Journal of
Marine Science and Engineering

Special Issue Reprint

Advances in Marine Geological and Geotechnical Hazards

Edited by
Lele Liu, Qingbing Liu and Dengfeng Fu

mdpi.com/journal/jmse

MDPI

Advances in Marine Geological and Geotechnical Hazards

Advances in Marine Geological and Geotechnical Hazards

Guest Editors

Lele Liu
Qingbing Liu
Dengfeng Fu

MDPI

Basel • Beijing • Wuhan • Barcelona • Belgrade • Novi Sad • Cluj • Manchester

Guest Editors

Lele Liu
Shandong Engineering
Research Center of Marine
Exploration and Conservation
Ocean University of China
Qingdao
China

Qingbing Liu
Badong National Observation
and Research Station
of Geohazards
China University
of Geosciences
Wuhan
China

Dengfeng Fu
College of Environmental
Science and Engineering
Ocean University of China
Qingdao
China

Editorial Office

MDPI AG
Grosspeteranlage 5
4052 Basel, Switzerland

This is a reprint of the Special Issue, published open access by the journal *Journal of Marine Science and Engineering* (ISSN 2077-1312), freely accessible at: https://www.mdpi.com/journal/jmse/special_issues/6039B3101H.

For citation purposes, cite each article independently as indicated on the article page online and as indicated below:

Lastname, A.A.; Lastname, B.B. Article Title. *Journal Name* **Year**, *Volume Number*, Page Range.

ISBN 978-3-7258-5641-1 (Hbk)
ISBN 978-3-7258-5642-8 (PDF)
https://doi.org/10.3390/books978-3-7258-5642-8

Contents

About the Editors

Lele Liu

Lele Liu is a professor at the Ocean University of China. His research focuses on the geomechanics and seepage mechanics of seabed energy resources, particularly natural gas hydrate exploitation and offshore wind energy development. He has led ten national and provincial projects, and his findings supported the offshore hydrate trial production that was listed among China's Top Ten Marine Science and Technology Advances. He currently serves as a corresponding member of TC209 and TC308 of the International Society for Soil Mechanics and Geotechnical Engineering and as an editorial board member of the journal *Advances in Geo-Energy Research*.

Qingbing Liu

Qingbing Liu is a professor at the China University of Geosciences and Deputy Director of the Badong National Observation and Research Station for Geohazards. He has led three general projects funded by the National Natural Science Foundation of China and over twenty industry-commissioned research programs. He is an active member of the IAEG Marine Engineering Geology Committee and a council leader within the Chinese Society for Rock Mechanics and Engineering. By merging large-scale physical modelling, high-resolution numerical simulation and long-term in situ geohazard monitoring, he has revealed how swelling clays, carbonate reef sediments and reservoir landslides deform, weaken and fail across scales. These insights now underpin early-warning systems and improved stability evaluation methods for national key projects such as the Three Gorges Project and South China Sea island-reef construction, delivering measurable reductions in geological risk and geohazard mitigation.

Dengfeng Fu

Dengfeng Fu is a professor and doctoral supervisor at the Ocean University of China. He has led two projects of the National Natural Science Foundation of China and over 20 industry-sponsored research initiatives addressing critical technological challenges. He has long been engaged in theoretical innovation and technological research and development in the fields of marine resource development and marine soil improvement. Dedicated to the study of seabed foundation stability and marine soil properties, he has conducted scientific research and engineering practice, driving innovative studies in areas such as the working and failure mechanisms of marine foundations throughout their life cycle, performance evaluation theories and design methods for new foundation types, and the improvement of marine soil properties. He has published over 50 papers and been granted 13 invention patents. He also serves as a committee member of the Youth Working Committee of the Soil Mechanics and Geotechnical Engineering Branch of the Chinese Civil Engineering Society, a council member of the Engineering Risk and Insurance Research Branch of the Chinese Civil Engineering Society, and an academic committee member of the Tunnel and Underground Space Operation Safety and Energy Conservation & Environmental Protection Technology Forum of the Tunnel and Underground Engineering Branch of the Chinese Civil Engineering Society.

Preface

This Reprint gathers the eleven rigorously peer-reviewed papers that emerged from the 2025 Special Issue "Advances in Marine Geological and Geotechnical Hazards" published in the *Journal of Marine Science and Engineering*. It focuses on the interplay between the geological complexity of the seafloor and the geotechnical performance of the infrastructure now being deployed to harvest oil, gas, hydrates, wind, wave and tidal energy. The scope extends from microscopic bubble–grain contacts to kilometer-long pipeline–fault crossings, and from single-suction-bucket centrifuge tests to global machine learning databases of pile response.

Our aim is to provide a concise, authoritative volume for engineers, researchers, regulators and graduate students seeking state-of-the-art methods for identifying, quantifying and mitigating marine hazards. Motivation for the work arose from a simple observation: floating turbines are already operating in 200 m water depths, hydrate production wells are being drilled through gas-charged, over-consolidated clays, and coral island airstrips are being extended with dynamically compacted calcareous sands, yet design practice still relies on empirical rules developed for onshore soils or sheltered offshore sites. Each contribution in this Reprint therefore couples high-quality experimental or field data with advanced numerical or analytical modelling to close the gap between offshore reality and current design codes.

We thank the authors for their patience during the iterative review process, the reviewers for their meticulous scrutiny and the MDPI editorial team for transforming a collection of manuscripts into a coherent reference work. It is our hope that the papers assembled here will accelerate the transition toward data–physics and uncertainty-aware design of safe, low-carbon ocean energy infrastructure.

Lele Liu, Qingbing Liu, and Dengfeng Fu
Guest Editors

Journal of
Marine Science and Engineering

MDPI

Editorial

Advances in Marine Geological and Geotechnical Hazards

Lele Liu [1,*], Qingbing Liu [2] and Dengfeng Fu [1]

[1] Shandong Engineering Research Center of Marine Exploration and Conservation, Ocean University of China, Qingdao 266100, China
[2] Badong National Observation and Research Station of Geohazards, China University of Geosciences, Wuhan 430074, China
* Correspondence: lele.liu@ouc.edu.cn

Since the first hearth was kindled, energy has steered human destiny, and today the ocean offers its own vast portfolio [1,2]. Along the surface, steady trade winds spin floating turbines; above, photovoltaic rafts drink in photons; within tides and swells, oscillating bodies harvest relentless mechanical power; across thermal gradients, warm and cold water drive closed-loop engines; and beneath the seabed, ancient organics have become oil, gas, and icy natural gas hydrates [3,4]. Each resource sits in a distinct physical niche, demanding tailored technologies, legal regimes, and environmental safeguards. Yet all share a common prerequisite: an intimate knowledge of the marine realm that hosts them.

Turning these gifts into usable power confronts geologic hazards that can erase decades of investment in seconds. Submarine landslides, triggered by earthquake or hydrate dissociation, can shear pipelines [5,6]; cyclic wave loading and scour undermine turbine foundations [7]; and unexpected pore pressures collapse wellbores [8]. To anticipate such threats, engineers must first characterize the seafloor soils and then understand complex interactions between the soils and structures for marine energy developments. Over the past decade, the surge in offshore renewable energy, port expansion, and deep-sea resource recovery has pushed coastal and geotechnical engineering into new frontiers. Floating wind turbines now operate in water depths exceeding 200 m; gravity-based foundations are being adapted for liquefiable seabed; and subsea pipelines cross active fault zones with unprecedented resilience [9]. These achievements, however, have also revealed gaps in our understanding of coupled hydrodynamic–geotechnical processes, from hydrate-rich sediments to cyclically loaded carbonate sands [10,11].

To capture these advances and catalyze further innovation, we have organized this Special Issue entitled "Advances in Marine Geological and Geotechnical Hazards" within the *Journal of Marine Science and Engineering*. For the Special Issue sixteen manuscripts were submitted for consideration, and all were subjected to a rigorous review process. In total, eleven research papers were finally accepted for publication and inclusion in this Special Issue. The contributions are listed as follows:

1. Jiang, J.; Luo, C.; Wang, D. Numerical Simulation of Vertical Cyclic Responses of a Bucket in Over-Consolidated Clay. *J. Mar. Sci. Eng.* **2024**, *12*, 1319. https://doi.org/10.3390/jmse12081319.
2. Gu, L.; Yang, W.; Wang, Z.; Wang, J.; Ye, G. Response of a Coral Reef Sand Foundation Densified through the Dynamic Compaction Method. *J. Mar. Sci. Eng.* **2024**, *12*, 1479. https://doi.org/10.3390/jmse12091479.

3. Tang, X.; Xin, D.; Lei, X.; Yao, T.; Meng, Q.; Liu, Q. Large-Scale Triaxial Test on Mechanical Behavior of Coral Sand Gravel Layered Samples. *J. Mar. Sci. Eng.* **2024**, *12*, 1784. https://doi.org/10.3390/jmse12101784.
4. Cao, L.; Zhao, H.; Yang, B.; Zhang, J.; Song, H.; Fu, X.; Liu, L. A Theoretical Model for the Hydraulic Permeability of Clayey Sediments Considering the Impact of Pore Fluid Chemistry. *J. Mar. Sci. Eng.* **2024**, *12*, 1937. https://doi.org/10.3390/jmse12111937.
5. Yan, Y.; Liu, H.; Dai, G.; Xiang, Y.; Xu, C. Analysis of the Vertical Dynamic Response of SDCM Piles in Coastal Areas. *J. Mar. Sci. Eng.* **2024**, *12*, 1950. https://doi.org/10.3390/jmse12111950.
6. Lei, J.; Leng, K.; Xu, W.; Wang, L.; Hu, Y.; Liu, Z. Effective Stress-Based Numerical Method for Predicting Large-Diameter Monopile Response to Various Lateral Cyclic Loadings. *J. Mar. Sci. Eng.* **2024**, *12*, 2260. https://doi.org/10.3390/jmse12122260.
7. Liu, T.; Qing, C.; Zheng, J.; Ma, X.; Chen, J.; Liu, X. Study on the Mechanical Behavior of Fine-Grained Gassy Soil Under Different Stress Conditions. *J. Mar. Sci. Eng.* **2025**, *13*, 373. https://doi.org/10.3390/jmse13020373.
8. Liu, T.; Liang, Y.; Peng, H.; Yu, L.; Xing, T.; Zhan, Y.; Zheng, J. Deformation Patterns and Control of Existing Tunnels Induced by Coastal Foundation Pit Excavation. *J. Mar. Sci. Eng.* **2025**, *13*, 773. https://doi.org/10.3390/jmse13040773.
9. Deng, X.; Wang, Z.; Qin, Y.; Cao, L.; Cao, P.; Xie, Y.; Xie, Y. Experimental Study on the Reinforcement of Calcareous Sand Using Combined Microbial-Induced Carbonate Precipitation (MICP) and Festuca arundinacea Techniques. *J. Mar. Sci. Eng.* **2025**, *13*, 883. https://doi.org/10.3390/jmse13050883.
10. Liu, T.; Zhu, L.; Zhang, Y.; Qing, C.; Zhan, Y.; Zhu, C.; Jia, J. Experimental Study on Strength Characteristics of Overconsolidated Gassy Clay. *J. Mar. Sci. Eng.* **2025**, *13*, 904. https://doi.org/10.3390/jmse13050904.
11. Lin, P.; Li, K.; Yu, X.; Liu, T.; Yuan, X.; Li, H. Analysis of Offshore Pile–Soil Interaction Using Artificial Neural Network. *J. Mar. Sci. Eng.* **2025**, *13*, 986. https://doi.org/10.3390/jmse13050986.

Contribution 1 numerically examines vertical cyclic responses of a single suction bucket in over-consolidated clay, relevant for tripod wind-turbine foundations. An undrained cyclic accumulation model is calibrated with direct simple shear tests and implemented in finite element analyses. Simulations reproduce centrifuge experiments, showing that displacement amplitude rises logarithmically with load cycles. A parametric investigation varying skirt length to diameter from half to double reveals that shorter skirts accumulate larger displacements. A compact predictive equation anchored at a unity aspect ratio is proposed and validated for practical ranges of geometry, soil strength, interface adhesion, and cyclic amplitude.

Contribution 2 evaluates dynamic compaction for strengthening coral reef sand foundations on remote sea islands. Pilot tests were conducted in two zones using varied impact energies. The field results showed crater depths up to forty-two centimeters, an allowable bearing capacity exceeding three hundred and sixty kilopascals, and effective improvement depths of three and a half meters. Shallow plate load tests and standard penetration tests confirmed densification. Two-dimensional particle flow simulations reproduced settlement and particle breakage patterns, revealing vertical force chains and progressive crushing beneath the impact point. The study validates dynamic compaction as a practical, economical method for large-scale coral sand improvement.

Contribution 3 examines coral sand, gravel, and two layered arrangements by using large-scale triaxial and step-loading tests. All samples showed strain hardening under drained shear. Clean gravel offered the highest peak strength and bearing capacity, fol-

lowed by gravel-over-sand layers, sand-over-gravel layers, and clean sand. Friction angles exceeded forty degrees for every group, while cohesion rose sharply from sand to gravel, with layered samples in between. Bulging failure concentrated in the gravel layer within composites. Step-loading p-s curves matched previous plate tests under a four hundred kilopascal confinement, confirming that placing gravel on top best enhances foundation performance in hydraulic fills.

Contribution 4 develops a new theoretical model which quantifies how pore fluid chemistry affects permeability in clayey sediments. Using electrokinetic flow theory, the model links salinity, ion mobility, surface potential, and pore size through tortuous capillary tubes. It accurately reproduces published permeability data for kaolinite, illite, smectite, and four bentonites under various salt concentrations. Sensitivity analyses reveal that permeability drops markedly only when the electric double-layer thickness approaches the pore size. During oceanic hydrate production, desalination couples with consolidation; salinity sensitivity strengthens for initially larger pores yet weakens for smaller ones.

Contribution 5 presents a rigorous theoretical framework for evaluating the vertical dynamic response of stiffened deep cement mixing piles embedded in unsaturated, viscoelastic coastal soils. Closed-form solutions for pile-head impedance are derived using elastic wave theory and a fractional-order soil model, and validated against published data. Parameter analyses reveal that reducing the core pile radius, increasing the pile length, raising soil saturation, lowering permeability, and enlarging the relaxation shear modulus markedly improve vibration resistance. Conversely, increasing the modulus of the cement–soil exterior pile harms performance, while the core pile modulus only benefits low-frequency excitation. The findings guide cost-effective design of resilient foundations for nearshore bridges and offshore energy structures.

Contribution 6 develops an effective stress-based finite element method to predict the response of large-diameter monopiles in clay under cyclic lateral loading. A bounding surface model is implemented and validated against centrifuge tests. The results show that cyclic loading causes soil stiffness degradation, permanent pile rotation, and excess pore pressure accumulation. The mean and amplitude of cyclic loads significantly influence pile behavior and pore pressure development. The method captures key soil–structure interaction mechanisms, offering insights for offshore wind turbine foundation design.

Contribution 7 investigates the mechanical behavior of fine-grained gassy soil under varied stress conditions through triaxial testing and modeling. The experiments reveal that initial pore water pressure strongly influences excess pore pressure and shear strength, with lower values enhancing strength via bubble flooding. Strength also improves under higher consolidation pressure. However, under reduced triaxial compression, both strength and pore pressure response decline.

Contribution 8 examines how coastal foundation pit excavation affects nearby shield tunnels in Qingdao's silty clay. Using statistical, numerical, and field data, it shows excavation drives tunnels toward the pit with increasing lateral and vertical displacement. Shallower tunnels and closer clearances experience larger deformation; widening the clearance from ten to twenty-five meters cuts displacement by one-third. Thicker diaphragm walls or deeper embedment alone offer only modest tunnel protection; supplementary tunnel-side reinforcement is needed. The work provides practical guidance for safeguarding existing metro lines during coastal construction.

Contribution 9 couples microbial carbonate precipitation with tall fescue to stabilize calcareous sand from reef islands. Laboratory tests show that higher cementation concentration and more cycles sharply improve water retention yet hinder seed emergence and root elongation by densifying the matrix. Optimal treatment balances plant growth and

wind resistance, achieving an almost ninety-eight percent erosion reduction at ten meters per second wind speed. The combined technique forms a mineralized surface layer and deep root anchorage, providing a low-carbon, economical alternative for slope protection in tropical maritime environments.

Contribution 10 investigates the strength and cyclic behavior of over-consolidated gassy clay through triaxial and simple shear tests combined with electron microscopy. The results show that increasing over-consolidation compresses gas bubbles, enhances dilatancy, raises shear strength, and reduces excess pore pressure. Cyclic tests reveal superior fatigue resistance compared with saturated clay, peaking at moderate over-consolidation. Microstructural analysis confirms bubble collapse and limited flooding. The findings provide essential data for modeling coastal geohazards and engineering design.

Contribution 11 compiles a global database of eighteen hundred offshore monopile tests and develops neural network models for predicting soil resistance and pile displacement. Trained networks achieve average errors below six percent, outperforming traditional curves and finite element methods by large margins. Sensitivity analyses highlight pile diameter and soil modulus as key drivers. A real project case confirms the model's superior accuracy and efficiency, offering a practical, uncertainty-aware tool for safer, cost-effective offshore wind foundation design.

The eleven research papers converge on offshore geotechnics and renewable-energy infrastructure—monopiles, calcareous slopes, over-consolidated gassy clay, coastal excavation, microbial stabilization, and neural network prediction—addressing how complex loading governs seabed–structure interaction, stability, and reliability. The shared driver is the urgent need for low-carbon, safe, and economical foundations for offshore wind, reef construction, and subsea pipelines, while conventional empirical or simplified methods falter under variable marine environments.

Future work should establish data-physics digital twins that assimilate real-time monitoring, laboratory tests, and machine learning for live model updating. Extensions to typhoon, seismic or long-term cyclic loading, and multi-scale multiphase coupling will move from laboratory to reef scale and from short-term response to whole-life sustainable offshore geotechnical engineering.

Author Contributions: Conceptualization, Q.L. and D.F.; methodology, L.L. and Q.L.; software, D.F.; validation, Q.L. and D.F.; formal analysis, L.L.; investigation, L.L.; resources, Q.L. and D.F.; data curation, L.L. and D.F.; writing—original draft preparation, L.L.; writing—review and editing, Q.L. and D.F.; visualization, L.L.; supervision, Q.L. and D.F.; project administration, D.F.; funding acquisition, L.L. All authors have read and agreed to the published version of the manuscript.

Funding: The support jointly provided by the Young Experts of Taishan Scholars (No. tsqn202211071) and the Natural Science Foundation of Shandong Province (No. ZR2022YQ54) is sincerely appreciated.

Acknowledgments: As Guest Editors of the Special Issue "Advances in Marine Geological and Geotechnical Hazards", we would like to express our deep appreciation to all the authors whose valuable work was published under this issue and thus contributed to the success of the edition.

Conflicts of Interest: The authors declare no conflicts of interest.

References

1. Cui, Y.; Zhao, H. Marine Renewable Energy Project: The Environmental Implication and Sustainable Technology. *Ocean Coast. Manag.* **2023**, *232*, 106415. [CrossRef]
2. Qiu, S.; Liu, K.; Wang, D.; Ye, J.; Liang, F. A Comprehensive Review of Ocean Wave Energy Research and Development in China. *Renew. Sustain. Energy Rev.* **2019**, *113*, 109271. [CrossRef]
3. Melikoglu, M. Current Status and Future of Ocean Energy Sources: A Global Review. *Ocean Eng.* **2018**, *148*, 563–573. [CrossRef]

4. Lu, C.; Qin, X.; Sun, J.; Wang, R.; Cai, J. Research Progress and Scientific Challenges in the Depressurization Exploitation Mechanism of Clayey-Silt Natural Gas Hydrates in the Northern South China Sea. *Adv. Geo Energy Res.* **2023**, *10*, 14–20. [CrossRef]
5. Dong, Y.; Wang, D.; Randolph, M.F. Investigation of Impact Forces on Pipeline by Submarine Landslide Using Material Point Method. *Ocean Eng.* **2017**, *146*, 21–28. [CrossRef]
6. Zhao, Y.; Kong, L.; Liu, L.; Liu, J. Influence of Hydrate Exploitation on Stability of Submarine Slopes. *Nat. Hazards* **2022**, *113*, 719–743. [CrossRef]
7. Zheng, H.; Liang, F.; Zhang, H.; Li, L. Combined Effects of Long-Term Cyclic Loading and Unidirectional Flow Induced Scour on the Mechanical Responses of Tetrapod Jacket Foundation Supported Offshore Wind Turbines. *Eng. Struct.* **2025**, *324*, 119378. [CrossRef]
8. Rahman, M.K.; Naseby, D.; Rahman, S.S. Borehole Collapse Analysis Incorporating Time-Dependent Pore Pressure Due to Mud Penetration in Shales. *J. Pet. Sci. Eng.* **2000**, *28*, 13–31. [CrossRef]
9. Hong, S.; McMorland, J.; Zhang, H.; Collu, M.; Halse, K.H. Floating Offshore Wind Farm Installation, Challenges and Opportunities: A Comprehensive Survey. *Ocean Eng.* **2024**, *304*, 117793. [CrossRef]
10. Tian, H.; Liu, W.; Ding, P.; Wei, W.; Li, X.; Cai, J. Numerical Simulation of Elastic Properties of Hydrate-Bearing Sediments with Digital Rock Technology. *Mar. Pet. Geol.* **2024**, *160*, 106592. [CrossRef]
11. He, S.-H.; Ding, Z.; Xia, T.-D.; Zhou, W.-H.; Gan, X.-L.; Chen, Y.-Z.; Xia, F. Long-Term Behaviour and Degradation of Calcareous Sand under Cyclic Loading. *Eng. Geol.* **2020**, *276*, 105756. [CrossRef]

Journal of
Marine Science and Engineering

MDPI

Article

Numerical Simulation of Vertical Cyclic Responses of a Bucket in Over-Consolidated Clay

Jun Jiang [1,2], Chengxi Luo [3] and Dong Wang [1,*]

[1] Shandong Engineering Research Center of Marine Exploration and Conservation, Ocean University of China, 238 Songling Road, Qingdao 266100, China; junjiang_hbcj@163.com
[2] School of Architectural Engineering, Hubei Urban Construction Vocational and Technological College, 28 Canglong Main Road, Wuhan 430205, China
[3] Power China Zhongnan Engineering Corporation Limited, Changsha 410014, China; luocx0150@126.com
* Correspondence: dongwang@ouc.edu.cn; Tel.: +86-13165325292

Abstract: Multi-bucket foundations have become an alternative for large offshore wind turbines, with the expansion of offshore wind energy into deeper waters. The vertical cyclic loading–displacement responses of the individual bucket of the tripod foundation are relevant to the deflection of multi-bucket foundations and crucial for serviceability design. Finite element analyses are used to investigate the responses of a bucket subjected to symmetric vertical cyclic loading in over-consolidated clay. The Undrained Cyclic Accumulation Model (UDCAM) is adopted to characterize the stress–strain properties of clay, the parameters of which are calibrated through monotonic and cyclic direct simple shear tests. The performance of the finite element (FE) model combined with UDCAM in simulating vertical displacement amplitudes is evaluated by comparison with existing centrifuge tests. Moreover, the impact of the bucket's aspect ratio on vertical displacement amplitude is investigated through a parametric study. A predictive equation is proposed to estimate the vertical displacement amplitudes of bucket foundations with various aspect ratios, based on the cyclic displacement amplitude of a bucket with an aspect ratio of unity.

Keywords: cyclic loading; bucket foundations; clay; offshore wind turbine; finite element method

1. Introduction

Bucket foundations have been used in Europe and Asia to support offshore wind turbines [1]. Compared to the large-diameter monopile, the most popular foundation of a fixed wind turbine in shallow water, the bucket foundation can be used in deposits with shallow bedrocks and offers the advantage of easy installation [2,3]. Bucket foundations are classified into mono-bucket and multi-bucket types, with the latter typically consisting of three or four buckets [4]. Bucket foundations are designed to withstand large horizontal loads and overturning moments transmitted from the wind turbine and upper structures [5,6]. For multi-bucket foundations with bucket diameter of D, interactions between buckets are reasonably negligible, given that the spacing between them typically exceeds $3.5D$ in practice [7,8]. In this case, the moment transferred directly to the individual bucket is negligible in magnitude, and the displacement of the individual bucket is primarily caused by the cyclic tension–compression loading (Figure 1). Therefore, the serviceability of multi-bucket foundations is controlled by the cyclic vertical load–displacement responses of the individual buckets [9–11]. In addition to the movement of foundations under cyclic loading, the vibration of the tower under dynamical loading [12] and the structural stability under survival loads [13] are also essential for the design of offshore wind turbines, but are beyond the scope of this study.

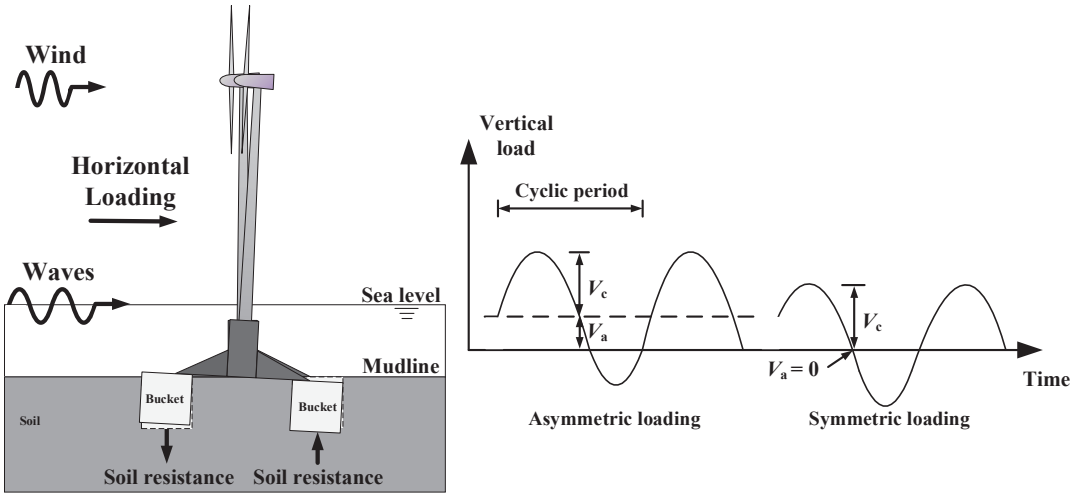

Figure 1. Response of multi-bucket foundation subjected to horizontal cyclic loading and definitions of vertical cyclic loading components.

To investigate the cyclic vertical displacements of a bucket in clay, conventional model tests [14,15] and model tests in centrifuge [16–18] have been conducted, where the bucket was usually displaced under nearly undrained conditions. Vertical cyclic loading was typically quantified through the vertical loading amplitude V_c and the average vertical loading V_a (Figure 1), causing the vertical displacement amplitude w_c and the average vertical displacement w_a. The accumulation of average vertical displacement and soil failure mechanisms depend on the direction of V_a; a zero or tensile V_a combined with arbitrary V_c value may lead to an upward w_a, which is more dangerous than the downward one [14,18,19]. Symmetric loading was the most dangerous condition since it would cause the most damaging strength loss [15,20]. Under symmetric loading with $V_a = 0$, the displacement amplitude w_c and average displacement w_a were both increased logarithmically with the number of cycles N, and the increases were more pronounced at higher V_c due to the more severe soil degradation [21]. However, a threshold of V_c may exist, below which the bucket is moved without significant accumulation of w_c and w_a after a large N [17,22].

Apart from the model tests, the cyclic responses of foundations in clay have been studied numerically [21,23]. The reliability of numerical results was dependent largely on whether the constitutive models could precisely describe the nonlinear response of soil under cyclic loading. Advanced constitutive models, such as the multi-surface model [23,24] and bounding surface model [18], have been developed to predict the displacements of foundations subjected to dozens of cycles [25]. However, the application of these models may be limited due to the large number of constitutive parameters and the potential computational errors accumulated during thousands of cycles [26]. An alternative option is the empirical approach simplifying the influence of a particular number of cycles through an equivalent static shear stress–strain relationship, e.g., the Undrained Cyclic Accumulation Model (UDCAM) that has been extensively used in practical applications over the last three decades [27–29]. In UDCAM, the cyclic shear strain contour diagrams are established via cyclic direct simple shear (DSS) tests or triaxial tests [30,31]. The program of UDCAM and the experimental database of a typical clay, Drammen clay [30], have been integrated into several commercial softwares, such as Bifurc [32] and Plaxis 3D Foundation Version 2.2 [33,34]. For other clays, the cyclic soil parameters can be determined from the existing database of Drammen clay [35]. The performance of UDCAM has been validated through comparisons with the model tests of gravity foundation [36,37] and then used to evaluate the undrained cyclic responses of monopiles [34]. Additionally, UDCAM was adopted in the design of monopiles in the Korean Western Sea, resulting in a more optimized solution than the conventional method recommended by the American Petroleum Institute [38,39].

However, it remains unclear whether UDCAM can be applied in the routine design of bucket foundations. As far as we know, the existing studies on the accumulation of vertical displacement amplitudes w_c of the bucket were mostly focused on a particular aspect ratio L/D (the ratio between skirt length L and diameter D of the bucket), for example, L/D of 0.5 in Zografou et al. [17] and 1 in Kou et al. [15]. The influence of L/D on w_c was quantified here.

In this paper, the responses of the individual bucket of the tripod foundation under symmetric cyclic vertical loading are investigated using finite element (FE) analyses. The cyclic properties of clay were represented by the UDCAM with shear strain contour diagrams. For verification of the numerical model, the simulated results of monotonic loading and cyclic loading tests for a bucket with aspect ratio L/D = 1 are compared with those obtained through centrifuge tests by Jiang et al. [18]. Subsequently, parameter analyses are conducted considering L/D ranging between 0.5 and 2, to investigate the effects of L/D on the simulated w_c. An equation is proposed to predict w_c for buckets with various L/D, based on the w_c of a bucket with L/D = 1. The validity of the proposed equation was further verified through additional cases featuring conditions beyond the scope of the parametric study. The process of the methodology is demonstrated in Figure 2.

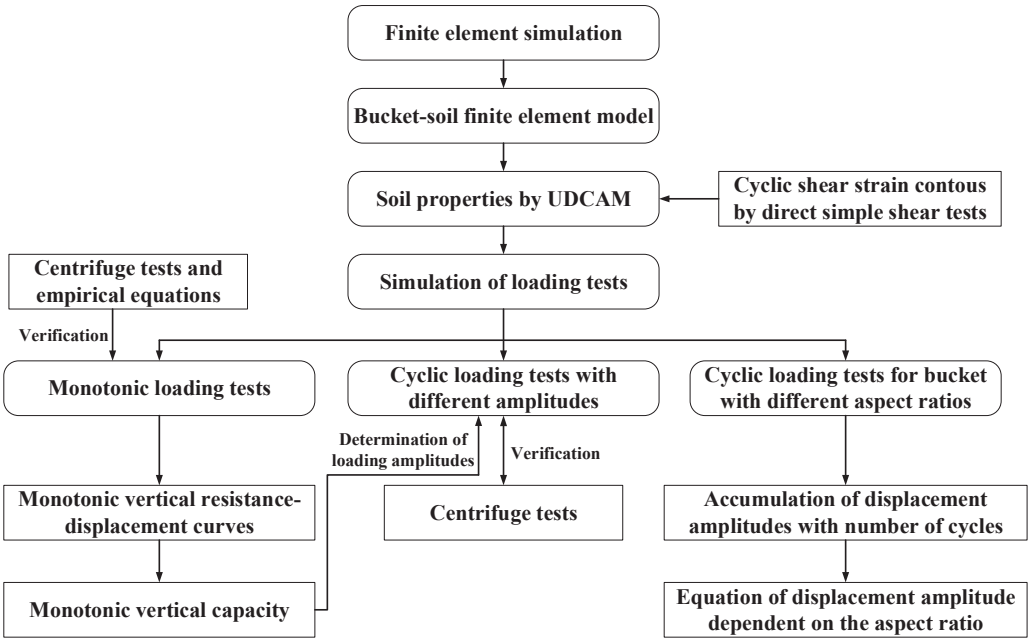

Figure 2. Process of the methodology.

2. Methodology

2.1. Finite Element Model

Commercial finite element package Plaxis 3D [33] was used to reproduce the interaction between the bucket and clay. The bucket was wished-in-place, whilst the installation effect was accounted for by reducing the shear stress along the skirt-soil interfaces with an adhesion factor [40,41]. The bucket diameter D was taken as 4 m (same as the bucket diameter in the prototype in Jiang et al. [18]), the skirt length L was 2, 4, 6, or 8 m, and skirt thickness was 0.1 m. The corresponding aspect ratios L/D were thus 0.5, 1, 1.5, and 2. Only half of the bucket and soil were modeled due to the symmetry of the foundation. The boundary conditions applied were as follows. Side surfaces of the soil were horizontally constrained and the soil base was fixed. The minimum and maximum aspect ratios selected, L/D = 0.5 and 2, were taken as examples and are shown in Figure 3. To avoid a boundary effect, the side edge of the soil was 3.4D away from the bucket skirt for all aspect ratios, while the soil bottom was 9L, 4L, 2.3L, and 1.5L away from the bucket tip at L/D = 0.5, 1, 1.5, and 2, respectively. Bucket and soil were discretized with ten-node tetrahedral

elements, with three degrees of freedom per node, referring to Banaszek et al. [42]. Four bucket–soil interfaces were set, including the ones outside and inside the bucket skirt and the ones below the cap and tip of the bucket. The interfaces were composed of twelve-node triangular interface elements formed by node pairs. One node of the pair belonged to the bucket and the other to soil. The shear stress of the interface was set as the undrained strength of the surrounding soil multiplied by an adhesion factor α. The value of α was calculated as $1/S_t$, where S_t denotes the soil sensitivity [10]. To meet the demands of convergence and accuracy, the coarseness factors of mesh were chosen as 0.1 for the bucket and soil inside the bucket, 0.3 for the soil near the bucket (0.5D horizontally and at least 0.5L vertically away from the bucket, as the red doted lines shown in Figure 3), and 1 for the rest, as shown in Figure 3.

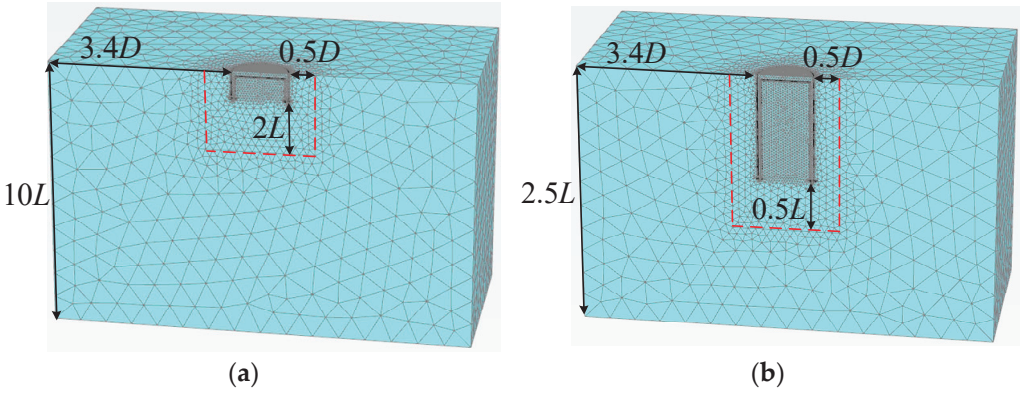

Figure 3. Mesh of the bucket and soil: (**a**) L/D = 0.5; (**b**) L/D = 2.

Total stress analyses were conducted, with clayey soil taken as undrained material. The bucket was simplified as a rigid body, with a reference point (RP) located at the center of the bucket cap. Consequently, the load–displacement responses of the bucket were characterized by the measurement at RP. Monotonic vertical loading tests were simulated using a displacement-controlled mode; vertical displacement w was applied at RP and the corresponding reaction force V was acquired. The vertical capacity of bucket V_0 was defined as the reaction force acquired when the vertical displacement reached quite a large value, for example, 0.25L adopted in Jiang et al. [18]. For cyclic vertical loading tests, a force-controlled mode was employed; the vertical loading amplitude V_c was applied at RP, leading to the corresponding displacement amplitude w_c. The specific values of V_c (expressed as the ratio between V_c and V_0) are shown in Table 1. At small w_c, the separation between bucket and soil interfaces was not allowed since suction was generated at the bucket base and the soil plug inside the bucket was moved along with it [18]. The simulations of large w_c, e.g., w_c between 0.1L and 0.25L, were only considered in Section 3 for verification purposes, but not discussed in the parametric study due to the deflection limit of wind turbines in practice.

Table 1. Conditions of centrifuge tests by Jiang et al. [18].

Case	s_u (kPa)	V_c/V_0
1	6.5 + 0.55z	0.42
2	6.5 + 0.55z	0.53
3	11.6	0.58
4	9.0 + 0.4z	0.37
5	9.0 + 0.4z	0.51
6	6.0 + 0.18z	0.64

2.2. Soil Properties

The properties of clay used in centrifuge tests included the following: a specific gravity of 2.70, an effective unit weight of 6.97 kN/m^3, a liquid limit of 42.8, a plastic limit of 20.8, and a soil sensitivity, S_t, of 2.1. The UDCAM was used to characterize the cyclic shear stress–strain response of clay. For symmetric cyclic loading with $V_a = 0$, only symmetric DSS tests exhibiting an average shear stress $\tau_a = 0$ were required to form the cyclic strain contours, which describe the relationship between the cyclic stress τ_c, the cyclic strain γ_c, and the number of cycles N. The DSS tests were carried out following the standards ASTM D6528-17 [43]. With comprehensive details reported by Andersen [30], the procedure of implementing the UDCAM for the clay used in the centrifuge tests [18] is as follows:

(a) The slurry with water content twice the liquid limit was moved into a strongbox, and the soil sample was prepared under consolidation pressure of 60 or 90 kPa. The overburden pressure at the skirt tip level in centrifuge tests was around 30 kPa, corresponding to an over-consolidation ratio (OCR) of 2 or 3. Therefore, the specimen for DSS test was consolidated at vertical stress of 60 or 90 kPa. Then, the specimen was unloaded to 30 kPa prior to the following shearing.

(b) The prepared specimens underwent shearing at a displacement rate of 0.015 mm/min to obtain the monotonic shear stress–strain responses (τ-γ responses), as shown in Figure 4. As a result, the static undrained shear strength s_u was defined as the shear stress at γ = 15% [44]. Then, s_u = 18.3 kPa for OCR = 2 and s_u = 22.9 kPa for OCR = 3.

(c) In symmetric cyclic shearing tests, various stress ratio amplitudes τ_c/s_u ranging from 0.2 to 0.7 were adopted, and the frequency was chosen as 0.1 Hz to match the typical wave frequency. Contour diagrams that describe the τ_c/s_u-N response are derived by connecting the data points from test results at the same γ_c values, e.g., γ_c = 0.08%, 0.14%, 0.5%, 1%, 1.5%, 3%, and 15%, as illustrated in Figure 5a,b.

(d) For a symmetric cyclic loading scenario with a uniform loading amplitude, the equivalent number of cycles was equal to the current number of cycles N. The typical γ_c values varying with τ_c/s_u can be obtained by linking the intersection points of lines at N = 1, 10, 100, and 1000 with the contours in Figure 5. As a result, the τ_c/s_u-γ_c curves for OCR = 3 are shown in Figure 6 as an example. The response of τ_c/s_u-γ_c at another relevant N can be interpolated automatically in Plaxis.

(e) To derive the dimensional τ_c-γ_c response, the static undrained shear strength s_u was required. The strength profiles of clay samples were inferred from cone penetration tests, with the cone factor taken as 15 [18]. As shown in Table 1, the undrained strength of clay, s_u, was increased with the soil depth z for most soil types, while a uniform clay sample had a constant s_u. The soil depth z and s_u are in units of m and kPa, respectively.

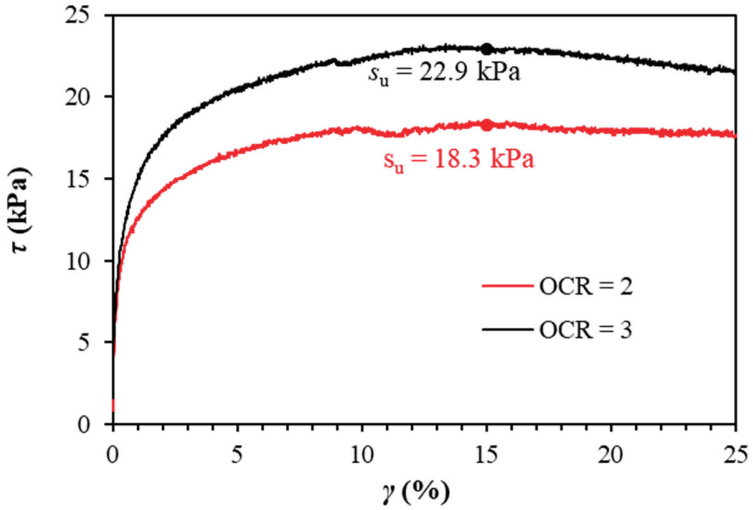

Figure 4. Static shear strength from monotonic DSS tests.

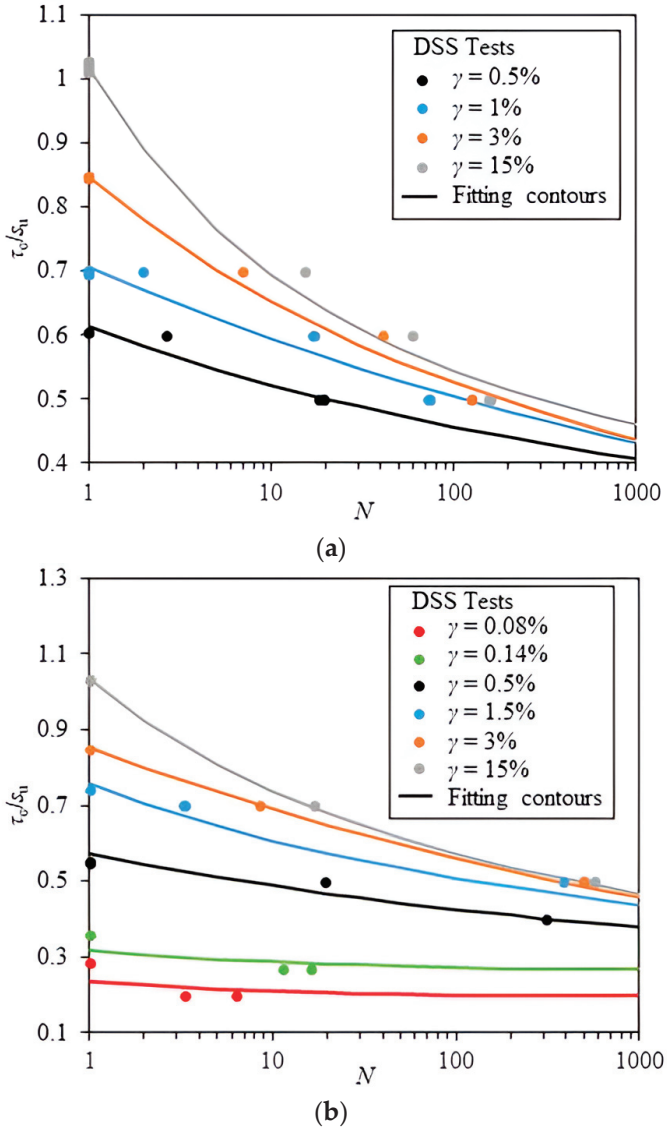

Figure 5. Contour diagrams at $\tau_a = 0$ deduced from cyclic DSS tests: (**a**) OCR = 2; (**b**) OCR = 3.

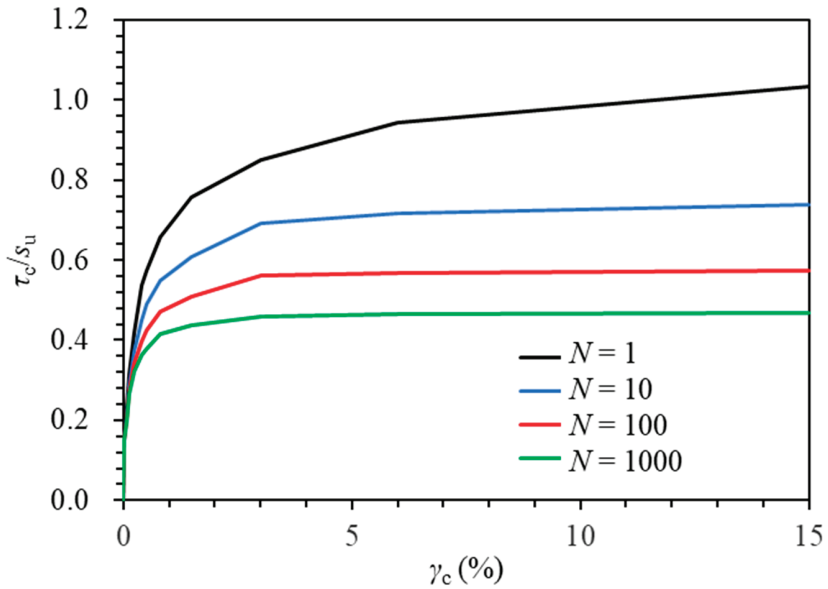

Figure 6. Typical γ_c values varying with τ_c/s_u at N = 1, 10, 100, and 1000 (OCR = 3).

3. Verification

3.1. Monotonic Loading Tests

To verify the reliability of the finite element model, monotonic vertical loading tests by Jiang et al. [18], named Tests 1-1, 2-1, 3-1, and 4-1 and carried out in four separate strongboxes, were simulated. Clay was regarded as a Tresca material under undrained conditions. The undrained shear strengths of clay samples were deduced from cone penetration tests. Specifically, $s_u = 6.5 + 0.55z$, 11.6, $9.0 + 0.4z$, and $6.0 + 0.18z$ for Samples 1–4, where soil depth z and s_u are in units of m and kPa, respectively. The adhesion factor α was set as $1/S_t = 0.5$, as the values of S_t in each strongbox are averaged as 2.1. A typical value of Young's modulus, $400s_u$, was adopted. The effective unit weight of clay γ_c' was 6.97 kN/m^3 and Poisson's ratio was taken as 0.495 to approximate constant volume under undrained conditions. The vertical force–displacement curves (V-w curves) of four tests by FE are shown in Figure 7. Similar to the centrifuge test results, the vertical force by FE increased rapidly with displacement at first, and then the increase trend became gentle. The vertical capacity V_0 of the bucket by FE was defined as the vertical reaction force V at vertical displacement $w = 0.25L$. V_0 by FE was very close to that by centrifuge tests. A simple equation was recommended in guidelines DNV RP E303 [45] to estimate the vertical force V:

$$V = z\alpha s_{ua}\pi D + (\gamma_c' z + s_{utip}N_c)A, \quad (1)$$

where A is the cross-section area of the bucket; s_{ua} is the average undrained shear strength along the bucket skirt; s_{utip} is the undrained shear strength at the bucket tip; N_c is the bearing capacity factor under plan strain conditions, usually taken as 7.5 [46]. The V_0 values in Equation (1) are presented as markers in Figure 7 for comparison purposes. The errors of V_0 values between FE and Equation (1) were less than 17%; it was reasonable for the reliability of the FE model [47], since the empirical equations were based on several simplifications.

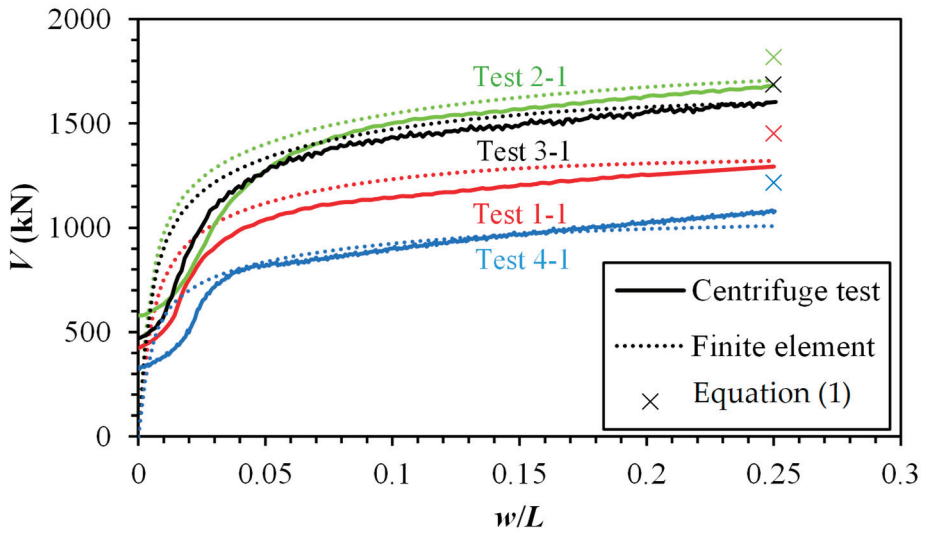

Figure 7. Monotonic vertical force–displacement curves from FE analyses and tests.

3.2. Cyclic Loading Tests

To further validate the FE model combined with UDCAM, six cyclic vertical loading tests with negligible V_a, named Tests 1-2, 1-3, 2-2, 3-2, 3-3, and 4-2 in Jiang et al. [18], were mimicked. Loading amplitudes for the six tests varied between $0.37V_0$ and $0.64V_0$, whereas the average loading values caused by the controlling error ranged from $0.01V_0$ to $0.05V_0$.

The cyclic vertical displacement amplitudes of the bucket w_c from centrifuge tests were normalized to the length of the bucket skirt L, represented by solid markers in Figure 8. Typical data points were used to illustrate the progression of w_c/L in relation to the number of cycles N throughout the tests, and the values of w_c/L exceeding $0.25L$ are not shown.

Observations indicated that w_c/L from centrifuge tests increased logarithmically with N. This phenomenon is attributed to the higher accumulation of pore pressure in centrifuge tests under larger N, consistent with the shear stress–strain curve at N = 1000, lower than that at N = 1, according to the DSS tests in Figure 6. The FE results of w_c/L are depicted as hollow markers in Figure 8. The predicted w_c/L exhibited a tendency similar to those observed in the centrifuge tests, highlighting the robustness of the UDCAM. For a low loading amplitude with V_c/V_0 = 0.37 or 0.42, the w_c/L values increased gently with the number of cycles in both centrifuge tests and FE simulations, and the bucket was actually under a stable state without significant accumulation of vertical displacement. As a comparison, a rapid failure of the bucket foundation was observed under a higher loading amplitude. For example, the failure occurred after 20 cycles with V_c/V_0 = 0.64 in the centrifuge, as demonstrated in Figure 8b, while the failure took place after 5 to 10 cycles in FE simulations. It was recognized that there existed divergences between the numerical and experimental data:

(a) At the early stage of loading, for example, N = 2, w_c/L predicted by the FE was lower than the measured value, and the divergence decreased with an increase in V_c/V_0. This phenomenon can be explained by the smaller cyclic shear strain at a lower cyclic shear stress given a certain number of cycles, as shown in Figure 6. As a result, w_c/L by centrifuge tests was larger at higher V_c/V_0 and more closely aligned with the simulations.

(b) Although the experimental w_c/L was higher than the value predicted by FE, the divergence became smaller with increasing cycles (e.g., V_c/V_0 = 0.37 and 0.51). In particular scenarios, V_c/V_0 = 0.42 at N > 650 and V_c/V_0 = 0.58 at N > 20, w_c/L measured in the tests appeared lower than the FE results. This phenomenon may be attributed to the potential consolidation effect which is caused by partial dissipation of pore pressures around the bucket during the long-term loading in centrifuge tests. For example, the loading duration amounted to 137 d in the prototype after 996 cycles with V_c/V_0 = 0.37, thereby allowing partially drained conditions in clay, which caused an increase in undrained shear strength and reduction in w_c/L. Conversely, the degradation of undrained strength induced by cyclic loading was accounted for in the UDCAM strategy, while the potential enhancement of undrained strength due to partial drainage within the long-term loading stage was ignored.

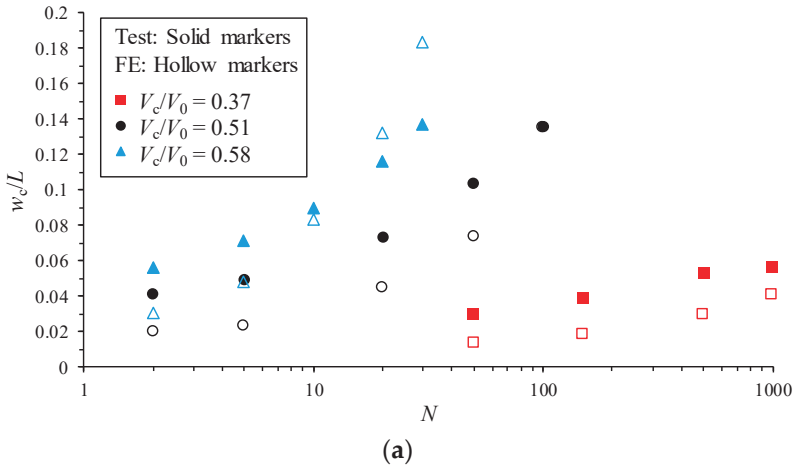

(**a**)

Figure 8. *Cont.*

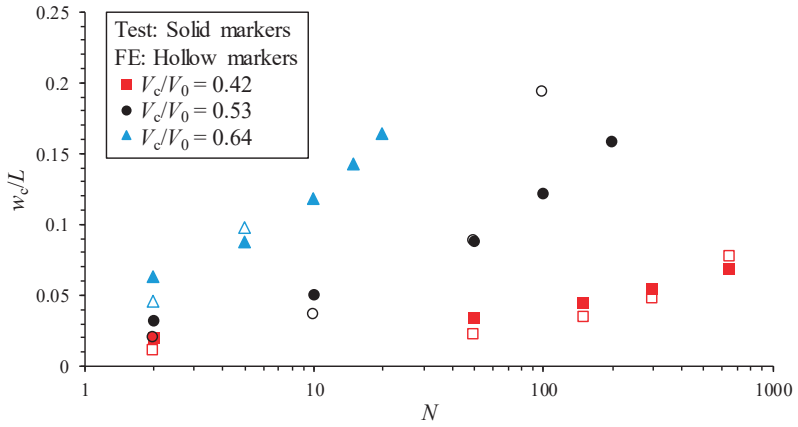

(**b**)

Figure 8. Comparison of cyclic displacement amplitudes by centrifuge test and FE: (**a**) V_c/V_0 = 0.37, 0.51, and 0.58; (**b**) V_c/V_0 = 0.42, 0.53, and 0.64.

4. Parametric Study

Various aspect ratios of the buckets with a diameter D of 4 m were employed in FE analyses to investigate the influence of the aspect ratio on w_c. The aspect ratio was 1 in the centrifuge tests by Jiang et al. [18], and here, it is changed to 0.5, 1.5, and 2, respectively. The FE results of two typical cases, Cases 1 and 3, are chosen to detail the findings. The combinations of clay properties and loading conditions of the two cases are listed in Table 1.

The vertical capacities V_0 against various aspect ratios need to be determined prior to simulating the vertical displacement amplitude w_c, by following the procedure addressed in Section 3.1. The V_0 values for Case 1 are 970.7, 1321.2, 1606.0, and 1897.3 kN against the aspect ratio of 0.5, 1, 1.5, and 2. For Case 3, V_0 values are identified as 1422.8, 1707.1, 1860.2, and 2024.3 kN for four aspect ratios, respectively.

According to the FE simulations combined with the UDCAM, w_c values under various numbers of cycles are predicted. As illustrated in Figure 9, w_c/L increases logarithmically with increasing N, but w_c/L is higher at lower L/D. The failure mechanisms of soil at various L/D values under cyclic loading, for instance, N = 300 for Case 1, are demonstrated in Figure 10. It is evident that the soil contained within the bucket moved along with the bucket, resulting in a reversed end bearing mechanism. The displacement of the mobilized soil in Figure 10 is larger with increasing L/D, resulting in an increased w_c of the bucket with increasing L/D. This trend is opposite to the decreased w_c/L with increasing L/D in Figure 9.

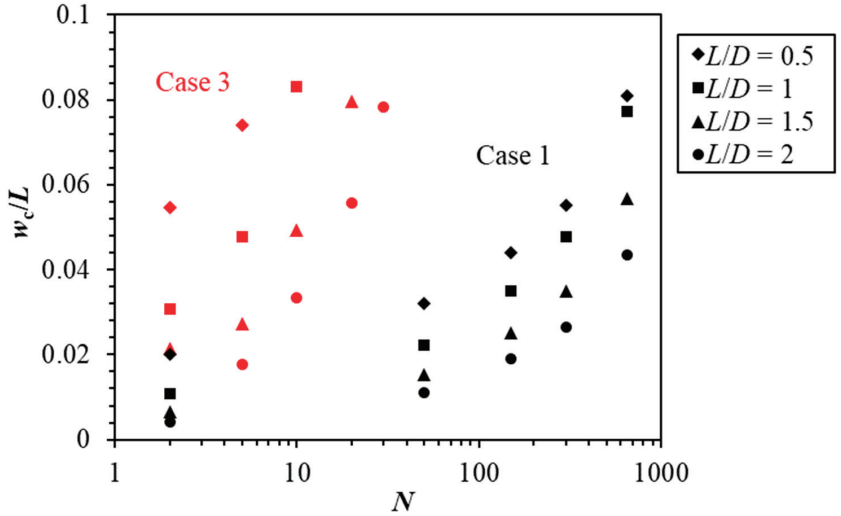

Figure 9. Comparison of cyclic loading amplitudes with N at different L/D values.

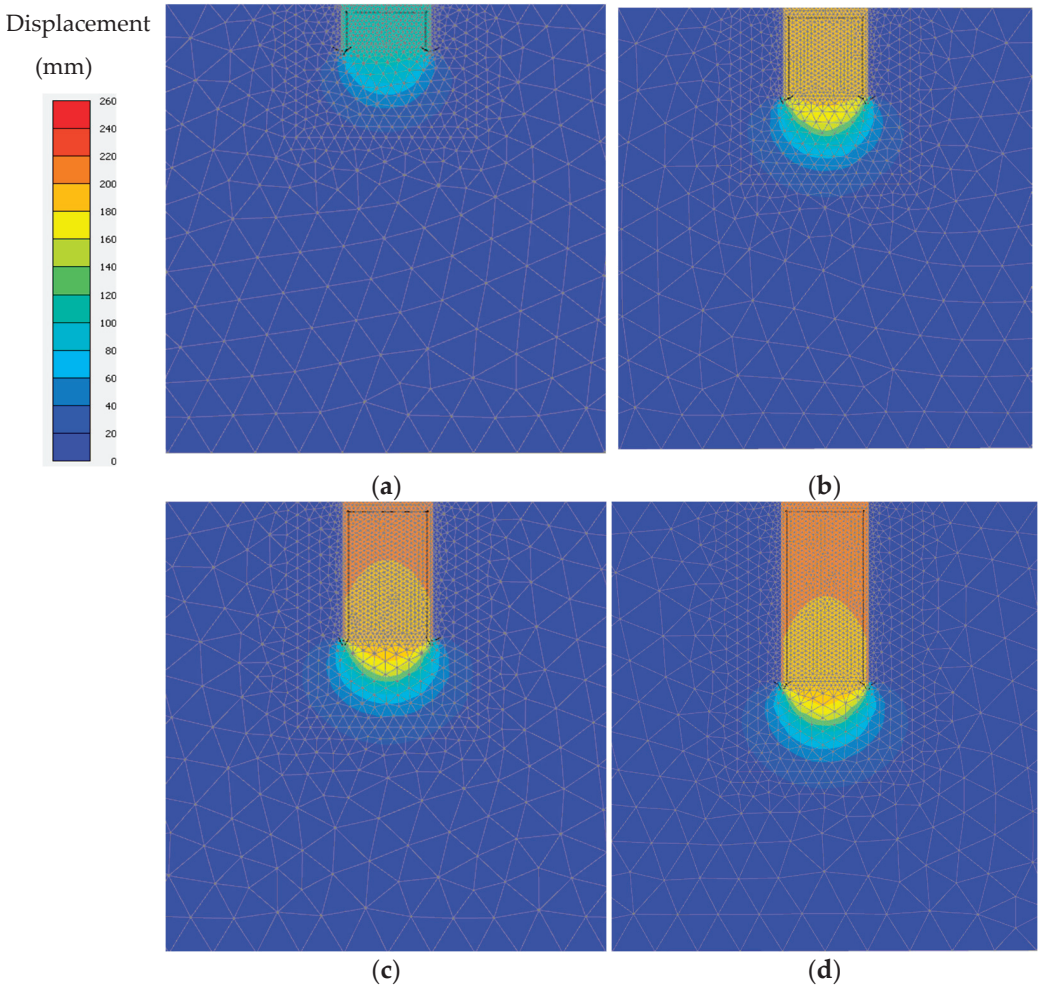

Figure 10. Displacement contours at N = 300 for Case 1: (**a**) L/D = 0.5; (**b**) L/D = 1; (**c**) L/D = 1.5; (**d**) L/D = 2.

By considering w_c/L at L/D = 1 as the reference displacement $(w_c/L)_{ref}$, w_c/L for varying L/D can be predicted using a fitting equation, as shown in Equation (2):

$$\frac{w_c/L}{(w_c/L)_{ref}} = 1 + 0.2\left(\frac{L}{D}\right)^2 \tanh\left[16.5\left(\frac{L}{D} - 1\right)\right] \quad (2)$$

The w_c/L values estimated by Equation (2) of the two cases are demonstrated in Figure 11. A reasonable agreement on w_c/L is achieved between the predictions of Equation (2) and FE results. The divergences for all cases are predominantly within the range of ±25%.

Despite reasonable agreement highlighted in Figure 11, it is not clear if Equation (2) is applicable for predicting w_c/L under the conditions beyond the scope of the above parametric study. The fatal factors include bucket sizes, undrained shear strengths and degradation behaviors of soil, the adhesion factors, and the amplitude of cyclic loading. Therefore, the reliability of Equation (2) is verified further through six additional cases listed in Table 2. In these six cases, the bucket diameter is selected deliberately as 2, 4, or 8 m to cover the practical applications. The aspect ratio of the bucket is extended to 3, as the aspect ratios of 0.5–2 are investigated already to deduce Equation (2). Two strength profiles representing undrained shear strength under over-consolidated and normally consolidated conditions are employed in Table 2. By following the recommendation of guidelines DNV-RP-E303 [45] and research by Shen et al. [41], the adhesion factor α is taken as 0.3 or 0.65, corresponding to the operation phases of immediately after the installation of the bucket and months or years after the installation of the bucket, respectively. The V_c/V_0

values are in the range of 0.3–0.58, to avoid the potential shakedown of the bucket under V_c/V_0 less than 0.3 or rapid failure of the bucket under V_c/V_0 larger than 0.58. It should be noted that V_0 values for the additional cases are determined using the same procedure addressed in Section 3.1. As a result, V_0 values are shown in the last column in Table 2.

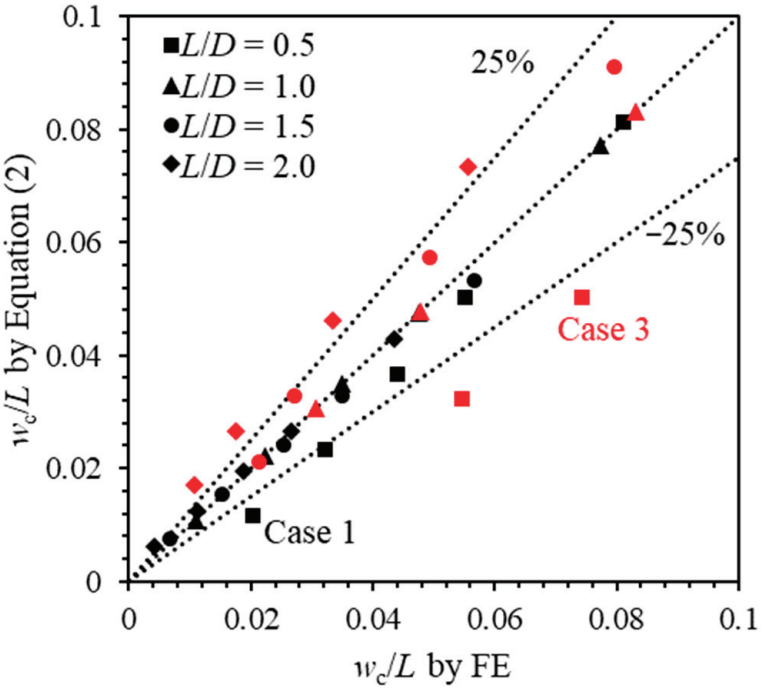

Figure 11. Comparison of w_c/L by FE and Equation (2) at D = 4 m and various L/D values.

Table 2. Additional cases for the reliability of Equation (2).

Case	D (m)	L/D	s_u (kPa)	α	V_c/V_0
A	8	0.5	6.5 + 0.55z	0.5	0.42
B	8	0.5	11.6	0.5	0.58
C	2	3	6.5 + 0.55z	0.5	0.42
D	2	3	11.6	0.5	0.58
E	4	1.5	30	0.65	0.30
F	4	1.5	10 + z	0.3	0.50

The w_c/L values by FE and Equation (2) are compared in Figure 12. It is evident in Figure 12a,b that Equation (2) is applicable for buckets with an aspect ratio ranging from 0.5 to 3 under the loading amplitudes considered, irrespective of the bucket diameter values. The w_c/L values predicted by Equation (2) are satisfactory in most cases, except for Case F in Figure 12c. A possible reason is that the clay in Case F is normally consolidated and the undrained shear strength increases more significantly with depth than that in other cases, whereas Equation (2) is more suitable for heavily over-consolidated soils with nearly uniform shear strength (s_u = 11.6 or 30 kPa) and slightly over-consolidated soils. Additionally, Equation (2) is valid for an adhesion factor ranging between 0.3 and 0.65, covering the typical operation phases of the bucket from the installation to a moderately long operational duration after the installation.

For practical application involving the predictions of w_c for buckets under symmetric vertical loading in clay using UDCAM, the following steps are suggested. (a) Establish the DSS cyclic strain contour diagrams through monotonic and cyclic DSS tests, to derive the normalized cyclic shear stress–strain relationship τ_c/s_u-γ_c. (b) Determine the static shear strength s_u through cone penetration tests. (c) Simulate w_c for a bucket with L/D = 1, utilizing the cyclic soil properties identified in Steps (a) to (c). (d) Calculate w_c for buckets

with relevant D and L/D using Equation (2). By employing the aforementioned steps, only a limited number of DSS tests, cone penetration tests, and numerical simulations are required to predict w_c for bucket foundations across various aspect ratios. This procedure is applicable for soils with different shear strengths and adhesion factors, and loading amplitudes V_c/V_0 in the range of 0.3–0.58.

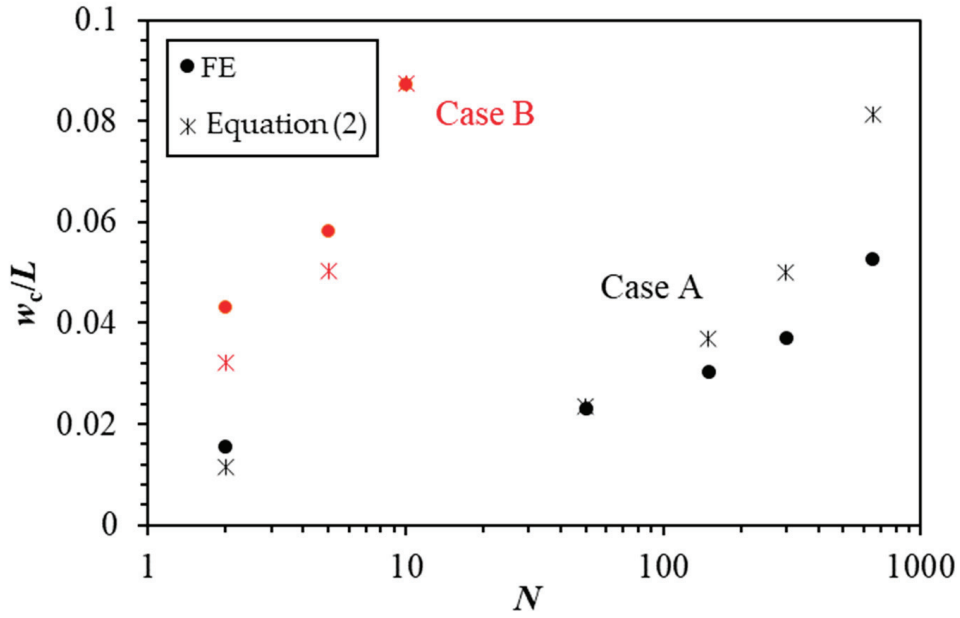

(**a**)

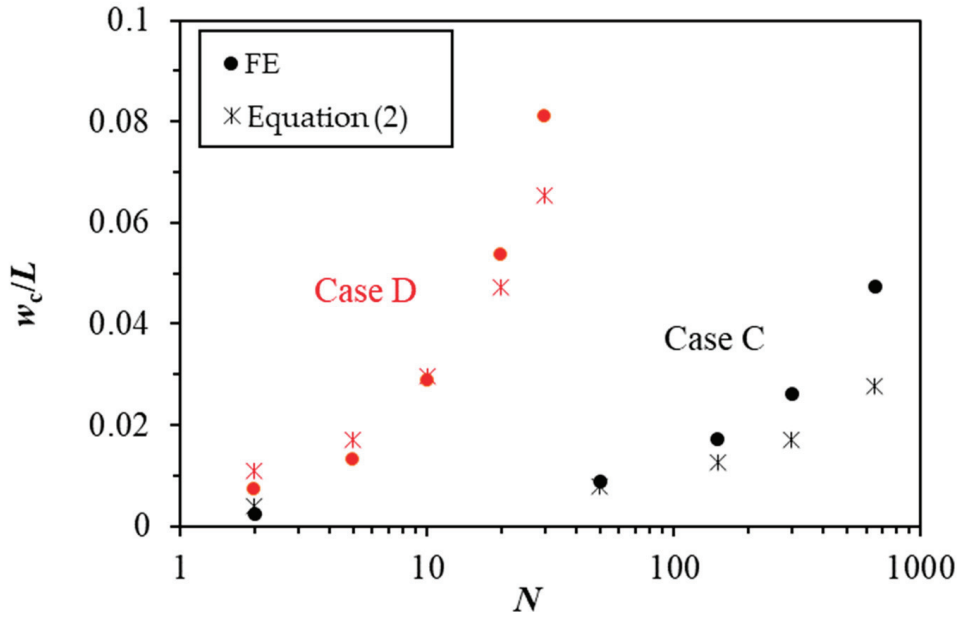

(**b**)

Figure 12. *Cont.*

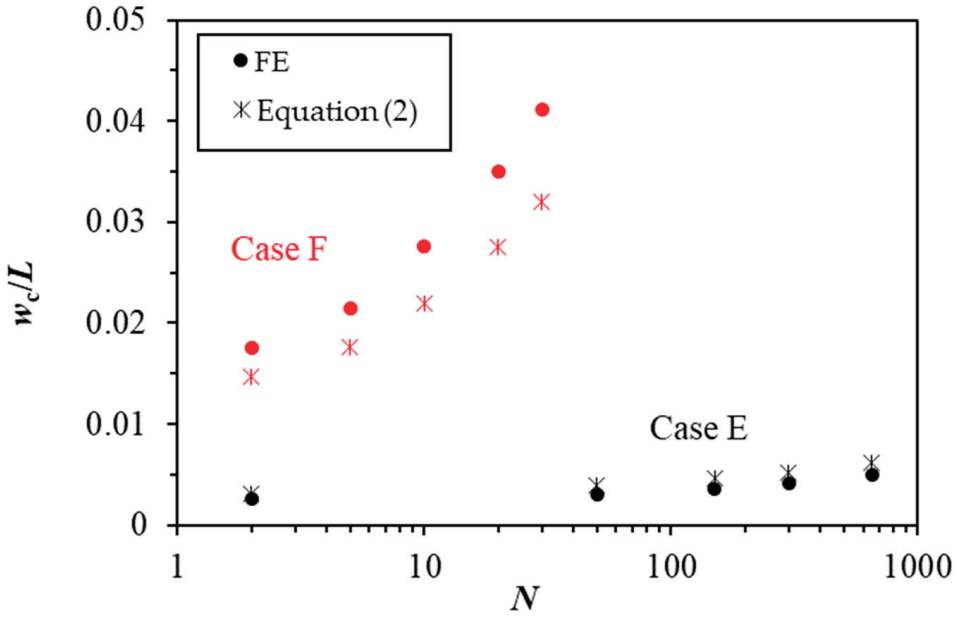

(**c**)

Figure 12. Performance of Equation (2) for cases in Table 2: (**a**) Cases A and B; (**b**) Cases C and D; (**c**) Cases E and F.

5. Conclusions

The accumulation of normalized vertical displacement amplitude w_c/L for buckets under symmetric vertical cyclic loading has been investigated through finite element (FE) analyses. Cyclic shear stress–strain relationships in clay are characterized using cyclic shear strain contour diagrams in a direct simple shear state. The results of w_c/L by FE are compared with those by centrifuge tests. In the parametric study, the aspect ratio L/D of the bucket is varied between 0.5 and 2 to investigate the effect of L/D on the prediction of w_c/L. The main conclusions are as follows:

(1) The w_c/L predicted by the FE model combined with UDCAM in this study exhibits reasonable agreement with the w_c/L obtained from existing centrifuge tests. The UDCAM is applicable for characterizing the cyclic shear stress–strain response of clay at a relevant number of cycles.

(2) The w_c/L in the parametric study decreases with increasing L/D. Taking w_c/L at L/D = 1 as a reference displacement, a predictive equation, Equation (2), for w_c/L at various L/D values has been proposed. It is proved that Equation (2) is applicable for buckets with L/D ranging between 0.5 and 3 and diameter D ranging between 2 and 8 m, normalized vertical loading amplitudes V_c/V_0 in the range of 0.3–0.58, and soil adhesion factors between 0.3 and 0.65. Equation (2) demonstrates better performance in soils with uniform or slightly increased undrained shear strength with depth than in soils with undrained shear strength increasing significantly with depth. In practical applications, a four-step procedure is suggested to predict w_c/L for bucket foundations across various aspect ratios, based on limited laboratory tests and FE simulations. The buckets with aspect ratios ranging between 0.5 and 3 are explored here, and the expansion of Equation (2) to larger aspect ratios needs to be testified in future. As for buckets under asymmetric vertical cyclic loading, the accumulation of w_c/L can be investigated through centrifuge tests at first and then compared with the predicted results by the proposed four-step procedure.

Author Contributions: Conceptualization, D.W., J.J. and C.L.; methodology, J.J.; software, D.W. and J.J.; validation, D.W. and J.J.; formal analysis, J.J.; investigation, J.J., D.W. and C.L.; data curation, J.J.; writing—original draft preparation, J.J.; writing—review and editing, D.W., C.L. and J.J.; funding acquisition, D.W. All authors have read and agreed to the published version of the manuscript.

Funding: This research was funded by the National Natural Science Foundation of China (grant Nos. 42025702 and 52394251).

Institutional Review Board Statement: Not applicable.

Informed Consent Statement: Not applicable.

Data Availability Statement: Data is contained within the article or supplementary material.

Conflicts of Interest: Author Chengxi Luo was employed by the company Power China Zhongnan Engineering Corporation Limited. The remaining authors declare that the research was conducted in the absence of any commercial or financial relationships that could be construed as a potential conflict of interest.

References

1. Bae, K.T.; Choo, Y.W.; Youn, H.; Kim, J.Y.; Choi, C.; Kwon, O. Geotechnical Perspective on Offshore Wind Plan, Strategy, Projects and Research in Korea. In Proceedings of the 19th International Conference on Soil Mechanics and Geotechnical Engineering: Technical Committee 209 Workshop, Seoul, Republic of Korea, 20 September 2017.
2. Houlsby, G.T.; Byrne, B.W. Suction Caisson Foundations for Offshore Wind Turbines and Anemometer Masts. *Wind Eng.* **2000**, *24*, 249–255. [CrossRef]
3. Zhu, F.Y.; O'Loughlin, C.D.; Bienen, B.; Cassidy, M.J.; Morgan, N. The Response of Suction Caissons to Long-Term Lateral Cyclic Loading in Single-Layer and Layered Seabeds. *Géotechnique* **2018**, *68*, 729–741. [CrossRef]
4. Faizi, K.; Faramarzi, A.; Dirar, S.; Chapman, D. Investigating the Monotonic Behaviour of Hybrid Tripod Suction Bucket Foundations for Offshore Wind Towers in Sand. *Appl. Ocean Res.* **2019**, *89*, 176–187. [CrossRef]
5. Achmus, M.; Kuo, Y.S.; Abdel-Rahman, K. Behavior of Monopile Foundations under Cyclic Lateral Load. *Comput. Geotech.* **2009**, *36*, 725–735. [CrossRef]
6. Petas, V.; Kolotsios, G.; Georgiadis, K.; Loukogeorgaki, E. Effect of Horizontal Loading on the Bearing Capacity of Tripod Skirted Foundations on Clay. In Proceedings of the 26th International Ocean and Polar Engineering Conference, Rhodes, Greece, 26 June 2016.
7. Zhao, Z.; Kouretzis, G.; Sloan, S.; Gao, Y. Ultimate Lateral Resistance of Tripod Pile Foundation in Clay. *Comput. Geotech.* **2017**, *92*, 220–228. [CrossRef]
8. Jeong, Y.H.; Kim, J.H.; Park, H.J.; Kim, D.S. Cyclic Behavior of Unit Bucket for Tripod Foundation System Supporting Offshore Wind Turbine via Model Tests. *Wind Energy* **2019**, *22*, 257–268. [CrossRef]
9. Kim, D.J.; Choo, Y.W.; Kim, J.H.; Kim, S.; Kim, D.S. Investigation of Monotonic and Cyclic Behavior of Tripod Suction Bucket Foundations for Offshore Wind Towers Using Centrifuge Modeling. *J. Geotech. Geoenviron. Eng.* **2014**, *140*, 04014008. [CrossRef]
10. He, B.; Jiang, J.; Cheng, J.; Zheng, J.; Wang, D. The Capacities of Tripod Bucket Foundation under Uniaxial and Combined Loading. *Ocean Eng.* **2021**, *220*, 108400. [CrossRef]
11. Carbon Trust. *Suction Installed Caisson Foundations for Offshore Wind: Design Guidelines*, 1st ed.; Carbon Trust: London, UK, 2019; pp. 1–92.
12. Elias, S.; Beer, M. Vibration Control and Energy Harvesting of Offshore Wind Turbines Installed with TMDI under Dynamical Loading. *Eng. Struct.* **2024**, *315*, 118459. [CrossRef]
13. Zakir, M.N.; Abasin, A.R.; Irshad, A.S.; Elias, S.; Yona, A.; Senjyu, T. Practical Wind Turbine Selection: A Multicriterion Decision Analysis for Sustainable Energy Infrastructure. *Pract. Period. Struct. Des. Constr.* **2024**, *29*, 04024028. [CrossRef]
14. Villalobos, F.A.; Byrne, B.W.; Houlsby, G.T. Model Testing of Suction Caissons in Clay Subjected to Vertical Loading. *Appl. Ocean Res.* **2010**, *32*, 414–424. [CrossRef]
15. Kou, H.; Fang, W.; Zhou, N.; Huang, J.; Zhang, X. Dynamic Response of Single-Bucket Foundation in Clay under Vertical Variable Amplitude Cyclic Loadings. *Ocean Eng.* **2023**, *273*, 113973. [CrossRef]
16. Chen, W.; Randolph, M.F. Uplift Capacity of Suction Caissons under Sustained and Cyclic Loading in Soft Clay. *J. Geotech. Geoenviron. Eng.* **2007**, *133*, 1352–1363. [CrossRef]
17. Zografou, D.; Gourvenec, S.; O'Loughlin, C. Vertical Cyclic Loading Response of Shallow Skirted Foundation in Soft Normally Consolidated Clay. *Can. Geotech. J.* **2019**, *56*, 473–483. [CrossRef]
18. Jiang, J.; Wang, D.; Fu, D. Vertical Monotonic and Cyclic Responses of a Bucket in Over-Consolidated Clay. *J. Mar. Sci. Eng.* **2023**, *11*, 2044. [CrossRef]

19. Randolph, M.F. Offshore Design Approaches and Model Tests for Sub-Failure Cyclic Loading of Foundations. In *Mechanical Behaviour of Soils under Environmentally Induced Cyclic Loads*; Di Prisco, C., Wood, D.M., Eds.; CISM Courses and Lectures; Springer: Vienna, Austria, 2012; pp. 441–480, ISBN 978-3-7091-1068-3.
20. Randolph, M.; Gourvenec, S. *Offshore Geotechnical Engineering*; CRC Press: London, UK, 2017; ISBN 978-1-315-27247-4.
21. Cheng, X.; Yang, A.; Li, G. Model Tests and Finite Element Analysis for the Cyclic Deformation Process of Suction Anchors in Soft Clays. *Ocean Eng.* **2018**, *151*, 329–341. [CrossRef]
22. Iskander, M.; El-Gharbawy, S.; Olson, R. Performance of Suction Caissons in Sand and Clay. *Can. Geotech. J.* **2002**, *39*, 576–584. [CrossRef]
23. Houlsby, G.T.; Abadie, C.N.; Beuckelaers, W.J.A.P.; Byrne, B.W. A Model for Nonlinear Hysteretic and Ratcheting Behaviour. *Int. J. Solids Struct.* **2017**, *120*, 67–80. [CrossRef]
24. Abadie, C. Cyclic Lateral Loading of Monopile Foundations in Cohesionless Soils. Ph.D. Thesis, University of Oxford, Oxford, UK, 2015.
25. Liu, H.; Pisanò, F.; Jostad, H.P.; Sivasithamparam, N. Impact of Cyclic Strain Accumulation on the Tilting Behaviour of Monopiles in Sand: An Assessment of the Miner's Rule Based on SANISAND-MS 3D FE Modelling. *Ocean Eng.* **2022**, *250*, 110579. [CrossRef]
26. Houlsby, G.T.; Kelly, R.B.; Huxtable, J.; Byrne, B.W. Field Trials of Suction Caissons in Clay for Offshore Wind Turbine Foundations. *Géotechnique* **2005**, *55*, 287–296. [CrossRef]
27. Andersen, K.H. Bearing Capacity under Cyclic Loading—Offshore, along the Coast, and on Land. *Can. Geotech. J.* **2009**, *46*, 513–535. [CrossRef]
28. Jostad, H.; Grimstad, G.; Andersen, K.; Saue, M.; Shin, Y.; You, D. A FE Procedure for Foundation Design of Offshore Structures—Applied to Study a Potential OWT Monopile Foundation in the Korean Western Sea. *Geotech. Eng.* **2014**, *45*, 63–72.
29. Zhang, C.; Wang, D.; Zheng, J. A Cyclic-Softening Macro Element Model for Mono-Bucket Foundations Supporting Offshore Wind Turbines in Clay. *Comput. Geotech.* **2023**, *161*, 105603. [CrossRef]
30. Andersen, A. Cyclic Soil Parameters for Offshore Foundation Design. In Proceedings of the 3rd International Symposium on Frontiers in Offshore Geotechnics, Oslo, Norway, 10 June 2015.
31. Skau, K.S.; Chen, Y.; Jostad, H.P. A Numerical Study of Capacity and Stiffness of Circular Skirted Foundations in Clay Subjected to Combined Static and Cyclic General Loading. *Géotechnique* **2018**, *68*, 205–220. [CrossRef]
32. Jostad, H.; Andresen, L. A FE Procedure for Calculation of Displacement and Capacity of Foundations Subject to Cyclic Loading. In Proceedings of the 1st International Symposium on Computational Geomechanics, Juan les Pins, France, 29 April 2009.
33. Manuals-PLAXIS-GeoStudio | PLAXIS Wiki-GeoStudio | PLAXIS-Bentley Communities. Available online: https://communities.bentley.com/products/geotech-analysis/w/wiki/46137/manuals---plaxis (accessed on 23 April 2024).
34. Khoa, H.D.V.; Jostad, H.P. Application of a Cyclic Accumulation Model UDCAM to FE Analyses of Offshore Foundations. In Proceedings of the 4th Congrès International de Géotechnique—Ouvrages-Structures, Ho Chi Minh City, Vietnam, 26 October 2017.
35. Andersen, K.H.; Engin, H.K.; D'Ignazio, M.; Yang, S. Determination of Cyclic Soil Parameters for Offshore Foundation Design from an Existing Data Base. *Ocean Eng.* **2023**, *267*, 113180. [CrossRef]
36. Skau, K.S.; Jostad, H.P. Application of the NGI-Procedure for Design of Bucket Foundations for Offshore Wind Turbines. In Proceeding of the 24th International Ocean and Polar Engineering Conference, Busan, Republic of Korea, 15 June 2014.
37. Rasch, C. Modelling of Cyclic Soil Degradation: Development of a Cyclic Accumulation Model and the Application to a Gravity Based Foundation. Master's Thesis, Delft University of Technology, Delft, The Netherlands, 2016.
38. API RP 2GEO Geotechnical and Foundtaion Design Considerations. Available online: https://www.intertekinform.com/en-au/standards/api-rp-2geo-2011-add-1-2014-97863_saig_api_api_206786/ (accessed on 3 July 2024).
39. Jostad, H.; Grimstad, G.; Andersen, K.; Sivasithamparam, N. A FE procedure for calculation of cyclic behaviour of offshore foundations under partly drained conditions. In Proceedings of the 3rd International Symposium on Frontiers in Offshore Geotechnics, Oslo, Norway, 10 June 2015.
40. Supachawarote, C. Inclined Load Capacity of Suction Caisson in Clay. Ph.D. Thesis, The University of Western Australia, Perth, Australia, 2006.
41. Shen, K.; Jiang, J.; Wang, D.; Zheng, J. Capacities of Tripod Bucket Foundation under Uniaxial and Combined Loading Considering Adhesion Factor. *Mar. Georesour. Geotechnol.* **2022**, *40*, 1520–1528. [CrossRef]
42. Banaszek, A.; Petrovic, R.; Zylinski, B. Finite Element Method Analysis of Pipe Material Temperature Changes Influence on Line Expansion Loops in Hydraulic Installations on Modern Tankers. *Therm. Sci.* **2011**, *15*, 81–90. [CrossRef]
43. *ASTM D6528-17*; Standard Test Method for Consolidated Undrained Direct Simple Shear Testing of Cohesive Soils. ASTM International: West Conshohocken, PA, USA, 2017.
44. Lunne, T.; Andersen, K.H. Soft clay shear strength parameters for deepwater geotechnical design. In Proceedings of the 6th International Offshore Site Investigation and Geotechnics Conference, London, UK, 11 September 2007.
45. DNV-RP-E303 Geotechnical Design and Installation of Suction Anchors in Clay. Available online: https://www.dnv.com/oilgas/download/dnv-rp-e303-geotechnical-design-and-installation-of-suction-anchors-in-clay/ (accessed on 3 July 2024).

46. Andersen, K.H.; Jostad, H.P. Foundation Design of Skirted Foundations and Anchors in Clay. In Proceedings of the 31st Offshore Technology Conference, Houston, TX, USA, 3 May 1999.
47. Wang, J.; Yang, H. Model Tests and Numerical Simulation on Bearing Capacity of Bucket Foundations in Soft Clay Under Vertical Static and Cyclic Loads. In Proceedings of the Seventeenth International Offshore and Polar Engineering Conference, Lisbon, Portugal, 1–6 July 2007; p. ISOPE-I-07-346.

Journal of
Marine Science and Engineering

MDPI

Article

Response of a Coral Reef Sand Foundation Densified through the Dynamic Compaction Method

Linlin Gu [1], Weihao Yang [1], Zhen Wang [2,*], Jianping Wang [3] and Guanlin Ye [4]

[1] Department of Emergency Support, Nanjing University of Science and Technology, Nanjing 210094, China; 15005666059@163.com (W.Y.)
[2] School of Mechanical Engineering, Nanjing University of Science and Technology, Nanjing 210094, China
[3] Naval Research Institute of PLA, Beijing 100161, China
[4] Department of Civil Engineering, Shanghai Jiaotong University, Shanghai 200030, China
* Correspondence: wangzhen2012@njust.edu.cn

Abstract: Dynamic compaction is a method of ground reinforcement that uses the huge impact energy of a free-falling hammer to compact the soil. This study presents a DC method for strengthening coral reef foundations in the reclamation area of remote sea islands. Pilot tests were performed to obtain the design parameters before official DC operation. The standard penetration test (SPT), shallow plate-load test (PLT), and deformation investigation were conducted in two improvement regions (A_1 and A_2) with varying tamping energies. During the deformation test, the depth of the tamping crater for the first two points' tamping and the third full tamping was observed at two distinct sites. The allowable ground bearing capacity at two disparate field sites was at least 360 kPa. The reinforcement depths were 3.5 and 3.2 m in the A_1 and A_2 zones, respectively. The DC process was numerically analyzed by the two-dimensional particle flow code, PFC2D. It indicated that the reinforcement effect and effective reinforcement depth were consistent with the field data. The coral sand particles at the bottom of the crater were primarily broken down in the initial stage, and the particle-crushing zone gradually developed toward both sides of the crater. The force chain developed similarly at the three tamping energies (800, 1500, and 2000 kJ), and the impact stress wave propagated along the sand particles primarily in the vertical direction.

Keywords: coral sand foundation; dynamic compaction; field test; particle flow discrete element; bearing capacity; improvement depth

1. Introduction

Coral reefs are a special type of rock mass formed after the death of reef-building coral communities through long geological processes [1]. Coral backfill is typically located on the surface of coral reefs and comprises biological debris from primary or secondary coral reef rocks, corals, and shells that have been eroded, broken, and deposited in nearshore environments [2]. Coral reef sand (CRS) is a widely graded soil with a distribution ranging from silt to gravel. The remote sea reef areas contain a large number of islands with loose deposits dominated by coral fragments and coral reef sand, accounting for 60–80% of the total. Using CRS as a reclamation material can effectively solve the problem of coral reef debris dumps and alleviate the shortage of reclamation fillers [3]. CRS is a particular type of soil with low particle hardness and high porosity and friability, making it challenging to use as the construction ground and backfill material for road embankments and airfield runways [4]. Thus, a CRS foundation cannot directly support structures or roads, necessitating an appropriate improvement method to strengthen it.

Research interest in improving coral sand foundations has increased in recent years. Traditional foundation reinforcement techniques, such as pile driving [5], which have been successfully adopted for other types of soils, have been proven to be ineffective for CRS owing to its crushability. Depending on the engineering requirements, a variety of additives,

including gypsum, limestone, calcite [6], Portland cement [7], and a chemical grout [8], can be utilized to stabilize CRS. In addition, various methods of improving soil, like microbially induced calcite precipitation (MICP) [9], which uses biomineralization processes to induce cementation, have significant advantages in decreasing subsidence [10], mitigating liquefaction [11], and reinforcing the foundation [12]. Stabilization and MICP improvement techniques could reinforce the mechanical capacity of CRS. However, they are generally not suitable for large built-up regions on islands and reefs owing to economic and environmental issues.

Among the aforementioned techniques, dynamic compaction (DC) is an appropriate reinforcement technique for large-scale foundation reinforcement owing to its feasibility, cost-effectiveness, and controllable thickness [13,14]. The DC technique involves repeatedly impacting a ground surface with a heavy steel or concrete rammer (generally 100–300 kN) dropped from a height of 10–40 m. The enormous stress exerted by the hammer's impact destroys the structure of the original soil particles and decreases the void ratio of the soil, effectively compacting the foundation. This decreases the compressibility and enhances the bearing capacity of the foundation. As a relatively mature foundation improvement method, it has been widely applied to sandy grounds. The DC approach was applied to reinforce the sandy foundation by Hu et al. [15], Zhou et al. [16], and Feng et al. [17], indicating its advantage for dissipating pore water pressure and strengthening deep sandy materials. Various coupling and nonlinear problems associated with the dynamic response of the DC process have led to the development of analytical and numerical models for demonstrating complex soil behavior during DC. Nashaed et al. [18] determined the post-improvement density and penetration resistance of sandy soils using energy-based numerical methods. The void ratio of granular soil can be effectively ascertained through the utilization of the discrete element method (DEM) in conjunction with a discontinuous deformation analysis methodology. Cundall and Strack [19] introduced an innovative algorithm called the particle flow code (PFC). The mechanical properties of material with granularity can be readily simulated by the implementation of the particle flow discrete element method. Wada et al. [20] analyzed the tampering crater on granular materials through a two-dimensional (2D) particle flow discrete element method. Ma et al. [21] employed the particle flow discrete element method to analyze the reinforcement effect of the gravelly soil foundation resulting from DC. Jia et al. [22] determined the granular soil mechanism during DC using the PFC/FLAC coupled method. Studies on the DC mechanism have mainly concentrated on terrigenous sand, while engineering experience and theoretical guidance on the reinforcement effect of CRS through DC remains in shortage. Thus, no matter whether from the perspective of forward-looking construction of island and reef projects, or from the perspective of promoting the comprehensive development of theory and technology in the field of engineering geology, it is greatly significant to investigate the scientific treatment of coral reef detrital sediments and the application of an engineering filler for DC.

This study comprehensively described a field investigation combined with a two-dimensional particle flow numerical analysis (PFC2D) method to study the effectiveness of DC on coral debris foundations in the remote sea islands. The field study consisted of a deformation test, shallow plate load test, and standard penetration test. The depth of a crater after each tamping pass in the two test zones after DC was measured during the deformation tests. On the basis of the data of the shallow plate load test, the CRS foundation's permissible bearing capacity reinforced through DC was acquired. In addition, the blow count was explored according to the SPT results in the investigation area, and the depth of reinforcement for DC was determined with respect to the variation in the blow count with depth. Numerical computations were performed to reproduce the DC process, and the reinforcement effect of the coral sand foundation was estimated.

2. On-Site Test Position and Test Procedures

2.1. Field Zones' Description and Subsoil Condition

The project proposed in the study is situated at a remote sea island and comprises many coral reefs, which are ideal platforms for oceanic resource exploitation. The site

is underlain by overlying reclaimed coral sand and a primitive reef and reef limestone formed by biological skeletons, as shown in Figure 1. The average thickness of the upper reclamation layer was approximately 6 m, which was loose and uneven, comprising coral sand dredged from the harbor pond. The original reef in the lower layer was undulating with approximately 10 m thickness, and the reef-limestone layer of cemented rock lay beneath the reef. The surface coral sand is a Holocene uncemented loose sedimentary layer, mainly composed of coral limbs, fragments, and biological gravel. It could be termed coral coarse-grained soil according to the national standard Geotechnical Engineering Investigation Code [23]. The engineering mechanical property of CRS is markedly poor, failing to meet the requirements for bearing capacity of the coral sand foundation. These defects can lead to foundation settlement and cracking of the superstructure. In this case, the foundation reinforcement needs to be implemented; otherwise, infrastructural construction on the reclaimed islands and reefs cannot be performed.

Considering the large construction area to be reinforced, two test zones, A_1 and A_2 (both at 30 m × 30 m), were sampled for particle sieving tests. According to the grading curve (Figure 2), the CRS gradings in the two disparate areas were approximately the same, with a coarse grain content of over 94%. The coefficient of curvature (C_c) ranged from 0.43 to 1.07, and the range of values for the coefficient of uniformity (C_u) were 3.84 to 16.70, respectively. The reclaimed coral sand layer at the study site was poorly graded. For the large area of reclaimed islands and reefs to be improved, DC was selected to treat the coral sand grounds for economic reasons. However, pilot tests were necessary before formal DC implementation to identify the crucial technical data. The design criterion for the allowable ground bearing capacity and reinforcement thickness after the DC reinforcement techniques were over 360 kPa and 3.0 m, respectively.

(**a**) Site topography (**b**) Site soil profile

Figure 1. Field site coral reef sand under dynamic compaction.

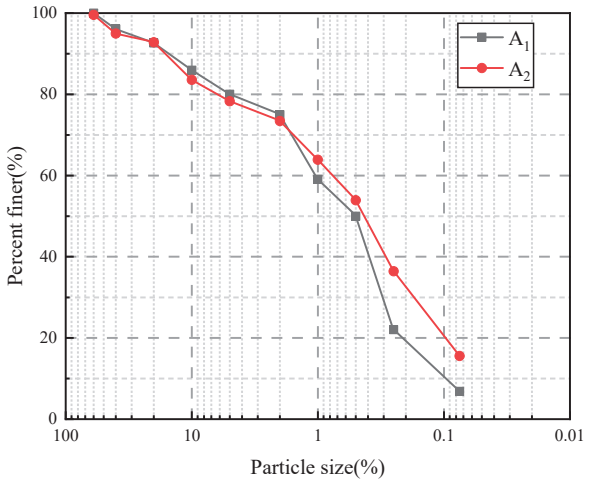

Figure 2. Grain size distribution in the two test zones.

2.2. DC Process on Coral Reef Sand

DC is a densification process; that is, the hammering energy produced by DC completely destroys the original structure of the soil sample and forces water and air out of the pores of the soil particles, causing the ground to become denser through a consolidation process. Lots of factors, including the tamper mass, fall height, tamping point sequence pass, pass numbers, the spacing of tamping points, the interval between each pass, and the ending rule of each tamping, can influence DC design. Owing to complex site-dependent conditions, the abovementioned construction data are often unavailable and are generally determined according to prior engineering experience. Therefore, field pilot tests were performed to ascertain the main technical parameters.

The overall configuration of the tamping points for the two sites (A_1, A_2) is shown in Figure 3. Three impact passes were conducted, and test tamping was performed to determine the impact times. During the first pass, hammering energy was applied to the impact points, as displayed by the solid circle. During the second pass, the heavy hammer's drop point position was halfway between the locations of the two adjacent tamping pits in the first pass. Finally, During the third pass, the tamping process was carried out thoroughly across the entire site. Table 1 lists the impact energy levels in the two DC zones. Figure 4 shows the cranes and tampers used in the pilot tests. The tamping energy applied to the A_1 region during the first two episodes of ramming reached 2000 kN·m per drop, which is roughly the free fall of a 200 kN hammer from a height of 10 m. As for the third full run of tamping, the tamping energy per drop was 800 kN·m, equivalent to an 80 kN rammer dropped from a 10 m height. The tamping energy for A_2 was 1500 kN·m for each drop in the two main tampings, with a full tamping of 600 kN·m per drop. The tamping points for the first two tampings were set up in a square-grid design with each center located 5 m apart. During the last full hammering, approximately one-quarter of the bottom area of the rammer was overlapped. For the last two impacts in the test tamping, the average tamping pit subsidence should have been less than 50 mm.

The average subsidence of the tamping pit for the last two drops in the test tamping should have been less than 50 mm, and the ground around the crater should not have bulged excessively. The drop numbers of the rammer were six for the first two passes and two for the last full pass.

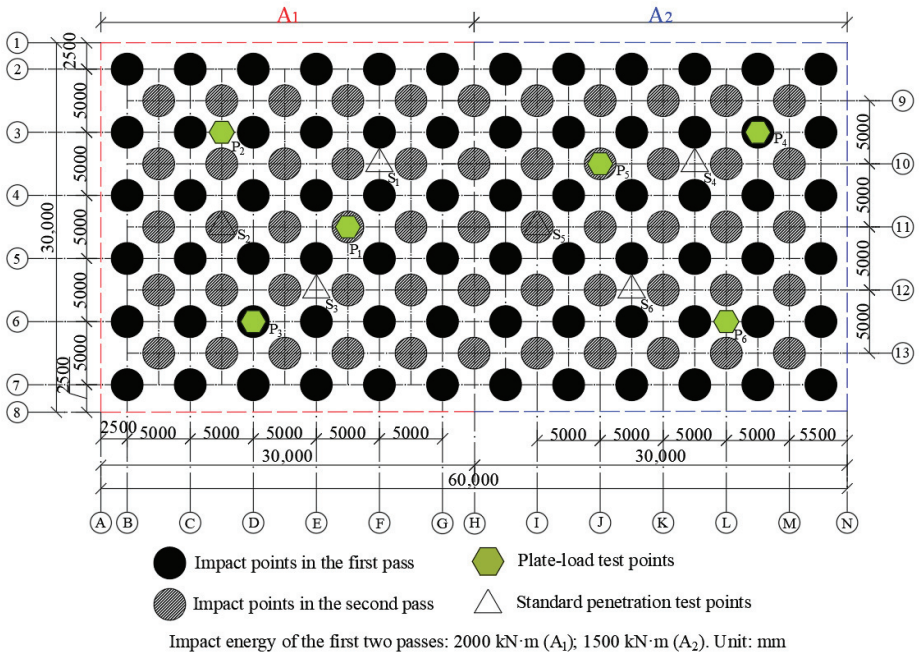

Figure 3. Layout of impact points and investigation points in two test zones.

(**a**) DC construction (**b**) crater depth measurement

Figure 4. DC site photos.

Table 1. Impact energy levels in two test zones.

Passes of Tamping	Impact Energy Level (kN·m)		Tamping Times	
	A_1	A_2	A_1	A_2
First pass	2000	1500	6	6
Second pass	2000	1500	6	6
Third pass	800	600	2	2

3. Field Test Results

To assess the tamping impact of the DC, lots of geological investigation methods have been employed to evaluate different aspects. Figure 3 illustrates the primary design and configuration of the investigation points. The settlement of tamping pits was monitored to assess the hammering energy applied during each pass. Through the execution of a shallow plate-load test, the permitted ground bearing capacity following DC implementation was verified. Meanwhile, the SPT was also performed to assess the improvement in depth after DC.

3.1. Ground Deformation

Ground settlement and the crater depth are the general and most direct indices of the reinforcement effect induced by the DC, as shown in Figure 4b. The initial position elevations were supplied with investigation points in the two testing regions. Thirty-two elevation observation points were installed in each zone. Following every tamping pass, the elevation of the observation points was recorded. The average aggregate settlement of the two distinct tamping areas after DC is depicted in Figure 5. The depth of tamping pits for the initial pass was the greatest, reaching averages of 0.224 and 0.188 m for zones A_1 and A_2, respectively. The depth increments of tamping pits for the second pass were significantly smaller than those for the first pass owing to the original tamping energy obtained by the first pass. The impact of compaction energy on the improvement effect gradually waned with point tamping during DC. After the third pass, the two sites were well-compacted, as demonstrated by the larger crater depth differences between the second and third passes. The last full tamping was essential and significant for strengthening the reclaimed sandy coral layer. According to the elevation measurements after the third full tamping in those two zones, the average total subsidence for A_1 and A_2 were 0.419 and 0.379 m, respectively, denoting that the coral sand ground underwent significant settlement. Thus, a higher tamping energy produces foundation compression more efficiently than a lower tamping energy.

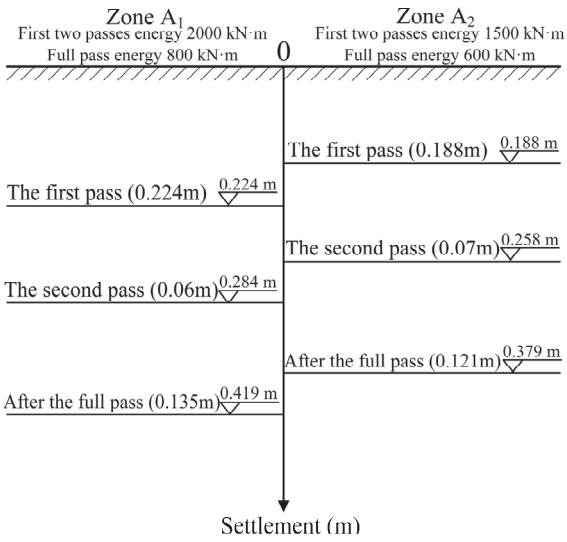

Figure 5. Average settlement of the two tamping zones in different passes.

3.2. Shallow Plate-Load Test and Foundation Bearing Capacity

Field load testing validated the coral sand foundation's bearing capabilities utilizing the ultimate load method. After DC implementation, three shallow plate load tests were performed in those two test zones, as illustrated in Figure 6. As illustrated in Figure 3, the two shallow plate load tests (P_2 and P_6) were conducted at the tamping points, while the other four plate load tests (P_1, P_3, P_4, and P_5) were performed in the middle of two adjacent tamping points. A circular loading plate with a 0.5 m^2 area was applied in each test region. The tests started from a plane 50 mm beneath the ground. A coarse sandy layer of 10–20 mm thickness was placed underneath circular loading plates to maintain the loading plate level, structure, and natural moisture content of the test soil. The maximum load applied was 720 kPa, which was twice the design's permitted bearing capability. The load was applied to the load plate incrementally, with each stage of the load generating settlement deformation larger than a tenth of the maximum load. When the settlement was stabilized, within two hours, the settlement per hour was less than 0.1 mm, then the next level of loading increment was imposed. Load-settlement curves can be utilized to determine the bearing capacity of the coral sand foundation after DC reinforcement according to shallow plate-load tests.

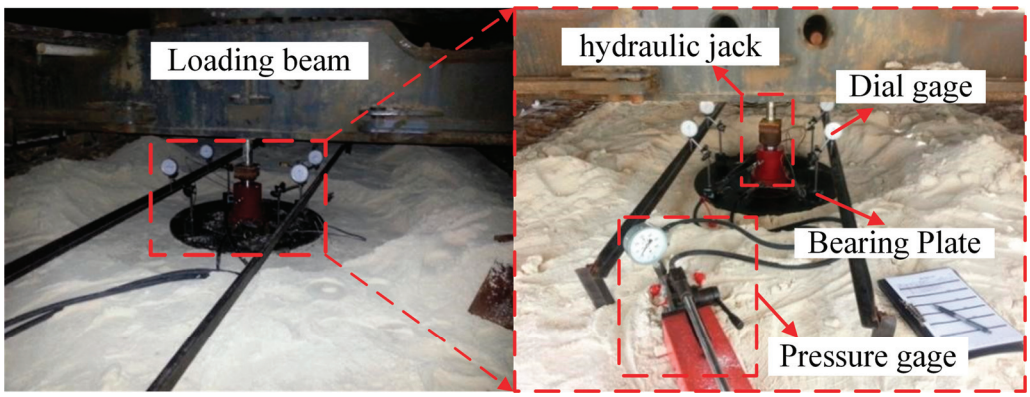

Figure 6. Shallow plate-load test at the field sites.

Table 2 lists detailed test data of the shallow plate-load test, and Figure 7 displays the load-settlement curves acquired from the shallow plate-load tests in six different test areas. At the maximum load of 720 kPa, the settlement values of test pits P_1, P_2, and P_3 in the A_1 area were 15.86, 12.45, and 19.03 mm, respectively. The corresponding settlements

for test pits P_4, P_5, and P_6 in A_2 were 14.9, 13.15, and 13.39 mm, respectively. In these two testing regions, none of the six test pits exhibited significant failure during loading to maximum loads. All the six load-settlement curves gradually decreased during the loading process. Smaller deviations were observed among curves P_4, P_5, and P_6, indicating a more homogeneous DC effect in A_2 than in A_1. Design requirements indicate that the characteristic value of the bearing capacity should be 50% of the value of the maximum loading. The allowable foundation bearing capacity of all six test pits exceeded 360 kPa, meeting the design requirement.

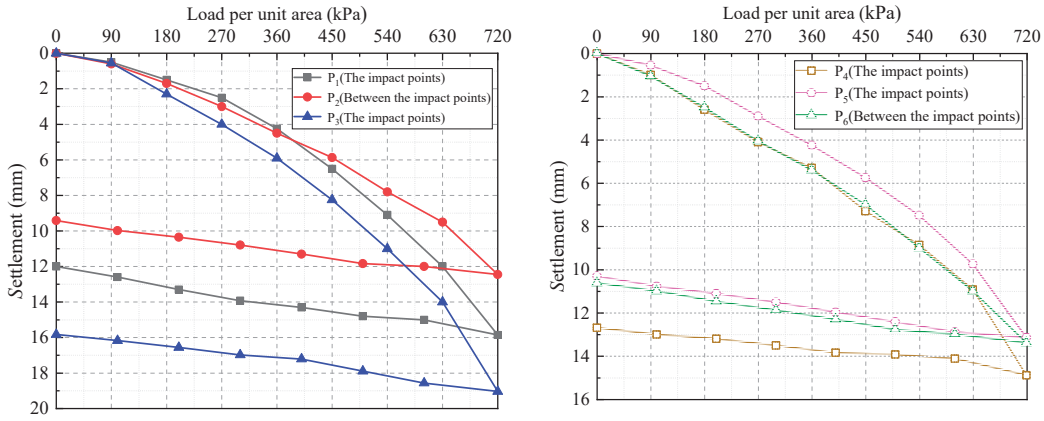

(**a**) Zone A_1 (**b**) Zone A_2

Figure 7. Load-settlement curves for shallow plate-load test at the field sites.

Table 2. Test results from shallow plate-load tests.

Test Zone	Test Site	Ultimate Load Method				
		Maximum Load (kPa)	Maximum Settlement (mm)	Maximum Resilience Value (mm)	Resilience Rate	Characteristic Value of Bearing Capacity (kPa)
A_1	P_1	720	15.86	3.86	24.34%	>360
	P_2	720	12.45	3.04	24.42%	>360
	P_3	720	19.03	3.2	16.82%	>360
A_2	P_4	720	14.9	2.2	14.77%	>360
	P_5	720	13.15	2.84	21.60%	>360
	P_6	720	13.39	2.76	20.61%	>360

3.3. Standard Penetration Test (SPT) and Reinforcement Depth

The SPT is a commonly employed field investigation method for evaluating the reinforcement depth by DC under sandy ground conditions. Each zone had three different test pits. The SPT was performed on the basis of the Chinese National Code for the design of a building foundation (GB50007-2011) [24]. During the test, the 63.5 kg donut hammer was lifted to a 0.76 m position, and the standard perforator with a length of 51 cm, an outer diameter of 5.1 cm, and an inner diameter of 3.49 cm was hit into the soil through free fall. Theoretically, the total potential energy of the drop hammer was 0.473 kN·m. Blow counts were directly used, considering that the SPT was performed to assess the compressibility of the subsoil after DC in the identical test area. Figure 8 shows the blow count curves at different depths in the two areas. The strengthening effect could be assessed by comparing the number of blows before and after DC. In the A_1 area, The SPT blow number grew to double within a depth of 3.5 m from the ground surface, demonstrating a significant reinforcing impact, and the average blow count reached approximately 36 after DC. In the A_2 area, the curves also exhibited a discrepancy before and after DC until the depth of about 3.2 m was achieved. The average blow count increased to approximately 30 at

depths over 3.2 m. Based on the blow count data of standard penetration tests, the effective reinforcement depths of the two test areas were 3.5 and 3.2 m, respectively. The blow count gradually decreased with an increasing depth until the density state of the ground soil before and after DC became homogeneous. The effective reinforcement depth was strongly correlated with the input energy; a higher tamping energy (2000 kJ) produced a larger effective reinforcement depth and better deep reinforcement effect on the coral reef foundation. Furthermore, on average, the locations at the impact points (S_2 in A_1 region, S_5 in A_2 region) underwent a better reinforcement effect than those between the impact points (S_1 and S_3 in A_1 region, S_4 and S_6 in A_2 region).

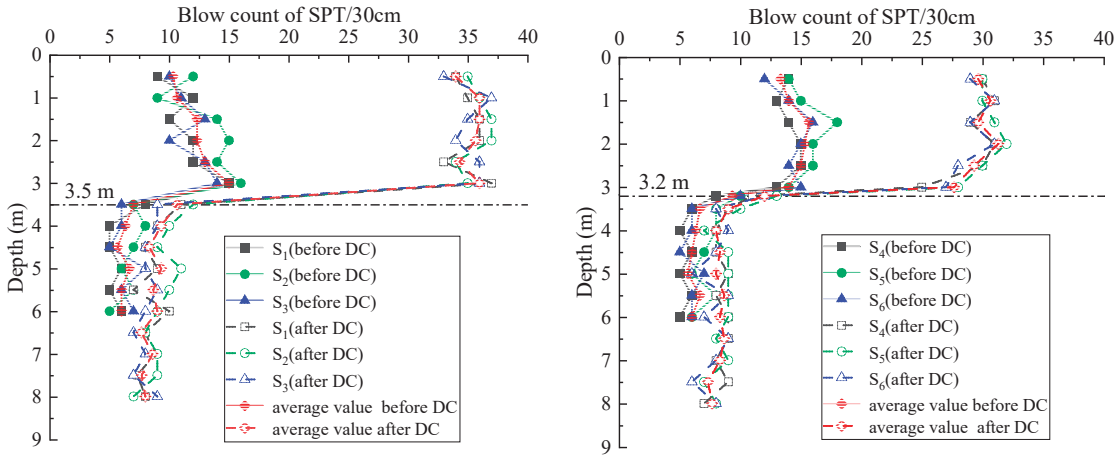

(**a**) Zone A_1 (**b**) Zone A_2

Figure 8. Variation in SPT blows against depth at the field sites before and after DC.

4. Numerical Study of DC Mechanism

4.1. Numerical Algorithm and Validation

PFC2D is a discrete element code for two-dimensional particle flow that uses a specific computational method. The motions and interactions for particles with the shape of a circle are computed in a large-deformation model, where the mechanical interactions between the particles in contact are considered. The linear contact relationship is defined by the contact stiffness in the tangential and radial directions between circular particles in PFC2D. This study adopted a parallel bonding contact model; that is, a parallel bonding contact was added. The advantage of a parallel bonding contact is that the determination method of particle breakage is simple and it is not necessary to manually select the flexible cluster failure criterion and sub-particle replacement mode. This can be used to characterize the complex and irregular particles to a certain extent and can solve the problem of large deformation [25–27]. The parallel bond contact adopted among particle elements is to bond sub-particles into a larger flexible cluster through bonds with a certain tensile strength and shear strength. When the surface spacing is less than 0, the parallel bonding contact is activated. A bonding force is generated between the circular particle elements. There are two forms of bonding force: a tensile stress and a shearing stress. When the maximum tensile stress is greater than the preset parallel bond tensile strength, the bond will have tensile failure; when the maximum shear stress is greater than the preset parallel bond shear strength, the bond will have shear failure. At this time, the bond breaks, and the flexible clusters are broken into a number of smaller sub-particles, forming a number of cracks. Under the continuous action of external force, these cracks will be linked; the macro performance is a certain number of broken zones. The number of cracks is monitored through the built-in FISH language to evaluate the breakage. A particle model of a coral sand foundation was developed according to gravitational deposition in a restricted space by walls. The soil particles were released and suspended in the assigned space, unaffected by gravitational forces, subsequently settling at the bottom of the container upon activation

of gravity (with a gravitational acceleration of 9.8 m/s^2 as per this study). Figure 9 shows the two-dimensional particle model of the coral sand foundation produced through gravity deposition. The calculation accuracy and calculation rate must be considered when using PFC2D for model test analysis. If the initial gradation is employed directly, the particle number will be large, and the calculation efficiency will be relatively low. Thus, the step-by-step method of equal-mass replacement of the finest particles was used to correct the initial gradation, and the final grain set used for modeling was obtained, as shown in Table 3.

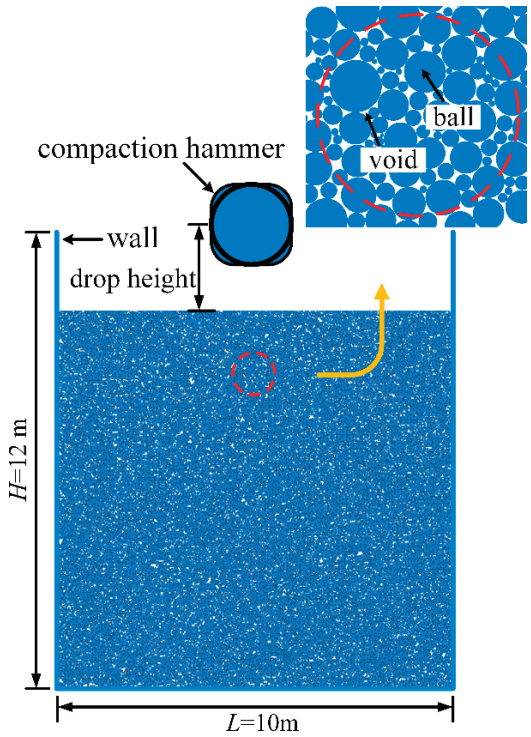

Figure 9. Two-dimensional particle model of coral sand foundation.

Table 3. Grain set used in the numerical simulation.

Grain Size (mm)	≥60	40~60	20~40	10~20	5~10	1~5	0.5~1.0	0~0.5
Content (%)	3.95	3.41	6.7	5.93	5.07	24.99	27.93	22.02

In the PFC2D program, a flexible cluster was used to simulate the coral sand, and a hammer model was formed using clump blocks combined with three ball elements with a 1 m radius. The hammer was set above the centerline of the model, which fell freely under the action of gravity, and its height was controlled to achieve different ramming energies. The hammer was deleted after each tamping was completed, and the model was self-balanced for a period to ensure the rebound time of the foundation. Monitoring points were set up at each depth to monitor the vertical displacement of the soil. Considering the influence of the tamping energy, hammer diameter, and particle size on the impact range and numerical calculation efficiency of DC, the model adopted a wall with a 12 m height and 10 m width to simulate the boundary of the numerical model. With both ball-to-ball and ball-to-wall contacts, the shear and normal stiffness (k_s, k_n) exhibited identical magnitudes. Table 4 lists the initial value of the microscopic variables used in the numerical calculations.

The numerical simulation of DC using PFC2D at a single point multiple times at 800, 1500, and 2000 kJ tamping energies was carried out to exhibit the development of crater settlement and breakage of coral reef sand. The results of the numerical calculation were contrasted with the data from the field investigation to verify the credibility of the numerical model. The proposed numerical methodology was employed to simulate the

initial six drops of the point tamping process during the first pass. The parameters in the numerical simulation were consistent with the field construction parameters. Figure 10 shows the comparative results of the average crater depth of each drop of tamping during the first pass. The crater settlement differences at the last drop for 2000 and 1500 kJ were 2.1 and 1.5 cm, respectively. There was only a slight discrepancy observed between the investigation data and the results of simulation, indicating that the numerical simulation results were credible and highly reliable.

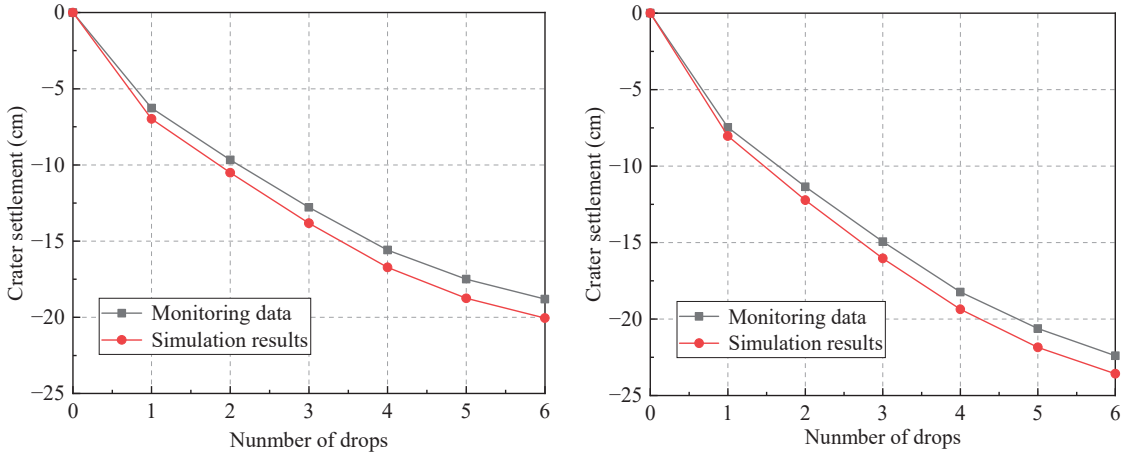

(**a**) 1500 kJ (**b**) 2000 kJ

Figure 10. Comparison between numerical results and field data.

Table 4. Initial microscopic parameters of coral sand.

Density/ρ (kg/m^3)	2730
Maximum porosity ratio/e_{max}	1.84
Minimum porosity ratio/e_{min}	0.88
Elongation index/EI	0.2–0.8
Effective modulus/E^* (kPa)	7.5×10^6
Stiffness ratio/k^*	15
Frictional coefficient/μ	0.65
Normal stiffness of parallel bond/$\overline{k_n}$ (kN·m^{-3})	8×10^5
Tangential stiffness of parallel bond/$\overline{k_s}$ (kN·m^{-3})	2×10^5
Parallel bond tensile strength/$\overline{\sigma_c}$ (kPa)	5×10^3
Parallel bond cohesion/$\overline{c}$ (kPa)	1×10^3
Internal friction angle of parallel bonding/$\overline{\phi}$ (°)	32

4.2. Numerical Analysis of Crater Settlement

In the numerical model, seven monitoring points were arranged at different depths below the centerline to monitor the crater settlement after six drops of tamping. Figure 11 shows the crater settlement curves for different tamping energies (800, 1500, and 2000 kJ). The deformation curves oscillated significantly under the three input energies and could be divided into three main stages: tamping settlement, resilient deformation, and soil equilibrium. After each drop of tamping, the coral sand foundation experienced resilient deformation, and the compaction of the foundation soil, plastic deformation, and an increase in soil density were all caused by the tamping energy. The first drop of tamping was extraordinary, producing a significantly larger crater depth than the other five drops; however, the individual settlement in the second drop appeared to be larger at a low input energy (800 kJ). This may have been because the coral sand in the first drop of tamping was partially broken when the energy was low (800 kJ), and it developed significant crushability and subsidence in the second tamping. With the increase in the tamping drops, the stiffer the foundation soil, the smaller the subsidence deformation and lager the rebound deformation. This trend became more pronounced as the depth increased.

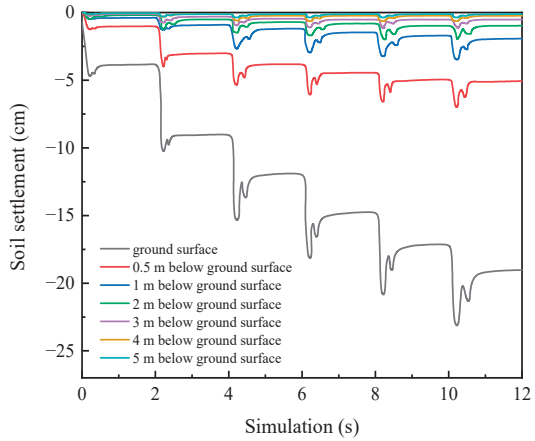

(**a**) 800 kJ

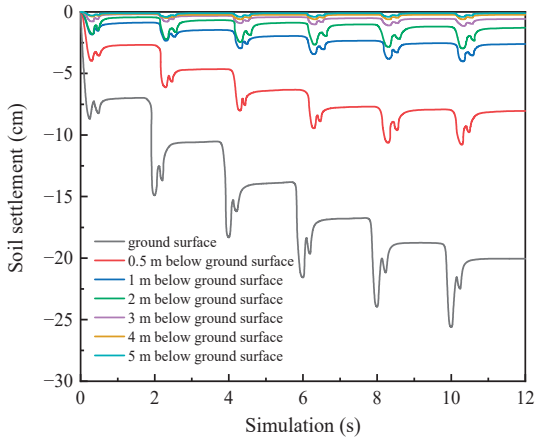

(**b**) 1500 kJ

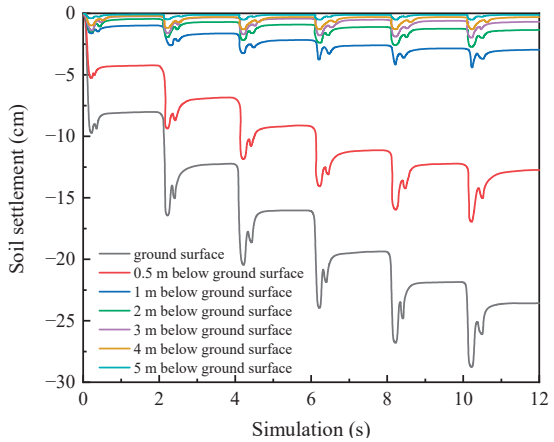

(**c**) 2000 kJ

Figure 11. Settlement curves of three tamping energies.

The vertical deformation response to the tamping energy varied at different depths. The surface subsidence was the largest and gradually decreased until it disappeared as the stress wave generated by the tamping energy propagated along the depth and was constantly attenuated. Furthermore, when the soil was compacted to its maximum possible density under the applied tamping energy, the rigid soil in the reinforced zone did not absorb the tamping energy but rather transmitted it. Moreover, most of the energy was consumed during the damping or shear deformation of the reinforced soil. This implies that additional drops of tamping would no longer produce compaction; thus, no further

improvement would be achieved. When the soil depth reached 3 m, the crater settlements at 800, 1500, and 2000 kJ tamping energies were only 0.50, 0.55, and 0.65 cm, respectively. The effective reinforcement depths under the three tamping energies were generally within the range of 3.0 m underground, which is consistent with the SPT data.

Figure 12 shows the displacement vector diagram of the coral sand foundation after tamping at different energies. The coral sand particles splashed around the tamping pit when the tamping energy was large (2000 kJ), and a certain degree of uplift on both sides of the crater was observed. This was because the coral sand on both sides was squeezed by the sand in the central reinforced area, resulting in an uplift caused by shear failure. The higher the tamping energy, the more noticeable the bulge. The displacement below the crater exhibited a radioactive distribution centered on the tamping point. The zone affected by tamping was primarily vertical, and the horizontal extension was subordinate. The settlement immediately below the rammer was the largest. The vertical deformation was smaller at a distance from the tamping center.

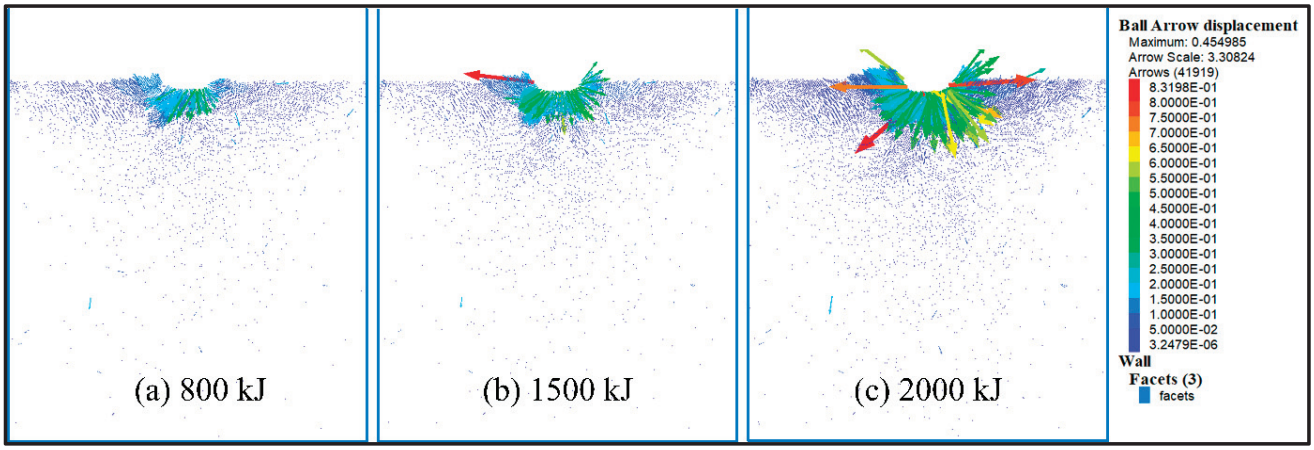

Figure 12. Displacement vector of coral foundation after tamping under different energy levels.

4.3. Numerical Analysis of Particle Breakage

Coral sand, a crushable granular material, produces large amounts of particle breakage at DC power. Therefore, investigating the development and evolution of particle breakage during DC is crucial. The number of cracks is monitored through the built-in FISH language to evaluate the breakage of the CRS. Figure 13 shows a cloud image of the particle breakage distribution under different hammering energies. At the end of tamping, the CRS particles were obviously broken, mainly by shear failure, indicating that the external force on the coral sand particles at this time was much greater than the parallel bond shear strength. With the increase in tamping energy d, the more thoroughly the coral sand was broken, the more cracks were significantly increased; the numbers of cracks under the three tamping energies were 540, 759, and 835, respectively. Under the tamping impact, the particle crushing zone was initially distributed below the ramming point, and it gradually developed toward both sides of the crater as the ramming number increased. The compaction energy also significantly influenced the particle breakage, primarily reflected in the depth and breadth of the coral sand ground. The particle crushing under 2000 kJ compaction was the highest; that is, the number of particles crushed after DC was the largest, with a wider impact range. Based on the coordinate data of the fracture zone, the depth at which the coral sand particles were broken under a 2000 kJ tamping energy was primarily distributed at approximately 3 m at the bottom of the crater.

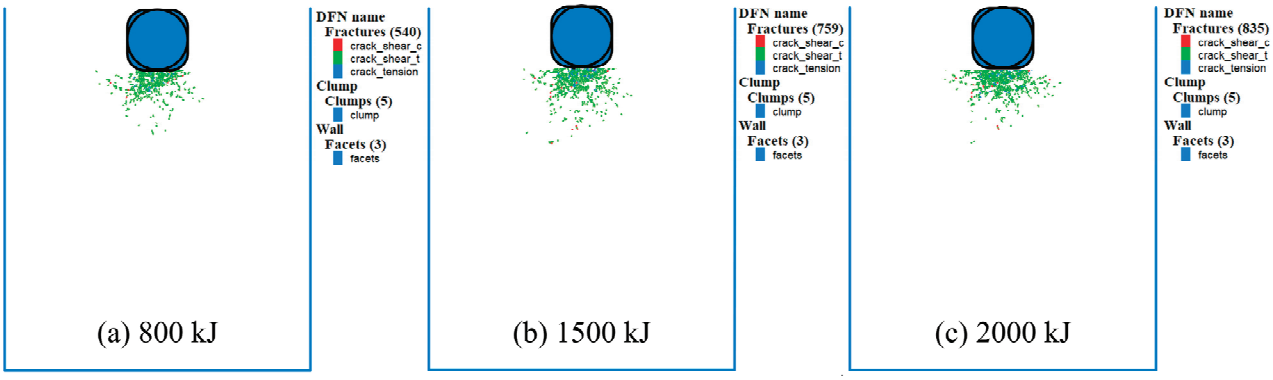

Figure 13. Development of particle breakage after tamping under different energy levels.

Particle overlap occurred among the coral sands under impact loading, and contact stress was generated. The numerical results revealed that the force chain development was relatively similar for all three hammering energies. Figure 14 shows that the force chains were tree-shaped and developed toward the ground depth. The thicknesses of the lines represent the contact stress between the particles. The force chains were primarily concentrated immediately below the tamping point, and the amount of vertical force chains started to increase, gradually thickened, and developed toward both sides as the ramming energy increased. This indicates that the dynamic stress squeezed the soil on both sides, forming a strong chain under the tamping crater and a weak force chain on both sides. The impact stress wave primarily propagated vertically along the sand particles, and the vertical dynamic stress was significantly higher than the horizontal dynamic stress. The pores of the soil below the tamping point decreased with closer contact, and vertical compression dominated. The particle contact force chains increased and developed deeply toward the ground with increased tamping energy until the damping of the soil completely expanded the dynamic stress.

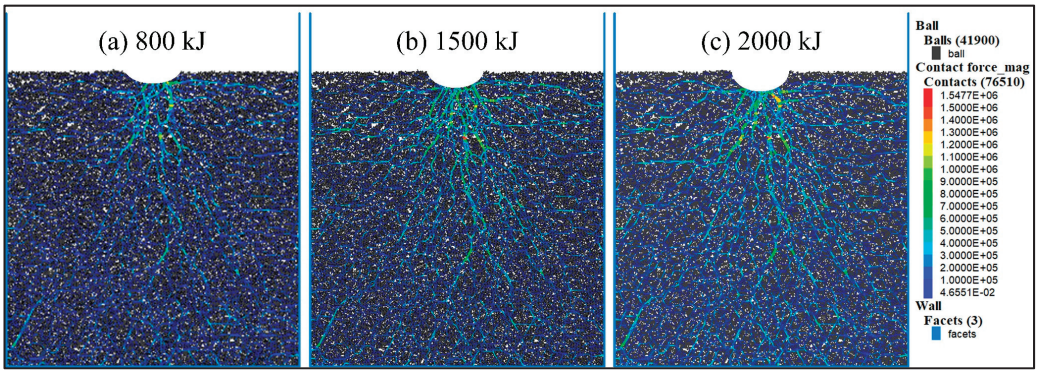

Figure 14. Cloud chart of force chain after tamping under different working conditions.

5. Conclusions

This study performed a series of field tests combined with the two-dimensional particle flow discrete element method to investigate the whole process of coral sand ground compacted by DC and demonstrated the reinforcement effect. The conclusions obtained are given below:

(1) In both reinforced regions (A_1 and A_2), the first drop in impact during the three passes (first two tamping points and last full tamping) produced the largest crater settlement, and the crater settlement gradually increased. Full tamping was necessary for the final tamping; the coral sand was well strengthened, and the average total settlements for A_1 and A_2 were 0.379 and 0.419 m, respectively.

(2) After ground treatment by DC, the allowable ground bearing capacity in both reinforced regions was at least 360 kPa, satisfying the design requirements. The DC method proved to be valid for dealing with reclaimed coral sand.
(3) The SPT field data indicated that the DC reinforcement depths at A_1 and A_2 were 3.5 and 3.2 m, respectively. The improvement at the impact points was commonly superior to that in the regions between the impact points in the two testing regions. Appropriate spacing of the impact points was necessary to guarantee a uniform strengthening effect in the construction areas.
(4) The DC process for coral sand grounds was reproduced using the particle flow discrete element method. The reinforcement effect and effective reinforced depth were numerically analyzed. The numerical results were consistent with the field investigation data. The fragmentation zone of coral sand caused by DC was primarily distributed immediately below the crater and gradually developed on both sides of the crater with increasing compaction time. The particle force chains after tamping were strong chains in the vertical direction of the crater and weak chains on both sides. This indicates that the particles directly below the ramming point were broken more thoroughly, and the contact between the particles was closer. The dynamic stress wave from the DC energy propagated primarily in the vertical direction.

The scientific results of this research serve as a relevant reference for further study on the DC mechanism involving CRS as a foundation for structures.

Author Contributions: Methodology, L.G.; Writing—original draft, L.G. and W.Y.; Writing—review & editing, L.G., W.Y., Z.W., J.W. and G.Y. All authors have read and agreed to the published version of the manuscript.

Funding: This research was funded by [The National Key Research and Development Program] grant number [No. 2023YFC3106502], [The National Natural Science Foundation of China] grant number [No. 42002266] and [The Fundamental Research Funds for the Central Universities] grant number [No. 30924010840]. And The APC was funded by [The Fundamental Research Funds for the Central Universities].

Institutional Review Board Statement: Not applicable.

Informed Consent Statement: This study did not involve humans.

Data Availability Statement: Data are contained within the article.

Acknowledgments: The authors would like to thank the worker who completed the sampling and field test for coral reef sand.

Conflicts of Interest: The authors declare no conflicts of interest.

References

1. Zhao, H.T. Researched of coral reef in modern China. *World SCI-Tech R&D* **1998**, *4*, 98–105. (In Chinese)
2. Mejia, L.; Yeung, R. Liquefaction of coralline soils during the 1993 Guam earthquake. Session on Seismically-Induced Movements of Foundations and Abutments. In Proceedings of the 1995 ASCE National Convention, San Diego, CA, USA, 22–26 October 1995; pp. 33–48.
3. Qiu, W.J.; Yang, H.P.; He, Y.X.; Yu, D.H. Experimental study on coral reef sand as foundation filling material and vibroflotation reinforcement. *J. Geotech. Eng.* **2017**, *39*, 1517–1523. (In Chinese)
4. Ohno, S.; Ochiai, H.; Yasufuku, N. Estimation of pile settlement in Calcareous sands. In *Engineering for Calcareous Sediments*; Al-Shafei, K.A., Ed.; Baklkema: Rotterdam, The Netherlands, 1999; pp. 1–6.
5. Lee, C.Y.; Poulos, H.G. Tests on model instrumented grouted piles in offshore calcareous soil. *J. Geotech. Eng.* **1991**, *117*, 1738–1753. [CrossRef]
6. Ismail, M.A.; Joer, H.A.; Sim, W.H.; Randolph, M.F. Effect of cement type on shear behavior of cemented calcareous soil. *J. Geotech. Geoenviron. Eng.* **2002**, *128*, 520–529. [CrossRef]
7. Consoli, N.C.; Cruz, R.C.; Floss, M.F.; Festugato, L. Parameters controlling tensile and compressive strength of artificially cemented sand. *J. Geotech. Geoenviron. Eng.* **2010**, *136*, 759–763. [CrossRef]
8. Xiao, Y.; Stuedlein, A.W.; Chen, Q.; Liu, H.L.; Liu, P. Stress-strain strength response and ductility of gravels improved by polyurethane foam adhesive. *J. Geotech. Geoenviron. Eng.* **2018**, *144*, 04017108. [CrossRef]

9. Liu, L.; Liu, H.L.; Stuedlein, A.W.; Evans, T.M.; Xiao, Y. Strength, stiffness, and microstructure characteristics of biocemented calcareous sand. *Can. Geotech. J.* **2019**, *56*, 1502–1513. [CrossRef]
10. DeJong, J.T.; Soga, K.; Kavazanjian, E.; Burns, S.; van Paassen, L.A.; Al Qabany, A.; Aydilek, A.; Bang, S.S.; Burbank, M.; Caslake, L.; et al. Biogeochemical processes and geotechnical applications: Progress, opportunities and challenges. *Géotechnique* **2013**, *63*, 287–301. [CrossRef]
11. Montoya, B.M.; DeJong, J.T.; Boulanger, R.W. Dynamic response of liquefiable sand improved by microbial-induced calcite precipitation. *Géotechnique* **2013**, *63*, 302–312. [CrossRef]
12. Van Paassen, L.A.; Ghose, R.; van der Linden, T.J.M.; van der Star, W.R.L.; van Loosdrecht, M.C.M. Quantifying biomediated ground improvement by ureolysis: Large-scale biogrout experiment. *J. Geotech. Geoenviron. Eng.* **2010**, *136*, 1721–1728. [CrossRef]
13. Feng, S.J.; Du, F.L.; Shi, Z.M.; Shui, W.H.; Tan, K. Field study on the reinforcement of collapsible loess using dynamic compaction. *Eng. Geol.* **2015**, *185*, 105–115. [CrossRef]
14. Zhou, C.; Yang, C.; Qi, H.; Yao, K.; Yao, Z.; Wang, K.; Ji, P.; Li, H. Evaluation on improvement zone of foundation after dynamic compaction. *Appl. Sci.* **2021**, *11*, 2156. [CrossRef]
15. Hu, B.; Wang, R.; Hu, M.J.; Wang, X.Z. Experimental study on dynamic compaction treatment of hydraulic reclamation sand foundation. *Rock Soil Mech.* **2007**, *28*, 89–92. (In Chinese)
16. Zhou, J.; Cui, J.H.; Jia, M.C.; Shi, D.D. Experimental study on soft foundation treatment with hydraulic fill fine sand. *Rock Soil Mech.* **2008**, *04*, 859–864. (In Chinese)
17. Feng, S.J.; Tan, K.; Shui, W.H.; Zhang, Y. Densification of desert sands by high energy dynamic compaction. *Eng. Geol.* **2013**, *157*, 48–54. [CrossRef]
18. Nashed, R.; Thevanayagam, S.; Martin, G.R. Dynamic compaction of saturated sands and silty sands: Results. *Ground Improv.* **2009**, *162*, 69–79. [CrossRef]
19. Cundall, P.A.; Strack, O.D.L. A discrete numerical model for granular assemblies. *Géotechnique* **1979**, *29*, 47–65. [CrossRef]
20. Wada, K.; Senshu, H.; Matsui, T. Numerical simulation of impact cratering on granular material. *Icarus* **2006**, *180*, 528–545. [CrossRef]
21. Ma, Z.Y.; Dang, F.N.; Liao, H.J. Numerical study of the dynamic compaction of gravel soil ground using the discrete element method. *Granul. Matter* **2014**, *16*, 881–889. [CrossRef]
22. Jia, M.; Yang, Y.; Liu, B.; Wu, S.J. PFC/FLAC coupled simulation of dynamic compaction in granular soils. *Granul. Matter* **2018**, *20*, 76. [CrossRef]
23. *National Standard GB 50021-2001*; Code for Geotechnical Engineering Investigation. Ministry of Housing and Urban-Rural Development of the People's Republic of China: Beijing, China, 2001. (In Chinese)
24. *National Standard GB 50007-2011*; Code for Design of Building Foundation. Ministry of Housing and Urban-Rural Development of the People's Republic of China: Beijing, China, 2011. (In Chinese)
25. Li, G.; Bodahi, F.; He, T.; Luo, F.; Duan, S.; Li, M. Sensitivity analysis of macroscopic mechanical behavior to microscopic parameters based on PFC simulation. *Geotech. Geol. Eng.* **2022**, *40*, 3633–3641. [CrossRef]
26. Wu, H.; Dai, B.; Zhao, G.; Chen, Y.; Tian, Y. A novel method of calibrating micro-scale parameters of PFC model and experimental validation. *Appl. Sci.* **2020**, *10*, 3221. [CrossRef]
27. Liu, X.Y. Macroscopic and Microscopic Study on Mechanical Properties and Fracture Mechanism of Volcanic Soil. Master's Thesis, Jilin University, Changchun, China, 2024. (In Chinese).

Journal of
Marine Science and Engineering

MDPI

Article

Large-Scale Triaxial Test on Mechanical Behavior of Coral Sand Gravel Layered Samples

Xinyue Tang [1,2], Dongfeng Xin [3], Xuewen Lei [1], Ting Yao [2,*], Qingshan Meng [2] and Qingbing Liu [4]

[1] School of Urban Construction, Wuhan University of Science and Technology, Wuhan 430065, China; tangxy@wust.edu.cn (X.T.); leixuewen@wust.edu.cn (X.L.)
[2] State Key Laboratory of Geomechanics and Geotechnical Engineering, Institute of Rock and Soil Mechanics, Chinese Academy of Sciences, Wuhan 430071, China; qsmeng@whrsm.ac.cn
[3] Huajin Aramco Petrochemical Company Limited, Panjin 124205, China; xindongfeng@hapco.com.cn
[4] Badong National Observation and Research Station of Geohazards, China University of Geosciences (Wuhan), Wuhan 430074, China; qingbing@cug.edu.cn
* Correspondence: tyao@whrsm.ac.cn

Abstract: Layered structures comprising coral sand and gravel have been observed in hydraulic filled foundations in the coral reefs in the South China Sea, leading to anisotropy in their physical and mechanical properties. However, the effect of a layered structure on the strength and deformation of the coral soil foundation remains unclear. In this study, a series of large-scale triaxial compression tests and step-loading tests were carried out on four types of samples, i.e., clean coral sand, clean coral gravel, sand-over-gravel layered sample, and gravel-over-sand layered sample, to investigate the impact of confining pressure and the layered structure on the strength and failure modes of these soils. The results indicate that the stress–strain relationships of all samples predominantly exhibit strain hardening under drained conditions. Under identical confining pressures, the peak strength of clean coral sand is the lowest, while that of coral gravel is the highest. The peak strengths of the two layered samples fall between these extremes, with the gravel-over-sand layered sample exhibiting higher strength. All four samples have similar peak friction angles, slightly exceeding 40°. The difference in peak strength among the four types of samples is attributed to the variations in cohesion, with the cohesion of clean coral gravel being up to four times that of clean sand, and the cohesion of layered samples falling between these two. Both clean sand and clean gravel samples exhibit a bulging phenomenon in the middle, while the layered samples primarily exhibit bulging near the coral gravel layer. In the step-loading tests, the bearing capacity of the layered samples falls between those of clean coral sand and coral gravel, with the gravel-over-sand layered samples demonstrating higher strength. Moreover, the *p-s* curve of the gravel-over-sand layered samples obtained from the large-scale triaxial apparatus under a confining pressure of 400 kPa resembles that from the plate load tests on the same samples.

Keywords: coral sand and gravel layered soil; large-scale triaxial test; step loading; failure mode

1. Introduction

In recent years, extensive land reclamation projects have been undertaken in the South China Sea. Due to the considerable distance from the mainland, coral sand is the only available hydraulic filling material. As a result, coral sand and debris from lagoons and outer reef flat were excavated by cutter suction dredgers or hopper suction dredgers and then pumped through pipelines onto the inner reef flat [1–6]. During the transportation and placement of the sand–water mixture, segregation occurred in both the horizontal and vertical directions, leading to heterogeneity in the foundation. In the horizontal direction, coarse particles are deposited near the pipeline, while finer particles tend to accumulate downstream [7]. Vertically, coarse particles settle rapidly at the bottom, whereas finer

particles are deposited at the top, as shown in Figure 1. Consequently, well-sorted gravel and sand layers are observed in the hydraulic filling areas in the coral reefs [8].

Figure 1. Layered coral sand and gravel structure in the hydraulic filling area in a coral reef in the South China Sea.

In nature, this kind of layered deposit is widely observed, particularly in river basins [9], reclaimed land areas [10], and tailing dams built using the up-stream method [11]. Yoshimine and Koike [12] found that the liquefaction resistance of stratified samples is higher than that of uniform sand samples. To date, limited research has focused on the monotonic mechanical behavior of sand with stratified structures. Naeini and Baziar [13] investigated the influence of fines content on the residual strength of layered sand samples and found that the normalized shear strength decreases with an increasing fines content up to 35%. Zhang et al. [14] examined the strength and deformation of tailings with fine-grained interlayers, discovering that the shear strength of the layered structures is significantly lower than that of coarse-grained tailings. Moreover, particle movement varied across different layers, with more pronounced movement observed in the upper layer. The thickness of the fine-grained soil layer significantly affected the stress–strain behavior and failure mode of the samples. Shen et al. [15] studied the undrained shearing behavior of artificial clay and silt layered samples and found that the friction angle of the layered samples lies between those of sand and clay. Therefore, the monotonic and dynamic mechanical behavior of layered samples may be either under-estimated or over-estimated when examining homogeneously reconstituted samples.

Coral deposits are mainly composed of coral, shells, and other marine biological remains, with calcium carbonate content higher than 90% [16]. So far, many studies have investigated the physical and mechanical behavior of coral sand. Due to its biological origin, coral sand displays distinct physical and mechanical behavior compared to terrigenous sediments such as quartz sand. The particle shape of coral sand is notably irregular, and the surface is quite rough due to the existence of intraparticle pores [17,18]. Yao and Li [19] found that the compressibility of coral sand at low stress levels is even lower than that of quartz sand. Under high stress levels, coral sand demonstrates high compressibility primarily due to particle fragmentation [20,21]. The shear strength of coral sand mainly depends on the cohesion and the internal friction angle. Due to the irregular shape of the coral sand particles, the internal friction angle is typically higher than that of quartz

sand [22]. The cohesion of coral sand, resulting from particle interlocking, is a significant factor that cannot be ignored, contributing to a substantially higher shear strength compared to quartz sand. The magnitude of the cohesion is influenced by the particle shape, particle size, and stress level [23]. The bearing capacity of coral sand is a crucial indicator to evaluate its engineering performance. Compared to quartz sand, coral sand exhibits a significantly higher bearing capacity [24]. Consequently, the dredged coral sand could provide satisfactory bearing capacity, with post-construction settlement being found to be insignificant [25].

Nevertheless, the quantity and quality of studies on the mechanical behavior of coral gravels, which are widely distributed in hydraulic filling areas in coral reefs, remain quite limited. Liu et al. [26] studied the single-particle strength of coral gravels with sizes ranging from 5 mm to 20 mm and found that the single-particle strength decreases with increasing particle size, while the apparent cohesion of coral gravel increases with increasing particle size [27]. Wu et al. [28] conducted large-scale dynamic triaxial tests on coral sand–gravel mixtures and discovered that the liquefaction resistance of the mixture is much higher than that of clean coral sand, as the addition of coral gravel forms a more stable structure. The mechanical properties of the layered samples differ from those of naturally deposited homogenous sand. Considering the segregation of coral sand and gravels, Fu et al. [29] examined the bearing characteristics of coral sand and gravel-layered samples through plate-loading tests. It was discovered that the bearing capacity of the layered sample increases with the thickness of the upper gravel layer. However, the effect of the anisotropy of the layered structure of coral gravel and sand on the shearing behavior of coral soil remains unknown.

In the current work, a series of monotonic large-scale triaxial tests was carried out on both homogenous samples and layered samples of coral sand and gravel to investigate the effect of the layered structure on the shearing behavior of coral deposits. The stress–strain relationship and the shear strength of the samples were carefully analyzed and compared. In addition to the triaxial tests, step-loading tests were performed using the large-scale triaxial apparatus to study the bearing capacity of the layered samples. Both the coral sand and gravel were collected from a dredged area in a coral reef in the South China Sea. The maximum particle size of the gravels used in this study was 60 mm, due to the size limitations of the triaxial apparatus.

2. Experimental Programs

2.1. Test Materials and Apparatus

In this study, the tested coral sand and coral gravel were sourced from a coral reef in the South China Sea. As shown in Figure 2, the particle shape of both the coral gravel and sand is quite irregular, and the surfaces are fairly rough with abundant intraparticle pores.

To quantitatively characterize the particle morphology of both materials, a Microtrac PartAn^{3D} Maxi (Montgomeryville, PA, USA) dynamic image analysis apparatus was employed. This system employs a high-speed, high-resolution camera to capture multiple images of each particle from arbitrary orientation. The images are then digitized and processed by the PartAn^{3D} (Version: PartDP-GC-20151002T143858) software, which measures particle length, width, thickness, perimeter, and area. Based on these measurements, morphological parameters, including aspect ratio, roundness, and sphericity, are calculated. This method allows for noncontact measurements of dry particles ranging in size from 0.16 to 135 mm.

Figure 3a presents multiple digital images of individual coral sand and gravel particles, offering a visual comparison of their morphological properties. In the current work, sphericity and roundness are employed to quantitatively assess the particle shape, which are defined as follows:

$$\text{Roundness R} = 4\text{A}/\pi FL^2 \tag{1}$$

$$\text{Sphericity S} = 4\pi\text{A}/P_{\text{p}}^2 \tag{2}$$

where A represents the particle's projected area; *FL* is the largest Feret diameter (the maximum distance between two paralleled planes that bound the particle perpendicularly), and P_p is the particle perimeter. In general, higher values of roundness (R) and sphericity (S) indicate that the particle is more rounded and closer to a sphere shape. As shown in Figure 3a, the roundness of branch-shaped particle 3 is only 0.29, which is much lower than that of rodlike particle 5 (0.84).

(**a**) (**b**)

Figure 2. The tested coral sand and gravel: (**a**) coral sand; (**b**) coral gravel.

However, an individual particle or a few particles is not representative of the entire sample. To provide a more comprehensive view, the cumulative distributions of roundness and sphericity of both coral gravel and sand are shown in Figure 3b. The mean values of sphericity of coral sand and gravel are similar, with both falling approximately at 0.83, which is similar to those found by Wei et al. [30]. The mean value of roundness of coral sand is 0.42, which is much higher than that of coral gravel (0.30), indicating that the particle shape of coral gravel is much more angular.

Mineral composition analysis of both materials was performed using a diffractometer (D8 Advance, Bruker, Karlsruhe, German) in accordance with the SY/T5163-201 standard [31]. Figure 4 shows the X-ray diffraction test results, revealing that the coral gravel and the coral sand are predominantly composed of aragonite and calcite, with calcium carbonate ($CaCO_3$) content in both materials exceeding 95%. The maximum particle size allowed by the large-scale triaxial apparatus used in this study is 60 mm; therefore, gravels coarser than 60 mm were removed prior to the test. Figure 5 shows the particle size distributions of coral sand and gravel. The particle size distribution curve of the coral sand is notably uneven, with a coefficient of uniformity (C_u) of 4.53 and a coefficient of curvature (C_c) of 0.9. According to the Unified Soil Classification System (ASTM D2487-00 2016) [32], the conditions of $C_u > 5$ and $1 < C_c < 5$ are not met, indicating poor gradation of coral sand. Similarly, the coral gravel sample also exhibits poor gradation. The minimum and maximum dry densities of the coral gravel were determined using the large-diameter cylinder method and surface vibration compaction method, respectively, in accordance with the Chinese National Standard of Soil Test Method (GB/T50123–2019) [33]. The basic physical parameters of the tested coral sand and gravel are summarized in Table 1.

The experiments were conducted using a large-scale static and dynamic triaxial apparatus (TAJ-2000, Tianshui Hongshan Test Machine Co., Tianshui, China), as depicted in Figure 6. This device comprises a confining pressure control system, an axial pressure control system, and a data acquisition system. It is capable of performing tests on coarse-grained soil with sizes finer than 60 mm, as the sample size is 300 mm in diameter and

600 mm in height. The maximum allowable confining pressure of the apparatus is 10 MPa, and the maximum axial loading force is 2000 kN. A linear variable displacement transducer (LVDT) (Sino Co., Guangzhou, China) with a resolution of 0.1 mm is located on the top of the chamber to measure the axial strain of the samples during shearing, and the maximum displacement range is 300 mm.

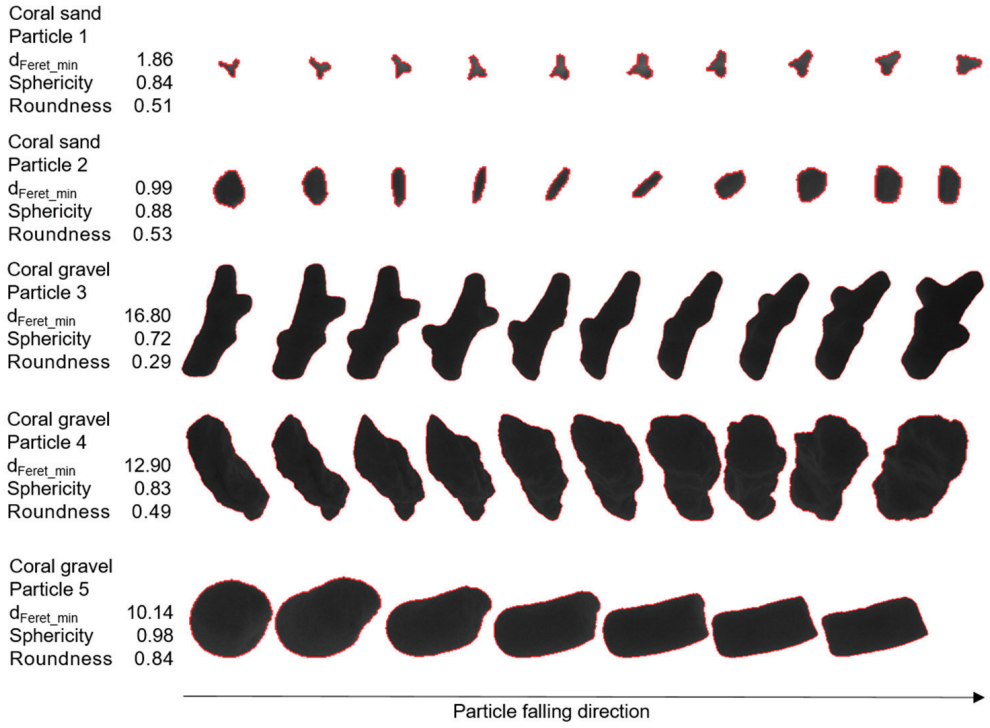

(**a**)

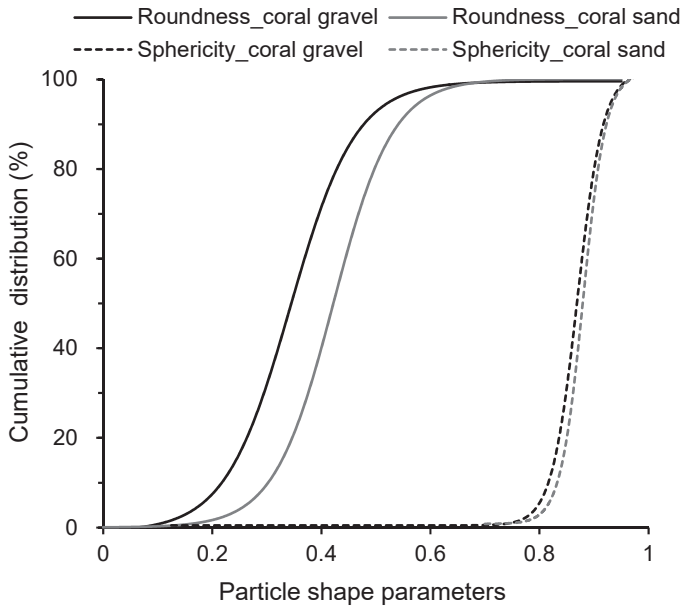

(**b**)

Figure 3. Quantification of particle shape of coral sand and gravel: (**a**) individual particles; (**b**) cumulative distributions of sphericity and roundness.

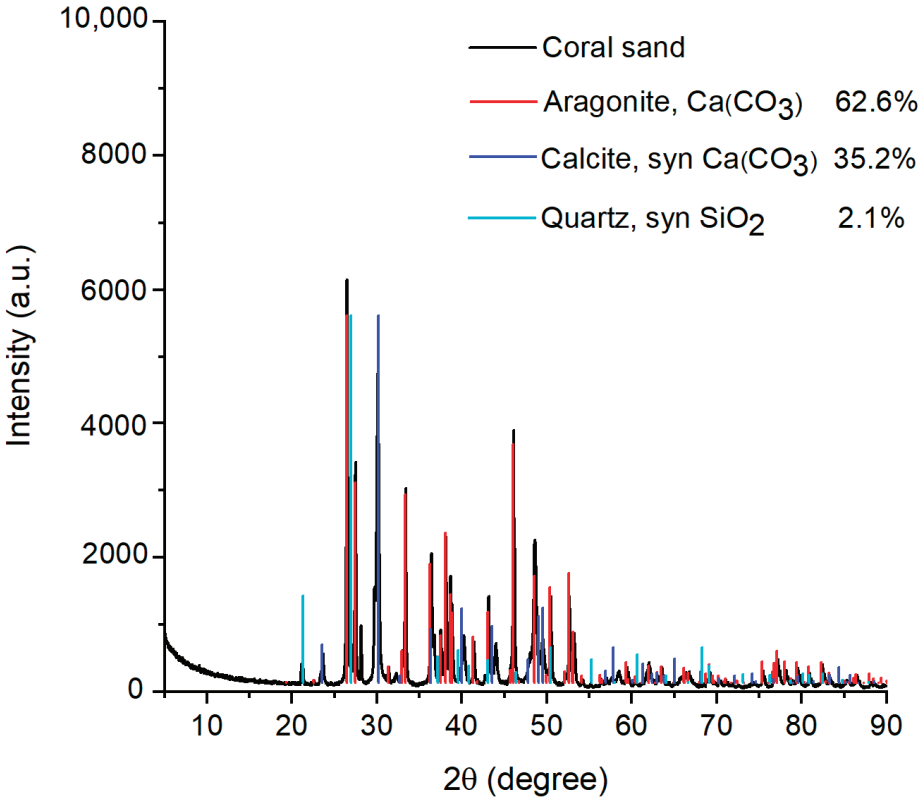

(a)

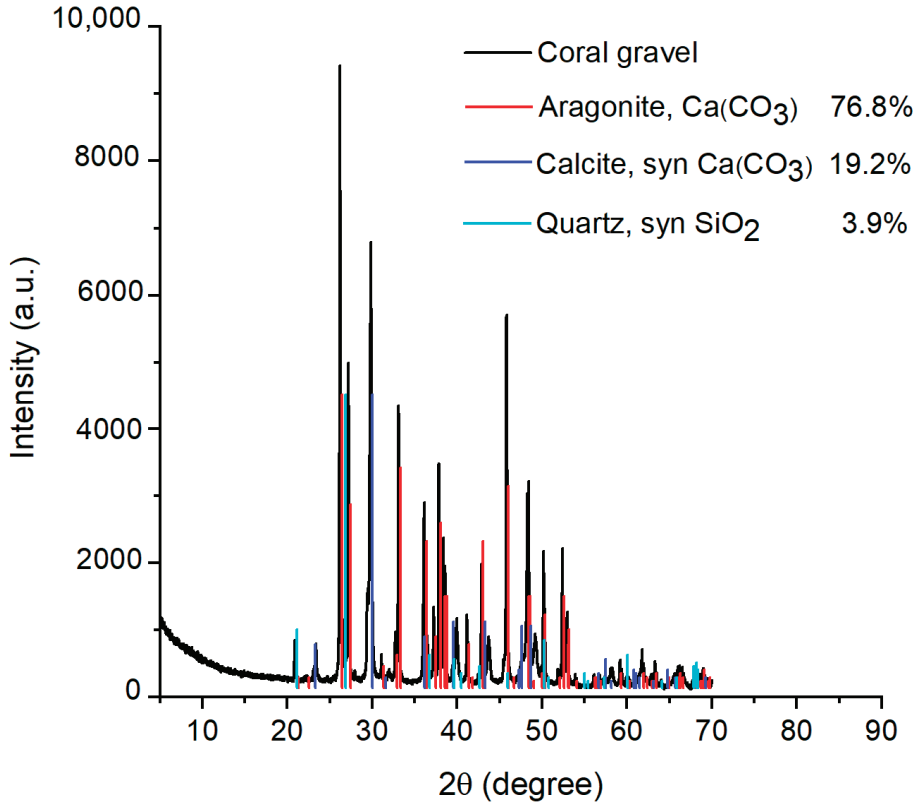

(b)

Figure 4. XRD test results of tested materials: (**a**) coral sand; (**b**) coral gravel.

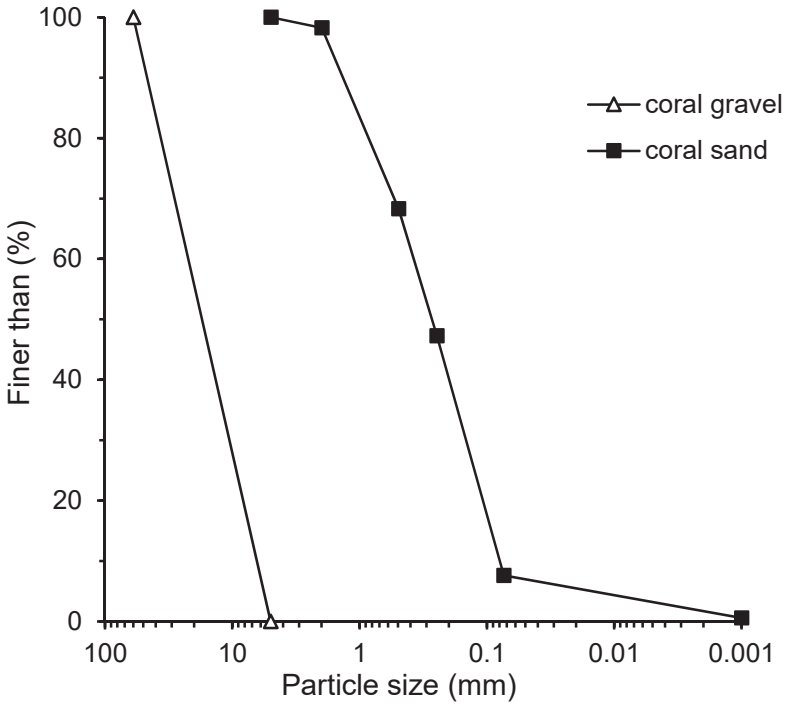

Figure 5. Particle size distributions of coral sand and gravel.

Table 1. Physical parameters of coral sand and gravel.

Sample	Maximum dry Density ρ_{d_max} (g/cm^3)	Minimum Dry Density ρ_{d_min} (g/cm^3)	Specific Gravity G_s	Water Content w (%)	C_u	C_c
Coral sand	1.80	1.25	2.79	0.5	4.53	0.9
Coral gravel	1.32	1.07	2.80	0.5	3.62	1.15

Figure 6. Large-scale triaxial test apparatus.

2.2. Test Procedure

In this study, a series of large-scale triaxial consolidation drained shearing tests was conducted on four types of samples, which are clean coral sand, clean coral gravel, a sand-over-gravel layered sample, and a gravel-over-sand layered sample, as shown in Figure 7. These tests aimed to understand the mechanical behavior of different foundation structures formed by hydraulic filling. During this process, hydraulic sorting results in a layered foundation structure with an alternating distribution of coral sand and gravel. Hence, two kinds of layered samples were tested: one sample with a sand layer on the top and the other one with a gravel layer on the top, as shown in Figure 7b,c.

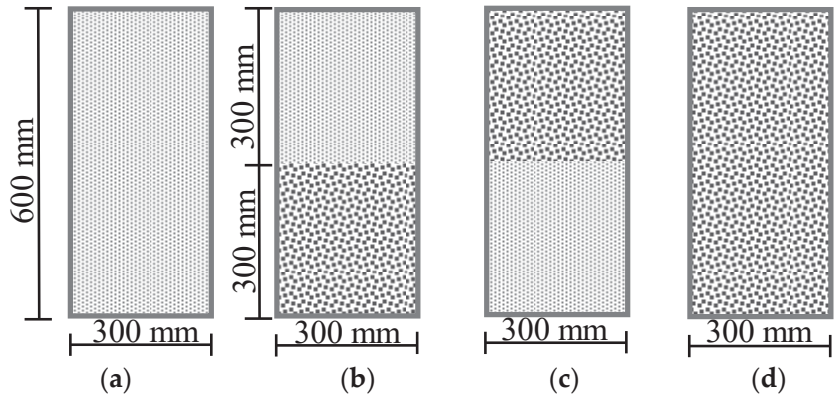

Figure 7. Schematic diagram of four types of samples: (**a**) coral sand; (**b**) sand-over-gravel layered sample; (**c**) gravel-over-sand layered sample; (**d**) coral gravel.

To compare the differences in the stress–strain relationship and peak strength between homogenous samples and layered samples, the relative densities of all samples were controlled as 80% according to the findings by Wang et al. [9] and Yao and Li [34]. The samples were directly prepared on the large-scale triaxial apparatus pedestal using the dry tamping method, where pre-determined quantities of oven-dried coral sand or gravel were compacted in 10 layers using a cylindrical tamper. To ensure the uniformity of the sample, the undercompaction technique introduced by Ladd [35] was adopted. Prior to sample reconstruction, the membrane was carefully marked at every 60 mm using an oil marker to strictly control the height of each layer. For the layered samples, both the thickness of the gravel and sand layers were 300 mm. To avoid particle breakage during sample preparation, care was taken during compaction based on the experience of Yao and Li [19]. After preparation, both the height and diameter of the sample were accurately measured to facilitate the calculation of the initial void ratio. The samples were flushed with carbon dioxide and then with de-aired water for approximately 6 h, and subsequently saturated with a back pressure higher than 200 kPa until the B value exceeded 0.95. After saturation, the samples experienced isotropic consolidation to the desired confining pressure and were subjected to shearing under drained conditions at a shearing rate of 0.5 mm/min until the axial strain stabilized or reached 15%. The confining pressures were 200 kPa, 400 kPa, 600 kPa, and 800 kPa; therefore, 16 tests were conducted in total. The testing program is summarized in Table 2.

In practical engineering projects, the bearing capacity of foundations is typically assessed using on-site plate-load tests. However, discrepancies exist between the stress states experienced by the soil under plate load and those under actual building foundations. Studies have shown that both the bearing capacity and the deformation modulus of the foundation increases with increasing confining pressure [36]. Moreover, the filling material is often non-homogenous, especially in reclaimed land areas. Nevertheless, the influence of the confining pressure and anisotropy on the bearing capacity of coral deposits foundation remains poorly understood. In addition to the conventional triaxial compression tests, step-loading tests using the large-scale triaxial apparatus were also conducted on the four

types of samples. During the step-loading tests, an axial load was applied to the samples in increments of 7 KN, and the vertical strain was recorded at each loading level. The resulting *p-s* curves of the gravel-over-sand layered samples were then compared with the plate load tests on the identical layered samples performed by Fu et al. [29].

Table 2. Test program.

Type of Sample	Confining Pressure (kPa)	Type of Test
Clean coral sand	200, 400, 600, 800	large-scale triaxial test
Clean coral gravel	200, 400, 600, 800	
Sand-over-gravel layered sample	200, 400, 600, 800	
Gravel-over-sand layered sample	200, 400, 600, 800	
Clean coral sand	400	step-loading tests
Clean coral gravel	400	
Sand-over-gravel layered sample	400	
Gravel-over-sand layered sample	200, 400, 600, 800	
23 tests in total		

3. Test Results

3.1. Stress–Strain Relationship

Figure 8 depicts the stress–strain relationship of four types of samples under drained conditions with increasing confining pressure. As can be seen from Figure 8a, the stress–strain relationship of coral sand exhibits strain hardening under different confining pressures without an obvious peak of the deviatoric stress ($\sigma_1 - \sigma_3$). At low stress levels ($\leq$200 kPa), the stress increases rapidly with axial strain, reaching a peak at a relatively low axial strain (3% to 8%) and then keeps constant at large strains. According to studies on the shearing behavior of uniform coral sand finer than 2.0 mm, the strain-hardening behavior usually occurs at high stress levels due to significant particle breakage [34,37]. In the current work, the tested coral sand contained more than 20% particles coarser than 5.0 mm. Under shearing, the inter-particle voids of the samples are compressed, and the volume of the samples decreases. As a result, the samples display strain hardening even under relatively low confining pressure. When the confining pressure increases up to 400 kPa, even the samples undergo strain hardening, the stresses keep on increasing with axial strain, and a less obvious stabilization can be observed at the end of the test. This behavior is possibly due to the particle breakage under high stress levels in coral sand and that the finer particles generated from the breakage fill the pores between larger particles, causing continued volumetric contraction and a consequent increase in deviatoric stress with axial strain [38]. In the current work, quantifying the particle breakage of coral sand or gravel is challenging due to the large sample mass (50–70 kg). However, information on the particle breakage of coral sand can be found in the literature [39–41].

Figure 8b shows the stress–strain relationship of coral gravel under drained conditions. Similar to those of clean coral sand, the coral gravel samples also displayed strain hardening under different stress levels. Differently from that of coral sand, under high stress levels ($\geq$400 kPa), the stress of clean coral gravel tends to stabilize at the axial strain around 8–10%. The maximum particle size of the gravels is up to 60 mm. According to the findings of Liu and Li [42], the single-particle strength of coral gravel increases with increasing particle size. Additionally, the particle shape of gravels is quite angular compared to coral sand as can be seen from Figures 2 and 3. During shearing, the inter-particle friction of coral gravels is much higher than those of coral sand. Consequently, it is hypothesized that the particle breakage of coral gravel is much lower than that of coral sand, resulting in less volumetric change under shearing.

In this study, two kinds of coral sand and gravel-layered samples were tested. The test results of the sand-over-gravel layered samples are illustrated in Figure 8c. Similar to those of clean coral sand and gravels, the sand-over-gravel layered samples also exhibited strain

hardening even under low confining pressures. When the samples sheared at 200 kPa, a much lower peak strength (734.4 kPa) can be observed in sand-over-gravel layered samples compared to the clean coral gravel (1071.5 kPa). The peak strength of clean coral sand (477.4 kPa) is slightly lower than that of clean coral gravel, resulting in a lower strength of sand-over-gravel layered samples. Figure 8d displays the stress–strain relationship of gravel-over-sand layered samples tested under drained conditions. It can be observed that although the stress–strain curves of the gravel-over-sand layered samples under different confining pressures also show strain hardening, the stresses of the samples at high confining pressures tend to stabilize at relatively lower axial strains. This indicates that for the layered samples, the position of the coral sand and gravel layer affects the stress–strain relationship of the samples, with the curves primarily influenced by the material in the upper layer.

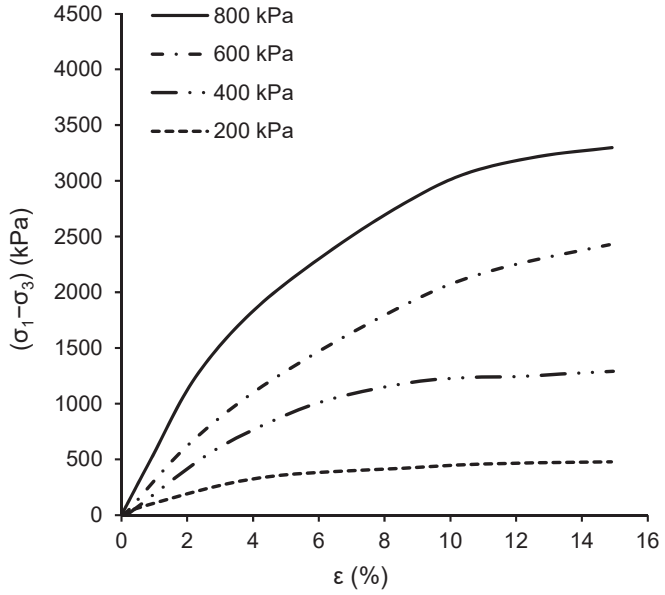

(**a**)

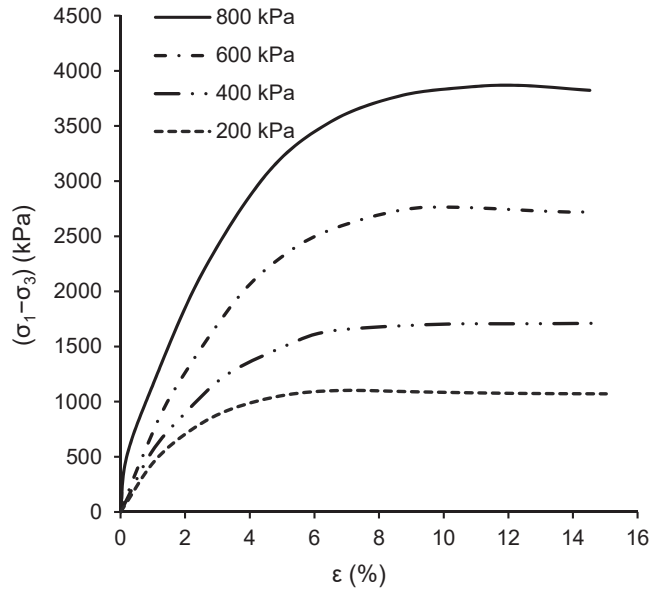

(**b**)

Figure 8. *Cont.*

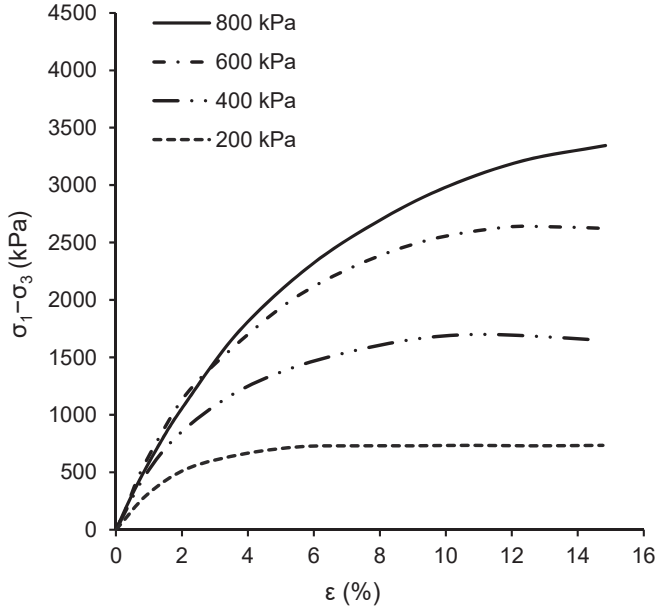

(**c**)

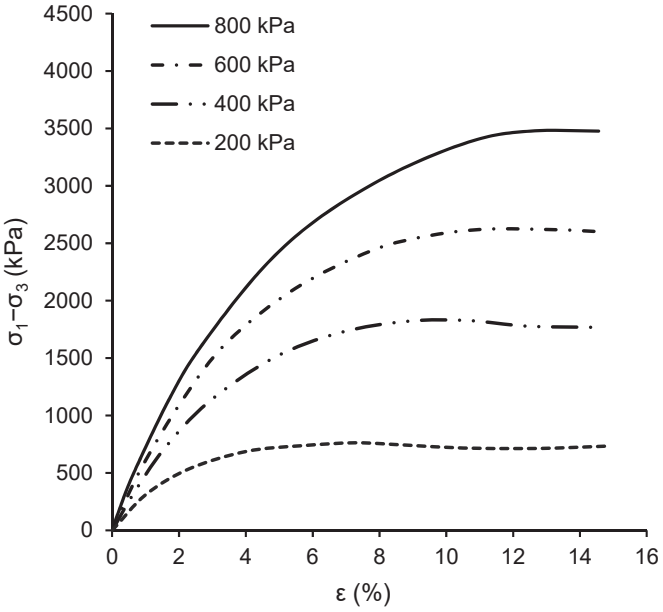

(**d**)

Figure 8. Stress–strain relationships for four types of tested samples: (**a**) coral sand; (**b**) coral gravel; (**c**) sand-over-gravel layered sample; (**d**) gravel-over-sand layered sample.

3.2. Shear Strength

According to the Chinese National Standard of Soil Test Method (GB/T 50123-2019) [33], if there is no distinct peak in the stress–strain curve of a sample under drained conditions, the deviatoric stress at 15% axial strain is generally taken as the peak strength. For samples where the deviatoric stress stabilizes before reaching 15% axial strain, the stabilized value is considered as the peak strength. If the deviatoric stress stabilizes only at 15% axial strain, the strength at 15% axial strain is taken as the peak strength [33]. The peak deviatoric stress of the samples under increasing confining pressures is shown in Figure 9. In the figure, the four variables in the *X*-axis represent the four types of the samples, i.e., clean coral sand, clean coral gravel, sand-over-gravel layered sample, gravel-over-sand layered sample. The peak strength of all the samples increases with increasing confining pressure. Under identical confining pressure, the peak strength of the layered samples falls between

those of clean coral sand and clean coral gravel. Furthermore, for layered samples with the gravel layer on top, the peak strength is higher. This finding suggests that, in layered coral sand and gravel samples, the peak strength is predominantly influenced by the material in the upper layer.

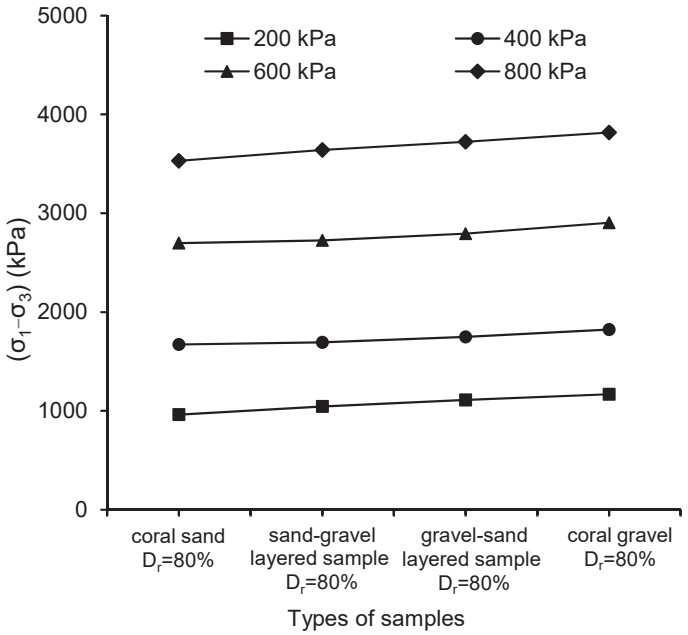

Figure 9. Relationship between peak deviatoric stress and confining pressure of four types of samples with relative density of 80%.

In geotechnical engineering, the Mohr–Coulomb criterion is a fundamental principle used to describe the failure criterion of materials under shear stress. The Mohr–Coulomb failure criterion is mathematically expressed by the following equation:

$$\tau_f = c + \sigma \tan \varphi \tag{3}$$

where τ_f is the shear strength; c denotes the cohesion of the material; σ is the normal stress, and φ is the internal friction angle of the soil.

Thus, the shear strength of soil is composed of cohesion and inter-particle friction. In general, cohesion reflects the inherent strength of the soil due to inter-particle bonding. Sand or gravel, being non-cohesive soil, are typically assumed to be cohesionless. However, in the shear test results of coral sand samples, significant cohesion is observed in the Mohr–Coulomb envelopes [43]. This cohesion primarily arises from the interlocking induced by the irregular shape of coral sand particles.

The Mohr–Coulomb theory is visually represented using Mohr's circle, a graphical method illustrating the relationship between normal stress and shear stress on different planes within the material. Figure 10 shows Mohr's circles for clean coral sand under different confining pressures. In this figure, the envelope tangent to Mohr's circles represents the failure criterion. The slope of the envelope corresponds to the friction angle (tan φ), and the intercept on the Y-axis represents the apparent cohesion (c). The internal friction angle of clean coral sand can be as high as 40°. This value is consistent with research findings on coral sand from other regions, which typically report peak friction angles ranging from 37.8° to 50° [44–46]. Although the single-particle strength of coral sand or gravel is considerably lower than that of quartz sand, its peak friction angle is significantly higher (28–29°) [47], which is attributed to the irregular shape of coral sand particles. The apparent cohesion of clean coral sand calculated from the envelope is around 8 kPa and is believed to result from particle interlocking.

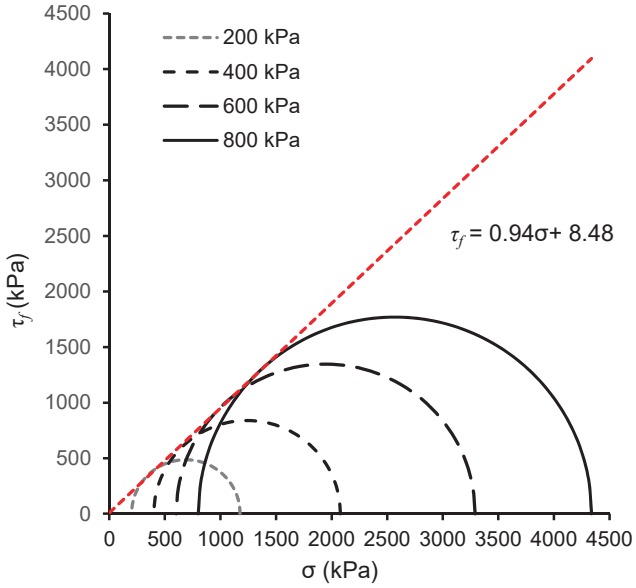

Figure 10. Shear strength envelopes of coral sand.

Based on the triaxial compression data under drained conditions for four types of samples, the shear strength parameters, notably the apparent cohesion and internal friction angle values, were calculated following the Mohr–Coulomb criterion and summarized in Table 3. The difference in the friction angle among the four types of samples is insignificant, while the apparent cohesion varies. Among these samples, coral gravel exhibits the highest apparent cohesion at 35.2 kPa, nearly four times that of clean coral gravel (8.4 kPa). Consequently, clean coral gravel exhibits the highest peak strength under identical confining pressure. Since the layered samples consist of both a coral sand layer and a coral gravel layer, their apparent cohesion falls between that of coral sand and gravel. Notably, the apparent cohesion is significantly higher in the layered samples with the gravel layer on top.

Table 3. Peak strength parameters of tested materials.

Type of Sample	*C* (kPa)	φ (°)
Clean coral sand	8.4	43.2
Clean coral gravel	35.2	44.3
Sand-over-gravel layered sample	13.4	42.8
Gravel-over-sand layered sample	25.8	43.6

3.3. Failure Mode

Due to the large size of the samples, the confining pressure chamber of the large-scale triaxial apparatus is made up of steel. To determine the failure mode of the samples, the chamber was removed, and photographs of the samples were taken. Figure 11 presents the failure modes of the four types of samples sheared at a confining pressure of 200 kPa. All samples exhibit bulging failure modes without the occurrence of strain localization (shear bands). However, the lateral deformation of the samples varies. The coral sand and coral gravel samples present bulging deformation in the middle, while in the layered samples, bulging deformation is mainly observed in the gravel layer. It is also found that the clean coral sand samples exhibit less lateral deformation, whereas the samples containing a gravel layer show more pronounced lateral deformation by visual observation. Figure 12 shows the failure mode of the gravel-over-sand layered sample sheared at a confining pressure of 400 kPa. A much more pronounced bulging phenomenon has been observed in the sample under higher confining pressure. At low confining pressures, the particles in the sample first experience slippage and rearrangement, followed by axial compaction, and then lateral expansion during shearing [48].

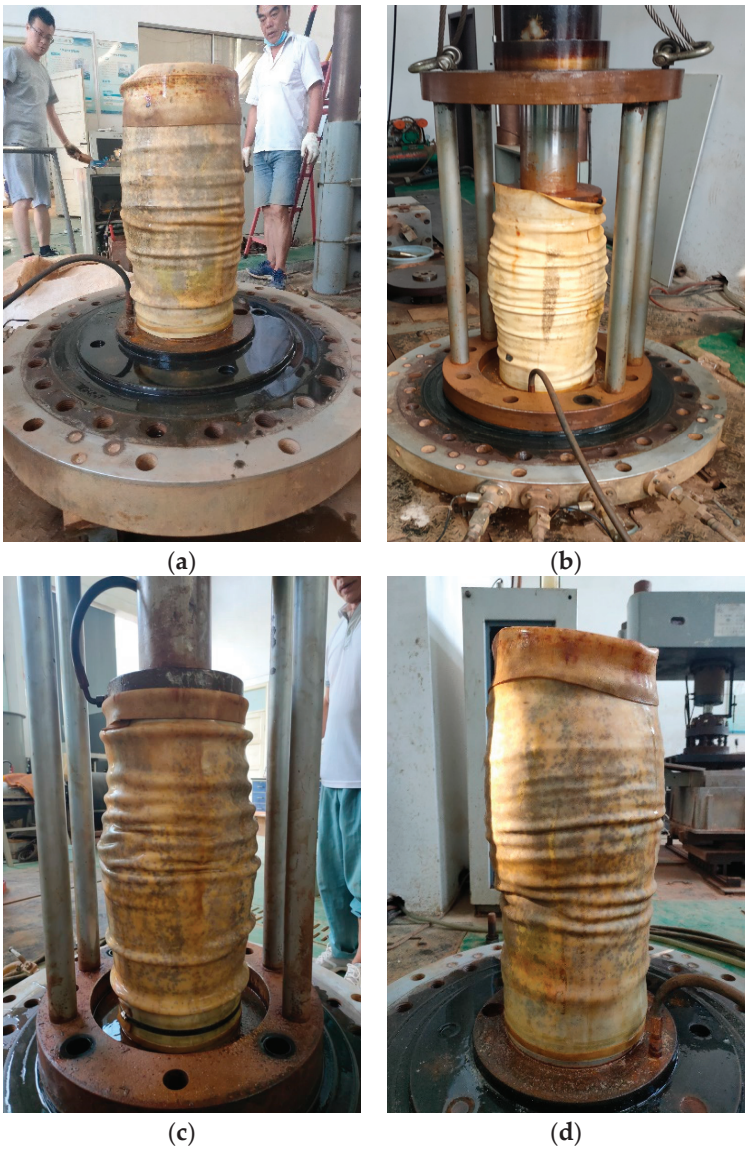

Figure 11. Failure modes of the samples under 200 kPa confining pressure: (**a**) coral sand; (**b**) coral gravel; (**c**) sand-over-gravel layered sample; (**d**) gravel-over-sand layered sample.

Figure 12. Failure mode of the gravel-over-sand layered sample under 400 kPa confining pressure.

4. Step-Loading Test by Large-Scale Triaxial Apparatus

Figure 13 presents the *p-s* curves of four types of samples under a confining pressure of 400 kPa, where *s* represents the axial displacement of the sample under loading, and *p* illustrates the vertical stress, calculated as the axial force over the cross-sectional area of the samples. The *p-s* curves of the four samples could be divided into three segments. Using the sand-over-gravel layered sample as an example, these segments can be described as: (I) the initial linear deformation stage, representing the elastic behavior of the soil in which stress and displacement are directly proportional; (II) the non-linear transition stage, indicating the onset of plastic deformation; (III) the inflection point, characterized by a sharp increase in displacement, which signifies the ultimate bearing capacity of the foundation, and reaching the peak stress before failure. Generally, the ultimate bearing capacity of the foundation is defined by the vertical stress at this inflection point.

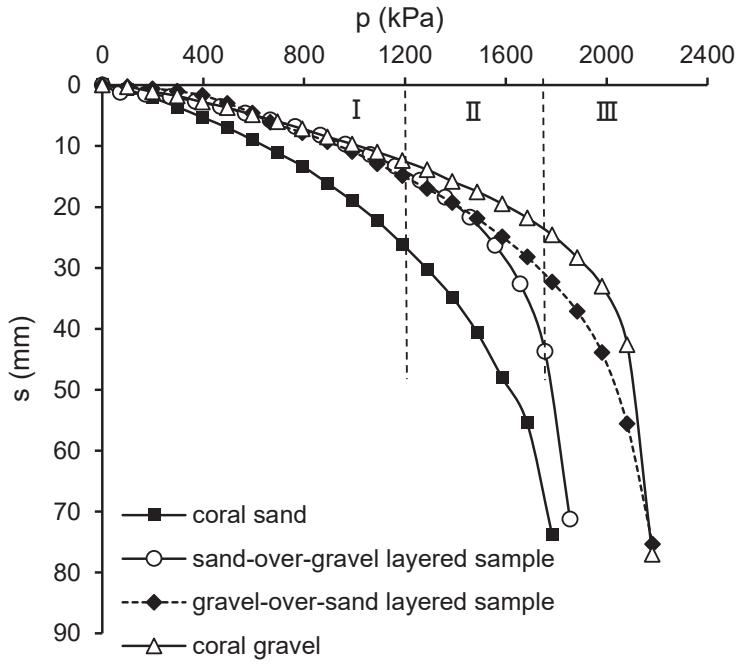

Figure 13. *p-s* curves of different samples under step loading with a confining pressure of 400 kPa.

In Figure 13, the clean coral sand sample exhibits elastic deformation within a load range of 0–792.64 kPa, reaching a settlement of 13.3 mm. By contrast, the layered sample and clean coral gravel sample under the same settlement can bear a load close to 1200 kPa. By comparing the *p-s* curves of the four types of samples, it is found that the bearing capacity of clean coral sand is the lowest, with an ultimate strength of 1684.36 kPa, while the bearing capacity of clean coral gravel is the highest among the four kinds of samples, with an ultimate strength of 2080.68 kPa. The bearing capacities of the layered samples fall between these two extremes, which is 1755.13 kPa for the sand-over-gravel layered sample, and 1981.6 kPa for the gravel-over-sand layered sample. Under the same vertical load, coral gravel exhibit less vertical deformation compared to clean coral sand, indicating higher stability. However, when the load exceeds 1500 kPa, the layered sample with the gravel layer on the top exhibits less axial deformation. In practical reclamation projects, arranging coral gravel on the surface is beneficial for enhancing the bearing capacity of the coral soil foundation.

Figure 14 presents the *p-s* curves of the gravel-over-sand layered samples under different confining pressures, compared with the results from the indoor plate load model tests conducted by Fu et al. [29]. The bearing capacity of the gravel-over-sand layered samples increases significantly with increasing confining pressure, while the deformation shows a decreasing trend. During the indoor plate load model tests, considering the

maximum output of the hydraulic jack and the safety of the reaction frame, the axial load did not exceed 2000 kPa. However, a comparison reveals that within the indoor plate load model tests, the *p-s* relation curve of the gravel-over-sand layered samples closely resembles the results from the triaxial stress staged loading tests under a confining pressure of 400 kPa. This demonstrates that the lateral confining pressure experienced by the soil beneath the loading plate in the indoor plate model tests is similar to 400 kPa.

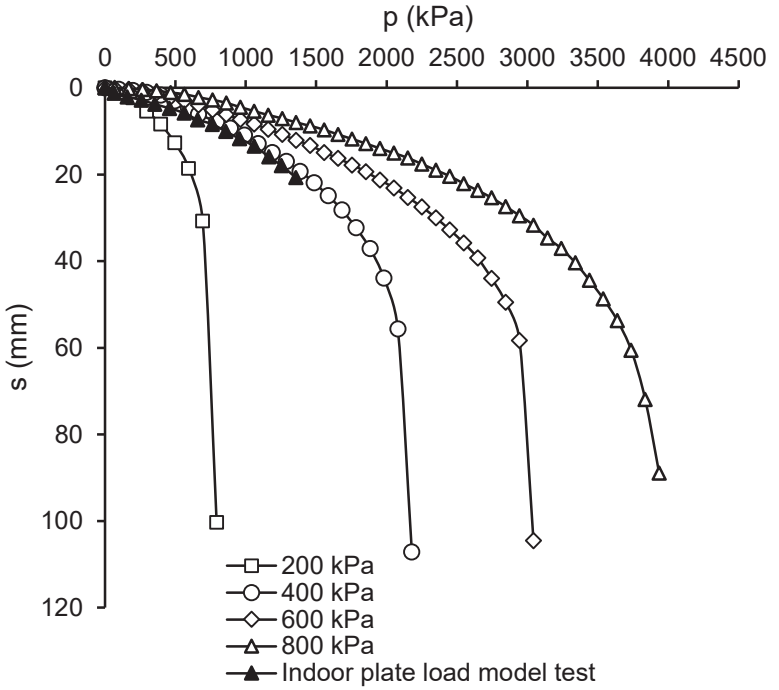

Figure 14. *p-s* curve of gravel-over-sand layered sample under step loading with different confining pressures.

5. Conclusions

In reclaimed foundations within coral reefs, layered structures composed of coral gravel and sand are frequently observed. This study conducted a series of consolidation drained shear test and step-loading test using a large-scale triaxial apparatus on four types of samples: clean coral sand, clean coral gravel, sand-over-gravel layered samples, and gravel-over-sand layered samples. The effect of the layered samples on the internal friction angle and cohesion of coral soil were examined, as well as the impact of confining pressure and the layered structure on the bearing capacity of coral soil foundations.

1. The stress–strain relationships of the four types of samples primarily exhibit strain hardening under drained conditions. Under identical confining pressure, the peak strength of coral sand is the lowest, while coral gravel has the highest peak strength. The strength of the layered samples falls between those two, with the layered samples having coral gravel on the top layer displaying much higher peak strength than those with a sand layer on top.
2. Based on the Mohr–Coulomb calculation, the four samples have similar peak friction angles, at slightly higher than 40°. However, the difference in cohesion is more significant. The cohesion of clean coral gravel can be four times that of clean sand. The layered samples' cohesion falls between these two, while the cohesion of the gravel-over-sand sample is relatively higher.
3. All samples exhibit a bulging failure mode after shearing, with bulging deformation observed in the middle of clean coral sand and gravel samples. In layered samples, bulging deformation is mainly observed in the gravel layer.

4. In the step-loading tests, under identical confining pressure, the bearing capacity of clean coral sand and clean coral gravel are the lowest and the highest, respectively, with the bearing capacity of the layered samples falling between of those two. The bearing capacity of the four types of samples increases with increasing confining pressure. The *p-s* curve obtained by the step-loading tests of the gravel-over-sand sample under 400 kPa confining pressure is close to that obtained in the plate load model tests.

Author Contributions: Investigation, X.T. and X.L.; Writing—original draft, X.T. and T.Y.; Methodology, X.T. and D.X.; Resources, D.X. and Q.M.; Funding acquisition, Q.M. and T.Y.; Data curation, X.T. and X.L.; Visualization, D.X.; Formal analysis, X.T. and X.L.; Writing—review and editing, T.Y. and Q.M., Supervision and Project Administration D.X. and Q.L. Validation, Q.L. All authors have read and agreed to the published version of the manuscript.

Funding: This research was funded by the National Natural Science Foundation of China (41877267, 42177154, 42377192) and the Natural Science Foundation of Hubei Province (2022CFB422).

Institutional Review Board Statement: Not applicable.

Informed Consent Statement: Not applicable.

Data Availability Statement: Data are contained within the article.

Conflicts of Interest: Author Dongfeng Xin was employed by Huajin Aramco Petrochemical Company Limited, Panjin, China. The remaining authors declare that the research was conducted in the absence of any commercial or financial relationships that could be construed as a potential conflict of interest.

References

1. Dong, Y.K.; Liu, C.L.; Wei, H.Z.; Meng, Q.S.; Zhou, H. Size segregation mechanism of reclamation fill sand due to rainbowing operations in hydraulic dredging activities. *Ocean Eng.* **2021**, *242*, 109957. [CrossRef]
2. Jafarian, Y.; Javdanian, H.; Haddad, A. Strain-dependent dynamic properties of Bushehr siliceous-carbonate sand: Experimental and comparative study. *Soil Dyn. Earthq. Eng.* **2018**, *107*, 339–349. [CrossRef]
3. Zhu, C.Q.; Wang, X.Z.; Wang, R.; Chen, H.Y.; Meng, Q.S. Experimental microscopic study of inner pores of calcareous sand. *Mater. Res. Innov.* **2014**, *18*, S2–S207. [CrossRef]
4. Shen, Y.; Zhu, Y.H.; Liu, H.L.; Li, A.; Ge, H.Y. Macro-meso effects of gradation and particle morphology on the compressibility characteristics of calcareous sand. *Bull. Eng. Geol. Environ.* **2018**, *77*, 1047–1055. [CrossRef]
5. Shahnazari, H.; Rezvani, R. Effective parameters for the particle breakage of calcareous sands: An experimental study. *Eng. Geol.* **2013**, *159*, 98–105. [CrossRef]
6. Ye, J.H.; Cao, M.; Li, G. Creep characteristics of undisturbed coral sand in the South China Sea. *Chin. J. Rock Mech. Eng.* **2019**, *38*, 1242–1251.
7. Ngan-Tillard, D.; Haan, J.; Laughton, D.; Mulder, A.; van der Kolff, A.N. Index test for the degradation potential of carbonate sands during hydraulic transportation. *Eng. Geol.* **2009**, *108*, 54–64. [CrossRef]
8. Van Ginkel, M.; Olsthoorn, T.N. Distribution of grain size and resulting hydraulic conductivity in land reclamations constructed by bottom dumping, rainbowing and pipeline discharge. *Water Resour. Manag.* **2019**, *33*, 993–1012. [CrossRef]
9. Wang, X.Z.; Ding, H.Z.; Meng, Q.S.; Wei, H.Z.; Wu, Y.; Zhang, Y. Engineering characteristics of coral reef and site assessment of hydraulic reclamation in the South China Sea. *Constr. Build. Mater.* **2021**, *300*, 124263. [CrossRef]
10. Marwan, A.; Aly, A. Pearl Jumeira project: A case study of land reclamation in Dubai, UAE. *Int. J. Jpn. Geotech. Soc. Spec. Publ.* **2015**, *2*, 1778–1783.
11. Li, W.; Coop, M.R. Mechanical behaviour of Panzhihua iron tailings. *Can. Geotech. J.* **2019**, *56*, 420–435. [CrossRef]
12. Yoshimine, M.; Koike, R. Liquefaction of clean sand with stratified structure due to segregation of particle size. *Soils Found.* **2005**, *45*, 89–98. [CrossRef] [PubMed]
13. Naeini, S.A.; Baziar, M.H. Effect of fines content on steady-state strength of mixed and layered samples of a sand. *Soil Dyn. Earthq. Eng.* **2004**, *24*, 181–187. [CrossRef]
14. Zhang, Q.G.; Yin, G.Z.; Wei, Z.A.; Fan, X.Y.; Wang, W.S.; Nie, W. An experimental study of the mechanical features of layered structures in dam tailings from macroscopic and microscopic points of view. *Eng. Geol.* **2015**, *195*, 142–154. [CrossRef]
15. Shen, Z.F.; Xu, Q.E.; Zhu, L.Y.; Wang, Z.; Gao, H. Study on static triaxial shear mechanical properties of artificially prepared interbedded soil. *Chin. J. Geotech. Eng.* **2023**, *45*, 840–846.
16. Giretti, D.; Fioravante, V.; Been, K.; Dickenson, S. Mechanical properties of a carbonate sand from a dredged hydraulic fill. *Géotechnique* **2018**, *68*, 410–420. [CrossRef]

17. Kong, D.; Fonseca, J. Quantification of the morphology of shelly carbonate sands using 3D images. *Géotechnique* **2018**, *68*, 249–261. [CrossRef]
18. Wu, M.M.; Zhou, B.; Wang, J.F. On the tracking of shelly carbonate sands using deep learning. *Géotechnique* **2022**, *73*, 974–985. [CrossRef]
19. Yao, T.; Li, W. Effect of initial fabric from sample preparation on the mechanical behaviour of a carbonate sand from the South China Sea. *Eng. Geol.* **2023**, *326*, 107311. [CrossRef]
20. Liu, Y.F.; Dong, X.G.; Gao, M. Experimental study on the shear strength characteristics of a transparent soil. *Hans J. Civ. Eng.* **2023**, *12*, 730–736. [CrossRef]
21. Wu, Y.; Cui, J.; Li, N.; Wang, X.; Wu, Y.H.; Guo, S.Y. Experimental study on the mechanical behavior and particle breakage characteristics of hydraulic filled coral sand on a coral reef island in the South China Sea. *Eng. Geol.* **2020**, *41*, 3181–3191.
22. Zhang, H.; Ren, H.; Mu, C.; Wu, X.; Huang, K.; Wang, F. Experiment study on the influence of density and confining pressure on triaxial shear properties of calcareous sand. *Materials* **2023**, *16*, 1683. [CrossRef] [PubMed]
23. Wang, X.; Zhu, C.Q.; Wang, X.Z. Experimental study on the coefficient of lateral pressure at rest for calcareous soils. *Mar. Georesour. Geotechnol.* **2020**, *38*, 989–1001. [CrossRef]
24. Wang, X.Z.; Jiao, Y.Y.; Wang, R.; Hu, M.J.; Meng, Q.S.; Tan, F.Y. Engineering characteristics of the calcareous sand in Nansha Islands, South China Sea. *Eng. Geol.* **2011**, *120*, 40–47. [CrossRef]
25. Wang, X.Z.; Tan, F.Y.; Jiao, Y.Y.; Wang, R. A new apparatus for testing the bearing capacity of calcareous sand in laboratory. *Mar. Georesour. Geotechnol.* **2014**, *32*, 379–386. [CrossRef]
26. Liu, X.; Li, S.; Yao, T. Laboratory investigation on the single particle crushing strength of carbonate gravel incorporating size and shape effects. *Géotechnique* **2023**, 1–17. [CrossRef]
27. Shang, G.W.; Sun, L.Q.; Li, S.; Liu, X.L.; Chen, W.W. Experimental study of the shear strength of carbonate gravel. *Bull. Eng. Geol. Environ.* **2020**, *79*, 2381–2394. [CrossRef]
28. Wu, Y.; Wu, Y.; Ma, L.; Cui, J.; Liu, J.; Dai, B. Experimental study on dynamic characteristics of coral sand and gravel mixtures in South China Sea. *Chin. J. Geotech. Eng.* **2024**, *46*, 63–71.
29. Fu, J.X.; Lei, X.W.; Meng, Q.S.; Pan, J.F. Model test study on bearing characteristics of coral gravel interlayer foundation. *Yangtze River* **2019**, *54*, 183–189.
30. Wei, H.Z.; Zhao, T.; Meng, Q.S.; Wang, X.Z.; Zhang, B. Quantifying the morphology of calcareous sands by dynamic image analysis. *Int. J. Geomech.* **2020**, *20*, 04020020. [CrossRef]
31. *SY/T5163*; Method for X-ray Diffraction Analysis of Clay Minerals and Common Non-Clay Minerals in Sedimentary Rocks. National Energy Administration of the People's Republic of China: Beijing, China, 2018.
32. *ASTM D2487-00*; Standard Practice for Classification of Soils for Engineering Purposes (Unified Soil Classification System). American Society for Testing and Materials: West Conshohocken, PA, USA, 2016.
33. *GB/T50123*; Standard for Soil Test Method. Chinese Ministry of Water Resources. China Planning Press: Beijing, China, 2019.
34. Yao, T.; Cao, Z.W.; Li, W. On the Mechanical behaviour of a coral silt from the South China Sea. *Géotechnique* **2024**, 1–40. [CrossRef]
35. Ladd, R.S. Preparing test specimens using undercompaction. *Geotech. Test J.* **1978**, *1*, 16–23. [CrossRef]
36. Lopez, M.; Quevedo, R. Modeling of settlement and bearing capacity of shallow foundations in overconsolidated clays. *J. GeoEng.* **2022**, *17*, 1–10.
37. Wu, Y.; Li, N.; Wang, X.; Cui, J.; Chen, Y.; Wu, Y.; Yamamoto, H. Experimental investigation on mechanical behavior and particle crushing of calcareous sand retrieved from South China Sea. *Eng. Geol.* **2021**, *280*, 105932. [CrossRef]
38. Yang, S.; Shen, X.; Liu, H.; Ge, H.; Rui, X. Gradation affects basic mechanical characteristics of Chinese calcareous sand as airport subgrade of reefs. *Mar. Georesour. Geotechnol.* **2020**, *38*, 706–715. [CrossRef]
39. Coop, M.R. The mechanics of uncemented carbonate sands. *Géotechnique* **1990**, *40*, 607–626. [CrossRef]
40. Yao, T.; Li, W. An Evaluation of treatment effectiveness for reclaimed coral sand foundation in the South China Sea. *J. Mar. Sci. Eng.* **2023**, *11*, 2288. [CrossRef]
41. Wei, H.Z.; Zhao, T.; He, J.Q.; Meng, Q.S.; Wang, X.Z. Evolution of particle breakage for calcareous sands during ring shear tests. *Int. J. Geomech.* **2018**, *18*, 04017153. [CrossRef]
42. Liu, X.; Li, S. A crushing index for granular soils based on comminution energy consumption theory. *Powder Technol.* **2024**, *434*, 119380. [CrossRef]
43. Wang, X.Z.; Weng, Y.L.; Wei, H.Z.; Meng, Q.S.; Hu, M.J. Particle obstruction and crushing of dredged calcareous soil in the Nansha Islands, South China Sea. *Eng. Geol.* **2019**, *261*, 105274. [CrossRef]
44. Shen, J.H.; Wang, X.Z.; Wang, X.; Yao, T.; Wei, H.Z.; Zhu, C.Q. Effect and mechanism of fines content on the shear strength of calcareous sand. *Bull. Eng. Geol. Environ.* **2021**, *80*, 7899–7919. [CrossRef]
45. Datta, M.; Gulhati, S.; Rao, G. Crushing of calcareous sands during drained shear. In Proceedings of the 11th Annual OTC, Houston, TX, USA, 30 April–3 May 1979; pp. 1459–1460.
46. Hull, T.S.; Poulos, H.G.; Alehossein, H. The static behavior of various calcareous sediments. In *Engineering for Calcareous Sediments, Proceedings of the International Conference on Calcareous Sediments, Perth, Australia, 15–18 March 1988*; Jewell, R.J., Khorshid, M.S., Eds.; CRC Press: Boca Raton, FL, USA, 1988; Volume 1, pp. 87–96.

47. Mitchell, J.K.; Soga, K. *Fundamentals of Soil Behavior*; Wiley: Hoboken, NJ, USA, 2005; p. 577.
48. Zhu, Y.; Liu, C.; Liu, H.; Huang, Y.H.; Qin, Y.; Deng, S. Experimental and discrete element numerical simulation of effect of particle morphology on shear strength of sand. *J. Eng. Geol.* **2019**, *28*, 490–499.

Journal of
Marine Science and Engineering

MDPI

Article

A Theoretical Model for the Hydraulic Permeability of Clayey Sediments Considering the Impact of Pore Fluid Chemistry

Lixue Cao [1,2,3], Hang Zhao [1,2,3], Baokai Yang [1,2,3], Jian Zhang [1,2,3], Hongzhi Song [1,2,3], Xiaomin Fu [1,2,3] and Lele Liu [4,*]

[1] Qingdao Key Laboratory of Groundwater Resources Protection and Rehabilitation, Qingdao 266101, China
[2] Key Laboratory of Geological Safety of Coastal Urban Underground Space, Qingdao 266101, China
[3] Qingdao Geo-Engineering Surveying Institute (Qingdao Geological Exploration Development Bureau), Qingdao 266101, China
[4] Shandong Engineering Research Center of Marine Exploration and Conservation, Ocean University of China, Qingdao 266100, China
* Correspondence: lele.liu@ouc.edu.cn

Abstract: The chemistry of the pore fluid within clayey sediments frequently changes in various processes. However, the impacts of pore fluid chemistry have not been well included in the hydraulic permeability model, and the physical bases behind the salinity sensitivity of the hydraulic permeability remains elusive. In this study, a theoretical model for the hydraulic permeability of clayey sediments is proposed, and impacts of the pore fluid chemistry are quantitatively considered by introducing electrokinetic flow theory. Available experimental data were used to verify the theoretical model, and the verified model was further applied as a sensitivity analysis tool to explore more deeply how hydraulic permeability depends on pore fluid chemistry under different conditions. Coupling effects of pore water desalination and the effective stress enhancement on the hydraulic permeability of marine sediments surrounding a depressurization wellbore during hydrate production are discussed. Results and discussion show that the hydraulic permeability reduction is significant only when the electric double layer thickness is comparable to the characteristic pore size, and the reduction becomes more obvious when the ion mobility of the saline solution is smaller and the surface dielectric potential of clay minerals is lower. During gas hydrate production in the ocean, the salinity sensitivity of the hydraulic permeability could become either stronger and weaker, depending on whether the original characteristic pore size of marine sediments is relatively large or small.

Keywords: seawater intrusion; gas hydrate; salinity; electro-viscous effect; electric double layer; pore size

1. Introduction

Clay minerals are hydrous silicates with layered structures, and layer silicates are essentially composed of silicon–oxygen tetrahedral and aluminum-bearing octahedral units which are stacked in a regular array as continuous two-dimensional sheets [1]. These distinctive structures largely determine the unique properties (e.g., swelling behavior, high cation exchange capacity, large specific surface area, etc.) of clay minerals, and the presence of clay minerals in soils could dramatically alter their chemical and physical properties [2,3]. Soil parent materials on the continent turn into clay minerals when subjected to weathering and erosion processes, and the clay minerals are carried by rivers, wind or ice into the sea [4]. On the seafloor, clay minerals continuously deposit, and the deposited clay minerals could be further transported to the ocean floor by gravitational flows (e.g., turbidity currents and debris flows) [5]. This results in an extremely wide distribution of clay minerals in marine sediments globally [5,6].

The pore fluid chemistry of clayey sediments frequently changes during various processes [7]. Clayey and silty sediments along the continental margins host more than 90% of global gas hydrate accumulation [8,9], and methane recovery from gas hydrates could reduce the pore fluid salinity, as one volume of gas hydrate would dissociate to about 0.8 volumes of freshwater [10]. Fresh groundwater salinization widely occurs in offshore and coastal regions due to seawater intrusion [11,12], and seawater–freshwater mixing zones would move landward if coastal aquifers were further overexploited or sea levels continuously increased [13,14]. Changes in pore fluid chemistry could alter the mechanical and hydraulic properties of clays or clayey sediments [7,15–20], and hydraulic permeability decreases dramatically when subjected to pore fluid desalination [21–24]. Accounting for the hydraulic permeability responses to changing salinities of pore fluid within clayey sediments is important for assessing the mechanical instability and production efficiency of methane extraction from gas hydrates, as well as for evaluating available freshwater storage volume and contamination of production wells under the threat of seawater intrusion. This is mainly because the hydraulic permeability of marine sediments is a major factor in controlling the multiple physical coupling processes of hydrate production [25–27] and seawater intrusion [28–30].

To numerically simulate the multiple physical coupling processes, theoretical or empirical models of hydraulic permeability are basically required and, in developments of the models, the interconnected pores within soils are frequently represented by using a bundle of capillary tubes [31,32]. In these capillary tubes, the fluid moves in parallel layers without disrupting or mixing (i.e., laminar fluid flow), and the flow rate of each capillary tube can be calculated by using the Hagen–Poiseuille equation [33]. Once the total flow rate of all the capillary tubes has been determined, Darcy's law [34,35] is adopted to calculate the hydraulic permeability of soils. In these hydraulic models, the Kozeny–Carman (KC) equation [36,37] is the most widely accepted and highly applicable model. The KC equation is roughly valid for sandy and silty soils but not for clayey soils [38]. The surface of clay particles in nature is negatively charged, and pore fluid (i.e., water molecules) near the clay particle surface is intensively constrained by electric field forces [39]. The constrained pore fluid and the pore fluid in unconnected pores make little contribution to the pore fluid transportation. For this reason, the porosity in the KC equation is modified as the effective porosity within clayey soils, in order to improve model usability [40]. The KC equation could also be modified by replacing the specific surface area with soil indexes, such as liquid limit [41], soil water characteristic curve [42], and cation exchange capacity [43]. As an alternative to the KC equation family, exponential models of hydraulic permeability have been proposed for clayey soils based on vast flushing data [44–46]. However, due to the empirical or semiempirical nature of these models for clayey soils, the impact of pore fluid chemistry has not been well addressed.

Clayey sediments inherently imply small pore sizes [47], and the equivalent pore diameter ranges from several hundred microns down to approximately several nanometers [48,49]. When a polar liquid (e.g., seawater) is forced through microchannels (e.g., small pores within clays) under an externally applied pressure gradient, an electrostatic potential (i.e., the streaming potential) is generated along the direction opposite to the pressure-driven flow due to the presence of an electrical double layer (EDL) near the solid–liquid interface [50,51]. The EDL is generally divided into two regions, a compact layer (also called the Stern or Helmholtz layer) and a diffuse layer (also called the Guoy–Chapman layer). Water molecules in the diffuse layer are pulled by ions moving under the induced streaming potential and a secondary liquid flow opposite to the pressure-driven flow occurs, resulting in an overall reduced flow rate in the external pressure gradient direction [52,53]. This retardation effect is usually referred to as the electro-viscous effect [54], and this electro-viscous effect becomes stronger when the characteristic dimensions of small pores and the EDL thickness become closer to each other [55]. The electro-viscous effect is treated as a factor inducing a non-flowing boundary layer coating capillary tubes (i.e., to shrink the tubes for fluid flow), and the behavior of fluid flow through low-permeability porous media

(e.g., clays) is analytically explored [56]. To the best of our knowledge, the electro-viscous effect has not been well included in developments of the hydraulic permeability model for clayey soils, and impacts of the pore fluid chemistry on hydraulic permeability have not been sufficiently explored.

This study proposes a theoretical model for the hydraulic permeability of clayey sediments, and impacts of the pore fluid chemistry are quantified by introducing the electrokinetic flow theory. The proposed theoretical model is firstly verified by experimental data, and sensitivity analyses are performed to explore how the hydraulic permeability alters with changing pore fluid salinity under different pore sizes, ion mobilities, and clayey minerals. Results are further extended by considering the consolidation behavior of clayey sediments, and insight is finally provided into the hydraulic permeability change when subjected to combined variations of pore fluid chemistry and external stress.

2. Model Development

The pore structure of clayey sediments is inherently complex, and the range of pore sizes can cover almost five orders of magnitude [48]. To simplify the problem and focus on the impact of pore fluid chemistry, the pore space within clayey sediments is represented by a bundle of tortuous capillary tubes, and the radii of all the capillary tubes are the same, which denotes the characteristic pore size. Inside, the walls of all the capillary tubes are uniformly and negatively charged to a potential ζ (i.e., the zeta potential) relative to the bulk saline solution filling the tubes, and an EDL with a thickness of κ^{-1} is developed near the inside wall (Figure 1). The thickness is temperature dependent [57], and the symbol κ represents the Debye–Hückel parameter [58], which could be calculated as

$$\kappa = \left(\frac{8\pi n_0 {e_0}^2}{\varepsilon_0 \epsilon k T} \right)^{\frac{1}{2}} \tag{1}$$

where n_0 stands for the bulk number concentration of ions in the saline solution (i.e., electrolyte concentration, ions·m^{-3}), e_0 for the proton charge (C), ε_0 for the vacuum permittivity (F·m^{-1}), ϵ for the dielectric constant of saline solution, k for the Boltzmann's constant, and T for the absolute temperature (K). The bulk number for concentration of ions is given by

$$n_0 = \frac{c_0 N_A}{M_s} \tag{2}$$

where N_A stands for the Avogadro constant, c_0 for the mass concentration (i.e., the salinity), and M_s for the molar mass of solute (i.e., sodium chloride in this study) in the saline solution (kg·mol^{-1}).

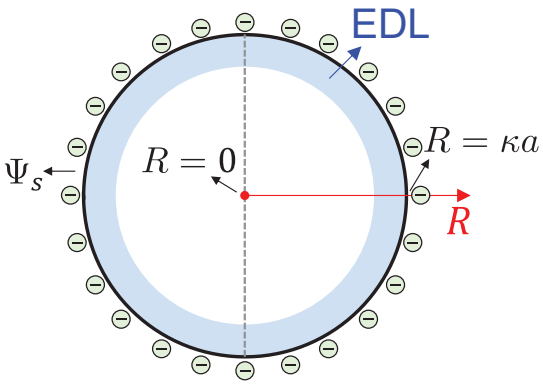

Figure 1. Illustration of a capillary tube with an electrical double layer (EDL) developed near the inside wall, which is uniformly and negatively charged to a dimensionless potential Ψ_s. Thickness of the EDL is expressed as κ^{-1}, and the capillary tube radius is demonstrated as a. A dimensionless radial coordinate R is set, starting at the center of the capillary tube.

For each capillary tube, the volumetric flow rate q is given by [54]

$$q = \frac{\pi a^4}{8\mu}\frac{\Delta P}{L_t} - \frac{{\varepsilon_0}^2\epsilon^2\zeta^2a^2(1-G)F}{16\pi\lambda\mu^2}\frac{\Delta P}{L_t} \quad (3)$$

where a stands for the capillary tube radius (m), μ for the saline solution viscosity (Pa·s), L_t for the capillary tube length (m), $\frac{\Delta P}{L_t}$ for the external pressure gradient (Pa·m^{-1}), and λ for the saline solution conductivity (S·m^{-1}), and this could be calculated as

$$\lambda = 2me_0n_0 \quad (4)$$

where m stands for the ion mobility (m^2·s^{-1}·V^{-1}). The symbol G in Equation (3) represents an integral function, which is given by [54]

$$G = \frac{2}{(\kappa a)^2\Psi_s}\int_0^{\kappa a} R\Psi(R)dR \quad (5)$$

where R stands for the dimensionless radial coordinate, and $R = \kappa r$ with the symbol r denoting the radial coordinate; $\Psi(R)$ represents the dimensionless potential due to the negatively charged inside wall; and $\Psi_s = \Psi(\kappa a) = \frac{e_0\zeta}{kT}$ denotes the dimensionless zeta potential. The symbol F in Equation (3) represents another integral function, which is given by [54]

$$F = \frac{\frac{1}{2}(\kappa a)^2(1-G)}{\int_0^{\kappa a} R\cosh\Psi(R)dR + \beta^*\int_0^{\kappa a} R\left(\frac{d\Psi(R)}{dR}\right)^2 dR} \quad (6)$$

where β^* represents a dimensionless parameter, which is defined as [54]

$$\beta^* = \frac{{\varepsilon_0}^2\epsilon^2k^2T^2\kappa^2}{16\pi^2\mu\lambda{e_0}^2} \quad (7)$$

The dimensionless potential $\Psi(R)$ is governed by the Poisson–Boltzmann equation [59], which is widely used to depict the ion distribution around a charged surface, and a dimensionless form of the Poisson–Boltzmann equation is given by [54]

$$\frac{1}{R}\frac{d}{dR}\left(R\frac{d\Psi(R)}{dR}\right) = \sinh\Psi(R) \quad (8)$$

The boundary conditions for a capillary tube with a negatively charged inside wall are

$$\Psi(R = \kappa a) = \Psi_s = \frac{e_0\zeta}{kT} \quad (9)$$

and

$$\left.\frac{d\Psi(R)}{dR}\right|_{R=0} = 0 \quad (10)$$

There is not a single simple analytical solution available for Equations (8)–(10), unless mathematical approximations are adopted [54,60]. In this study, mathematical approximations are not used, and Equations (8)–(10) are numerically solved by using an iteration method. Prior to iterative computations, the hyperbolic sine function $\sinh\Psi(R)$ is written as a truncated series, and Equation (8) turns into

$$\frac{1}{R}\frac{d}{dR}\left(R\frac{d\Psi(R)}{dR}\right) = \Psi(R) + \frac{\Psi(R)^3}{3!} + \frac{\Psi(R)^5}{5!} + \frac{\Psi(R)^7}{7!} + \frac{\Psi(R)^9}{9!} \quad (11)$$

Once the volumetric flow rate q is determined, the total volumetric flow rate Q of the capillary tube bundle could be calculated as

$$Q = \frac{A\phi}{\pi a^2} q \tag{12}$$

where A stands for the cross-sectional area (m^2) of the representative volume element (REV) of clayey sediments, and ϕ for the porosity of clayey sediments. According to Darcy's law [34,35], the hydraulic permeability K of clayey sediments is given by

$$K = \frac{\mu Q}{A\frac{\Delta P}{L}} \tag{13}$$

where L denotes the REV side length (m) along the porous flow direction, and $L = \frac{L_t}{\tau}$, where τ represents the hydraulic tortuosity.

To reexamine the polynomial on the right-hand side of Equation (3), the first term is exactly consistent with the Hagen–Poiseuille equation, and the second term is solely as a result of the electrokinetic phenomena. The reduced volumetric flow rate resembles the volumetric flow rate of a fluid with an increased viscosity (i.e., the electro-viscous effect), and an apparent viscosity μ_a is used to recalculate the volumetric flow rate as

$$q = \frac{\pi a^4}{8\mu_a} \frac{\Delta P}{L_t} \tag{14}$$

By comparison of Equations (3) and (14), the apparent viscosity μ_a is given by

$$\frac{\mu_a}{\mu} = \left(1 - \frac{8\beta^* {\Psi_s}^2 (1-G)F}{(\kappa a)^2}\right)^{-1} \tag{15}$$

Equation (11) and the boundary conditions (Equations (9) and (10)) are firstly dispersed by using the finite difference method, and the iterative computations use the following equation

$$\begin{gathered}\left(1 - \frac{1}{2(i-1)}\right)\Psi_{i-1} - (2 + \Delta R \Delta R)\Psi_i + \left(1 + \frac{1}{2(i-1)}\right)\Psi_{i+1} \\ = (\Delta R \Delta R)\left(\frac{{\Psi_i}^3}{3!} + \frac{{\Psi_i}^5}{5!} + \frac{{\Psi_i}^7}{7!} + \frac{{\Psi_i}^9}{9!}\right)\end{gathered} \tag{16}$$

where ΔR stands for the spatial step, i for the node number, and $\Psi_N = \Psi_s$ while $\Psi_1 = \Psi_2$ according to Equations (9) and (10). Then, the symbols G and F could be calculated according to Equations (5) and (6), followed by computation of the apparent viscosity μ_a according to Equation (15). Finally, the hydraulic permeability K could be calculated according to Equation (13). All the computations in this study are accomplished by using a self-developed code based on the programming platform of MATLAB R2016a.

3. Model Verification

Numerical computations are conducted with different total grid numbers to study the grid dependency, and values of the model parameter are summarized in Table 1. Calculated results for the dimensionless dielectric potential Ψ, the dimensionless parameters G and F, and the normalized viscosity $\Gamma = \frac{\mu_a}{\mu}$ are shown in Figure 2. It is obvious that, when the total grid number is larger than 100, the dimensionless dielectric potential curves overlap each other (Figure 2a), and values of G, F, and Γ are fully independent of the total grid number. In this study, a total grid number of 10,001 is applied to the following computations.

Table 1. Values of the model parameters.

Parameters	Values	References
Proton charge, e_0 (C)	1.6028×10^{-19}	[61]
Dielectric constant of saline solution, ϵ (dimensionless)	80	[54]
Avogadro constant, N_A (dimensionless)	6.0221×10^{23}	[62]
Boltzmann's constant, k ($J \cdot K^{-1}$)	1.38065×10^{-23}	[61]
Ion mobility, m ($m^2 \cdot s^{-1} \cdot V^{-1}$)	5.19×10^{-8}	[63]
Surface dielectric potential, ζ (V)	-49.3×10^{-3}	[39]
Viscosity, μ (Pa·s)	1.0×10^{-3}	[54]
Mass concentration of sodium chloride, c_0 (dimensionless)	3.5×10^{-2}	[64]
Hydraulic tortuosity, τ (dimensionless)	1.15	[65]
Molar mass of sodium chloride, M_s ($kg \cdot mol^{-1}$)	58.5×10^{-3}	
Capillary tube radius, a (m)	1.0×10^{-8}	
Temperature, T (K)	293	

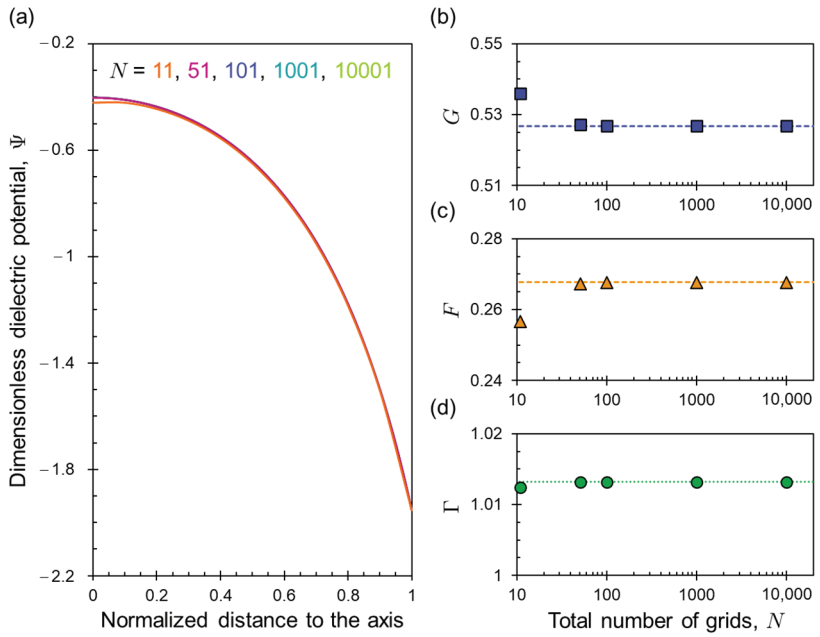

Figure 2. Results of the dimensionless dielectric potential Ψ (**a**), the dimensionless parameters G (**b**) and F (**c**), and the normalized viscosity Γ (**d**) under different conditions of the total grid number N.

Mesri and Olson [45] prepared slurries of kaolinite, illite, and smectite (mainly montmorillonite) in water by repeatedly washing with concentrated saline solutions. The slurries were first consolidated to pressures ranging from 4.309 kPa to 5.985 kPa in a special sedimentation tube and then further consolidated to a pressure of 3.064 MPa through eight steps in a consolidation ring with a diameter of 63.5 mm. When subjected to consolidation pressure changes, the measured settlement data are used to extract the coefficient of permeability. Coefficients of permeability of all three clay minerals in saline solutions with different salinities were reported, and these experimental results are used to verify the model proposed in this study. The coefficient of permeability K^* (i.e., the hydraulic conductivity, $m \cdot s^{-1}$) is transformed into the hydraulic permeability K (m^2) by $K = \frac{\mu}{\rho g} K^*$, where ρ is the fluid density and g is the gravitational acceleration. The void ratio e_v of clay minerals was measured and used to calculate the porosity $\phi = \frac{e_v}{1+e_v}$. The surface potential of kaolinite, illite, and montmorillonite minerals is -0.0538×10^{-3} V, -49.3×10^{-3} V, and -19.3×10^{-3} V, respectively [39]. The hydraulic tortuosity and the characteristic pore size of clay minerals were unfortunately not measured, a common value of 1.15 was set for the hydraulic tortuosity (Table 1), and the characteristic pore size was acquired by fitting the hydraulic permeability.

Experimental and theoretical permeabilities are compared in Figure 3, and the fitted capillary radius is also included. It is obvious that the theoretical permeability is very

consistent with the experimental permeability for all three clay minerals under different conditions of sodium chloride concentration, and values of the Lin's Concordance Correlation Coefficient (LCCC) [66,67] are all larger than 0.999 (Table 2). The fitted capillary radius (i.e., the characteristic pore size) generally ranges from 0.1 μm to 1.8 μm for kaolinite (Figure 3d), from 0.01 μm to 0.20 μm for illite (Figure 3e), and from 0.005 μm to 0.08 μm for smectite (Figure 3f). These values of the characteristic pore size are quite comparable with published data [48,49,68,69]. For example, the characteristic pore size of three clayey soils located in China generally ranges from 0.004 μm to 0.01 μm [68], the pore size of compacted Edgar Plastic kaolinite mostly ranges from 0.03 μm to 3.0 μm, the characteristic pore size of Macon kaolinite is roughly 0.2 μm, and the characteristic pore size of Fithian illite is roughly 0.1 μm [48]; The characteristic pore size of natural clays is about 0.2 μm [49], the characteristic pore size of Wyoming montmorillonite is 0.07 μm, and the characteristic pore size of Georgia kaolinite is roughly 0.15 μm [69]. In addition, the fitted capillary radius generally decreases with decreasing void ratio due to consolidation, and the overall trend is consistent with the theoretical analyses [70,71], which offer an equation depicting the trend as

$$\log_{10}\Omega \;=\; \log_{10}\left(\frac{a}{a^*}\right) \;=\; \chi(e_v - {e_v}^*) \tag{17}$$

where ${e_v}^*$ stands for a reference void ratio, a^* for the corresponding capillary radius, and χ for a fitting parameter. Fitting curves and experimental data are shown in Figure 4. It is obvious that Equation (17) can capture the physical bases of the characteristic pore size change due to consolidation. The fitting parameter $\chi = 0.741$, $\chi = 0.231$, and $\chi = 0.0958$ for kaolinite, illite, and smectite minerals, respectively.

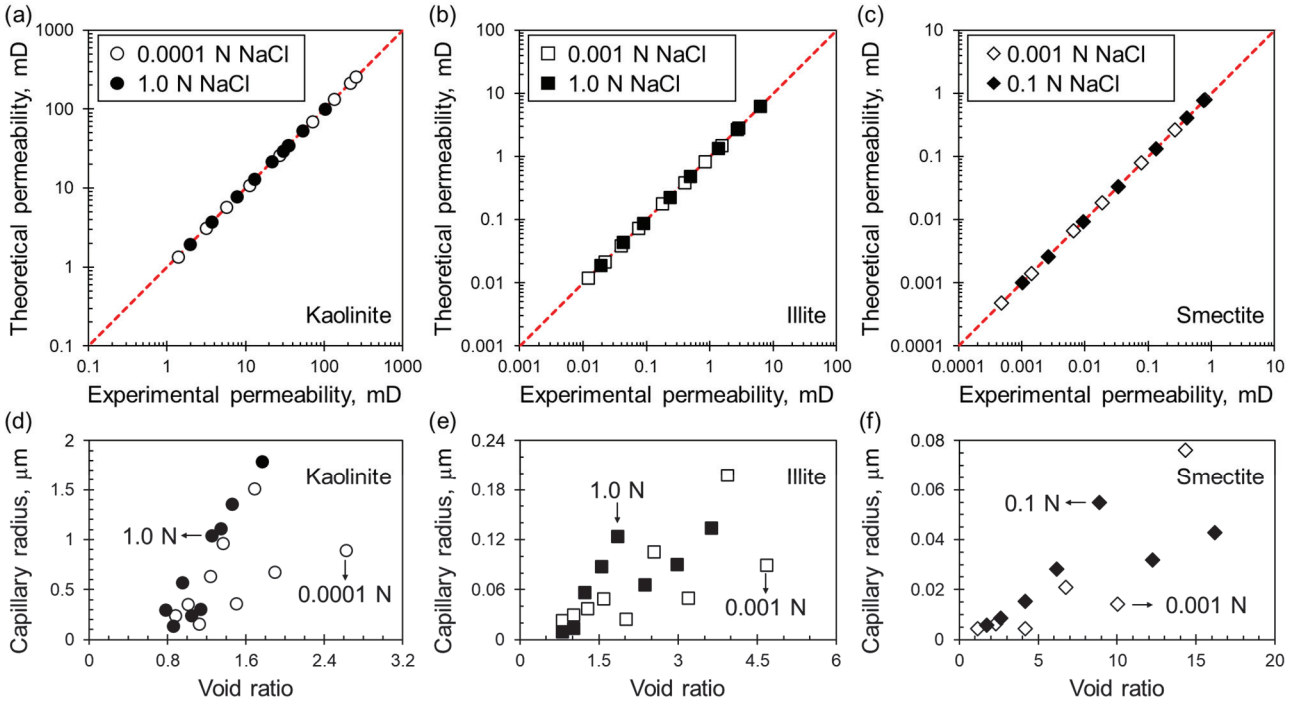

Figure 3. Comparisons of experimental and theoretical permeabilities of kaolinite (**a**), illite (**b**), and smectite (**c**) minerals when subjected to consolidation in an oedometer cell. The fitted capillary radius (i.e., the characteristic pore size) changes with the void ratio of kaolinite (**d**), illite (**e**), and smectite (**f**) minerals. The dimension N represents normality and, for the sodium chloride (NaCl) solution, 1.0 N stands for a mass concentration of 0.0585. The dimension mD represents millidarcy, and 1.0 mD $= 0.987 \times 10^{-15}$ m^2.

Table 2. Values of the Lin's Concordance Correlation Coefficient (LCCC).

Experimental Conditions	LCCC	Figure	Reference
Kaolinite (0.0001 N NaCl) Kaolinite (1.0 N NaCl)	0.99982 0.99978	Figure 3a	[45]
Illite (0.001 N NaCl) Illite (1.0 N NaCl)	0.99984 0.99997	Figure 3b	
Smectite (0.001 N NaCl) Smectite (0.1 N NaCl)	0.99993 0.99999	Figure 3c	
Bentonite A (D. I. Water) Bentonite A (0.1 N NaCl) Bentonite A (1.0 N NaCl)	0.99982 0.99982 0.99980	Figure 5a	[21]
Bentonite B (D. I. Water) Bentonite B (0.1 N NaCl) Bentonite B (1.0 N NaCl)	0.99992 0.99980 0.99989	Figure 5b	
Bentonite C (D. I. Water) Bentonite C (0.1 N NaCl) Bentonite C (1.0 N NaCl)	0.99996 0.99962 0.99990	Figure 5c	
Bentonite D (D. I. Water) Bentonite D (0.1 N NaCl) Bentonite D (1.0 N NaCl)	0.99984 0.99974 0.99987	Figure 5d	

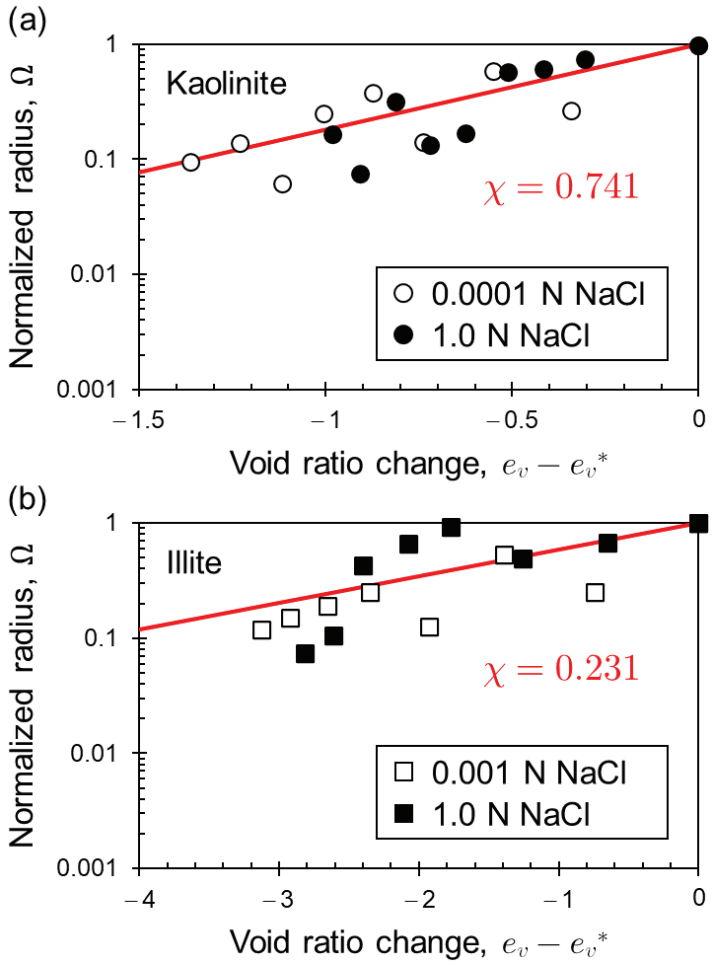

Figure 4. *Cont.*

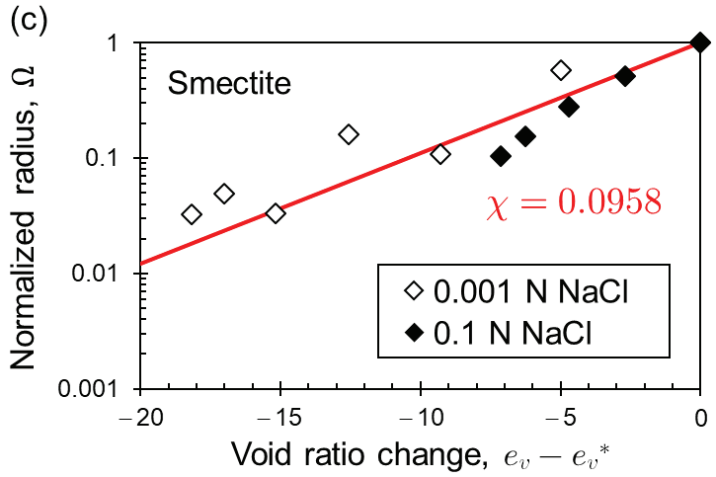

Figure 4. Normalized capillary radius $\Omega = \frac{a}{a^*}$ decreasing with decreasing void ratio change $e_v - e_v^*$ for kaolinite (**a**), illite (**b**), and smectite (**c**). The symbol e_v^* stands for a reference void ratio, and a^* represents the corresponding capillary radius. The red curve is drawn by Equation (17) with different values of the fitting parameter χ.

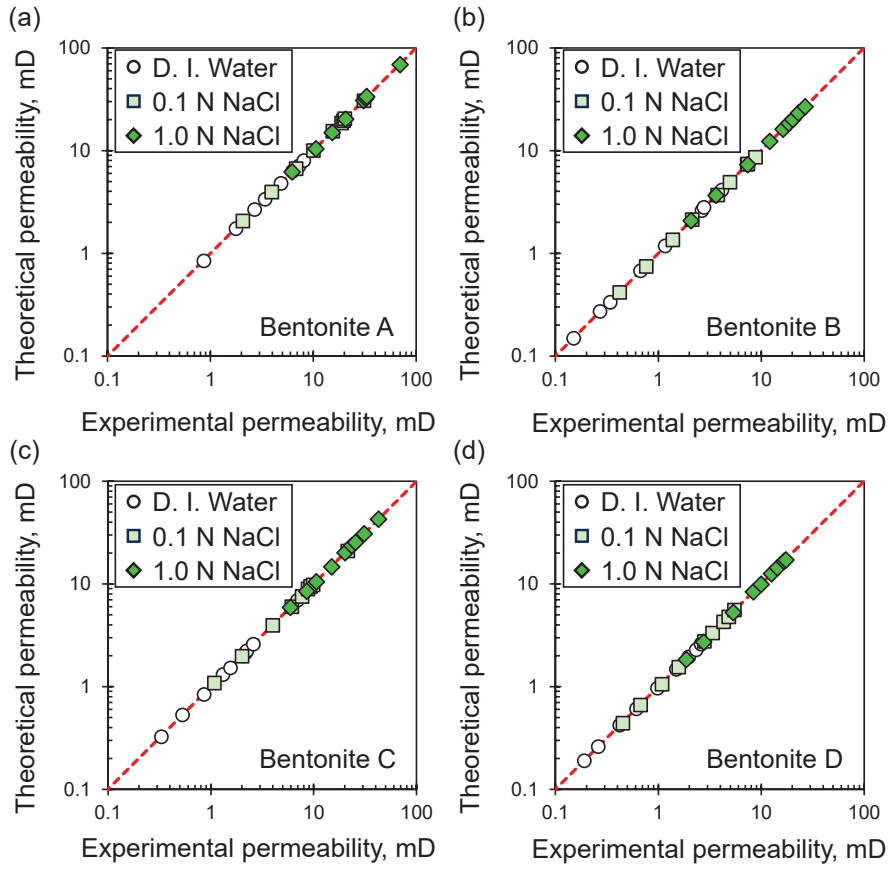

Figure 5. Comparisons of experimental and theoretical permeabilities of bentonites A (**a**), B (**b**), C (**c**), and D (**d**) when subjected to consolidation in an oedometer cell. The abbreviation "D. I. Water" in the legend denotes deionized water. The dimension N represents normality and, for the sodium chloride (NaCl) solution, 1.0 N stands for a mass concentration of 0.0585. The dimension mD represents millidarcy, and 1.0 mD $= 0.987 \times 10^{-15}$ m^2.

Mishra et al. [21] prepared samples of bentonite A, B, C, and D with the initial water content equal to their respective liquid limits and consolidated the samples in an oedometer cell with a diameter of 60 mm. The vertical loading increased from 4.9 kPa to 1.254 MPa

through seven steps with a unit incremental ratio, and the hydraulic conductivity of bentonites under different conditions of sodium chloride concentration is obtained according to the method used by Mesri and Olson [45]. The experimental results are used to further verify the model proposed in this study. All these bentonite samples are mixtures of basalt soil and bentonite with a mixing ratio of 100:20 by dry weight, and the liquid limit of all these samples ranges from 310.5% to 615.5%. The clay content of all these samples ranges from 61.4% to 82.8%, and the major mineral component of the clay is montmorillonite. Thus, the surface potential ζ of clay minerals is selected as -19.3×10^{-3} V [39] in this study.

Experimental and theoretical permeabilities are compared in Figure 5. It is obvious that the theoretical permeability is also very consistent with the experimental permeability for all these bentonites under different conditions of sodium chloride concentration, and all the LCCC values are larger than 0.999 (Table 2). The fitted capillary radius (i.e., the characteristic pore size) of all these bentonites is demonstrated in Figure 6. It is demonstrated that the fitted characteristic pore size mostly ranges from 0.1 μm to 1.6 μm for bentonite A (Figure 6a), from 0.03 μm to 0.84 μm for bentonite B (Figure 6b), from 0.04 μm to 1.05 μm for bentonite C (Figure 6c), and from 0.02 μm to 0.84 μm for bentonite D (Figure 6d). These values for the characteristic pore size are also quite comparable with the published data [48,49,68,69]. The fitted characteristic pore size also decreases with decreasing void ratio due to consolidation, and experimental data of the normalized capillary radius Ω together with fitting curves are shown in Figure 7. It is obvious that Equation (17) could also capture the physical bases of the characteristic pore size change due to consolidation. The fitting parameter $\chi = 1.123$, $\chi = 0.675$, $\chi = 0.811$, and $\chi = 0.438$ for bentonite A, B, C, and D, respectively.

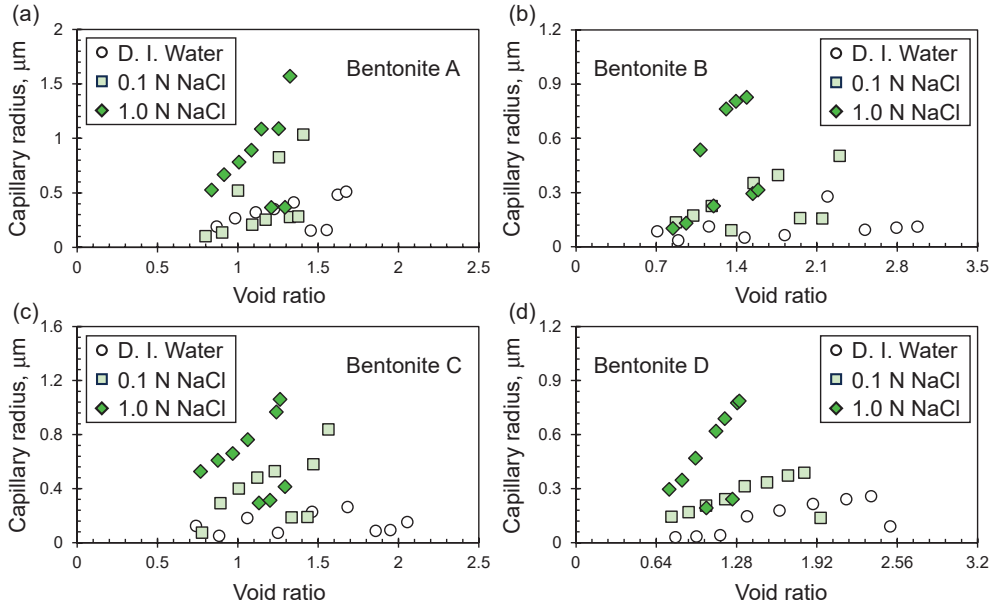

Figure 6. The fitted capillary radius (i.e., the characteristic pore size) changes with void ratio of bentonites A (**a**), B (**b**), C (**c**), and D (**d**). The abbreviation "D. I. Water" denotes deionized water. For the sodium chloride (NaCl) solution, the normality 1.0 N stands for a mass concentration of 0.0585.

In addition to the void ratio dependent data, Mishra et al. [21] provided the hydraulic conductivity of bentonites at a particular void ratio of 1.2 to show the dependence on the sodium chloride concentration. For each concentration, the fitted capillary radii corresponding to neighbor void ratios just lower and higher than 1.2 are used to calculate the hydraulic permeability of bentonites. The calculated results, together with corresponding experimental data, are shown in Figures 8 and 9. It is demonstrated that the experimental data of all these bentonites mostly occur between the theoretical results, which are acquired by using the lower and higher neighbor void ratios. This further demonstrates the capabil-

ity of the proposed model to predict the void ratio dependent hydraulic permeability of clayey sediments considering the impact of pore fluid chemistry.

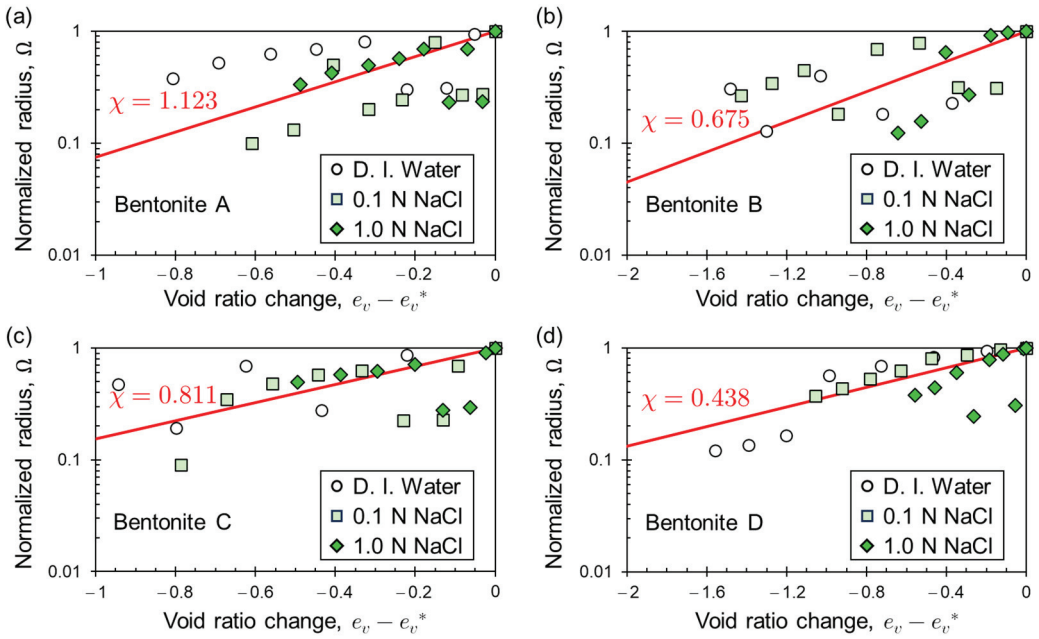

Figure 7. Normalized capillary radius $\Omega = \frac{a}{a^*}$ decreasing with decreasing void ratio change $e_v - e_v{}^*$ for bentonites A (**a**), B (**b**), C (**c**), and D (**d**). The symbol $e_v{}^*$ stands for a reference void ratio, and a^* represents the corresponding capillary radius. The red curve is drawn by Equation (17) with different χ values.

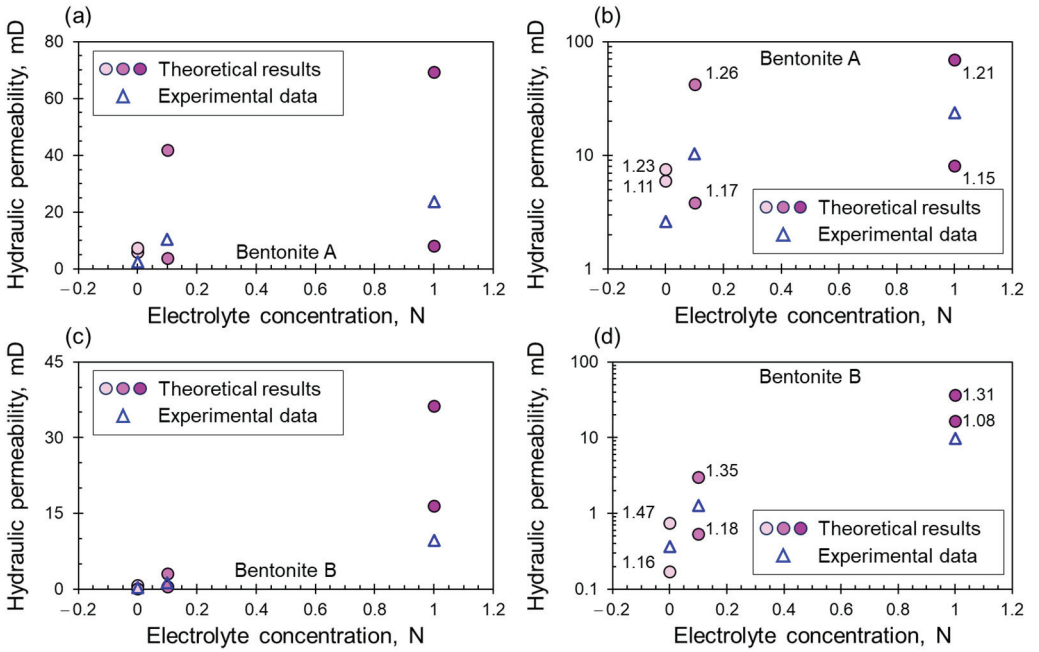

Figure 8. The electrolyte concentration-dependent hydraulic permeability of bentonites A (**a**,**b**) and B (**c**,**d**). The experimental data are obtained at a particular void ratio of 1.2, and the theoretical results are acquired by substituting lower and higher neighbor void ratios into the model. The lower and higher void ratios neighboring the void ratio of 1.2 are denoted as black decimals in the semilogarithmic coordinate system (**b**,**d**).

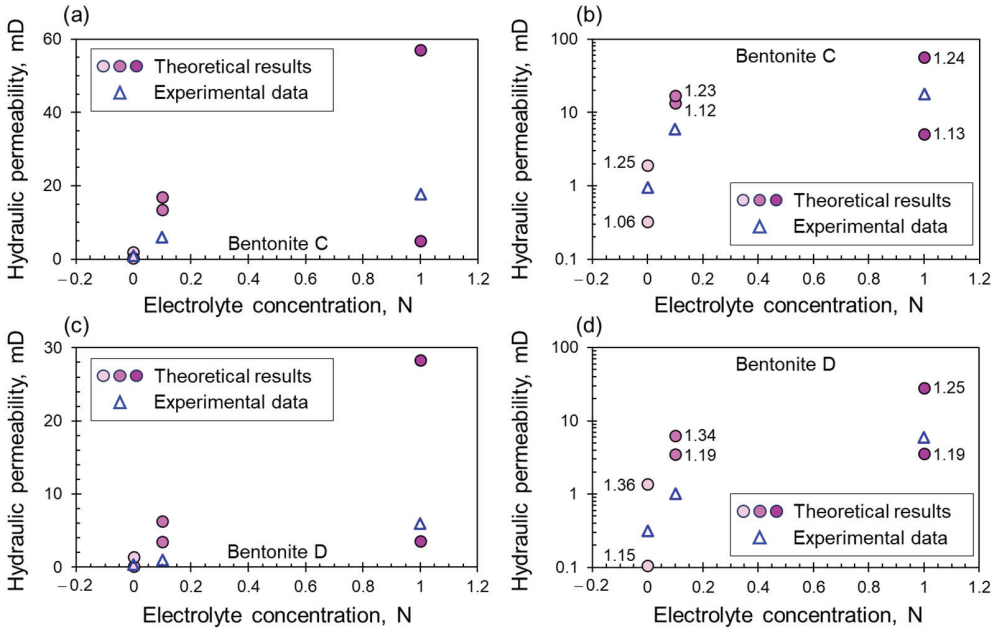

Figure 9. The electrolyte concentration dependent hydraulic permeability of bentonites C (**a**,**b**) and D (**c**,**d**). The experimental data are obtained at a particular void ratio of 1.2, and the theoretical results are acquired by substituting lower and higher neighbor void ratios into the model. The lower and higher void ratios neighboring the void ratio of 1.2 are denoted as black decimals in the semilogarithmic coordinate system (**b**,**d**).

4. Sensitivity Analysis

4.1. Effects of the Characteristic Pore Size

A dimensionless hydraulic permeability $\Pi = \frac{K}{\widetilde{K}}$ is defined to characterize the electrokinetic phenomena effect, and the symbol $\widetilde{K}$ represents the hydraulic permeability of clayey sediments when the electrokinetic phenomena are not considered. It is easy to deduce a brief formulation $\Pi = \Gamma^{-1}$. The normalized viscosity Γ and the dimensionless hydraulic permeability Π, changing with the electrolyte concentration n_0 under different conditions of the capillary radius, are shown in Figure 10. It is demonstrated that the normalized viscosity Γ and the dimensionless hydraulic permeability Π are independent of the electrolyte concentration n_0 when the capillary radius a (i.e., the characteristic pore size) is large (i.e., $a = 1.0$ μm) or small (i.e., $a = 0.0001$ μm). For the medium sized capillary radii, the normalized viscosity Γ and the dimensionless hydraulic permeability Π are dependent on the electrolyte concentration n_0. More specifically, the normalized viscosity Γ decreases while the dimensionless hydraulic permeability Π increases with increasing electrolyte concentration for $a = 0.1$ μm. For $a = 0.01$ μm, the normalized viscosity Γ firstly increases and then decreases with increasing electrolyte concentration, but the dimensionless hydraulic permeability Π changes inversely. With the capillary radius further decreasing to $a = 0.001$ μm, the normalized viscosity Γ increases, while the dimensionless hydraulic permeability Π decreases with increasing electrolyte concentration.

The dimensionless capillary radius κa and the hydraulic permeability K, changing with the electrolyte concentration n_0, are shown in Figure 11. It is demonstrated that the dimensionless capillary radius κa is far from the unit line for $a = 1.0$ μm and $a = 0.0001$ μm. For the medium sized capillary radii, the dimensionless capillary radius κa approaches the unit line to some extent, or even crosses the unit line ($a = 0.01$ μm). This indicates that effects of the electrokinetic phenomena are significant when the dimensionless capillary radius κa is close to the unit, and the effects should be considered. The capillary radius a largely controls the hydraulic permeability of clayey sediments. When the capillary radius is unchanged, the hydraulic permeability changes along with the electrolyte concentration

are small. It could be inferred that the characteristic pore size is not only a major factor denoting effects of the electrokinetic phenomena but also directly controls the hydraulic permeability of clayey sediments.

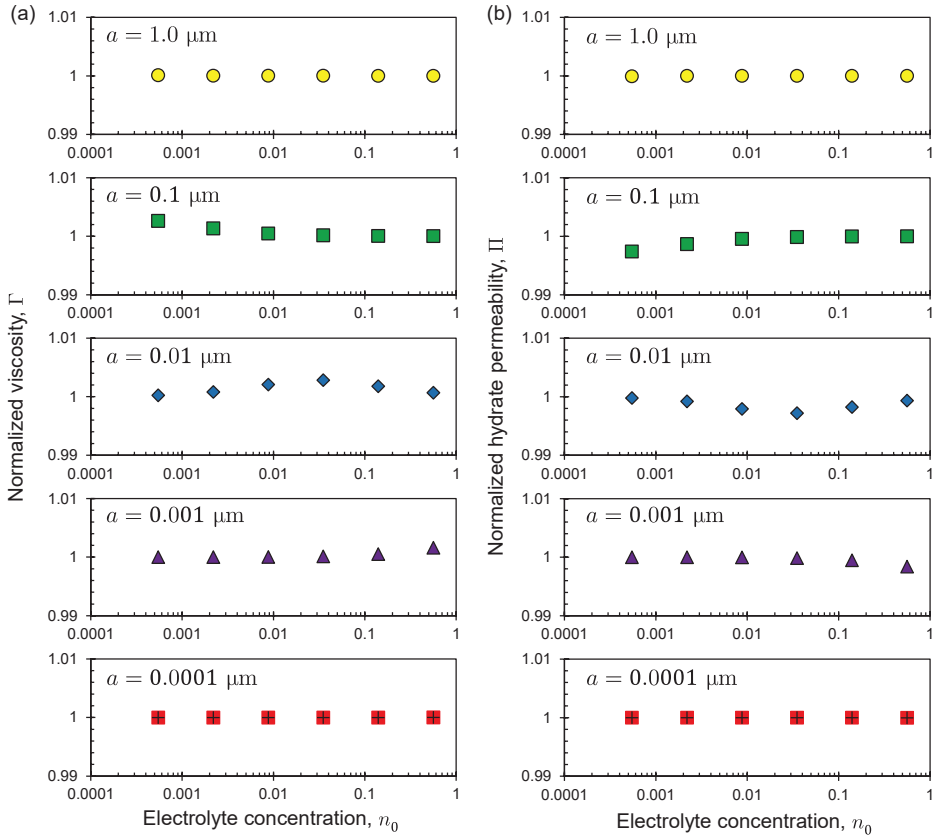

Figure 10. The normalized viscosity Γ (**a**) and the normalized hydraulic permeability Π (**b**) changes with the electrolyte concentration n_0 under different conditions of the capillary radius a.

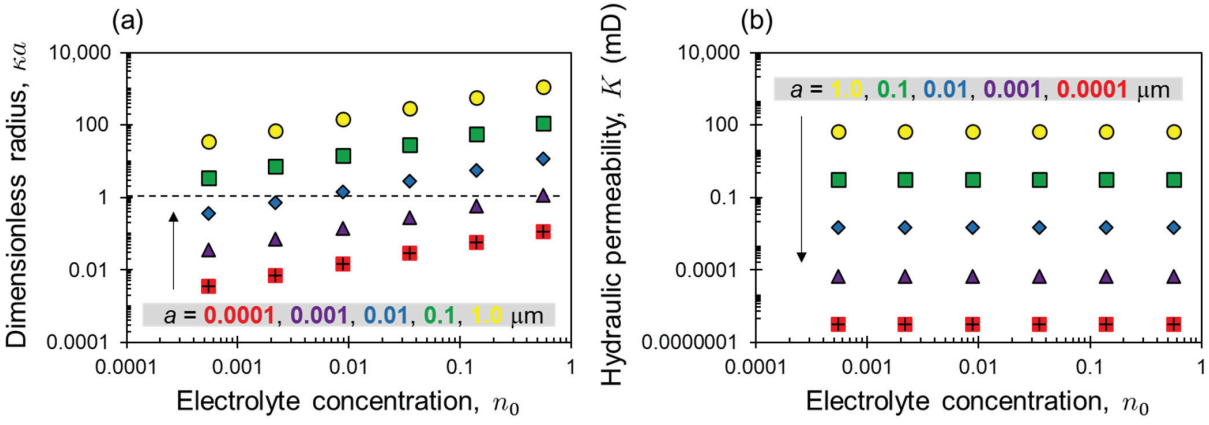

Figure 11. The dimensionless capillary radius κa (**a**) and the hydraulic permeability K (**b**) changes with the electrolyte concentration n_0 under different conditions of the capillary radius a.

4.2. Effects of Ion Mobility

The normalized viscosity Γ and the dimensionless hydraulic permeability Π, changing with the electrolyte concentration n_0 under different conditions of ion mobility, are shown in Figure 12. It is demonstrated that the normalized viscosity Γ decreases (Figure 12a), while the dimensionless hydraulic permeability Π increases (Figure 12b) with increasing electrolyte concentration for $a = 0.1$ μm. For $a = 0.01$ μm, the normalized viscosity Γ firstly increases

and then decreases (Figure 12c) with increasing electrolyte concentration, but the dimensionless hydraulic permeability Π firstly decreases and then increases (Figure 12d) with increasing electrolyte concentration. The normalized viscosity Γ increases (Figure 12e), while the dimensionless hydraulic permeability Π decreases (Figure 12f) with increasing electrolyte concentration for $a = 0.001$ μm. These responses to the electrolyte concentration change become much stronger when a smaller ion mobility is applied. The dimensionless capillary radius κa and the hydraulic permeability K, changing with the electrolyte concentration n_0, are shown in Figure 13. It is obvious that the dimensionless capillary radius κa increases with increasing electrolyte concentration, and the change process is independent of the ion mobility (Figure 13a,c,e). The hydraulic permeability K decreases (Figure 13b) with increasing electrolyte concentration for $a = 0.1$ μm. The hydraulic permeability K firstly decreases and then increases (Figure 13d) with increasing electrolyte concentration for $a = 0.01$ μm. The hydraulic permeability K decreases (Figure 13f) with increasing electrolyte concentration for $a = 0.001$ μm. In addition, the maximal change in hydraulic permeability decreases with increasing ion mobility.

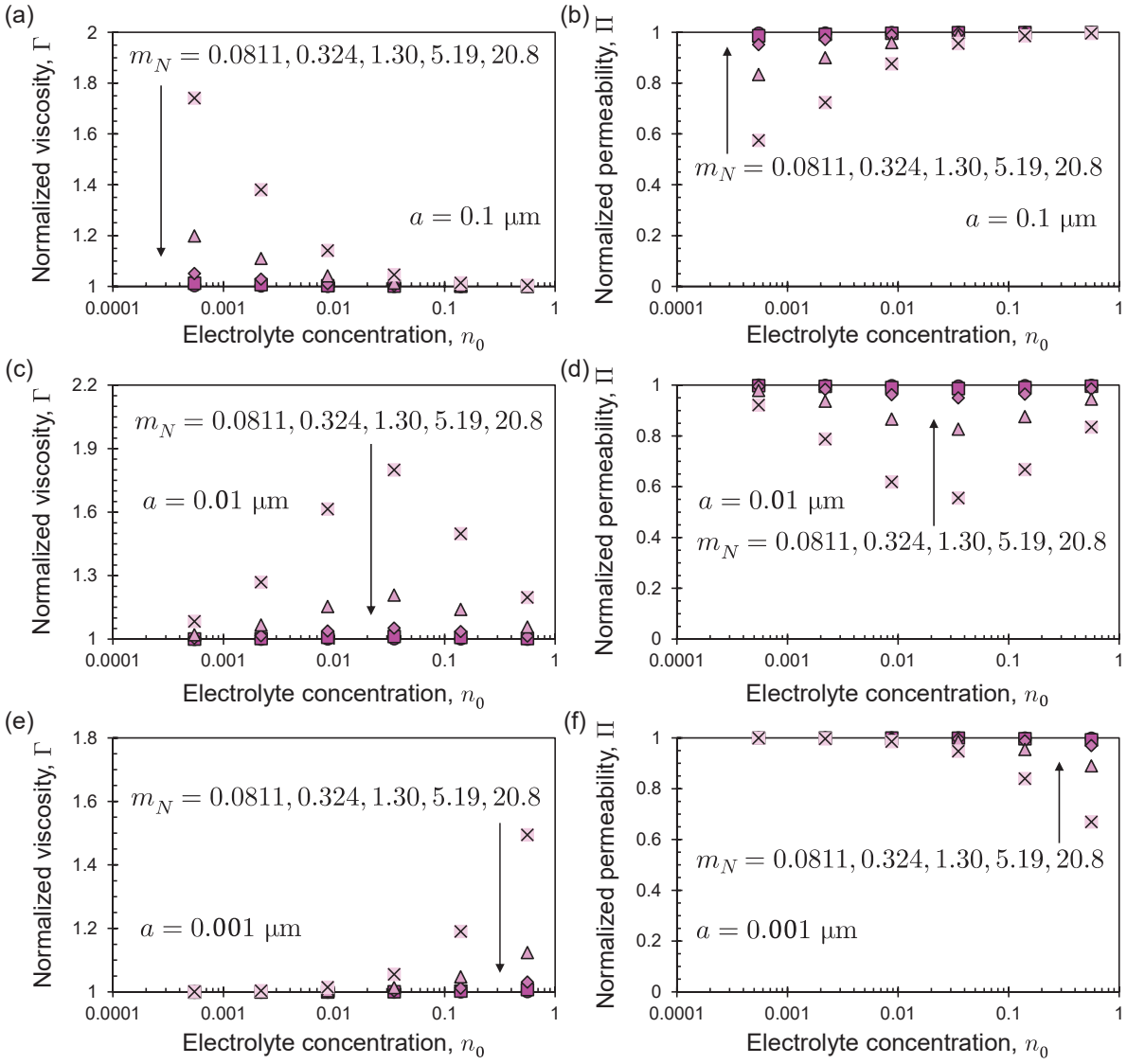

Figure 12. The normalized viscosity Γ (**a**,**c**,**e**) and the normalized hydraulic permeability Π (**b**,**d**,**f**) change with the electrolyte concentration n_0 under different conditions of dimensionless ion mobility $m_N = \frac{m}{m^*}$, where $m^* = 1.0 \times 10^{-8}$ m^{2}s^{-1}V^{-1}. The capillary radius $a = 0.1$ μm (**a**,**b**), $a = 0.01$ μm (**c**,**d**), and $a = 0.001$ μm (**e**,**f**).

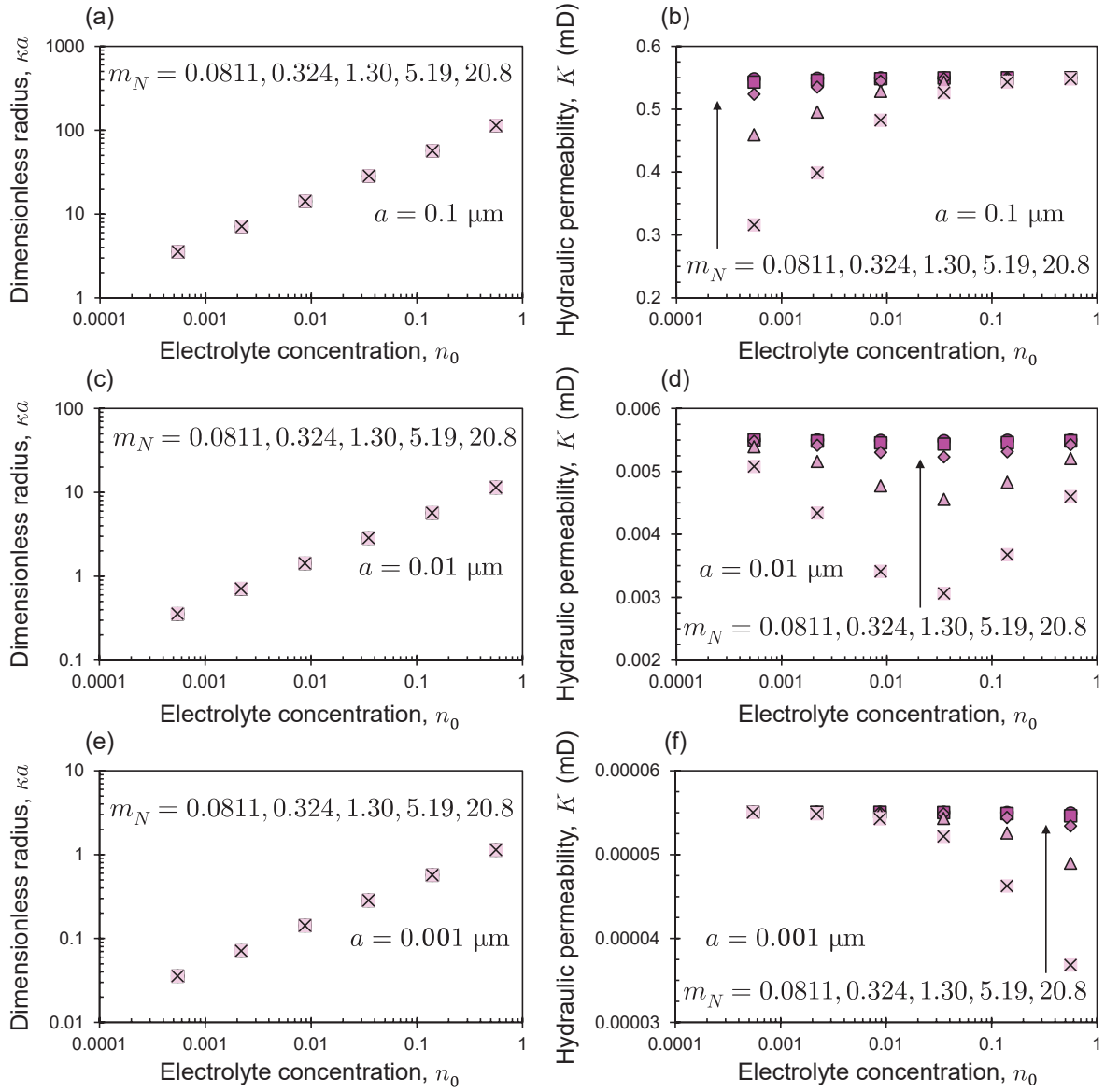

Figure 13. The dimensionless capillary radius κa (**a**,**c**,**e**) and the hydraulic permeability K (**b**,**d**,**f**) change with the electrolyte concentration n_0 under different conditions of the dimensionless ion mobility $m_N = \frac{m}{m^*}$, where $m^* = 1.0 \times 10^{-8}$ m^{2}s^{-1}V^{-1}. The capillary radius $a = 0.1$ μm (**a**,**b**), $a = 0.01$ μm (**c**,**d**), and $a = 0.001$ μm (**e**,**f**).

4.3. Effects of the Surface Dielectric Potential

The normalized viscosity Γ, the dimensionless hydraulic permeability Π, the dimensionless capillary radius κa, and the hydraulic permeability K, changing with the electrolyte concentration n_0 under different conditions of the surface dielectric potential ζ, are shown in Figure 14. It is demonstrated that the normalized viscosity Γ firstly increases and then decreases (Figure 14a), the dimensionless hydraulic permeability Π firstly decreases and then increases (Figure 14b), the dimensionless capillary radius κa increases (Figure 14c), and the hydraulic permeability K firstly decreases and then increases (Figure 14d) with increasing electrolyte concentration. The maximal change in the normalized viscosity Γ, dimensionless hydraulic permeability Π, and the hydraulic permeability K decreases with increasing surface dielectric potential ζ. In addition, dependence of the dimensionless capillary radius on the electrolyte concentration is unchanged when different values are assigned to the surface dielectric potential.

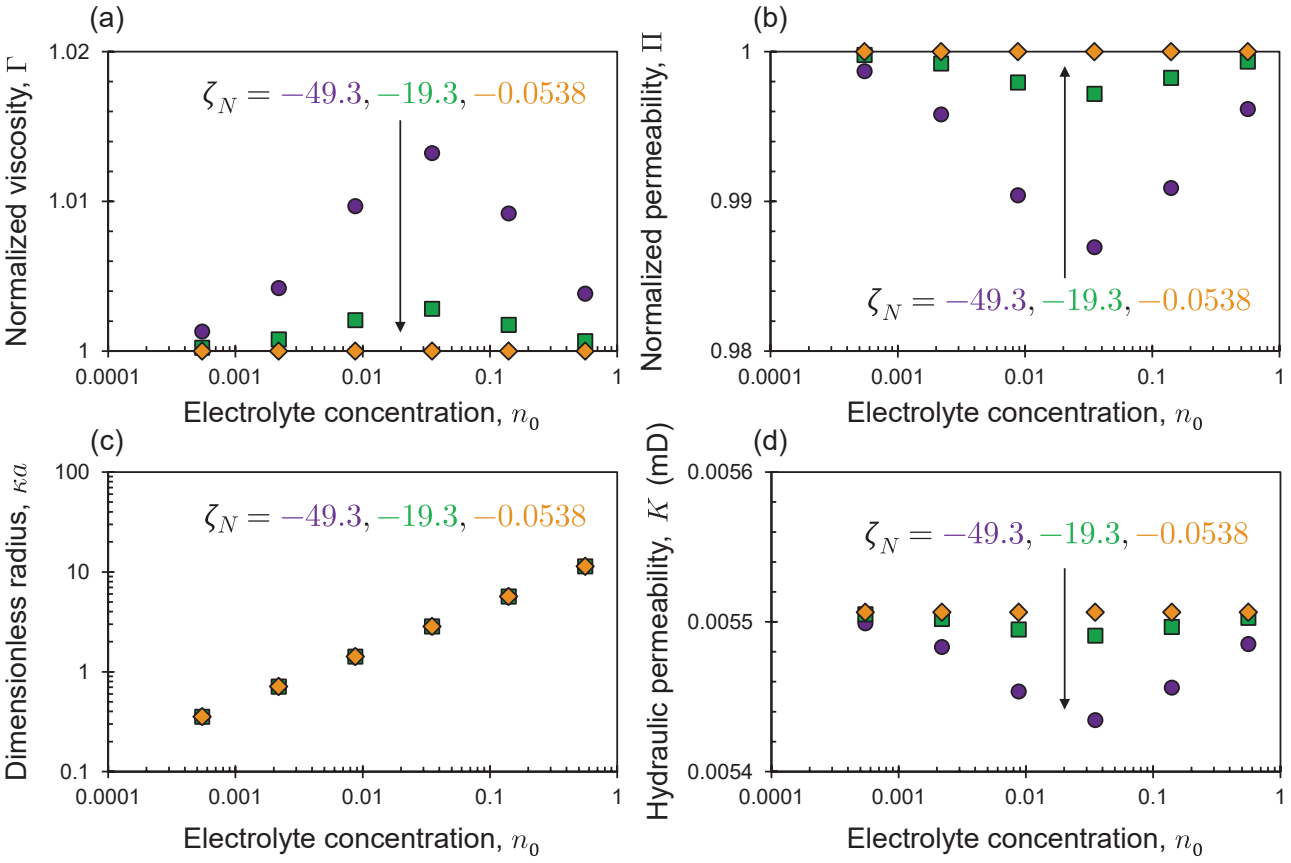

Figure 14. The normalized viscosity Γ (**a**), the normalized hydraulic permeability Π (**b**), the dimensionless capillary radius κa (**c**), and the hydraulic permeability K (**d**), changing with the electrolyte concentration n_0 under different conditions of the dimensionless surface dielectric potential $\zeta_N = \frac{\zeta}{\zeta^*}$, where $\zeta^* = 1.0 \times 10^{-3}$ V. The capillary radius $a = 0.01$ μm.

5. Discussion

Depressurization is currently a preferred method to recover natural gas from hydrate deposits in the ocean, and marine sediments surrounding the wellbore experience pore fluid chemistry changes (e.g., desalination) and increased effective stress, which causes further consolidation. During the consolidation, the characteristic pore size of marine sediments generally decreases. Results of the sensitivity analyses have shown that the decreased characteristic pore size and the decreased pore fluid salinity could jointly affect the hydraulic permeability of clayey sediments, and the coupling effects of pore fluid desalination and increased effective stress during gas hydrate production by depressurization are discussed in this section.

Dependence of the hydraulic permeability K on pore fluid salinity c_0 is characterized by defining a salinity sensitivity index η as

$$\eta = \frac{1}{K}\frac{\partial K}{\partial c_0} \tag{18}$$

If values of the salinity sensitivity index are negative, it is indicated that the hydraulic permeability increases when the pore fluid salinity decreases (i.e., negatively correlated). Positive values of the salinity sensitivity index mean that the hydraulic permeability is positively correlated to the pore fluid salinity. Whether the values are negative or positive, the larger the absolute value of the salinity sensitivity index, the higher the level of the salinity sensitivity of the hydraulic permeability.

The salinity sensitivity index η, changing with the normalized pore fluid salinity Λ under different conditions of the capillary radius a, is demonstrated in Figure 15a. The

normalized pore fluid salinity Λ is defined as the ratio of the pore fluid salinity after desalination over the original pore fluid salinity (i.e., the seawater salinity), and $\Lambda = 100\%$ indicates that the seawater has not been desalinized. It is demonstrated that the salinity sensitivity index η barely changes with the normalized salinity Λ for $a = 0.001$ μm. When the capillary radius increases to $a = 0.01$ μm, the salinity sensitivity index η decreases with decreasing normalized salinity Λ (i.e., increasing desalination degree). The salinity sensitivity index η obviously increases with decreasing normalized salinity Λ for $a = 0.1$ μm. When the capillary radius further increases to $a = 1.0$ μm, the salinity sensitivity index η slightly increases with decreasing normalized salinity desalination degree Λ. These responses could be explained by the dimensionless capillary radius change (Figure 15b). It is demonstrated that the dimensionless capillary radius for $a = 1.0$ μm is much larger than the unit, and the dimensionless capillary radius for $a = 0.001$ μm is much smaller than the unit. For medium-sized capillary radii (i.e., $a = 0.1$ μm and $a = 0.01$ μm), the dimensionless capillary radius is much closer to the unit. The salinity sensitivity index η and its absolute value $|\eta|$, changing with the capillary radius a, are shown in Figure 15c,d, respectively. It is demonstrated that the salinity sensitivity index η increases when the capillary radius decreases from $a = 1.0$ μm to $a = 0.1$ μm and from $a = 0.01$ μm to $a = 0.001$ μm. However, when the capillary radius decreases from $a = 0.1$ μm to $a = 0.01$ μm, the salinity sensitivity index η decreases. In addition, the absolute salinity sensitivity index $|\eta|$ increases when the capillary radius decreases from $a = 1.0$ μm to $a = 0.1$ μm and decreases when the capillary radius decreases from $a = 0.01$ μm to $a = 0.001$ μm. This indicates that the salinity sensitivity of the hydraulic permeability is characteristic pore size dependent, and whether the salinity sensitivity becomes stronger or weaker highly depends on the original characteristic pore size of clayey sediments when subjected to consolidation.

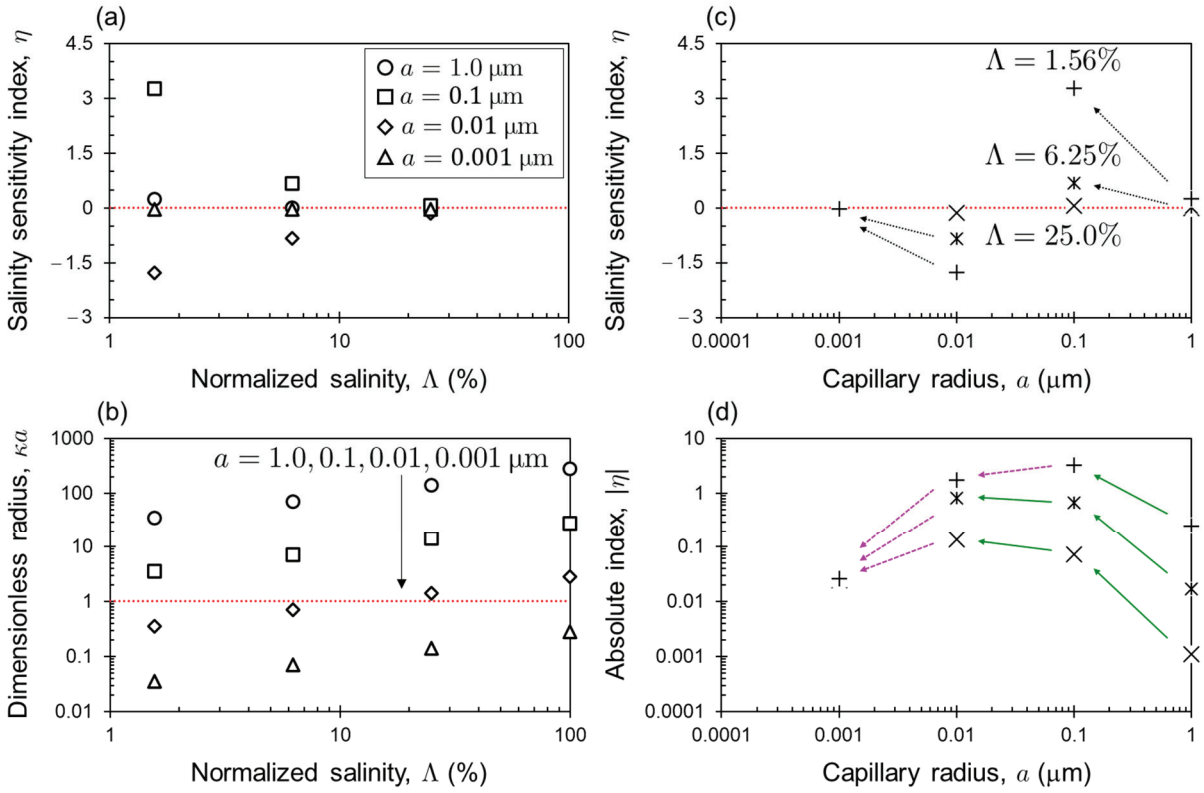

Figure 15. The salinity sensitivity index η of the hydraulic permeability (**a**) and the dimensionless capillary radius κa (**b**) change with the normalized pore fluid salinity Λ under different conditions of the capillary radius a. The salinity sensitivity index η (**c**) and its absolute value $|\eta|$ (**d**) change with the capillary radius a.

6. Conclusions

This study derives and verifies a theoretical model for the hydraulic permeability of clayey sediments, and the verified model is used as a base for sensitivity analyses to deepen the understanding of how hydraulic permeability depends on the pore fluid salinity. Results are further extended to discuss responses of the hydraulic permeability to combined changes in the effective stress and pore fluid salinity during gas hydrate production. The main conclusions are drawn as follows:

The hydraulic permeability of clayey sediments saturated with a saline solution is reduced, due to the development of an electric double layer near the surface of clay minerals, and the permeability reduction is significant only when the electric double layer thickness is comparable to the characteristic pore size. In addition, a smaller ion mobility of the saline solution and a lower surface dielectric potential of the clay minerals both lead to a bigger reduction in hydraulic permeability.

During hydrate production by depressurization in the ocean, sensitivity of the hydraulic permeability to the decreasing salinity of seawater within marine sediments is dependent on the desalination degree and the reduction history of pore sizes. When subjected to a desalination of seawater within marine sediments, with decreasing void ratio due to consolidation, the salinity sensitivity becomes stronger if the original characteristic pore size is relatively large (e.g., several microns) but becomes weaker if relatively small (e.g., several nanometers).

Although the pore size distribution and the fabric of clay particles are excluded, the theoretical model could certainly calculate the macroscopic hydraulic permeability of clayey sediments from the microscopic thickness of an electric double layer near the surface of clay minerals. Impacts of the pore fluid chemistry are properly considered, and the theoretical model has significant potential in gas hydrate production and seawater intrusion prevention.

Author Contributions: Conceptualization, L.L.; methodology, L.C. and L.L.; software, L.L.; validation, L.C., H.Z. and L.L.; formal analysis, H.Z. and B.Y.; investigation, B.Y. and J.Z.; resources, H.S. and X.F.; data curation, H.S.; writing—original draft preparation, L.C. and L.L.; writing—review and editing, H.Z., B.Y. and J.Z.; visualization, L.L.; supervision, X.F.; project administration, X.F.; funding acquisition, X.F. and L.L. All authors have read and agreed to the published version of the manuscript.

Funding: This study is jointly supported by the Qingdao Key Laboratory of Groundwater Resources Protection and Rehabilitation (grant DXSKF2022Z03), the Natural Science Foundation of Shandong Province (grant ZR2022YQ54), the Qingdao Science and Technology Demonstration Project for Benefiting the People (grant 24-1-8-cspz-14-nsh), and the Taishan Scholars Program (grant tsqn202306297).

Institutional Review Board Statement: Not applicable.

Informed Consent Statement: Not applicable.

Data Availability Statement: The original contributions presented in this study are included in the article. Further inquiries can be directed to the corresponding author.

Conflicts of Interest: The authors declare no conflict of interest.

References

1. Kumari, N.; Mohan, C. Basics of Clay Minerals and Their Characteristic Properties. In *Clay and Clay Minerals*; IntechOpen: London, UK, 2021; ISBN 978-1-83969-564-3.
2. Ghosh, B.; Chakraborty, D. An Overview of the Clay Minerals: Composition, Classification, Internal Structure and Properties. In *Clay Minerals: Their Antimicrobial and Antitoxic Applications*; Ghosh, B., Chakraborty, D., Eds.; Springer International Publishing: Cham, Switzerland, 2023; pp. 1–24. ISBN 978-3-031-22327-3.
3. Iranfar, S.; Karbala, M.M.; Shakiba, M.; Shahsavari, M.H. Effects of Type and Distribution of Clay Minerals on the Physico-Chemical and Geomechanical Properties of Engineered Porous Rocks. *Sci. Rep.* **2023**, *13*, 5837. [CrossRef] [PubMed]
4. Brown, G. Structure, Crystal Chemistry, and Origin of the Phyllosilicate Minerals Common in Soil Clays. In *Soil Colloids and Their Associations in Aggregates*; De Boodt, M.F., Hayes, M.H.B., Herbillon, A., De Strooper, E.B.A., Tuck, J.J., Eds.; Springer US: Boston, MA, USA, 1990; pp. 7–38. ISBN 978-1-4899-2611-1.

5. Fagel, N. Chapter Four Clay Minerals, Deep Circulation and Climate. In *Developments in Marine Geology*; Hillaire–Marcel, C., De Vernal, A., Eds.; Proxies in Late Cenozoic Paleoceanography; Elsevier: Amsterdam, The Netherlands, 2007; Volume 1, pp. 139–184.
6. Thiry, M. Palaeoclimatic Interpretation of Clay Minerals in Marine Deposits: An Outlook from the Continental Origin. *Earth-Sci. Rev.* **2000**, *49*, 201–221. [CrossRef]
7. Jang, J.; Cao, S.C.; Stern, L.A.; Jung, J.; Waite, W.F. Impact of Pore-Fluid Chemistry on Fine-Grained Sediment Fabric and Compressibility. *J. Geophys. Res. Solid. Earth* **2018**, *123*, 5495–5514. [CrossRef]
8. Li, Y.; Liu, L.; Jin, Y.; Wu, N. Characterization and Development of Marine Natural Gas Hydrate Reservoirs in Marine Clayey-Silt Reservoirs: A Review and Discussion. *Adv. Geo-Energy Res.* **2021**, *5*, 75–86. [CrossRef]
9. Boswell, R. Is Gas Hydrate Energy Within Reach? *Science* **2009**, *325*, 957–958. [CrossRef]
10. Sloan, E.D. Fundamental Principles and Applications of Natural Gas Hydrates. *Nature* **2003**, *426*, 353–363. [CrossRef]
11. Cunillera-Montcusí, D.; Beklioğlu, M.; Cañedo-Argüelles, M.; Jeppesen, E.; Ptacnik, R.; Amorim, C.A.; Arnott, S.E.; Berger, S.A.; Brucet, S.; Dugan, H.A.; et al. Freshwater Salinisation: A Research Agenda for a Saltier World. *Trends Ecol. Evol.* **2022**, *37*, 440–453. [CrossRef]
12. Post, V.E.A.; Groen, J.; Kooi, H.; Person, M.; Ge, S.; Edmunds, W.M. Offshore Fresh Groundwater Reserves as a Global Phenomenon. *Nature* **2013**, *504*, 71–78. [CrossRef]
13. Fang, Y.; Zheng, T.; Wang, H.; Zheng, X.; Walther, M. Influence of Dynamically Stable-Unstable Flow on Seawater Intrusion and Submarine Groundwater Discharge Over Tidal and Seasonal Cycles. *J. Geophys. Res. Ocean* **2022**, *127*, e2021JC018209. [CrossRef]
14. Werner, A.D.; Bakker, M.; Post, V.E.A.; Vandenbohede, A.; Lu, C.; Ataie-Ashtiani, B.; Simmons, C.T.; Barry, D.A. Seawater Intrusion Processes, Investigation and Management: Recent Advances and Future Challenges. *Adv. Water Resour.* **2013**, *51*, 3–26. [CrossRef]
15. Deng, Y.; Zhang, T.; Cui, Y.; Chen, Y.; Deng, T.; Zhou, X. Pore Water Salinity Effect on the Intrinsic Compression Behaviour of Artificial Soft Soils. *Appl. Clay Sci.* **2018**, *166*, 299–306. [CrossRef]
16. Musso, G.; Scelsi, G.; Della Vecchia, G. Chemo-Mechanical Behaviour of Non-Expansive Clays Accounting for Salinity Effects. *Géotechnique* **2024**, *74*, 632–646. [CrossRef]
17. Song, M.-M.; Zeng, L.-L.; Hong, Z.-S. Pore Fluid Salinity Effects on Physicochemical-Compressive Behaviour of Reconstituted Marine Clays. *Appl. Clay Sci.* **2017**, *146*, 270–277. [CrossRef]
18. Tang, S.; She, D.; Wang, H. Effect of Salinity on Soil Structure and Soil Hydraulic Characteristics. *Can. J. Soil. Sci.* **2021**, *101*, 62–73. [CrossRef]
19. Cai, W.; Bordoloi, S.; Zhu, C.; Gupt, C.B. Influence of Plasticity and Porewater Salinity on Shrinkage and Water Retention Characteristics of Biochar-Engineered Clays. *Soil Sci. Soc. Am. J.* **2023**, *87*, 1285–1303. [CrossRef]
20. Bayesteh, H.; Hezareh, H. Behavior of Cement-Stabilized Marine Clay and Pure Clay Minerals Exposed to High Salinity Grout. *Constr. Build. Mater.* **2023**, *383*, 131334. [CrossRef]
21. Mishra, A.K.; Ohtsubo, M.; Li, L.Y.; Higashi, T.; Park, J. Effect of Salt of Various Concentrations on Liquid Limit, and Hydraulic Conductivity of Different Soil-Bentonite Mixtures. *Environ. Geol.* **2009**, *57*, 1145–1153. [CrossRef]
22. Quirk, J.P.; Schofield, R.K. The Effect of Electrolyte Concentration on Soil Permeability. *J. Soil. Sci.* **1955**, *6*, 163–178. [CrossRef]
23. Jo, H.Y.; Benson, C.H.; Edil, T.B. Hydraulic Conductivity and Cation Exchange in Non-Prehydrated and Prehydrated Bentonite Permeated with Weak Inorganic Salt Solutions. *Clays Clay Miner.* **2004**, *52*, 661–679. [CrossRef]
24. Yilmaz, G.; Yetimoglu, T.; Arasan, S. Hydraulic Conductivity of Compacted Clay Liners Permeated with Inorganic Salt Solutions. *Waste Manag. Res.* **2008**, *26*, 464–473. [CrossRef]
25. Wan, Y.; Yuan, Y.; Zhou, C.; Liu, L. Multiphysics Coupling in Exploitation and Utilization of Geo-Energy: State-of-the-Art and Future Perspectives. *Adv. Geo-Energy Res.* **2023**, *10*, 7–13. [CrossRef]
26. Liu, L.; Lu, X.; Zhang, X. A Theoretical Model for Predicting the Spatial Distribution of Gas Hydrate Dissociation under the Combination of Depressurization and Heating without the Discontinuous Interface Assumption. *J. Pet. Sci. Eng.* **2015**, *133*, 589–601. [CrossRef]
27. Zhang, H.; Bian, H.; Qi, S.; Wang, J. A Comprehensive Analysis of Formation Conditions, Intrinsic Properties, and Mechanical Responses of Gas Hydrate-Bearing Sediments. *Rock Mech. Bull.* **2024**, *3*, 100114. [CrossRef]
28. Strack, O.D.L.; Stoeckl, L.; Damm, K.; Houben, G.; Ausk, B.K.; de Lange, W.J. Reduction of Saltwater Intrusion by Modifying Hydraulic Conductivity. *Water Resour. Res.* **2016**, *52*, 6978–6988. [CrossRef]
29. Kerrou, J.; Renard, P. A Numerical Analysis of Dimensionality and Heterogeneity Effects on Advective Dispersive Seawater Intrusion Processes. *Hydrogeol. J.* **2010**, *18*, 55–72. [CrossRef]
30. Lu, C.; Chen, Y.; Zhang, C.; Luo, J. Steady-State Freshwater–Seawater Mixing Zone in Stratified Coastal Aquifers. *J. Hydrol.* **2013**, *505*, 24–34. [CrossRef]
31. Liu, L.; Dai, S.; Ning, F.; Cai, J.; Liu, C.; Wu, N. Fractal Characteristics of Unsaturated Sands—Implications to Relative Permeability in Hydrate-Bearing Sediments. *J. Nat. Gas. Sci. Eng.* **2019**, *66*, 11–17. [CrossRef]
32. Golparvar, A.; Zhou, Y.; Wu, K.; Ma, J.; Yu, Z. A Comprehensive Review of Pore Scale Modeling Methodologies for Multiphase Flow in Porous Media. *Adv. Geo-Energy Res.* **2018**, *2*, 418–440. [CrossRef]
33. Pisano, A. From Tubes and Catheters to the Basis of Hemodynamics: The Hagen–Poiseuille Equation. In *Physics for Anesthesiologists: From Daily Life to the Operating Room*; Pisano, A., Ed.; Springer International Publishing: Cham, Switzerland, 2017; pp. 55–61. ISBN 978-3-319-57330-4.

34. Darcy, H. *The Public Fountains of the City of Dijon (Translated by Patricia Bobeck)*; Kendall Hunt Publishing Co.: Dubuque, IA, USA, 2004; ISBN 978-0-7575-0540-9.
35. Brown, G.O. Henry Darcy and the Making of a Law. *Water Resour. Res.* **2002**, *38*, 11-1–11-12. [CrossRef]
36. Kozeny, J. Uber Kapillare Leitung Des Wassers Im Boden. *Sitzungsberichte Der Akad. Der Wiss. Math.-Naturwissenschaftliche Kl.* **1927**, *136*, 271–306.
37. Carman, P.C. Fluid Flow through Granular Beds. *Trans. Inst. Chem. Eng.* **1937**, *15*, 150–167. [CrossRef]
38. Chapuis, R.P. Predicting the Saturated Hydraulic Conductivity of Soils: A Review. *Bull. Eng. Geol. Environ.* **2012**, *71*, 401–434. [CrossRef]
39. Qin, Z.; Nie, X.; Yu, W.; Yang, S.; Zhou, Z.; Yang, S.; Wan, Q. Probing the Surface Electrical Properties of Clay Minerals with Electrostatic Force Microscopy and Kelvin Probe Force Microscopy. *Mater. Res. Express* **2024**, *11*, 025501. [CrossRef]
40. Carcione, J.M.; Gei, D.; Yu, T.; Ba, J. Effect of Clay and Mineralogy on Permeability. *Pure Appl. Geophys.* **2019**, *176*, 2581–2594. [CrossRef]
41. Akin, I.D.; Likos, W.J. Single-Point and Multi-Point Water-Sorption Methods for Specific Surface Areas of Clay. *Geotech. Test. J.* **2016**, *39*, 291–300. [CrossRef]
42. Maček, M.; Mauko, A.; Mladenovič, A.; Majes, B.; Petkovšek, A. A Comparison of Methods Used to Characterize the Soil Specific Surface Area of Clays. *Appl. Clay Sci.* **2013**, *83–84*, 144–152. [CrossRef]
43. Sharma, A.; Hazra, B.; Spagnoli, G.; Sekharan, S. Probabilistic Estimation of Specific Surface Area and Cation Exchange Capacity: A Global Multivariate Distribution. *Can. Geotech. J.* **2021**, *58*, 1077–1094. [CrossRef]
44. Taylor, D.W. Fundamentals of Soil Mechanics. *Soil Sci.* **1948**, *66*, 161. [CrossRef]
45. Mesri, G.; Olson, R.E. Mechanisms Controlling the Permeability of Clays. *Clays Clay Miner.* **1971**, *19*, 151–158. [CrossRef]
46. Nagaraj, T.S.; Pandian, N.S.; Narashimha Raju, P.S.R. Stress State-Permeability Relationships for Fine-Grained Soils. *Géotechnique* **1993**, *43*, 333–336. [CrossRef]
47. Dai, S.; Santamarina, J.C. *Hydrate-Bearing Clayey Sediments: Morphology, Physical Properties, Production and Engineering/Geological Implications*; Georgia Institute of Technology: Atlanta, GA, USA, 2017.
48. Diamond, S. Pore Size Distributions in Clays. *Clays Clay Miner.* **1970**, *18*, 7–23. [CrossRef]
49. Zhang, X.; Wang, G.; Liu, X.; Xu, Y.; Kong, L. Microstructural Analysis of Pore Characteristics of Natural Structured Clay. *Bull. Eng. Geol. Environ.* **2022**, *81*, 473. [CrossRef]
50. van der Heyden, F.H.J.; Bonthuis, D.J.; Stein, D.; Meyer, C.; Dekker, C. Power Generation by Pressure-Driven Transport of Ions in Nanofluidic Channels. *Nano Lett.* **2007**, *7*, 1022–1025. [CrossRef]
51. Wu, J. Understanding the Electric Double-Layer Structure, Capacitance, and Charging Dynamics. *Chem. Rev.* **2022**, *122*, 10821–10859. [CrossRef] [PubMed]
52. Olthuis, W.; Schippers, B.; Eijkel, J.; van den Berg, A. Energy from Streaming Current and Potential. *Sens. Actuators B Chem.* **2005**, *111–112*, 385–389. [CrossRef]
53. Yang, J.; Kwok, D.Y. Microfluid Flow in Circular Microchannel with Electrokinetic Effect and Navier's Slip Condition. *Langmuir* **2003**, *19*, 1047–1053. [CrossRef]
54. Levine, S.; Marriott, J.R.; Neale, G.; Epstein, N. Theory of Electrokinetic Flow in Fine Cylindrical Capillaries at High Zeta-Potentials. *J. Colloid Interface Sci.* **1975**, *52*, 136–149. [CrossRef]
55. Bhattacharyya, A.; Masliyah, J.H.; Yang, J. Oscillating Laminar Electrokinetic Flow in Infinitely Extended Circular Microchannels. *J. Colloid Interface Sci.* **2003**, *261*, 12–20. [CrossRef]
56. Cheng, H.; Wang, F.; Guan, X.; Yang, G.; Yuan, Y.; Feng, G. A Mathematical Model for Pre-Darcy Flow in Low Permeability Porous Media with Stress Sensitivity and the Boundary-Layer Effect. *Eng. Geol.* **2023**, *324*, 107257. [CrossRef]
57. Hasan, M.F.; Abuel-Naga, H. Effect of Temperature and Water Salinity on Electrical Surface Conduction of Clay Particles. *Minerals* **2023**, *13*, 1110. [CrossRef]
58. Costa Reis, M. Ion Activity Models: The Debye-Hückel Equation and Its Extensions. *ChemTexts* **2021**, *7*, 9. [CrossRef]
59. Blossey, R. The Poisson–Boltzmann Equation. In *The Poisson–Boltzmann Equation: An Introduction*; Blossey, R., Ed.; Springer International Publishing: Cham, Switzerland, 2023; pp. 1–25. ISBN 978-3-031-24782-8.
60. Rice, C.L.; Whitehead, R. Electrokinetic Flow in a Narrow Cylindrical Capillary. *J. Phys. Chem.* **1965**, *69*, 4017–4024. [CrossRef]
61. Kim, S.I.; Kim, S.J. Analysis of the Electroviscous Effects on Pressure-Driven Flow in Nanochannels Using Effective Ionic Concentrations. *Microfluid. Nanofluid.* **2017**, *22*, 12. [CrossRef]
62. Murrell, J.N. Avogadro and His Constant. *Helv. Chim. Acta* **2001**, *84*, 1314–1327. [CrossRef]
63. Zhang, P. *Physical Chemistry*, 2nd ed.; Chemical Industry Press Co., Ltd.: Beijing, China, 2023; ISBN 978-7-122-42316-0.
64. Gould, W.J.; Cunningham, S.A. Global-Scale Patterns of Observed Sea Surface Salinity Intensified since the 1870s. *Commun. Earth Environ.* **2021**, *2*, 1–7. [CrossRef]
65. Iversen, N.; Jørgensen, B.B. Diffusion Coefficients of Sulfate and Methane in Marine Sediments: Influence of Porosity. *Geochim. Cosmochim. Acta* **1993**, *57*, 571–578. [CrossRef]
66. Lin, L.I.-K. A Concordance Correlation Coefficient to Evaluate Reproducibility. *Biometrics* **1989**, *45*, 255–268. [CrossRef]
67. Lin, L.; Hedayat, A.S.; Wu, W. *Statistical Tools for Measuring Agreement*; Springer: New York, NY, USA, 2012; ISBN 978-1-4614-0561-0.
68. Zaffar, M.; Lu, S.-G. Pore Size Distribution of Clayey Soils and Its Correlation with Soil Organic Matter. *Pedosphere* **2015**, *25*, 240–249. [CrossRef]

69. Kuila, U.; Prasad, M. Specific Surface Area and Pore-Size Distribution in Clays and Shales. *Geophys. Prospect.* **2013**, *61*, 341–362. [CrossRef]
70. Cheng, Q.; Ng, C.W.W.; Zhou, C.; Tang, C.S. A New Water Retention Model That Considers Pore Non-Uniformity and Evolution of Pore Size Distribution. *Bull. Eng. Geol. Environ.* **2019**, *78*, 5055–5065. [CrossRef]
71. Zhou, C.; Ng, C.W.W. A New and Simple Stress-Dependent Water Retention Model for Unsaturated Soil. *Comput. Geotech.* **2014**, *62*, 216–222. [CrossRef]

Journal of
Marine Science and Engineering

MDPI

Article

Analysis of the Vertical Dynamic Response of SDCM Piles in Coastal Areas

Yeyu Yan [1,2], Hongbo Liu [1,2], Guoliang Dai [1,2,*], Yufan Xiang [1,2] and Chenhu Xu [1,2]

[1] Key Laboratory of Concrete and Prestressed Concrete Structures, Ministry of Education, Southeast University, Nanjing 211189, China
[2] School of Civil Engineering, Southeast University, Nanjing 211189, China
* Correspondence: daigl@seu.edu.cn; Tel.: +86-139-1298-7757

Abstract: The stiffened deep cement mixing (SDCM) pile, as a new type of rigid–flexible composite pile, significantly enhances the vertical bearing capacity of traditional precast piles, thus holding broad application prospects in the substructure construction of nearshore bridges and marine energy structures. This paper investigates the vertical dynamic response of SDCM piles through theoretical derivation and parameter analysis. Firstly, based on elastic dynamics theory and the three-phase porous media model, vertical vibration control equations for both SDCM piles and fractional-order viscoelastic unsaturated soils are established. Secondly, theoretical derivations yield exact analytical solutions for the surrounding dynamic impedance, top dynamic stiffness, and dynamic damping of the SDCM pile. Finally, through numerical examples and parameter studies, the impact mechanisms of physical parameters in the SDCM pile–unsaturated soil dynamic coupling system on the top dynamic stiffness and dynamic damping of the SDCM pile are analyzed. The research results presented in this paper indicate that reducing the radius of the rigid core pile while increasing the thickness of the exterior pile has a positive effect on enhancing its vibration resistance. Additionally, increasing the length of SDCM piles contributes to improved vibration performance. However, an increase in the elastic modulus of the cement–soil exterior pile is detrimental to the vibration resistance of the rigid composite pile. On the other hand, an increase in the elastic modulus of the concrete core pile only enhances its ability to resist vibration under low-frequency load excitation. Furthermore, enlarging the soil saturation, decreasing the intrinsic permeability, and enlarging the soil relaxation shear modulus have a significant positive impact on improving the vibration resistance of SDCM piles. In contrast, changes in porosity have a negligible effect on the ability to resist vertical vibrations of SDCM piles.

Keywords: stiffened deep cement mixing (SDCM) pile; unsaturated soil; cyclic load

1. Introduction

Stiffened deep cement mixing (SDCM) piles represent an innovative category of composite pile foundations [1]. The introduction of SDCM piles addresses the poor bearing performance of traditional DCM piles when the soil at the pile tip is of low quality [2,3]. SDCM piles incorporate a stiffened core made of concrete or steel pipe into the DCM pile [4,5], thereby extending the load transfer path and creating a composite pile where the core and exterior piles reinforce each other [6,7]. This design improves the reinforcement effect and bearing capacity of the pile foundation in weak soil layers.

The SDCM pile exhibits remarkable bearing capacity, attributable to the synergistic benefits of integrating single large-diameter deep cement mixing (DCM) with rigid pile, even under challenging soil conditions [8–11], which renders it highly suitable for use in coastal soft soil regions for infrastructure such as bridges, buildings, and constructions on artificial islands, as well as for foundations supporting offshore wind and photovoltaic installations. Bridges and energy facilities are subjected to dynamic loads, which include

those resulting from vehicle vibrations, wind forces, and the rotational effects of wind turbine blades [12–15].

Since the inception of SDCM piles, they have been extensively applied [16–18]. Experimental studies, numerical simulations, and theoretical analyses, as the most commonly used methods for addressing geotechnical engineering issues [19], have led numerous researchers to investigate SDCM piles through these approaches. Existing research demonstrates that the inclusion of a core pile substantially enhances the load-bearing capacity of DCM piles. Building on this foundation, some researchers have explored different concrete core piles. For instance, Liu et al. [20] proposed a T-shape core pile that enhances load-bearing capacity while saving costs. Jamsawang et al. [21] conducted field tests on the SDCM pile incorporating a rectangular core pile, showing that the presence of the rectangular core significantly increased the side resistance of the SDCM pile compared to the DCM pile, thereby enhancing the structural load capacity of pile foundations set in weak support layers. Zhou et al.'s [22,23] research on concrete nodular column core piles indicated that using SDCM piles provides an improvement compared to traditional cast-in-place piles.

Furthermore, numerous researchers have conducted extensive studies on the factors influencing the load-bearing performance of SDCM piles. Jamsawang et al.'s [24] investigations confirmed that longer core piles can significantly enhance the structural capacity of SDCM piles to support loads. Wonglert and Jongpradist [9] conducted numerical simulations and laboratory experiments to study the effects of core length and materials on the structural capacity of SDCM piles to support loads. Their results imply that the optimal core length is related to the surrounding soil and the strength of the DCM socket. Tang et al. [25] have shown through experimental and numerical simulations that the length of the core pile is a critical determinant of the load-bearing capacity of SDCM piles. The structural capacity of SDCM piles to support loads can be significantly enhanced at the optimal core pile length. Bao et al. [26] performed model experiments to examine how lateral pressure influences the shear mechanical characteristics of the inner interface. Their research indicates that even when the inner pile is a smooth steel pipe, it can achieve a close bond with the surrounding cement–soil. The upper load is transmitted downward through the rigid core pile, and during this transmission, it diffuses through the exterior pile to the surrounding soil, with only a small portion of the load reaching the pile tip. Dai et al. [4] utilized finite element software (Diana, https://dianafea.com/) capable of simulating Mohr–Coulomb friction to study SDCM piles, revealing a significant group pile effect in foundations composed of SDCM piles. Moreover, they found that SDCM piles still exhibit some characteristics of flexible piles, with potential negative skin friction occurring at the top. Peng et al.'s [27] model testing demonstrates that while increasing the cement content in the outer cement–soil piles and utilizing ribbed steel pipe piles significantly enhances the load-bearing capacity of SDCM piles, the use of ribbed steel pipe piles as core piles can also considerably improve the bond strength conversion factor. Additionally, based on experimental results and the load transfer method, they proposed a calculation formula for the structural capacity of model piles to support loads. Gong et al. [28] established and validated the calculation model for SDCM piles through theoretical research, proposing the optimal ratio of lengths and radii of the core and exterior piles. The study also indicated that the elastic modulus of the pile does not significantly affect its bearing capacity. In the recent years, the bearing capacity for soils have been investigated through machine learning approaches, which can be a useful tool for engineers [29,30].

The aforementioned experimental studies, numerical simulations, and theoretical analyses indicate that the compressive, tensile, and lateral load-bearing characteristics of SDCM piles surpass those of the same-diameter bored cast-in-place piles and precast piles, offering significant economic benefits. However, compared to the research on conventional pile foundations, existing studies on SDCM piles have primarily focused on their static properties, while research under dynamic loading conditions is still relatively lacking [31–35]. This issue is particularly prominent in theoretical analyses. Limited research has already

demonstrated that SDCM piles exhibit a substantial improvement in resistance to cyclic loads compared to DCM piles [36]. In addition, some scholars have also studied the seismic resistance of SDCM piles [37]. Given the extensive application of SDCM piles in bridge foundations and land-based wind power foundations in coastal and soft clay areas, as well as the wide application prospects in offshore bridges and offshore energy facilities, it is important to undertake a theoretical study of the dynamic response of pile apex of SDCM piles to support their implementation.

This research aims to assess the vertical dynamic response of SDCM piles—composed of concrete pipe piles (core pile) and cement–soil columns (exterior pile)—subjected to dynamic loads applied at the top of the pile. This study assumes that the surrounding soil is modeled as a fractional-order viscoelastic unsaturated porous medium. Through theoretical derivations, numerical examples, and parameter analyses, this research aims to provide references for the applications of SDCM piles in bridges and offshore energy facility construction in coastal areas and to offer suggestions for improving the vertical cyclic load capacity of SDCM piles.

2. Research Process

As shown in Figure 1, this paper first establishes a computational model for the SDCM pile resisting vertical dynamic loads in viscoelastic unsaturated soil. Subsequently, based on this model, the micro-unit equilibrium equations for the core pile and the exterior pile are obtained. Following this, the axial vibration equation of the SDCM pile is derived based on mechanical equilibrium. By introducing the motion control equations of the viscoelastic unsaturated soil, the analytical solution for the dynamic impedance at the top of the SDCM pile is finally deduced.

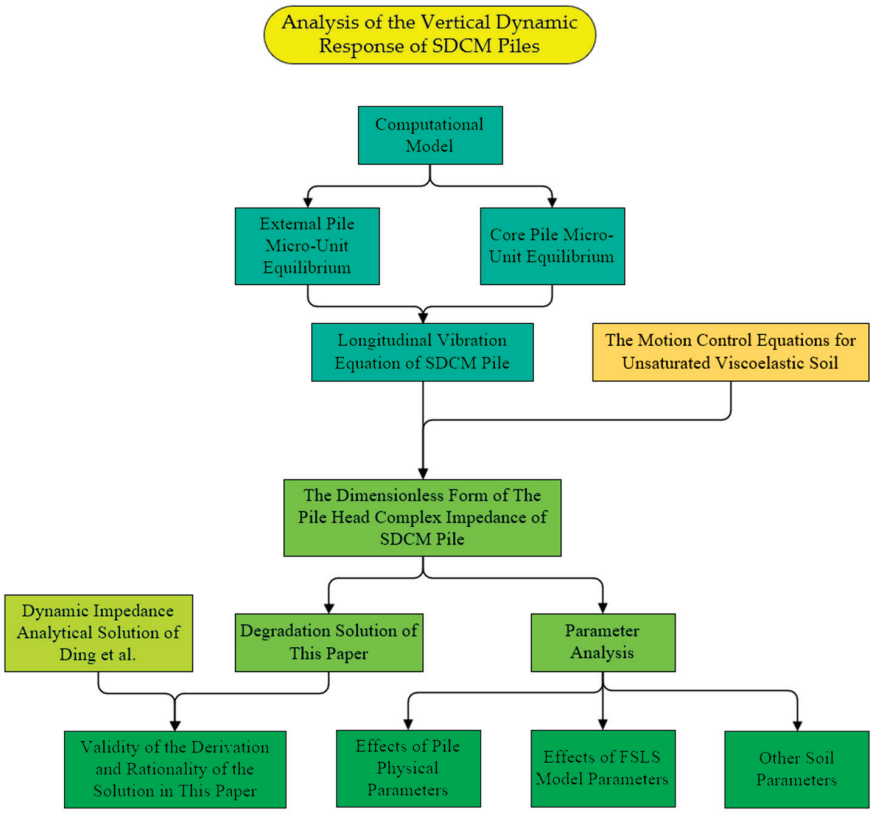

Figure 1. Mind map of this paper. (The comparative validation section in this figure references Ding et al. [38]).

Based on the analytical solution for dynamic impedance, the degradation solution presented in this paper is derived and compared with the research results of Ding et al. [38]

to verify the validity and rationality of the proposed solutions. After confirming the correctness of the analytical solution obtained in this paper, parameter analysis is conducted based on this solution from three aspects: pile physical parameters, the fractional standard linear solid (FSLS) parameters, and other soil parameters, investigating how variations in these parameters affect the vibration resistance capacity of the SDCM pile.

3. Computational Models and Fundamental Equations

3.1. Computational Models and Assumptions

The configuration of the pile–soil interaction system considered in this paper is depicted in Figure 2. The pile shown in the figure is a bottom-closed stiffened composite pile, including a core pile made of concrete pipe pile and an external pile made of cement–soil pile, which are fully bonded along their entire length at the interface to form an integrated unit. The concrete core pile has a density of ρ_c, cross-sectional area A_c, and inner and external radii r_1 and r_2, respectively. The exterior pile has a density of σ_m, cross-sectional area A_m, and inner and outer radii r_2 and r_3, respectively. The SDCM pile has a total length L and is subjected to a uniformly distributed harmonic dynamic load $P(t)$ applied at its top. The pile end is supported on a dense soil layer (considered as a rigid base).

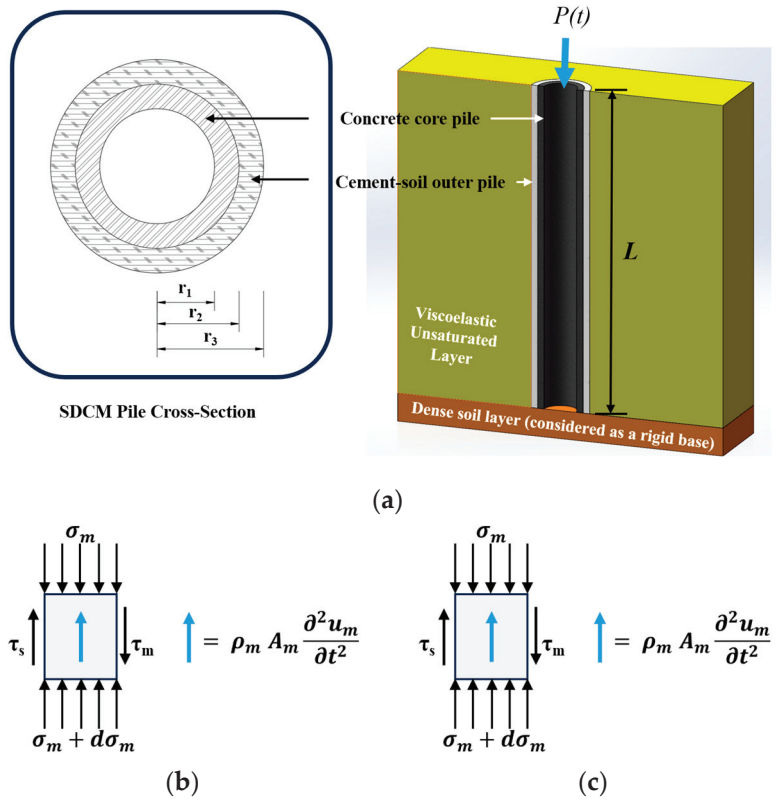

Figure 2. Simplified model of pile–soil interaction (**a**) schematic diagram of the computational model; (**b**) micro unit of the cement–soil exterior pile; (**c**) micro unit of the concrete core pile.

The longitudinal stress acting on the top of the micro unit of the core pile is denoted by σ_c, and the frictional resistance affecting the outer wall of the micro unit of the core pile is denoted by τ_m. The longitudinal displacement of the concrete core pile is denoted by u_c.

The primary assumptions are as follows:

(1) The soil adjacent to the pile is homogeneous, isotropic, viscoelastic, and unsaturated;
(2) The cement–soil exterior pile and concrete core pile are linear elastic mediums, neglecting their viscosity;

(3) Deformations induced by vibration in the pile–soil interaction system are small deformations. During vibration, displacements and stresses at the pile–soil interface remain continuous and coordinated;
(4) There is sufficient adhesive strength between the cement–soil exterior pile and concrete core pile, and the interface between them does not detach or experience mutual misalignment during vibration;
(5) At the initial moment, the pile–soil interaction system is in a static state;
(6) The compaction effects due to pile driving are neglected.

3.2. Longitudinal Vibration Equation of SDCM Pile

For the cement–soil exterior pile, the longitudinal force balance of the microelement shown in Figure 2 can be obtained.

$$A_m\sigma_m + 2\pi r_2\tau_m = A_m(\sigma_m + \mathrm{d}\sigma_m) + 2\pi r_3\tau_s + \rho_m A_m\frac{\partial^2 u_m}{\partial t^2} \tag{1}$$

Similarly, the longitudinal force equilibrium of the microelement of the concrete core pile shown in Figure 2 can be derived.

$$A_c\sigma_c = A_c(\sigma_c + \mathrm{d}\sigma_c) + 2\pi r_2\tau_m + \rho_c A_c\frac{\partial^2 u_c}{\partial t^2} \tag{2}$$

From the stress–strain relationship and combined with Hooke's law, the following equation can be derived.

$$\begin{cases} \sigma_m = E_m\varepsilon_m = -E_m\frac{\partial u_m}{\partial z} \\ \sigma_c = E_c\varepsilon_c = -E_c\frac{\partial u_c}{\partial z} \end{cases} \tag{3}$$

In the equation, E_m and E_c represent the elastic moduli of the exterior pile and the core pile, respectively.

Substituting Equation (3) into Equations (1) and (2) gives

$$E_m A_m\frac{\partial^2 u_m}{\partial z^2} + \rho_m A_m\omega^2 u_m = 2\pi(r_3\tau_s - r_2\tau_m) \tag{4}$$

$$E_c A_c\frac{\partial^2 u_c}{\partial z^2} + \rho_c A_c\omega^2 u_c = 2\pi r_2\tau_m \tag{5}$$

In the equation, $\omega = 2\pi f$ defines angular frequency, where f is frequency (Hz).

Considering sufficient interfacial bond strength between the cement grout pile and the concrete core pile, mutual slippage between them can be neglected. Therefore, $u_c = u_m = u_p$ can be assumed. Combining Equations (4) and (5) yields the longitudinal vibration equation for the composite cement grout pile.

$$(E_m A_m + E_c A_c)\frac{\partial^2 u_p}{\partial z^2} + (\rho_m A_m + \rho_c A_c)\omega^2 u_p - 2\pi r_3\tau_s = 0 \tag{6}$$

3.3. The Governing Equation for Soil at the Pile Side

Considering the soil at the pile side as a non-saturated, porous, viscoelastic medium composed of solid, liquid, and gas phases, this paper introduces the motion control equations for unsaturated viscoelastic soil established by Liu et al. [39].

$$\begin{cases} \overline{\mu}(\omega)u_{i,jj} + [C_{11}(\omega) + \overline{\mu}(\omega)]u_{j,ji} + C_{12}(\omega)w_{j,ji} + C_{13}(\omega)v_{j,ji} = \rho\ddot{u}_i + \rho_w\ddot{w}_i + \rho_g\ddot{v}_i \\ C_{21}(\omega)u_{j,ji} + C_{22}(\omega)w_{j,ji} + C_{23}(\omega)v_{j,ji} = \rho_w\ddot{u}_i + \rho_w\ddot{w}_i/(\phi S_w) + \mu_w\dot{w}_i/(k_{rw}k) \\ C_{31}(\omega)u_{j,ji} + C_{32}(\omega)w_{j,ji} + C_{33}(\omega)v_{j,ji} = \rho_g\ddot{u}_i + \rho_g\ddot{v}_i/(\phi S_g) + \mu_g\dot{v}_i/(k_{rg}k) \end{cases} \tag{7}$$

Pore water pressure and pore air pressure can be expressed as

$$\begin{cases} p_w = -C_{21}(\omega)u_{i,i} - C_{22}(\omega)w_{i,i} - C_{23}(\omega)v_{i,i} \\ p_g = -C_{31}(\omega)u_{i,i} - C_{32}(\omega)w_{i,i} - C_{33}(\omega)v_{i,i} \end{cases} \tag{8}$$

In this formula

$$C_{11}(\omega) = \overline{\lambda}(\omega) + S_w\overline{a}(\omega)C_{21}(\omega) + S_g\overline{a}(\omega)C_{31}(\omega)$$

$$C_{12}(\omega) = \overline{a}(\omega)\left[S_w\overline{B}_{12}(\omega) + S_g\overline{B}_{22}(\omega)\right]/(\phi S_w)$$

$$C_{13}(\omega) = \overline{a}(\omega)\left[S_w\overline{B}_{13}(\omega) + S_g\overline{B}_{23}(\omega)\right]/\phi S_g$$

$$C_{21}(\omega) = \overline{B}_{11}(\omega) + \overline{B}_{12}(\omega) + \overline{B}_{13}(\omega)$$

$$C_{22}(\omega) = \overline{B}_{12}(\omega)/(\phi S_w)$$

$$C_{23}(\omega) = \overline{B}_{13}(\omega)/\left(\phi S_g\right)$$

$$C_{31}(\omega) = \overline{B}_{21}(\omega) + \overline{B}_{22}(\omega) + \overline{B}_{23}(\omega)$$

$$C_{32}(\omega) = \overline{B}_{22}(\omega)/(\phi S_w)$$

$$C_{33}(\omega) = \overline{B}_{23}(\omega)/\left(\phi S_g\right)$$

$$k_{rw} = \sqrt{S_e}\left[1 - \left(1 - {S_e}^{1/m}\right)^m\right]^2$$

$$k_{rg} = \sqrt{1 - S_e}\left(1 - {S_e}^{1/m}\right)^{2m}$$

$$\rho = (1-\phi)\rho_s + \phi S_w\rho_w + \phi(1 - S_w)\rho_g$$

In this formula:

u_i, w_i, and v_i are displacement components of the solid phase, relative displacement components of the liquid phase, and relative displacement components of the gas phase, respectively.

ρ_s, ρ_w, and ρ_g are absolute mass densities, where the subscript s*s* represents the absolute mass density of the solid phase, and w*w* and g*g* represent the liquid phase and gas phase, respectively.

ϕ refers to the measure of void spaces within unsaturated soil, indicating its porosity.

S_w and S_g are saturation degrees of the liquid phase and gas phase, respectively.

k is the intrinsic permeability coefficient of the unsaturated soil.

μ_w and μ_g are dynamic viscosities of the liquid phase and gas phase, respectively.

k_{rw} and k_{rg} are relative permeability coefficients of the liquid phase and gas phase, respectively.

m represents a parameter within the V-G model.

In the equation $S_e = (S_w - S_{res})/(1 - S_{res})$, S_e represents the effective saturation of the liquid phase, while S_{res} signifies the residual saturation of that liquid phase.

p_w refers to the pressure exerted by the water within the pores s, while p_g signifies the pressure exerted by the gas present in the pore spaces.

The expressions for other parameters $\overline{B}_{11}(\omega) \sim \overline{B}_{13}(\omega)$ $\overline{B}_{21}(\omega) \sim \overline{B}_{23}(\omega)$ are detailed in Appendix A.

Equation (7) in the context of unsaturated soil dynamics introduces the fractional standard linear solid (FSLS) model. The model is selected due to its ability to accurately characterize the viscoelastic properties of materials with a parsimonious set of model parameters and a straightforward stress–strain relationship. This model is particularly effective in capturing the frequency-dependent viscoelastic features of the soil skeleton. The FSLS model represents the stress–strain relationship of viscoelastic solid media as shown in Equation (9) [39]:

$$\overline{\sigma}(\omega) = E_0 \frac{1 + (\mathrm{i}\omega\tau_\varepsilon)^r}{1 + (\mathrm{i}\omega\tau_\sigma)^r} \overline{\varepsilon}(\omega) \tag{9}$$

In the equation, $\overline{\sigma}(\omega)$ and $\overline{\varepsilon}(\omega)$, respectively, denote the Fourier transforms of stress and strain in the medium; r represents the fractional order; τ_σ and τ_ε signify the relaxation times for stress and strain; E_0 represents the relaxation modulus; $i = \sqrt{-1}$ is the imaginary unit.

Similarly, $\overline{\lambda}(\omega)$, $\overline{\mu}(\omega)$ and $\overline{a}(\omega)$ can be represented as

$$\begin{cases} \overline{\mu}(\omega) = \mu_0 \frac{1+(\mathrm{i}\omega\tau_\varepsilon)^r}{1+(\mathrm{i}\omega\tau_\sigma)^r} \\ \overline{\lambda}(\omega) = \left(K_{b0} - \frac{2\mu_0}{3}\right) \frac{1+(\mathrm{i}\omega\tau_\varepsilon)^r}{1+(\mathrm{i}\omega\tau_\sigma)^r} \\ \overline{a}(\omega) = 1 - \frac{K_{b0}}{K_s} \frac{1+(\mathrm{i}\omega\tau_\varepsilon)^r}{1+(\mathrm{i}\omega\tau_\sigma)^r} \end{cases} \tag{10}$$

In the equation:

μ_0 and K_{b0}, respectively, represent the relaxed shear modulus and relaxed bulk modulus of the soil skeleton;

K_s signifies the modulus of compression for the soil particles.

4. Equation Solution

4.1. Pile–Soil System Boundary Conditions

Equation (11) can be derived under the assumption that the soil at the pile's side at an infinite distance is in a state of no displacement, no strain, and no stress.

$$\begin{cases} u_r|_{r\to\infty} = w_r|_{r\to\infty} = v_r|_{r\to\infty} = 0 \\ u_z|_{r\to\infty} = w_z|_{r\to\infty} = v_z|_{r\to\infty} = 0 \\ \varepsilon_s|_{r\to\infty} = \varepsilon_w|_{r\to\infty} = \varepsilon_g|_{r\to\infty} = 0 \\ \sigma_{zr}|_{r\to\infty} = \sigma_z|_{r\to\infty} = \sigma_r|_{r\to\infty} = 0 \end{cases} \tag{11}$$

In the equation, r represents the radial direction, while z denotes the axial direction.; ε_{xx} and ε_9, respectively, denote the relative volumetric strain of the liquid phase and gas phase in the pore; σ_z, σ_r, and σ_{zr}, respectively, represent axial stress, radial stress, and shear stress.

Considering zero axial stress on the soil surface and zero pore fluid pressure, the following expression can be derived:

$$\sigma_z|_{z=0} = p_w|_{z=0} = p_g|_{z=0} = 0 \tag{12}$$

Considering that the soil's longitudinal displacement at the pile end is zero, the following expression can be derived:

$$u_z|_{z=L} = w_z|_{z=L} = v_z|_{z=L} = 0 \tag{13}$$

Considering the longitudinal dynamic load $P(t)$ acting at the pile head and the displacement being zero at the end of the SDCM pile, the following expression can be derived:

$$(E_m A_m + E_c A_c)\frac{\partial u_p}{\partial z}\bigg|_{z=0} = -P(t),\ u_p|_{z=L} = 0 \tag{14}$$

Considering the displacement continuity and impermeability at the interface between the pile and the soil, the following expression can be derived:

$$u_z|_{r=r_3} = u_p,\ u_r|_{r=r_3} = w_r|_{r=r_3} = v_r|_{r=r_3} = 0 \tag{15}$$

4.2. Analysis of Soil Behavior Adjacent to Piles

The dynamic governing equation of pile–soil interaction described by Equation (7) can be rewritten in cylindrical coordinates.

$$\overline{\mu}(\omega)\left(\nabla^2 - \frac{1}{r^2}\right)u_r + [C_{11}(\omega) + \overline{\mu}(\omega)]\frac{\partial \varepsilon_s}{\partial r} + C_{12}(\omega)\frac{\partial \varepsilon_w}{\partial r} + C_{13}(\omega)\frac{\partial \varepsilon_g}{\partial r} = -\rho\omega^2 u_r - \rho_w\omega^2 w_r - \rho_g\omega^2 v_r \tag{16a}$$

$$\overline{\mu}(\omega)\nabla^2 u_z + [C_{11}(\omega) + \overline{\mu}(\omega)]\frac{\partial \varepsilon_s}{\partial z} + C_{12}(\omega)\frac{\partial \varepsilon_w}{\partial z} + C_{13}(\omega)\frac{\partial \varepsilon_g}{\partial z} = -\rho\omega^2 u_z - \rho_w\omega^2 w_z - \rho_g\omega^2 v_z \tag{16b}$$

$$C_{21}(\omega)\frac{\partial \varepsilon_s}{\partial r} + C_{22}(\omega)\frac{\partial \varepsilon_w}{\partial r} + C_{23}(\omega)\frac{\partial \varepsilon_g}{\partial r} = -\rho_w\omega^2 u_r - \rho_w\omega^2 w_r/(\phi S_w) + \mu_w \mathrm{i}\omega w_r/(k_{rw}k) \tag{16c}$$

$$C_{21}(\omega)\frac{\partial \varepsilon_s}{\partial z} + C_{22}(\omega)\frac{\partial \varepsilon_w}{\partial z} + C_{23}(\omega)\frac{\partial \varepsilon_g}{\partial z} = -\rho_w\omega^2 u_z - \rho_w\omega^2 w_z/(\phi S_w) + \mu_w \mathrm{i}\omega w_z/(k_{rw}k) \tag{16d}$$

$$C_{31}(\omega)\frac{\partial \varepsilon_s}{\partial r} + C_{32}(\omega)\frac{\partial \varepsilon_w}{\partial r} + C_{33}(\omega)\frac{\partial \varepsilon_g}{\partial r} = -\rho_g\omega^2 u_r - \rho_g\omega^2 v_r/(\phi S_g) + \mu_g \mathrm{i}\omega v_r/(k_{rg}k) \tag{16e}$$

$$C_{31}(\omega)\frac{\partial \varepsilon_s}{\partial z} + C_{32}(\omega)\frac{\partial \varepsilon_w}{\partial z} + C_{33}(\omega)\frac{\partial \varepsilon_g}{\partial z} = -\rho_g\omega^2 u_z - \rho_g\omega^2 v_z/(\phi S_g) + \mu_g \mathrm{i}\omega v_z/(k_{rg}k) \tag{16f}$$

In the formula:

$$\nabla^2 = \frac{\partial^2}{\partial r^2} + \frac{1}{r}\frac{\partial}{\partial r} + \frac{\partial^2}{\partial z^2}$$

$$\varepsilon_s = \frac{\partial u_r}{\partial r} + \frac{u_r}{r} + \frac{\partial u_z}{\partial z}$$

$$\varepsilon_w = \frac{\partial w_r}{\partial r} + \frac{w_r}{r} + \frac{\partial w_z}{\partial z}$$

$$\varepsilon_g = \frac{\partial v_r}{\partial r} + \frac{v_r}{r} + \frac{\partial v_z}{\partial z}$$

In the equation, ∇^2 represents the Laplace operator.

Based on the potential function decomposition theorem, the displacement within the solid–liquid–gas three-phase system can be decoupled into the following equation:

$$\begin{cases} u_r = \frac{\partial \varphi_s}{\partial r} + \frac{\partial^2 \psi_s}{\partial z \partial r},\ u_z = \frac{\partial \varphi_s}{\partial z} - \frac{1}{r}\frac{\partial}{\partial r}\left(r\frac{\partial \psi_s}{\partial r}\right) \\ w_r = \frac{\partial \varphi_w}{\partial r} + \frac{\partial^2 \psi_w}{\partial z \partial r},\ w_z = \frac{\partial \varphi_w}{\partial z} - \frac{1}{r}\frac{\partial}{\partial r}\left(r\frac{\partial \psi_w}{\partial r}\right) \\ v_r = \frac{\partial \varphi_g}{\partial r} + \frac{\partial^2 \psi_g}{\partial z \partial r},\ v_z = \frac{\partial \varphi_g}{\partial z} - \frac{1}{r}\frac{\partial}{\partial r}\left(r\frac{\partial \psi_g}{\partial r}\right) \end{cases} \tag{17}$$

In the equation, φ_s, φ_w, φ_g and ψ_s, ψ_w, ψ_g, respectively, denote the scalar potential functions and vector potential functions of each phase.

The volumetric strains ε_s, ε_w, and ε_g of each phase medium can be further expressed as

$$\varepsilon_s = \nabla^2\varphi_s,\ \varepsilon_w = \nabla^2\varphi_w,\ \varepsilon_g = \nabla^2\varphi_g \tag{18}$$

When Equations (17) and (18) are substituted into Equation (16), the resulting equation is as follows:

$$\begin{bmatrix} a_1\nabla^2 + a_2 & a_3\nabla^2 + a_4 & a_5\nabla^2 + a_6 \\ a_7\nabla^2 + a_4 & a_8\nabla^2 + a_9 & a_{10}\nabla^2 \\ a_{11}\nabla^2 + a_6 & a_{12}\nabla^2 & a_{13}\nabla^2 + a_{14} \end{bmatrix} \begin{Bmatrix} \varphi_s \\ \varphi_w \\ \varphi_g \end{Bmatrix} = \begin{Bmatrix} 0 \\ 0 \\ 0 \end{Bmatrix} \tag{19}$$

$$\begin{bmatrix} a_{15}\nabla^2 + a_2 & a_4 & a_6 \\ a_4 & a_9 & 0 \\ a_6 & 0 & a_{14} \end{bmatrix} \begin{Bmatrix} \psi_s \\ \psi_w \\ \psi_g \end{Bmatrix} = \begin{Bmatrix} 0 \\ 0 \\ 0 \end{Bmatrix} \tag{20}$$

The expressions for coefficients a_1 to a_{15} are outlined in Appendix B.

The necessary condition for Equations (19) and (20) to have non-trivial solutions is that the coefficient matrix must have a determinant of zero; therefore, the following equation can be obtained:

$$\begin{cases} \left(h_1\nabla^6 + h_2\nabla^4 + h_3\nabla^2 + h_4\right)\varphi_s = 0 \\ \left(h_1\nabla^6 + h_2\nabla^4 + h_3\nabla^2 + h_4\right)\varphi_w = 0 \\ \left(h_1\nabla^6 + h_2\nabla^4 + h_3\nabla^2 + h_4\right)\varphi_g = 0 \end{cases} \tag{21}$$

$$\begin{cases} \left(\nabla^2 - h_5\right)\psi_s = 0 \\ \left(\nabla^2 - h_5\right)\psi_w = 0 \\ \left(\nabla^2 - h_5\right)\psi_g = 0 \end{cases} \tag{22}$$

The expressions for coefficients h_1 to h_5 are detailed in Appendix C.

According to the method of separating variables, the scalar potential and vector potential functions for each medium can be expressed as:

$$\begin{aligned} \varphi_s = {} & [E_1K_0(q_1r) + F_1I_0(q_1r)](G_1\mathrm{e}^{g_1z} + H_1\mathrm{e}^{-g_1z}) \\ & +[E_2K_0(q_2r) + F_2I_0(q_2r)](G_2\mathrm{e}^{g_2z} + H_2\mathrm{e}^{-g_2z}) \\ & +[E_3K_0(q_3r) + F_3I_0(q_3r)](G_3\mathrm{e}^{g_3z} + H_3\mathrm{e}^{-g_3z}) \end{aligned} \tag{23}$$

$$\begin{aligned} \varphi_w = {} & [E_4K_0(q_1r) + F_4I_0(q_1r)](G_4\mathrm{e}^{g_1z} + H_4\mathrm{e}^{-g_1z}) \\ & +[E_5K_0(q_2r) + F_5I_0(q_2r)](G_5\mathrm{e}^{g_2z} + H_5\mathrm{e}^{-g_2z}) \\ & +[E_6K_0(q_3r) + F_6I_0(q_3r)](G_6\mathrm{e}^{g_3z} + H_6\mathrm{e}^{-g_3z}) \end{aligned} \tag{24}$$

$$\begin{aligned} \varphi_g = {} & [E_7K_0(q_1r) + F_7I_0(q_1r)](G_7\mathrm{e}^{g_1z} + H_7\mathrm{e}^{-g_1z}) \\ & +[E_8K_0(q_2r) + F_8I_0(q_2r)](G_8\mathrm{e}^{g_2z} + H_8\mathrm{e}^{-g_2z}) \\ & +[E_9K_0(q_3r) + F_9I_0(q_3r)](G_9\mathrm{e}^{g_3z} + H_9\mathrm{e}^{-g_3z}) \end{aligned} \tag{25}$$

$$\psi_s = \begin{bmatrix} E_{10}K_0(q_4r) + \\ F_{10}I_0(q_4r) \end{bmatrix}\left(G_{10}\mathrm{e}^{g_4z} + H_{10}\mathrm{e}^{-g_4z}\right) \tag{26}$$

$$\psi_w = \begin{bmatrix} E_{11}K_0(q_4r) + \\ F_{11}I_0(q_4r) \end{bmatrix}\left(G_{11}\mathrm{e}^{g_4z} + H_{11}\mathrm{e}^{-g_4z}\right) \tag{27}$$

$$\psi_g = \begin{bmatrix} E_{12}K_0(q_4r) + \\ F_{12}I_0(q_4r) \end{bmatrix}\left(G_{12}\mathrm{e}^{g_4z} + H_{12}\mathrm{e}^{-g_4z}\right) \tag{28}$$

In the equations

$$q_1^2 + g_1^2 = \beta_1^2,\ q_2^2 + g_2^2 = \beta_2^2,\ q_3^2 + g_3^2 = \beta_3^2,\ q_4^2 + g_4^2 = h_5,$$

β_1^2, β_2^2, and β_3^2 represent three solutions corresponding to the coefficient matrix in Equation (19);

$I_0(\cdot)$ and $K_0(\cdot)$, respectively denote the modified Bessel functions of the first kind and second kind of zero order;

E_1 through E_{12}, F_1 through F_{12}, G_1 through G_{12}, and H_1 through H_{12} are unknown coefficients.

Under the boundary conditions given by Equation (11), it follows that $F_1 = F_2 = \ldots = F_{12} = 0$. Substituting Equations (23) through (25) into Equation (19), and Equations (26) through (28) into Equation (20) leads to following equation:

$$\begin{cases} G_4 = \chi_{w1} G_1,\ G_5 = \chi_{w2} G_2,\ G_6 = \chi_{w3} G_3 \\ G_7 = \chi_{g1} G_1,\ G_8 = \chi_{g2} G_2,\ G_9 = \chi_{g3} G_3 \end{cases} \tag{29}$$

$$\begin{cases} H_4 = \chi_{w1} H_1,\ H_5 = \chi_{w2} H_2,\ H_6 = \chi_{w3} H_3 \\ H_7 = \chi_{g1} H_1,\ H_8 = \chi_{g2} H_2,\ H_9 = \chi_{g3} H_3 \end{cases} \tag{30}$$

$$\begin{cases} G_{12} = \chi_{g4} G_{10},\ G_{11} = \chi_{w4} G_{10} \\ H_{12} = \chi_{g4} H_{10},\ H_{11} = \chi_{w4} H_{10} \end{cases} \tag{31}$$

The expressions for the coefficients χ_{w1} to χ_{w4} and χ_{g1} to χ_{g4} are detailed in Appendix D.

From boundary conditions (12) and (13), the following equations can be derived.

$$G_1 = -H_1,\ G_2 = -H_2,\ G_3 = -H_3,\ G_{10} = H_{10} \tag{32}$$

$$g_n = g_1 = g_2 = g_3 = g_4 = (2n-1)\pi \mathrm{i}/(2L) \tag{33}$$

In the equations, n = 1, 2, 3...

From boundary condition (15), the following equations can be derived.

$$G_2 = \xi_1 G_1,\ G_3 = \xi_2 G_1,\ G_{10} = \xi_3 G_1 \tag{34}$$

The expressions for the coefficients ξ_1, ξ_2, and ξ_3 are detailed in Appendix D.

The longitudinal displacement of the soil skeleton can be derived from the above analysis in the form of a closed-form series solution.

$$u_z = 2\sum_{n=1}^{\infty} \begin{bmatrix} g_n K_0(q_{1n} r) + \\ \xi_{1n} g_n K_0(q_{2n} r) + \\ \xi_{2n} g_n K_0(q_{3n} r) - \\ \xi_{3n} q_{4n}^2 K_0(q_{4n} r) \end{bmatrix} G_{1n} \cosh(g_n z) \tag{35}$$

Consequently, the frictional resistance τ_s at the interface of the pile with the soil can be formulated as follows:

$$\tau_s = -\overline{\mu}(\omega)\,(\partial u_z/\partial r)|_{r=r_3} = \overline{\mu}(\omega) \sum_{n=1}^{\infty} \vartheta_n G_{1n} \cosh(g_n z) \tag{36}$$

In the equation:

$$\vartheta_n = 2 g_n q_{1n} K_1(q_{1n} r_3) + 2\xi_{1n} g_n q_{2n} K_1(q_{2n} r_3) + 2\xi_{2n} g_n q_{3n} K_1(q_{3n} r_3) - 2\xi_{3n} q_{4n}^3 K_1(q_{4n} r_3) \tag{37}$$

4.3. Solution of SDCM Pile

Substituting Equation (36) into Equation (6), the following equation can be derived:

$$(E_m A_m + E_c A_c)\frac{\partial^2 u_p}{\partial z^2} + (\rho_m A_m + \rho_c A_c)\omega^2 u_p = 2\pi r_3 \overline{\mu}(\omega) \sum_{n=1}^{\infty} \vartheta_n G_{1n} \cosh(g_n z) \tag{38}$$

The longitudinal displacement of the SDCM pile can be determined using Equation (38), which is formulated as follows:

$$u_p = J_1 \cos(\varpi z) + J_2 \sin(\varpi z) + \sum_{n=1}^{\infty} v_n G_{1n} \cosh(g_n z) \tag{39}$$

In the equation:

$$\varpi = \sqrt{\frac{(\rho_m A_m + \rho_c A_c)\omega^2}{E_m A_m + E_c A_c}} \tag{40}$$

$$v_n = \frac{2\pi r_3 \overline{\mu}(\omega)\vartheta_n}{(E_m A_m + E_c A_c)g_n^2 + (\rho_m A_m + \rho_c A_c)\omega^2} \tag{41}$$

Based on the boundary condition of continuity of pile–soil interface displacement (Equation (15)), the following equation can be derived:

$$J_1 \cos(\varpi z) + J_2 \sin(\varpi z) + \sum_{n=1}^{\infty} v_n G_{1n} \cosh(g_n z) = \sum_{n=1}^{\infty} \eta_n G_{1n} \cosh(g_n z) \tag{42}$$

In the equation:

$$\begin{array}{l} \eta_n = 2g_n K_0(q_{1n} r_3) + 2\xi_{1n} g_n K_0(q_{2n} r_3) \\ +2\xi_{2n} g_n K_0(q_{3n} r_3) - 2\xi_{3n} q_{4n}^2 K_0(q_{4n} r_3) \end{array} \tag{43}$$

The hyperbolic cosine functions exhibit a specific orthogonality property, as shown by the following equation:

$$\begin{cases} \int_0^L \cosh(g_m z)\cosh(g_n z)\mathrm{d}z = \dfrac{L}{2},\ m = n \\ \int_0^L \cosh(g_m z)\cosh(g_n z)\mathrm{d}z = 0,\ m \neq n \end{cases} \tag{44}$$

Substituting Equation (44) into Equation (42) results in the following equation:

$$G_{1n} = L_{1n} J_1 + L_{2n} J_2 \tag{45}$$

In the equation:

$$L_{1n} = \frac{2g_n \cos(\varpi L)\sinh(g_n L)}{(g_n^2 + \varpi^2)(\eta_n - v_n)L} \tag{46}$$

$$L_{2n} = \frac{2g_n \sin(\varpi L)\sinh(g_n L) + 2\varpi}{(g_n^2 + \varpi^2)(\eta_n - v_n)L} \tag{47}$$

By substituting the boundary conditions at the ends of the SDCM pile, as outlined in Equation (14), into Equation (39), the derivation proceeds as follows:

$$\begin{cases} J_1 = \frac{\overline{P}(\omega)\tan(\varpi L)}{\varpi(E_m A_m + E_c A_c)} \\ J_2 = \frac{-\overline{P}(\omega)}{\varpi(E_m A_m + E_c A_c)} \end{cases} \tag{48}$$

In the equation, $\overline{P}(\omega)$ indicates the Fourier transform of $P(t)$.

According to the above derivation, the longitudinal displacement of the SDCM pile is given by:

$$u_p = \frac{\tan(\varpi L)\cos(\varpi z) - \sin(\varpi z) + S(z)}{\varpi(E_m A_m + E_c A_c)} \overline{P}(\omega) \tag{49}$$

In the equation:

$$S(z) = \sum_{n=1}^{\infty} v_n [L_{1n} \tan(\varpi L) - L_{2n}] \cosh(g_n z) \tag{50}$$

The pile apex complex impedance can be expressed as:

$$K_d = \frac{\overline{P}(\omega)}{u_p|_{z=0}} = \frac{\varpi(E_m A_m + E_c A_c)}{\tan(\varpi L) + S(0)} \tag{51}$$

In the equation:

$$S(0) = \sum_{n=1}^{\infty} v_n [L_{1n} \tan(\varpi L) - L_{2n}] \tag{52}$$

Ultimately, the dimensionless form of the pile head complex impedance can be expressed as

$$k_{re} + \mathrm{i}k_{im} = \frac{K_d}{E_c A_c / L} \tag{53}$$

The equation specifies that k_{re} denotes the dynamic stiffness and k_{imkim} signifies the dynamic damping of the pile apex.

5. Case Study Analysis

5.1. Comparative Verification of Solutions

Before conducting specific numerical examples and parameter analyses, it is essential to first validate the effectiveness and correctness of the theoretical derivation in this paper. The established pile–soil model in this study can be degraded and compared with existing solutions to verify its accuracy. By setting $\phi \to 0$, $\rho_w = 0$, $\rho_g = 0$, $\tau_\sigma = 0$, and $r = 1$, the viscoelastic unsaturated soil model developed in this paper is degraded to a single-phase viscoelastic soil model. By setting $r_1 \to 0$, $r_2 = r_3$, $E_m = \rho_m = 0$, the SDCM pile model in this paper is degraded to a single-pile model. The values of other parameters for soil and pile are consistent with those used by Ding et al. [38]. The comparison curve of the degraded solution in this paper with the analytical solution of dynamic impedance obtained by Ding et al. [38] is shown in Figure 3, where $a_0 = \omega L / \sqrt{(E_m + E_c)/(\rho_m + \rho_c)}$ is the dimensionless frequency.

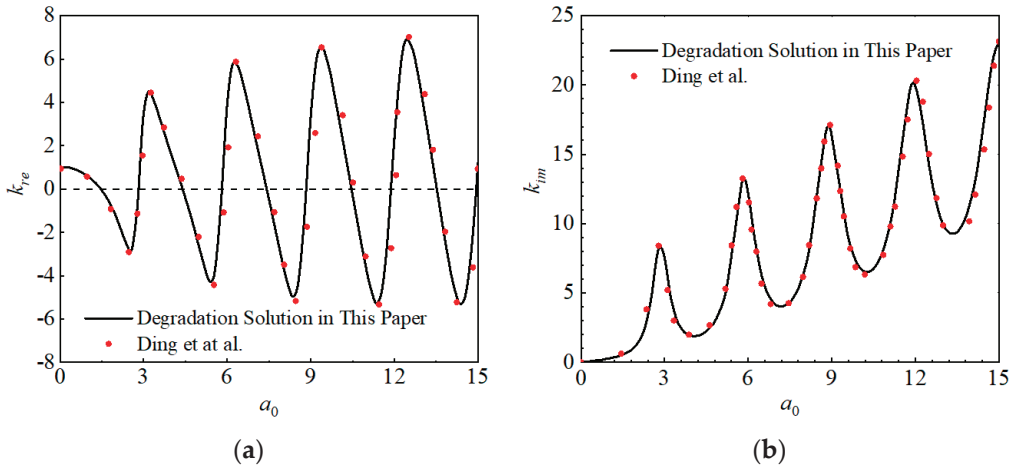

Figure 3. The comparison curves (Comparison with Ding et al. [38]): (**a**) the comparison curves of pile head dynamic stiffness; (**b**) the comparison curves of dynamic damping.

As shown in Figure 3, the comparison curves of pile apex dynamic stiffness and dynamic damping indicate that the degraded solution obtained in this paper qualitatively and quantitatively matches well with the existing solutions by Ding et al. [38].

5.2. Parameter Analysis

This section presents numerical examples and parameter analyses discussing the influence of physical characteristics of SDCM piles and the adjacent soil on the pile apex

dynamic impedance. The physical parameters of SDCM piles include radius, length, and elastic modulus, while those of the surrounding soil include parameters from the the fractional standard linear solid (FSLS) model, saturation degree, intrinsic permeability coefficient, relaxation shear modulus, and porosity. Unless specified otherwise, the values of the parameters for the pile–side soil and SDCM piles are based on the values listed in Table 1. It is noteworthy that the intrinsic permeability mentioned in this paper represents the pore capacity through which fluids can flow in porous materials. This is a quantitative property of porous materials, and its value is related to the pore structure of the materials [39]. The other parameters in the table are determined based on the existing literature [15].

Table 1. Computation parameters.

Medium	Parameter Name/Symbol	Value
Soil particles	Bulk modulus/K_s	35 GPa
	Density/ρ_s	2650 kg/m^3
Water	Bulk modulus/K_w	2.25 GPa
	Density/ρ_w	997 kg/m^3
	Dynamic viscosity/μ_w	0.001 Pa·s
Air	Porosity/K_g	0.145 MPa
	Density/ρ_g	1.1 kg/m^3
	Dynamic viscosity/μ_g	1.8×10^{-5} Pa·s
Soil skeleton	Porosity/ϕ	0.45
	Saturation/S_w	0.6
	Residual saturation/S_{res}	0.0913
	V-G model parameters/α_v	0.0001
	V-G model parameters/m	0.5338
	V-G model parameters/d	2.145
	Intrinsic permeability/k	5.3×10^{-13} m^2
	Fractional order/r	0.6
	Stress relaxation time/τ_σ	4.24×10^{-5} s
	Strain relaxation time/τ_ε	5.39×10^{-5} s
	Relaxation shear modulus/μ_0	3.85 MPa
	Bulk relaxation modulus/K_{b0}	8.33 MPa
Concrete core pile	Elastic modulus	20,000 MPa
	Density	2350 kg/m^3
	Inner radius	0.1 m
	Outer radius	0.2 m
	Pile length	10 m
Concrete–soil exterior pile	Elastic modulus	300 MPa
	Density	2010 kg/m^3
	Inner radius	0.2 m
	Outer radius	0.4 m
	Pile length	10 m

5.2.1. Effects of Pile Physical Parameters

Figure 4 shows the variation curve of the pile apex dynamic impedance with respect to the dimensionless frequency when the inside diameter r_1 of the concrete core pile and the outer diameter r_3 of the SDCM pile remain constant, while changing the outer diameter r_3 of the core pile. This indicates the change in pile top dynamic impedance as the ratio of the area of the cross-section of the core pile to that of the exterior pile varies, with the area of the cross-section of the SDCM pile is fixed. Figure 4 illustrates that at lower frequencies, an increase in the radius r_2 of the core pile enhances the dynamic stiffness of the composite pile. This phenomenon occurs because, in the context of low frequencies, the stiffness of the foundation pile is predominantly influenced by its static characteristics, and core piles with larger radii demonstrate increased static stiffness.

At higher frequencies, maintaining the external radius r_3 of the cement–soil exterior pile while decreasing the external radius r_2 of the core pile reduces the resonant frequency of the pile head dynamic stiffness and dynamic damping variation curve, significantly decreasing the peak value of the curves at the resonant frequency. It is evident that increasing the exterior pile cross-sectional area slightly reduces the dynamic stiffness of the SDCM pile, but significantly enhances vibration reduction due to increased flexibility.

Additionally, it is worth mentioning that increasing the wall thickness of cement–soil exterior piles requires significantly less manpower, resources, and cost compared to augment the cross-sectional area of core piles. Moreover, increasing the wall thickness of concrete core piles not only complicates the pile driving process but also induces substantial soil squeezing effects. Therefore, for larger radius concrete pipe piles, when the bearing capacity requirements are met, it is advantageous to prioritize appropriately sized composite piles to reduce construction costs and difficulty, while enhancing the foundation's seismic performance.

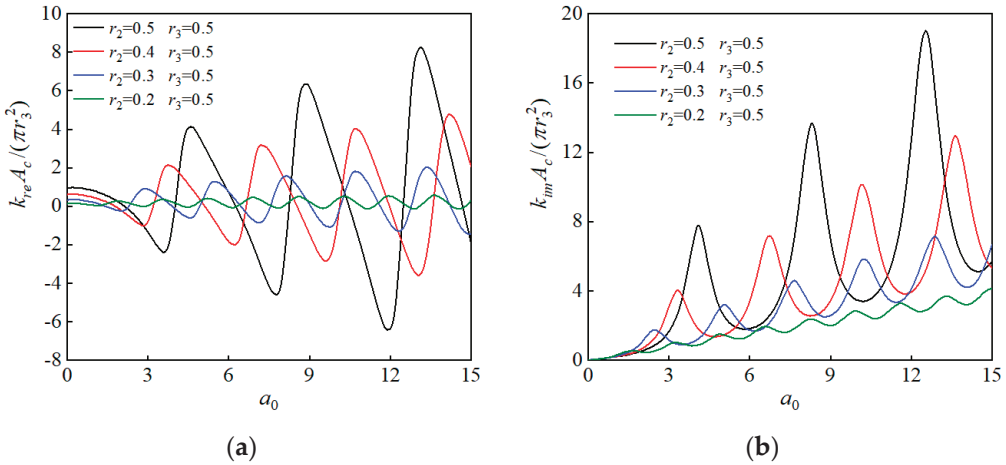

Figure 4. The impact of changing the outer diameter of the inner pile on the pile top dynamic impedance while keeping the total cross-section of the SDCM pile constant: (**a**) the impact of this parameter's variation on dynamic impedance; (**b**) the influence of this parameter's variation on dynamic damping.

Figure 5 shows the variation curve of dynamic impedance with respect to the dimensionless frequency when the thickness of the exterior pile is changed while keeping the inner and outer radius of the concrete core pile unchanged. This is achieved by maintaining the inner and outer diameters r_1 and r_2 of the concrete core pile constant while varying r_3. It is noteworthy that since the radius r_2 of the concrete core pile is 0.2 m, the result when r_3 is also 0.2 m represents the calculation result of the concrete pipe pile. Figure 5 indicates that at lower frequencies, augmenting the crossing-area of the exterior pile can slightly amplify the dynamic stiffness of the SDCM pile. This is because, in the low-frequency range, the stiffness of the pile foundation mainly hinges upon its static characteristics, and increasing the thickness of the exterior pile can marginally improve the static stiffness of the SDCM pile.

Moreover, expanding the thickness of the concrete exterior pile will lower the resonance frequency of the curve representing dynamic stiffness and dynamic damping variations at pile apex. However, under high-frequency oscillation conditions, it can significantly increase the amplitude of oscillation below the resonance frequency. This phenomenon indicates that whether increasing the thickness of the cement–soil exterior pile enhances its ability to resist vibrations depends on the load excitation frequency. Although the anti-vibration performance can be slightly improved at lower load excitation frequencies, the oscillation amplitude increases significantly at high frequencies. Therefore, it is not recommended to enhance the anti-vibration performance of the SDCM pile simply by augmenting the thickness of the exterior pile.

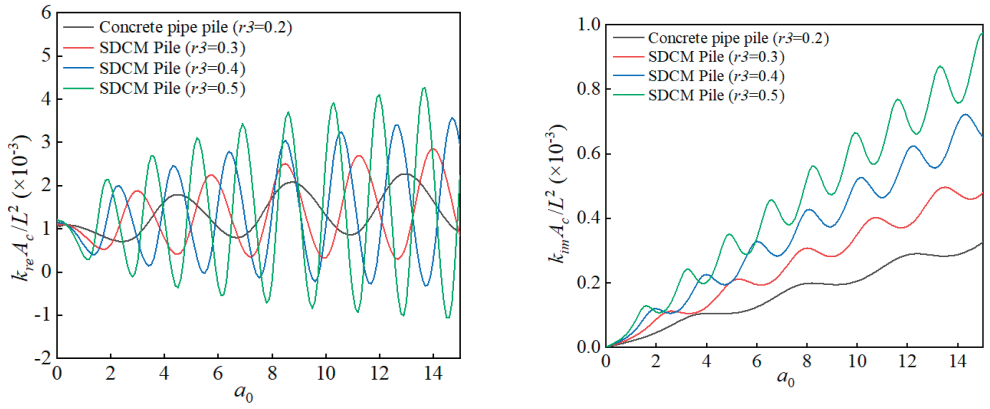

Figure 5. The impact of varying the thickness of the cement–soil exterior pile on the dynamic impedance at the top of the pile when the cross-section of the concrete inner pile remains constant: (**a**) the impact of this parameter's variation on dynamic impedance; (**b**) the influence of this parameter's variation on dynamic damping.

Figure 6 illustrates the variation in pile head dynamic impedance with dimensionless frequency a_1 $\left(a_1 = \omega r_3/\sqrt{\mu/\rho}\right)$ for different pile lengths. From Figure 6, it is observed that at lower frequencies, shorter composite piles exhibit relatively higher dynamic stiffness. The explanation for this is that at lower frequencies, the dynamic stiffness of the foundation pile, primarily due to its static properties, and shorter piles under end-bearing conditions demonstrate greater stiffness.

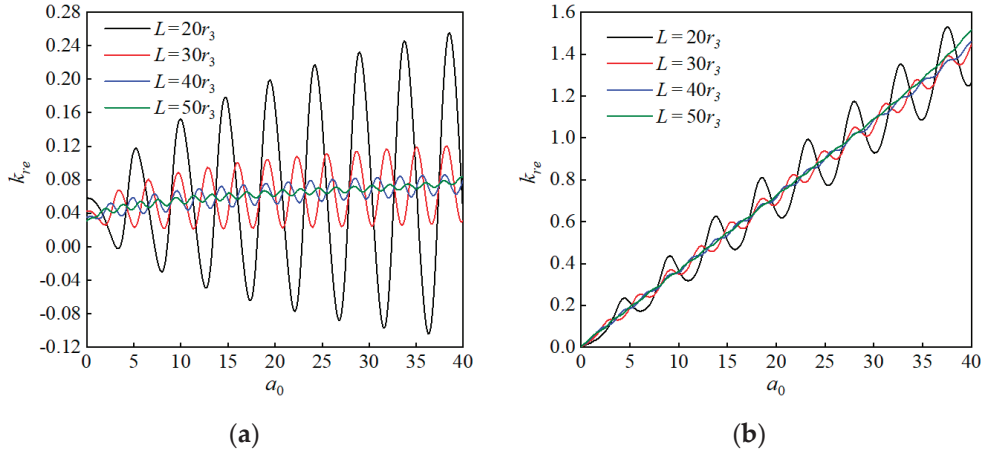

Figure 6. The impact of pile length on the dynamic impedance at the pile apex: (**a**) the influence of this parameter's variation on dynamic impedance; (**b**) the impact of this parameter's variation on dynamic damping.

Additionally, at higher frequencies, the resonant frequency of pile apex dynamic stiffness and dynamic damping, as well as the oscillation amplitude at the resonant frequency, significantly decrease with increasing pile length. This is mainly due to longer piles experiencing greater soil frictional resistance around their perimeter and increased flexibility, thereby enhancing the pile's vibration attenuation capability and seismic performance.

However, it is crucial to emphasize that that once the pile length reaches a certain threshold, the oscillation amplitude of the variation curve may become very small, and it may even be impossible to observe the fluctuations of the curve. When this situation occurs, the benefits gained from further increasing the pile length can be considered negligible.

Figure 7 depicts the curve of pile head dynamic impedance variation with dimensionless frequency a_1 for varied elastic modulus values of the surrounding cement–soil

piles (E_m). Figure 6 shows that with enlarged elastic modulus of the exterior piles, the resonant frequency of dynamic stiffness and dynamic damping at pile apex, along with the oscillation amplitude at the resonant frequency, significantly increase. Additionally, the average values of dynamic stiffness and dynamic damping slightly raise.

These results reveal that increasing the elastic modulus of the exterior piles (E_m) has a negative impact on enhancing the seismic performance of SDCM piles. However, at lower frequencies, increasing E_m has a positive impact on improving the dynamic stiffness of SDCM piles, which is primarily related to the static properties of the pile foundation.

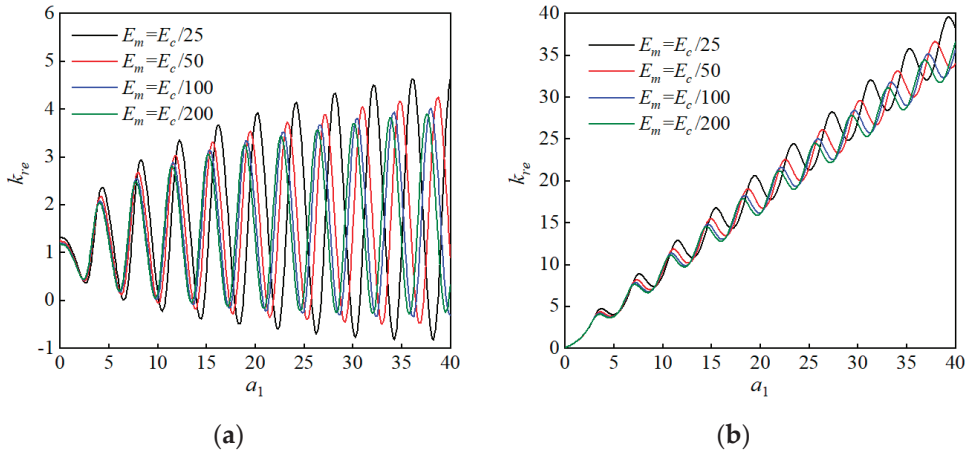

Figure 7. The impact of variations in the modulus of the cement–soil exterior pile on the dynamic impedance at the top of the pile: (**a**) the impact of this parameter's variation on dynamic impedance; (**b**) the impact of this parameter's variation on dynamic damping.

Figure 8 reveals the variation curve of pile top dynamic impedance with respect to the dimensionless frequency when the elastic modulus of the exterior pile E_m remains constant while the elastic modulus of the core pile E_c changes. Comparing Figure 8 with Figure 7, it becomes clear that that the trend of the dynamic impedance with respect to dimensionless frequency caused by the enlargement of the elastic modulus of the concrete core pile is consistent with the trend of the curve when the modulus of the cement–soil exterior pile increases. Specifically, as the elastic modulus E_c of the concrete inner pile increases, both the resonance frequency and the oscillation peak value at resonance frequency of the pile top dynamic stiffness and dynamic damping significantly increase, and the average values of dynamic impedance at the pile top also show a marked increase.

Therefore, when the strength and seismic requirements of SDCM piles are clearly defined, cost savings can be achieved by appropriately reducing the elastic modulus of the concrete core piles while simultaneously increasing the elastic modulus E_m of the exterior piles.

Based on the integrated findings from Figures 4–8, it is discernible that achieving optimal anti-vibration performance and substantial cost savings in SDCM piles necessitates the meticulous configuration of core and exterior pile parameters. It is generally recommended that the radius of the concrete core pile falls within 40% to 60% of the total radius of the SDCM pile. The effective pile length should ideally be between 30 to 50 times its radius.

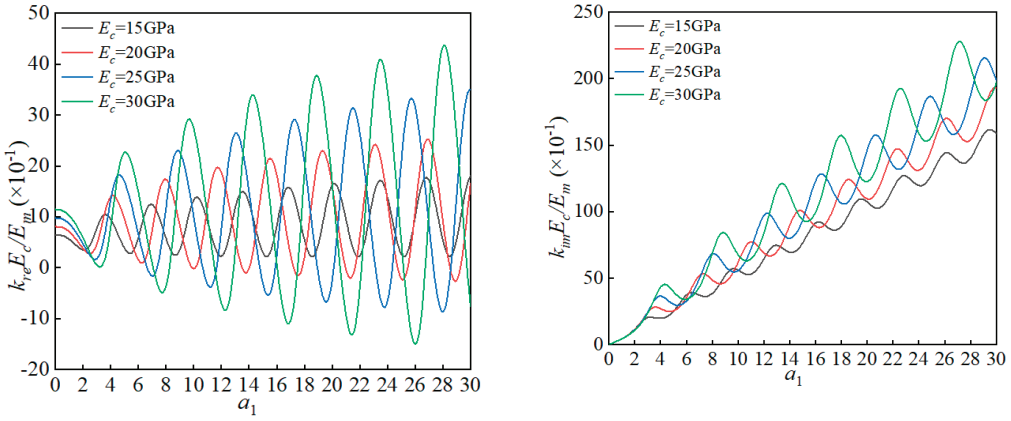

(**a**) (**b**)

Figure 8. The effect of variations in the modulus of the concrete core pile on the dynamic impedance at the top of the pile: (**a**) the influence of this parameter's variation on dynamic impedance; (**b**) the impact of this parameter's variation on dynamic damping.

5.2.2. Effects of FSLS Model Parameters

The FSLS model represented consists of three key parameters: the fractional order r, the stress relaxation time τ_σ, and the strain relaxation time τ_ε. These parameters collectively characterize the frequency-dependent viscoelastic properties of the soil skeleton, encompassing instantaneous response, creep behavior, and strain relaxation. In this section, numerical examples and parameter analysis are employed to discuss how variations in the FSLS model affect the pile head dynamic impedance of SDCM piles.

Figure 9 illustrates the variation in pile apex dynamic stiffness and damping of SDCM piles with dimensionless frequency under different fractional orders. From Figure 9, it is evident that there is a significant correlation between the pile head dynamic impedance and stiffness of SDCM piles with the fractional order of the soil skeleton. Specifically, as the fractional order of the soil skeleton increases, the resonance frequency slightly decreases for the variation curves. Moreover, the amplitude of oscillation of dynamic stiffness and damping at resonance frequency notably reduces.

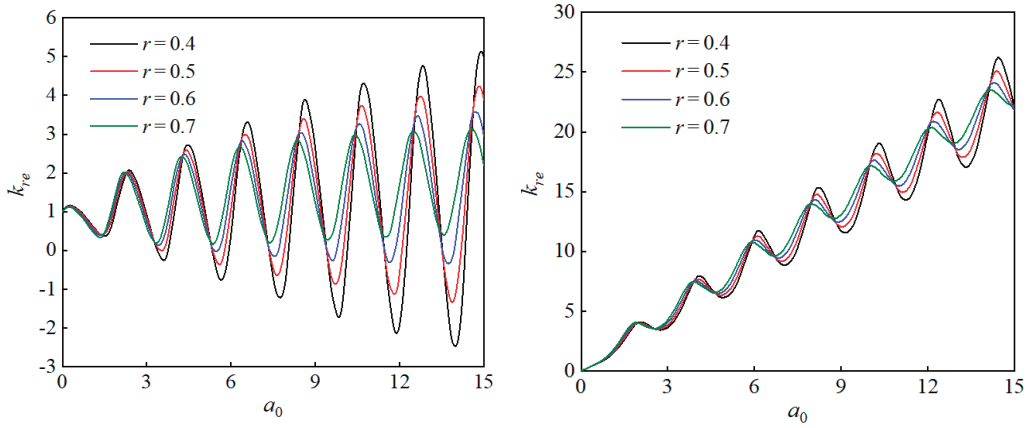

(**a**) (**b**)

Figure 9. The impact of fractional order on the dynamic impedance at the pile apex: (**a**) the impact of this parameter's variation on dynamic impedance; (**b**) the impact of this parameter's variation on dynamic damping.

These observations illustrate that increasing the fractional order positively enhances the vibration resistance of SDCM piles, with a more pronounced effect at higher frequencies.

However, it is worth mentioning that while increasing the fractional order of the soil skeleton benefits the vibration resistance of SDCM piles, it also leads to soil softening and reduced strength. Therefore, careful consideration is required regarding the implications of fractional order on these aspects.

The above results are closely associated with the physical mechanism of changes in the stiffness of the soil skeleton with varying fractional orders. Generally, as the fractional order approaches zero, the soil skeleton exhibits properties that closely resemble those of an elastic solid. The shear modulus of the soil skeleton approaches the initial shear modulus, and its correlation with frequency weakens. Consequently, the ability of the soil skeleton to dissipate energy from dynamic disturbances weakens, and in elastic solids, there is no energy dissipation capability. Clearly, this is detrimental to enhancing the pile head dynamic impedance of SDCM piles.

Conversely, as the fractional order approaches 1, the viscosity of the soil skeleton increases, and the correlation between frequency and shear modulus strengthens. At this point, the soil skeleton's ability to dissipate energy from dynamic disturbances improves, which positively impacts the vibration resistance of pile foundations. This mechanism corroborates the trends observed in the curves shown in Figure 9.

Figure 10 depicts the variation curves for the dynamic stiffness and dynamic damping of SDCM piles at the pile head, plotted against dimensionless frequency for various stress and strain relaxation times.

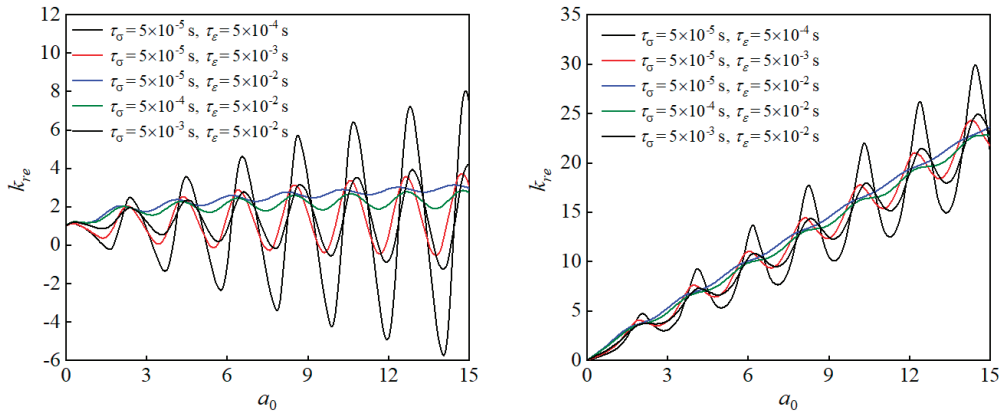

Figure 10. The impact of stress and strain relaxation times on the dynamic impedance at the pile apex: (**a**) the influence of this parameter's variation on dynamic impedance; (**b**) the influence of this parameter's variation on dynamic damping.

Figure 10 shows that when the stress relaxation time of the soil skeleton is increased, there is a slight reduction in the resonance frequency of the curves for SDCM piles. This increase also causes a decrease in the peak value of oscillation for both dynamic stiffness and damping at the resonance frequency, while notably raising the mean dynamic stiffness at the pile head. This implies that an increased stress relaxation time contributes positively to the vibration resistance performance of SDCM piles.

Conversely, Figure 10 shows that increasing the strain relaxation time of the soil skeleton alone increases the resonance frequency of variation curves of SDCM piles. It also significantly increases the amplitude of oscillation of dynamic stiffness and damping at resonance frequency, while notably decreasing the mean dynamic stiffness of the pile head. Therefore, an increase in strain relaxation time has a detrimental effect on the vibration resistance performance of SDCM piles.

Furthermore, the impact of strain relaxation time on pile head dynamic impedance is more pronounced compared to the impact of stress relaxation time.

From a fundamental mechanistic perspective, an increase in the strain relaxation time of the soil skeleton will extend the duration required for soil particles to reach a stable state,

thereby delaying soil deformation. Consequently, this results in an increase in the soil's shear modulus and frictional damping. Such effects positively contribute to enhancing the dynamic impedance of the pile cap in SDCM piles. Increasing the stress relaxation time of the soil skeleton diminishes the interactions among soil particles, resulting in a decrease in the soil's shear modulus and frictional damping, which, in turn, lowers the dynamic impedance of the pile cap.

5.2.3. Impact of Other Soil Parameters

The variation in soil saturation and permeability coefficient will alter the coupling interactions among the solid–liquid–gas three-phase medium, thus changing the dynamic response of the soil. In this section, the effects of soil saturation and the permeability coefficient on the dynamic impedance at the heads of SDCM piles will be explored through numerical analysis.

The curves showing the dynamic impedance at the pile head of SDCM piles with respect to the dimensionless frequency for different soil saturations and intrinsic permeabilities are depicted in Figures 11 and 12, respectively.

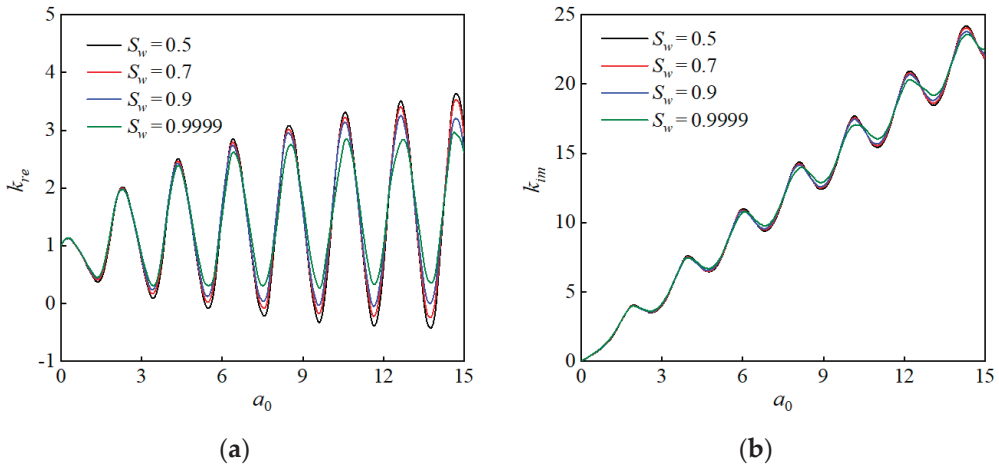

Figure 11. The effect of soil saturation on the dynamic impedance at the pile head: (**a**) the impact of this parameter's variation on dynamic impedance; (**b**) the influence of this parameter's variation on dynamic damping.

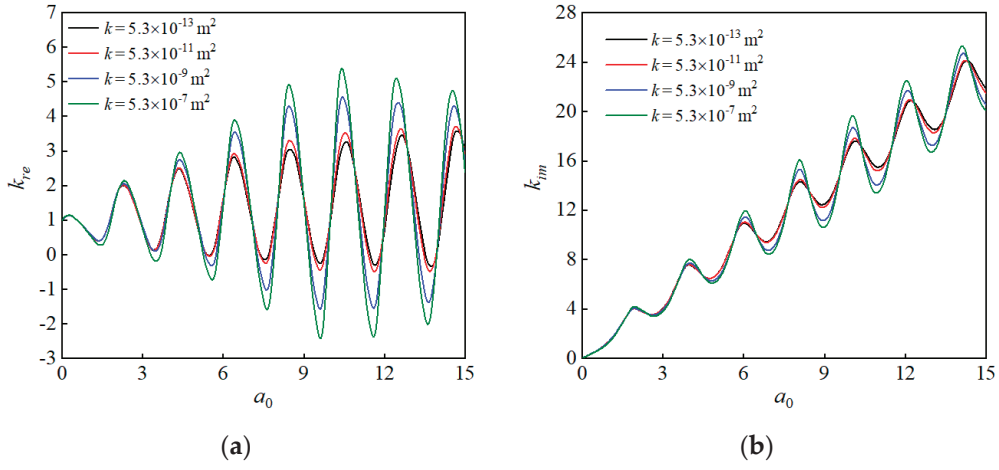

Figure 12. The effect of soil intrinsic permeability on the dynamic impedance at the pile head: (**a**) the impact of this parameter's variation on dynamic impedance; (**b**) the influence of this parameter's variation on dynamic damping.

According to Figure 11, higher soil saturation levels result in a marked reduction in the oscillation amplitude of the curve at resonance frequency, which enhances the vibration resistance of the pile foundation. From a deeper mechanism perspective, increased soil saturation enhances the constraints on the soil skeleton's movement and softens the skeleton due to the higher liquid volume fraction, improving the energy dissipation of the surrounding soil and reducing the oscillation peak value of the dynamic impedance curves.

As illustrated in Figure 12, higher intrinsic permeability of the soil leads to a significant increase in the oscillation amplitude of curves at resonance frequency, adversely affecting the vibration resistance of the pile foundation. Mechanistically, intrinsic permeability represents the void capacity for fluid flow within the medium and serves as a quantitative parameter for porous materials. As this parameter increases, soil permeability improves, diminishing the constraints on the movement of the soil skeleton and reducing the softening impact of the liquid. Consequently, this leads to a decrease in energy dissipation and an enlargement in the peak value of the stiffness and damping curves.

The effects of changes in the soil relaxation shear modulus and porosity on the dynamic impedance at the top of the pile are also worthy of investigation. The results of these two studies are presented in Figures 13 and 14.

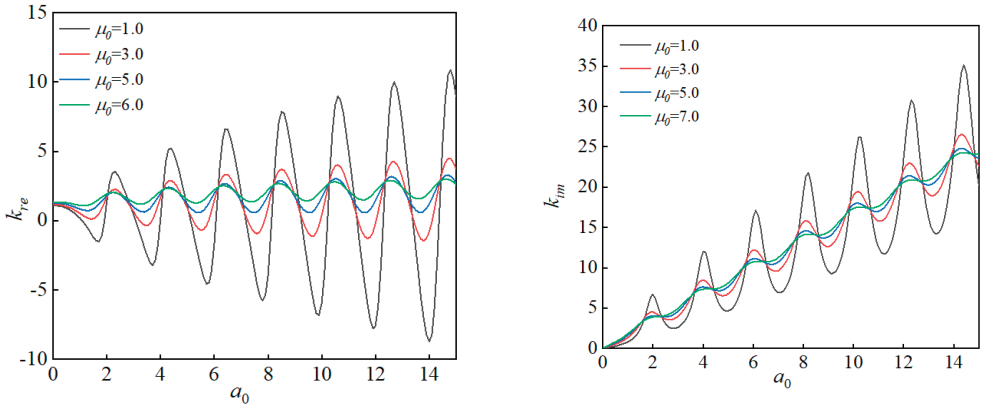

(**a**) (**b**)

Figure 13. The effect of changes in the soil relaxation shear modulus on the dynamic impedance at the top of the pile: (**a**) the influence of this parameter's variation on dynamic impedance; (**b**) the impact of this parameter's variation on dynamic damping.

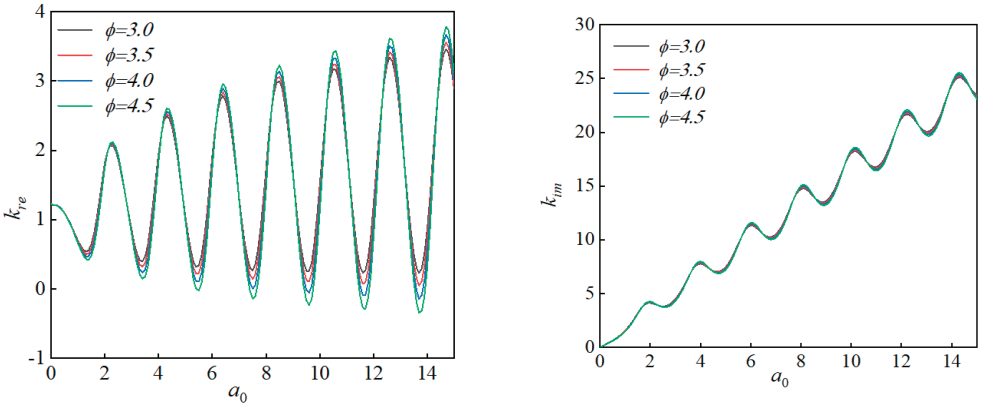

(**a**) (**b**)

Figure 14. The effect of changes in soil porosity on the dynamic impedance at the pile apex: (**a**) the influence of this parameter's variation on dynamic impedance; (**b**) the impact of this parameter's variation on dynamic damping.

As depicted in Figure 13, the curves representing dynamic stiffness and damping at the top of the SDCM pile change with dimensionless frequency for various soil relaxation shear moduli. It can be seen from the figure that as the soil relaxation shear modulus increases, in the context of low frequencies, the dynamic slightly increases, while the oscillation amplitude at the resonance frequency significantly decreases. This phenomenon indicates that the increase in soil relaxation shear modulus can significantly enhance the dynamic stiffness and damping of the SDCM pile at its top.

Figure 14 illustrates the curves of dynamic stiffness and damping of the pile apex of the SDCM pile varying with the dimensionless frequency under changes in soil porosity alone. It is apparent that the influence of porosity changes on dynamic stiffness within the low-frequency spectrum and resonance frequency is negligible. However, as the frequency increases, it can be observed that higher porosity contributes to a slight increase in the oscillation amplitude at the resonance frequency. Thus, it can be concluded that an increase in porosity is detrimental to the vibration resistance performance of the SDCM pile, but the impact is not significant and can generally be ignored.

6. Discussion

This paper derives the theoretical solution for the dynamic impedance at the top of the SDCM pile based on mechanical equilibrium and the governing equations for unsaturated soil motion through rigorous derivation. By comparing the degenerated solution of the derived formula with the dynamic impedance analytical solution proposed by Ding et al. [38], it is shown that both results are in high agreement, confirming the correctness and rationality of the findings in this paper. Finally, parameter analyses based on the proposed analytical solution for the dynamic impedance indicate the following: (1) reducing the radius of the concrete core pile or increasing the length of the SDCM pile is beneficial for enhancing its resistance to vertical dynamic loads; (2) in the FSLS model, raising the fractional order and strain relaxation time, alongside lowering the stress relaxation time, can significantly bolster the SDCM pile's capacity to resist vertical dynamic loads; and (3) increasing soil saturation and decreasing the intrinsic permeability coefficient can also enhance its vibration resistance.

Unlike previous studies focusing on the bearing capacity of SDCM piles, this paper theoretically investigates the ability of SDCM piles to resist vertical dynamic loads, which is significant for the application of SDCM piles in the foundations of bridges and energy facilities in coastal areas.

According to our research findings, increasing the length of the SDCM pile can enhance its ability to resist vertical vibration loads. Previous research on the bearing performance of SDCM piles has also shown that this measure can improve their load-bearing capacity. Therefore, in practical engineering applications, increasing the pile length is a simple and effective approach to simultaneously enhance both the bearing capacity and vibration resistance of SDCM piles. However, increasing the pile length also implies an increase in cost. The results of this study show that reducing the radius of the concrete core pile can also improve its vibration resistance, allowing for cost savings while meeting load-bearing capacity requirements. According to the research by Tang et al. [25], when the volume of the core pile is fixed, a smaller radius and longer core pile can provide higher bearing capacity. Therefore, in the foundations of bridges and energy facilities in coastal areas, the core pile should be designed to be slender, achieving higher bearing capacity and vibration resistance while controlling costs.

Moreover, we examined the impact of various soil parameters on the vibration resistance of SDCM piles, which can assist engineers in making reasonable designs when facing different geological conditions. Although this paper theoretically investigates the vibration resistance of SDCM piles composed of equal-length circular concrete core piles and cement outer casings, numerous scholars have proposed various forms of SDCM piles, such as T-shaped concrete core piles and rib-reinforced core piles. Further research is required on the vibration resistance of these types of SDCM piles. Comparing the vibration

performance of these differently shaped SDCM piles is crucial for their application in the foundations of bridges and energy facilities in coastal areas.

Additionally, this study focuses on vertical dynamic loads; however, bridges and energy facilities also experience horizontal dynamic loads, such as wind and wave loads, while bearing vertical dynamic loads. Therefore, studying horizontal dynamic loads is equally important. In future research, we will examine the horizontal vibration resistance performance of SDCM piles.

7. Conclusions

Based on the theory of elastic dynamics and considering the special structure of SDCM piles and the non-flowable viscosity of the unsaturated soil framework, this paper investigates the axial dynamic response of SDCM piles in an unsaturated viscoelastic foundation through theoretical derivations and parameter analysis. The primary findings are outlined below:

(1) Reducing the radius of the concrete core pile while maintaining a constant total cross-sectional area of the SDCM pile positively contributes to enhancing its vibration resistance and helps to reduce construction costs and difficulties. However, expanding the radius of the exterior pile without changing the cross-section of the concrete core pile does not effectively improve its vibration resistance.

(2) Increasing the length of the SDCM pile aids in enhancing its vibration resistance. Conversely, an rise in the elastic modulus of the exterior pile is detrimental to the ability to resist vertical vibrations of the SDCM pile. The enlargement in the elastic modulus of the core pile only enhance its vibration resistance under low-frequency load excitation.

(3) In the FSLS model, an increase in the fractional order and strain relaxation time, along with a decrease in stress relaxation time, both contribute to improving the ability to resist vertical vibrations of the SDCM pile.

(4) An increase in soil saturation and a decrease in the intrinsic permeability coefficient have a significantly positive effect on enhancing the ability to resist axial dynamic loads of the SDCM pile. Additionally, an surge in the relaxed shear modulus of the surrounding soil has a markedly positive impact on the ability to resist vertical vibrations of the SDCM pile. However, the impact of porosity changes on the ability to resist vertical vibrations of the SDCM pile can be considered negligible.

Author Contributions: Manuscript writing: Y.Y.; chart creation: Y.Y.; data analysis: Y.Y.; literature search: Y.Y.; monitoring progress: G.D.; finalizing the manuscript: G.D.; literature search: H.L.; chart creation: H.L.; data analysis: H.L.; literature search: Y.X.; literature search: C.X. All authors have read and agreed to the published version of the manuscript.

Funding: This research was funded by National Natural Science Foundation of China (52378328, 52178317, and 52078128).

Institutional Review Board Statement: Not applicable.

Informed Consent Statement: Not applicable.

Data Availability Statement: Data are contained within the article.

Conflicts of Interest: The authors declare no conflicts of interest.

Symbols and Abbreviations

Symbols and Abbreviations	Description
SDCM	Stiffened deep cement mixing
DCM	Deep cement mixing
ρ_c	The density of concrete core pile
A_c	Cross-sectional area of core pile
A_m	Cross-sectional area of exterior pile
r_1	Inner radii of concrete core pile
r_2	External radii of concrete core pile
r_3	External radii of exterior pile
L	The length of the stiffened composite pile
$P(t)$	Uniformly distributed harmonic dynamic load
τ_m	The frictional resistance acting on the inner wall of the micro unit of the exterior pile
τ_s	The frictional resistance acting on the exterior wall of the micro unit of the exterior pile
u_m	The axial displacement of the cement–soil exterior pile
u_c	The axial displacement of the concrete core pile
σ_m	The axial stress acting on the top of the micro unit of the cement–soil exterior pile
σ_c	The axial stress acting on the top of the micro unit of the concrete core pile
E_m	The elastic moduli of the concrete core pile
E_c	The elastic moduli of the cement–soil exterior pile
ω	Angular frequency
f	Frequency
u_i	Displacement components of the solid phase
w_i	Relative displacement components of the liquid phase
v_i	Relative displacement components of the gas phase
ρ_s	Absolute mass densities of the solid phase
ρ_w	Absolute mass densities of the liquid phase
ρ_g	Absolute mass densities of the gas phase
ϕ	The porosity of the unsaturated soil
S_w	Saturation degrees of the liquid phase
S_g	Saturation degrees of the gas phase
k	The intrinsic permeability coefficient of the unsaturated soil
μ_w	Dynamic viscosities of the liquid phase
μ_g	Dynamic viscosities of the gas phase
k_{rw}	Relative permeability coefficients of the liquid phase
k_{rg}	Relative permeability coefficients of the gas phase
m	The parameter of the V-G model
S_e	The effective saturation of the liquid phase
S_{res}	The residual saturation of the liquid phase
p_w	Pore water pressure
p_g	Pore gas pressure
$\overline{\sigma}(\omega)$	Fourier transforms of stress
$\overline{\varepsilon}(\omega)$	Strain in the medium
r	The fractional order
τ_σ	Stress relaxation time
τ_ε	Strain relaxation time
μ_0	The relaxed shear modulus
K_{b0}	Relaxed bulk modulus of the soil skeleton
K_s	The compressive modulus of the soil particles
ε_s	The volumetric strain of the soil skeleton
ε_{xx}	The relative volumetric strain of the liquid phase
ε_9	The relative volumetric strain of the gas phase
σ_z	Axial stress
σ_r	Radial stress
σ_{zr}	Shear stress
∇^2	The Laplace operator
$\overline{P}(\omega)$	The Fourier transform form of $P(t)$

Appendix A

$$\begin{cases} \overline{B}_{11}(\omega) = \frac{\overline{A}_{13}(\omega)\overline{A}_{22}(\omega)-\overline{A}_{23}(\omega)\overline{A}_{12}(\omega)}{\overline{A}_{11}(\omega)\overline{A}_{22}(\omega)-\overline{A}_{21}(\omega)\overline{A}_{12}(\omega)} \\ \overline{B}_{12}(\omega) = \frac{A_{14}\overline{A}_{22}(\omega)}{\overline{A}_{11}(\omega)\overline{A}_{22}(\omega)-\overline{A}_{21}(\omega)\overline{A}_{12}(\omega)} \\ \overline{B}_{13}(\omega) = \frac{A_{25}\overline{A}_{12}(\omega)}{\overline{A}_{11}(\omega)\overline{A}_{22}(\omega)-\overline{A}_{21}(\omega)\overline{A}_{12}(\omega)} \end{cases} \tag{A1}$$

$$\begin{cases} \overline{B}_{21}(\omega) = \frac{\overline{A}_{13}(\omega)\overline{A}_{21}(\omega)-\overline{A}_{23}(\omega)\overline{A}_{11}(\omega)}{\overline{A}_{12}(\omega)\overline{A}_{21}(\omega)-\overline{A}_{22}(\omega)\overline{A}_{11}(\omega)} \\ \overline{B}_{22}(\omega) = \frac{A_{14}\overline{A}_{21}(\omega)}{\overline{A}_{12}(\omega)\overline{A}_{21}(\omega)-\overline{A}_{22}(\omega)\overline{A}_{11}(\omega)} \\ \overline{B}_{23}(\omega) = \frac{-A_{25}\overline{A}_{11}(\omega)}{\overline{A}_{12}(\omega)\overline{A}_{21}(\omega)-\overline{A}_{22}(\omega)\overline{A}_{11}(\omega)} \end{cases} \tag{A2}$$

In the equation:

$$\begin{cases} \overline{A}_{11}(\omega) = \phi A_s + [\overline{a}(\omega) - \phi]S_w^2/K_s + \phi S_w/K_w \\ \overline{A}_{12}(\omega) = [\overline{a}(\omega) - \phi]S_w S_g/K_s - \phi A_s \\ \overline{A}_{13}(\omega) = [\overline{a}(\omega) - \phi]S_w, A_{14} = \phi S_w, A_{15} = 0 \end{cases} \tag{A3}$$

$$\begin{cases} \overline{A}_{21}(\omega) = [\overline{a}(\omega) - \phi]S_w S_g/K_s - \phi A_s \\ \overline{A}_{22}(\omega) = \phi A_s + [\overline{a}(\omega) - \phi]{S_g}^2/K_s + \phi S_g/K_g \\ \overline{A}_{23}(\omega) = [\overline{a}(\omega) - \phi]S_g, A_{24} = 0, A_{25} = \phi S_g \end{cases} \tag{A4}$$

$$A_s = \alpha_v m d(1 - S_{res}){S_e}^{(m+1)/m}\left({S_e}^{-1/m} - 1\right)^{(d-1)/d} \tag{A5}$$

In the equation, K_w and K_g represent the volume moduli of the liquid phase and the gas phase, respectively; α_v, m, and d are the fitting parameters of the V-G model.

Appendix B

$$\begin{cases} a_1 = C_{11}(\omega) + 2\overline{\mu}(\omega), a_2 = \rho\omega^2, a_3 = C_{12}(\omega) \\ a_4 = \rho_w\omega^2, a_5 = C_{13}(\omega), a_6 = \rho_g\omega^2 \\ a_7 = C_{21}(\omega), a_8 = C_{22}(\omega) \\ a_9 = \rho_w\omega^2/(\phi S_w) - \mu_w \mathrm{i}\omega/(k_{rw}k) \end{cases} \tag{A6}$$

$$\begin{cases} a_{10} = C_{23}(\omega), a_{11} = C_{31}(\omega), a_{12} = C_{32}(\omega) \\ a_{13} = C_{33}(\omega), a_{15} = \overline{\mu}(\omega) \\ a_{14} = \rho_g\omega^2/\left(\phi S_g\right) - \mu_g \mathrm{i}\omega/\left(k_{rg}k\right) \end{cases} \tag{A7}$$

Appendix C

$$h_1 = a_1(a_8a_{13} - a_{10}a_{12}) + a_3(a_{10}a_{11} - a_7a_{13}) + a_5(a_7a_{12} - a_8a_{11}) \tag{A8}$$

$$\begin{aligned} h_2 = {} & a_3(a_6a_{10} - a_7a_{14}) + a_{11}(a_4a_{10} - a_5a_9) + a_8[a_1a_{14} + a_2a_{13} - a_6(a_5 + a_{11})] \\ & + a_{12}(a_4a_5 + a_6a_7 - a_2a_{10}) + a_{13}[a_1a_9 - a_4(a_3 + a_7)] \end{aligned} \tag{A9}$$

$$\begin{aligned} h_3 = {} & a_8\left(a_2a_{14} - a_6^2\right) + a_9(a_1a_{14} + a_2a_{13}) - a_6a_9(a_5 + a_{11}) \\ & + a_4a_6(a_{10} + a_{12}) - a_4a_{14}(a_3 + a_7) - a_4a_4a_{13} \end{aligned} \tag{A10}$$

$$h_4 = a_9\left(a_2a_{14} - a_6^2\right) - a_4^2a_{14} \tag{A11}$$

$$h_5 = \left[a_4^2a_{14} - a_9\left(a_2a_{14} - a_6^2\right)\right]/(a_9a_{14}a_{15}) \tag{A12}$$

Appendix D

$$\chi_{wj} = \frac{a_{10}\beta_j^2\left(a_1\beta_j^2 + a_2\right) - \left(a_7\beta_j^2 + a_4\right)\left(a_5\beta_j^2 + a_6\right)}{\left(a_8\beta_j^2 + a_9\right)\left(a_5\beta_j^2 + a_6\right) - a_{10}\beta_j^2\left(a_3\beta_j^2 + a_4\right)} \tag{A13}$$

$$\chi_{gj} = \frac{a_{12}\beta_j^2\left(a_7\beta_j^2 + a_4\right) - \left(a_{11}\beta_j^2 + a_6\right)\left(a_8\beta_j^2 + a_9\right)}{\left(a_{13}\beta_j^2 + a_{14}\right)\left(a_8\beta_j^2 + a_9\right) - a_{10}\beta_j^2 a_{12}\beta_j^2} \tag{A14}$$

$$\chi_{w4} = -a_4/a_9,\ \chi_{g4} = -a_6/a_{14} \tag{A15}$$

In the equation, the subscript j = 1, 2, 3.

$$\xi_1 = \frac{\theta_1 - \theta_2}{\theta_3 - \theta_4}\frac{q_1 K_1(q_1 r_3)}{q_2 K_1(q_2 r_3)} \tag{A16}$$

$$\xi_2 = \frac{\theta_5 - \theta_6}{\theta_7 - \theta_8}\frac{q_1 K_1(q_1 r_1)}{q_3 K_1(q_3 r_1)} \tag{A17}$$

$$\xi_3 = \frac{q_1 K_1(q_1 r_3) + \xi_1 q_2 K_1(q_2 r_3) + \xi_2 q_3 K_1(q_3 r_3)}{-g_n q_4 K_1(q_4 r_3)} \tag{A18}$$

In the equation:

$$\begin{cases} \theta_1 = (\chi_{w4} - \chi_{w1})(\chi_{g4} - \chi_{g3}) \\ \theta_2 = (\chi_{w4} - \chi_{w3})(\chi_{g4} - \chi_{g1}) \\ \theta_3 = (\chi_{w4} - \chi_{w3})(\chi_{g4} - \chi_{g2}) \\ \theta_4 = (\chi_{w4} - \chi_{w2})(\chi_{g4} - \chi_{g3}) \end{cases} \tag{A19}$$

$$\begin{cases} \theta_5 = (\chi_{w4} - \chi_{w1})(\chi_{g4} - \chi_{g2}) \\ \theta_6 = (\chi_{w4} - \chi_{w2})(\chi_{g4} - \chi_{g1}) \\ \theta_7 = (\chi_{w4} - \chi_{w2})(\chi_{g4} - \chi_{g3}) \\ \theta_8 = (\chi_{w4} - \chi_{w3})(\chi_{g4} - \chi_{g2}) \end{cases} \tag{A20}$$

References

1. Zhu, R.; Zhou, F.; Wang, X.D.; Wei, X.; Deng, Y.G. Pore Water Pressure and Stress Changes During the Construction of Stiffened Deep Cement Mixing Piles. *Int. J. Civ. Eng.* **2024**, *22*, 1481–1492. [CrossRef]
2. Zhu, S.M.; Chen, C.F.; Cai, H.; Mao, F.S. Analytical modeling for the load-transfer behavior of stiffened deep cement mixing (SDCM) pile with rigid cap in layer soils. *Comput. Geotech.* **2022**, *144*, 104618. [CrossRef]
3. Voottipruex, P.; Suksawat, T.; Bergado, D.T.; Jamsawang, P. Numerical simulations and parametric study of SDCM and DCM piles under full scale axial and lateral loads. *Comput. Geotech.* **2011**, *38*, 318–329. [CrossRef]
4. Dai, Z.H.; Liu, Z.E.; Zhang, H.; Qin, Z.Z. Numerical analysis of load-transfer mechanism of stiffened deep cement mixing pile foundation. *Int. J. Geotech. Eng.* **2023**, *17*, 583–593. [CrossRef]
5. Tao, F.; Zhu, H.Q.; Dong, F.B.; Chai, S.Q.; Liu, F.; Zhang, M. Experimental study on the bearing property of the composite foundation with stiffened deep cement mixing pile based on the PHC pile. *Front. Mater.* **2023**, *10*, 1237190. [CrossRef]
6. Han, Y.S.; Cheng, J.Y.; Zhou, M.; Ni, P.P.; Wang, Y.L. Experimental Study of Compaction and Expansion Effects Caused by Penetration of Core Pile During Construction of SDCM Pile. *Int. J. Geomech.* **2022**, *22*, 04022041. [CrossRef]
7. Zhuang, X.X.; Zong, Z.L.; Huang, Y.H.; Wang, C.S.; Lin, X.J. Parametric Study on Analyzing the Effect of Soil-Cement Strength on the Uplifting Behavior of HSCM Piles Installed in Marine Soft Clay. *Appl Sci.* **2023**, *13*, 330. [CrossRef]
8. Sukkarak, R.; Jongpradist, P.; Kongkitkul, W.; Jamsawang, P.; Likitlersuang, S. Investigation on load-carrying capacity of geogrid-encased deep cement mixing piles. *Geosynth. Int.* **2021**, *28*, 450–463. [CrossRef]
9. Wonglert, A.; Jongpradist, P. Impact of reinforced core on performance and failure behavior of stiffened deep cement mixing piles. *Comput. Geotech.* **2015**, *69*, 93–104. [CrossRef]
10. Jiu, Y.Z.; Gao, Y.F.; Lei, F.G.; Zhu, Y.Z.; Zhang, Z.Z. Nonlinear Analysis of Bearing Characteristics of Stiffened Deep Cement Mixing Piles under Vertical Loading. *Buildings* **2024**, *14*, 816. [CrossRef]
11. Zhou, M.; Li, Z.T.; Han, Y.S.; Ni, P.P.; Wang, Y.L. Experimental Study on the Vertical Bearing Capacity of Stiffened Deep Cement Mixing Piles. *Int. J. Geomech.* **2022**, *22*, 04022043. [CrossRef]
12. Wang, C.; Wu, Q.; Zhang, H.; Liang, F. Effect of scour remediation by solidified soil on lateral response of monopile supporting offshore wind turbines using numerical model. *Appl. Ocean. Res.* **2024**, *150*, 104143. [CrossRef]

13. Dai, G.L.; OuYang, H.R.; Gao, L.C.; Liu, H.B.; Guo, Q.; Gong, W.M. Monotonic and cyclic lateral behavior of semi-rigid pile in cement-improved clay: Centrifuge tests and numerical investigation. *Acta. Geotech.* **2023**, *18*, 4157–4181. [CrossRef]
14. Zhang, C.R.; Zhang, X.; Huang, M.S.; Tang, H.W. Responses of caisson-piles foundations to long-term cyclic lateral load and scouring. *Soil Dyn. Earthq. Eng.* **2019**, *119*, 62–74. [CrossRef]
15. Liu, H.B.; Dai, G.L.; Zhou, F.X.; Ouyang, H.R.; Liu, J. Analytical approach for lateral dynamic behaviours of pipe piles enhanced by cement-improved soil in unsaturated ground. *Acta. Geotech.* **2024**, *19*, 6747–6772. [CrossRef]
16. Wang, C.; Xu, Y.F.; Dong, P. Working characteristics of concrete-cored deep cement mixing piles under embankments. *J. Zhejiang Univ. Sci. A* **2014**, *15*, 419–431. [CrossRef]
17. Phutthananon, C.; Jongpradist, P.; Dias, D.; Guo, X.F.; Jamsawang, P.; Baroth, J. Reliability-based settlement analysis of embankments over soft soils reinforced with T-shaped deep cement mixing piles. *Front. Struct. Civ. Eng.* **2022**, *16*, 638–656. [CrossRef]
18. Phutthananon, C.; Jongpradist, P.; Yensri, P.; Jamsawang, P. Dependence of ultimate bearing capacity and failure behavior of T-shaped deep cement mixing piles on enlarged cap shape and pile strength. *Comput. Geotech.* **2018**, *97*, 27–41. [CrossRef]
19. Papadimitriou, A.G.; Valsamis, A.I.; Limnaiou, T.G. Liquefaction mitigation methods for existing shallow-founded elongated structures on horizontal or mildly-inclined ground. *Soil Dyn. Earthq. Eng.* **2022**, *162*, 107453. [CrossRef]
20. Liu, S.Y.; Du, Y.J.; Yi, Y.L.; Puppala, A.J. Field Investigations on Performance of T-Shaped Deep Mixed Soil Cement Column-Supported Embankments over Soft Ground. *J. Geotech. Geoenviron.* **2012**, *138*, 718–727. [CrossRef]
21. Jamsawang, P.; Bergado, D.T.; Voottipruex, P. Field behaviour of stiffened deep cement mixing piles. *Proc. Inst. Civ. Eng. Ground Improv.* **2011**, *164*, 33–49. [CrossRef]
22. Zhou, J.J.; Gong, X.N.; Wang, K.H.; Zhang, R.H. A field study on the behavior of static drill rooted nodular piles with caps under compression. *J. Zhejiang Univ. Sci. A* **2015**, *16*, 951–963. [CrossRef]
23. Zhou, J.J.; Wang, K.H.; Gong, X.N.; Zhang, R.H. Bearing capacity and load transfer mechanism of a static drill rooted nodular pile in soft soil areas. *J. Zhejiang Univ. Sci. A* **2013**, *14*, 705–719. [CrossRef]
24. Jamsawang, P.; Bergado, D.T.; Voottipruex, P. Chapter 2—Full-Scale Tests on Stiffened Deep Cement Mixing Piles Including Three-Dimensional Finite Element Simulation. In *Ground Improvement Case Histories*; Indraratna, B., Chu, J., Rujikiatkamjorn, C., Eds.; Butterworth-Heinemann: Oxford, UK, 2015; pp. 31–77.
25. Tang, X.J.; Zhao, W.; Dong, M.M.; Su, H.; Cai, X.L.; Chen, Y.; Li, W.W. Experimental and Numerical Study of the Mechanical Behavior of Cemented Soil Stiffened with Large-Size Prestressed High-Strength Concrete Pile Under Compression. *Arab. J. Sci. Eng.* **2024**. [CrossRef]
26. Bao, H.; Peng, J.; Cheng, Z.J.N.; Hong, J.Q.; Gao, Y. Experimental Study on Inner Interface Mechanical Properties of the ESDCM Pile with Steel Core. *Buildings* **2023**, *13*, 486. [CrossRef]
27. Peng, J.; Gao, Y.; Bao, H.; Liu, Y.M.; Shao, Q.H. Influence of the ribbed steel core on the inner Interface mechanical behavior of the ESDCM pile. *Case Stud. Constr. Mater.* **2024**, *21*, e03554. [CrossRef]
28. Gong, Z.Y.; Dai, G.L.; Liu, H.B.; Chen, X.S.; Ouyang, H.R.; Jiang, J.X. Theoretical Analysis and Field Investigation on Bearing Characteristics of the Long-Core SDCM Pile Under Vertical Load in Multilayered Soil. *Int. J. Numer. Anal. Methods Geomech.* **2024**. [CrossRef]
29. Savvides, A.A.; Papadopoulos, L. A neural network approach for the reliability analysis on failure of shallow foundations on cohesive soils. *Int. J. Geotech. Eng.* **2024**, *15*, 15. [CrossRef]
30. Zhang, P.; Yin, Z.Y.; Sheil, B. Interpretable data-driven constitutive modelling of soils with sparse data. *Comput. Geotech.* **2023**, *160*, 105511. [CrossRef]
31. Zheng, C.J.; Kouretzis, G.; Ding, X.M.; Luan, L.B. Vertical vibration of end-bearing single piles in poroelastic soil considering three-dimensional soil and pile wave effects. *Comput. Geotech.* **2022**, *146*, 104740. [CrossRef]
32. Liu, H.B.; Dai, G.L.; Zhou, F.X.; Li, Z.W.; Liang, Y.W. Vertical dynamic response of pipe pile embedded in unsaturated soil based on fractional-order standard linear solid model and Rayleigh-Love rod model. *Int. J. Numer. Anal. Methods Geomech.* **2023**, *47*, 325–348. [CrossRef]
33. Meng, K.; Cui, C.Y.; Liang, Z.M.; Li, H.J.; Pei, H.F. A new approach for longitudinal vibration of a large-diameter floating pipe pile in visco-elastic soil considering the three-dimensional wave effects. *Comput. Geotech.* **2020**, *128*, 103840. [CrossRef]
34. Shan, Y.; Ma, W.J.; Xiang, K.; Wang, B.L.; Zhou, S.H.; Guo, H.J. Vertical dynamic response of a floating pile in unsaturated poroelastic media based on the fictitious unsaturated soil pile model. *Appl. Math. Model.* **2022**, *109*, 209–228. [CrossRef]
35. Lü, S.H.; Wang, K.H.; Wu, W.B.; Leo, C.J. Longitudinal vibration of a pile embedded in layered soil considering the transverse inertia effect of pile. *Comput. Geotech.* **2014**, *62*, 90–99. [CrossRef]
36. Raongjant, W.; Jing, M. Field testing of stiffened deep cement mixing piles under lateral cyclic loading. *Earthq. Eng. Eng. Vib.* **2013**, *12*, 261–265. [CrossRef]
37. Zhang, D.W.; Wang, A.H.; Ding, X.M. Seismic response of pile groups improved with deep cement mixing columns in liquefiable sand: Shaking table tests. *Can. Geotech. J.* **2022**, *59*, 994–1006. [CrossRef]

38. Ding, X.M.; Zheng, J.H.; Luan, L.B. *Principles of Pile Dynamics*; Science Press: Beijing, China, 2021; pp. 118–142.
39. Liu, H.; Dai, G.; Zhou, F.; Cao, X.; Wang, L. Effect of flow-independent viscosity on the propagation behavior of Rayleigh wave in partially saturated soil based on the fractional standard linear solid model. *Comput. Geotech.* **2022**, *147*, 104763. [CrossRef]

Journal of
Marine Science and Engineering

MDPI

Article

Effective Stress-Based Numerical Method for Predicting Large-Diameter Monopile Response to Various Lateral Cyclic Loadings

Jichao Lei [1,2], Kehua Leng [2,*], Wei Xu [3], Lixian Wang [2], Yu Hu [2] and Zhen Liu [4]

[1] Sanya Science and Education Innovation Park of Wuhan University of Technology, Sanya 572000, China; leijichao88@whut.edu.cn
[2] School of Naval Architecture, Ocean and Energy Power Engineering, Wuhan University of Technology, Wuhan 430063, China; lixianwang@whut.edu.cn (L.W.); huyu1012@hotmail.com (Y.H.)
[3] Naval Research Institute, Beijing 100161, China; weixu06@163.com
[4] Naval Logistics Academy, Tianjin 300450, China; zliu@tju.edu.cn
* Correspondence: lengkehua2024@whut.edu.cn

Abstract: Extreme marine environmental cyclic loading significantly affects the serviceability of monopiles applied for the foundation of offshore wind turbines (OWTs). Existing research has primarily used p-y methods or total stress-based models to investigate the behavior of monopile–marine clay systems, overlooking the pore pressure development in subsea clay. Studies on the effective stress-based behavior of clay under various lateral cyclic loading conditions are limited. This paper presents an effective stress-based 3D finite element numerical method developed to predict key behaviors of pile–clay systems, including permanent pile rotation under cyclic loading, pile bending moment, and the evolution of pore pressure in subsea clay. The model is verified by contrasting the simulations results to centrifuge experimental results. Cyclic lateral loading is divided into average cyclic load and amplitude of cyclic load to investigate their impacts on the pile–clay system response. The research findings offer insights for the design of large-diameter monopiles under complex cyclic loading conditions.

Keywords: effective stress model; large diameter monopile; cyclic lateral load; excess pore pressure; numerical simulation

1. Introduction

Some offshore wind turbines (OWTs) rely on monopiles as foundational supports. These monopiles, embedded into the seabed, are designed to withstand not only the weight of the turbines but also the cyclic lateral loads from environmental factors such as wind, current, and waves. For the purpose of meeting the serviceability limit state (SLS) criteria, as outlined in current OWT guidelines, it is necessary to conduct a thorough analysis of monopile response to complex lateral cyclic loading.

To simulate the behavior of offshore wind turbines (OWTs) under cyclic loading, the nonlinear *p-y* method, which is recommended by current codes for its simplicity, is commonly used [1–5]. However, this method is primarily based on investigations on small-diameter piles. It is questionable to use it to reasonably predict the behavior of monopiles under various patterns of cyclic loading. Additionally, this method is a quasi-static method that simplifies the complicated load–displacement behavior of a pile under cyclic loading, overlooking important characteristics such as the pile's hysteresis behavior, cyclic load paths, and plastic strain accumulation in subsea soil. These important characteristics also significantly affect the serviceability of monopiles under cyclic loading, in addition to the permanent displacement of piles. Similar limitations are found in modified models of the *p-y* method [6,7] and other simplified analysis methods [8] that attempt to consider the cyclic stiffness degradation.

For investigating the detailed evolution of the load–displacement characteristics of monopiles under cyclic loading, dynamic constitutive models are utilized in the numerical calculation of monopile–soil interaction. The majority of these dynamic models are elastic–plastic models [3,9–15]. These models incorporate the plastic flow law in the soil model to consider the hysteresis behavior of the pile, plastic strain development, and the effects of cyclic loading history. However, these models are total stress models, which cannot consider the plastic strain development in the direction of mean principal stress, thereby failing to account for changes in the effective stress and pore pressure. Previous investigations [16–19] have shown that the development of excess pore pressure decreases the effective stress in clay, resulting in the degradation of its strength and stiffness. Damgaard et al. [20] observed that the pore pressure and permeability of the subsoil have a strong influence on the stiffness of the wind turbine which can demonstrate the deviations between measured and calculated results. Therefore, accurately predicting pore pressure in the foundation with advanced constitutive models is important for predicting the response of OWTs under cyclic loading. While some researchers have investigated the development of pore pressure in the subsea clay around monopiles using independent pore pressure models [21,22], these models are established based on Biot theory and cannot consider the hydro-mechanical coupling behavior of soil. In addition, some researchers focus on the dynamic behavior of monopiles subjected to seismic load in liquefiable soil [23,24], however, the mechanical response will be significantly different from that of a monopile in a clay foundation. Therefore, the application of a model simulating the effective stress-based behavior of clay is necessary to accurately predict the behavior of the monopile–soil system subjected to lateral cyclic loading.

Some researchers have employed effective stress-based advanced models to investigate the coupled response of load–displacement of monopiles and excess pore pressure in subsea soil in a specific loading condition. Charlton and Rouainia [25] used a kinematic hardening constitutive model to investigate the cyclic performance of a monopile in spatially variable clay. They observed an increase in the cyclic secant stiffness, which was attributed to the development of negative excess pore pressures in the clay, as well as the accumulation of excess pore water pressure over time due to the buildup of plastic strain. Duque et al. [26] used a hypoplastic model for clay to study the post-cyclic reconsolidation behavior of subsoil. Through applying the multi-stage of post-cyclic reconsolidation, the development of pore pressure is simulated. Ding et al. [27] employed the bounding surface model to examine the behavior of the soil–monopile–offshore wind turbine (OWT) system, taking into account the cyclic hydro-mechanical response of clay. The study revealed a significant accumulation of excess pore pressure in the upper half of the soil domain and near the bottom of the monopile. Zhang et al. [28] used the elastic–plastic model to analyze the bearing capacity of a monopile and excess pore pressure of seabed soil under seismic load. The studies above considered the hydro-mechanical coupling behavior of clay. Esfeh and Kaynia [29] used the Sanisand model to investigate the evolution of pore water pressure in sand around OWTs during earthquake shaking.

The existing research based on effective stress analysis has primarily focused on specific cyclic loading conditions or sand foundations. However, there is a lack of studies that address the coupled responses of load–displacement of piles and the evolution of pore pressure in clay under complex cyclic loading cases. Therefore, it is necessary to employ an effective stress-based model to investigate the behavior of clay. Additionally, the lateral cyclic load can be either a typical one-way or two-way cyclic loading or an asymmetric two-way cyclic loading. Hence, the cyclic load is divided into cyclic mean values and cyclic amplitudes to study the influence of cyclic load patterns in this study. Consequently, the primary objectives of this paper are: (a) to develop and validate a 3D finite element method based on effective stress for analyzing the response of monopile–clay systems, utilizing an effective stress-based bounding surface model; and (b) to examine the response of monopile–clay systems, including pile load–displacement and excess pore pressure in subsea clay, under different combinations of average cyclic load and cyclic load amplitude.

2. Effective Stress-Based Bounding Surface Model Framework

To accurately predict the changes in the pore water and effective stress of saturated clay around a large-diameter monopile subjected to cyclic load, the effective stress-based constitutive models applied in numerical analysis are crucial. An effective stress-based model with a vanishing elastic domain derived from the classical bounding surface model is applied. The model can predict the essential behavior of saturated clay under monotonic and cyclic loading, including growth in elastic and plastic strain, evolution of effective stress paths, development of pore pressure, and monotonic shear strength softening. Furthermore, the model was successfully implemented in ABAQUS 2020 software using a UMAT subroutine.

The model, developed using a radial return algorithm, operates as an elastic–plastic incremental framework. During loading, the model first performs an elastic prediction followed by a plastic correction. Due to the absence of a defined elastic domain, purely elastic strain does not occur during the loading process. In contrast, during unloading, the model assumes a purely elastic response, with the elastic behavior governed by the generalized Hooke's law. The elastic bulk modulus K and shear modulus G are defined to calculate the elastic incremental strain and plastic incremental strain:

$$K = \frac{1+e}{\kappa} p;\ G = \frac{3K}{2}\frac{1-2\mu}{1+\mu} \tag{1}$$

where μ donates the Poisson's ratio; κ is the swelling line slope in e-ln p plane; and e is the void ratio.

Due to the absence of an elastic domain of the model, pure elastic strain does not occur during the loading process and plastic correction is needed. The novelty of the effective stress-based model lies in its ability to predict plastic strain increments even when the stress point is located inside the bounding surface. It is achieved by applying the mapping rule in the elastic–plastic model. For simplicity, the conventional radial mapping rule $\overline{\sigma}_{ij} = \beta\sigma_{ij}$, with the origin of the stress plane as the projection center, was employed, where σ_{ij} and $\overline{\sigma}_{ij}$ are the actual stress tensor and image stress tensor, respectively. It is widely applied by many bounding surface models [30,31]. The positions of the current stress point A located on the loading surface and the image stress point $\overline{\text{A}}$ located on the bounding surface in σ_1-σ_2-σ_3 stress space are depicted in Figure 1.

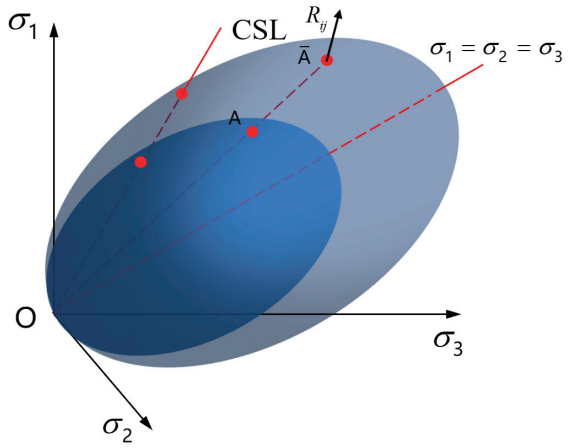

Figure 1. Bounding and loading surface in stress space in σ_1-σ_2-σ_3 space.

The bounding surface is formulated by an ellipsoidal function in the stress space, similar to the yield function of the modified Cam-clay (MCC) model. Based on the Einstein summation convention, this function of the bounding surface for the model is:

$$F\left(\overline{\sigma}_{ij}, p_0\right) = \overline{s}_{ij}\overline{s}_{ij} - \frac{2}{3}M^2\overline{p}(p_0 - \overline{p}) = 0 \tag{2}$$

where $\bar{s}_{ij}$ represents the image deviator stress tensor; $\overline{p}$ represents the image mean effective pressure; p_0 is the hardening parameter. M represents the slope of the critical state line. The loading surface function form is consistent with that of the bounding surface model, except for changing the image stress variable to the current stress variable and changing the p_0 to p_1 which indicates the size of the loading surface.

The associated flow rule is applied in this paper. A significant feature of the model is its ability to capture the cyclic response of marine clay, including hysteresis characteristics, cyclic pore pressure development, and plastic strain accumulation. The hardening rule incorporating this parameter is presented below:

$$p_0 = p_{0(0)} \cdot \eta \cdot \exp\left(\frac{v}{\lambda - \kappa}\varepsilon_v^p\right) \tag{3}$$

where $p_{0(0)}$ represents the initial value of the p_0. The calculation function for η is given by:

$$\eta = \Lambda_0 + (1 - \Lambda_0)\exp(\frac{-\omega_0 v_0}{\lambda - \kappa}\varepsilon_d^p) \tag{4}$$

where Λ_0 and ω_0 are shear softening constants that govern the degree and rate of shear strength degradation, respectively.

Following the classical bounding surface theory [32,33], the plastic modulus is defined as follows:

$$K_P = \overline{K}_P + h(\overline{p})\left(\sqrt{\beta} - 1\right) \tag{5}$$

where $h(\overline{p})$ is the scalar function related to $\overline{p}$. The function of $h(\overline{p})$ is chosen in the form [30] and is as follows:

$$h(\overline{p}) = H_0 \frac{16}{9}\frac{M^4 \nu}{\lambda - \kappa}\overline{p}^3 \tag{6}$$

where H_0 is the plastic modulus parameter. The plastic modulus at the image stress point following the form of [34] is given below:

$$\overline{K}_P = \frac{8}{9}M^2\overline{p}p_0\left[\left(\overline{p} - \frac{1}{2}p_0\right)\frac{vM^2}{\lambda - \kappa} + \frac{\eta - \Lambda_0}{\eta}\frac{-\omega_0 v}{\lambda - \kappa}\sqrt{\frac{3}{2}\bar{s}_{ij}\bar{s}_{ij}}\right] \tag{7}$$

3. Numerical Methods

3.1. Introduction of Centrifuge Tests

To validate the numerical methods presented in this study, centrifuge model tests on monopiles under lateral monotonic and cyclic loading were conducted by Yang et al. [35] using Malaysian kaolin clay. These experiments were conducted at a 100 g acceleration level. The strongbox dimensions were 1.2 m in length, 0.9 m in width, and 1.0 m in height. The Malaysian kaolin clay specimens in the tests were prepared via the mud consolidation method, undergoing 8 h of consolidation at 100 g. The specific gravity of the clay is 2.6. The liquid limit and plastic limit are 80% and 35%, respectively. The coefficient of permeability is 2×10^{-8} m/s. Its internal friction angle is 23 degrees and its unit weight is 15.5–16.4 KN/m^3. The coefficient of consolidation is 40 m^2/year. The monopile model is open-ended and made of aluminum alloy. The pile's diameter is 0.059 m and its length is 0.83 m. An aluminum alloy pipe is used to make the model pile. Its elastic modulus is 68.9 GPa. The depth of the monopile buried in the clay is 0.55 m and the position of the loading point is 0.05m below the pile top.

Monotonic experiments were conducted with a loading velocity of 0.003 m/s, which can be considered as an undrained condition. The cyclic loading test consisted of three cases numbered C1, C2, and C3. The cyclic loading period of 5s was applied. The valley and peak values of cyclic load for C1, C2, and C3 episodes are 25 N–100 N, 45 N–175 N, 45 N–370 N, respectively. The numbers of cycles for C1, C2, and C3 episodes were 100, 100, and 180, respectively.

Note that, although drainage in the soil ground under cyclic loading is allowed, the time interval between each cyclic stage is limited to just 30 s, and a total of 380 cycles in the cyclic loading process last only about 30 min. Considering a permeability coefficient of Malaysian kaolin clay of 2×10^8 m/s, the drainage during the cyclic loading process is extremely limited. Therefore, the effect of drainage in the clay ground is not considered during the cyclic loading process in this paper.

3.2. Model Parameter Calibration

The bounding surface model requires seven parameters, which can be divided into two categories: the first category includes the Cambridge parameters (λ, κ, μ, M) and the second category includes the parameters related to plastic modulus (H_0, Λ_0, ω_0). The above parameters can be determined through the constants provided in the centrifuge tests and the indoor triaxial test results of Malaysian kaolin clay found by Duque et al. [36].

M is the critical state line slope and has the following form:

$$M = \frac{6 \sin \varphi_{cs}}{3 - \sin \varphi_{cs}} \tag{8}$$

where φ_{cs} is the internal friction angle. As Malaysian kaolin clay's φ_{cs} is 23 degrees, it can be inferred that M of the clay is 0.898. Although Poisson's ratio can vary with loading conditions, particularly in soils subjected to significant stress changes, it is assumed to be constant at 0.3 for simplicity. This assumption is a common practice in many geotechnical studies involving marine clay.

λ and κ can be determined by 1D oedometric compression tests. λ can be calculated using its relationship with the compression index (C_c): $\lambda = C_c/2.303$, and κ can be calculated using its relationship with the swelling index (Cs): κ = Cs/2.303. Cc and Cs are the normal consolidation and swelling line slopes in the e-log p plane, respectively. According to the indoor oedometric compression test conducted by Duque et al. [36] on Malaysian kaolin clay, as shown in Figure 2, C_c = 0.539 and C_s = 0.152. Therefore, λ = 0.234 and κ = 0.066.

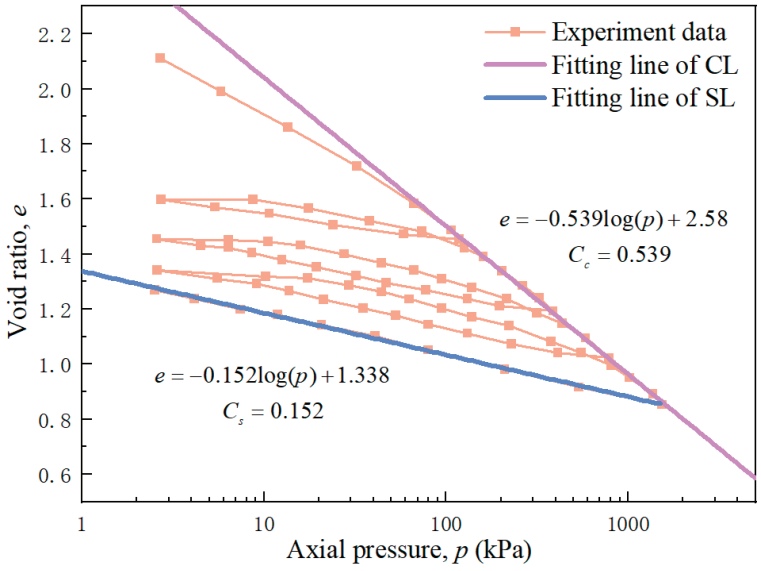

Figure 2. Fitting results of oedometric compression test conducted by Duque et al. [36].

The parameters H_0, Λ_0, and ω_0 can be calibrated using triaxial undrained monotonic shear tests conducted on marine clay. Parameters H_0, Λ_0, and ω_0 can be calibrated by trial-and-error simulation for the shear characteristics of normally consolidated clay. Based on the stress–strain triaxial test results of Malaysian kaolin clay found by Duque et al. [36], values of H_0 = 5, Λ_0 = 1, and ω_0 = 0.1 can be obtained, as shown in Figure 3a. The comparisons between the test and prediction of effective stress paths and pore pressure

development during shearing for normally consolidated clay are illustrated in Figure 3b,c. The comparisons demonstrate that the model can generally predict the stress paths and pore pressure evolution of normally consolidated Malaysian kaolin clay. It forms the basis for predicting the evolution of pore pressure in subsea clay around the monopile in this paper.

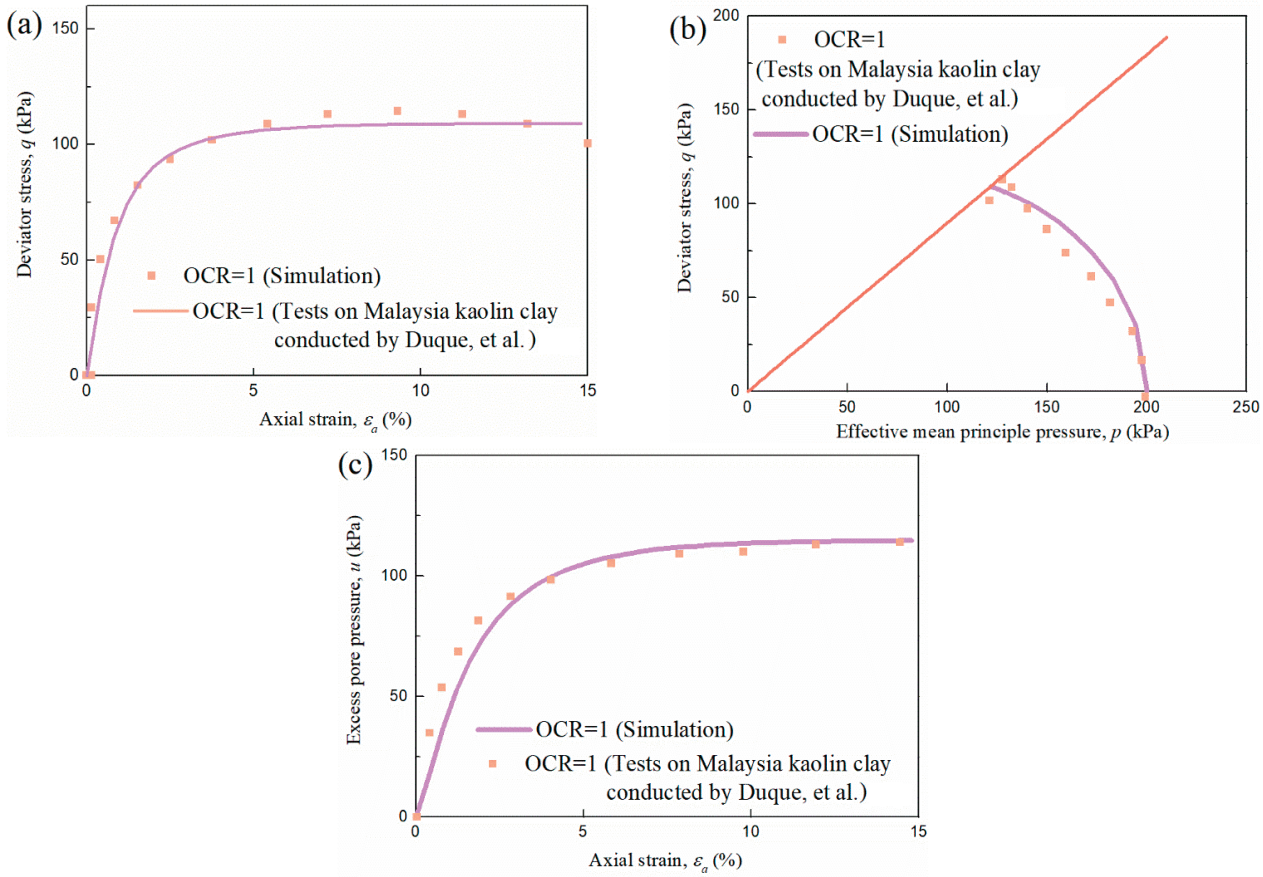

Figure 3. Comparison between predicted results with bounding surface model and test results of Malaysian kaolin clay found by Duque et al. [36] with different OCR: (**a**) q versus ε_a; (**b**) q versus p; (**c**) u versus ε_a.

In addition to the constitutive model parameters, several clay parameters must be specified when establishing the monopile–clay numerical model.

The lateral pressure coefficient during the initial consolidation of clay is determined by the following equation:

$$K_0 = 1 - \sin \varphi_{cs} \tag{9}$$

As φ_{cs} = 23, K_0 = 0.61 is taken.

As the monopile–clay model must account for the effective stress changes in the soil ground, it is necessary to account for the variations in the void ratio of clay. The confining effective stress in the ground increases gradually along the mud surface, resulting in the decrease in clay's void ratio. Given the bounding surface expression, the e_0 of clay can be calculated with the following equation:

$$e_0 = e_1 - \lambda \ln\left(\frac{{q_c}^2}{M^2} + p_c\right) + \kappa \ln\left(\frac{{q_c}^2}{p_c^2 M^2} + 1\right) \tag{10}$$

where q_c and p_c are the deviator stress and mean effective stress in situ, respectively; e_1 is the initial void ratio of the clay when the effective stress p' equals 1 kPa. According to the fitting result of the e_0-p curve in Figure 2, e_1 is equal to 2.58. The initial stresses p_c and q_c of

the clay at different burial depths can be calibrated based on the stress state after the clay's gravity is applied.

The initial size of the yield envelope is prescribed as a function of the initial stresses in the clay ground. It can be calculated using the bounding surface expression and takes the following form:

$$p_{0(0)} = \frac{{q_c}^2}{p_c M^2} + p_c \tag{11}$$

In the centrifuge test, the unit weight is considered to be 15.5–16.4 KN/m^3. Numerical simulation takes a saturation density of 1.6×10^3 kg/m^3 for calculation. As the initial void ratio e_0 decreases with the depth of the ground, the initial dry density of the clay will also gradually change along the depth direction from the mud surface. The dry density of clay at different burial depths can be calculated by Equation (12):

$$\rho_d = \rho_{sat} - \rho_w \frac{e_0}{1 + e_0} \tag{12}$$

where ρ_d is the dry density of clay; ρ_{sat} is the saturation density; ρ_w is the density of water.

3.3. Effective Stress-Based Numerical Method Implementation in UMAT

The bounding surface model is implemented in ABAQUS using the subroutine interface UMAT for structure–soil interaction numerical calculation. Implicit analysis in ABAQUS/Standard has the feature of pore pressure analysis by using the C3D8P element, which can divide the total stress into pore pressure and effective stress. Therefore, only the effective stress increment needed to be updated by inputting it into the UMAT subroutine. The calculation chart of the user-defined UMAT subroutine is illustrated in Figure 4, where STATEVs are the solution-dependent state variables that can store the intermediate variables such as void ratio, bounding surface size p_0, and internal parameter η. The control error tolerance (TOL) is set as 10^{-5}. When the determinant of the residual matrix R_n of the nth iteration is less than TOL, the current variables will be output from UMAT to ABAQUS.

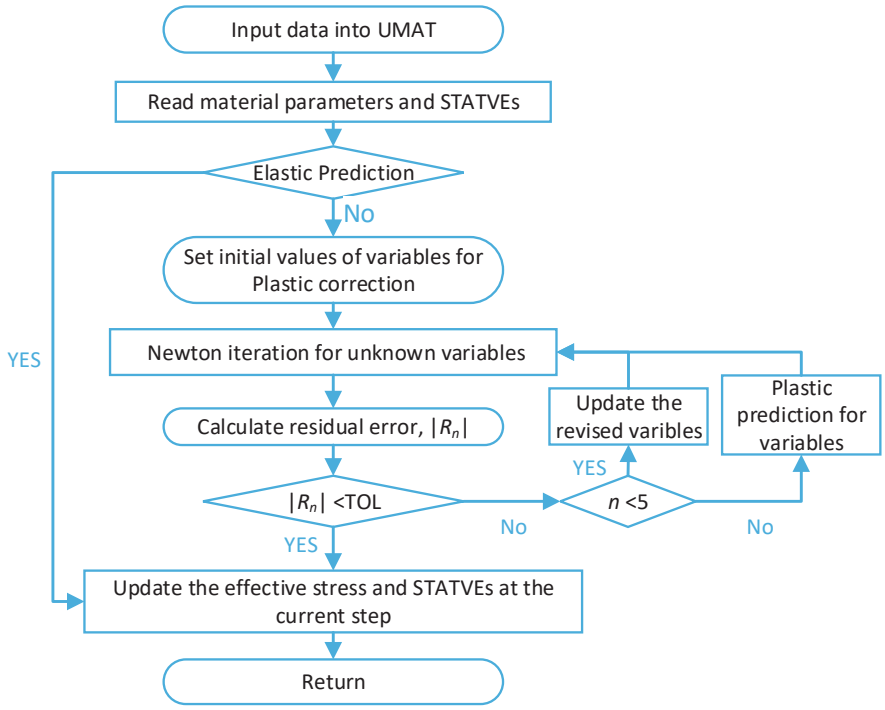

Figure 4. Flow chart of user-defined UMAT subroutine.

3.4. Finite Element Mesh of Centrifuge Tests

Three-dimensional (3D) finite element meshes were employed to model the centrifuge tests using the commercial software Abaqus. Due to symmetry along the vertical centerline of the monopile, only half of the problem was modeled. The model geometry can be determined based on the centrifuge modeling similarity rate. A schematic representation of the monopile–soil finite element model is presented in Figure 5. Following the size of the centrifuge test strongbox and the simulation approach of Cheng et al. [11], the mesh boundaries extend 10D (D is the pile diameter) horizontally from the pile's centerline and 14D vertically from the mudline in order to ensure that the response of the large-diameter monopile is not influenced by the boundaries. All mesh boundaries and the pile were prescribed as undrained boundaries. The pile was modeled using 3D 8-node linear brick elements (C3D8), while the soils were modeled using 3D 8-node trilinear displacement and trilinear pore pressure brick elements (C3D8P). Normal horizontal displacement was constrained on the vertical mesh boundaries. Horizontal and vertical displacements were constrained across the base of the mesh. The pile–clay interface was modeled as a surface-to-surface contact, allowing for separation and sliding between the pile and clay, a method commonly used in offshore applications. The normal direction behavior between the two surfaces was governed by a "hardening contact" algorithm, which prevents any penetration. The tangential behavior was governed by Coulomb's friction law, with a friction coefficient of 0.4. The initial total pore pressure in subsea soil must be specified before analysis. In clay foundations, the effective stress is influenced by the excess pore pressure rather than the hydrostatic pressure. Thus, a zero initial static pore pressure is set at the mud surface, which increases with depth. The initial static pore pressure at any depth is calculated as the product of the bulk density of water (10 kN/m^3) and the depth at that location.

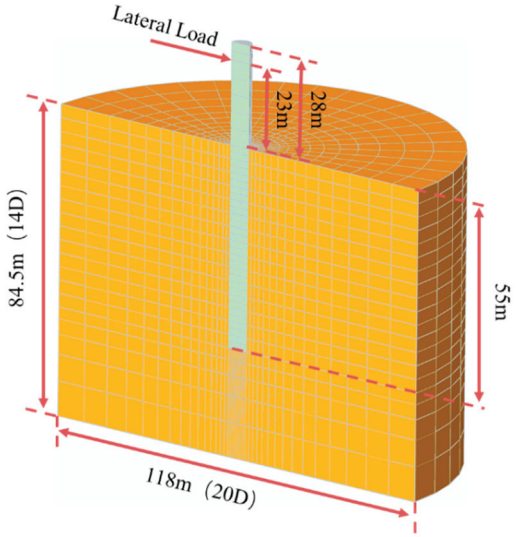

Figure 5. Illustration of 3D finite element model for large-diameter monopile.

4. Validation

4.1. Monotonic Load Behavior

According to the centrifuge test investigation of Hong et al. [37], the soil failure mechanisms around a pile consist of a wedge-flow mechanism near the mud surface and a full-flow mechanism and a rotation-flow mechanism in the bottom region of the pile. Figure 6 illustrates the simulation results of lateral displacement of the pile–clay system. It can be easily observed that the three distinct soil flow mechanisms are present in the lateral displacement contour. This demonstrates that the pile–clay numerical model can reasonably predict the deformation mode of the soil. Figure 7 displays the simulation contour of total displacement of the monopile. To enhance clarity, a scale factor of 5 is applied. The deformation mode of the monopile is observed to be rotational, with the

rotation center slightly ahead of the pile rather than on the pile itself. At the same depth as the rotation center, zero lateral deflection is observed, indicating zero lateral soil resistance at that point.

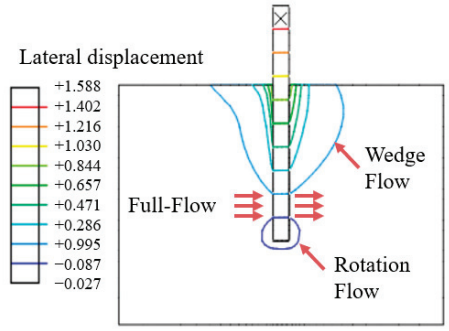

Figure 6. Simulation result of lateral displacement of the pile–clay system.

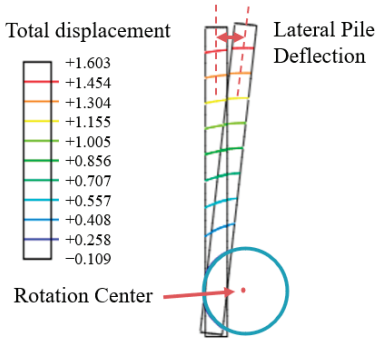

Figure 7. Simulation result of deformation mode of monopile with a scale factor of 5.

Figure 8a compares simulation results with test results of load–displacement curves under monotonic lateral load. The pile-head lateral displacement has been normalized by the pile diameter. It is evident that the relationship between lateral load and normalized displacement is nearly linear in the early stage of lateral loading. As loading continues, the soil stiffness degrades, leading to a decrease in the slope of the curves. Overall, the development of the load–displacement relationship between tests and predictions is consistent.

The bending moments along the pile shaft of the test and prediction are plotted in Figure 8b. The results under lateral loading of 1 MN, 3 MN, and 8 MN are compared. It can be seen that the bending moment increases with the growth in lateral load. The maximum bending moment occurs at a depth of 15~20 m below the mud surface, which is above the rotation center. The predicted development of the bending moment along the pile shaft is consistent with test results, except for that under 3 MN lateral loading which is underestimated. This difference may be attributed to inconsistencies in the nonlinear stress–strain relationship of the subsea soil between the test and simulation.

Figure 8c displays the lateral pile deflection along the pile shaft under lateral loads of 1 MN, 2 MN, 4 MN, 6 MN, and 9 MN. It can be seen that the lateral deflection increases with the increase in lateral load. The rotation center remains unchanged under different lateral loads. It can be inferred that the passive soil pressure occurs on the right side of the pile above the rotation center and on the left side below the rotation center. The prediction results agree with the measured results in the overall trend.

4.2. Cyclic Load Behavior

A centrifuge model test applying three episodes of lateral cyclic loading (C1, C2, and C3) was conducted by Yang et al. [35], whose load–displacement curves are shown in Figure 9a. These curves exhibit significant nonlinearity and hysteresis under cyclic loading.

As cyclic amplitude grows from C1 to C3, the nonlinear trend gradually increases. Due to the accumulated plastic strain in subsea soil under cyclic loading, the pile undergoes irreversible permanent displacement along the loading direction and the permanent displacement rises as the cyclic load level increases. To predict the behavior of the pile under lateral cyclic loading, simulation load–displacement results with the same loading conditions as those in Figure 9a are plotted in Figure 9b. It can be found that the predicted results are generally consistent with the test results. The increase in permanent displacement from C1 to C3 is reasonably reflected in the simulation. However, the predicted accumulated displacement in C1 and C2 is slightly smaller than that in the centrifuge tests. This difference may be attributed to the elastic unloading criterion used by the bounding surface model, which may have underestimated the accumulated permanent strain in subsea soil. Additionally, the predicted permanent displacement is slightly larger than that in the test, which may be due to the overestimation of the degradation of the plastic modulus of the bounding surface model compared to the experiments.

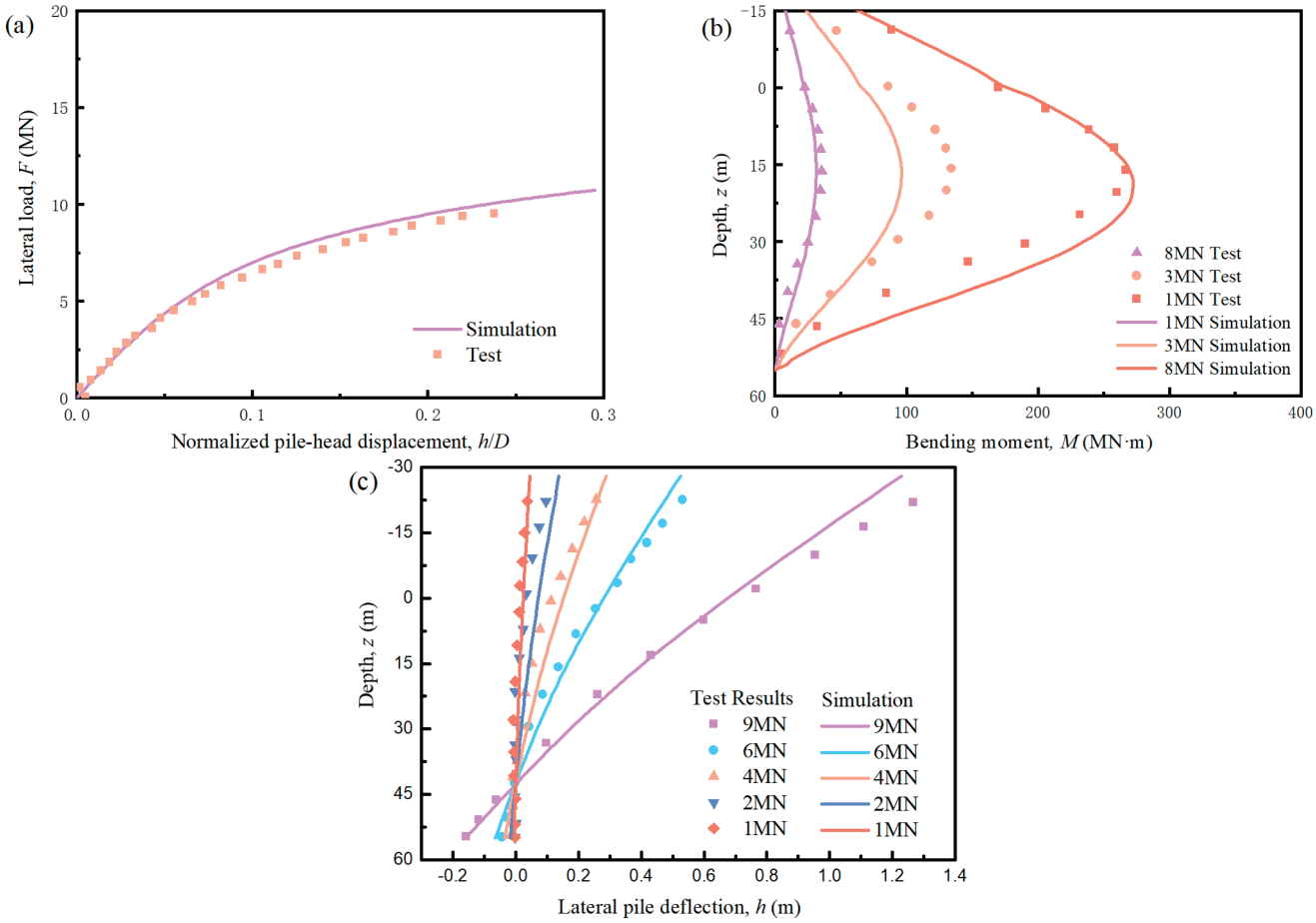

Figure 8. Comparison between simulation results and test results under monotonic lateral load: (**a**) load–displacement curve; (**b**) bending moment along pile shaft; (**c**) lateral pile deflection at different loads.

Figure 9c illustrates the comparison between the test results and prediction results of the bending moment along the pile shaft under different numbers of cycles in C1 (N = 1, 20, 50, and 90). It can be seen that the development trends of the bending moment along the pile as N increases of tests and predictions are consistent in general. The simulated results can capture the location of the maximum bending moment and the increase in it with the growth in N. However, there still are some deviations between tests and predicted results. This difference may contribute to the underestimation of accumulated displacement during C1 cyclic loading, as mentioned above.

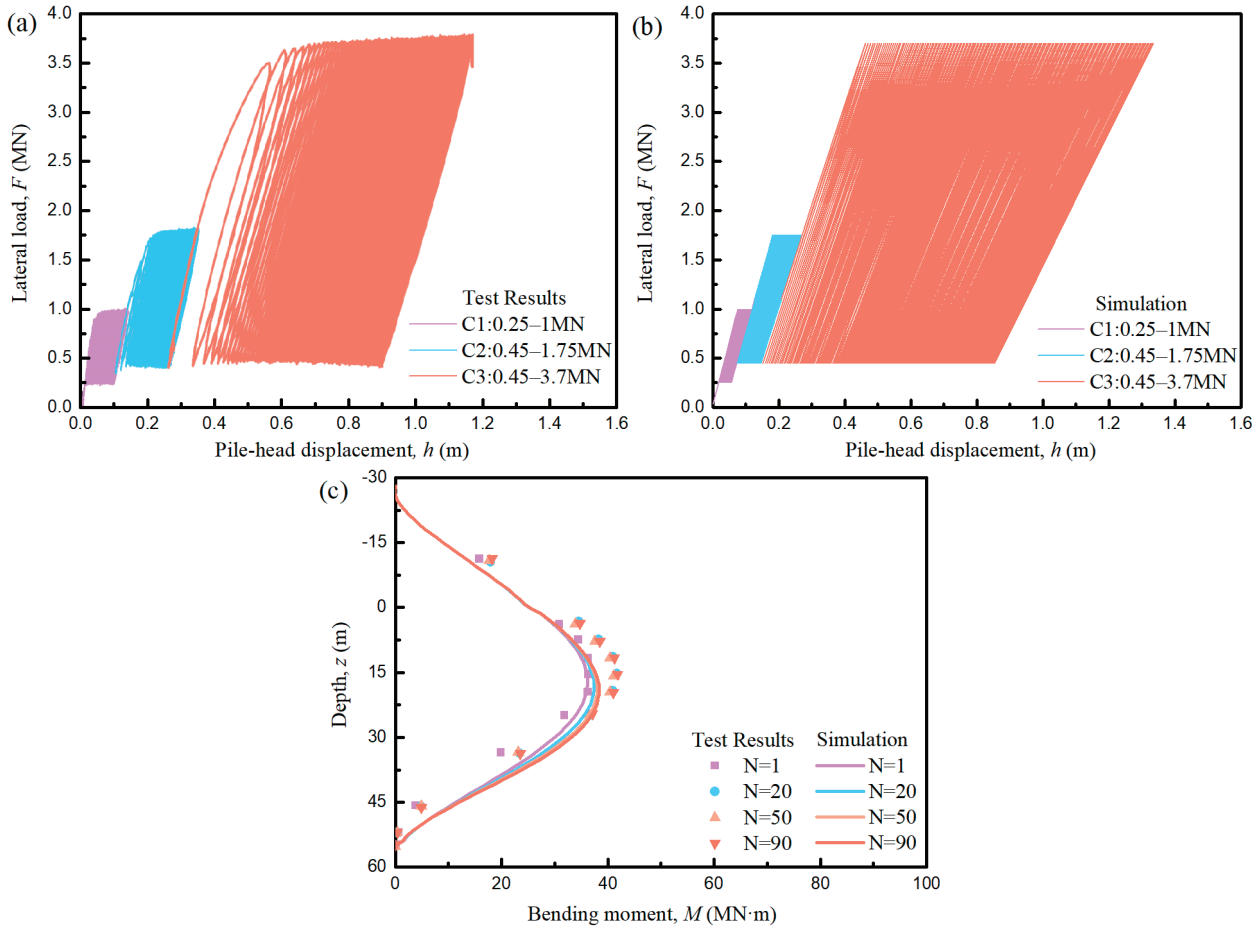

Figure 9. Comparison between predicted and test results of pile under multi-level cyclic loading: (**a**) experimental load–displacement curves of pile head; (**b**) simulated load–displacement curves of pile head; (**c**) bending moment profile along pile shaft under different N.

Because the bounding surface model applied in this paper is based on an effective stress algorithm, it can also simulate the development of pore pressure in the subsea soil. To demonstrate the evolution of pore pressure at different locations within the subsea soil, a schematic diagram depicting the node numbers for measuring excess pore pressure (u) is presented in Figure 10. In clay foundations, the effective stress is influenced by the excess pore pressure rather than the hydrostatic pressure. Therefore, development curves of u for the 10 points (A to F3) during cyclic loading of C1, C2, and C3 are provided in Figure 11 to illustrate the pattern of excess pore pressure development in the clay foundation.

Figure 11a shows the excess pore pressure development at points B, E1, and A of clay nodes located on the bottom of the pile. Due to the initial rotation of the pile causing tension at point B, the clay initially experiences a significant negative excess pore pressure, while point A initially experiences a significant positive u under compression. The direction of offset vibration of excess pore pressure from the average excess pore pressure of the previous episode for points A and B is opposite, resulting in a noticeable difference in the final accumulated average excess pore pressure (value at the centerline of cyclic vibration, abbreviated as AESOP for simplicity). Since point E1 is not subjected to a normal cyclic load but to a frictional load, its initial excess pore pressure is near zero and its cyclic pore pressure vibration amplitude is relatively small compared to that of points A and B. However, the small u of E1 does not affect its final AESOP, which is slightly larger than that of point A. Additionally, the growth rate of excess pore pressure is relatively high in the initial stages of cyclic loading and decreases with the increase in the accumulated number of cycles, N_{cyc} (the total number of cycles applied). The development of excess

pore pressure tends to be stable for point B that is on the tension side of the pile, but for points A and C, it still shows a growth trend.

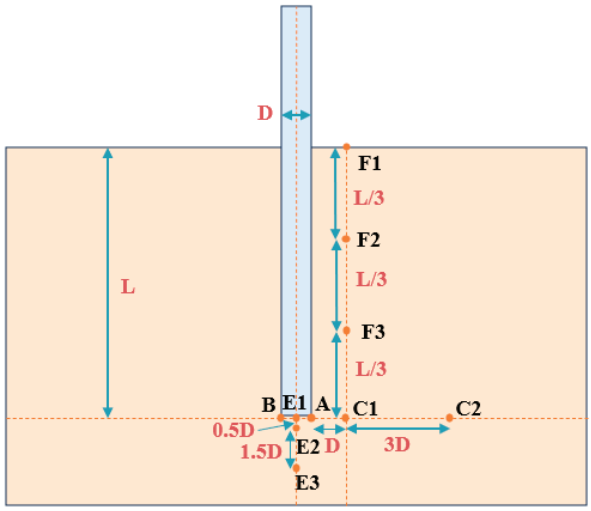

Figure 10. Schematic diagram of node numbers for measuring excess pore pressure.

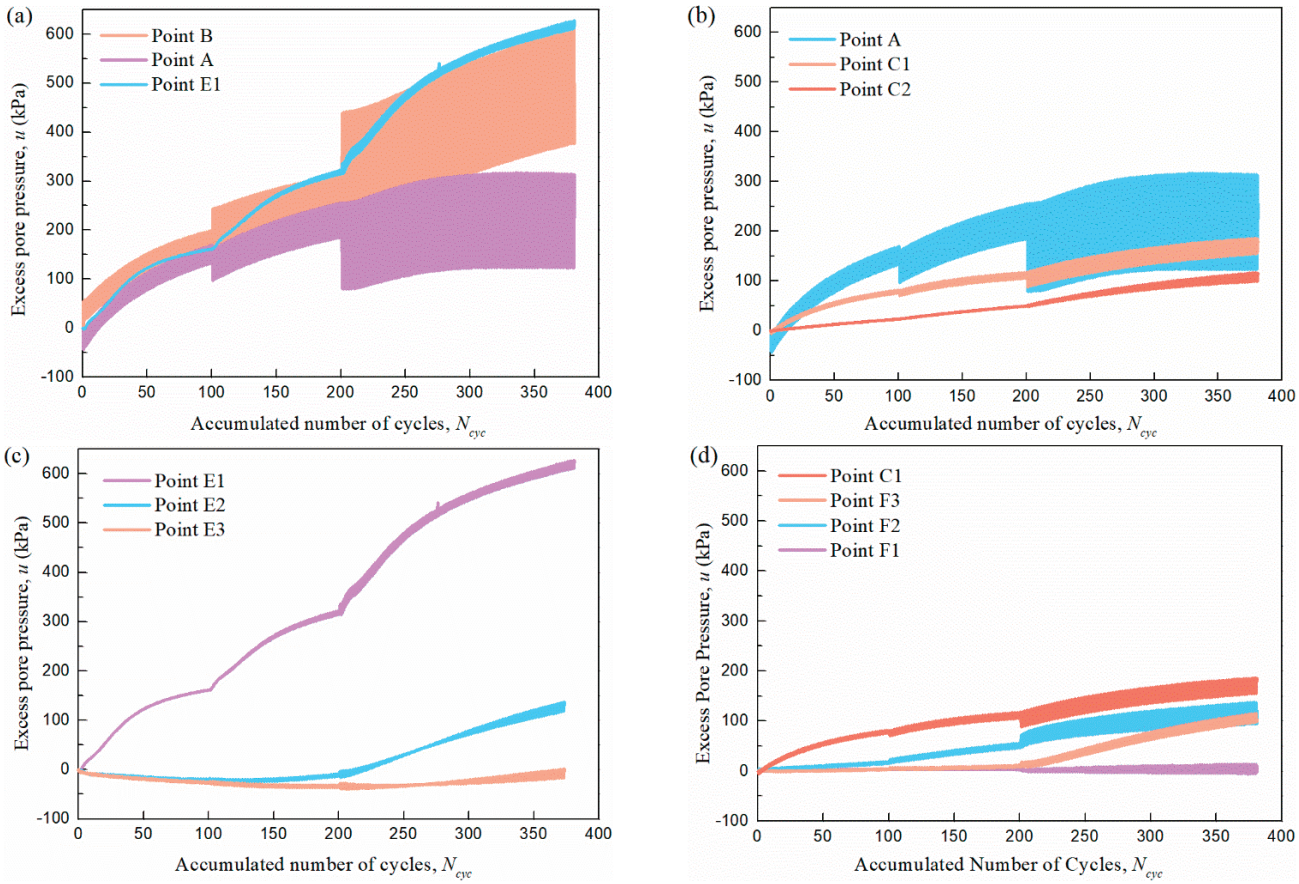

Figure 11. The development of excess pore pressure with accumulated number of cycles at different positions. (**a**) point A, B and E1; (**b**) point A, C1 and C2; (**c**) point E1, E2 and E3; (**d**) point C1, F1, F2 and F3.

Figure 11b displays the excess pore pressure development of points A, C1, and C2 located on the horizontal plane of the pile bottom. It can be found that the initial negative excess pore pressure decreases as the distance from the pile increases. The shorter the

distance from the pile, the greater the amplitude of cyclic vibration of excess pore pressure, resulting in a greater final AESOP.

Figure 11c illustrates the pore pressure development at points E1, E2, and E3 located below the pile bottom on the centerline of the pile. The developments of excess pore pressure of E1, E2, and E3 are significantly different. The excess pore pressure at E1, attached to the bottom of the pile, increases with the number of cycles. However, at points E2 and E3 located 0.5D and 2D away from the bottom of the pile, respectively, the negative excess pore pressure first increases and then gradually decreases until it becomes positive (as seen in E2). The cyclic amplitudes of excess pore pressure at points E1, E2, and E3 are similar and relatively small, as they are not subjected to normal cyclic load.

Figure 11d demonstrates the pore pressure development of points F1, F2, E3, and D1 at a distance of 1D from pile. The maximum excess pore pressure is at point D1 and the minimum is at point F1. However, the accumulation of excess pore pressure of F3 is smaller than that of F2, which has a smaller depth. This is mainly because point F3 is near the rotation center, resulting in little development of pore pressure in loading C1 and C2. With the application of C3, the plastic strain in subsea soil gradually accumulates, resulting in a rapid development of pore pressure at F3.

5. Predicted Response of Pile–Clay System Subjected to Various Lateral Cyclic Loadings

The lateral cyclic load on the pile can be divided into two parts: the mean value of cyclic load (F_a) and the cyclic amplitude of the load (F_{cyc}), as illustrated in Figure 12. This section simulates the response of the pile–clay system to various combinations of F_a and F_{cyc}. The 3D finite element model used previously is still utilized to assess the impact of different cyclic loading patterns on the responses of large-diameter monopiles and the development of pore pressure in the subsea clay.

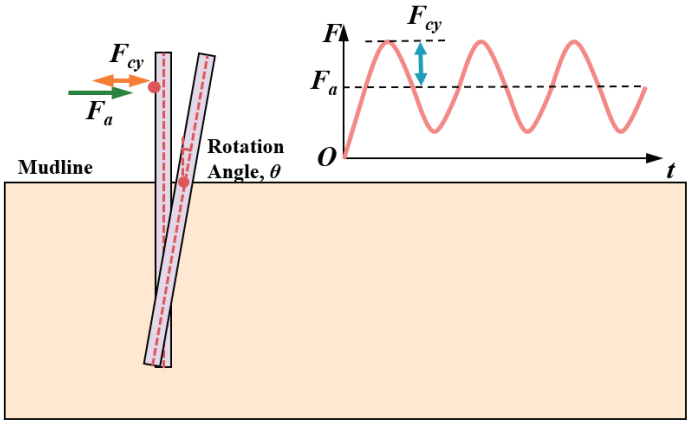

Figure 12. Illustration of lateral cyclic load and rotation angle at the mud surface.

A sinusoidal cyclic load with constant amplitude and frequency, representing wave loading, is applied in this study. This approach, consistent with previous research, facilitates a clear interpretation of the effective stress-based numerical method and the cyclic response of the monopile–clay system under regular wave action. The maximum number of cyclic loads considered in this section is limited to 100, based on two primary considerations. First, the study focuses on the cyclic response of the monopile–clay system under short-term extreme loading conditions, aiming to capture its early-to-intermediate behavior. Second, simulating a larger number of cycles would significantly impact computational efficiency; therefore, 100 cycles were selected as a practical and effective limit.

When the rotation of monopiles at the mudline reaches 0.25 degrees, it is considered that the OWTs have reached their serviceability limit state (SLS) [11]. At this point, the lateral monotonic load on the pile is denoted as F_{sls}. In order to investigate the response of large-diameter monopiles and the development of pore pressure in the subsea soil under different kinds of cyclic loading, the cyclic lateral loads are normalized by F_{sls} to clarify

the difference in the response of the pile under monotonic and cyclic loads. Here, in the prototype of the monotonic loading centrifuge test, F_{sls} is 3.06 MN when the rotation angle reaches 0.25 degrees.

Figure 13 illustrates various patterns of lateral cyclic loading. Figure 13a presents specific loading conditions under different F_a values but with the same F_{cyc}. In this study, F_a/F_{sls} = 0, F_a/F_{sls} = 0.3, and F_a/F_{sls} = 0.6 are applied. Figure 13b demonstrates specific loading conditions under different F_{cyc} values but with the same F_a. The values of F_{cyc}/F_{sls} employed are 0.3, 0.6, and 0.9. The number of cyclic loading cycles for each loading condition is consistently set to 100.

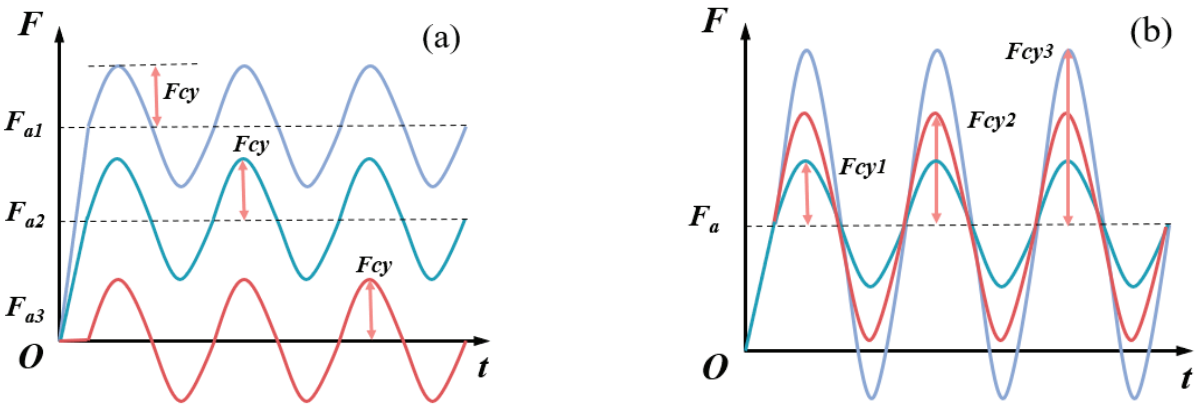

Figure 13. Different patterns of lateral cyclic load: (**a**) different F_a and same F_{cy}; (**b**) same F_a and different F_{cy}.

5.1. Different Cyclic Amplitudes with F_a = 0

From Figures 14–16, the response of the pile–clay system under F_a/F_{sls} = 0 and F_{cyc}/F_{sls} = 0.3, 0.6, and 0.9 is presented. Under these conditions, the monopile is subjected to typical two-way cyclic loading. Figure 14a illustrates that the pile undergoes lateral cyclic loading with equal positive and negative amplitudes, and the mud surface point shows the same rotation amplitude in both clockwise and counterclockwise directions. The rotation amplitude increases with the increase in F_{cyc}. The rotation–cycle curves are shown in Figure 14b, where the centerlines of the cyclic rotation curves, representing the average trend of a large amount of cyclic rotation data points, are plotted. It is evident that the centerlines of rotation curves under different F_{cyc} overlap and consistently register zero due to the two-way cyclic load with F_a = 0. However, the cyclic rotation amplitude is larger with the increase in the number of cycles and its growth rate increases with higher F_{cyc}, reflecting the degradation of stiffness of subsea soil under cyclic loading. Additionally, within the 100 cycles of loading, the maximum rotation angle remains below 0.25 degrees, meeting the serviceability limit state requirements.

Figure 15 shows the development of excess pore pressure at points A and B with different numbers of cycles under F_a = 0 and different F_{cyc}. It is evident that the centerline of cyclic excess pore pressure and its peak value for A and B are generally consistent under two-way cyclic loading, as shown in Figure 15a–c. However, the minimum cyclic pore pressure of A is slightly lower than that of B, possibly because the initial loading results in a significant negative initial pore pressure at A and it will continue to exist throughout the subsequent process. The comparison of excess pore pressure at B under different F_{cyc} is presented in Figure 15d. It demonstrates that the amplitude, peak value, and minimum value of cyclic excess pore pressure are larger with a higher F_{cyc}. The development trend of the centerline of cyclic pore pressure indicates the growth rate in excess pore pressure is higher in the initial loading stage and decreases to a lower rate as the loading progresses.

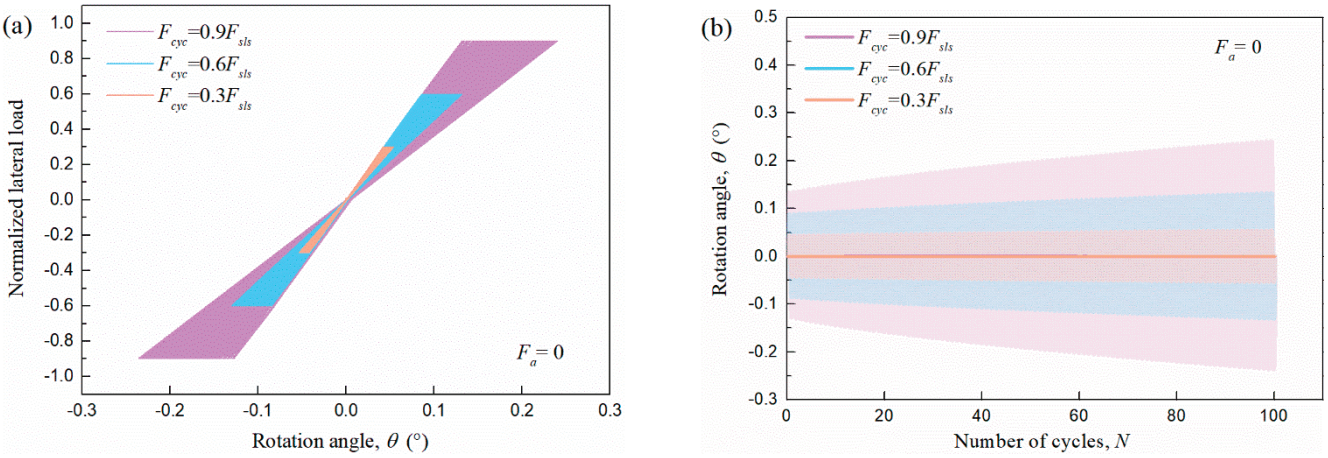

Figure 14. Load–rotation and rotation–cycle curves at the mudline under F_a = 0 and different F_{cyc}. (**a**) F/F_{sls} versus θ; (**b**) θ versus N_{cyc}.

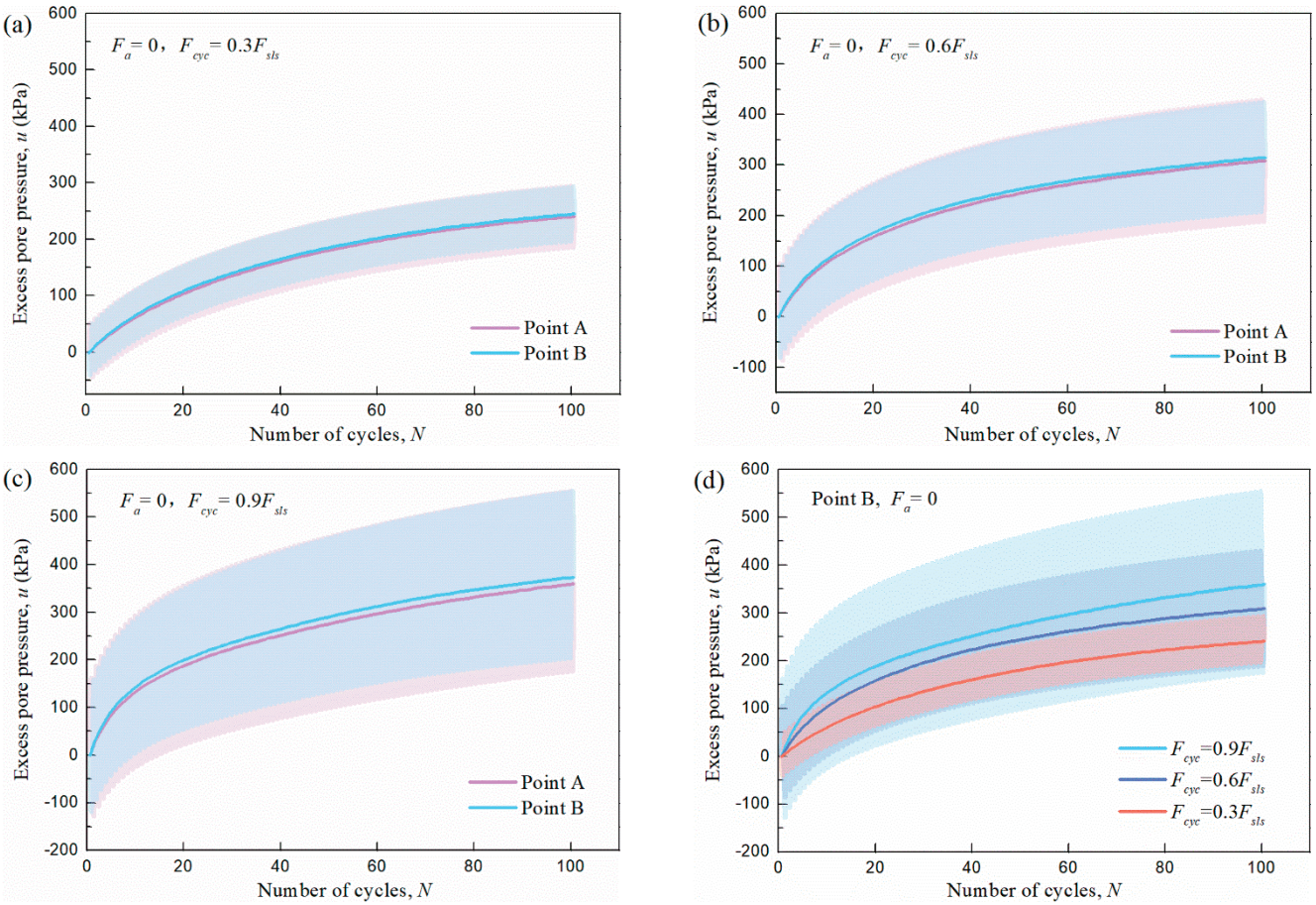

Figure 15. The development of excess pore pressure at points A and B under F_a = 0 and different F_{cyc}. (**a**) F_{cyc} = 0.3F_{sls}; (**b**) F_{cyc} = 0.6F_{sls}; (**c**) F_{cyc} = 0.9F_{sls}; (**d**) u under different F_{cyc} at point B.

The accumulated excess pore pressure (AESOP) after cyclic loading with F_a = 0 and different F_{cyc} is shown in Figure 16. It is evident that the accumulated excess pore pressure increases with higher F_{cyc} values. The distribution of AESOP is symmetric due to the two-way cyclic loading. The maximum of AESOP is located at the level of the pile bottom plane, which is consistent with the experimental result found by Español-Espinel et al. [38] on a sand foundation and the simulation results found by Ding et al. [27]. The soil area around the pile end below the rotation center is where the pore pressure grows rapidly,

while its development near the rotation center is restricted. The pore pressure in the area between the mudline and rotation center on the sides of the pile also develops rapidly.

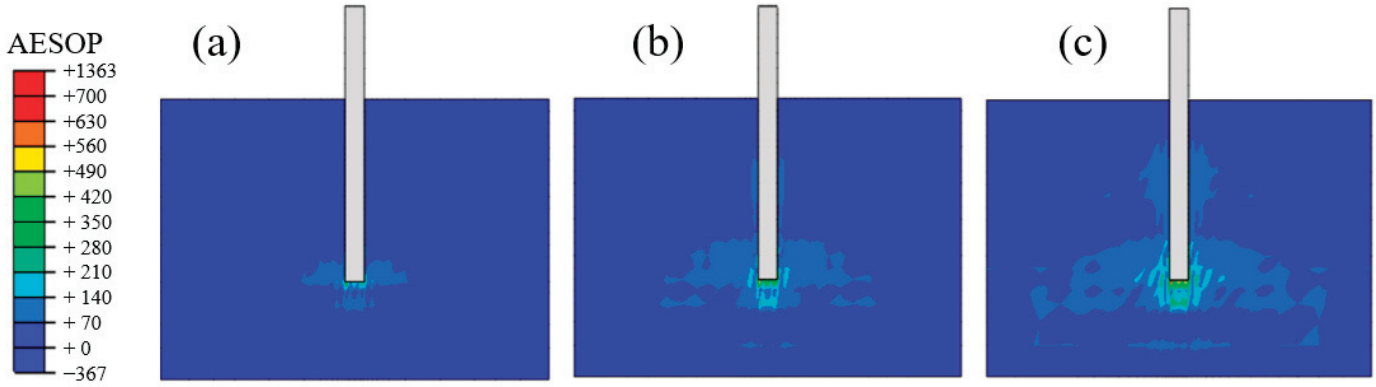

Figure 16. Distribution of accumulated excess pore pressure (AESOP) after cyclic loading with $F_a = 0$ and different F_{cyc}: (**a**) $F_{cyc} = 0.3F_{sls}$; (**b**) $F_{cyc} = 0.6F_{sls}$; (**c**) $F_{cyc} = 0.9F_{sls}$.

5.2. Different Cyclic Amplitudes with $F_a = 0.3F_{sls}$

Figure 17a illustrates the load–rotation behavior at the mudline for $F_a = 0.3F_{sls}$ and varying F_{cyc} value. Due to the asymmetric nature of these cyclic loading conditions, the rotation angle accumulates during continuous cyclic loading, in contrast to the behavior observed in Figure 14a. The accumulation of rotation angle increases with a higher number of cycles, and noticeable cyclic stiffness degradation occurs. The rotation–cycle curves under $F_a = 0.3F_{sls}$ and various F_{cyc} values are depicted in Figure 17b. The average cyclic rotation angle increases with the number of cycles, and the final accumulated average rotation angle increases with the number of cycles as well, due to the plastic strain development in subsea soil. This contrasts from the two-way cyclic behaviors depicted in Figure 14b. The cyclic rotation amplitude increases with higher F_{cyc}. It is observed that the peak cyclic rotation angle of curves under $F_{cyc} = 0.9F_{sls}$ exceeds 0.25 degrees after 12 cycles and its average cyclic rotation angle after 56 cycles exceeds this threshold. Although the peak lateral load $F_a + F_{cyc} = 1.2F_{sls} > F_{sls}$, exceeding the serviceability limit state still requires a certain number of cycles. This highlights the distinct response under dynamic load compared to that under static loading. Additionally, within the total 100 cycles of loading, the average rotation angle remains below the serviceability limit state for curves of $F_{cyc} = 0.3F_{sls}$ and $F_{cyc} = 0.6F_{sls}$. The peak cyclic rotation angle of curves under $F_{cyc} = 0.6F_{sls}$ exceeds 0.25 degrees after 38 cycles, where the peak lateral load $F_a + F_{cyc} = 0.9F_{sls} < F_{sls}$.

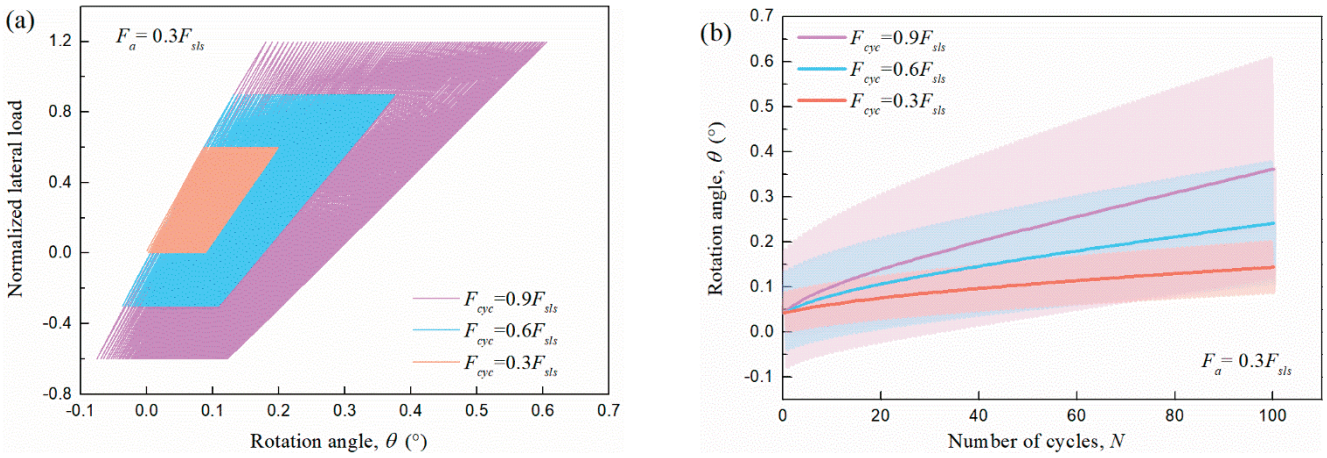

Figure 17. Load–rotation and rotation–cycle curves at the mudline under $F_a = 0.3F_{sls}$ and different F_{cyc}. (**a**) F/F_{sls} versus θ; (**b**) θ versus N_{cyc}.

Figure 18 shows the development of excess pore pressure at points A and B under $F_a = 0.3F_{sls}$ and different F_{cyc}. Due to applying the average lateral load of $F_a = 0.3F_{sls}$, the initial negative excess pore pressure for point A and positive excess pore pressure for point B are evident, as shown in Figure 18a–c. However, the developments of excess pore pressure during continuous cyclic loading are generally consistent for A and B under the same amplitude of cyclic loading. The trend of the curves in Figure 18 is similar to that in Figure 15d, but the accumulated pore pressure of clay under $F_a = 0.3F_{sls}$ is higher than that under $F_a = 0$ and the same F_{cyc}.

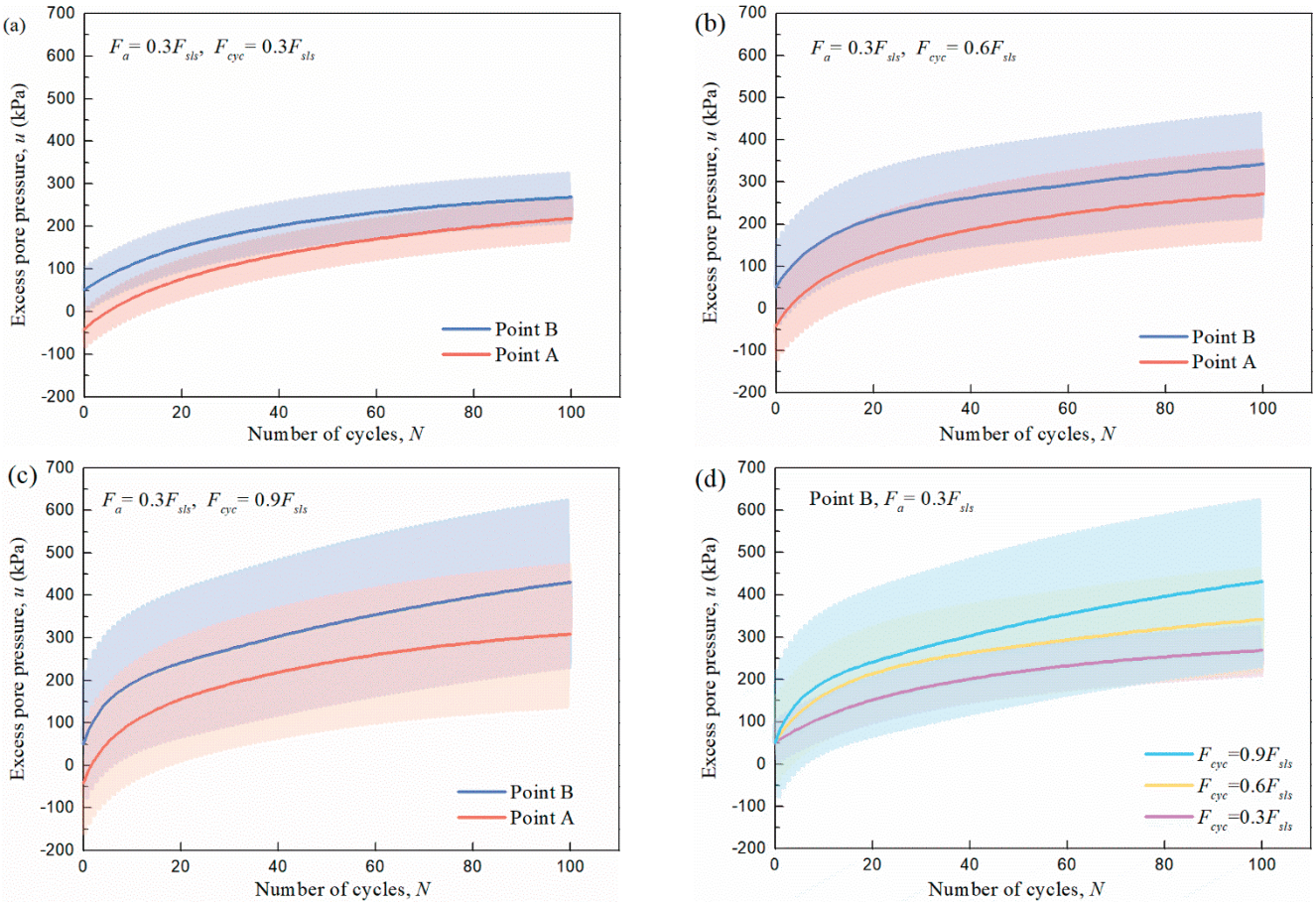

Figure 18. The development of excess pore pressure at points A and B under $F_a = 0.3F_{sls}$ and different F_{cyc}. (**a**) $F_{cyc} = 0.3F_{sls}$; (**b**) $F_{cyc} = 0.6F_{sls}$; (**c**) $F_{cyc} = 0.9F_{sls}$; (**d**) u under different F_{cyc} at point B.

Figure 19 shows the distribution of AESOP after cyclic loading under $F_a = 0.3F_{sls}$ and various F_{cyc} values. The distribution of accumulated excess pore pressure in Figure 19 resembles that in Figure 16. However, the pore pressure in subsea soil is asymmetric. It is evident that the AESOP on the right side of the pile is greater than that on the left side above the rotation angle. Conversely, the opposite is observed below the rotation point. This phenomenon arises from the presence of an average lateral cyclic load, resulting in greater compression on the right side of the pile above the rotation angle and on the left side of the pile below the rotation angle.

5.3. Different Cyclic Amplitudes with $F_a = 0.6F_{sls}$

Figure 20 illustrates the load–rotation and rotation–cycle curves at the mudline under $F_a = 0.6F_{sls}$ and different F_{cyc}. The development trend of the rotation angle is similar to that under $F_a = 0.3F_{sls}$ shown in Figure 17, but with a larger accumulated rotation angle and a higher increase rate of rotation angle as the cycles progress. Moreover, within the

total 100 cycles of loading, both the average and peak rotation angle of all curves with $F_{cyc} = 0.6F_{sls}$ exceed the serviceability limit state.

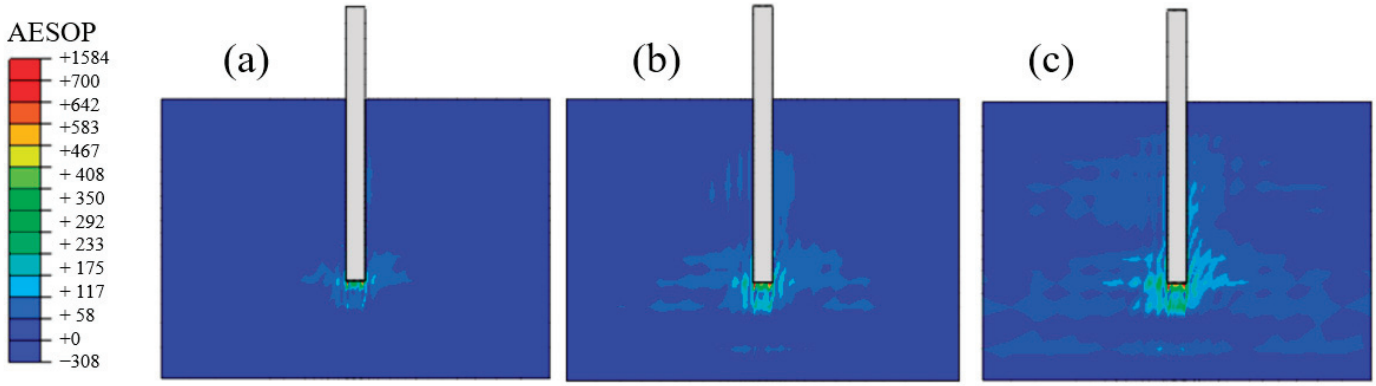

Figure 19. Distribution of accumulated excess pore pressure (AESOP) after cyclic loading with $F_a = 0.3F_{sls}$ and different F_{cyc}: (**a**) $F_{cyc} = 0.3F_{sls}$; (**b**) $F_{cyc} = 0.6F_{sls}$; (**c**) $F_{cyc} = 0.9F_{sls}$.

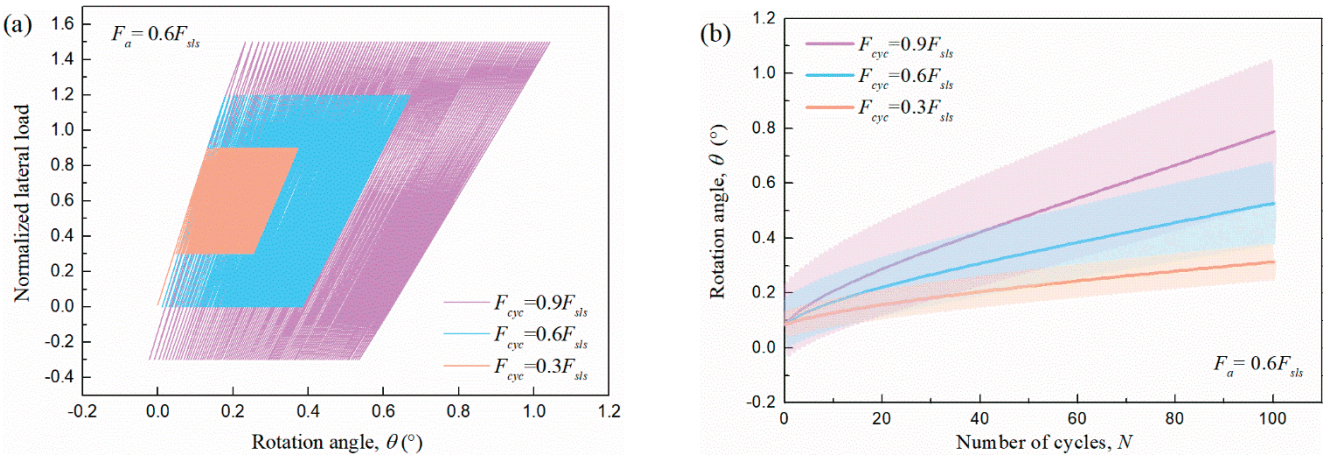

Figure 20. Load–rotation and rotation–cycle curves at the mudline under $F_a = 0.6F_{sls}$ and different F_{cyc}: (**a**) F/F_{sls} versus θ; (**b**) θ versus N_{cyc}.

Figure 21 shows the development of excess pore pressure at points A and B under $F_a = 0.6F_{sls}$ and different F_{cyc}. The trend of excess pore pressure development at points A and B is similar to that in Figure 18, except for a higher initial negative or positive pore pressure and a higher accumulated excess pore pressure at the same number of cycles.

Figure 22 illustrates the distribution AESOP after cyclic loading under $F_a = 0.6F_{sls}$ and various F_{cyc} values. The distribution of AESOP in Figure 22 resembles that in Figure 19 but is more asymmetrical due to the larger average lateral cyclic load. Additionally, the value of AESOP after 100 cycles is larger than that in Figure 19 due to the larger peak cyclic load.

5.4. Different Average Cyclic Loads

For comparisons of the response of the pile–clay system under the same cyclic amplitude but different average lateral loads, the load–rotation, rotation–cycle, and pore pressure development curves are plotted in Figures 23–25.

Figure 23 illustrates the load–rotation curves at the mudline with the same F_{cyc} but various F_a in each graph. It can be seen that with the increase in average lateral load, the accumulated rotation angles increase as the cycles progress, even if with the same cyclic amplitude. With the increase in cyclic amplitude, the relationships between curves with $F_a = 0$, $0.3F_{sls}$, and $0.6F_{sls}$ resemble each other, but with a higher accumulation rotation angle.

Figure 24 illustrates the rotation–cycle curves at the mudline with the same F_{cyc} but different F_a in each graph. The amplitudes of cyclic rotation angle for $F_a = 0$, $0.3F_{sls}$, and

$0.6F_{sls}$ are consistent with each other, regardless of the amplitude of cyclic load. The initial rotation value increases with the mean value of cyclic load. Moreover, the accumulated value and the rate of increase in rotation angle increase with a higher mean value of cyclic load.

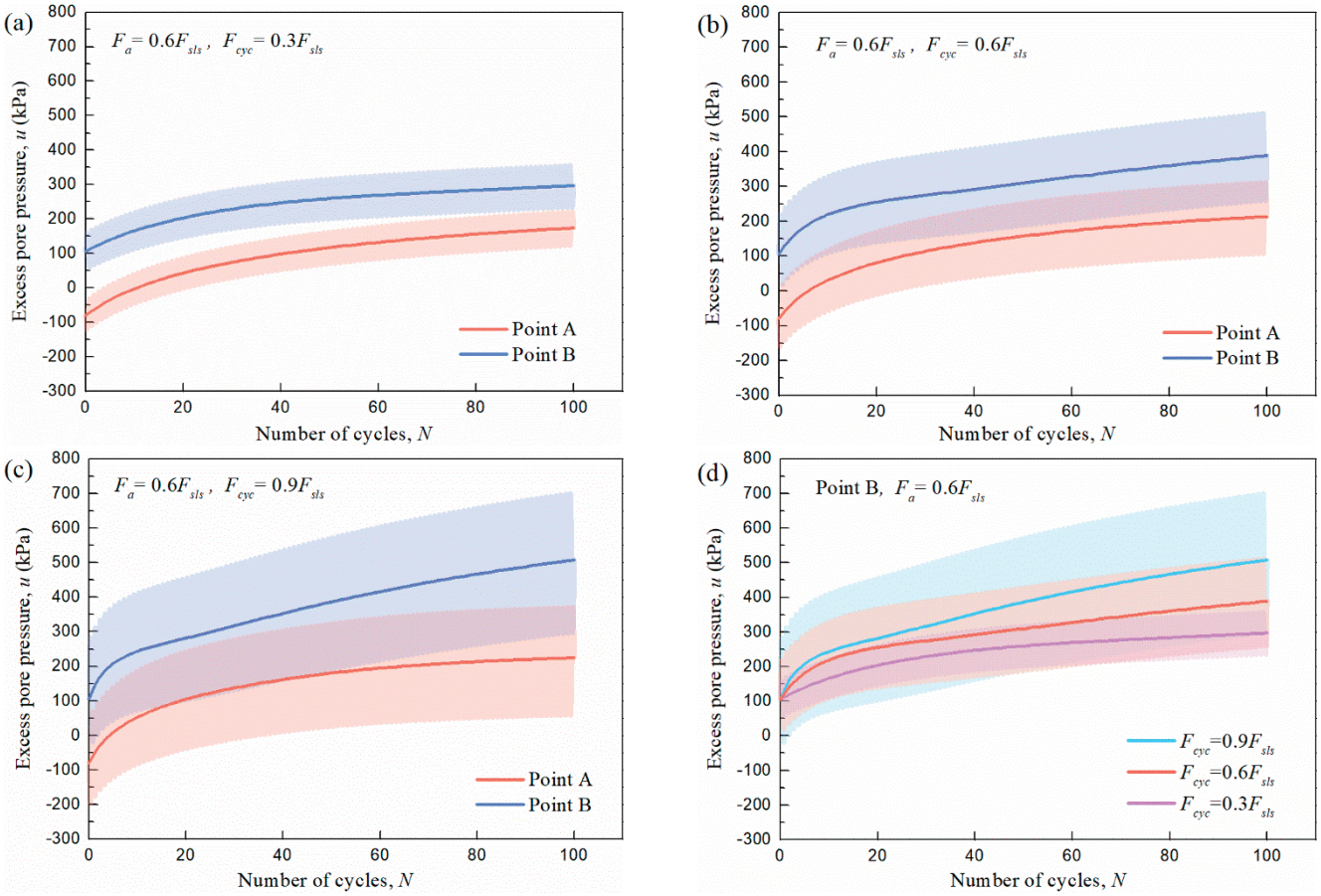

Figure 21. The development of excess pore pressure at points A and B under $F_a = 0.6F_{sls}$ and different F_{cyc}: (**a**) $F_{cyc} = 0.3F_{sls}$; (**b**) $F_{cyc} = 0.6F_{sls}$; (**c**) $F_{cyc} = 0.9F_{sls}$; (**d**) u under different F_{cyc} at point B.

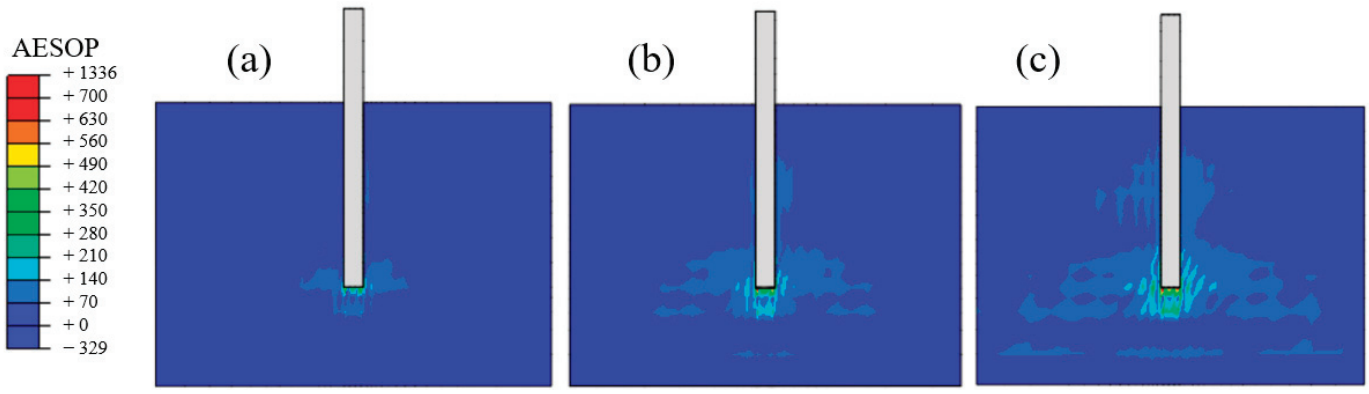

Figure 22. Distribution of accumulated excess pore pressure (AESOP) after cyclic loading with $F_a = 0.6F_{sls}$ and different F_{cyc}: (**a**) $F_{cyc} = 0.3F_{sls}$; (**b**) $F_{cyc} = 0.6F_{sls}$; (**c**) $F_{cyc} = 0.9F_{sls}$.

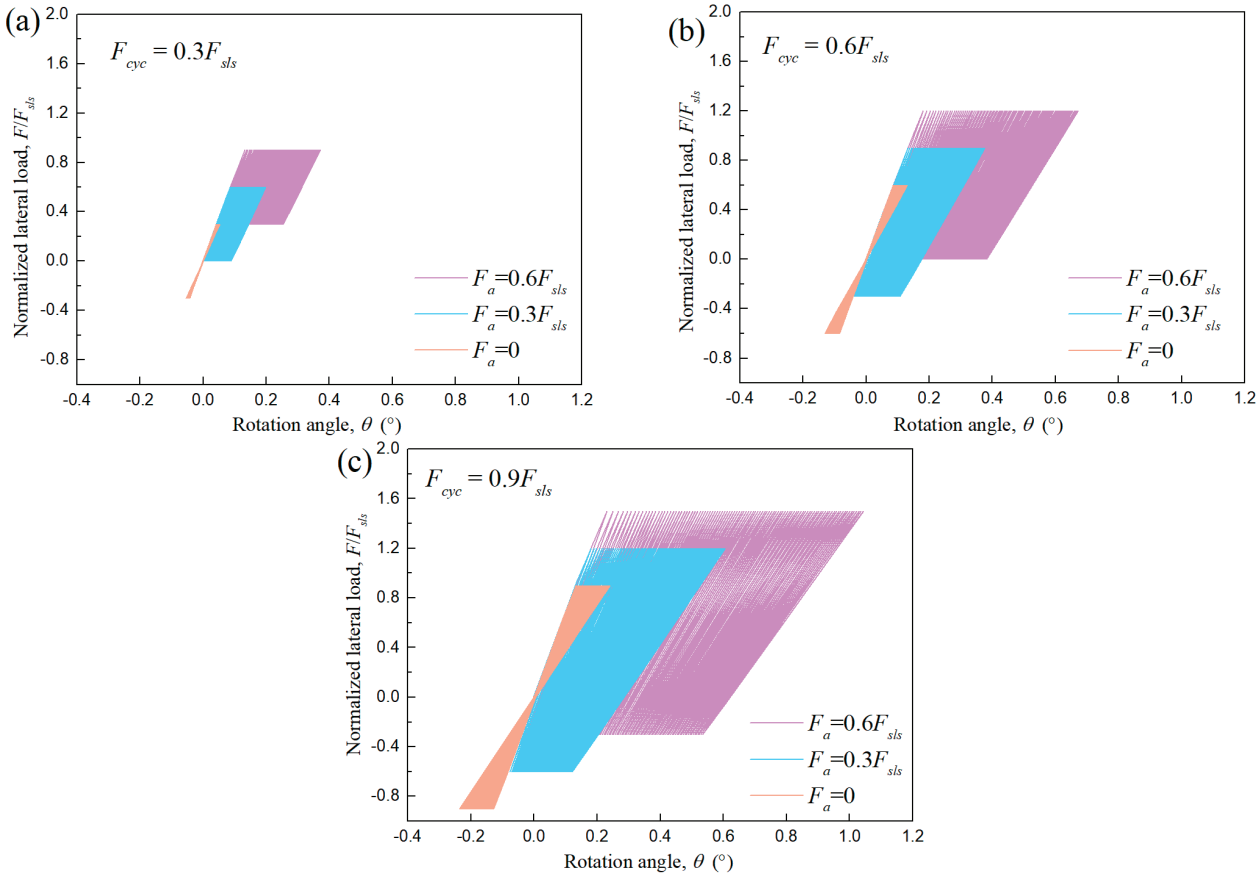

Figure 23. Load–rotation curves at the mudline under different F_a and F_{cyc}: (**a**) F_{cyc} = 0.3F_{sls}; (**b**) F_{cyc} = 0.6F_{sls}; (**c**) F_{cyc} = 0.9F_{sls}.

Figure 25 shows the development of pore pressure at point B for different values of F_a, while keeping F_{cyc} constant. It can be found that the cyclic amplitude and development trend of pore pressure for constant F_{cyc} but varying F_a are consistent with each other. However, different initial pore pressure values for varying F_a cause the curves to diverge. This demonstrates that the mean value of cyclic load primarily affects the initial pore pressure in subsea soil but has less impact on the cyclic amplitude and development trend of pore pressure.

Additionally, for a small cyclic amplitude of F_{cyc} = 0.3F_{sls}, the large initial increase rate of pore pressure gradually decreases to reach a plateau state as the cycles progress. However, with a larger F_{cyc}, the growth rate of pore pressure increases continuously with the cycles and stays relatively high during the final stage of loading.

5.5. Discussion

Based on the calculation results, the effects of cyclic loading on the behavior of the monopile–clay system are summarized. The combined effects of F_a and F_{cyc} on the rotation angle, θ, accumulated excess pore pressure, u, amplitude of θ, and amplitude of u after 100 cycles of cyclic loading are illustrated in Figure 26. It is evident that cyclic loading significantly influences the accumulation of permanent plastic strain and pore pressure in the subsoil, leading to the development of the absolute values of θ, u, and their respective amplitudes. However, there is a special case with F_a = 0 that has no increment in accumulation of θ, which is also consistent with previous studies. Under two-way symmetric cyclic loading, the accumulation of displacement in the clay foundation is negligible or zero. Different mean values of cyclic load F_a have a significant impact on the accumulation of θ, u but only a minimal effect on their amplitudes.

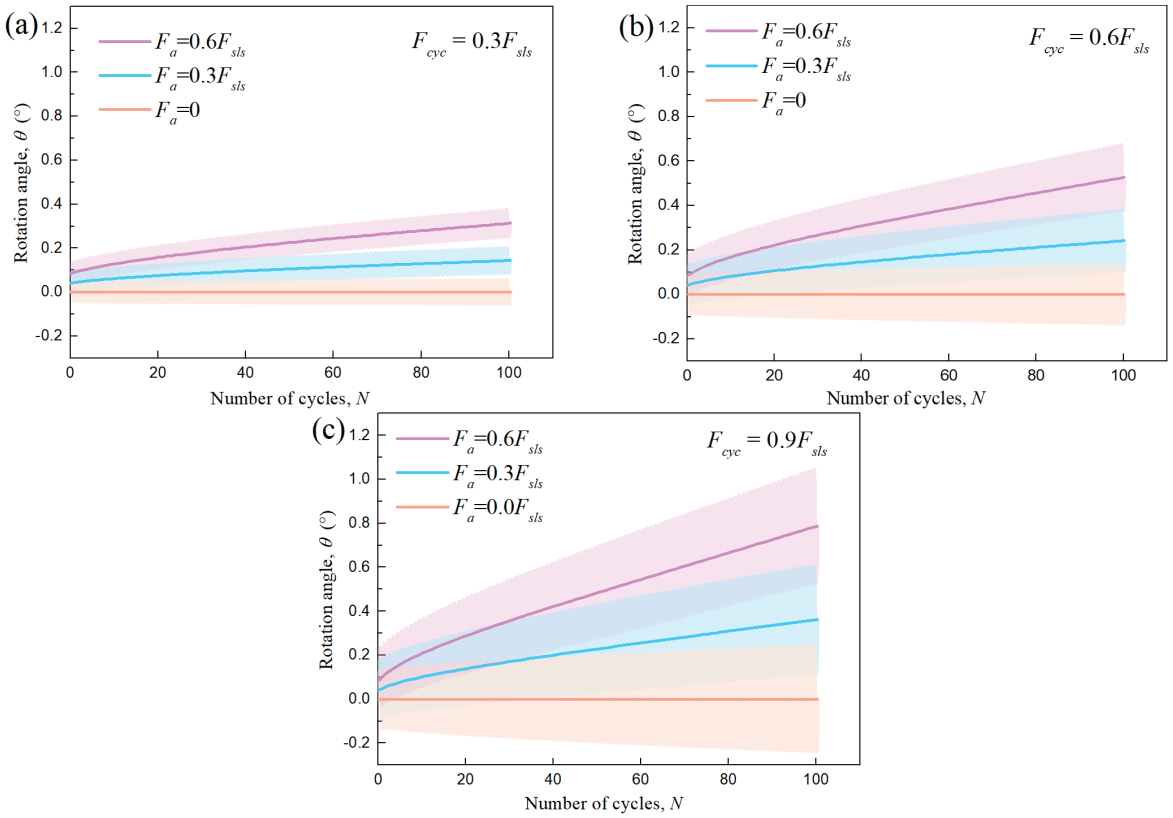

Figure 24. Rotation–cycle curves at mudline under different F_a and F_{cyc}: (**a**) $F_{cyc} = 0.3F_{sls}$; (**b**) $F_{cyc} = 0.6F_{sls}$; (**c**) $F_{cyc} = 0.9F_{sls}$.

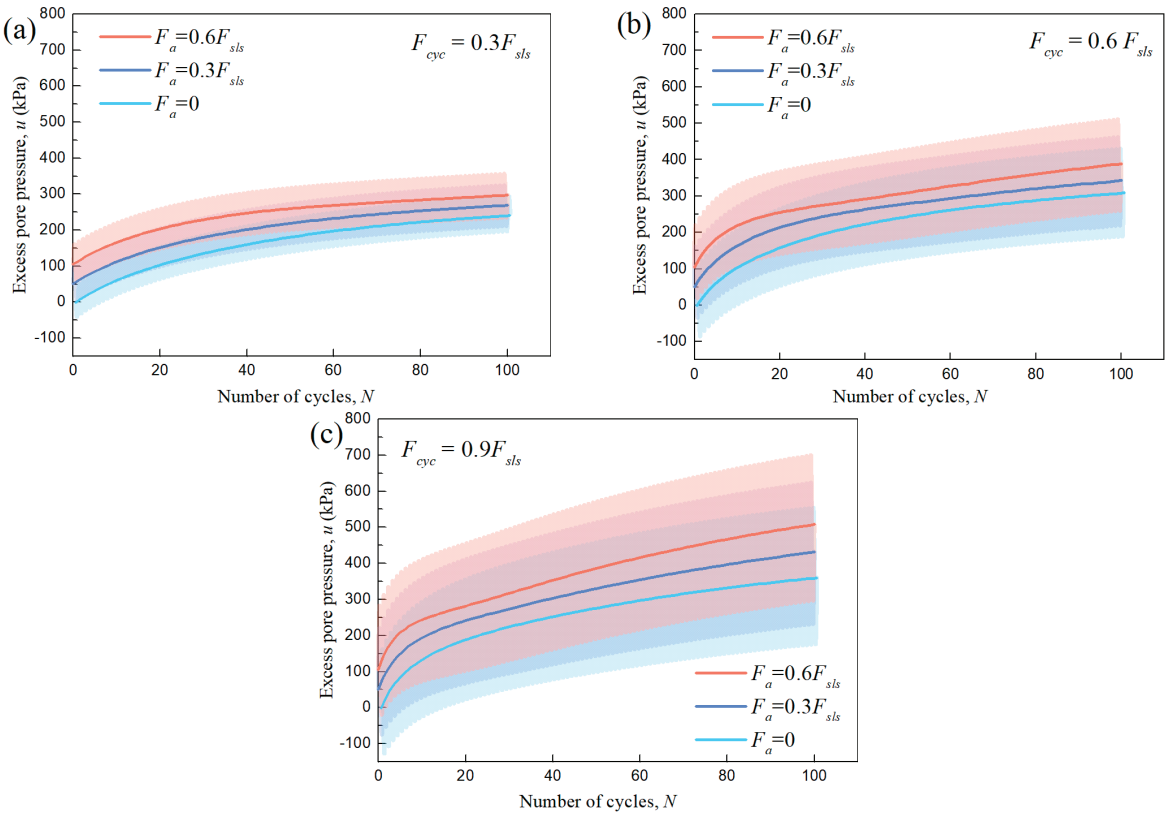

Figure 25. The development of u at point B under different F_a and F_{cyc}: (**a**) $F_{cyc} = 0.3F_{sls}$; (**b**) $F_{cyc} = 0.6F_{sls}$; (**c**) $F_{cyc} = 0.9F_{sls}$.

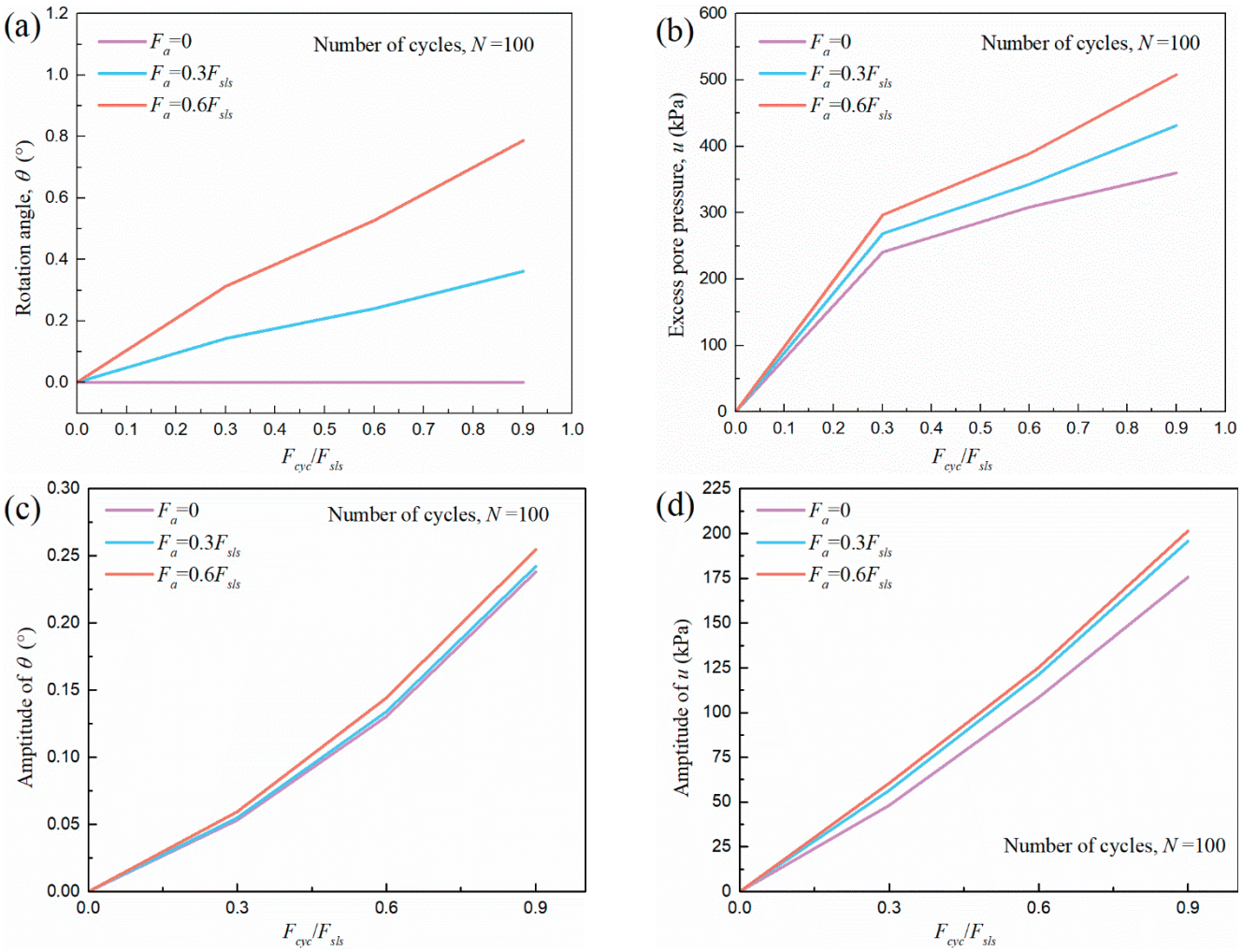

Figure 26. The response of monopile–clay system after 100 cycles of cyclic loading under various cyclic loading conditions: (**a**) accumulated rotation angle; (**b**) accumulated pore pressure; (**c**) rotation angle amplitude; (**d**) pore pressure amplitude.

The prediction results can be compared with the study by Xinglei Cheng et al. [11], which used a simplified constitutive model implemented in ABAQUS to predict the response of a monopile–clay system under various cyclic loading conditions. The results show that the predicted trends for lateral displacement and bending moment under two-way and one-way cyclic loading are consistent with those predicted by the model in this paper. However, the study in [11], which employs a total stress-based numerical method, does not predict the development of pore pressure in the soil foundation. This highlights the effectiveness of the effective stress-based numerical method proposed in this paper.

It should be noted that while the proposed model effectively captures the overall behavior of marine clay under cyclic loading, it has certain limitations, particularly in accounting for the unloading plastic behavior, which is a critical aspect of the marine clay response under cyclic loading. The elastic unloading assumption for the model is inconsistent with the previous research and the movable mapping center should be incorporated in the effective stress model for more accurate prediction results of the cyclic response of a monopile–clay system.

Additionally, this study lacks direct comparisons with field observations, which are essential for validating the model under real-world conditions. The primary limitation is the absence of field data that matches the specific cyclic loading conditions, soil properties, and boundary conditions considered in this study. While laboratory data were used

for validation, field validation is crucial for assessing the model's accuracy in practical applications. Future work should focus on validating the effective stress-based method with field data from monopile–clay systems to enhance its applicability and reliability for real-world scenarios.

6. Conclusions

This paper presents a numerical analysis based on effective stress to study the response of large-diameter monopiles under various lateral cyclic loading conditions. The following conclusions can be drawn from this study.

(1) The effective stress-based finite element method is proposed for predicting the response of monopile–clay foundation systems under lateral cyclic loading. This method is founded on a modified bounding surface model capable of predicting changes in the effective stress of clay elements under monotonic or cyclic loading conditions. The model has been successfully incorporated into the ABAQUS software using the UMAT subroutine. The calibration of model parameters is discussed, and the finite element method is validated by comparing results of pile–clay centrifuge tests with corresponding simulations. This method not only accurately predicts the nonlinear load–displacement relationship and bending moment of piles under lateral cyclic loading but also forecasts the growth of cyclic excess pore water pressure in the soil.

(2) Simulation results for load–rotation and rotation–cycles under various combinations of F_a and F_{cyc} indicate that the cyclic rotation amplitude increases with the number of cycles and its growth rate increases with a higher amplitude of cyclic load. This trend reflects the degradation of stiffness of subsea soil under cyclic loading. This degradation can be found under two-way or one-way cyclic loadings, irrespective of the level of F_a and F_{cyc}.

(3) Exceeding the serviceability limit state is the result of the combined effect of mean cyclic load and the amplitude of cyclic load. The presence of cyclic load amplitude causes the permanent rotation angle to exceed the threshold after a certain number of cycles where $F_a + F_{cyc} < F_{sls}$. Moreover, an increase in the mean cyclic load also accelerates the accumulation of permanent rotation angle as the cycles progress. Conversely, the condition where $F_a + F_{cyc} > F_{sls}$ will not reach the serviceability limit state until the number of cycles to failure is reached.

(4) The maximum excess pore pressure is located at the level of the monopile bottom plane, which agrees with the previous experimental result. The soil area around the pile end below the rotation center experiences rapid pore pressure growth, while development near the rotation center is limited. Pore pressure between the mudline and rotation center on the sides of the pile develops faster than in other areas, except for the area around the pile bottom.

(5) The application of average cyclic load induces initial positive and negative pore pressure on the loaded and unloaded sides, respectively, of the bottom of the monopile. However, the accumulation of positive excess pore pressure occurs as the cycles progress.

(6) The simulation results of cyclic excess pore pressure under various combinations of F_a and F_{cyc} indicate that the mean value of cyclic load primarily affects the initial pore pressure in subsea soil but has less impact on the cyclic amplitude and development trend of pore pressure. The cyclic amplitude and development trend of pore pressure are mainly affected by the amplitude of the cyclic load. The amplitude, peak value, and average value of cyclic excess pore pressure are larger with a higher amplitude of the cyclic load.

Author Contributions: Conceptualization, Y.H.; Methodology, J.L.; Software, K.L.; Validation, J.L. and W.X.; Formal analysis, J.L. and K.L.; Investigation, L.W. and Z.L.; Resources, W.X.; Writing—original draft, J.L.; Visualization, K.L. and L.W.; Supervision, Y.H. All authors have read and agreed to the published version of the manuscript.

Funding: This work was supported by the Hainan Provincial Joint Project of Sanya Yazhou Bay Science and Technology City (Grant No. 2021JJLH0088); the Open Fund of State Key Laboratory of Hydraulic Engineering Intelligent Construction and Operation, Tianjin University (Grant No. HESS-2105); the Hainan Provincial Natural Science Foundation of China (Grant No. 522QN341).

Data Availability Statement: The original contributions presented in the study are included in the article, further inquiries can be directed to the corresponding author.

Conflicts of Interest: The authors declare no conflict of interest.

References

1. Choo, Y.; Kim, D. Experimental development of the p-y relationship for large-diameter offshore monopiles in sands: Centrifuge tests. *J. Geotech. Geoenvironmental Eng.* **2016**, *142*, 04015058. [CrossRef]
2. Amar Bouzid, D. Numerical Investigation of Large-Diameter Monopiles in Sands: Critical Review and Evaluation of Both API and Newly Proposed p-y Curves. *Int. J. Geomech.* **2018**, *18*, 04018141. [CrossRef]
3. Kim, J.; Kim, G.; Lee, J. Dynamic p-y analysis method based on cone penetration test results for monopiles in sand. *Soil Dyn. Earthq. Eng.* **2022**, *163*, 107503. [CrossRef]
4. Cheng, X.; El Naggar, M.H.; Lu, D.; Wang, P.; Tu, W. A cyclic p–y elastoplastic model applied to lateral loaded pile in soft clays. *Can. Geotech. J.* **2023**, *60*, 885–901. [CrossRef]
5. Xia, Q.; Hu, C.; Zeng, E.X.; Tang, H.Y.; Dong, J.J.; Xu, F.; Yi, J.T. An enhanced understanding of the lateral response of large-diameter monopile: Development of a new *P*-y curve. *Mar. Georesources Geotechnol.* **2024**, 1–16. [CrossRef]
6. Tsai, C.-C.; Li, Y.-P.; Lin, S.-H. p-y based approach to predicting the response of monopile embedded in soft clay under long-term cyclic loading. *Ocean Eng.* **2023**, *275*, 114144. [CrossRef]
7. Achmus, M.; Kuo, Y.-S.; Abdel-Rahman, K. Behavior of monopile foundations under cyclic lateral load. *Comput. Geotech.* **2009**, *36*, 725–735. [CrossRef]
8. Naggar, M.H.E.; Shayanfar, M.A.; Kimiaei, M.; Aghakouchak, A.A. Simplified BNWF model for nonlinear seismic response analysis of offshore piles with nonlinear input ground motion analysis. *Can. Geotech. J.* **2005**, *42*, 365–380. [CrossRef]
9. Cheng, X.; Wang, T.; Zhang, J.; Wang, P.; Tu, W.; Li, W. Dynamic response analysis of monopile offshore wind turbines to seismic and environmental loading considering the stiffness degradation of clay. *Comput. Geotech.* **2023**, *155*, 105210. [CrossRef]
10. Kaynia, A.M.; Hebig, J.; Pein, T.; Shin, Y. Numerical model for dynamic installation of large diameter monopiles. *Soil Dyn. Earthq. Eng.* **2022**, *161*, 107393. [CrossRef]
11. Cheng, X.; Wang, T.; Zhang, J.; Liu, Z.; Cheng, W. Finite element analysis of cyclic lateral responses for large diameter monopiles in clays under different loading patterns. *Comput. Geotech.* **2021**, *134*, 104104. [CrossRef]
12. Yu, J.; Zhu, J.; Shen, K.; Huang, M.; Leung, C.F.; Jorgin Tan, Q.W. Bounding-surface-based p-y model for laterally loaded piles in undrained clay. *Ocean Eng.* **2020**, *216*, 107997. [CrossRef]
13. Zhang, Y.; Andersen, K.H. Soil reaction curves for monopiles in clay. *Mar. Struct.* **2019**, *65*, 94–113. [CrossRef]
14. Huang, M.; Liu, L.; Shi, Z.; Li, S. Modeling of laterally cyclic loaded monopile foundation by anisotropic undrained clay model. *Ocean Eng.* **2021**, *228*, 108915. [CrossRef]
15. Wang, G.; Sitar, N. Static and Dynamic Axial Response of Drilled Piers. II: Numerical Simulation. *J. Geotech. Geoenvironmental Eng.* **2011**, *137*, 1143–1153. [CrossRef]
16. Wang, Y.; Lei, J.; Wang, Y.; Li, S. Post-cyclic shear behavior of reconstituted marine silty clay with different degrees of reconsolidation. *Soil Dyn. Earthq. Eng.* **2019**, *116*, 530–540. [CrossRef]
17. Wang, Y.; Lei, J.; Gong, X.; Wang, Y.; Yang, P. Post-cyclic undrained shear behavior of marine silty clay under various loading conditions. *Ocean Eng.* **2018**, *158*, 152–161. [CrossRef]
18. Yasuhara, K.; Murakami, S.; Hyde, A.F.L. Post-cyclic degradation of saturated plasticity silts. *Cycl. Behav. Soils Liq. Phenom.* **2004**, 275–286. [CrossRef]
19. Andersen, K.H.; Lauritzsen, R. Bearing capacity for foundations with cyclic loads. *J. Geotech. Eng.* **1988**, *114*, 540–555. [CrossRef]
20. Damgaard, M.; Bayat, M.; Andersen, L.V.; Ibsen, L.B. Assessment of the dynamic behaviour of saturated soil subjected to cyclic loading from offshore monopile wind turbine foundations. *Comput. Geotech.* **2014**, *61*, 116–126. [CrossRef]
21. Liao, C.; Chen, J.; Zhang, Y. Accumulation of pore water pressure in a homogeneous sandy seabed around a rocking mono-pile subjected to wave loads. *Ocean Eng.* **2019**, *173*, 810–822. [CrossRef]
22. Lin, Z.; Pokrajac, D.; Guo, Y.; Jeng, D.-s.; Tang, T.; Rey, N.; Zheng, J.; Zhang, J. Investigation of nonlinear wave-induced seabed response around mono-pile foundation. *Coast. Eng.* **2017**, *121*, 197–211. [CrossRef]
23. Patra, S.K.; Haldar, S. Seismic response of monopile supported offshore wind turbine in liquefiable soil. *Structures* **2021**, *31*, 248–265. [CrossRef]
24. Sahraeian, S.M.S.; Masoumi, M.A.; Najafgholipour, M.A.; Shafiee, A. Seismic response of monopile foundation of offshore wind turbines in liquefiable soils. *Structures* **2024**, *64*, 106591. [CrossRef]
25. Charlton, T.S.; Rouainia, M. Cyclic performance of a monopile in spatially variable clay using an advanced constitutive model. *Soil Dyn. Earthq. Eng.* **2021**, *140*, 106437. [CrossRef]

26. Duque, J.; Ochmański, M.; Mašín, D.; Hong, Y.; Wang, L. On the behavior of monopiles subjected to multiple episodes of cyclic loading and reconsolidation in cohesive soils. *Comput. Geotech.* **2021**, *134*, 104049. [CrossRef]
27. Ding, X.; Chian, S.C.; Lian, J.; Cao, G.; Shen, J.; Luan, L. Wind-wave combined effect on dynamic response of soil-monopile-OWT system considering cyclic hydro-mechanical clay behavior. *Comput. Geotech.* **2023**, *154*, 105124. [CrossRef]
28. Zhang, Q.; Zhang, Y.; Lin, H.; Feng, L. Numerical investigation on bearing capacity of OWT foundation with large diameter monopile under Seismic load. *Appl. Ocean Res.* **2021**, *108*, 102518. [CrossRef]
29. Esfeh, P.K.; Kaynia, A.M. Earthquake response of monopiles and caissons for Offshore Wind Turbines founded in liquefiable soil. *Soil Dyn. Earthq. Eng.* **2020**, *136*, 106213. [CrossRef]
30. Manzari, M.; Nour, M. On implicit integration of bounding surface plasticity models. *Comput. Struct.* **1997**, *63*, 385–395. [CrossRef]
31. Wang, Y.; Lei, J.; Wang, Y. A post-cyclic strength degradation model for saturated soft clay. *Ocean Eng.* **2019**, *186*, 106072. [CrossRef]
32. Dafalias, Y.F. Bounding surface plasticity. I: Mathematical foundation and hypoplasticity. *J. Eng. Mech.* **1986**, *112*, 966–987. [CrossRef]
33. Dafalias, Y.F.; Popov, E.P. A model of nonlinearly hardening materials for complex loading. *Acta Mech.* **1975**, *21*, 173–192. [CrossRef]
34. Lei, J.; Liu, C.; Li, F.; Sun, L. A united hardening rule considering monotonic and cyclic strength degradation of clay. *Soil Dyn. Earthq. Eng.* **2023**, *166*, 107754. [CrossRef]
35. Yang, Q.-j.; Gao, Y.-f.; Kong, D.-q.; Zhu, B. Centrifuge modelling of lateral loading behaviour of a "semi-rigid" Mono-pile in soft clay. *Mar. Georesources Geotechnol.* **2019**, *37*, 1205–1216. [CrossRef]
36. Duque, J.; Roháč, J.; Mašín, D.; Najser, J. Experimental investigation on Malaysian kaolin under monotonic and cyclic loading: Inspection of undrained Miner's rule and drained cyclic preloading. *Acta Geotech.* **2022**, *17*, 4953–4975. [CrossRef]
37. Hong, Y.; He, B.; Wang, L.; Wang, Z.; Ng, C.W.W.; Mašín, D. Cyclic lateral response and failure mechanisms of semi-rigid pile in soft clay: Centrifuge tests and numerical modelling. *Can. Geotech. J.* **2017**, *54*, 806–824. [CrossRef]
38. Español-Espinel, C.; Haigh, S.K.; Madabhushi, G.S.P.; Abadie, C.N.; Go, J.E.; Morrison, P.R.J. Evolution of excess pore water pressures around monopiles subjected to moderate seismic loading. *Soil Dyn. Earthq. Eng.* **2024**, *176*, 108316. [CrossRef]

Journal of
Marine Science and Engineering

MDPI

Article

Study on the Mechanical Behavior of Fine-Grained Gassy Soil Under Different Stress Conditions

Tao Liu [1], Chengrong Qing [1], Jianguo Zheng [2,*], Xiufen Ma [3], Jiawang Chen [4] and Xiaolei Liu [2]

[1] Shandong Engineering Research Center of Marine Exploration and Conservation, Ocean University of China, Qingdao 266100, China; ltmilan@ouc.edu.cn (T.L.); qcr@stu.ouc.edu.cn (C.Q.)
[2] Shandong Provincial Key Laboratory of Marine Environment and Geological Engineering, Ocean University of China, Qingdao 266100, China; xiaolei@ouc.edu.cn
[3] Qingdao Robotfish Marine Technology Co., Ltd., Qingdao 266100, China
[4] Ocean College, Zhejiang University, Zhoushan 316000, China; arwang@zju.edu.cn
* Correspondence: jianguo@ouc.edu.cn

Abstract: Gassy soil is prevalent in coastal regions, and the presence of gas bubbles can significantly alter the mechanical properties of soil, potentially leading to various marine engineering geological hazards. In this study, a series of triaxial tests were conducted on fine-grained gassy soils under different consolidation pressures ($p_{c'}$), stress paths, and initial pore water pressures (u_{w0}). These tests were also used to verify the applicability of a newly proposed constitutive model. According to the test results, the response to excess pore pressure and the stress–strain relationship of fine-grained gassy soils strongly depend on the initial pore water pressure (u_{w0}), with the degree of variation being influenced by the consolidation pressure ($p_{c'}$) and stress path. As u_{w0} decreases, the undrained shear strength (c_u) of fine-grained gassy soils gradually increases, and this is lower under the reduced triaxial compression (RTC) path compared to the conventional triaxial compression (CTC) path, which can be attributed to the destruction of the pore structure due to an increase in gas volume. The newly proposed model accurately predicts the pore pressure and stress–strain relationship of fine-grained gassy soils at low consolidation pressures ($p_{c'}$), but it falls short in predicting the mechanical behavior during shear progression under high $p_{c'}$ or the RTC path. Although the model effectively predicts the excess pore pressure and deviator stress at the shear failure point (axial strain = 15%), further improvement is still required.

Keywords: gassy soil; triaxial testing; constitutive model; pore water pressure; stress path

1. Introduction

Gassy soils are widely distributed in the coastal areas of five continents around the world [1,2]. Unlike conventional unsaturated soils, gassy soil has a continuous water phase, while the gas phase exists as isolated bubbles [3,4].

These bubbles, comprised mainly of methane, nitrogen, or carbon dioxide, are primarily formed through the anaerobic fermentation of submarine microorganisms or the thermal decomposition of deep organic matter [5–8]. The presence of these bubbles results in the rearrangement of soil particles and the alteration of the mechanical properties, including consolidation behavior and strength properties [9–13], which usually reduce the strength of gassy soil since the bubbles have no shear stiffness or shear strength. This reduction

in strength can lead to abnormal settlement, lateral or rotational slipping, and even instability and failure of the seabed, ultimately resulting in a series of marine geological disasters [14–16]. Consequently, the safety of offshore facilities built on gassy sediments is significantly jeopardized.

The bubble size in fine-grained gassy soil is significantly larger than that of soil particles and voids, with these sizable bubbles directly contacting multiple soil particles [17–19]. This distinctive structural arrangement is illustrated in Figure 1 and leads to instances where pore water within fine-grained gassy soil partially discharges into the gas cavities. This phenomenon results in a reduction in bubble volume and an elevation in gas pressure, while the bubble itself remains stationary, a phenomenon commonly referred to as "bubble flooding" [20]. It has been experimentally confirmed that bubble flooding exerts a positive influence on the undrained shear strength of fine-grained gassy soils [21,22].

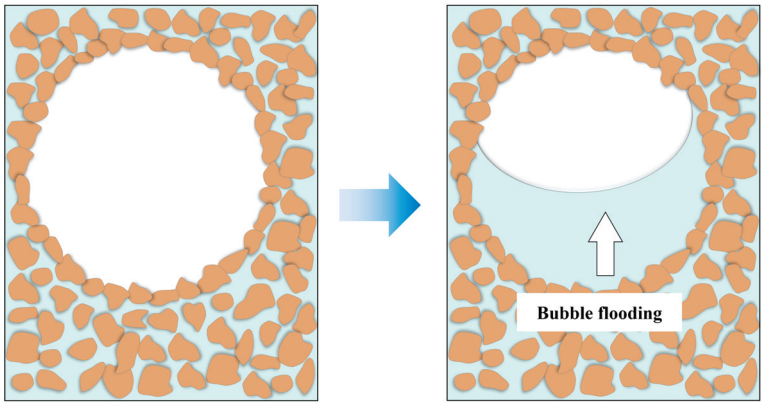

Figure 1. A schematic diagram of bubble flooding which is adapted from Hong et al. (2017) [23].

To comprehensively capture the opposite effects of the specific soil structure and bubble flooding, Wheeler [20] initially established upper and lower bounds for the undrained shear strength of fine-grained gassy soil, but it could not be used to predict the stress–strain characteristics and the undrained shear strength for specific stress conditions. Some recent studies have proposed constitutive models that can describe both the harmful and beneficial effects of bubbles on fine-grained gassy soil based on Cam-Clay models [21,24,25], and the simulation results of the mechanical response have been proven to be in good agreement with most of the reported conventional triaxial compression (short for CTC) tests [20,23,26,27]. Hong et al. [23,26] conducted a series of CTC tests under identical initial mean effective stress but varying initial pore water pressures and gas contents. Sham [27] and Wheeler [20] have also conducted numerous CTC tests, although only one complete dataset has been reported. Additionally, several other scholars have performed specialized undrained triaxial compression tests related to deep-water sampling (short for TC), as opposed to in situ stress conditions [28–30].

It is important to note that all of these aforementioned studies have concentrated solely on the mechanical behavior of fine-grained gassy soils under loading stress paths, but less attention has been paid to the reduced triaxial compression test (short for RTC) which is used to simulate soil under reduced confining pressure conditions such as the tunnel face and side wall of a foundation pit. The differences among the above three stress paths are shown in Figure 2.

Therefore, the adequacy of these newly proposed constitutive models in accurately depicting the mechanical behavior of fine-grained soils under high initial mean effective stress or RTC stress paths remains uncertain. To investigate the mechanical behavior of

fine-grained gassy soil under diverse stress conditions, the triaxial tests of fine-grained gassy soil at different stress paths, different initial mean effective stresses, and different initial pore water pressures were conducted, and the newly proposed constitutive model was used to verify the applicability to a wider range of stress conditions.

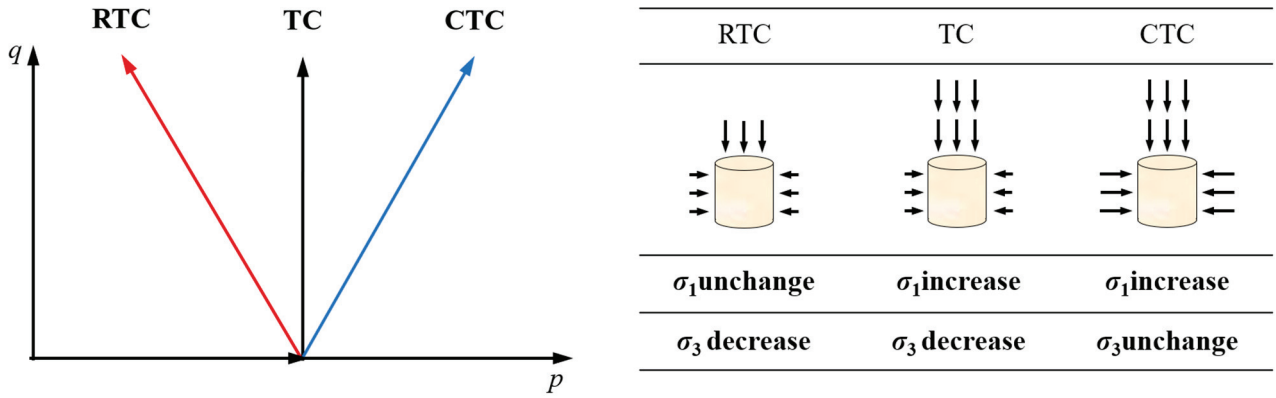

Figure 2. Schematic diagram of stress path in triaxial test.

2. Experimental Programs

The gassy soil includes three different matrixes: bubbles, pore water, and soil particles. To conveniently regard the volume of the whole gas-bearing soil as V, the volume of bubbles, pore water, and soil particles is regarded as V_g, V_w, and V_s, respectively. S_r is the saturation of the water phase, and e_w and ψ are the water void ratio and gas volume fraction, respectively. The three-phase composition of gassy soil per unit volume is shown in Figure 3.

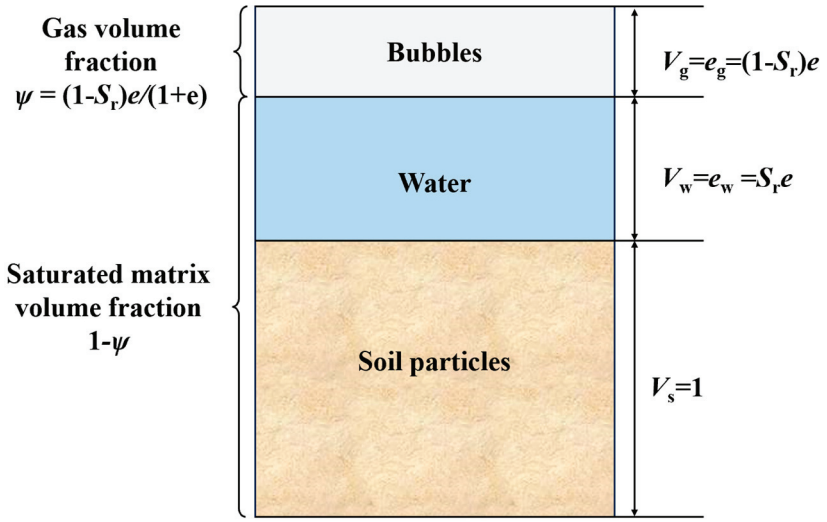

Figure 3. Three-phase composition diagram of gas-bearing soil per unit volume.

2.1. Testing Material and Preparation of Gassy Specimens

Gassy soils are typically found in deep water environments. When in situ samples are extracted from these sites, pressure variations lead to the exsolution and expansion of gases within the gassy soil, resulting in alterations to the soil structure and, in some cases, the development of cracks [30–32]. Therefore, it is difficult to obtain undisturbed gassy soil samples under in situ conditions, so reproduced gassy soil in the laboratory is usually used in triaxial tests. In this study, Malaysian kaolin was used to prepare gassy specimens

by the zeolite molecular sieve technique which was justified by Sills et al. [33]. The soil parameters are shown in Table 1.

Table 1. Index properties and mechanical parameters of Malaysia kaolin.

Parameter	Measured Value
Liquid limit: %	56
Plastic limit: %	35
Plasticity index	21
The angle of friction: °	24.3
Coefficient of earth pressure at rest	0.59
Critical stress ratio	1

The procedure for preparing gassy soil is shown in Figure 4. This method is mainly through the affinity of zeolite to polar water molecules to discharge non-polar nitrogen molecules from zeolite pores, thereby introducing gas into soil samples. The process involves the following steps: (a) The zeolite powder is dried at a high temperature (100 °C, 24 h). (b) The dried zeolite is placed into a sealed tank and subjected to vacuuming (−100 kPa, 24 h). Afterward, the vacuum pump is turned off, and nitrogen is injected under high pressure (200 kPa, 24 h). (c) Malaysian kaolin is dried (105 °C, 24 h), and the dried soil is mixed with airless water at a ratio of twice the liquid limit. Vacuum saturation is performed while stirring (24 h). The saturated slurry is then mixed with nitrogen-filled zeolite powder (equivalent to 20% of dry soil mass) to ensure that water and nitrogen are exchanged so that gas is generated inside the slurry. (d) The gassy soil mixture is gradually poured into the loading device, and a specific load (80 kPa) is applied to achieve initial consolidation. This technique is simple and effective, and the loading history is known [27,34]. It allows for the production of specimens that exhibit physical properties similar to in situ conditions in a batch manner. However, it is worth noting that the gas content of the prepared samples cannot be precisely controlled.

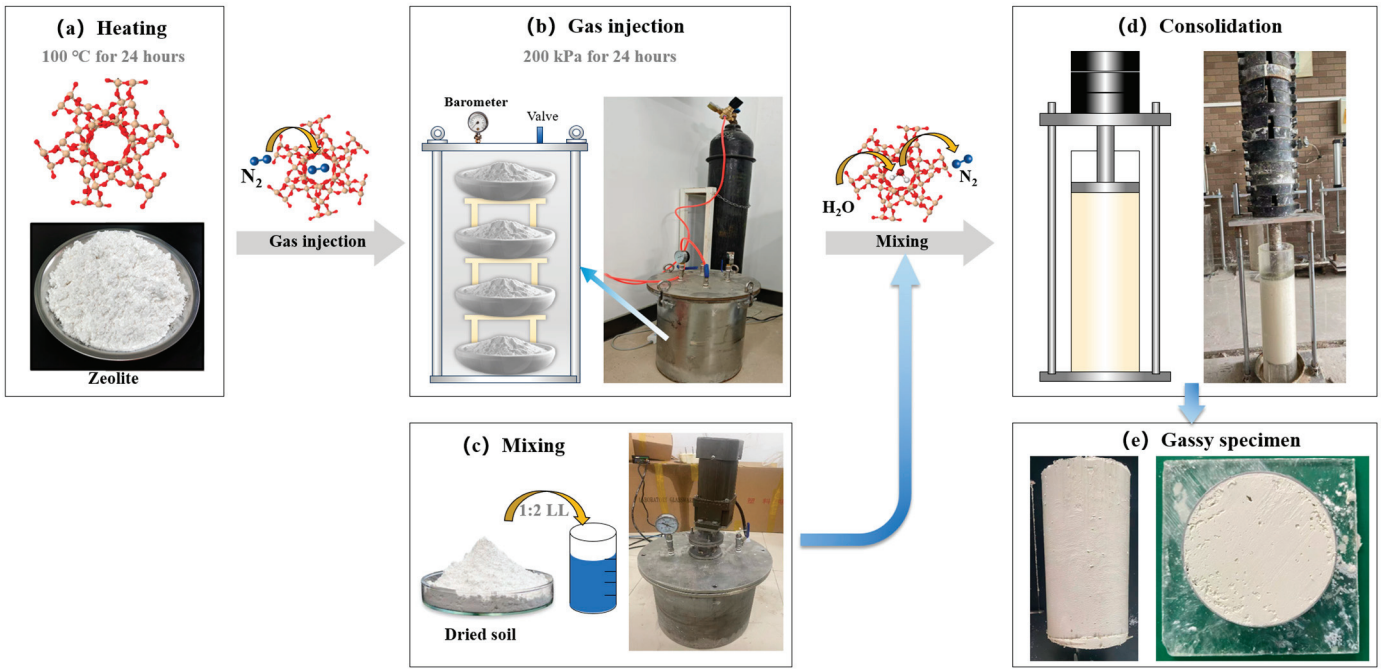

Figure 4. The main process of gassy soil preparation using the zeolite molecular sieve technique.

2.2. Consolidated Drained Triaxial Compression Test

One-dimensionally consolidated gassy soils were carefully trimmed into standard triaxial specimens of 50 mm in diameter and 100 mm in height and then set to different initial pore water pressures (u_{w0} = 0, 60, 120, 250, 500 kPa) in the consolidation stage and consolidated to a certain confining pressure ($p_{c'}$ = 200, 400 kPa) according to the set average effective stress to complete isotropic consolidation. After consolidation is complete (as judged by pore pressure dissipation or drainage), the triaxial axial strain rate is set to 1.5% per hour (CTC tests), and the confining pressure unloading rate is set to 15 kPa per hour (RTC tests) until the shear failure occurs. A reference saturated soil test ($p_{c'}$ = 200 kPa, u_{w0} = 200 kPa) was also performed for comparison.

All tests were conducted using the GDS triaxial test system, which was equipped with a HKUST double cell. As shown in Figure 5, the confining pressure during the test is controlled by the air pressure controller to ensure that the pressure in the inner and outer chambers is equal (minimizing the deformation caused by pressure changes). During the test, the water level in the inner chamber changes due to the volume change in the specimen in the inner chamber, while the reference water level remains constant, so the difference between the water level in the inner chamber and the reference water level changes. Through the high-precision differential pressure sensor, the water level change in the inner chamber can be accurately measured, to determine the total volume and water volume change in the sample during the consolidation process. This method can be used to determine the initial saturation (S_{r0}), water void ratio (e_{w0}), and gas volume fraction (ψ_0) of the gassy specimen after isotropic consolidation. The specific test scheme is shown in Table 2.

Table 2. A summary of the experimental program.

Sample Type	Initial Pore Water Pressure (kPa)	Initial Degree of Saturation (%)	Initial Water Void Ratio	Initial Gas Volume Fraction (%)	Initial Mean Operative Stress (kPa)	Test Type
Saturated	200	100	1.39	0	200	CTC
Gassy	0	90.7	1.36	5.4	200	CTC
	60	92.5	1.34	4.3		
	120	95.3	1.35	2.7		
	250	95.9	1.36	2.2		
	500	97.5	1.37	1.4		
Gassy	0	94.7	1.30	3.0	400	CTC
	120	96.1	1.29	2.2		
	250	98.2	1.30	1.0		
Gassy	0	91.6	1.35	4.8	200	RTC
	120	94.5	1.33	3.1		
	250	96.3	1.34	2.1		

Before commencing the tests, the double cell and the differential pressure sensor underwent calibration using the method proposed by Ng et al. [35]. The accuracy of the HKUST double cell can reach 31.4 mm^3, which is about 0.02% of the volume of the test specimens (diameter = 50 mm, height = 100 mm).

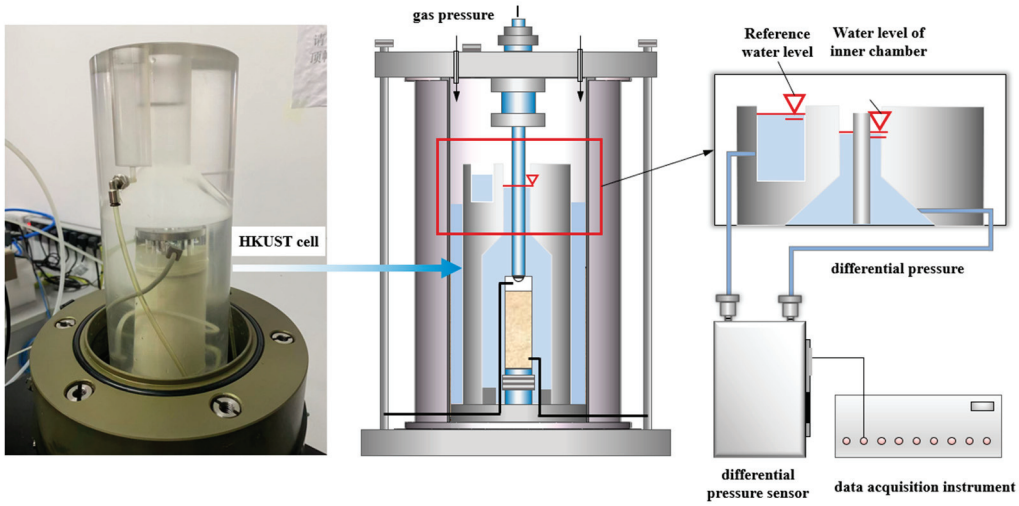

Figure 5. The main process of gassy soil preparation using the zeolite molecular sieve technique.

3. Experimental Results and Discussion

Since the effective stress principle is theoretically and experimentally proven to be usable for gassy soil with S_r values over 90% [33,36–39], the tests of gassy soil in this study are still designed and explained according to the effective stress principle.

3.1. Excess Pore Pressure

Figure 6 shows the variation in excess pore pressure (Δu) under different stress conditions, including different stress paths (CTC and RTC) and different consolidation pressures ($p_{c'}$ = 200, 400 kPa). The data of gassy Combwich mud [20] are also included for comparison. The Δu is normalized by the effective consolidation pressure ($p_{c'}$).

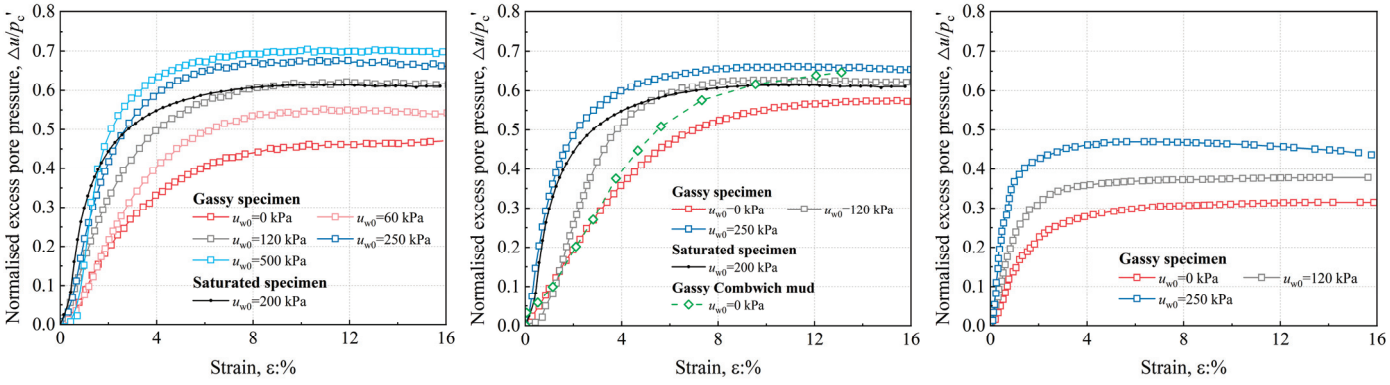

(**a**) CTC ($p_{c'}$ = 200 kPa) (**b**) CTC ($p_{c'}$ = 400 kPa) (**c**) RTC ($p_{c'}$ = 200 kPa)

Figure 6. The excess pore pressure responses under different stress conditions.

The gassy specimens under different stress conditions all show a positive excess pore pressure response. At higher u_{w0} (≥250 kPa), the Δu of gassy specimens under the CTC path is close to the peak at the beginning of shearing (ε = 2%~3%). As u_{w0} decreases, the rate of pore pressure accumulation gradually slows down, and the $\Delta u/p_{c'}$ of the gassy specimens also decreases significantly. When u_{w0} is reduced from 500 kPa to 0 kPa, the Δu generated by shearing is reduced by 33% (Figure 6a). Compared to the saturated specimen, the $\Delta u/p_{c'}$ decreases by 23% at zero u_{w0}. This may be because the bubble pressure is lower and the bubble size is larger at lower u_{w0}, so the water can easily enter the bubble from the soil matrix, resulting in bubble flooding.

Figure 6b shows the excess pore pressure responses of the gassy and saturated specimens at higher $p_{c'}$ (400 kPa). Regardless of the u_{w0}, the $\Delta u/p_{c'}$ of gassy specimens is closer to that of the saturated specimen, as the gas volume fraction in the soil decreases and the void ratio (e) of the gassy specimens is closer to that of the saturated specimen, making bubble flooding less likely to occur. In particular, the gassy specimen at zero u_{w0} exhibits a notable increase in $\Delta u/p_{c'}$, as the compression of bubbles becomes more pronounced at low u_{w0}. In comparison to gassy Combwich mud, the Δu of gassy Malaysian kaolin is smaller and peaks earlier.

As shown in Figure 6c, the $\Delta u/p_{c'}$ under the RTC path is lower compared to the CTC path. Specifically, at the same $p_{c'}$ (200 kPa), the $\Delta u/p_{c'}$ of gassy specimens under the RTC path is approximately 33% to 39% lower than that of the CTC tests. On the one hand, this may be due to the decrease in confining pressure. On the other hand, it may be because gas expansion or exsolution may occur during the shear process under the RTC path, resulting in an increase in the gas volume fraction in the gassy specimens. As a result, bubble flooding is more likely to occur, which in turn decreases the excess pore pressure.

3.2. Stress–Strain Relationship

Figures 7 and 8 show the stress–strain relationship and effective stress paths of gassy and saturated specimens under different values of u_{w0} and $p_{c'}$ during the CTC test. The data of gassy Kaolin clay [27] and gassy Combwich mud [20] are also included for comparison.

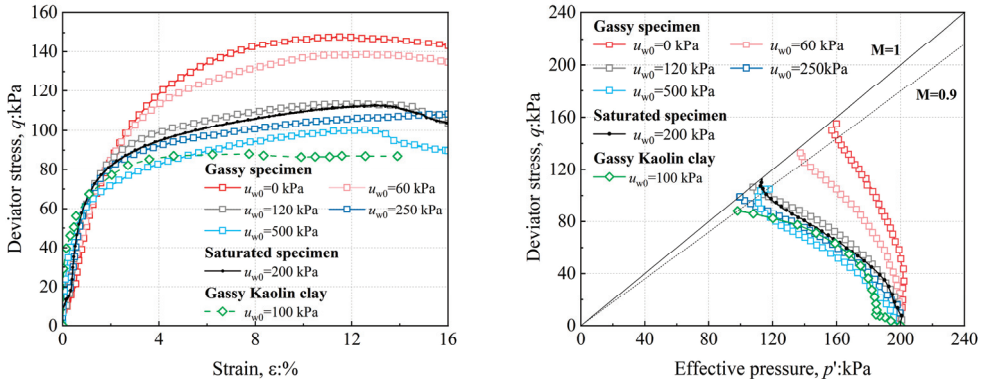

(**a**) Stress–strain relationship. (**b**) Effective stress paths.

Figure 7. Stress–strain relationship and effective stress paths of specimens at different u_{w0} during the CTC test ($p_{c'}$ = 200 kPa).

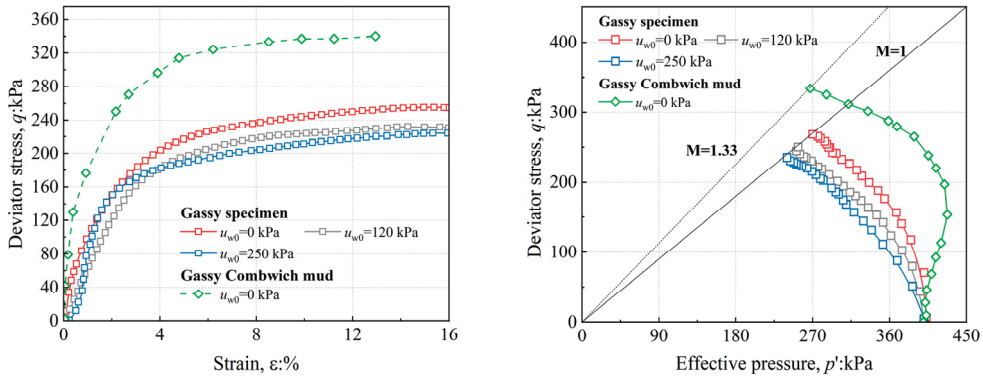

(**a**) Stress–strain relationship (**b**) Effective stress paths.

Figure 8. Stress–strain relationship and effective stress paths of specimens at different u_{w0} during the CTC test ($p_{c'}$ = 400 kPa).

The stress–strain characteristics of gassy Malaysian kaolin and gassy Kaolin clay exhibit similarities due to the comparable nature of these two soils (Figure 7). Conversely, the stress–strain relationship and effective stress paths of gassy Malaysian kaolin differ significantly, despite the minor disparity in pore pressure response between the two. This dissimilarity might be attributed to the higher plasticity index (28) of Combwich mud. Previous studies have indicated that, in most cases, clay with a higher plasticity index exhibits greater undrained shear strength [40,41]. Furthermore, the stress–strain characteristics of gassy soils rely more on the soil matrix, as the presence of gas bubbles does not visibly impact the overall shape of the stress–strain curves [20].

As u_{w0} increases, the ultimate deviatoric stress (equal to two times the undrained shear strength c_u) of gassy specimens consistently decreases (Figure 7). Specifically, as u_{w0} increases from 0 kPa to 500 kPa, the undrained shear strength decreases by 43% due to the higher excess pore pressure (Figure 6). Because the gas is compressed into a flat shape under high u_{w0}, it is easier to destroy the structure of the soil and form micro-cracks, which means greater excess pore pressure (Figure 6). Under high axial strain, the damage to the soil is more obvious, resulting in a sudden drop in deviatoric stress.

The deviatoric stress of the gassy specimens is enhanced at higher $p_{c'}$ (400 kPa) due to the effect of compactness (Figure 8). For gassy specimens with different u_{w0}, the strengthening effect of compactness is different. At a higher u_{w0} (250 kPa), the ultimate deviatoric stress of the gassy specimens increases by 108%, whereas at zero u_{w0}, it increases by 78%. This discrepancy is likely attributed to the more pronounced effect of compactness at higher u_{w0}, as the size of the gas bubbles decreases and subsequently reduces the shear shrinkage effect caused by pore collapse during the shear process.

Figure 9 shows the stress–strain relationship and effective stress paths of gassy specimens at the same $p_{c'}$ (200 kPa) but different u_{w0} (0, 120, 250 kPa) during the RTC test. Compared with the CTC test, the undrained shear strength of gassy specimens at different u_{w0} exhibits a certain decrease, with the amplitude of the decrease falling within 10%. The primary reason for this decrease could be the reduction in confining pressure during the shear process, which leads to the exsolution and expansion of gas, thereby increasing the overall gas volume and disrupting the pore structure. Simultaneously, the release of confining pressure promotes bubble growth, resulting in increased soil compressibility, reduced effective stress, and a weakening of its strength.

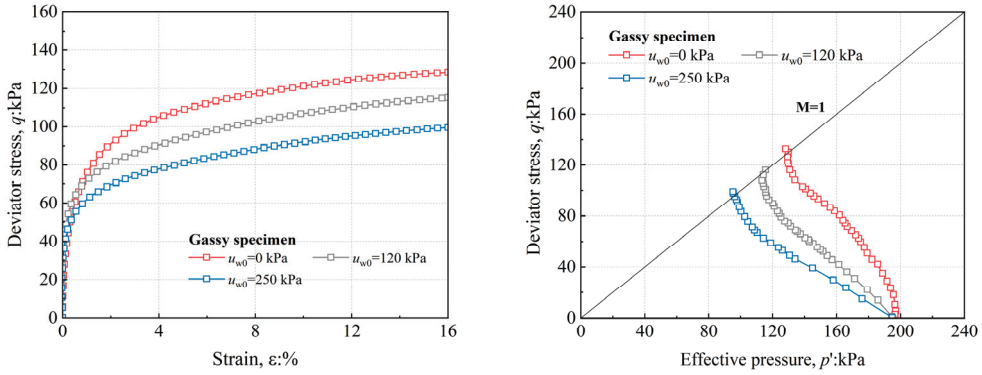

(**a**) Stress–strain relationship. (**b**) Effective stress paths.

Figure 9. Stress–strain relationship and effective stress paths of specimens at different u_{w0} during the RTC test ($p_{c'}$ = 200 kPa).

4. Model Validation and Discussion

The model proposed by Gao et al. [21,24] introduces only one or two new parameters to the Modified Cam-Clay (MCC) model to describe the two opposite mechanical behaviors of fine-grained gassy soils. However, these models fall short in capturing the response of gassy soils under unloading situations as they only provide a purely elastic response. In contrast, Hong et al. [25] developed an elastoplastic constitutive model for fine-grained gassy soils (Hong-model for short) by incorporating the stress–dilatancy function into the versatile yield surface within the framework of the critical state theory.

This model effectively accounts for the influence of u_{w0} and ψ_0 on the yield curve and dilatancy characteristics of fine-grained gassy soils (Figure 10, Equations (1)–(3)) (i.e., gas-bearing soils under different water depths). The yield surface of saturated soil is elliptical. At high u_{w0} and low ψ_0 (i.e., deep water environment), bubbles will reduce the strength of the soil. The yield surface is bullet-shaped, and there is more shear shrinkage than saturated soil. At low u_{w0} and high ψ_0 (i.e., shallow water environment), bubbles will enhance the strength of the soil. The yield surface is water droplet-shaped, and there is more dilatancy than saturated soil. Hong-model introduces more parameters (five new parameters), but Hong et al. derived the yield points needed to determine the shape of the yield curve and the directions of plastic strain increment from a series of saturated and gassy specimens (24 specimens in total) with the same $p_{c'}$ (200 kPa) and isotropically unloaded them to confining pressures of 120, 140, 160, 170, 180, and 190 kPa, which can better capture the unloading behavior of fine-grained gassy soils. For further details regarding the model, refer to Hong et al. [25].

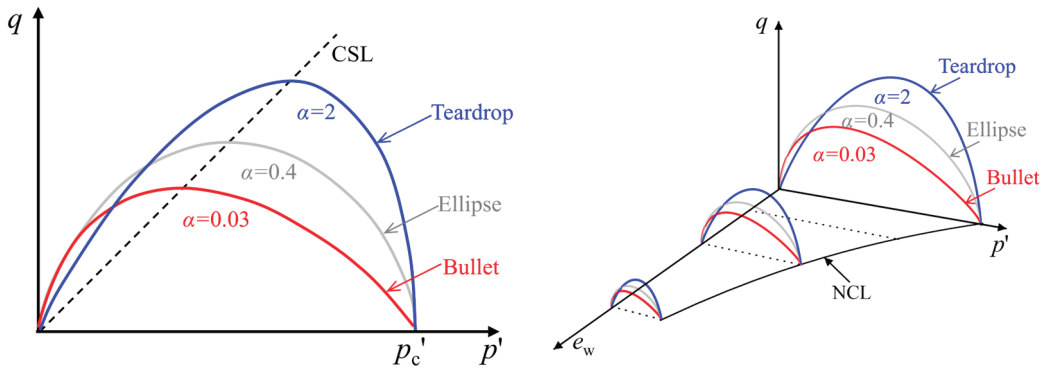

(**a**) p'-q space (**b**) p'-q-e_w

Figure 10. Varying shapes of yield surface in p'-q space and p'-q-e_w at different values of shape parameter α.

Hong-model contains ten parameters, five of which are identical to the parameters utilized in the MCC model (λ, κ, N, M, and v). Two new parameters, denoted as a and b, are introduced to control the shape of the yield surface. Furthermore, two new parameters, denoted as ξ and χ, are introduced to capture the influence of u_{w0} and ψ_0 on the dilatancy characteristics of gassy soil. Lastly, one parameter (δ) is associated with the initial gas pressure and is not essential if the volumetric behavior of gassy soil is not a concern.

The functions for the parameters controlling the shape of the yield surface are as follows:

$$\alpha\left(\frac{u_{w0}-u_{w0\_ref}}{p_c'},\psi_0\right)=0.4\times exp\left(-5\times\Lambda\psi_0^{a+h(\Lambda)b}\right) \quad (1)$$

$$\Lambda = \frac{u_{w0} - u_{w0\_ref}}{p'_c} \tag{2}$$

where Λ is used to describe the normalized difference between the u_{w0} and the virtual reference initial pore water pressure (u_{w0_ref}).

The stress–dilatancy function (D) is as follows:

$$D = \left[1 + \xi \frac{u_{w0} - u_{w0\_ref}}{p'_c} exp\left(-\frac{\chi}{\psi_0}\right)\right] \frac{M^2 - \eta^2}{2\eta} \tag{3}$$

where M is the stress ratio at the critical state, and η is the stress ratio ($\eta = q/p'$). When u_{w0} of gassy soil is equal to u_{w0_ref}, Equation (3) will return to the dilatancy equation of the MCC model, which is independent of the value of ψ_0.

According to the procedure proposed by Hong et al., ξ and χ require fine-tuning to align the stress–dilatancy function (Equation (3)) with the measured stress–dilatancy relationships. Parameters a and b can be derived by calibrating the effective stress paths using the seven parameters obtained, which include those from the MCC model. To determine these parameters, two sets of test results of gassy specimens ($p_{c'}$ = 200 kPa, u_{w0} = 60, and 500 kPa) were employed (Figure 11), while the remaining results were utilized for model validation. The dilatancy (D) can be determined experimentally using the following equation proposed by Hong et al. [26]:

$$D = \frac{-\frac{\kappa dp'}{(1+e_{w0})p'}}{d\varepsilon_q - \frac{2\kappa(1+\nu)dq}{9(1-2\nu)(1+e_{w0})p'}} \tag{4}$$

where κ is the slope of swelling line in the $e_w - \ln p'$ plane, dp' and dq are increments of effective mean normal stress and deviatoric stress, respectively, $d\varepsilon_q$ denotes increments of deviatoric strain, and v is Poisson's ratio.

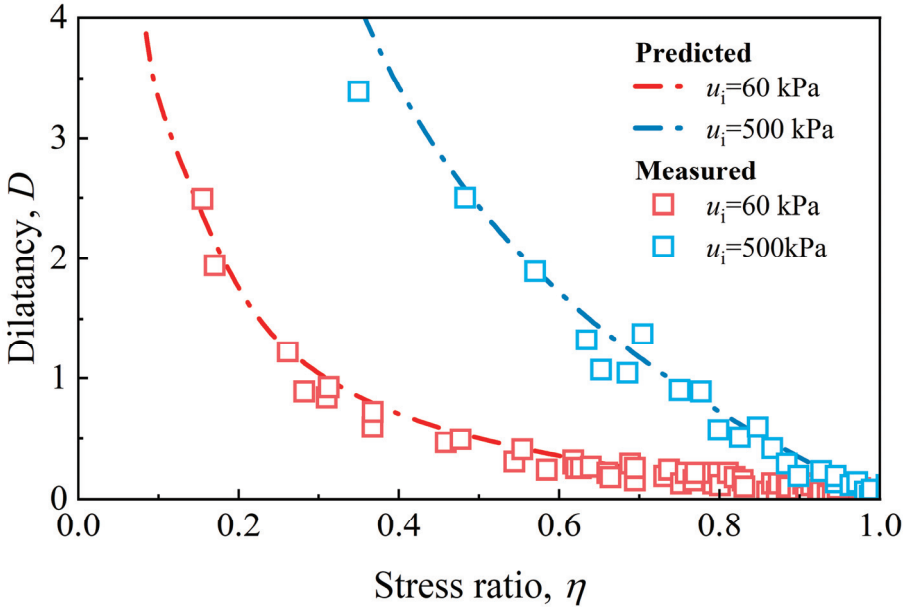

Figure 11. Stress–dilatancy relationship of gassy Malaysian kaolin.

Table 3 presents the model parameters of gassy Malaysian kaolin.

Table 3. Model parameters.

Type of Parameter	Meaning of Parameters	Parameter	Value
MCC parameters	Slope of compression line in $e_w - \ln p'$ plane	λ	0.24
	Slope of swelling line in $e_w - \ln p'$ plane	κ	0.05
	Intercept of NCL in $e_w - \ln p'$ plane	N	2.74
	Stress ratio at the critical state	M	1
	Poisson's ratio	v	0.30
Hong-model parameters	Shape parameters of the yield surface	a	0.15
		b	0.35
	Parameters of dilatancy function	ξ	1.45
		χ	0.02
	Parameter of initial gas pressure	δ	0.7

4.1. Shear Behavior

Figures 12–14 show the comparison between the predicted and measured shear behavior (pore pressure response, stress–strain relationship, and effective stress paths) of the gassy specimens under different $p_{c'}$, u_{w0}, and stress paths.

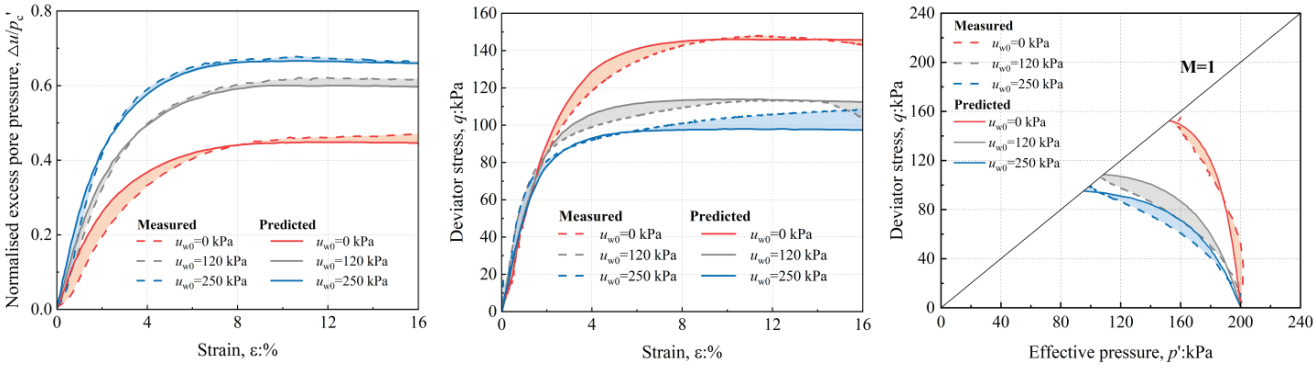

(**a**) Pore pressure response. (**b**) Stress–strain relationship. (**c**) Effective stress paths.

Figure 12. Comparison between the predicted and measured shear behavior of gassy soil at $p_{c'}$ = 200 kPa and CTC stress path.

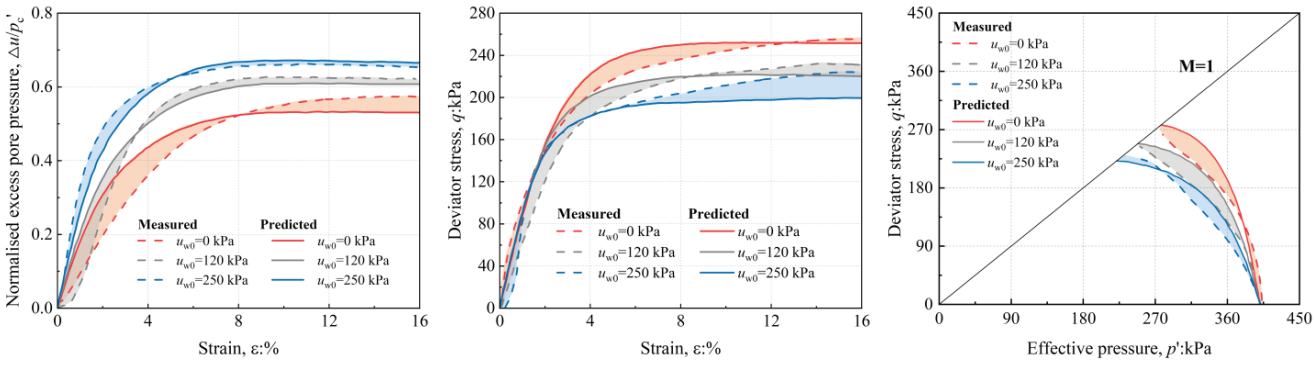

(**a**) Pore pressure response. (**b**) Stress–strain relationship. (**c**) Effective stress paths.

Figure 13. Comparison between the predicted and measured shear behavior of gassy soil at $p_{c'}$ = 400 kPa and CTC stress path.

The shear behaviors of the gassy specimens were all reasonably predicted under the CTC path. However, it is important to note that prediction errors in the stress–strain relationship gradually increase as u_{w0} rises, while the opposite is observed for the pore pressure response. At lower $p_{c'}$ (200 kPa), the effective stress paths of gassy specimens with

higher u_{w0} (120, 250 kPa) exhibit a more noticeable delayed incline when compared to the gassy specimen with zero u_{w0} (Figure 12).

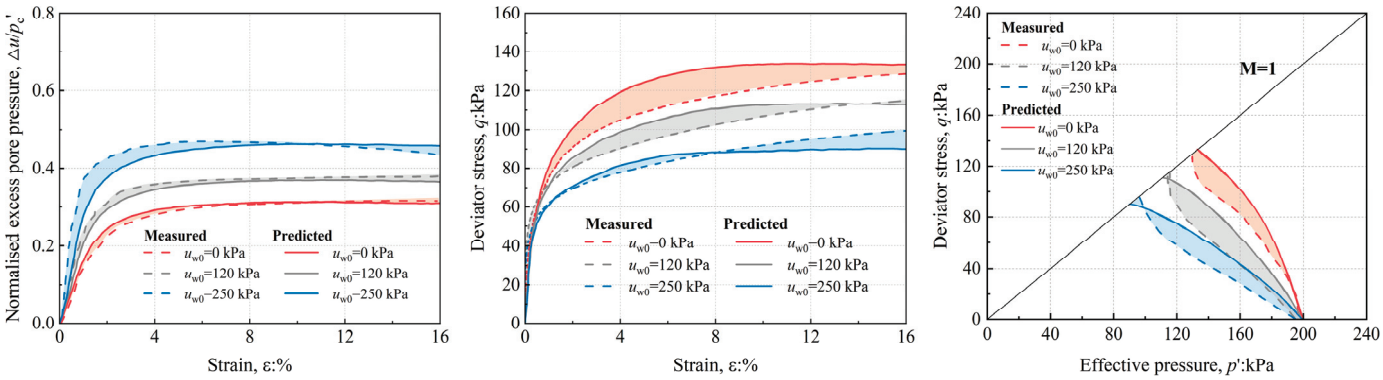

(**a**) Pore pressure response. (**b**) Stress–strain relationship. (**c**) Effective stress paths.

Figure 14. Comparison between the predicted and measured shear behavior of gassy soil at $p_{c'}$ = 200 kPa and RTC stress path.

As shown in Figure 13, errors in predicting the stress–strain characteristics of gassy specimens at higher $p_{c'}$ (400 kPa) are higher than those of gassy specimens at lower $p_{c'}$ (200 kPa). Nevertheless, these errors remain within acceptable limits, staying below 12%. However, the prediction error for the pore pressure response of gassy specimens at higher $p_{c'}$ (400 kPa) and zero u_{w0} in the early stage of shearing (ε = 1~4%) is considerably higher, nearing 30%.

As shown in Figure 14, compared with the CTC test, the excess pore pressure of the gassy specimens under the RTC path is better simulated. However, the prediction error of the stress–strain relationship in the middle stage of shearing is much higher, especially in the case of low u_{w0}. Although the endpoints of the effective stress paths are basically coincident, the development trend of the stress paths is not well predicted, and the model still needs to be further extended to simulate a wider range of stress conditions.

The undrained shear strengths of all specimens were well predicted. Quantitatively, the prediction errors were all less than 15%, although Hong-model has a large error in predicting the excess pore pressure and stress–strain relationship at certain stages of the shearing process of gassy specimens under different stress paths and $p_{c'}$.

4.2. Parameter Sensitivity

Hong-model contains five new parameters (a, b, ξ, χ, and δ). The parameter δ, which only relates to the initial gas pressure, is optional and may be omitted. Equation (3) incorporates a Heaviside step function $h(\Lambda)$ to account for the impact of different initial conditions on fine-grained gassy soils. When the u_{w0} is low ($\Lambda < 0$), the exponent of ψ_0 is represented by parameter a. For high u_{w0}, the exponent of ψ_0 is determined by the sum of a and b. From this, it can be seen that only parameter a is affected by the low u_{w0}, while a and b have the same influence by the high u_{w0}. Therefore, the sensitivity analysis primarily focuses on parameters a, ξ, and χ.

Since Hong-model predicts better for fine-grained gassy soils under lower $p_{c'}$ (200 kPa) and CTC path, two gassy specimens with low and high u_{w0} (0, 500 kPa) were analyzed for this condition. During the sensitivity analysis, it was assumed that each parameter was independent of the others, and only one corresponding parameter was altered while keeping the rest unchanged. By increasing or decreasing the parameter values provided in Table 3, different results were obtained.

Figure 15 shows the pore pressure response of fine-grained gassy soils after changing the parameters. When parameter a is increased, the $\Delta u/p_{c'}$ exhibits a slight increase, with the effect being more pronounced at zero u_{w0}. Regardless of whether parameter a is increased or decreased, the change in $\Delta u/p_{c'}$ is less than 5% (Figure 15a,d). At zero u_{w0}, when ξ increases from 1.45 to 2.3, there is a significant decrease in $\Delta u/p_{c'}$, while decreasing ξ has a minimal effect on $\Delta u/p_{c'}$ (Figure 15b). At high u_{w0}, altering the values of parameters ξ and χ significantly affects the rate of cumulative pore pressure in fine-grained gassy soils, reaching the peak $\Delta u/p_{c'}$ value at ε around 4%. However, these changes show only a small effect on the final value of $\Delta u/p_{c'}$ value (Figure 15e,f). At zero u_{w0}, parameter χ has almost no effect on the pore pressure response of fine-grained gassy soils (Figure 15c).

Figure 16 shows the stress–strain relationship of fine-grained gassy soils after changing the parameters. The parameter changes have a minimal impact on the slope of the stress–strain relationship in fine-grained gassy soils. The undrained shear strength decreases as the parameter increases, especially at zero u_{w0}, but the magnitude of this change remains less than 5% (Figure 16a,d). At zero u_{w0}, an increase in ξ from 1.45 to 2.3 results in more pronounced delayed shear damage in the predicted values, while a decrease in ξ from 1.3 to 0.87 does not significantly alter the stress–strain characteristics (Figure 16b). At high u_{w0}, changes in parameters ξ and χ significantly affect the hardening rate of fine-grained gassy soils but have a negligible effect on the undrained shear strength (Figure 16e,f). At zero u_{w0}, parameter χ exhibits a minimal impact on the stress–strain relationship of fine-grained gassy soils (Figure 16c).

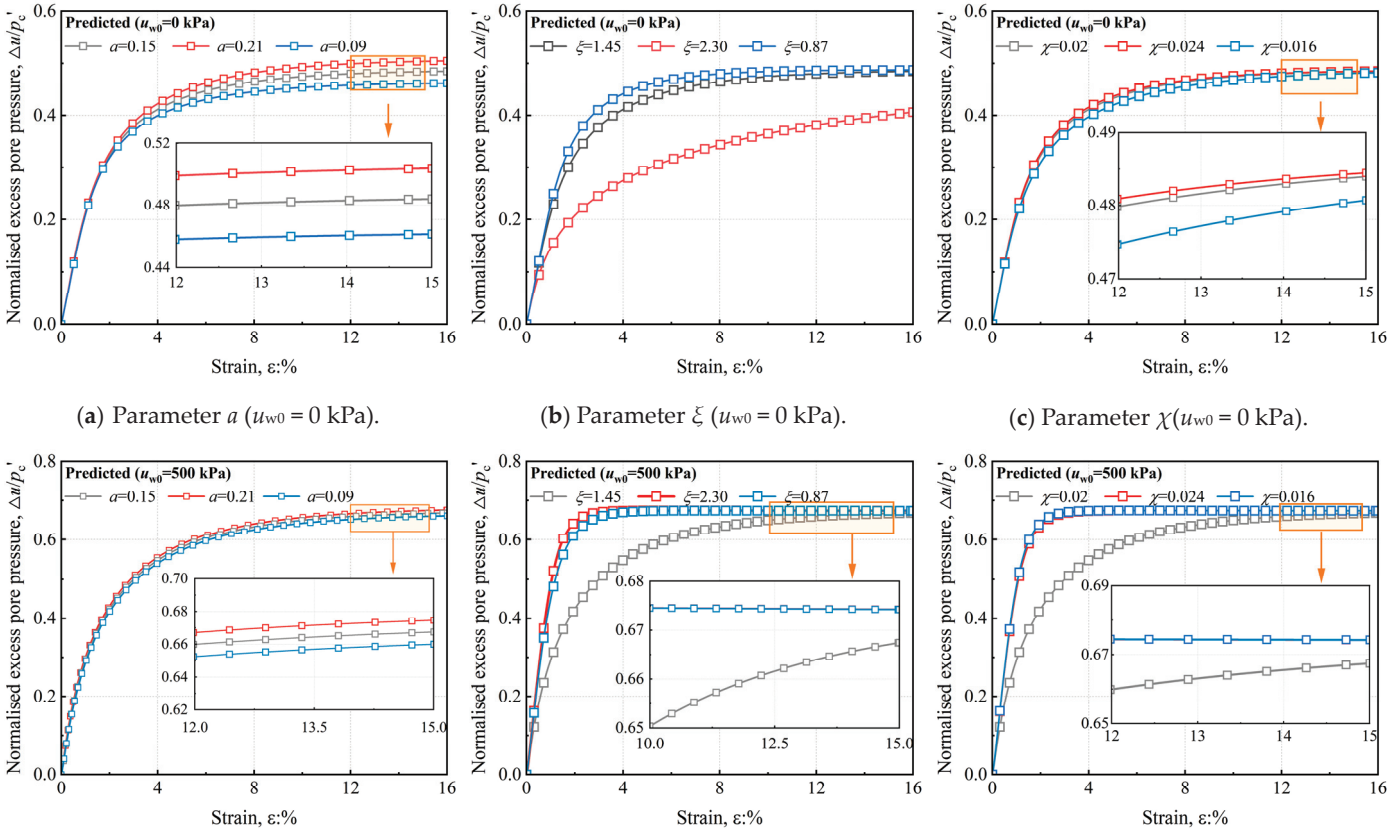

(**a**) Parameter a (u_{w0} = 0 kPa). (**b**) Parameter ξ (u_{w0} = 0 kPa). (**c**) Parameter χ(u_{w0} = 0 kPa).

(**d**) Parameter a (u_{w0} = 500 kPa). (**e**) Parameter ξ (u_{w0} = 500 kPa). (**f**) Parameter χ(u_{w0} = 500 kPa).

Figure 15. Pore pressure response results under different parameters (the grey line is the prediction result corresponding to the unadjusted parameters).

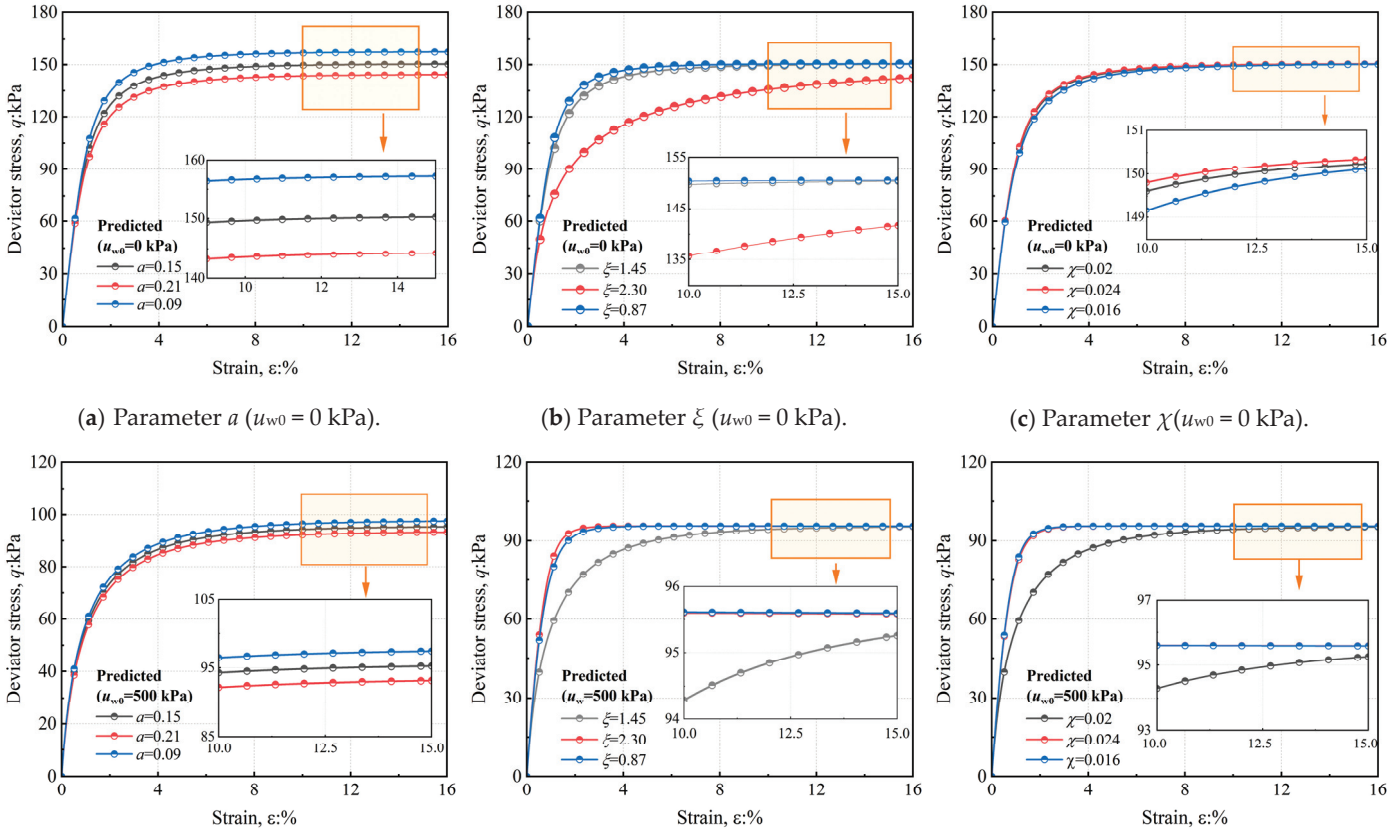

(**a**) Parameter a (u_{w0} = 0 kPa). (**b**) Parameter ξ (u_{w0} = 0 kPa). (**c**) Parameter χ(u_{w0} = 0 kPa).

(**d**) Parameter a (u_{w0} = 500 kPa). (**e**) Parameter ξ (u_{w0} = 500 kPa). (**f**) Parameter χ(u_{w0} = 500 kPa).

Figure 16. Deviator stress results under different parameters (the grey line is the prediction result corresponding to the unadjusted parameters).

5. Conclusions

In this study, a series of triaxial tests of fine-grained gassy soil at different initial pore water pressures (u_{w0}), stress paths (CTC, RTC), and consolidation pressures ($p_{c'}$) were carried out. Based on the results of these tests, the new constitutive model was utilized to predict the mechanical behavior of fine-grained gassy soils. The following conclusions can be drawn from this research:

(1) The mechanical response of fine-grained gassy soil is significantly influenced by u_{w0} under different stress paths and $p_{c'}$ values. At higher u_{w0}, due to the collapse of the cavity and the destruction of the soil structure, the excess pore pressure increases, and the strength decreases. At lower u_{w0}, bubble flooding occurs, whereby excess pore pressure (Δu) is dissipated to larger bubbles, resulting in increased strength.

(2) For fine-grained gassy soils with higher $p_{c'}$, its excess pore pressure response is closer to that of saturated soil, and the undrained shear strength is enhanced. This enhancement effect is more pronounced for higher u_{w0} values, as the reduction in bubble size reduces the shear shrinkage effect.

(3) Under the RTC path, the undrained shear strength (c_u) and excess pore pressure (Δu) of fine-grained gassy soils show a certain reduction compared with the CTC test. Quantitatively, the reduction in c_u is less than 10% while the reduction in Δu is about 33~39%. This may be mainly due to the reduction in the confining pressure in the shear process, leading to the exsolution and expansion of the gas and destroying the cavity structure, resulting in a reduction in the strength and an increase in the volume

fraction of the gas, which makes it easier for the phenomenon of bubble flooding to occur, decreasing the Δu.

(4) The detrimental effect of gas bubbles on the mechanical behavior of fine-grained gassy soils is most significant at shallow seabed depths (i.e., lower $p_{c'}$), deeper water regions (i.e., higher u_{w0}), and during excavations (i.e., unloading path).

(5) The constitutive model proposed by Hong et al. effectively simulates the mechanical response of fine-grained gassy soils under different u_{w0} and $p_{c'}$ values along the CTC path. However, the model exhibits relatively high prediction errors in capturing the stress–strain characteristics of gas-containing specimens under the RTC path and fails to effectively simulate changes in stress paths during unloading conditions. Further improvements are needed to address these limitations. Additionally, careful selection of parameters controlling the stress–shear relationship (ξ and χ) is crucial, as errors in predicting the mechanical behavior of fine-grained gassy soil in the early stages of the shear process can arise from these parameters.

Author Contributions: Conceptualization, T.L., C.Q. and J.Z.; methodology T.L. and J.C.; software, X.M.; validation, C.Q. and X.L.; formal analysis, T.L. and J.C.; investigation C.Q. and X.M.; resources, T.L., C.Q. and J.Z.; data curation, C.Q.; writing—original draft preparation, C.Q.; writing—review and editing, T.L., C.Q. and J.Z.; visualization, C.Q.; supervision, T.L. and J.Z.; project administration T.L.; funding acquisition, T.L. All authors have read and agreed to the published version of the manuscript.

Funding: This research was funded by the National Natural Science Foundation of China (NO. 42277139, NO. U2006213).

Institutional Review Board Statement: Not applicable.

Informed Consent Statement: Not applicable.

Data Availability Statement: The original contributions presented in this study are included in the article; further inquiries can be directed to the corresponding author.

Acknowledgments: The authors would like to thank Xiaotong Yang and Jun Han for their help during the experiment. Thanks to Shandong Engineering Research Center of Marine Exploration and Conservation for providing the test equipment.

Conflicts of Interest: Xiufen Ma was employed by Qingdao Robotfish Marine Technology Company Limited. The remaining authors declare that the research was conducted in the absence of any commercial or financial relationships that could be construed as a potential conflict of interest.

References

1. Fleischer, P.; Orsi, T.H.; Richardson, M.D.; Anderson, A.L. Distribution of free gas in marine sediments: A global overview. *Geo-Mar. Lett.* **2001**, *21*, 103–122. [CrossRef]
2. Grozic, J.L.H.; Robertson, P.K.; Morgenstern, N.R. Cyclic liquefaction of loose gassy sand. *Can. Geotech. J.* **2000**, *37*, 843–856. [CrossRef]
3. Boudreau, B.P.; Algar, C.; Johnson, B.D.; Croudace, I.; Reed, A.; Furukawa, Y.; Dorgan, K.M.; Jumars, P.A.; Grader, A.S.; Gardiner, B.S. Bubble growth and rise in soft sediments. *Geology* **2005**, *33*, 517–520. [CrossRef]
4. Sobkowicz, J.; Morgenstern, N. The undrained equilibrium behaviour of gassy sediments. *Can. Geotech. J.* **1984**, *21*, 439–448. [CrossRef]
5. Boetius, A.; Ravenschlag, K.; Schubert, C.J.; Rickert, D.; Widdel, F.; Gieseke, A.; Amann, R.; Jorgensen, B.B.; Witte, U.; Pfannkuche, O. A marine microbial consortium apparently mediating anaerobic oxidation of methane. *Nature* **2000**, *407*, 623–626. [CrossRef]
6. Floodgate, G.; Judd, A. The origins of shallow gas. *Cont. Shelf Res.* **1992**, *12*, 1145–1156. [CrossRef]
7. Jones, G.B.; Floodgate, G.; Bennell, J. Chemical and microbiological aspects of acoustically turbid sediments: Preliminary investigations. *Mar. Georesour. Geotechnol.* **1986**, *6*, 315–332. [CrossRef]
8. Judd, A.; Hovland, M. *Seabed Fluid Flow: The Impact on Geology, Biology and the Marine Environment*; Cambridge University Press: Cambridge, UK, 2009.

9. Barden, L. Consolidation of compacted and unsaturated clays. *Geotechnique* **1965**, *15*, 267–286. [CrossRef]
10. Duffy, S.M.; Wheeler, S.J.; Bennell, J.D. Shear modulus of kaolin containing methane bubbles. *J. Geotech. Eng. Asce* **1994**, *120*, 781–796. [CrossRef]
11. Johns, M.W. Geotechnical Properties of Mississippi River Delta Sediments Utilizing In Situ Pressure Sampling Techniques. Ph.D. Thesis, Texas A&M University, College Station, TX, USA, 1985.
12. Puzrin, A.M.; Tront, J.; Schmid, A.; Hughes, J.B. Engineered use of microbial gas production to decrease primary consolidation settlement in clayey soils. *Geotechnique* **2011**, *61*, 785–794. [CrossRef]
13. Wheeler, S.J.; Gardner, T.N. Elastic moduli of soils containing large gas bubbles. *Geotechnique* **1989**, *39*, 333–342. [CrossRef]
14. Nisbet, E.G.; Piper, D.J.W. Giant submarine landslides. *Nature* **1998**, *392*, 329–330. [CrossRef]
15. Riboulot, V.; Cattaneo, A.; Sultan, N.; Garziglia, S.; Ker, S.; Imbert, P.; Voisset, M. Sea-level change and free gas occurrence influencing a submarine landslide and pockmark formation and distribution in deepwater Nigeria. *Earth Planet. Sci. Lett.* **2013**, *375*, 78–91. [CrossRef]
16. Sultan, N.; Cochonat, P.; Foucher, J.P.; Mienert, J. Effect of gas hydrates melting on seafloor slope instability. *Mar. Geol.* **2004**, *213*, 379–401. [CrossRef]
17. Boudreau, B.R. The physics of bubbles in surficial, soft, cohesive sediments. *Mar. Pet. Geol.* **2012**, *38*, 1–18. [CrossRef]
18. Choi, J.H.; Seol, Y.; Boswell, R.; Juanes, R. X-ray computed-tomography imaging of gas migration in water-saturated sediments: From capillary invasion to conduit opening. *Geophys. Res. Lett.* **2011**, *38*, L17310. [CrossRef]
19. Guo, Z.; Liu, T.; Guo, L.; Su, X.; Zhang, Y.; Li, S. An experimental study on microscopic characteristics of gas-bearing sediments under different gas reservoir pressures. *Acta Oceanol. Sin.* **2021**, *40*, 144–151. [CrossRef]
20. Wheeler, S.J. The Stress-Strain Behaviour of Soils Containing Gas Bubbles. Ph.D. Thesis, University of Oxford, Oxford, UK, 1986.
21. Gao, Z.W.; Hong, Y.; Wang, L.Z. Constitutive modelling of fine-grained gassy soil: A composite approach. *Int. J. Numer. Anal. Methods Geomech.* **2020**, *44*, 1350–1368. [CrossRef]
22. Wheeler, S.J. The undrained shear strength of soils containing large gas bubbles. *Géotechnique* **1988**, *38*, 399–413. [CrossRef]
23. Hong, Y.; Wang, L.Z.; Ng, C.W.W.; Yang, B. Effect of initial pore pressure on undrained shear behaviour of fine-grained gassy soil. *Can. Geotech. J.* **2017**, *54*, 1592–1600. [CrossRef]
24. Gao, Z.; Cai, H.; Hong, Y.; Lu, D. A critical state constitutive model for gassy clay. *Can. Geotech. J.* **2021**, *59*, 1033–1045. [CrossRef]
25. Hong, Y.; Wang, L.Z.; Zhang, J.F.; Gao, Z.W. 3D Elastoplastic Model for Fine-Grained Gassy Soil Considering the Gas-Dependent Yield Surface Shape and Stress-Dilatancy. *J. Eng. Mech.* **2020**, *146*, 04020037. [CrossRef]
26. Hong, Y.; Wang, L.Z.; Yang, B.; Zhang, J.F. Stress-dilatancy behaviour of bubbled fine-grained sediments. *Eng. Geol.* **2019**, *260*, 105196. [CrossRef]
27. Sham, W.K. The Undrained Shear Strength of Soils Containing Large Gas Bubbles. Ph.D. Thesis, Queen's University Belfast, Belfast, UK, 1989.
28. Hight, D.; Leroueil, S. Characterisation of soils for engineering purposes. In *Characterisation and Engineering Properties of Natural Soils*; Balkema: Lisse, The Netherlands, 2003; Volume 1, pp. 255–362.
29. Lunne, T.; Berre, T.; Strandvik, S.; Andersen, K.; Tjelta, T. Deepwater sample disturbance due to stress relief. In Proceedings of the OTRC 2001 International Conference, Houston, TX, USA, 6–9 April 2001; pp. 64–85.
30. Sultan, N.; De Gennaro, V.; Puech, A. Mechanical behaviour of gas-charged marine plastic sediments. *Geotechnique* **2012**, *62*, 751–766. [CrossRef]
31. Dueck, Y.; Lorke, A.; Jokiel, C.; Gierse, J. Laboratory and field investigations on freeze and gravity core sampling and assessment of coring disturbances with implications on gas bubble characterization. *Limnol. Oceanogr. Methods* **2019**, *17*, 585–606. [CrossRef]
32. Zhang, R.T.; Tom, L. Deepwater sample disturbance due to stress relief. *Chin. J. Geotech. Eng.* **2003**, *25*, 356–360.
33. Sills, G.C.; Wheeler, S.J.; Thomas, S.D.; Gardner, T.N. Behavior Of Offshore Soils Containing Gas-Bubbles. *Geotechnique* **1991**, *41*, 227–241. [CrossRef]
34. Liu, T.; Yang, X.; Zhang, Y. A Review of Gassy Sediments: Mechanical Property, Disaster Simulation and In-Situ Test. *Front. Earth Sci.* **2022**, *10*, 915735. [CrossRef]
35. Ng, C.W.W.; Zhan, L.T.; Cui, Y.J. A new simple system for measuring volume changes in unsaturated soils. *Can. Geotech. J.* **2002**, *39*, 757–764. [CrossRef]
36. Esrig, M.I.; Kirby, R.C. Implications of gas content for predicting the stability of submarine slopes. *Mar. Georesour. Geotechnol.* **1977**, *2*, 81–100. [CrossRef]
37. Finno, R.J.; Zhang, Y.; Buscarnera, G. Experimental Validation of Terzaghi's Effective Stress Principle for Gassy Sand. *J. Geotech. Geoenviron. Eng.* **2017**, *143*, 04017092. [CrossRef]
38. Xu, H.-F.; Ying, H.-W.; Xie, X.-Y.; Xie, K.-H. Analysis on effective stress formula and consolidation of gassy muddy clay. *J. Cent. South Univ.* **2014**, *21*, 1594–1599. [CrossRef]

39. Xu, H.F.; Xie, K.H. Effective stress in soils under different saturation conditions. *J. Cent. South Univ. Technol.* **2011**, *18*, 2137–2142. [CrossRef]
40. Nakase, A.; Kamei, T. Undrained shear strength anisotropy of normally consolidated cohesive soils. *Soils Found.* **1983**, *23*, 91–101. [CrossRef]
41. Silva, I.N.; Indraratna, B.; Nguyen, T.T.; Rujikiatkamjorn, C. Shear behaviour of subgrade soil with reference to varying initial shear stress and plasticity index. *Acta Geotech.* **2022**, *17*, 4207–4216. [CrossRef]

Journal of
Marine Science and Engineering

MDPI

Article

Deformation Patterns and Control of Existing Tunnels Induced by Coastal Foundation Pit Excavation

Tao Liu [1,2], Yunlong Liang [1,3], Huadong Peng [1,*], Liucheng Yu [1,3], Tongju Xing [1,3], Yuanzhe Zhan [1,3] and Jianguo Zheng [1,2]

[1] Shandong Engineering Research Center of Marine Exploration and Conservation, Ocean University of China, Qingdao 266100, China; ltmilan@ouc.edu.cn (T.L.); liangyunlong9271@stu.ouc.edu.cn (Y.L.); yuliucheng@stu.ouc.edu.cn (L.Y.)
[2] Laboratory for Marine Geology, Qingdao Marine Science and Technology Center, Qingdao 266237, China
[3] Shandong Provincial Key Laboratory of Marine Environment and Geological Engineering, Ocean University of China, Qingdao 266100, China
* Correspondence: phd1214@163.com

Abstract: The rapid development of coastal cities has intensified land resource constraints and is leading to an increasing number of foundation pit projects near existing operational tunnels. This necessitates careful consideration of coastal excavation impacts on adjacent tunnels. Taking a foundation pit project in Qingdao as a case study, this paper investigates tunnel deformation through statistical analysis, numerical simulation, and field monitoring. By adjusting numerical model parameters, the research examines the influence of horizontal clearance distances, existing structure burial depths, and different retaining structure configurations on tunnel deformation, providing guidance for deformation control. Key findings include the following: (1) Statistical analysis reveals that tunnels in silty clay strata experience more significant excavation-induced deformation compared to those in silt strata, with relative positional relationships between pits and tunnels playing a critical role. (2) Numerical and monitoring results demonstrate that pit excavation induces tunnel displacement towards the excavation zone. Maximum lateral displacement reached 3.57 mm (simulated) and 4.79 mm (measured), while maximum vertical displacement was 3.11 mm (simulated) and 3.85 mm (measured), all within safety thresholds. (3) Sensitivity analysis shows that shallower tunnels exhibit more pronounced deformations. Increasing horizontal separation distance from 10 m to 25 m reduces deformation by one-third. However, adjusting diaphragm wall thickness and retaining structure embedment depth proves limited in deformation control, necessitating reinforcement measures on the tunnel side. These findings provide valuable references for protecting coastal silty clay stratum tunnels.

Keywords: coastal foundation pit; tunnel deformation; existing shield tunnel; control measures; silty clay stratum

1. Introduction

Coastal cities serve as critical transitional zones between continental and marine areas and are characterized by rapid economic development and increasingly severe challenges such as traffic congestion and land resource scarcity [1]. Efficient utilization of urban underground space has been identified as a key solution to these issues [2,3]. As a major coastal city in northern China, Qingdao has witnessed extensive construction of coastal metro foundation pits to meet urban development demands amid rapid urbanization

(Figure 1a). The impact of these coastal foundation pits on adjacent existing metro tunnels cannot be overlooked [4]. The soil layers in coastal areas exhibit characteristics such as low strength, low bearing capacity, lengthy consolidation processes, and weak permeability compared to typical geological formations [5]. Additionally, groundwater-level fluctuations caused by tidal action significantly influence foundation pit excavation (Figure 1b). These coastal soil layers demonstrate more complex deformation patterns than conventional strata, which may exert a more pronounced impact on adjacent existing subway tunnels.

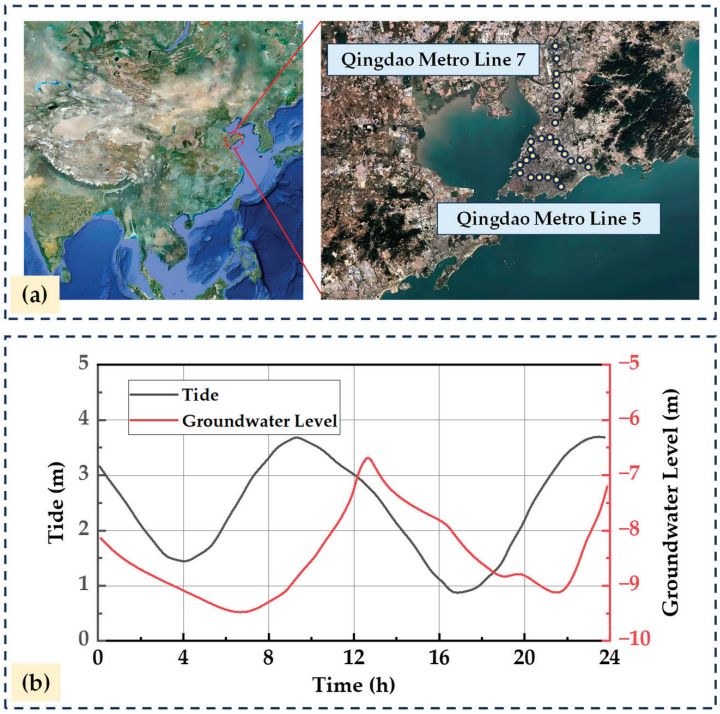

Figure 1. (**a**) Distribution map of metro foundation pits in the coastal area of Qingdao. (**b**) Groundwater level of a coastal foundation pit on Qingdao Metro Line 5.

Regarding the deformation and control of adjacent tunnels induced by foundation pit excavation, multiple scholars have conducted analyses based on various theoretical models. Liu B et al. [6] adopted a Winkler foundation beam–Timoshenko beam equivalent model [7], incorporating the shear effects of special soil layers, and revealed the additional stress distribution in adjacent tunnels caused by soil unloading during excavation. Liang et al. [8] derived the relationship between tunnel burial depth and subgrade reaction coefficients using a Euler–Bernoulli beam model, providing parametric references for subsequent studies. Fu Y et al. [9] investigated the impact of excavation on tunnels via a two-stage analytical method and validated the reliability of pile horizontal/vertical displacement calculations through engineering cases. Schweiger [10] systematically analyzed the differential impacts of excavation types, support methods, and excavation sequences on tunnel displacement and internal forces based on practical engineering. Additionally, Sun H et al. [11] demonstrated through theoretical and case comparisons that the longitudinal deformation of existing tunnels is predominantly governed by curvature parameters.

Numerous scholars have investigated the impact of foundation pit excavation on tunnels through experimental and simulation approaches. Bian X et al. [12] employed model tests to equate soil unloading during excavation to surface loading/unloading, revealing distinct deformation patterns between medium sand (unloading) and cohesive soil (loading). Wei G et al. [13] estimated effective approximations of tunnel segment

stiffness via model tests. Masayasu Hisatake [14] combined centrifuge tests with numerical simulations to validate the effectiveness of the circular excavation method in controlling tunnel deformation and ground settlement. Yu Z [15] designed centrifuge tests for weak soil layers and established a 3D model, quantifying the sensitivity of tunnel displacement at different positions to support structures and surrounding soil settlement. Additionally, Shi J [16] demonstrated through superplastic soil model simulations that optimizing tunnel structural parameters can mitigate displacements induced by soil unloading.

Numerous scholars have investigated the mechanical effects of foundation pit excavation on adjacent tunnels through numerical simulations. Li [16] utilized ABAQUS modeling to validate the controllability of the DAEM excavation scheme on existing tunnel deformation. Huang [10] employed 3D models to reveal the correlation between tunnel–pit spatial relationships, structural parameters, excavation depth, and displacement patterns. Shi [17,18] integrated excavation types and soil properties (stiffness and sand density) to predict the displacement and tensile thresholds of adjacent tunnels. Zhang [19] proposed a regression-based simplified model for maximum tunnel displacement, verifying its reliability with engineering monitoring data. Li et al. [20] developed a multi-phase, multi-parameter array-based simulation method for refined modeling of foundation pit excavation to assess impacts on adjacent buildings during excavation, while Zhuang Y [21] confirmed a significant positive correlation between lining stiffness and tunnel displacement. He et al. [22] combined field data from Fuzhou soft soil riverbank engineering with 3D numerical simulations to propose deformation control strategies for adjacent metro tunnels. Zhang et al. [23] employed 3D finite element models to analyze the deformation patterns of underlying pipelines induced by excavation. Additionally, Zhao et al. [24] implemented shaft excavation combined with friction pile–slab techniques for Shenzhen collinear long foundation pits, demonstrating effective suppression of tunnel heave and settlement.

Regarding field measurement studies, Zhang X et al. [25] established a longitudinal deformation–additional surrounding pressure model for shield tunnels based on real-time monitoring data during excavation, quantifying the variation patterns of segment internal forces. Niu Y et al. [26], focusing on a project adjacent to Shenzhen Metro Line 5, identified cracks/misalignment defects in shield segments caused by soil unloading and revealed the sensitivity of tunnel displacement to geological parameters. Zhang et al. [27] found through comparative analysis of field monitoring and numerical simulations that zoning and sectional excavation methods can effectively reduce displacement deformation in adjacent subway tunnels. Chen et al. [28,29] demonstrated that using the TRD (Trench Remixing Deep) method in adjacent excavation projects not only controls the impact of high confined groundwater but also meets deformation control requirements for track beds and precision standards of lining structures in shield tunnel design.

Current research on the deformation effects of foundation pit excavation on adjacent tunnels predominantly focuses on soft soil regions, while the influence mechanisms in coastal silty clay strata remain underexplored. This study takes a foundation pit excavation project in Qingdao City as a case study, combining numerical simulations with field measurements to investigate the impact of excavation processes on existing metro tunnels in typical coastal silty clay strata. The research aims to ensure the safe operation of the tunnel and provide a reference source for similar future engineering projects.

2. Materials and Methods

2.1. Project Overview

The proposed project involves a foundation pit in Qingdao City. As shown in Figure 2, the shield tunnel is located at the corner of the foundation pit, making its deformation

highly susceptible to the spatiotemporal effects of excavation. The pit covers an area of approximately 6204.6 m^2, with a depth ranging from 12.5 m to 14 m. Its dimensions are approximately 65 m in the east–west direction and 82 m in the north–south direction. During excavation, unevenly distributed artificial fill layers were encountered, with thicknesses varying between 2.7 m and 5.4 m. These layers primarily consist of construction debris and clay fill materials, characterized by complex composition and high compressibility. Beneath the artificial fill layers lie Quaternary strata and sedimentary layers formed by alluvial and diluvial processes. The geological composition mainly includes silty clay, silty clay interbedded with gravel, and cobble layers.

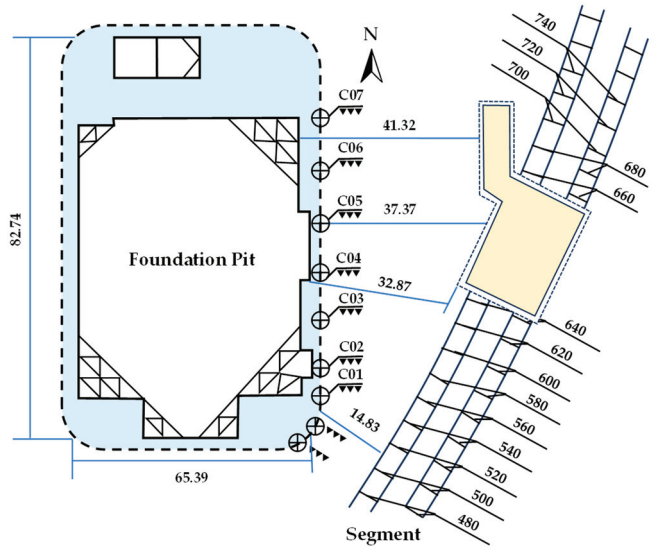

Figure 2. Schematic diagram of the location of a foundation pit and tunnel in Qingdao.

2.2. Test Method and Procedure

2.2.1. Statistical Evaluation of Tunnel Deformation Impacts

The impact of foundation pit construction on surrounding geotechnical bodies varies significantly across different strata in terms of disturbance range and intensity. In practical engineering scenarios, multiple factors, including excavation depth, horizontal clearance from existing structures, burial depth, diverse retaining systems, and geological conditions, collectively influence tunnel deformation patterns. This study therefore conducts statistical analysis on tunnel deformation data from typical soft soil region projects, aiming to investigate the effects of foundation pit excavation on existing tunnel deformations. The findings are expected to provide valuable insights for related research in coastal areas.

2.2.2. Numerical Simulation and Computation

This study employs MIDAS-GTS/NX 2021 software to conduct three-dimensional finite element calculations regarding the deformation of existing tunnels and corresponding control measures during foundation pit excavation construction. The study investigates tunnel displacement and bending moments in this engineering project. Furthermore, through parameter variations including horizontal clear distance between the foundation pit and tunnel, tunnel burial depth, and foundation pit enclosure structures (diaphragm wall thickness and embedment ratio of retaining structures), a sensitivity analysis is performed to examine the influence of critical factors on tunnel deformation.

The soil in the model adopts a modified Mohr–Coulomb constitutive material. By defining the unloading deformation modulus of the soil, the model simulates various foundation types, particularly silty soil and muddy soil strata. To mitigate the base heave

phenomenon caused by stress release during excavation, the unloading modulus was set to three times the loading modulus in the calculations. The soil parameters in the model adopted were simplified based on the engineering geological survey report. Strata with similar mechanical properties were merged, and the model was ultimately simplified into five layers. The mechanical parameters of the strata are listed in Table 1.

Table 1. Mechanical parameters of modeled soils.

Properties of the Soil	Unit Weight (kN/m^3)	Cohesion (kPa)	Friction Angle (°)	Elastic Modulus (kN/m^2)
Miscellaneous fill	19	10	18	5000
Silty clay	19.2	15	20	4830
Silty clay	19.3	37.5	18	5630
Silty clay with gravel	19.6	37.5	20	6270
Completely weathered diorite	20	45	20	25,000

Given the large dimensions of the excavation in this project, the bored pile retaining structure was converted into a diaphragm wall using the equivalent stiffness method for simplified calculations. The conversion formula is as follows [30]:

$$h = 0.838D\sqrt[3]{\frac{D}{(D+t)}}$$

where h is the thickness of the equivalent diaphragm wall, m; D is the pile diameter, m; and t is the clear spacing between piles, m.

The equivalent diaphragm wall thickness is calculated to be 0.8 m.

In the numerical simulation analysis, the supporting structures—such as diaphragm walls and ground anchors, as well as shield tunnel linings—are categorized into distinct structural types and modeled using elastic constitutive models to describe their behavior. For diaphragm walls, which exhibit plate-like characteristics, plate elements are selected for simulation. The tunnel structure, due to its three-dimensional geometry, is simulated with solid elements. Horizontal struts in the excavation are modeled using beam elements to accurately capture their lateral load-bearing capacity. Ground anchors are represented through embedded truss models, which effectively describe the interaction between the anchors and surrounding soil. All parameters required for these simulations—including material properties and dimensions—are configured based on the data provided in Table 2 to ensure the accuracy of the results.

Table 2. Structural element parameters.

Structures	Element Type	Elastic Modulus (GPa)	Poisson's Ratio
Shield segment	Plate	34.5	0.2
Diaphragm wall	Plate	30	0.2
Internal strut	Beam	30	0.2
Ground anchor	Embedded Truss	210	0.3

The model establishes a coordinate system with the center of the excavation as the origin. To mitigate boundary effects, the model boundaries were set at 3 to 5 times the excavation width in depth. Considering the relative positional relationships of the tunnel, the X-axis direction was defined as 200 m, the Y-axis direction as 200 m, and the Z-axis

direction as 50 m. To simulate potential boundary conditions in actual engineering, horizontal displacement constraints were applied to the lateral sides of the model, vertical constraints to the bottom, and the top boundary was set as free. The mesh generation of the model is illustrated in Figure 3a, with detailed meshing of the shield tunnel and excavation support structures shown in Figure 3b. This meshing approach facilitates precise capture of structural interactions and their mechanical responses under loading.

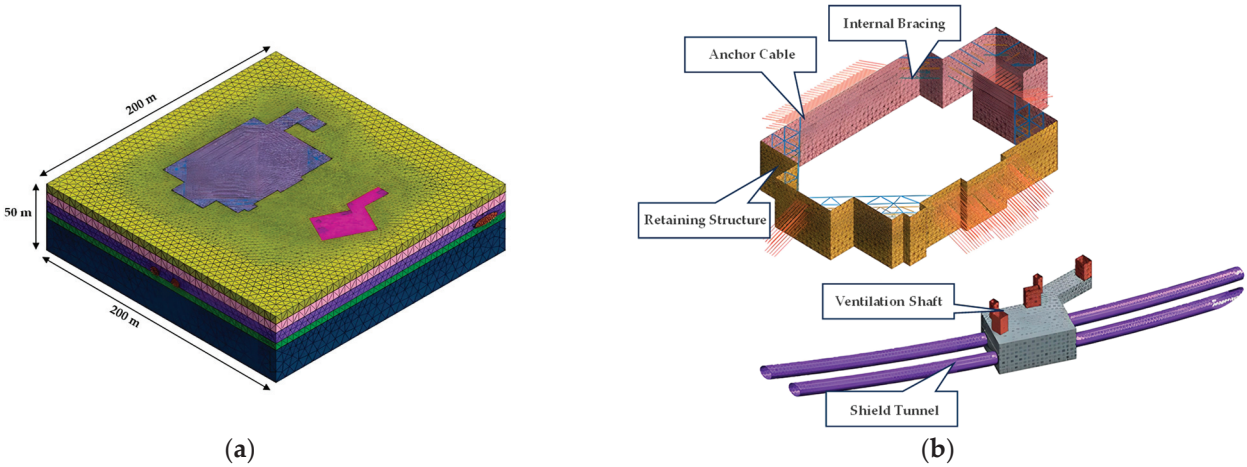

Figure 3. Mesh generation of the numerical computational model: (**a**) integrated model and (**b**) shield tunnel and excavation supporting structures.

2.2.3. Field Measurement Study

The advantages of the field measurement method lie in its authenticity and reliability. Through actual monitoring, the most accurate field data can be obtained to evaluate the practical impacts of foundation pit excavation on existing tunnels. Based on the affected zone in this project, displacement analysis of shield tunnels during different construction phases was conducted. The configuration of monitoring cross-sections is illustrated in Figure 2. The layout of monitoring points within tunnel cross-sections is shown in Figure 4.

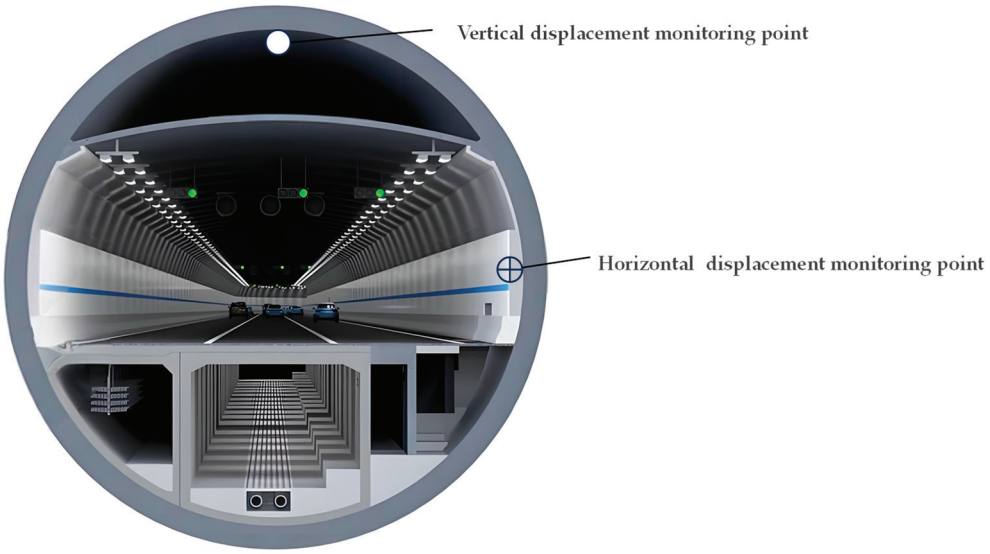

Figure 4. Layout of tunnel cross-section monitoring points.

Simultaneously determining appropriate monitoring control values and warning thresholds for surveillance items is a comprehensive process that requires consideration of

specific project conditions and relevant construction specifications. Through consultation between the construction unit and the monitoring unit, the finalized monitoring plan is shown in Table 3.

Table 3. Tunnel structural monitoring control values.

Monitoring Items	Control Values		
	Accumulated Values	Variation Rate	Alert Thresholds
Horizontal displacement	5 mm	1 mm/d	10 mm
Vertical displacement	5 mm	1 mm/d	10 mm
Total displacement	5 mm	1 mm/d	10 mm

3. Results

3.1. Results of the Statistical Evaluation of Tunnel Deformation Impacts

Statistical analysis was conducted on tunnel deformation characteristics in 30 foundation pit projects adjacent to existing tunnels within typical soft soil regions, with partial data summarized in Table 4 [31].

Table 4. Partial list of foundation pit projects adjacent to tunnels [31].

Foundation Pit Project	Excavation Depth (m)	Relative Position to Tunnel	Minimum Clear Distance (m)	Tunnel Deformation (Max. Uplift, mm)	Main Stratigraphic Conditions
A foundation pit adjacent to Hangzhou metro Station	16.8	Tunnel above the side of the pit	9.3	−7.8	Sandy silt
Hangzheng storage plots 86-1,2	15.8	Tunnel above the side of the pit	4.5	+9.0	Sandy silt
Jianggan district Weidong pit, Hangzhou	12.55	Tunnel above the side of the pit	17.3	+5.3	Clayey silt
A building foundation pit, Jianggan district, Hangzhou	5.7	Tunnel below the side of the pit	24	+3.1	Clayey silt
Xiasha economic zone pit, Hangzhou	11.8	Tunnel below the side of the pit	11	−4.5	Sandy silt
Hangzheng storage plot No. 16	10.7	Tunnel below the side of the pit	10.5	−4.4	Silty clay
Shanghai Dongfang Road interchange project	6.5	Up/Down Tunnels in Sections No. 1/No. 2	2.76	Up: +11.56, Down: +12.3	Silty clay
Shanghai East-West underground express tunnel (Pudong Section)	10.2	45° diagonally crossing below the pit	4	Up: +12.10, Down: +14.20	Silty clay
Nanjing Longpan Road tunnel (South Section) West Pit	7.9	70° diagonally crossing below the pit	Left 2.73, Right 2.15	Left: +3.20, Right: +5.50	Silty clay
Tianjin West Station underground tunnel	4.75	Below existing metro box structure	0.3	Cumulative uplift: +8.10	Silty clay

The statistical results revealed a maximum excavation depth of 17.3 m, a minimum depth of 4.75 m, and an average depth of 10.2 m. Among these projects, 70% exhibited vertical tunnel deformations below 10 mm, with the maximum vertical deformation not exceeding 16 mm. Geographically, 47% of the projects were situated in silt layers, while 50% were in silty clay layers. Notably, 93% of projects in silt layers demonstrated deformations below 10 mm, compared to only 40% in silty clay layers. This disparity suggests that existing tunnels in silty clay are more significantly affected by adjacent excavations than those in silt. Mechanistically, silt's low cohesion renders it highly susceptible to disturbance, whereas silty clay—with its high water and clay contents and plasticity—exhibits greater deformation resistance under specific conditions. The observed statistical variations arise from regional geological heterogeneity and additional factors such as the relative position, horizontal distance, and burial depth between excavations and tunnels. Therefore, a comprehensive sensitivity analysis integrating these variables is essential for accurate risk assessment and mitigation.

3.2. Analysis of Numerical Simulation Results

3.2.1. Numerical Simulation Results of Field Working Conditions

Based on the parameters from Section 2 and the established site condition model, the influence of foundation pit excavation on the bending moments of shield tunnels obtained through phased excavation is illustrated in Figure 5, revealing that after the completion of the first soil layer excavation the bending moments at the crown and invert of the shield tunnel decreased, while those at the haunches increased. However, the overall variation in bending moments was not significant, with changes limited to approximately 5 kN·m. Following the second soil layer excavation, the bending moment changes slightly increased compared to the first excavation stage. These observations indicate that during the early stages of foundation pit excavation, the impact on the shield tunnel remains relatively minor. After the third and fourth soil layer excavations, the bending moments at various points of the tunnel gradually increased and exhibited specific patterns. Bending moments at the haunches increased significantly, while bending moments at the crown and invert decreased. Adjacent points to the crown and invert showed slightly larger bending moments, while other points exhibited smaller values. The tunnel's long axis elongated, and the short axis shortened, resulting in a "flattened duck egg" shape (compressed vertically and elongated horizontally). Upon completion of the foundation pit excavation, the bending moments further expanded. The "flattened duck egg" shape became more elongated, with bending moments at the top, bottom, left, and right points fluctuating around 80 kN·m. Since the bending moment value is significantly less than the design bending moment value, the entire foundation pit excavation process will not induce durability-related cracking in the tunnel segments.

The displacement response of shield tunnels induced by foundation pit excavation is illustrated in Figure 6. As shown in Figure 6a, during the first two excavation stages, tunnel displacements preferentially develop toward the excavation side with magnitudes below 1 mm. Commencing with the third excavation stage, displacement magnitudes exhibit progressive amplification, particularly demonstrating maximum offset in the upper-right quadrant. Post-excavation monitoring reveals significant horizontal displacement expansion, where left-side displacements (maximum 3.57 mm at point 3) systematically exceed right-side values (minimum 0.2 mm at point 11), confirming non-uniform deformation characteristics.

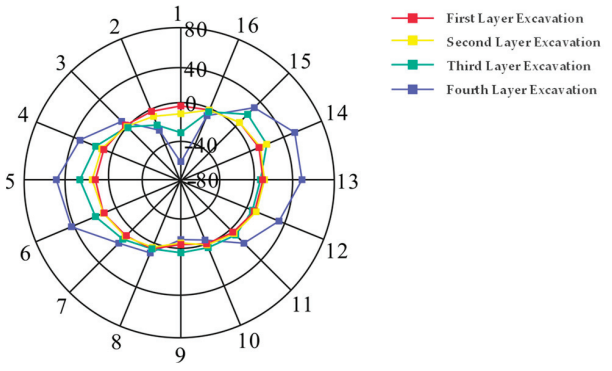

Figure 5. Variation of tunnel bending moments for field conditions. The radial coordinate denotes the bending moment (kN·m), and the circumferential coordinate indicates the measurement point ID.

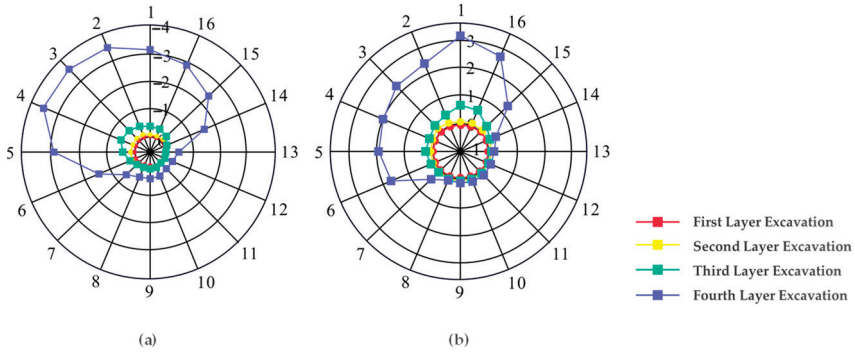

Figure 6. Variation of tunnel displacement under field conditions. The radial coordinate denotes displacement and the circumferential coordinate indicates measurement point ID. (**a**) Horizontal displacement. (**b**) Vertical displacement.

Figure 6b delineates the evolutionary pattern of vertical displacements. Initial excavation phases (Stages 1–2) induce generalized heave with limited magnitude (<0.8 mm). Transitioning to Stage 3, differential vertical movements emerge with crown settlement and invert heave developing synchronously, though constrained within 1.2 mm. Final excavation completion triggers predominant subsidence, particularly above the demarcation line connecting Points 6–14, where maximum settlement reaches 3.11 mm at Point 1. Contrastingly, displacements below this boundary remain sub-0.5 mm (minimum 0.2 mm at Point 8), establishing pronounced vertical deformation heterogeneity.

3.2.2. Influence of Horizontal Clear Distance Between Foundation Pit and Tunnel

Under constant conditions for other factors, this study set horizontal clear distances between the foundation pit and tunnel at 10 m, 15 m, 20 m, and 25 m to observe the impact of excavation on adjacent tunnel deformation.

Based on the analysis in Figure 7, it can be observed that as the excavation depth of the foundation pit increases, the horizontal clear distance between the pit and the tunnel also increases, leading to a gradual reduction in both the total and vertical displacements of the tunnel. During the initial stages of excavation (e.g., at depths of 3 m and 6 m), the horizontal displacement of the tunnel initially increased and then gradually decreased with an increase in the horizontal clear distance. Notably, the maximum displacement occurred at a horizontal clear distance of 15 m, after which displacement began to diminish. This phenomenon primarily arises because the increasing horizontal clear distance alters the spatial angle between the tunnel and the excavation center as excavation progresses. These angular changes influence the force distribution and displacement patterns acting on the

tunnel, thereby driving the observed displacement trends. In summary, increasing the horizontal clear distance between the foundation pit and the tunnel effectively mitigates displacement during excavation.

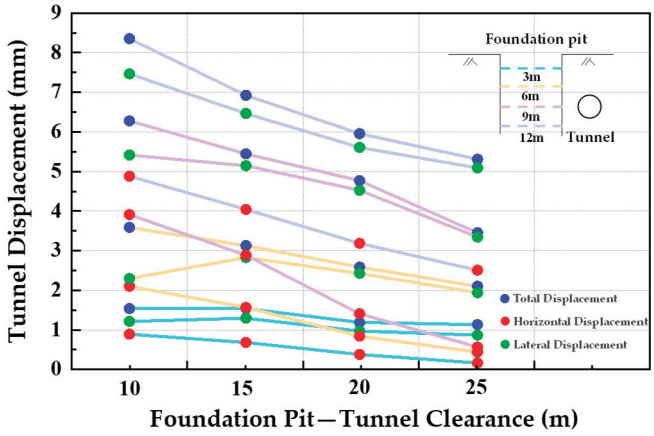

Figure 7. Influence of horizontal clear distance on the central displacement of the tunnel.

3.2.3. Influence of Tunnel Burial Depth

Two numerical models were established with a fixed horizontal clear distance of 7.4 m between the tunnel and foundation pit, and tunnel burial depths of 10 m and 15 m, respectively. Based on prior analyses indicating negligible tunnel deformation during the first two excavation stages, this study focused on the third and fourth excavation layers to investigate the impact of tunnel burial depth on shield tunnel behavior.

A comparative analysis of bending moment variations in tunnels with different burial depths in the same excavation layer (as shown in Figure 8) reveals that tunnels with shallower burial depths are more sensitive to excavation impacts. For the tunnel with a burial depth of 10 m, during the third excavation layer compression and tension phenomena began to emerge, and in the fourth excavation layer significant tension was observed at the left and right ends of the shield tunnel, accompanied by pronounced compression at the crown and invert. In contrast, for the tunnel with a burial depth of 15 m, compression effects during the third excavation layer were negligible, and while bending moment changes increased substantially in the fourth layer they remained smaller than those for the 10 m burial depth. This indicates that the bending moments at all tunnel sections for the 10 m burial depth consistently exceeded those for the 15 m burial depth across excavation stages. As excavation progressed from the third layer onward, the lateral bending moments of the shield tunnel increased, while vertical bending moments exhibited a decreasing trend. The tunnel displayed marked tension at its left and right ends and significant compression at the crown and invert, forming a distinct "flattened duck egg" shape. This deformation pattern became even more pronounced following the completion of the fourth excavation layer.

An analysis of displacement variations in tunnels with different burial depths during each excavation stage (Figure 9) reveals that tunnels with shallower burial depths are more significantly affected by foundation pit excavation, exhibiting more pronounced displacement changes. As the excavation progresses, displacements at all tunnel points gradually increase, reaching their maximum variations at the completion of excavation. Furthermore, a demarcation line connecting Points 6–14 highlights that both horizontal and vertical displacements on the upper-right side of the tunnel exceed those on the lower-left side, resulting in non-uniform displacement distribution. The settlement deformation of the tunnel predominantly orients toward the excavation side, emphasizing the spatial bias in displacement patterns.

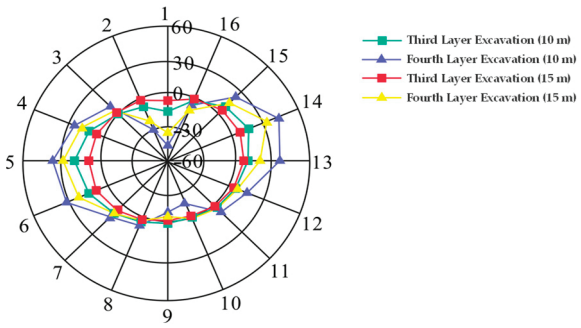

Figure 8. Variation of bending moments in tunnels with different excavation depths. The radial coordinate denotes bending moment (kN·m), and the circumferential coordinate indicates the measurement point ID.

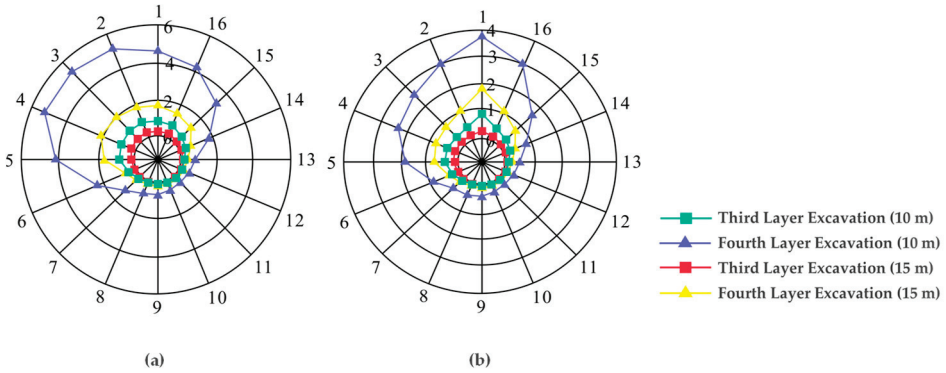

Figure 9. Variation of tunnel displacement for different excavation depths. The radial coordinate denotes displacement; and the circumferential coordinate indicates measurement point ID. (**a**) Horizontal displacement. (**b**) Vertical displacement.

3.2.4. Influence of Diaphragm Wall Thickness

The retaining pile structure of foundation pits exhibits a strong correlation in deformation with adjacent existing subway tunnels, where variations in diaphragm wall thickness significantly influence the deformations of both the excavation and tunnels. This section employs the aforementioned numerical model to analyze the influence of diaphragm wall thickness on the deformations of the foundation pit and tunnels.

Analysis of the data in Figure 10 shows that when the thickness of the diaphragm wall increases from 0.8 m to 1.2 m, the surface settlement decreases from 16.9 mm to 6.3 mm (a reduction of 62.7%), and the horizontal displacement of the diaphragm wall decreases from 24.7 mm to 14.6 mm (a reduction of 40.9%). This indicates that increasing the thickness of the diaphragm wall significantly enhances the control of foundation pit deformation. However, when comparing the maximum base heave of the foundation pit, it is found that as the diaphragm wall thickness increases, the maximum base heave decreases only slightly from 36.5 mm to 33.2 mm, representing a mere 9% reduction. This suggests that variations in diaphragm wall thickness have limited effectiveness in controlling base heave. This phenomenon may be attributed to the fact that base heave is influenced by other factors, such as soil properties and the support system of the foundation pit, which remained unchanged in this study.

Following the completion of foundation pit excavation, observation of the data in Figure 11 reveals that as the thickness of the diaphragm wall increases from 0.8 m to 1.2 m, the total displacement, horizontal displacement, and vertical displacement of the tunnel all exhibit a downward trend, albeit with relatively minor reductions. Specifically, the total displacement decreases by 12.7%, horizontal displacement by 9.6%, and vertical

displacement by 12.1%, none of which represent substantial reductions. This indicates that altering the thickness of the diaphragm wall has limited effectiveness in controlling tunnel displacement deformation.

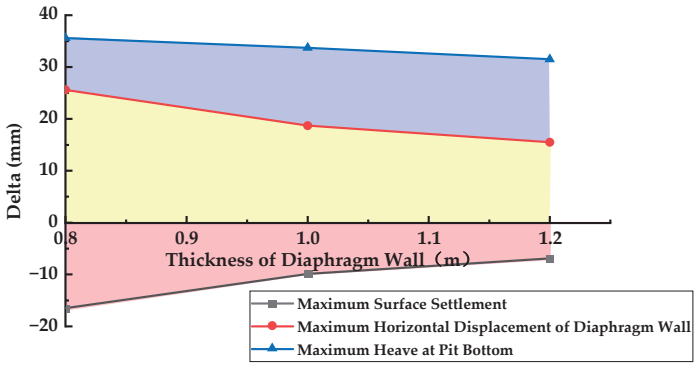

Figure 10. Influence of diaphragm wall thickness on foundation pit deformation.

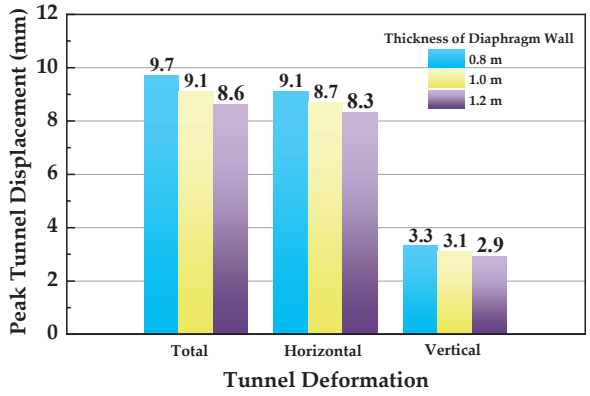

Figure 11. Influence of diaphragm wall thickness on tunnel deformation.

Therefore, in practical foundation pit excavation projects, selecting an appropriate thickness for the diaphragm wall is crucial. This approach not only ensures the safety of adjacent tunnels but also achieves cost-effectiveness. Comprehensive consideration of all factors reveals that a diaphragm wall thickness of 1.0 m provides a relatively optimal balance between controlling excavation-induced deformations and minimizing economic costs. This implies that excessively increasing the diaphragm wall thickness during design and construction is unnecessary, as a 1.0 m thickness effectively balances economic efficiency and structural safety.

3.2.5. Influence of Retaining Structure Embedment Ratio

The embedment ratio of retaining structures is introduced to analyze the deformation impact on adjacent metro tunnels after the completion of foundation pit excavation. Based on the computational model mentioned above, calculations were performed for embedment ratios of 0.8, 1.0, 1.2, and 1.4.

As shown in Figure 12, both surface settlement and horizontal displacement of the diaphragm wall are notably influenced, with significant base heave observed at the foundation pit bottom. When the embedment ratio of the retaining structure increases from 0.8 to 1.2, the surface settlement decreases by 11.4%, the maximum horizontal displacement of the diaphragm wall decreases by 8.2%, and the maximum base heave reduces by 5.2%. While increasing the embedment ratio positively controls surface settlement, base heave, and maximum horizontal displacement of the diaphragm wall, the rate of deformation reduction

slows progressively. These results demonstrate that modifying the embedment ratio of retaining structures has limited effectiveness in mitigating excavation-induced deformations.

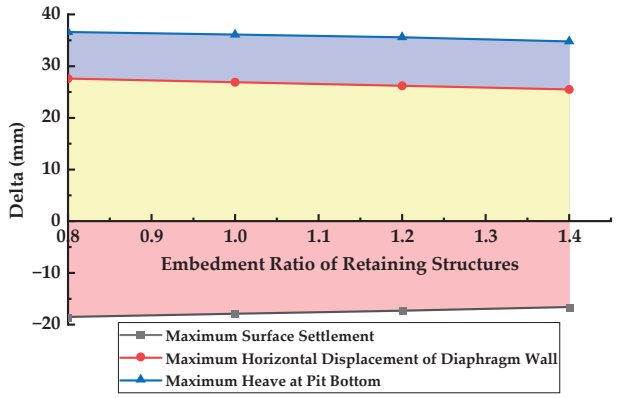

Figure 12. Influence of retaining structure embedment ratio on foundation pit deformation.

As the embedment ratio of the retaining structure varies, the displacement deformation of the tunnel remains relatively minor (Figure 13). When the embedment ratio increases from 0.8 to 1.4, the total displacement changes by 0.4 mm (a variation magnitude of 4.1%), the horizontal displacement increases by 0.5 mm (4.1%), and the vertical displacement decreases by 0.6 mm (8.8%). These results indicate that altering the embedment ratio of the retaining structure exerts moderate effectiveness in controlling the deformation of adjacent tunnels, yet the overall impact on tunnel displacement mitigation remains limited.

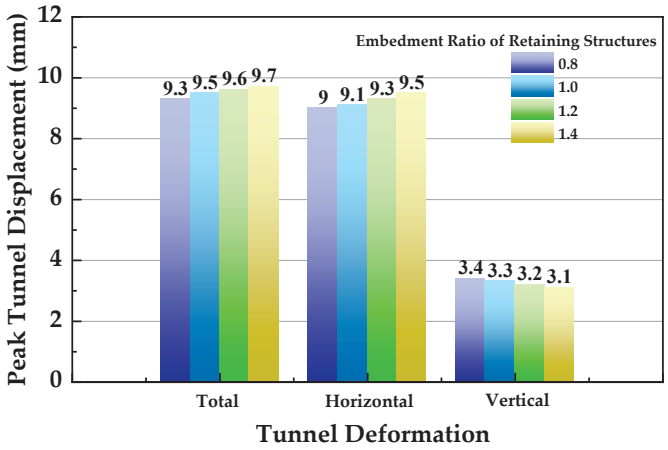

Figure 13. Influence of retaining structure embedment ratio on tunnel deformation.

Based on a comprehensive comparison, under the premise of ensuring excavation stability, adjusting the thickness of the diaphragm wall and the embedment ratio of the retaining structure has a significant impact on controlling foundation pit deformation, but exhibits relatively minor influence on controlling the deformation of adjacent tunnels.

3.3. Analysis of Field Measurement Data

3.3.1. Vertical Displacement Analysis of Shield Tunnel

Figure 14 shows the vertical settlement variation curves of the tunnel during different construction stages. As observed from the figure, slight upward displacement (maximum approximately 1 mm) occurred in the tunnel during the construction of the retaining structure. This phenomenon is primarily attributed to disturbances in the stable underground soil layers caused by retaining structure construction activities, resulting in tunnel uplift.

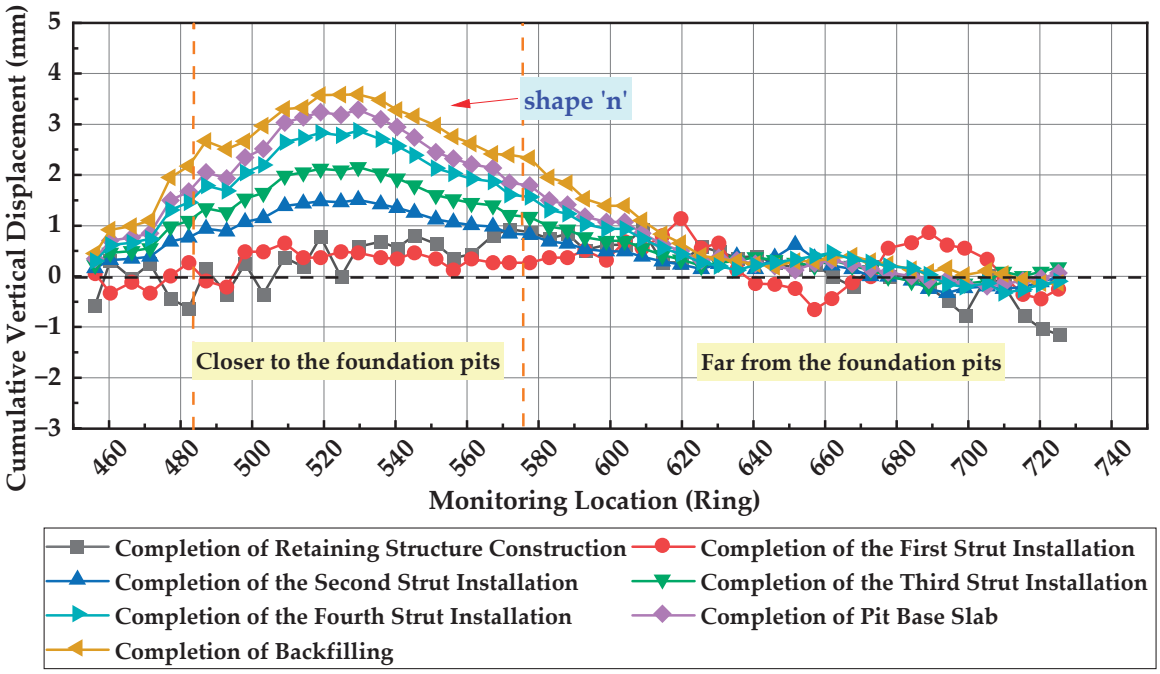

Figure 14. The vertical settlement variation curves of the tunnel during different construction stages.

Following foundation pit excavation completion, the tunnel deformation pattern transitioned to settlement, exhibiting a characteristic "n"-shaped heave profile where uplift zones predominantly concentrated on the pit-proximal side. The maximum tunnel heave induced by excavation reached 3.85 mm at the closest ring (Ring 530) to the pit, with the heave zone spanning Rings 480–575. This indicates that the influence range of foundation pit excavation on adjacent tunnels extends approximately 114 m.

3.3.2. Shield Tunnel Horizontal Displacement Analysis

Figure 15 presents the horizontal displacement curves of the tunnel across various construction phases. Positive values indicate tunnel displacement away from the foundation pit, while negative values correspond to displacement towards the pit.

Following the completion of retaining structure construction, tunnel horizontal displacements remained within ±1 mm, indicating negligible deformation. As excavation proceeded, these displacements transitioned from positive to negative values with progressive escalation. This phenomenon is primarily attributed to stress relief in the soil mass due to pit unloading, which reduced lateral earth pressure on the tunnel segment adjacent to the excavation zone, consequently inducing inward deformation toward the pit.

During backfilling operations, horizontal displacements exhibited cumulative growth, peaking at near 6 mm upon completion of the pit base slab casting. Although displacements gradually stabilized post-backfilling, persistent monitoring remained crucial throughout this phase due to continued deformation risks.

The finalized horizontal displacement profile manifested a distinct "√"-shaped curve characterized by significantly amplified displacements (approaching 6 mm) with rapid deformation rates in pit-proximal tunnel segments, and progressively diminished displacements and decelerated deformation rates in distal sections. Maximum horizontal displacement occurred precisely at the tunnel location nearest to the excavation boundary.

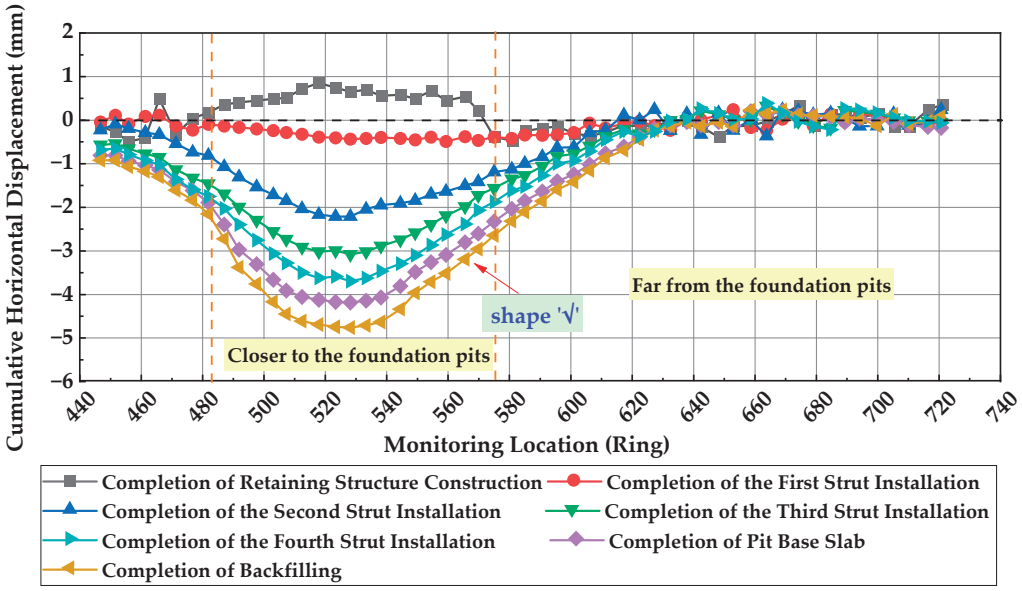

Figure 15. The horizontal displacement curves of the tunnel across various construction phases.

4. Discussion

4.1. Analysis of Tunnel Deformation

Through the combined analysis of numerical simulation and field measurement data, the deformation influence patterns of coastal silty clay foundation pit excavation on adjacent existing tunnels were derived. As excavation progressed, the horizontal displacement of shield tunnels consistently developed towards the pit side, gradually increasing with excavation depth while exhibiting uneven transverse displacement variations. The maximum simulated horizontal displacement reached 3.57 mm, compared with a measured value of 4.79 mm. Regarding vertical displacement, monitoring points initially displayed an upward heave trend during early excavation stages, transitioning to subsidence after pit completion. The maximum simulated vertical displacement was 3.11 mm versus a measured 3.85 mm. Within the same monitoring plane, vertical displacements demonstrated bias towards the pit side, mirroring horizontal displacement patterns.

This trend aligns with observations reported in Reference [32]. The settlement non-uniformity primarily stems from stress redistribution in soil layers within a limited range around the excavation pit during deep excavation, which induces strain redistribution. This process triggers deformation of retaining structures, base heave at the pit bottom, and subsequent displacement of external soils, ultimately leading to tunnel deformation. When the retaining structure displacement is minor, the frictional resistance between the structure and surrounding soil effectively constrains surface settlement, resulting in smaller subsidence near the retaining walls. However, when retaining structure displacement becomes significant, this frictional resistance loses its restraining capacity, leading to pronounced subsidence near the external side of the retaining structure. Additionally, deformation of protective structures expands the elastic zone in external soils, enhancing soil movement toward the pit interior and exacerbating base heave. As excavation scope and depth increase, these effects progressively propagate through soil layers before transferring to adjacent tunnels and strata. During deep excavation, strain transmission occurs from the pit periphery toward excavated soils, while ground deformation propagates outward from excavated zones. This mechanism ultimately drives shield tunnel displacement toward the excavation side, as shown in Figure 16.

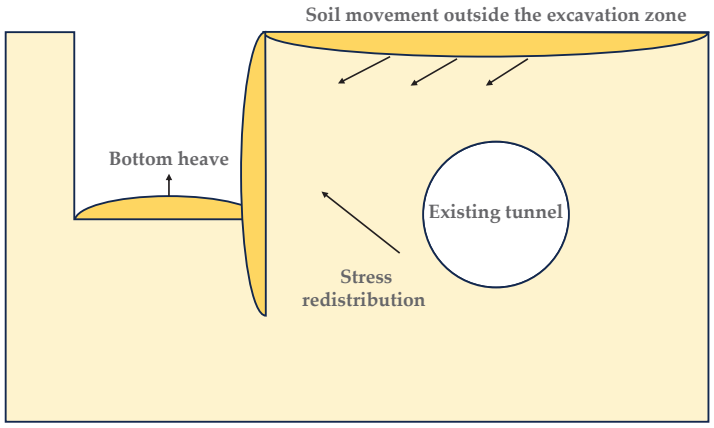

Figure 16. Deformation and stress variation patterns in adjacent tunnels induced by foundation pit excavation and unloading.

4.2. Sensitivity Analysis of Key Factors

The field-measured data in this study validated the accuracy of the numerical model. By adjusting parameters in the numerical simulation, the research investigated the effects of various factors including horizontal clear distance, burial depth of existing structures, and different retaining systems of foundation pits on tunnel deformation. Furthermore, it systematically analyzed the influence mechanisms of coastal foundation pit excavation on the deformation patterns of adjacent existing tunnels.

The influences of various factors on total tunnel displacement after foundation pit excavation are illustrated in Figure 17. As shown in the figure, all parameters exert varying degrees of influence on tunnel deformation. The maximum total displacement of shield tunnels progressively decreases with increasing horizontal clear distance between pit and tunnel, while simultaneously demonstrating a decreasing trend with greater tunnel burial depth. Regarding the pit's retaining system, adjusting diaphragm wall thickness and embedment ratio can partially mitigate the maximum tunnel displacement. However, the mitigation extent remains limited. Practical engineering should adopt holistic consideration of tunnel displacement thresholds and economic factors when selecting parameters. Due to experimental constraints, this study primarily investigated deformation patterns of adjacent shield tunnels in coastal silty clay through numerical simulations, with more comprehensive multivariate analysis and field validation requiring further research.

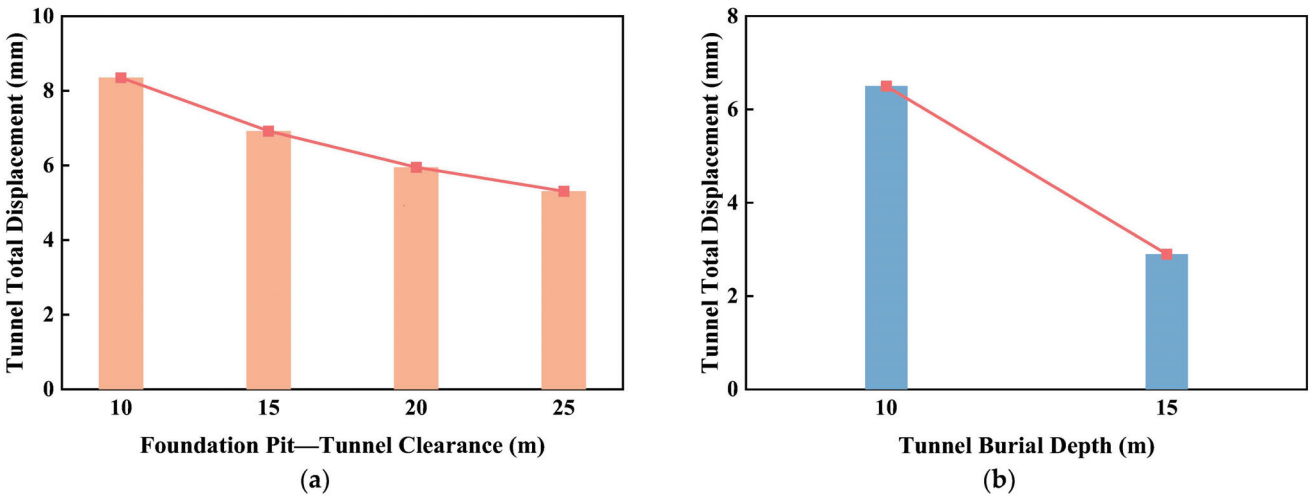

Figure 17. *Cont.*

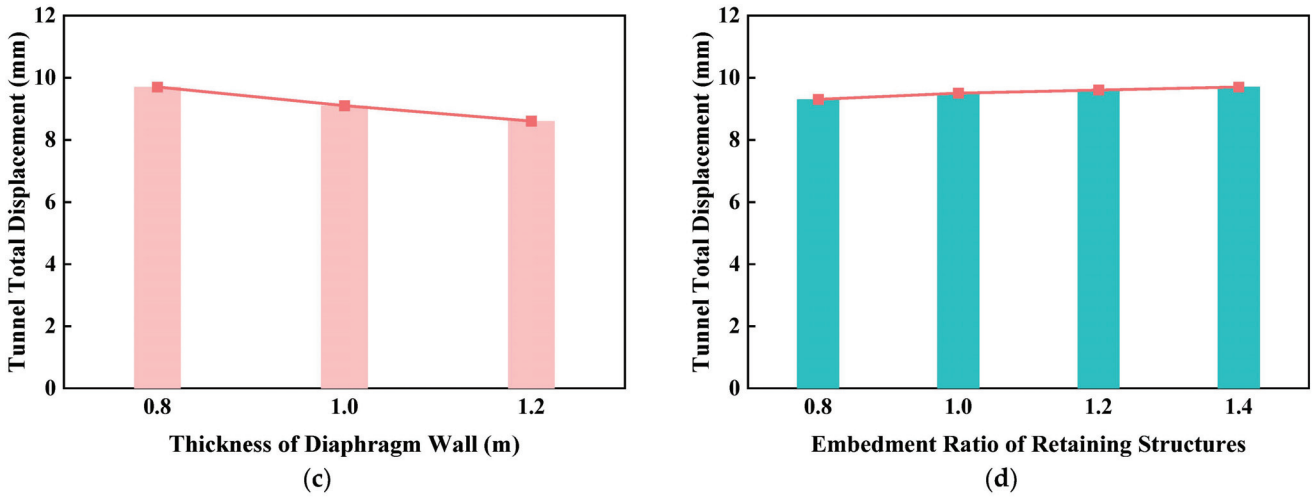

Figure 17. Impact analysis of key geological and construction factors on tunnel deformation. (**a**) Foundation pit–tunnel clearance. (**b**) Tunnel burial depth. (**c**) Thickness of diaphragm wall. (**d**) Embedment ratio of retaining structures.

5. Conclusions

Based on a foundation pit excavation project in Qingdao City, this study investigates the deformation patterns of adjacent existing tunnels induced by pit excavation through integrated approaches including statistical analysis, numerical simulation, and field monitoring. Sensitivity analysis was performed on critical factors influencing tunnel deformation to provide practical insights for deformation prevention and control. The main conclusions are as follows:

(1) Analysis of 30 excavation cases near existing tunnels in different soft strata indicates that tunnels in silt strata exhibit deformation magnitudes below 10 mm with higher frequency compared to those in silty clay strata, suggesting greater susceptibility of tunnels in silty clay to adjacent excavations. Considering regional geological variations and influential factors including relative positioning, separation distance, and burial depth between excavations and existing tunnels, comprehensive sensitivity analysis incorporating multiple parameters is recommended.

(2) With increasing excavation depth, both bending moments and displacements of adjacent tunnels progressively intensify. During initial excavation stages, tunnel deformations remain relatively minor. Upon completion of excavation, lateral bending moments increase while vertical bending moments decrease, forming a horizontal oval bending moment distribution pattern. The tunnel demonstrates a global tendency to displace towards the excavation zone.

(3) Monitoring data confirm that excavation-induced stress relief drives deep soil movement towards the pit, consequently displacing shield tunnels in the same direction. Both vertical and horizontal tunnel displacements progressively accumulate during excavation, exhibiting magnitude–distance correlation. Maximum tunnel settlement (3.85 mm) occurs at Ring 530 nearest to excavation, with the affected zone extending approximately 114 m. Maximum horizontal displacement approaches 5 mm, satisfying relevant code requirements. These findings provide scientific references for deformation control in existing tunnels within coastal silty clay strata.

(4) Sensitivity analysis of tunnel deformation in coastal silty clay. Within the same stratum, the horizontal clear distance between the excavation pit and the tunnel exerts significant influence on tunnel deformation. When the excavation is completed, the

deformation of tunnels spaced 10 m apart increases by one-third compared to those spaced 25 m apart. The displacement vectors of the tunnel rotate counterclockwise from the upper left, with the maximum displacement gradually approaching the left haunch of the tunnel arch. Furthermore, tunnel burial depth also demonstrates notable impacts on displacement—shallower tunnels experience more severe deformation and greater displacement under excavation effects. However, under stable excavation conditions, modifying diaphragm wall thickness and the embedment ratio of pit retaining structures show limited effectiveness in controlling adjacent tunnel deformation. Additional measures targeting the tunnel side are required for effective deformation control. Field measurements are also necessary to further validate the sensitivity factors affecting tunnel deformation in coastal silty clay environments.

Author Contributions: Data curation, Y.L.; funding acquisition, T.L. and H.P.; investigation, Y.L., L.Y., Y.Z. and T.X.; methodology, Y.L. and J.Z.; project administration, Y.L., H.P., T.L. and J.Z.; writing—original draft, Y.L.; writing—review and editing, Y.L., H.P., L.Y. and T.L. All authors contributed to the article and approved the submitted version. All authors have read and agreed to the published version of the manuscript.

Funding: This research was funded by the Laoshan Laboratory (LSKJ202203500) and the National Natural Science Foundation of China (NO.42277139, NO.U2006213).

Data Availability Statement: The data used to support the findings of this study are included in the article.

Acknowledgments: The authors would like to thank Tongju Xing and Yuanzhe Zhan for their help during the experiment. Thank you to the Laoshan Laboratory and the National Natural Science Foundation of China for funding the project. Thanks to Shandong Engineering Research Center of Marine Exploration and Conservation for providing the test equipment.

Conflicts of Interest: The authors declare no conflicts of interest.

References

1. Tian, P.; Wang, Z.; Li, J.; Cao, L.; Liu, Y.; Zhang, H.; Ai, S. Spatiotemporal characteristics and driving mechanism of high-intensity development of continental coastal zones in the East China Sea. *Geogr. Res.* **2023**, *42*, 156–171.
2. Chen, X.; Li, K.; Bao, X.; Hong, C.; Fu, Y.; Cui, H. Innovations in the development of digital and intelligent Construction of urban shield tunnels. *J. Basic Sci. Eng.* **2021**, *29*, 1057–1074. [CrossRef]
3. Su, D.; Huang, M.; Han, W.; Li, A.; Wang, E.; Chen, X. Suitability evaluation of underground space development in Shenzhen: Urban geoenvironmental considerations. *Earth Sci. Front.* **2023**, *30*, 514–524. [CrossRef]
4. Wang, C.; Liu, L. Analysis on the future development trend of urban rail transit in China. *Urban Rail Transit* **2019**, *22*, 22–24. [CrossRef]
5. Xu, X.; Deng, Y.; Zhou, L.; Ming, W.; Zhang, H.; Xia, C. Experimental study on temperature effect of consolidation and permeability of coastal soft soil. *J. Eng. Geol.* **2023**, *2023*, 1–8. [CrossRef]
6. Liu, B.; Yu, Z.; Han, Y.; Wang, Z.; Zhang, R.; Wang, S. Analytical solution for the response of an existing tunnel induced by above-crossing shield tunneling. *Comput. Geotech.* **2020**, *124*, 103624. [CrossRef]
7. Zhang, Z.G.; Huang, M.S.; Wang, W.D. Evaluation of deformation response for adjacent tunnels due to soil unloading in excavation engineering. *Tunn. Undergr. Space Technol.* **2013**, *38*, 244–253. [CrossRef]
8. Liang, R.; Wu, W.; Yu, F.; Jiang, G.; Liu, J. Simplified method for evaluating shield tunnel deformation due to adjacent excavation. *Tunn. Undergr. Space Technol.* **2018**, *71*, 94–105. [CrossRef]
9. Fu, Y.; Wang, B.; Wu, H.; Chen, X.; Sun, X.; Bian, Y.; Shen, X. Theoretical analysis on horizontal rectification of tunnel near deep foundation pit by grouting. *Tunn. Undergr. Space Technol.* **2023**, *133*, 104977. [CrossRef]
10. Huang, X.; Schweiger, H.F.; Huang, H. Influence of Deep Excavations on Nearby Existing Tunnels. *Int. J. Geomech.* **2013**, *13*, 170–180. [CrossRef]
11. Sun, H.; Chen, Y.; Zhang, J.; Kuang, T. Analytical investigation of tunnel deformation caused by circular foundation pit excavation. *Comput. Geotech.* **2019**, *106*, 193–198. [CrossRef]

12. Bian, X.; Hu, H.; Zhao, C.; Ye, J.; Chen, Y. Protective effect of partition excavations of a large-deep foundation pit on adjacent tunnels in soft soils: A case study. *Bull. Eng. Geol. Environ.* **2021**, *80*, 5693–5707. [CrossRef]
13. Wei, G.; Feng, F.; Cui, Y.; Wang, X.; Diao, H.; Wu, Y. Research on the influence of foundation pit excavation on the lateral force and deformation of side shield tunnels based on full-scale experiments. *Tunn. Undergr. Space Technol.* **2023**, *140*, 105236. [CrossRef]
14. Masayasu, H.; Shiro, O.; Tatsuaki, K.; Ohmae, Y. Effects of the ring-cut excavation method on ground displacements and stability of a tunnel face. *J. Tunn. Eng.* **2017**, *17*, 1–8.
15. Yu, Z.T.; Wang, H.Y.; Wang, W.; Ling, D.S.; Zhang, X.D.; Wang, C.; Qu, Y.H. Experimental and Numerical Investigation on the Effects of Foundation Pit Excavation on Adjacent Tunnels in Soft Soil. *Math. Probl. Eng.* **2021**, *2021*, 5587857. [CrossRef]
16. Li, M.; Chen, J.; Wang, J.; Zhu, Y. Comparative study of construction methods for deep excavations above shield tunnels. *Tunn. Undergr. Space Technol.* **2018**, *71*, 329–339. [CrossRef]
17. Shi, J.; Ng, C.W.W.; Chen, Y. Three-dimensional numerical parametric study of the influence of basement excavation on existing tunnel. *Comput. Geotech.* **2015**, *63*, 146–158. [CrossRef]
18. Shi, J.; Ng, C.W.W.; Chen, Y. A simplified method to estimate three-dimensional tunnel responses to basement excavation. *Tunn. Undergr. Space Technol.* **2017**, *62*, 53–63. [CrossRef]
19. Zhang, D.; Xie, X.; Li, Z.; Zhang, J. Simplified analysis method for predicting the influence of deep excavation on existing tunnels. *Comput. Geotech.* **2020**, *121*, 103477. [CrossRef]
20. Li, D.; Liao, F.; Wang, L.; Lin, J.; Wang, J. Multi-Stage and Multi-Parameter Influence Analysis of Deep Foundation Pit Excavation on Surrounding Environment. *Buildings* **2024**, *14*, 297. [CrossRef]
21. Zhuang, Y.; Cui, X.; Hu, S. Numerical simulation and simplified analytical method to evaluate the displacement of adjacent tunnels caused by excavation. *Tunn. Undergr. Space Technol.* **2023**, *132*, 104879. [CrossRef]
22. He, C.; Cai, Y.; Pu, C.; Zhou, S.; Di, H.; Zhang, X. Deformation analysis and protection measures of existing metro tunnels effected by river channel excavation in soft soils. *Tunn. Undergr. Space Technol.* **2024**, *144*, 105504. [CrossRef]
23. Zhang, J.; Xie, R.; Zhang, H. Mechanical response analysis of the buried pipeline due to adjacent foundation pit excavation. *Tunn. Undergr. Space Technol.* **2018**, *78*, 135–145. [CrossRef]
24. Zhao, Y.; Chen, X.; Hu, B.; Wang, P.; Li, W. Evolution of tunnel uplift induced by adjacent long and collinear excavation and an effective protective measure. *Tunn. Undergr. Space Technol.* **2023**, *131*, 104846. [CrossRef]
25. Zhang, X.; Wei, G.; Lin, X.; Xia, C.; Wei, X. Transverse Force Analysis of Adjacent Shield Tunnel Caused by Foundation Pit Excavation Considering Deformation of Retaining Structures. *Symmetry* **2021**, *13*, 1478. [CrossRef]
26. Niu, Y.; Wang, Q.; Ma, F. Study on the Influence of Foundation Pit Excavation on the Deformation of Adjacent Subway Tunnel in the Affected Area of Fault Zones. *Sustainability* **2023**, *15*, 9462. [CrossRef]
27. Zhang, S.; Li, X. Numerical analysis of deep foundation pit zoned excavation. *Low Temp. Archit. Technol.* **2012**, *2012*, 113–115.
28. Chen, J.J.; Wang, J.H.; Xiang, G.W.; Wen, S.L.; Du, Y. Numerical study on the movement of existing tunnel due to deep excavation in Shanghai. *Geotech. Eng. J. SEAGS AGSSEA* **2011**, *42*, 30–40.
29. Chen, J.; Liu, W.; Sun, X. Effects of Tuned Rail Damper on Track Dynamic Characteristics Optimization. *Procedia Eng.* **2017**, *199*, 1616–1622. [CrossRef]
30. Ruan, H.T.; Zhao, J.H.; Huang, W.D.; Liu, L. Design and analysis of concurrent excavation of adjacent deep foundation pits. *Chin. J. Geotech. Eng.* **2010**, *32*, 146–150.
31. Wei, G. Measurement and analysis of impact of foundation pit excavation on below existed shield tunnels. *Rock Soil Mech.* **2013**, *34*, 1421–1428. [CrossRef]
32. Jian, R.; Huang, R.; Xu, C.X. Influence of deep excavation on the adjacent existing shielded tunnel in Hangzhou area. *Soil Eng. Found.* **2023**, *37*, 982–986.

Journal of
Marine Science and Engineering

MDPI

Article

Experimental Study on the Reinforcement of Calcareous Sand Using Combined Microbial-Induced Carbonate Precipitation (MICP) and *Festuca arundinacea* Techniques

Xiuqiong Deng [1], Ziyu Wang [1,*], Yuchun Qin [1], Liang Cao [2], Peng Cao [2], Yu Xie [1] and Yingqi Xie [1]

[1] Yazhou Bay Innovation Institute, College of Marine Science and Technology, Hainan Tropical Ocean University, Sanya 572022, China; deng06141005@163.com (X.D.); 18910966832@163.cm (Y.Q.); 17373175594@163.com (Y.X.); luckyluckyxyq@163.com (Y.X.)
[2] College of Architecture and Civil Engineering, Beijing University of Technology, Beijing 100124, China; liangcao988@emails.bjut.edu.cn (L.C.); caopeng@bjut.edu.cn (P.C.)
* Correspondence: zywang@hntou.edu.cn

Abstract: Combining the Microbial-Induced Calcium Carbonate Precipitation (MICP) technique with plants to reinforce calcareous sand slopes on reef islands is expected to achieve both reinforcement and economic benefits. In this study, MICP was combined with *Festuca arundinacea* (MICP-FA) for calcareous sand reinforcement. Based on water retention and scanning electron microscopy (SEM) tests, the water retention performance and mechanism of MICP-reinforced calcareous sand under different cementation solution concentrations and cementation cycles were analyzed. The growth adaptability of *Festuca arundinacea* was evaluated under different bacteria solution concentrations, cementation solution concentrations and cementation cycles. The engineering applicability of MICP-FA-reinforced calcareous sand was evaluated by wind erosion tests, and the synergistic reinforcement mechanism was analyzed. The results show that with the increase in the cementation solution concentration and cementation cycles, more calcium carbonate filled and adhered to the calcareous sand particles, significantly improving the water retention performance. MICP-FA can enhance the wind erosion resistance of calcareous sand. This synergistic mechanism lies in the surface cementation effect of MICP and the deep anchoring effect of plant roots. This study provides theoretical basis and technical guidance for engineering applications in calcareous sand areas.

Keywords: calcareous sand; MICP; *Festuca arundinacea*; synergistic reinforcement; wind erosion

1. Introduction

With the vigorous development of reef construction, the stability and sustainability of reef structures have drawn extensive attention. As a natural foundation material, calcareous sand is widely applied for constructing reef infrastructure, including slopes, airport runways, and military bases [1–5]. Due to its characteristics of irregular particle shapes, high crushability, and high porosity [6–11], calcareous sand is prone to erosion under hydraulic and aeolian forces, which renders the slopes constructed with it susceptible to reduced stability and subsequent collapses or landslides. Conventional reinforcement methods such as chemical grouting [12,13] and cement stabilization [14,15] are associated with inherent drawbacks, including high construction costs, substantial energy consumption, and significant environmental pollution. Therefore, there is an urgent need to explore more environmentally friendly methods for reinforcing calcareous sand slopes on reefs.

Microbial-Induced Calcite Precipitation (MICP), a novel soil stabilization technology, has been applied to foundation treatment research [16–19] and is characterized by low cost, low energy consumption, rapid reaction kinetics, and environmental friendliness [20,21]. The primary mechanism of action [22–27] involves microbial production of urease during metabolism, which catalyzes the decomposition of urea to generate CO_3^{2-} ions. These ions then react with ambient Ca^{2+} ions to form $CaCO_3$ precipitates through the following chemical reaction equations:

$$CO(NH_2)_2 + 2H_2O \rightarrow 2NH_4^+ + CO_3^{2-} \quad (1)$$

$$Ca^{2+} + CO_3^{2-} \rightarrow CaCO_3 \quad (2)$$

Scholars have applied MICP technology to soil stabilization to enhance erosion resistance. Li et al. reported that as the number of cementation cycles increases, sand particles are encapsulated by precipitated calcium carbonate generated from microbial reactions, thereby enhancing the mechanical strength of the sand matrix [28]. Chen et al. found that after MICP treatment, a dense hard-shell layer composed of calcium carbonate and soil particles formed on the surface of the specimen, which effectively enhanced the strength and scouring resistance of the sandy soils [29]. He et al. found that the MICP technique bonded loose sand particles with piles to form bio-enhanced piles with larger diameters in the shallow soil layer, which significantly improved the bearing capacity and strength of the original piles [30]. Zhang et al. found that MICP can enhance the shear strength of rock joints. The peak shear strength increased with curing time [31]. Liu et al. treated loess samples with bacterial solutions and cementing solutions of varying concentrations, resulting in a significant improvement in the mechanical properties of the treated loess [32]. Liu et al. treated sandy slopes by varying the Ca^{2+} concentration in the cementing solution, demonstrating that slopes treated with higher concentration exhibited superior erosion resistance compared to those treated with lower concentrations [33]. Huang et al. reinforced slopes using MICP technology, demonstrating that cemented sands remained intact under simulated rainfall erosion and maintained enhanced slope integrity [34]. Dagliya et al. demonstrated that cementing solutions can enhance the strength of desert sands. Through comparative SEM analysis of MICP-treated and untreated samples, crystalline growth was observed in interparticle pores of the sand matrix. Based on these findings, temperature effect analysis was conducted to lay a foundation for field-scale wind erosion tests [35]. Qu et al. reported that precipitated calcium carbonate generated by MICP reactions is distributed on soil particle surfaces and within interparticle pores, enabling aeolian sands to exhibit satisfactory wind erosion resistance at wind speeds of 13 m/s [36]. Hang et al. demonstrated that with increasing temperature and cementation solution concentration, the surface penetration resistance of the specimens was significantly enhanced, leading to improved wind erosion resistance [37].

MICP technology is affected by many factors due to its complex biochemical process, which leads to differences in the engineering properties of MICP-treated soils, so many scholars have performed many studies on the factors affecting MICP. Wang et al. observed the effect of bacterial density on the growth rate and properties of precipitates based on the pore size model of microfluidics, and concluded that the precipitation rate of calcium carbonate increases with the increase in bacterial density, and that bacterial density also has an effect on the size and number of calcium carbonate crystals [38]. Jiang et al. treated artificial slopes with three cementation solution concentrations (0.2, 1.0, and 2.0 mol/L), and after spraying the slopes for 30 min at a rainfall rate of 5 mm/min, it was

concluded that the resistance of the slopes with the 0.2 mol/L and 1.0 mol/L treatments to erosion resistance was significantly enhanced, while a large amount of soil was lost from the 2.0 mol/L-treated slopes and the erosion resistance was not improved [39]. Li et al. studied the effects of bacterial concentration, urea concentration, mass concentration, curing temperature, and curing time on the compressive strength based on the microbial-induced calcite precipitation (MICP) technology. The study found that all these factors can enhance compressive strength; however, an excessively high urea concentration and curing temperature will lead to a decrease in compressive strength [40].

According to the above studies, although MICP technology can significantly improve soil strength and stiffness [41–45] and enhance erosion resistance, the reinforcement effect is susceptible to a variety of factors such as bacteria solution concentration, temperatures, and cementing liquids, which makes the treated specimens prone to uneven curing strength. Therefore, its application in large-scale reef slope reinforcement is constrained by increased treatment costs and limited treatment depth.

Vegetative slope stabilization, a sustainable slope protection technique combining slope reinforcement and ecological restoration [46,47], influences slope stability primarily through mechanical and hydrological reinforcement [48–50]. Plant roots intertwine with soil particles to form root-soil composites, enhancing soil strength [51,52] and improving slope reinforcement. Rahman et al. demonstrated that plant roots enhance soil strength in slopes through mechanical interlocking between roots and soil particles [53]. Cardoza et al. demonstrated that the strength of natural silty sand soil was significantly increased when reinforced with plant roots [54]. *Festuca arundinacea*, a commonly used slope protection plant, features an extensive root system, heat tolerance, drought resistance, and cost-effectiveness [55,56]. During plant growth, the soil is blown by wind erosion, covering and burying plant seedlings, which can easily cause seedling death [57], while MICP technology can stabilize the soil surface layer to provide protection during the pre-growth period. Therefore, integrating MICP technology and vegetative reinforcement can achieve dual objectives of soil reinforcement, erosion resistance enhancement, and environmental remediation.

This study investigates the feasibility and reinforcement mechanism of combining MICP with *Festuca arundinacea* (MICP-FA) for calcareous sand reinforcement. By systematically investigating the effects of bacterial concentration, cementation solution concentration, and cementation cycles on soil water retention capacity and *Festuca arundinacea* growth performance, the optimal growth conditions for the vegetation will be determined. Wind erosion tests will then be conducted to identify optimal reinforcement parameters, followed by a mechanistic analysis of the combined MICP-FA treatment. The findings of this research are expected to provide a novel eco-friendly solution for sustainable infrastructure reinforcement in reef slope engineering.

2. Materials and Methods

2.1. Test Materials

(1) Sand selection: The sand used in the experiments was calcareous sand collected from a reef island in the South China Sea. The dry density of the specimens ranged from 1.22 to 1.65 g/cm^3, with a void ratio between 0.63 and 1.29. The specific gravity of the sand was determined to be 2.69. The particle size distribution is presented in Figure 1a.

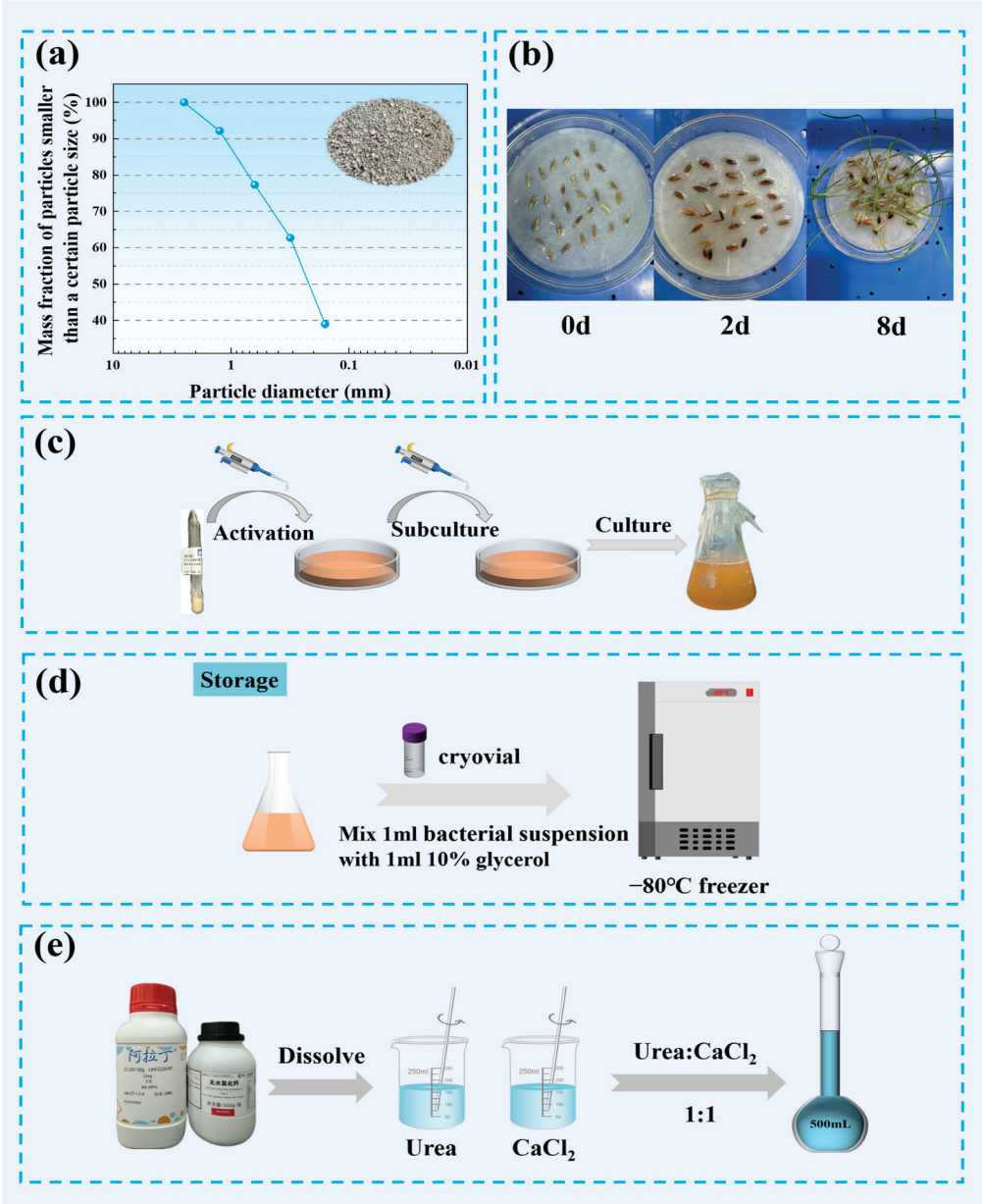

Figure 1. Summary of experimental materials: (**a**) Particle size distribution plot; (**b**) photograph of germinated *Festuca arundinacea* seeds; (**c**) bacterial activation, subculture, and cultivation; (**d**) bacterial storage; (**e**) cementation solution preparation.

(2) Experimental grass seeds: The germination quality of *Festuca arundinacea* seeds (Jiangsu Yunzhigu Landscape Engineering Co. Ltd., Suzhou, China) was evaluated using the paper towel method. Germination performance is shown in Figure 1b. Seedlings emerged starting on day 2 of the experiment, and no further germination was observed after day 8, yielding a germination rate of 96.67%. These results indicate that the purchased seeds met high quality standards.

(3) Bacterial strain and cementation solution: The *Bacillus pasteurii* strain BNCC337394, obtained from the BeNa Culture Collection (Guangdong Province Microbial Culture Collection Center, Guangzhou, China), was used in this study. The strain was preserved as lyophilized powder in ampoules via vacuum-drying. The procedures for bacterial activation, cultivation, and storage are illustrated in Figure 1c,d. The cementation solution was prepared by mixing calcium chloride ($CaCl_2$, Shanghai Xilong Chemical Co. Ltd., Shanghai,

China) and urea (Shanghai Aladdin Biochemical Technology Co. Ltd., Shanghai, China) at a molar ratio 1:1. The solution must be allowed to cool before being combined with the urea solution because the dissolution of calcium chloride in water is an exothermic reaction. These reagents provide CO_3^{2-} and Ca^{2+} ions for microbial-induced calcite precipitation. The cementation solution preparation process is shown in Figure 1e.

2.2. Test Methods

2.2.1. Water Retention Test

This study systematically analyzed the effects of cementation solution concentration and cycles on water retention capacity by applying different treatment protocols. A pressurized spray bottle was used to uniformly apply bacterial and cementation solutions at 0.1 mL/cm^2 and 0.2 mL/cm^2, respectively. Each cementation cycle consisted of (1) spraying bacterial solution followed by a 12 h rest and (2) spraying cementation solution followed by a 24 h reaction. Specimen labeling and testing procedures are detailed in Table 1 and Figure 2.

Table 1. Specimen labeling scheme for water retention tests.

CSC (mol/L) \ CC	1 Cycle	2 Cycles	3 Cycles	4 Cycles
0 mol/L	J11	J12	J13	J14
0.1 mol/L	J21	J22	J23	J24
0.25 mol/L	J31	J32	J33	J34
0.4 mol/L	J41	J42	J43	J44
0.5 mol/L	J51	J52	J53	J54

(Note: Each treatment group was replicated twice. Cementation solution concentration is abbreviated as CSC; cementation cycles is abbreviated as CCs. The first number in the labeling scheme J21 indicates that the cementation solution concentration is 0.1 mol/L, and the second number indicates that the number of cementation cycles is one.)

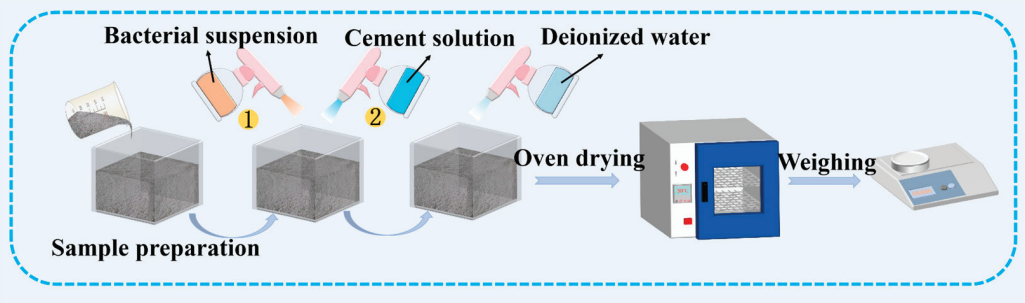

Figure 2. Water retention test procedure.

2.2.2. SEM Analysis

This experiment observes and analyzes the microstructure of the cementation on the specimen surface through a field emission scanning electron microscope (SEM) with the model JSM-7610FPlus (JEOL Ltd., Tokyo, Japan.).

2.2.3. Growth Adaptability Test of *Festuca arundinacea*

This study aimed to investigate the effects of bacterial concentration, cementation solution concentration, and cementation cycles on the growth characteristics of *Festuca arundinacea* (including emergence rate, root length, shoot height, and root–shoot ratio) and determine the optimal treatment conditions for plant growth. The emergence rate was calculated as the percentage of germinated seeds relative to the total number of tested seeds after 28 days of experimentation. Root length was defined as the total length of root

systems below the rhizome. Shoot height was measured as the distance from the rhizome emerging above the soil surface to the plant apex. The root–shoot ratio was calculated as the biomass ratio of root systems to above-ground parts (including stems, leaves, flowers, and fruits).

Root length: In combination with the software ImageJ (version 1.52a), we measured the length of the root system of each *Festuca arundinacea* plant with a ruler and calculated the average value.

Shoot height: In combination with the software ImageJ (version 1.52a), the length of each *Festuca arundinacea* plant was measured from the surface of the soil to the top of the plant with a ruler, and the average value was calculated.

Root–shoot ratio: We separated the root system of *Festuca arundinacea* from the above-ground part, put it into the oven at 105 °C for 30 min to kill the green treatment, and then transferred it into the oven at 80 °C to dry to the constant weight, and then we weighed the root system and the above-ground part with the balance, and then calculated the ratio of the two as the root–shoot ratio.

In the experiment, bacterial and cementation solutions were applied using a pressurized spray bottle at 0.1 mL/cm^2 and 0.2 mL/cm^2, respectively. After curing, deionized water was sprayed onto the soil surface at 0.3 mL/cm^2 every other day to provide moisture for plant growth. Table 2 and Figure 3 present the specimen labeling and testing procedures.

Table 2. Specimen labeling scheme for growth adaptability tests.

CSC (mol/L) \ BSC	Y	xs10	xs20
0 mol/L	J11-n	J21-n	J31-n
0.1 mol/L	J12-n	J22-n	J32-n
0.25 mol/L	J13-n	J23-n	J33-n
0.4 mol/L	J14-n	J24-n	J34-n
0.5 mol/L	J15-n	J25-n	J35-n

(Note: cementation solution concentration is abbreviated as CSC; bacterial solution concentration is abbreviated as BSC; Y, xs10, and xs20 represent bacterial concentrations with OD_{600} values of 2.2, 0.22, and 0.11, respectively. "n" represents cementation cycles (1–4). The first number in the labeling scheme J12-n indicates that the bacteria solution concentration OD600 value is Y, i.e., 2.2, the second number indicates that the cementation solution concentration is 0.1 mol/L, and "n" indicates the different cementation cycles).

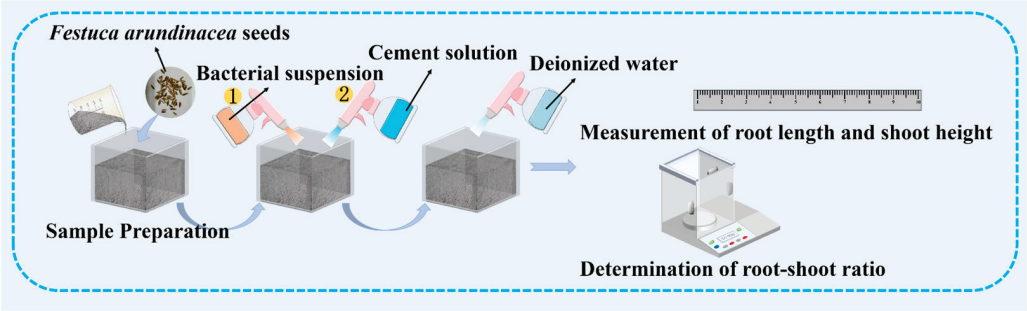

Figure 3. *Festuca arundinacea* growth adaptability test procedure.

2.2.4. Wind Erosion Test

The wind erosion device used in this experiment is shown in Figure 4. The model of the fan (KALAIKE Pump Industry (Zhejiang) Co. Ltd., Wenling, China) is SF4-4, and the model of the anemometer (UNI-TREND Technology (CHINA) Co. Ltd., Dongguan, China) is UT363-BT. Xu et al. selected representative sites on the South China Sea reefs. Based on data from the National Oceanic and Atmospheric Administration (NOAA) of the United States from 2006 to 2016, their analysis revealed that the lowest annual average wind speed

at the sites was 3.5 m/s, and the highest was 5.9 m/s [58]. According to this, different test wind speeds of 3 m/s, 5 m/s, and 10 m/s were set in the experiment. The specimens under optimal treatment conditions were determined by analyzing the changes in the specimens' mass over time and the mass loss rate at the end of the experiment.

$$\text{Percentage mass loss due to wind erosion}(\%) = \frac{m_1 - m_2}{m_1} \times 100\% \quad (3)$$

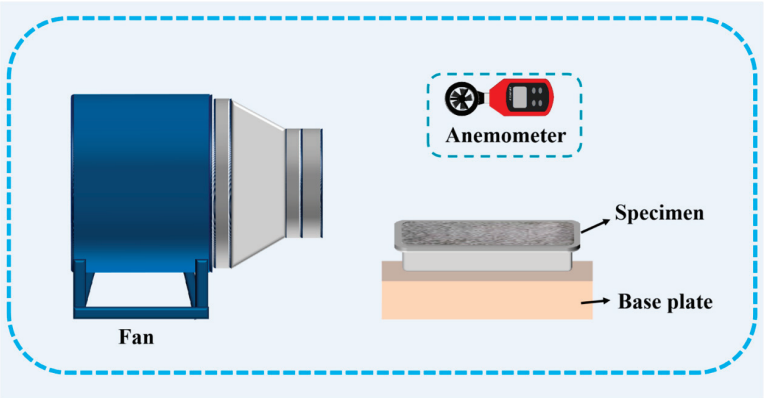

Figure 4. Wind erosion test device.

In the formula, m_1 is the mass of the sample before wind erosion and m_2 is the mass of the sample after wind erosion.

3. Results and Discussion

3.1. Effects of Cementation Solution Concentration and Cycles on Water Content

The results in Figure 5 demonstrate that water content in the soil gradually decreased over time. Increasing the cementation solution concentration within the same cementation cycle led to a higher water retention capacity. Moreover, the decline in water content slowed significantly as the number of cementation cycles increased. Increasing the cementation solution concentration [59] and cementation cycles [60] increased calcium carbonate precipitation. More loose calcareous sand particles were cemented into an integrated structure, and the compactness of the sand increased. This effectively inhibited water evaporation and improved soil water retention capacity. Among all groups, the untreated control (CK) showed the most significant water loss, while the specimen treated with 0.5 mol/L cementation solution for four cycles achieved the highest water content, demonstrating a 56.72% improvement compared with the CK group.

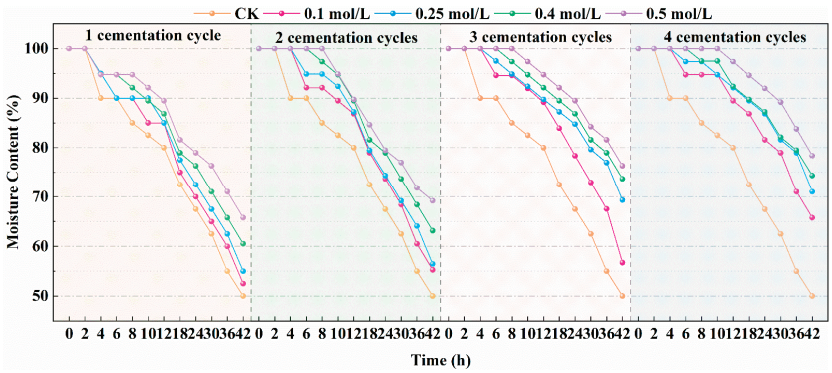

Figure 5. Effect of cementation solution concentration on water content at different cementation cycles.

These results indicate that MICP technology significantly enhances soil water retention capacity [61]. This enhancement makes it easier for plants to gain access to enough water during their growth and development, which benefits the plants' overall development.

3.2. Microstructural Analysis

Figure 6 shows SEM images of calcareous sand treated with 0.1 mol/L and 0.5 mol/L cementation solutions for one and four cycles. The images reveal calcium carbonate precipitation on sand surfaces increases with cementation solution concentration and cycles. This is attributed to the enhanced calcite formation resulting from higher reagent dosages and repeated MICP reactions, which improve particle bonding and water retention capacity.

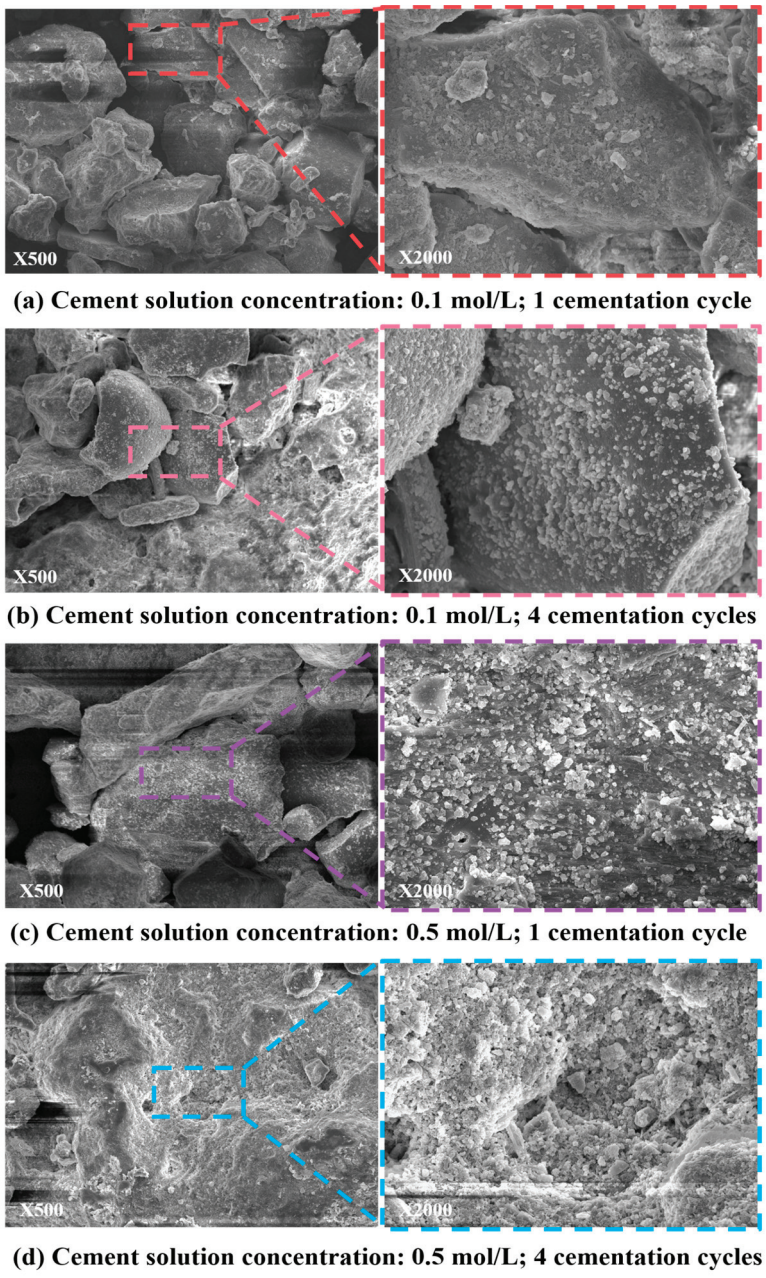

Figure 6. SEM images of surface reinforcement in specimens treated with cementation solution at different cycles.

3.3. Impact on Festuca Arundinacea Growth

As shown in Figures 7 and 8, the seedling emergence rate of the untreated control (CK) was 43%, indicating that *Festuca arundinacea* can generally grow in calcareous sand substrates. Notably, when the cementation solution concentration was 0 mol/L (i.e., only bacterial solution was applied), specimens treated with low bacterial concentrations (xs10, xs20) exhibited higher emergence rates than CK. This suggests that low bacterial concentrations promote plant growth, likely due to urea hydrolysis by microbes generating NH_4^+, an essential nitrogen source for plant development [62].

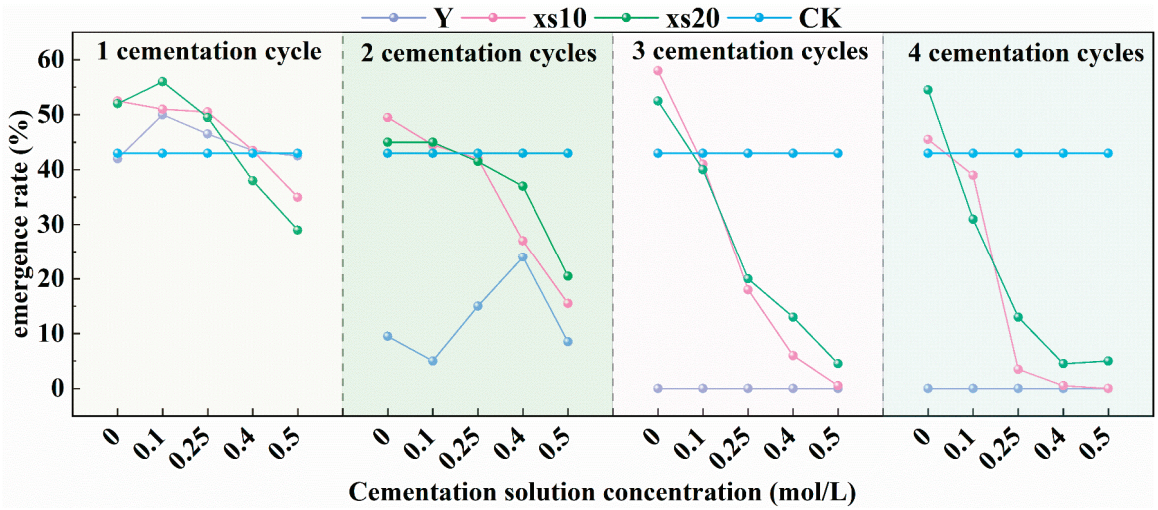

Figure 7. Effect of different treatments on seedling emergence rate of specimens.

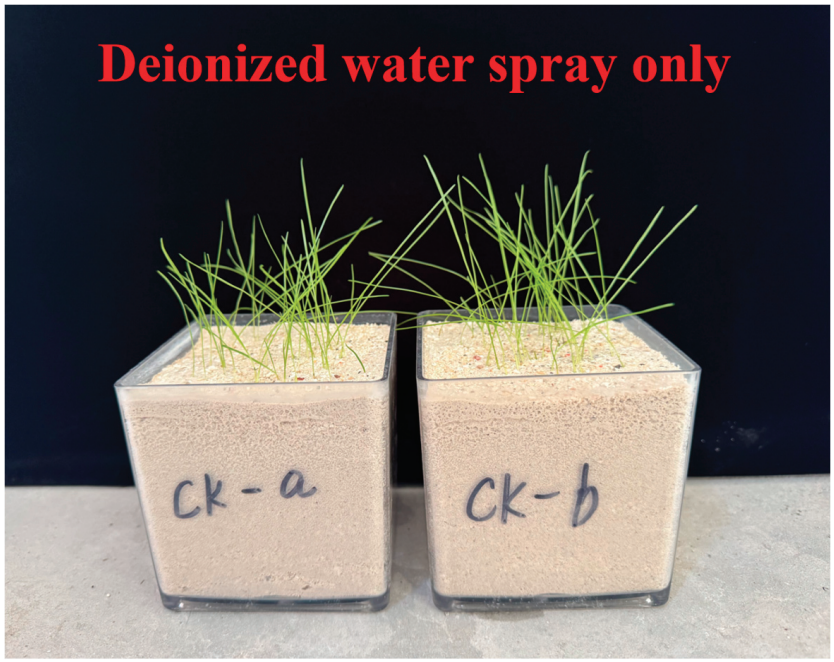

(**a**)

Figure 8. *Cont.*

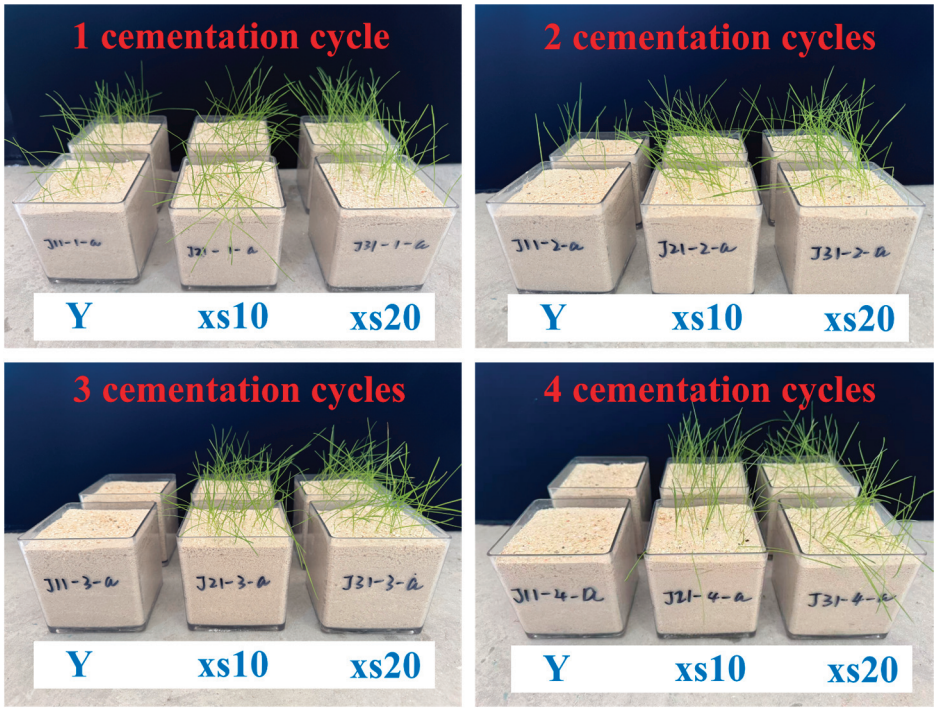

(**b**)

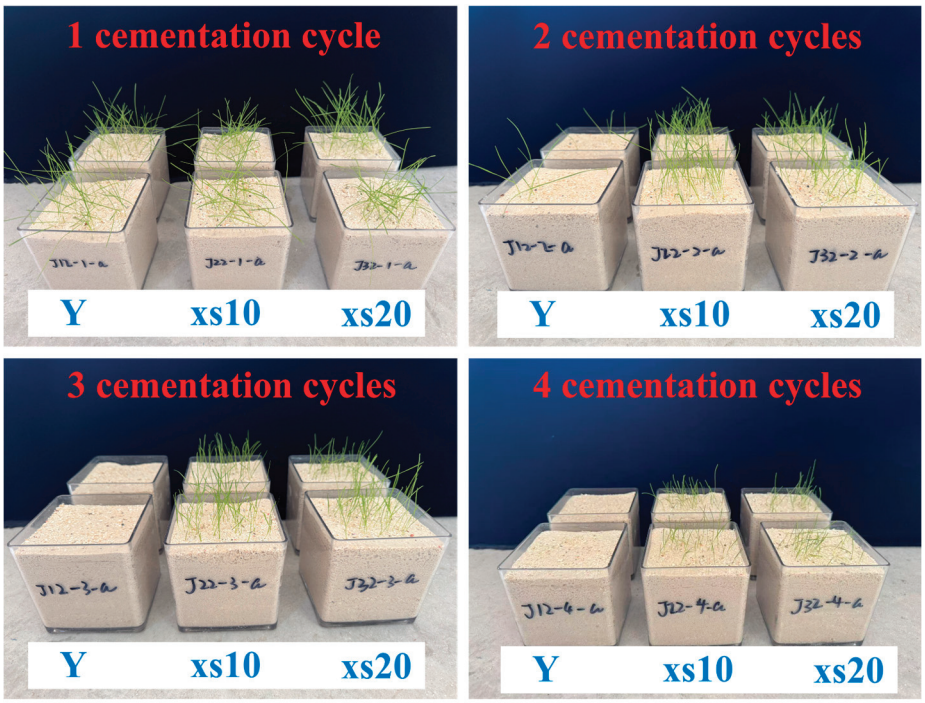

(**c**)

Figure 8. *Cont.*

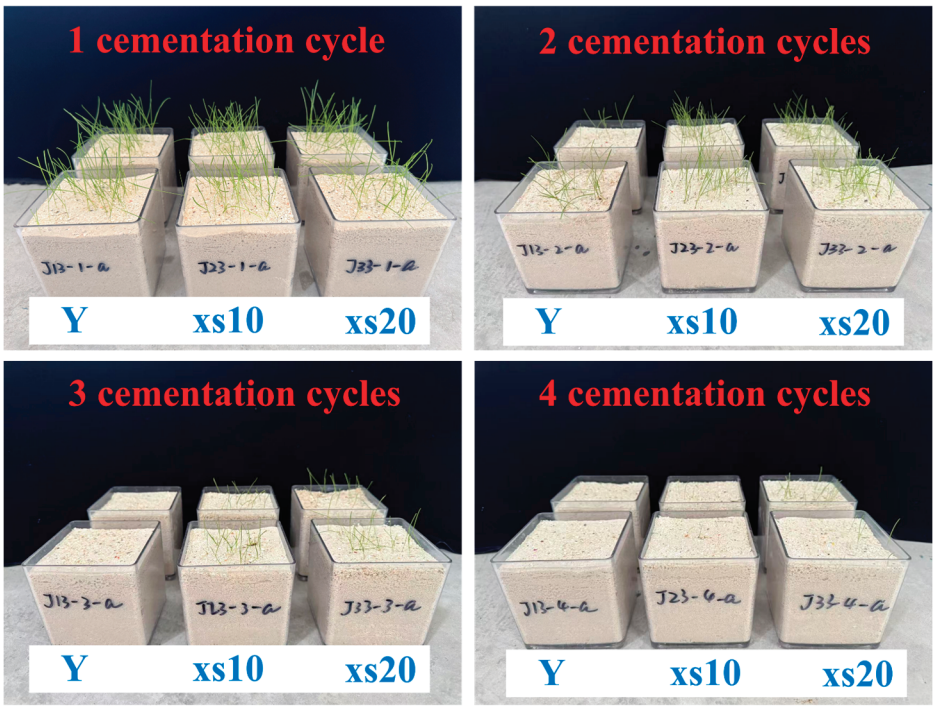

(**d**)

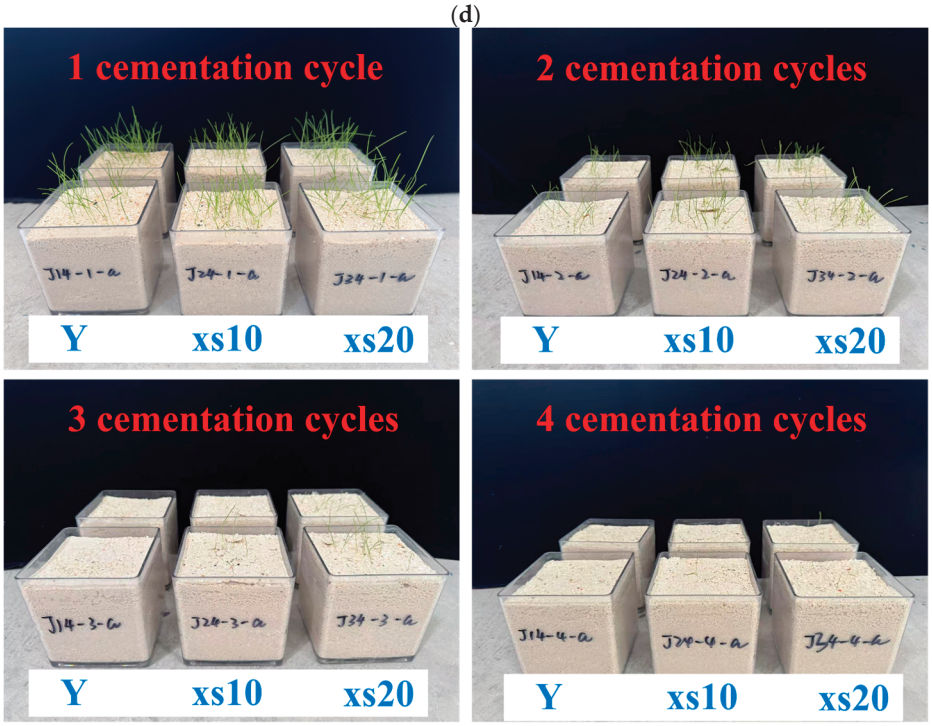

(**e**)

Figure 8. *Cont.*

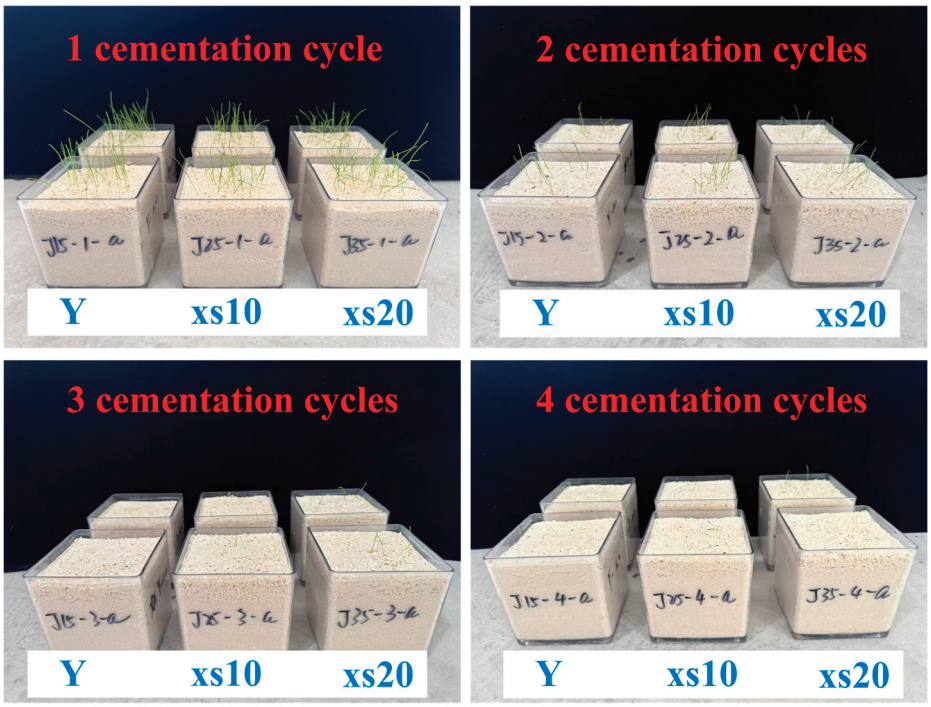

(**f**)

Figure 8. Growth performance of *Festuca arundinacea* under different treatments. (**a**) CK. (**b**) Cement solution concentration: 0 mol/L; bacterial suspension concentration: Y/xs10/xs20; cementation cycles: 1/2/3/4. (**c**) Cement solution concentration: 0.1 mol/L; bacterial suspension concentration: Y/xs10/xs20; cementation cycles: 1/2/3/4. (**d**) Cement solution concentration: 0.25 mol/L; bacterial suspension concentration: Y/xs10/xs20; cementation cycles: 1/2/3/4. (**e**) Cement solution concentration: 0.4 mol/L; bacterial suspension concentration: Y/xs10/xs20; cementation cycles: 1/2/3/4. (**f**) Cement solution concentration: 0.5 mol/L; bacterial suspension concentration: Y/xs10/xs20; cementation cycles: 1/2/3/4.

Figure 8 illustrates that the emergence rate of the specimens decreased as the number of cementation cycles and the concentration of the cementation solution increased. Taking J23-3 (a cementation solution concentration of 0.25 mol/L, bacteria solution concentration of xs10, and three cementation cycles) in Figure 8d as an example, it can be seen in conjunction with Figure 7 that the emergence rate of the specimens under this treatment condition was 18%, which was 58.14% lower than that of the CK group. The reason is that as they increase, more calcium carbonate is generated in the reaction, causing more loose calcareous sand to be cemented into a whole, which increases the strength of the sample [63]. This makes it difficult for the seeds to break through the soil, resulting in a decrease in the seedling emergence rate. As shown in Figure 7, the seedling emergence rate declined significantly when the cementation solution concentration exceeded 0.25 mol/L, whereas the suppressive effect was relatively mild at 0.1 mol/L. At this concentration, treatments with 1–2 cementation cycles and bacterial concentrations Y, xs10, xs20 (specimen IDs: J12-1, J22-1, J32-1, J22-2, J32-2) increased emergence rates by 16.28%, 18.6%, 30.23%, 3.49%, and 4.65%, respectively, compared to the CK.

As shown in Figure 7, seedling emergence rates were extremely low or zero in specimens treated with $\geq$0.4 mol/L cementation solution and three cementation cycles. Therefore, these concentrations were excluded from subsequent experiments.

As shown in Figure 9a, the mean root length of *Festuca arundinacea* decreased with increasing bacterial concentration, cementation solution concentration, and cementation

cycles. This is primarily due to the progressive filling of soil pores by calcium carbonate precipitates, which increases soil compactness [64]. Consequently, restricted growth space in the densified matrix impeded root elongation. Specimens treated with 0.1 mol/L cementation solution exhibited a less inhibitory effect on root length than higher concentrations.

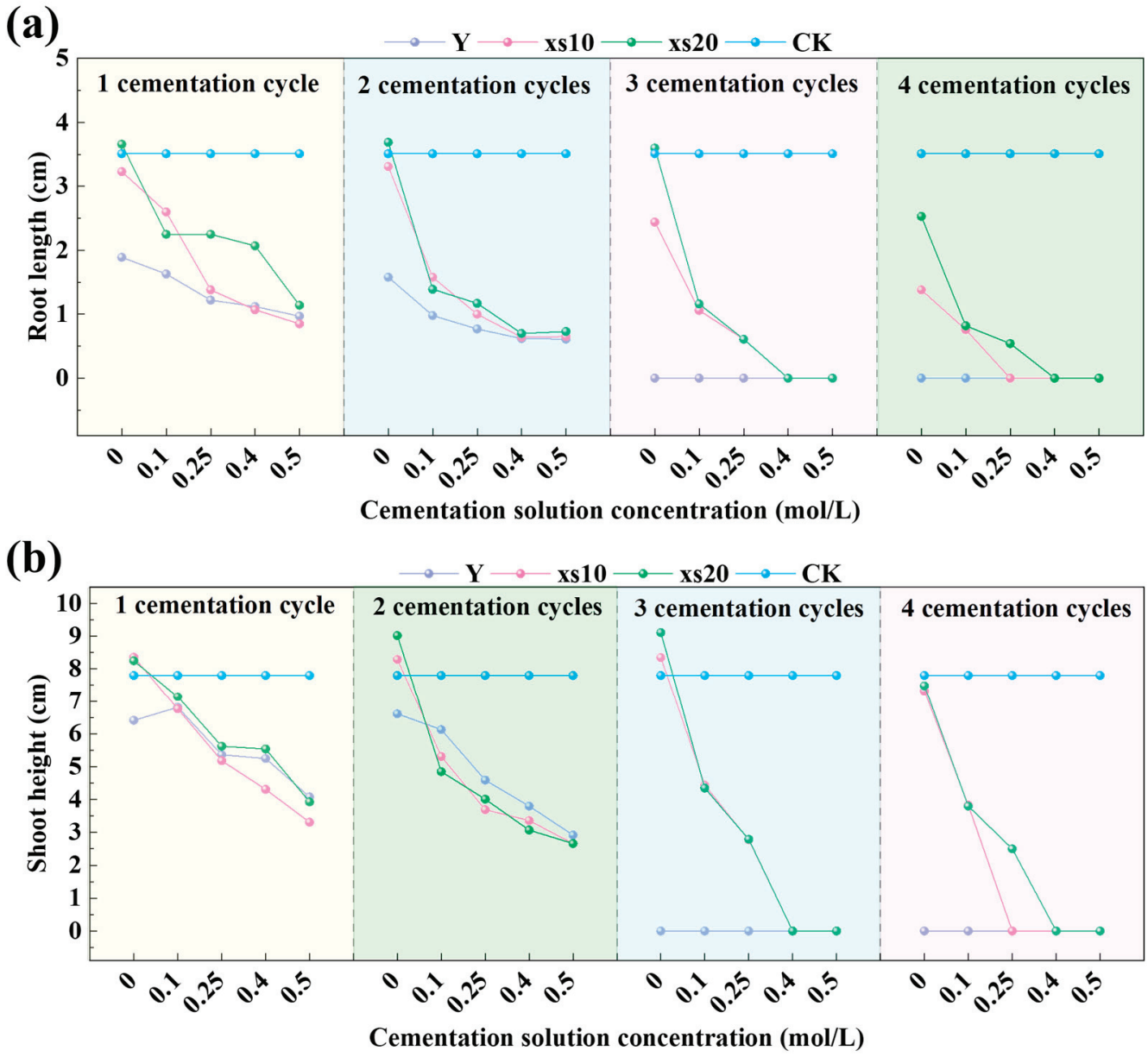

Figure 9. Effect of different treatments on root length and shoot height of specimens: (**a**) root length; (**b**) shoot height.

The effect of different treatments on the average shoot height of *Festuca arundinacea* is presented in Figure 9b. Lower bacterial concentrations promoted shoot elongation, with the xs20 bacterial treatment combined with three cementation cycles showing a 16.79% increase compared to CK. At consistent bacterial concentrations and cementation cycles, shoot height progressively decreased as the cementation solution concentration increased, with higher cycles exacerbating this decline relative to CK. This phenomenon is attributed to the nitrogenous compounds generated during microbial growth acting as fertilizer to enhance plant development, while excessive nitrogen supply inhibited nutrient uptake

balance. Additionally, increased alkalization of soil matrices with higher reagent dosages and cycles negatively impacted plant growth.

As shown in Figure 10, within the cementation solution concentration range of 0.1–0.5 mol/L, the root–shoot ratio of *Festuca arundinacea* generally decreased as the concentration increased, except for a notable upward trend observed for one cementation cycle. Taking the Y bacterial concentration combined with one cementation cycle as an example, specimens treated with 0.1–0.5 mol/L cementation solution showed increases of 0.94%, 1.18%, 9.22%, and 28.98% in the root–shoot ratio compared to the CK. This phenomenon arises from the altered osmotic pressure in soil solutions caused by high cementation solution concentrations, impairs shoot water and nutrient uptake. Roots exhibit enhanced growth to compensate, leading to an increased root–shoot ratio. With additional cementation cycles, accumulating calcium carbonate precipitates and densifies the matrix, reducing porosity and degrading soil aeration and water permeability. This restricts root growth space and impedes respiration, slowing root elongation. As shoot development is less affected, the root–shoot ratio stabilizes or decreases.

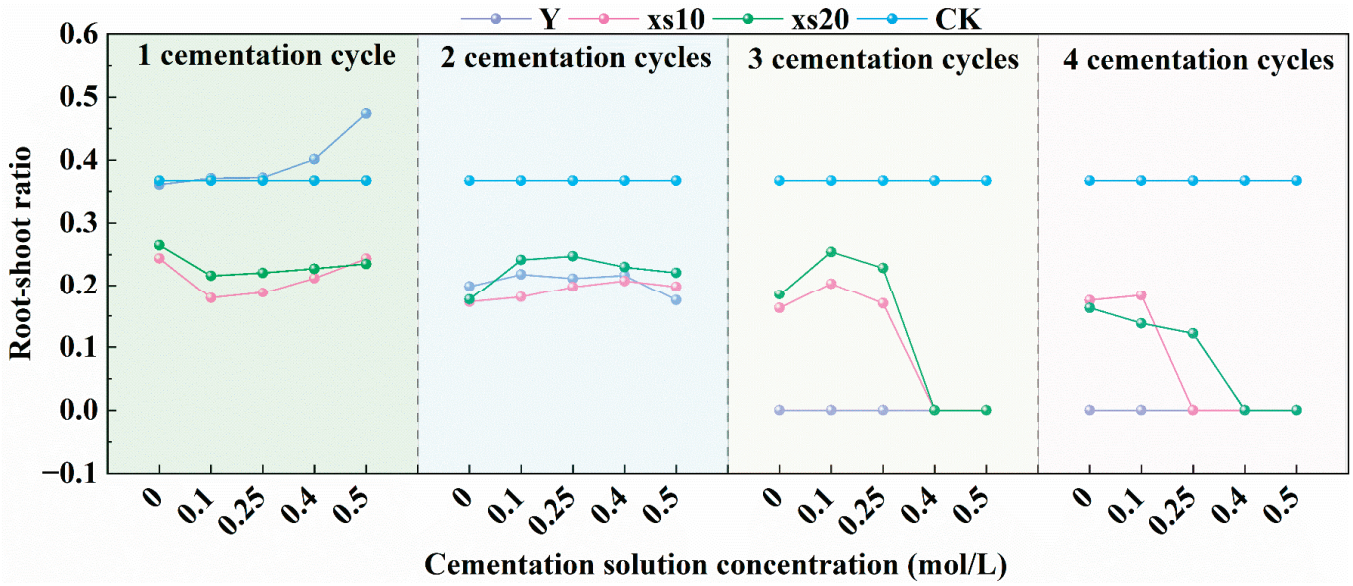

Figure 10. Effect of different treatments on the root–shoot ratio of specimens.

In summary, to balance soil reinforcement and promote *Festuca arundinacea* growth, specimens treated with 0.1 mol/L cementation solution were selected. Although low bacterial concentrations enhanced plant development, diluting bacterial solutions reduced overall urease activity, decreasing CO_3^{2-} production and calcium carbonate precipitation [65] and compromising reinforcement efficacy. Increasing cementation cycles augmented calcite formation. Therefore, the optimal treatments were (1) J12-1: Y bacterial concentration +0.1 mol/L solution +1 cycle. (2) J22-3: xs10 bacterial concentration +0.1 mol/L solution +3 cycles. (3) J32-3: xs20 bacterial concentration +0.1 mol/L solution +3 cycles.

3.4. Wind Erosion Test Results

Based on previous experiments, the optimized treatments combining soil reinforcement and *Festuca arundinacea* growth promotion were identified as J12-1, J22-3, and J32-3. Figure 11 shows the time-dependent mass changes in these specimens and their wind erosion mass loss rates after 20 min erosion at varying wind speeds. As revealed in Figure 11a, specimen mass increased progressively over time, with more pronounced upward trends at higher wind speeds. Figure 12 demonstrates that at low wind speeds, surface

erosion was negligible, whereas higher velocities caused significant surface damage, which was particularly severe in the CK group. These results indicate that MICP-FA-treated specimens exhibit superior wind erosion resistance, confirming effective reinforcement of calcareous sand. This improvement is attributed to vegetation increasing surface roughness to reduce wind velocity [66], root systems stabilizing soil through the anchorage and reinforcement mechanisms, and MICP-treated surfaces forming mineralized layers that resist erosive forces.

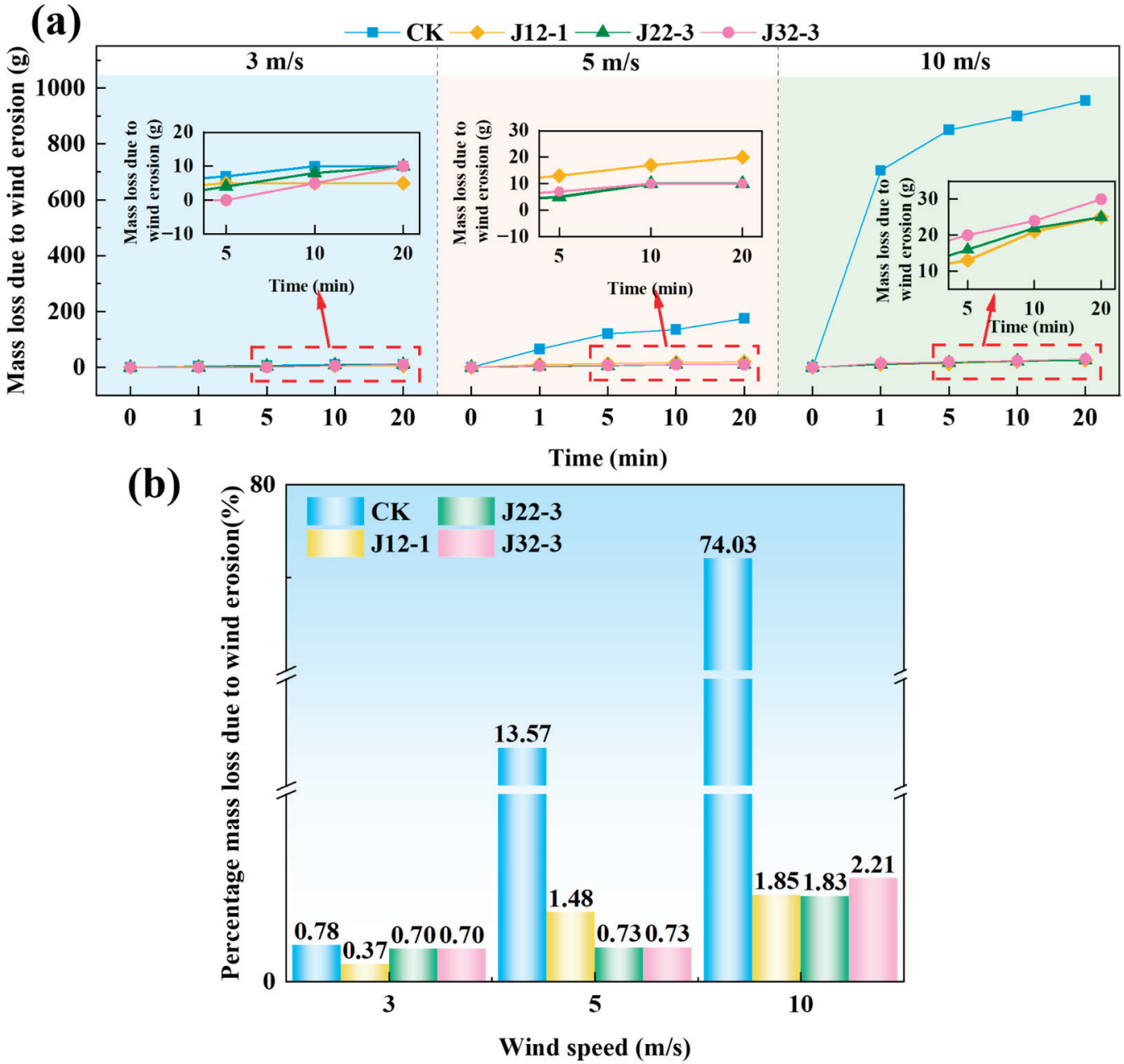

Figure 11. Wind erosion mass changes in specimens under different treatments: (**a**) Temporal variation in wind erosion mass loss; (**b**) percentage mass loss due to wind erosion.

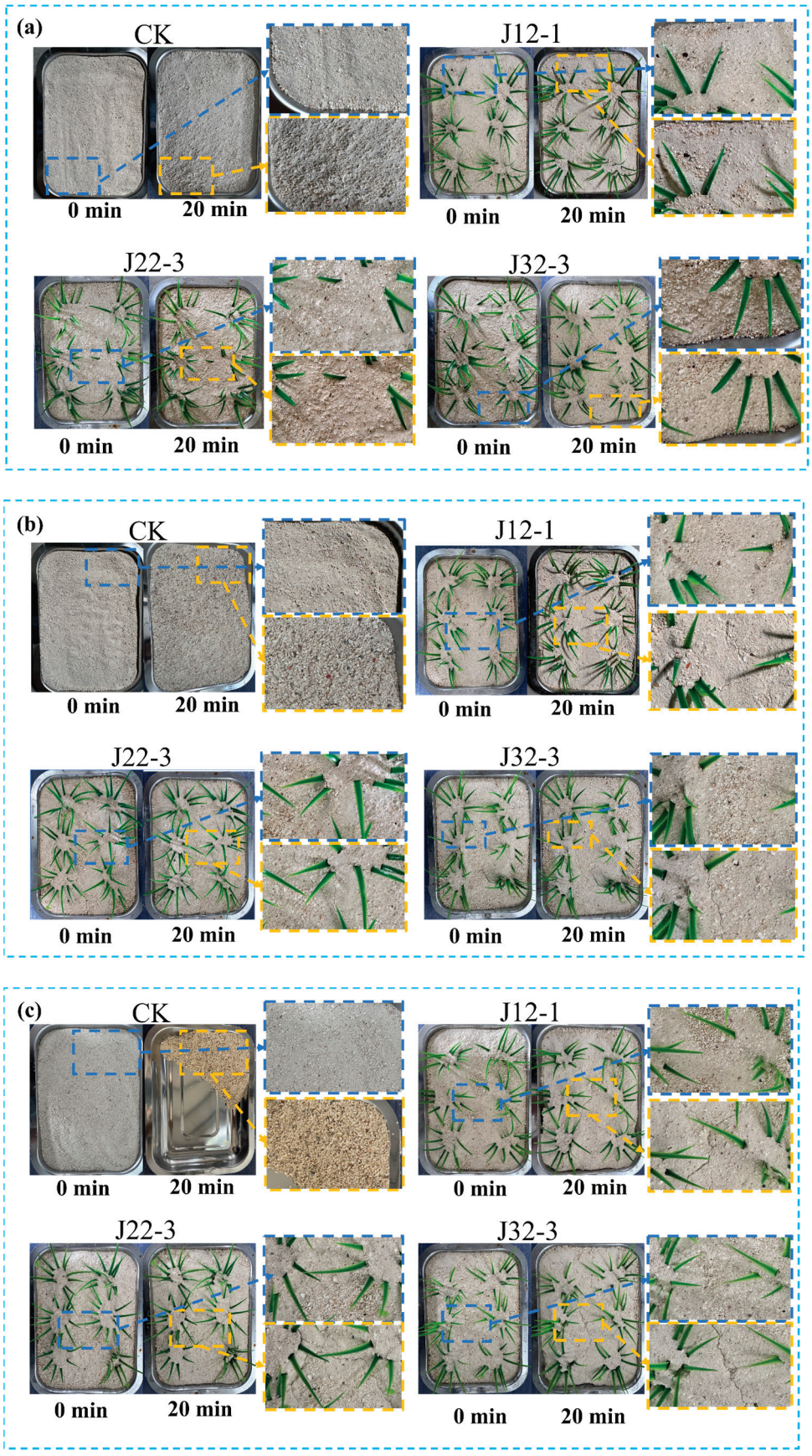

Figure 12. Visual changes in specimen wind erosion: (**a**) 3 m/s. (**b**) 5 m/s. (**c**) 10 m/s.

As shown in Figure 11b, wind erosion mass loss rates increased with rising wind speeds for all three groups (J12-1, J22-3, J32-3), though the J12-1 group demonstrated a significantly gentler growth trend. From 3 m/s to 5 m/s, J12-1's mass loss rate increased from 0.37% to 1.48% (Δ1.11 percentage points), while J22-3 and J32-3 only experienced 0.3 percentage point increases. During this phase, J22-3 and J32-3 showed smaller increments, but when wind speed rose from 5 m/s to 10 m/s, J12-1, J22-3, and J32-3 increased by 0.37, 1.1, and 1.48 percentage points. Notably, J22-3 and J32-3 exhibited much steeper increases than J12-1 at high wind speeds. This indicates that J12-1 maintained consistently lower mass loss rates across all wind speeds, demonstrating superior stability in wind erosion resistance and, thus, better reinforcement efficacy.

Qu et al. conducted a wind tunnel test on MICP-treated wind sand, and when the wind speed was 13 m/s, the wind erosion mass loss rate of the specimen was 63.6% [36]. Chen et al. conducted a wind tunnel test on desert sand treated by combining *Caragana korshinskii Kom* with SICP technology, and after blowing for 1 min at a wind speed of 15 m/s and cementation solution concentration of 0.1 mol/L, the soil mass loss was 7968 g/min/m^2 [67]. In this study, under the conditions of wind speed of 10 m/s and 20 min of erosion, the wind erosion mass loss rate of J21-1 group was only 1.85%. This indicates that the MICP-FA technique can significantly improve the wind erosion resistance of calcareous sand soils.

3.5. Synergistic Reinforcement Mechanism Analysis

A schematic diagram of MICP-FA reinforced calcareous sand is presented in Figure 13a. As shown in Figure 13b, calcium carbonate precipitated through MICP reactions fills soil pores, cementing loose particles into an integrated structure and forming a dense mineralized layer. This process enhances soil strength and stability, thereby providing effective reinforcement. As shown in Figure 13c, primary and coarse roots provide anchorage during plant growth, while fine roots offer reinforcement. Root systems interpenetrate soil particles to form a root–soil composite, significantly enhancing overall soil stability [68,69]. Root systems treated with MICP were shorter than untreated roots. Additionally, the root systems of the MICP-treated plants were slightly shorter than those of the untreated group when bacterial solution, cementation solution, and cementation cycles were at their appropriate levels. Excessive reagent dosages and cycles further reduced root length. This reduction is attributed to increased soil strength and density restricting root penetration [70]. The combined application of MICP-FA creates a dual-layer reinforcement system where the surface mineralized layer formed by microbial calcite precipitation provides wind erosion resistance. The underlying root networks mechanically stabilize deeper soil layers through anchorage and interlocking. This integrated mechanism enhances overall soil structural integrity across the entire profile.

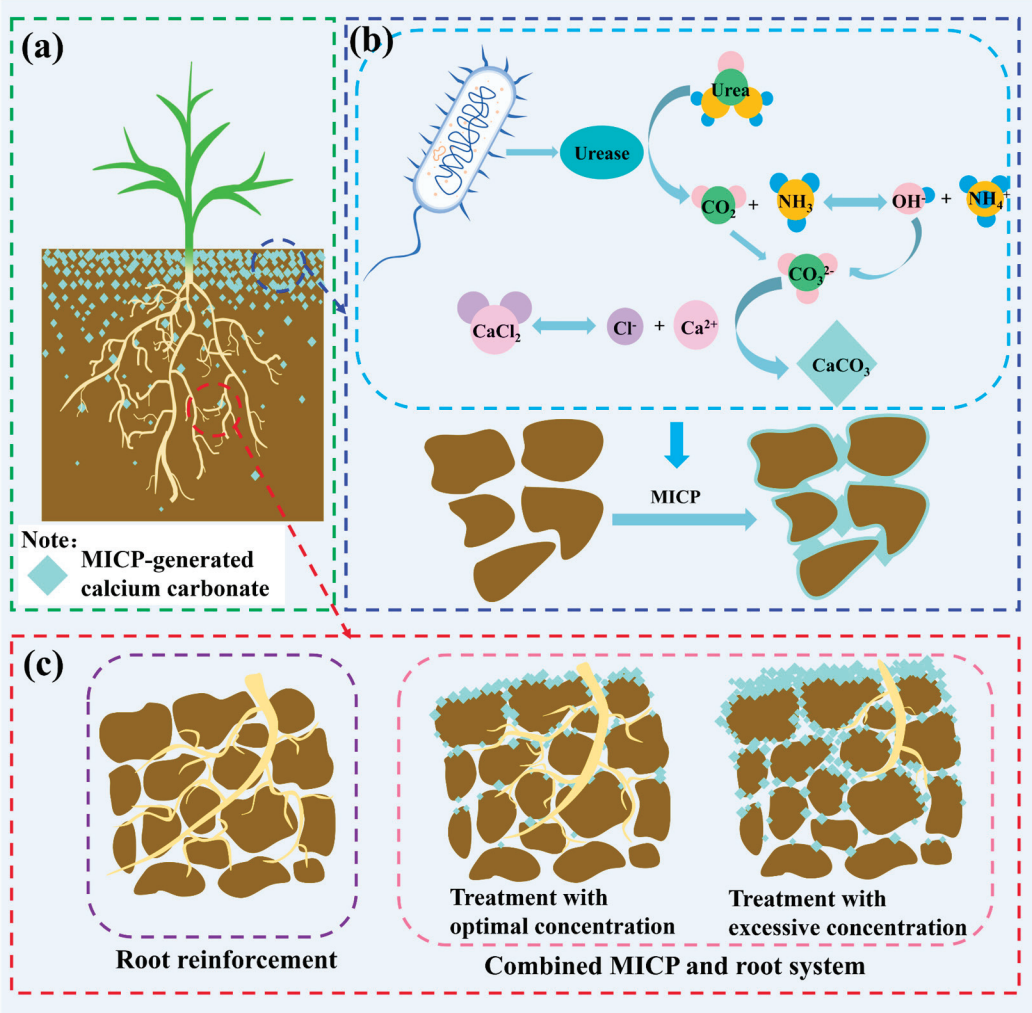

Figure 13. Schematic diagram of combined reinforcement mechanisms: (**a**) Overall reinforcement; (**b**) MICP-induced mineralization; (**c**) root system reinforcement.

4. Conclusions

This study uses MICP-FA technology to reinforce calcareous sand and evaluates the water retention ability of the treated soil, *Festuca arundinacea* growth adaptability, and wind erosion resistance. The key conclusions derived from the research results are as follows:

(1) Based on the water retention test and scanning electron microscope images, it can be seen that with the increase in cementation solution concentration and the number of cementation cycles, more calcium carbonate adheres to and fills in the surface and interstitial space of calcareous sand particles, which effectively improves the water retention performance of the calcareous sand soil body. The best water retention performance is achieved with a 0.5 mol/L cementation solution concentration and four cementation cycles, which is 56.72% higher than that of control group.

(2) Based on the results of *Festuca arundinacea* growth adaptation test, lower bacterial solution concentration, cementation solution concentration, and cementation cycles promote the growth of *Festuca arundinacea*, and increasing these parameters gradually inhibits the development of plants.

(3) According to the results of the wind erosion test, MICP-FA reinforcement can enhance the wind erosion resistance of calcareous sand soil body. Under an OD_{600} = 2.2 bacterial concentration, 0.1 mol/L cementation solution concentration,

and one cementation cycle (J12-1), the best wind erosion resistance of the reinforced soil was obtained, and favorable plant growth was maintained. At this time, under a 10 m/s wind speed, the specimen wind erosion mass loss rate was only 1.85%, which was 97.5% lower than that of the control group. (4) MICP-FA reinforcement significantly improves the wind erosion resistance of calcareous sand. The synergistic mechanism includes the surface bonding of MICP and the deep soil anchoring/reinforcement of the *Festuca arundinacea* root system.

5. Discussion

This study shows that MICP-FA-reinforced calcareous sand can significantly improve the wind erosion resistance of soil. However, this experiment was conducted indoors and has some limitations. Therefore, the following points can be considered in future experiments:

(1) Only *Festuca arundinacea* was selected as a test plant in this study, and there are significant differences in its root morphology, secretion and growth habit among different plants, and the synergistic mechanism with MICP technology may be different. The combination of different plants and MICP technology can be considered in the subsequent experiments.

(2) The wind speed set in the wind erosion test did not adequately simulate the extreme wind speed conditions during typhoons on the South China Sea islands. Further evaluation of the wind erosion resistance of MICP-FA0-reinforced calcareous sand can be considered in the subsequent study by referring to the wind speed of the typhoon in the South China Sea islands and reefs.

(3) The issue of how the enhancement of soil strength following MICP treatment influences plant root extension and distribution can be measured in greater detail in subsequent experiments.

(4) This study was carried out under controlled conditions in the laboratory, and the uniformity of the microbial solution and the initial state of the calcareous sand were strictly controlled. However, in actual island projects with a wide range of calcareous sand sites and complex environmental conditions (e.g., temperature), the implementation effect of the MICP-FA technique may change due to scale-up. While plant growth space and conditions are controllable in a laboratory setting, plant root competition, microbial community diversity, and interactions with other environmental factors (e.g., wave wash, tidal action) are more complex in real island ecosystems. It is necessary to conduct simulated field experiments to further investigate the influence of scale changes on the effectiveness of reinforcement, in order to realize an effective transition from the laboratory to the actual project.

Author Contributions: Investigation, writing—original draft preparation, data curation, formal analysis and methodology, X.D.; funding acquisition, project administration, supervision, resources and writing—review and editing, Z.W.; supervision and data curation, Y.Q.; supervision, writing—review and editing, L.C.; visualization and formal analysis, P.C.; Data curation, Y.X. (Yu Xie) and Y.X. (Yingqi Xie). All authors contributed to the writing of the paper. All authors have read and agreed to the published version of the manuscript.

Funding: This research was funded by the National Natural Science Foundation of China (Grant No. 42162024), the Hainan Provincial Natural Science Foundation of China (Grant No. 421RC592), the Major Science and Technology Plan Project of Yazhou Bay Innovation Research Institute of Hainan Tropical Ocean College (2022CXYZD003).

Data Availability Statement: The data used during the study are available from the first author and corresponding author by request.

Conflicts of Interest: The authors declare no conflicts of interest.

References

1. Wang, X.; Liu, J.-Q.; Cui, J.; Wang, X.-Z.; Shen, J.-H.; Zhu, C.-Q. Particle Breakage Characteristics of a Foundation Filling Material on Island-Reefs in the South China Sea. *Constr. Build. Mater.* **2021**, *306*, 124690. [CrossRef]
2. Cao, L.; Cao, P.; Wang, Z.; Tan, Z.; Shi, F.; Wang, J.; Liu, S. Application of SCMs and Seawater to Cement-Bonded Calcareous Sand: Macro Performance, Micro Mechanism, and Strength Prediction. *Constr. Build. Mater.* **2024**, *419*, 135560. [CrossRef]
3. Zhang, P.; Liu, M.; Yang, Y.; Liu, H.; Gao, X.; Cheng, L. In Situ Microbially Induced Ca-Alginate Polymeric Sealant in Calcareous Sand and Potential Engineering Applications. *Acta Geotech.* **2024**, *19*, 4217–4226. [CrossRef]
4. Sun, T.; Wang, F.; Liu, J.; Chen, Z.; Tuo, M.; Yang, Y. Research on the Bearing Performance of HSCA High-Strength Preloaded Expansion Piles in Calcareous Sand Foundation. *Sci. Rep.* **2025**, *15*, 3155. [CrossRef] [PubMed]
5. Wang, X.; Wen, D.; Ding, H.; Liu, K. Improving Erosion Resistance of Calcareous Sand Slope with Zinc Sulfate Solution. *Constr. Build. Mater.* **2024**, *447*, 138113. [CrossRef]
6. Li, X.; Liu, J. One-Dimensional Compression Feature and Particle Crushability Behavior of Dry Calcareous Sand Considering Fine-Grained Soil Content and Relative Compaction. *Bull. Eng. Geol. Environ.* **2021**, *80*, 4049–4065. [CrossRef]
7. Wu, Y.; Wang, X.; Shen, J.-H.; Cui, J.; Zhu, C.-Q.; Wang, X.-Z. Experimental Study on the Impact of Water Content on the Strength Parameters of Coral Gravelly Sand. *J. Mar. Sci. Eng.* **2020**, *8*, 634. [CrossRef]
8. Xu, D.; Shen, G.; Liu, Q.; Du, W. Dynamic Mechanical Response and Particle Breakage Characteristics of Calcareous Sand. *Soil Dyn. Earthq. Eng.* **2024**, *181*, 108653. [CrossRef]
9. He, S.-H.; Goudarzy, M.; Ding, Z.; Sun, Y. Strength, Deformation, and Particle Breakage Behavior of Calcareous Sand: Role of Anisotropic Consolidation. *J. Geotech. Geoenviron. Eng.* **2023**, *149*, 04023002. [CrossRef]
10. Wei, H.; Liu, H.; Li, X.; Tao, Z.; Wu, Y.; Shen, J.; Yin, M. Effect of Stress Path on the Mechanical Properties of Calcareous Sand. *Undergr. Space* **2023**, *9*, 20–30. [CrossRef]
11. Ma, G.; Xiao, Y.; He, X.; Li, J.; Chu, J.; Liu, H. Kaolin-Nucleation-Based Biotreated Calcareous Sand through Unsaturated Percolation Method. *Acta Geotech.* **2022**, *17*, 3181–3193. [CrossRef]
12. Cao, D.; Fan, L.; Huang, R.; Guo, C. Investigation of the Mechanical Properties of Reinforced Calcareous Sand Using a Permeable Polyurethane Polymer Adhesive. *Materials* **2024**, *17*, 5277. [CrossRef] [PubMed]
13. Tao, G.; Yuan, J.; Chen, Q.; Peng, W.; Yu, R.; Basack, S. Chemical Stabilization of Calcareous Sand by Polyurethane Foam Adhesive. *Constr. Build. Mater.* **2021**, *295*, 123609. [CrossRef]
14. Gu, J.; Lyu, H.; Li, B.; Chen, H.; Xu, X.; Du, X. Assessment of Mechanical Behavior and Failure Criteria under Varied Confining Pressures in Treated Calcareous Sand. *Geomech. Energy Environ.* **2024**, *38*, 100548. [CrossRef]
15. Gu, J.; Lyu, H.; Yang, J.; Zeng, C. Effects of Cement Content and Curing Period on Geotechnical Properties of Cement-Treated Calcareous Sands. *Transp. Geotech.* **2022**, *33*, 100732. [CrossRef]
16. Fang, X.; Shen, C.; Wang, C.; Guo, Y.; Wang, L. Study on Bearing Characteristic of Multi-Pile Composite Foundation with Biocemented Coral Sand Pile. *J. Build. Eng.* **2024**, *98*, 111297. [CrossRef]
17. Shen, C.; Fang, X.; Guo, Y.; Hu, F.; Xiong, P.; Wang, C. Effects of Area Replacement Ratio and Pile Length on Composite Foundation with Biocemented Coral Sand Pile. *Geomicrobiol. J.* **2025**, *42*, 286–296. [CrossRef]
18. Arnepalli, S.K.K.; Gondu, V.R.; Chinthala, S. Sustainable Improvement of Granite Sludge Dust Properties Using Microbially Induced Carbonate Precipitation (MICP): Strength Enhancement, Erosion Prevention, and Dust Mitigation. *Environ. Sci. Pollut. Res.* **2025**, 1–24. [CrossRef]
19. Fang, X.; Yang, Y.; Chen, Z.; Liu, H.; Xiao, Y.; Shen, C. Influence of Fiber Content and Length on Engineering Properties of MICP-Treated Coral Sand. *Geomicrobiol. J.* **2020**, *37*, 582–594. [CrossRef]
20. Rahman, M.M.; Hora, R.N.; Ahenkorah, I.; Beecham, S.; Karim, M.R.; Iqbal, A. State-of-the-Art Review of Microbial-Induced Calcite Precipitation and Its Sustainability in Engineering Applications. *Sustainability* **2020**, *12*, 6281. [CrossRef]
21. Wang, Z.; Qin, H.; Dong, X.; Zhang, W. Classification of Additives and Their Influence Mechanisms in Improving the Performance of Biologically Induced Carbonate Precipitation. *Environ. Res.* **2025**, *275*, 121376. [CrossRef] [PubMed]
22. Liu, J.; Li, G.; Li, X.A. Geotechnical Engineering Properties of Soils Solidified by Microbially Induced $CaCO_3$ Precipitation (MICP). *Adv. Civ. Eng.* **2021**, *2021*, 6683930. [CrossRef]
23. Wen, K.; Li, Y.; Amini, F.; Li, L. Impact of Bacteria and Urease Concentration on Precipitation Kinetics and Crystal Morphology of Calcium Carbonate. *Acta Geotech.* **2020**, *15*, 17–27. [CrossRef]

24. Zhang, K.; Tang, C.-S.; Jiang, N.-J.; Pan, X.-H.; Liu, B.; Wang, Y.-J.; Shi, B. Microbial-induced Carbonate Precipitation (MICP) Technology: A Review on the Fundamentals and Engineering Applications. *Environ. Earth Sci.* **2023**, *82*, 229. [CrossRef]
25. Zhang, X.; Wang, H.; Wang, Y.; Wang, J.; Cao, J.; Zhang, G. Improved Methods, Properties, Applications and Prospects of Microbial Induced Carbonate Precipitation (MICP) Treated Soil: A Review. *Biogeotechnics* **2025**, *3*, 100123. [CrossRef]
26. Wang, Y.; Konstantinou, C.; Tang, S.; Chen, H. Applications of Microbial-Induced Carbonate Precipitation: A State-of-the-Art Review. *Biogeotechnics* **2023**, *1*, 100008. [CrossRef]
27. Wu, H.; Wu, W.; Liang, W.; Dai, F.; Liu, H.; Xiao, Y. 3D DEM Modeling of Biocemented Sand with Fines as Cementing Agents. *Int. J. Numer. Anal. Methods Geomech.* **2023**, *47*, 212–240. [CrossRef]
28. Li, G.; Zhang, Y.; Hua, X.; Liu, J.; Liu, X. Mechanical Properties of Aeolian Sand Cemented via Microbially Induced Calcite Precipitation (MICP). *Sci. Rep.* **2024**, *14*, 22745. [CrossRef]
29. Chen, R.; Li, G.; Mi, Z.; Wei, K. Experimental Study of Erosion Prevention Model by Bio-Cement Sand. *Appl. Sci.* **2024**, *14*, 9571. [CrossRef]
30. He, S.; Zheng, J.; He, R.; Hosseini, S.M.J.; Zhu, T.; Cheng, L.; Guo, Z. Influence of Edge Scour on Lateral Responses of Monopiles with Precast Microbial Reinforcement. *Ocean Eng.* **2024**, *313*, 119493. [CrossRef]
31. Zhang, S.; Wang, S.; Ahmed, Z.; Alshawmar, F. Application of Microbially Induced $CaCO_3$ on the Reinforcement of Rock Discontinuity. *Appl. Sci.* **2024**, *14*, 8952. [CrossRef]
32. Liu, X.; Fan, J.; Yu, J.; Gao, X. Solidification of Loess Using Microbial Induced Carbonate Precipitation. *J. Mt. Sci.* **2021**, *18*, 265–274. [CrossRef]
33. Liu, S.; Du, K.; Wen, K.; Armwood-Gordon, C.; Li, L. Influence of Rainfall-induced Erosion on the Stability of Sandy Slopes Treated by MICP. *Adv. Civ. Eng.* **2022**, *2022*, 5105206. [CrossRef]
34. Huang, M.; Zhang, Y.; Hu, J.; Hei, Y.; Xu, Z.; Su, J. Experimental Study on Pore Pressure Variation and Erosion Stability of Sandy Slope Model under Microbially Induced Carbonate Precipitation. *Sustainability* **2023**, *15*, 12650. [CrossRef]
35. Dagliya, M.; Satyam, N.; Garg, A. Experimental Study on Optimization of Cementation Solution for Wind-Erosion Resistance Using the MICP Method. *Sustainability* **2022**, *14*, 1770. [CrossRef]
36. Qu, J.; Li, G.; Ma, B.; Liu, J.; Zhang, J.; Liu, X.; Zhang, Y. Experimental Study on the Wind Erosion Resistance of Aeolian Sand Solidified by Microbially Induced Calcite Precipitation (MICP). *Materials* **2024**, *17*, 1270. [CrossRef]
37. Hang, L.; Yang, E.; Zhou, Y.; Song, W.; He, J. Microbially Induced Calcite Precipitation (MICP) for Stabilization of Desert Sand against the Wind-Induced Erosion: A Parametric Study. *Sustainability* **2022**, *14*, 11409. [CrossRef]
38. Wang, Y.; Soga, K.; DeJong, J.T.; Kabla, A.J. Effects of Bacterial Density on Growth Rate and Characteristics of Microbial-Induced $CaCO_3$ Precipitates: Particle-Scale Experimental Study. *J. Geotech. Geoenviron. Eng.* **2021**, *147*, 04021036. [CrossRef]
39. Jiang, N.-J.; Tang, C.-S.; Yin, L.-Y.; Xie, Y.-H.; Shi, B. Applicability of Microbial Calcification Method for Sandy-Slope Surface Erosion Control. *J. Mater. Civ. Eng.* **2019**, *31*, 04019250. [CrossRef]
40. Li, M.; Peng, Y.; Zhang, J.; Zhao, Y.; Wang, Z.; Guo, Q.; Guo, S. Properties of a Backfill Material Prepared by Cementing Coal Gangue and Fly Ash through Microbial-Induced Calcite Precipitation. *Constr. Build. Mater.* **2023**, *384*, 131329. [CrossRef]
41. Karimian, A.; Hassanlourad, M. Mechanical Behaviour of MICP-Treated Silty Sand. *Bull. Eng. Geol. Environ.* **2022**, *81*, 285. [CrossRef]
42. Yang, Z.; Liu, L.; Dong, Y.; Liu, X.; Wang, X. Analysis of Unconfined Compressive Strength and Environmental Impact of MICP-Treated Lead-Zinc Tailings Sand Instead of Sand as Embankment Material. *Sci. Total Environ.* **2024**, *931*, 172809. [CrossRef] [PubMed]
43. Zhang, W.; Shi, F.; Duan, X.; Kang, W.; Feng, C.; Su, F. Effect of Microbially Induced Carbonate Precipitation (MICP) on the Early Strength Enhancement and Micromechanical Properties in Fly Ash Blended Cement. *Constr. Build. Mater.* **2024**, *423*, 135675. [CrossRef]
44. Abbasi, M.; Hosseinpour, I.; Barari, A.; Mirmoradi, S.H. Mechanical Properties of Silty Sand Treated with MICP Technique Subjected to Freeze-Thaw Cycles. *Transp. Infrastruct. Geotechnol.* **2025**, *12*, 34. [CrossRef]
45. Naskar, J.; Sharma, A.K. Assessment of Enhanced Strength and Stiffness Properties of Bio-Engineered Coal Fly Ash. *Constr. Build. Mater.* **2024**, *413*, 134793. [CrossRef]
46. Kumar, P.; Debele, S.E.; Sahani, J.; Rawat, N.; Marti-Cardona, B.; Alfieri, S.M.; Basu, B.; Basu, A.S.; Bowyer, P.; Charizopoulos, N.; et al. Nature-Based Solutions Efficiency Evaluation against Natural Hazards: Modelling Methods, Advantages and Limitations. *Sci. Total Environ.* **2021**, *784*, 147058. [CrossRef]
47. Gong, C.; Ni, D.; Liu, Y.; Li, Y.; Huang, Q.; Tian, Y.; Zhang, H. Herbaceous Vegetation in Slope Stabilization: A Comparative Review of Mechanisms, Advantages, and Practical Applications. *Sustainability* **2024**, *16*, 7620. [CrossRef]
48. Su, X.; Zhou, Z.; Cao, L.; Liu, J.; Wang, P. Estimating Slope Stability by the Root Reinforcement Mechanism of Artemisia Sacrorum on the Loess Plateau of China. *Ecol. Model.* **2021**, *444*, 109473. [CrossRef]

49. Li, S.; Wang, Z.; Stutz, H.H. State-of-the-Art Review on Plant-Based Solutions for Soil Improvement. *Biogeotechnics* **2023**, *1*, 100035. [CrossRef]
50. DiBiagio, A.; Capobianco, V.; Oen, A.; Tallaksen, L.M. State-of-the-Art: Parametrization of Hydrological and Mechanical Reinforcement Effects of Vegetation in Slope Stability Models for Shallow Landslides. *Landslides* **2024**, *21*, 2417–2446. [CrossRef]
51. Gan, F.; Wei, J.; Li, S. Root–Soil Friction Mechanism of Typical Grasses on Purple Soil Bunds in the Three Gorges Reservoir Area, China. *J. Soil Sci. Plant Nutr.* **2023**, *23*, 3381–3392. [CrossRef]
52. Saadati, N.; Mosaddeghi, M.R.; Sabzalian, M.R.; Jafari, M. Soil Mechanical Reinforcement by the Fibrous Roots of Selected Rangeland Plants Using a Large Soil-Root Shear Apparatus. *Soil Tillage Res.* **2023**, *234*, 105852. [CrossRef]
53. Rahman, E.K.A.; Jeludin, M.; Ratnayake, U.; Musthapa, S.M. *Impact of Roots on the Shear Strength of Root-Reinforced Soil on Slopes*; IOP Publishing: Bristol, UK, 2024; Volume 1369, p. 012022.
54. Cardoza, R.; Oka, L. *Measuring the Effect of Grass Roots on Shear Strength Parameters of Sandy Soils*; American Society of Civil Engineers: Reston, VA, USA, 2020; pp. 214–223.
55. Chakrabarti, M.; Nagabhyru, P.; Schardl, C.L.; Dinkins, R.D. Differential Gene Expression in Tall Fescue Tissues in Response to Water Deficit. *Plant Genome* **2022**, *15*, e20199. [CrossRef] [PubMed]
56. Li, X.; Wu, F.; Xiang, Y.; Fan, J. Transcriptomic Analysis of Antimony Response in Tall Fescue (*Festuca arundinacea*). *Agriculture* **2024**, *14*, 1504. [CrossRef]
57. Cornelis, W.M. Hydroclimatology of Wind Erosion in Arid and Semiarid Envirmonments. In *Dryland Ecohydrology*; Springer: Dordrecht, The Netherlands, 2006; pp. 141–159.
58. Xu, Y.; Li, Q.; Meng, Q.A.Z.L. Meteorological Parameters and Building Energy Consumption Analysis of South China Sea Islands. *J. Civ. Environ. Eng.* **2018**, *40*, 42–47.
59. Wang, Y.; Wang, G.; Wan, Y.; Yu, X.; Zhao, J.; Shao, J. Recycling of Dredged River Silt Reinforced by an Eco-Friendly Technology as Microbial Induced Calcium Carbonate Precipitation (MICP). *Soils Found.* **2022**, *62*, 101216. [CrossRef]
60. Zhu, W.; Yuan, M.; He, F.; Zhao, Y.; Xiao, Z.; Wang, Q.; Meng, F.; Tang, Q. Effects of Hydroxypropyl Methylcellulose (HPMC) on the Reinforcement of Sand by Microbial-Induced Calcium Carbonate Precipitation (MICP). *Appl. Sci.* **2022**, *12*, 5360. [CrossRef]
61. Liu, B.; Tang, C.S.; Pan, X.H.; Zhu, C.; Cheng, Y.J.; Xu, J.J.; Shi, B. Potential Drought Mitigation through Microbial Induced Calcite precipitation-MICP. *Water Resour. Res.* **2021**, *57*, e2020WR029434. [CrossRef]
62. Luo, L.; Zhang, Y.; Xu, G. How Does Nitrogen Shape Plant Architecture? *J. Exp. Bot.* **2020**, *71*, 4415–4427. [CrossRef]
63. Xie, L.; Zhou, J.; Shen, L.; Ji, Y.; Li, W.; Cheng, Y. Discrete Element Study on Mechanical Properties of MICP-Treated Sand under Triaxial Compression. *J. Mar. Sci. Eng.* **2024**, *12*, 1503. [CrossRef]
64. Hu, Q.; Chen, Q. Experimental Study of Synergistic Reinforcement of Silty Clay with Glutinous Rice Paste and MICP. *PLoS ONE* **2023**, *18*, e0284633. [CrossRef] [PubMed]
65. Lai, Y.; Liu, S.; Cai, Y.; Yu, J. Reinforcement of Different Sands by Low-pH Bio-Mineralization. *Materials* **2023**, *16*, 6211. [CrossRef] [PubMed]
66. Jiang, N.; Cheng, H.; Liu, C.; Fang, Z.; Zou, X. A Wind Tunnel Study of the Effects of Vegetation Structural Characteristics on the Airflow Field. *CATENA* **2024**, *242*, 108064. [CrossRef]
67. Chen, Y.; Liu, B.; Bian, Y.; Gao, Y.; Liu, Y.; Cheng, M.; Wang, L.; Hang, L. Effects of Soybean Urease Induced Carbonate Precipitation on the Seed Emergence and Seedling Growth of Caragana Korshinskii Kom and Its Application in Wind Erosion Control. *Plant Soil* **2025**, *507*, 629–653. [CrossRef]
68. Ji, X. GDS Triaxial Test on the Reinforcement Effects of Bermudagrass Root-Soil Complex. *IOP Conf. Ser. Earth Environ. Sci.* **2019**, *304*, 032106. [CrossRef]
69. Wang, B.; Wang, S. Shear Strength Analysis and Slope Stability Study of Straight Root Herbaceous Root Soil Composite. *Appl. Sci.* **2023**, *13*, 12632. [CrossRef]
70. Ghasemi, P.; Montoya, B.M. Effect of Treatment Solution Chemistry and Soil Engineering Properties Due to Microbially Induced Carbonate Precipitation Treatments on Vegetation Health and Growth. *ACS EST Eng.* **2022**, *2*, 2196–2205. [CrossRef]

Journal of
Marine Science and Engineering

MDPI

Article

Experimental Study on Strength Characteristics of Overconsolidated Gassy Clay

Tao Liu [1,2], Longfei Zhu [1], Yan Zhang [3,*], Chengrong Qing [1], Yuanzhe Zhan [1], Chaonan Zhu [1] and Jiayang Jia [1]

[1] Shandong Engineering Research Center of Marine Exploration and Conservation, Ocean University of China, Qingdao 266100, China; ltmilan@ouc.edu.cn (T.L.); zhulongfei@stu.ouc.edu.cn (L.Z.); qcr@stu.ouc.edu.cn (C.Q.); zhanyuanzhe@stu.ouc.edu.cn (Y.Z.); 21231013039@stu.ouc.edu.cn (C.Z.); jiajiayang@stu.ouc.edu.cn (J.J.)
[2] Laboratory for Marine Geology, Qingdao Marine Science and Technology Center, Qingdao 266237, China
[3] Key Laboratory of Intelligent Underground Detection Technology, Anhui Jianzhu University, Hefei 230000, China
* Correspondence: zhangyan4850@ahjzu.edu.cn

Abstract: Gassy clay, commonly encountered in coastal areas as overconsolidated deposits, demonstrates distinct mechanical properties posing risks for submarine geohazards and engineering stability. Consolidated undrained triaxial tests combined with cyclic simple shear tests were performed on specimens with varying overconsolidation ratios (OCRs) and initial pore pressures, supplemented by SEM microstructural analysis. Triaxial results indicate that OCR controls the transitions between shear contraction and dilatancy, which govern both stress–strain responses and excess pore pressure development. Higher OCR with lower initial pore pressure increases stress path slope, raises undrained shear strength (s_u), reduces pore pressure generation, and induces negative pore pressure at elevated OCR. These effects originate from compressed gas bubbles and limited bubble flooding under overconsolidation, intensifying dilatancy during shear. Cyclic tests reveal gassy clay's superior cyclic strength, slower pore pressure accumulation, reduced stiffness softening, and enhanced deformation resistance relative to saturated soils. Cyclic pore pressure amplitude increases with OCR, while peak cyclic strength and anti-softening capacity occur at OCR = 2, implying gas bubble interactions.

Keywords: overconsolidated gassy clay; consolidation test; triaxial test; cyclic simple shear test; numerical simulation

1. Introduction

Submarine shallow gas refers to methane and other gases continuously generated through microbial degradation of sediments with high organic content buried at certain depths below the seabed [1,2]. These gases predominantly exist in the form of gas pockets and gassy sediments, widely distributed in global coastal and alluvial plain regions [3]. As shown in Figure 1, coastal gassy soil is characterized by discontinuous gas phases and interconnected water phases, with saturation levels typically exceeding 85% [4,5]. Advanced techniques such as scanning electron microscopy (SEM) and computed tomography (CT) scanning reveal that gas bubbles are trapped within the soil matrix in clay-dominated fine-grained gassy soil, exhibiting sizes significantly larger than soil particles and gas pressures reaching 5–6 times the standard atmospheric pressure. The presence of gas profoundly alters the geomechanical properties of gassy soil, including critical parameters such as

settlement behavior, liquefaction potential, and shear strength. This results in a marked increase in internal pore pressure, reduced effective stress, and subsequent soil expansion and structural weakening of the soil skeleton [6], collectively diminishing bearing capacity and posing severe risks to engineering safety. Furthermore, under dynamic loads, such as wave action, these conditions may trigger submarine geohazards [7]. For example, the Deepwater Horizon drilling platform in the Gulf of Mexico suffered a catastrophic shallow gas explosion, resulting in severe environmental and economic losses [8]. A water conservancy facility in Anhui Province, China, experienced foundation settlement and structural cracking due to the presence of gassy soil strata [9]. In recent years, some scholars have carried out visual analysis on the microstructure of different types of gassy soil [10–13]. The unique meso-structure of gassy soil introduces a more complex multiphase coupling mechanism compared to conventional unsaturated soils [14,15].

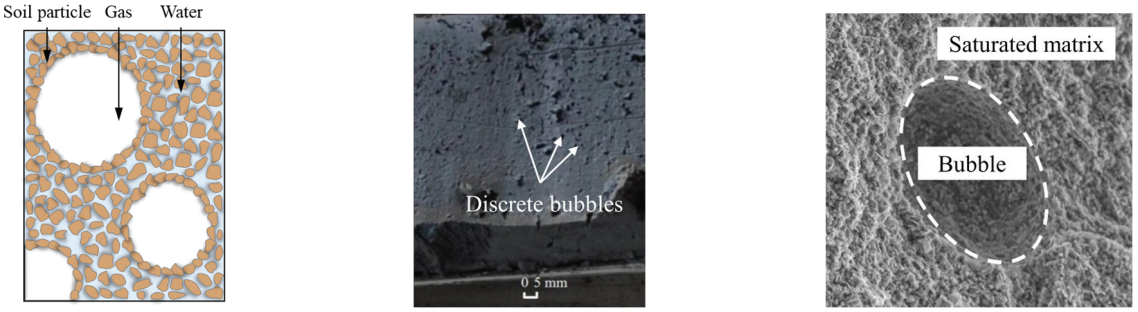

Figure 1. Typical gassy clay and its microscopic scanning image [14]: (**a**) Gassy clay structure; (**b**) gassy clay samples in Zhoushan sea area; (**c**) SEM image of typical gassy soil.

Research indicates that the effective stress principle remains applicable to gassy soil under high saturation conditions (S_r > 90%), effectively explaining their mechanical behaviors, including compressibility [7] and constitutive relationships [16–18]. For fine-grained gassy soil, the total volumetric strain generated under shear loading is attributed to both the saturated soil matrix and gas bubbles [19]. However, since the shear stiffness of gas bubbles is generally negligible, it is conventionally assumed that the total volumetric strain is entirely contributed by the saturated soil matrix. Figure 2 illustrates a representative volume element of fine-grained gassy soil, including three different matrixes: bubbles, pore water, and soil particles. To conveniently regard the volume of the whole gas-bearing soil as V, the volume of bubbles, pore water, and soil particles is regarded as V_g, V_w, and $V_{s,}$ respectively. S_r is the saturation of the water phase, and e_w and ψ are the water void ratio and gas volume fraction, respectively [20]. The three-phase composition of gassy soil per unit volume is shown in Figure 2.

Thomas [21] demonstrated, through one-dimensional consolidation tests, that increased gas content significantly enhances soil compressibility, with compression curves asymptotically approaching those of saturated soils without altering matrix properties. Puzrin et al. [7] emphasized that gas bubbles solely influence the consolidation process without altering the ultimate settlement. Hong [16], utilizing triaxial testing, confirmed that initial gas content and compressibility exhibit negative correlations with increasing initial pore pressure, while enhanced effective stress drives the compressibility of gassy soil to converge toward saturated soil behavior. Ye et al. [22] observed that the ultimate settlement of gassy soil exceeds that of saturated soils and demonstrates a negative correlation with initial pore pressure, with water intrusion into gas cavities accelerating pore pressure dissi-

pation. Notably, large, occluded bubbles drastically modify compression characteristics, inducing post-dissipation creep and long-term consolidation, due to delayed gas pressure equilibration [23–25].

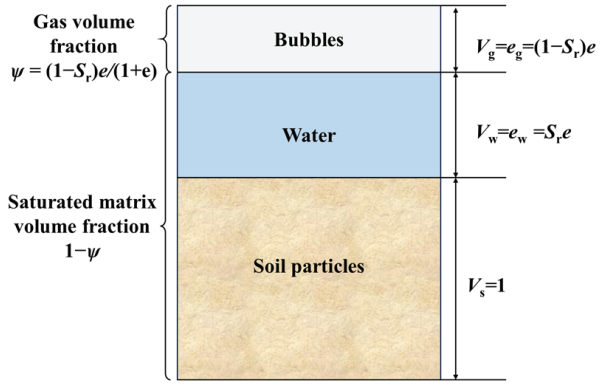

Figure 2. Three-phase composition diagram of gas-bearing soil per unit volume.

Wheeler [26] revealed through undrained shear tests that gas bubbles influence shear strength by modulating the coupled relationship between initial pore pressure and mean effective stress. Hong [16] proposed that gas–liquid interactions dominate the excess pore pressure response: under high initial pore pressure, gas bubble compression induces fracture collapse, reducing strength and amplifying excess pore pressure; under low initial pore pressure, the "bubble flooding" effect is triggered, enhancing strength and suppressing excess pore pressure. Based on continuum mechanics theory, Wheeler [27,28] established two critical pressure models for gas bubbles, elucidating the evolutionary relationship between gas content and gas pressure thresholds, and demonstrated that increasing gas content reduces both the shear modulus and bulk modulus of gassy soil.

Liu [29] demonstrated fine-grained gassy soils' excess pore pressure and shear strength dependency on initial pore water pressure through triaxial tests, showing higher strength under CTC than RTC. Wang [30] revealed that 3.5% gas content enhanced undrained strength by 18% and reduced consolidation coefficient by 50% via triaxial-consolidation tests, further establishing cone factor-gas content correlations through CPT simulations. Hong et al. [31] demonstrated, through cyclic triaxial tests, that saturated clay's cyclic stress ratio decayed to 0.74 (50 cycles); low-pressure gassy clay showed CSR = 0.5/slope = 4 (partial drainage); high-pressure specimens exhibited CSR > 1 with higher pore pressure than saturated clay due to micro-crack instability.

Building upon Gao's critical state model [32], Cai [33] developed an overconsolidated gassy clay bounding surface model, revealing gas cavity-induced soil structure degradation that reduces plastic modulus and shear strength, while partial drainage under undrained conditions enhances stiffness. Validation via undrained triaxial tests on Malaysian and Specwhite Kaolin confirmed model accuracy. In marine environments, overconsolidated gassy soil subjected to geological sedimentation, hydrodynamic conditions, and engineering disturbances [34] may trigger gas segregation and migration as well as geohazards, such as submarine landslides and pipeline ruptures [35,36]. Existing studies predominantly focus on the influence of gas content, saturation, and initial pore pressure on strength, while the effects and mechanisms of overconsolidation states on the mechanical and cyclic behaviors of gassy soil remain unclear. To investigate the mechanical strength characteristics and response mechanisms of overconsolidated gassy clay, this study conducted consolidated undrained triaxial tests and cyclic simple shear tests on gassy clay specimens with different

overconsolidation ratios and initial pore pressures. Scanning electron microscopy (SEM) was employed to observe their microstructural characteristics.

2. Experimental Programs

2.1. Testing Material and Preparation of Gassy Specimens

During in situ sampling, gases in gassy soil are prone to exsolution and expansion under pressure variations, causing disturbance and damage to soil specimens [37,38]. This study employed the zeolite molecular sieve technique to prepare reconstituted gassy clay specimens. Chinese kaolin clay was selected as the test soil, wherein gas-absorbed zeolite was incorporated into the slurry to release adsorbed gases [39,40]. Table 1 presents the basic physical property indices of the Chinese kaolin used in the experiments.

Table 1. Index properties and mechanical parameters of Chinese kaolin.

Parameter	Measured Value
Liquid limit: %	40
Plastic limit: %	23
Plasticity index	17
The angle of friction: °	25.4
Coefficient of earth pressure at rest	0.59
Critical stress ratio	1

The zeolite molecular sieve technique (as illustrated in Figure 3) provides a straightforward and effective methodology with traceable stress history, enabling large-scale preparation of gassy soil specimens whose physical and mechanical properties closely resemble in situ gassy clay. However, this technique exhibits limitations in gas-phase parameter regulation accuracy, particularly in achieving precise quantitative control of gas content. The detailed procedure comprises the following steps: (a) Subject pre-weighed molecular sieve material (zeolite powder, 20% of dry soil mass) to high-temperature drying (105 °C for 24 h), followed by vacuum saturation (−100 kPa for 24 h). Subsequently, introduce N_2 into the molecular sieve under high-pressure conditions (200 kPa for 24 h). (b) Mix dry soil (kaolin) with deaerated water at a mass ratio of 1:2 times the Liquid Limit (LL) through thorough homogenization, followed by vacuum saturation under −100 kPa for 24 h. (c) Blend the N_2-saturated zeolite powder with the saturated slurry under thorough mixing, facilitating gas–water exchange between the zeolite and slurry to induce bubble nucleation. This process closely replicates bubble formation mechanisms observed in marine sediments. (d) Transfer the slurry to a cylindrical chamber and apply 60 kPa of vertical stress incrementally until pre-consolidation completion.

2.2. Scanning Electron Microscope Test

Microstructural characterization of overconsolidated gassy clay was conducted using a ZEISS Sigma 360 scanning electron microscope (Germany), which enables secondary electron imaging, backscattered electron observation, and morphological analysis under variable vacuum conditions. This study focused on gassy clay with overconsolidation ratios (OCR) of 1, 2, and 4. Specimen preparation utilized a GDS Advanced Consolidation System through the following protocol: normally consolidated samples (OCR = 1) were obtained by incrementally loading gassy clay specimens to 100 kPa. For overconsolidated specimens (OCR = 2 and 4), samples were first loaded incrementally to 200 kPa and 400 kPa, respectively, then unloaded to 12.5 kPa, and, subsequently, reloaded to 100 kPa.

The prepared overconsolidated gassy clay was dried, and a 1 cm^3 sample was carefully extracted. Using tweezers, the specimen was adjusted to maintain the fresh fracture surface facing upward and fixed to the specimen stub with double-sided adhesive tape, minimizing disturbances such as contact or vibration. The stub was gently transferred to the vacuum chamber for gold sputtering. The vacuum pump was activated to evacuate air and maintain vacuum conditions. Gold sputtering was then performed on the specimen surface to enhance conductivity, improve image quality, protect the sample, and reduce charging effects, thereby providing optimal conditions for observation and analysis. The workflow is illustrated in Figure 4.

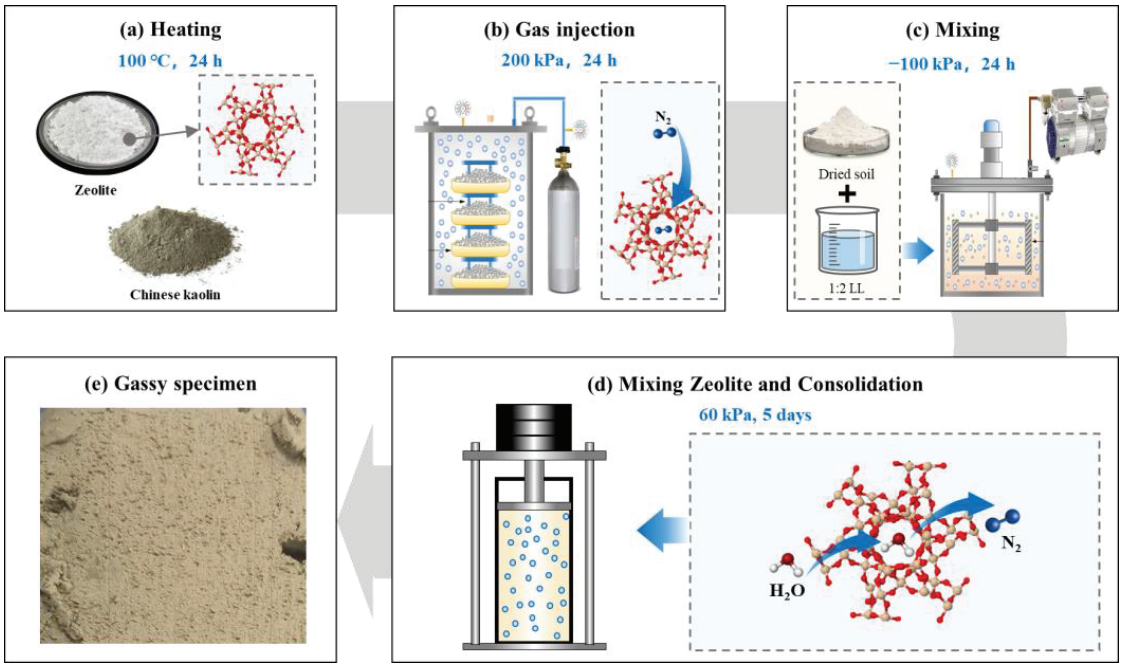

Figure 3. The main process of gassy soil preparation using the zeolite molecular sieve technique.

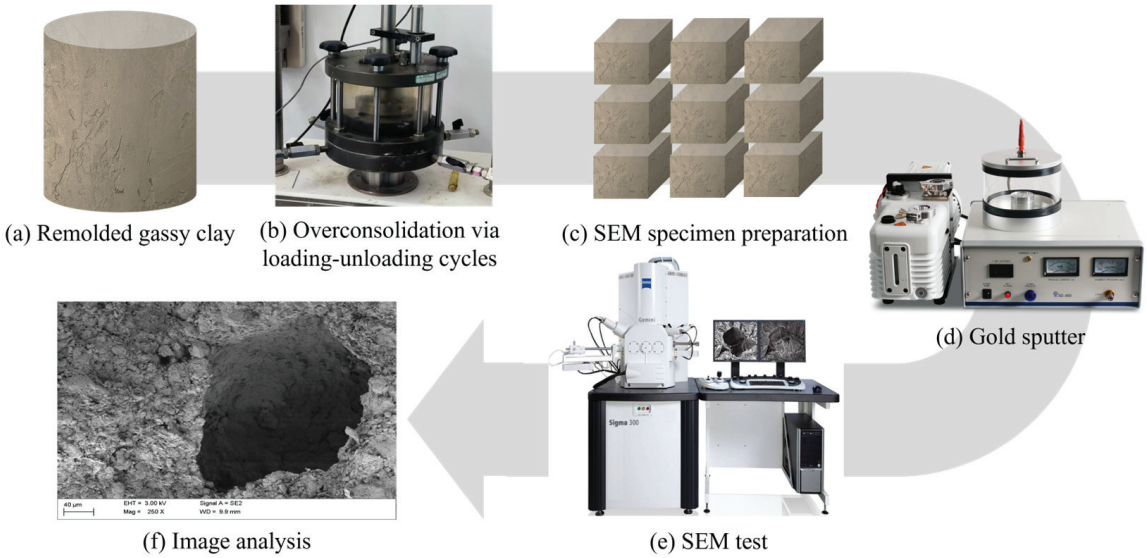

Figure 4. The main process of SEM test.

2.3. Consolidated-Undrained Triaxial Compression Test

Consolidated undrained compression tests were conducted on overconsolidated gassy clay using the GDS dynamic triaxial testing system, as illustrated in Figure 5.

The remolded gassy clay specimens were trimmed into triaxial samples with dimensions of 50 mm in diameter and 100 mm in height. During the consolidation phase, initial pore water pressures were set to u_0 = 0 kPa and 200 kPa, with a mean effective stress p'_0 = 100 kPa. Normally consolidated specimens (OCR = 1) underwent isotropic consolidation under 100 kPa effective confining pressure for 48 h. Overconsolidated specimens (OCR = 2 and 4) were first consolidated isotropically under 200 kPa and 400 kPa effective confining pressures for 48 h, respectively, followed by unloading to 100 kPa and reconsolidation for 48 h. Consolidation completion criteria required full dissipation of excess pore pressure or negligible volumetric change. Post-consolidation, drainage valves were closed, and undrained shear testing commenced at a controlled axial strain rate of 0.05%/min until shear failure occurred or axial strain reached 20%. The experimental program and specimen numbering are detailed in Table 2.

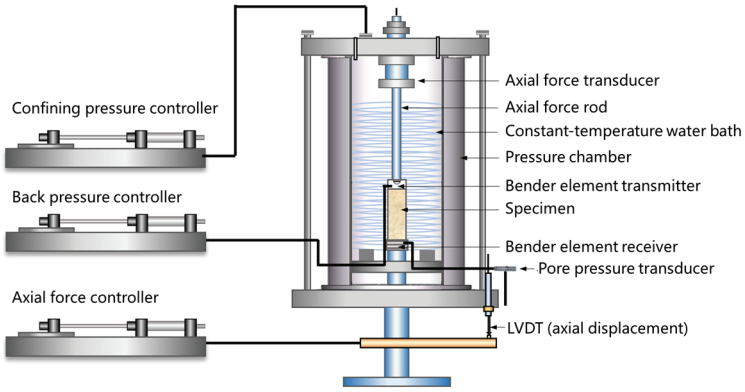

Figure 5. Schematic diagram of GDS dynamic triaxial apparatus.

Table 2. Triaxial test scheme.

Sample Type	Zeolite Content (%)	Initial Pore Water Pressure (kPa)	OCR	Initial Mean Operative Stress (kPa)
Saturated (SS)	0	Saturation	1, 2, 4	100
Gassy (G0)	20	0		
Gassy (G2)	20	200		

2.4. Cyclic Simple Shear Test

Cyclic simple shear tests on overconsolidated gassy clay were conducted using the GDS cyclic simple shear apparatus, as illustrated in Figure 6a. Figure 6c illustrates the parameter definitions for mean shear stress (τ_a) and cyclic shear stress (τ_{cy}) in cyclic simple shear testing, expressed mathematically as follows:

$$\tau_a = (\tau_{max} + \tau_{min})/2 \quad (1)$$

$$\tau_{cy} = (\tau_{max} - \tau_{min})/2 \quad (2)$$

where τ_a is the mean shear stress (static shear stress), τ_{cy} is the cyclic shear stress (dynamic shear stress), and τ_{max} and τ_{min} are the maximum and minimum shear stresses within a single cycle.

This study conducted cyclic simple shear tests on gassy soil and saturated soils with varying overconsolidation ratios (OCRs) under two dynamic shear stress ratios (τ_{cy}/τ_{max}), excluding mean shear stress. The experimental program is detailed in Table 3, where τ_{max} represents the maximum shear stress measured via static simple shear tests. The procedure comprises the following: (a) Preparation of simple shear specimens using a ring knife method: samples (70 mm diameter × 20 mm height) were trimmed with filter papers placed on both top and bottom surfaces. (b) Mounting of the rubber membrane-encased specimen onto the shear apparatus base, followed by sequential installation of lubricated shear rings. (c) Consolidation under vertical stresses of 100, 200, and 400 kPa with drainage valves open. Upon vertical displacement stabilization (24 h), unloading to 100 kPa achieved OCR = 1, 2, and 4. Specimens were then equilibrated for 24 h. (d) The vertical loading system was locked to maintain a constant volume. Horizontal shear force was applied at 0.1 mm/min until shear strain reached 16%, with τ_{max} recorded at termination. (f) Repeating steps (a)–(c), followed by application of sinusoidal cyclic shear stresses with amplitudes of $0.5\tau_{max}$ or $0.25\tau_{max}$ at 0.1 Hz until the cumulative shear strain attained 16%.

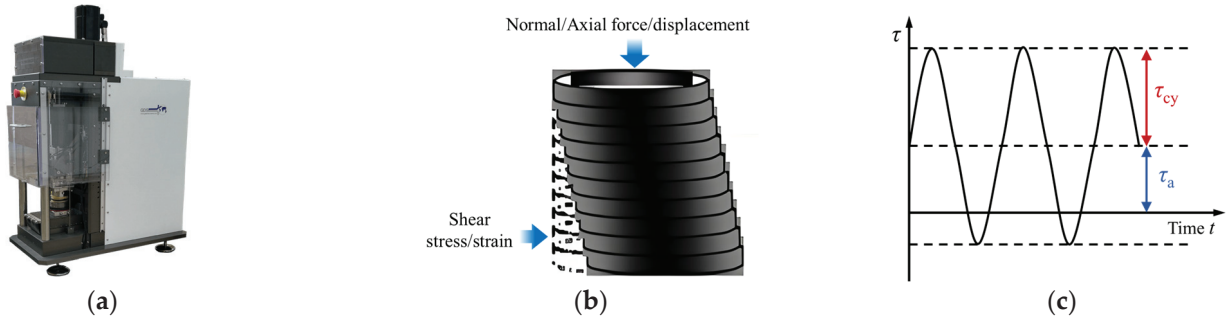

Figure 6. Schematic diagram of GDS cyclic shear test system: (**a**) GDS cyclic simple shear apparatus; (**b**) schematic diagram of shear deformation; (**c**) shear stress parameters.

Table 3. Cyclic simple shear test scheme.

Sample Type	Zeolite Content (%)	Dynamic Shear Stress Ratios (τ_{cy}/τ_{max})	OCR	Cyclic Shear Stress τ_{cy} (kPa)
Saturated (SS)	0	0.5	1	14.6
			2	24.8
			4	34.9
Gassy (G05)	20	0.5	1	15.5
			2	22.9
			4	37.0
Gassy (G025)	20	0.25	1	7.8
			2	11.5
			4	18.5

3. Experimental Results and Discussion

3.1. Micromorphological Characteristics

Microstructural analysis of remolded gassy clay was conducted through scanning electron microscopy (SEM) at 250× and 500× magnifications (Figure 7), revealing distinct gas bubble structures (the dashed line boxs in white) and their spatial distribution relative to soil particles. The observed microstructure aligns with natural gassy clay reported by Hong [10] from Zhoushan sediments at 5 m water depth, validating the reliability of the

specimen preparation method. With increasing overconsolidation ratio (OCR), bubble volume decreased progressively: at OCR = 2, bubble volume reduced to approximately 30% of the normally consolidated state (OCR = 1), transitioning from spherical to collapsed configurations (Figure 7b,d); at OCR = 4, bubble volume further diminished to below 10% of the baseline, exhibiting pronounced collapse (Figure 7c,f).

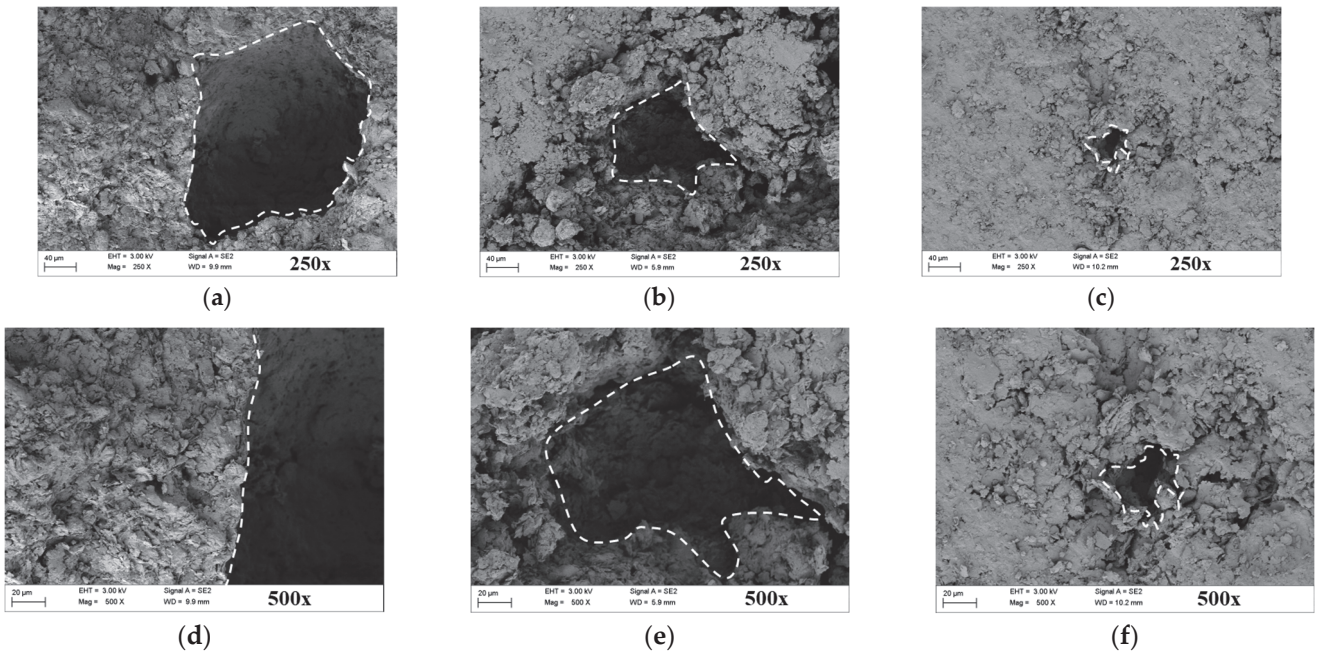

Figure 7. Microstructure of overconsolidated gassy soil: (**a**) OCR = 1, 250×; (**b**) OCR = 2, 250×; (**c**) OCR = 4, 250×; (**d**) OCR = 1, 500×; (**e**) OCR = 2, 500×; (**f**) OCR = 4, 500×.

The observed microstructural alterations may be attributed to the elevated preconsolidation pressure inducing significant irrecoverable plastic deformation in the gassy clay, resulting in tighter particle packing, reduced void ratio, and disruption of stress concentration at soil particle–gas bubble interfaces. Under sustained external pressure (as schematized in Figure 8), gas bubbles underwent volumetric compression accompanied by partial gas dissolution into pore water. Post-unloading, the dissolved gas exhibited negligible re-entrainment into bubbles, while both bubble volume and intergranular porosity demonstrated limited rebound capacity, rendering the microstructure irrecoverable to its pre-overconsolidation state.

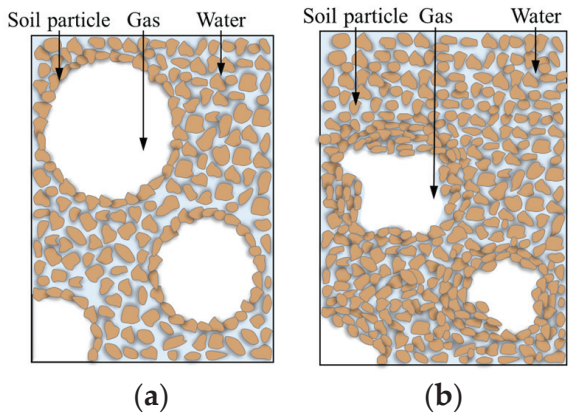

Figure 8. Schematic diagram of microstructure change in overconsolidated gassy soil: (**a**) normal consolidation; (**b**) overconsolidation.

3.2. Consolidated Undrained Shear Characteristics

3.2.1. Excess Pore Pressure

The excess pore water pressure (Δu) in soils exhibits a critical relationship with shear strength, directly influencing the shear process. Figure 9 compares Δu evolution during undrained shear between gassy soil and saturated soils across varying overconsolidation ratios (OCR = 1, 2, 4) and initial pore water pressures (u_0 = 0, 200 kPa), where Δu is normalized by the effective consolidation pressure p'.

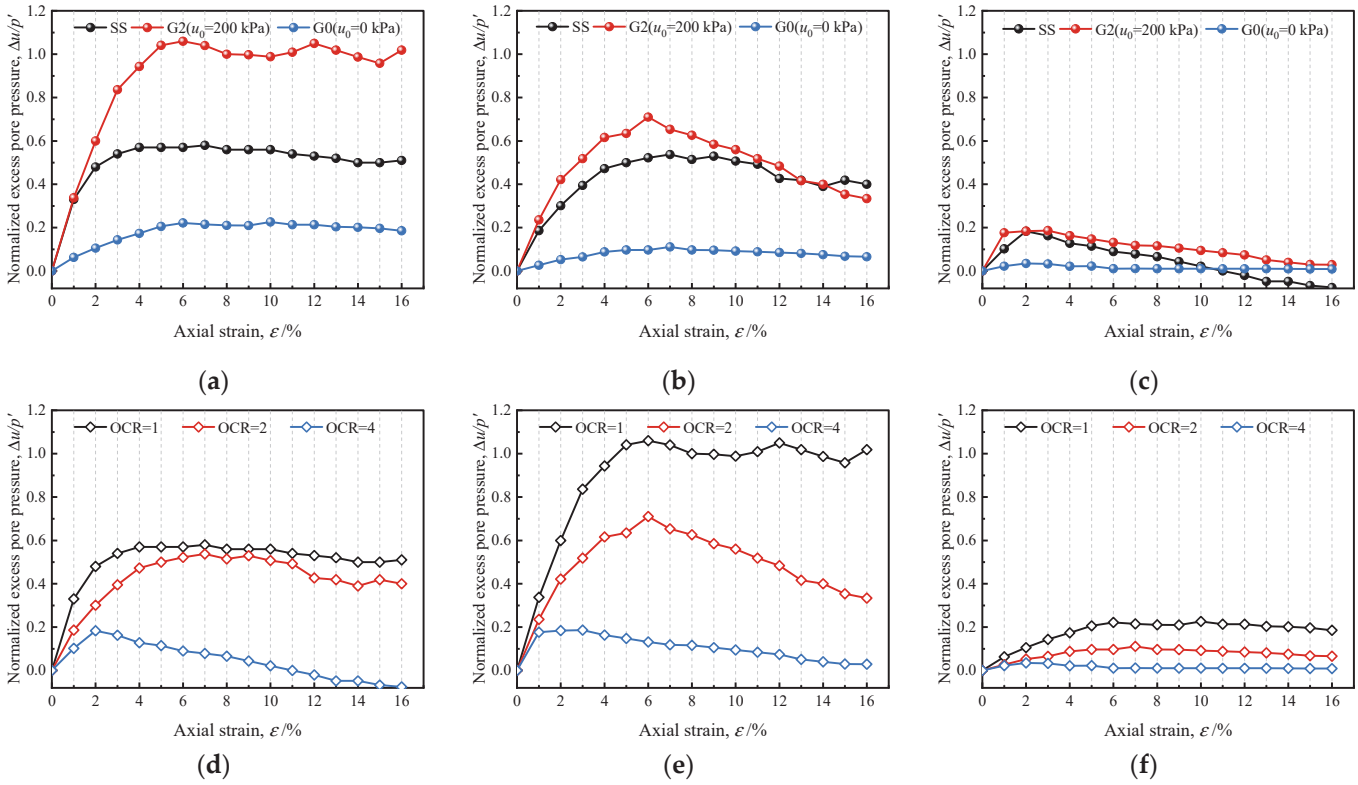

Figure 9. Excess pore pressure response of gassy soil with different overconsolidation ratios and initial pore pressure: (**a**) OCR = 1; (**b**) OCR = 2; (**c**) OCR = 4; (**d**) SS; (**e**) G2; (**f**) G0.

Figure 9 demonstrates that gassy soil and saturated soil with OCR = 1 both exhibited positive excess pore pressure ($\Delta u/p'$) with analogous response trends. At axial strains below 5%, $\Delta u/p'$ increased rapidly in a near-linear manner with strain; beyond 5% axial strain, the $\Delta u/p'$ growth rate decelerated and stabilized, maintaining a plateau until specimen failure. As OCR increased, Δu evolution diverged markedly: specimens with OCR = 2 displayed lower peak $\Delta u/p'$ than normally consolidated counterparts, followed by $\Delta u/p'$ reduction upon exceeding 10% axial strain before eventual stabilization. For OCR = 4 specimens, peak $\Delta u/p'$ further diminished, with $\Delta u/p'$ commencing decline at just 2% axial strain and exhibiting significant decline, particularly in saturated soils, where negative $\Delta u/p'$ emerged.

The generation of excess pore pressure arises from shear-induced contraction, progressive particle rearrangement, and pore collapse, which promotes shear contraction tendencies, thereby generating positive excess pore pressure. In overconsolidated specimens, preconsolidation pressure enhances initial compaction (lower void ratio), leading to shear dilatancy tendencies. At higher OCR, pronounced dilatancy dominates: initial shear generates positive excess pore pressure until peak strength, followed by excess pore pressure reduction or even negative excess pore pressure due to volumetric expansion

exceeding pore water replenishment. For gassy soil, gas bubbles mitigate both the attenuation of shear contraction (at lower OCR) and the intensification of shear dilatancy (at higher OCR). Specifically, at OCR = 2, gassy soils exhibit higher peak excess pore pressure than saturated soils due to the delay of the weakening of shear contraction; at OCR = 4, the excess pore pressure reduction amplitude in gassy soil is significantly smaller than in saturated soils, with no marked negative excess pore pressure observed, as bubbles buffer the enhancement shear dilatancy and the dissipation pore pressure.

Figure 9 reveals that the excess pore pressure ($\Delta u/p'$) response of gassy soil correlates with initial pore pressure conditions. At higher initial pore pressure (u_0 = 200 kPa), gassy soils exhibit greater $\Delta u/p'$ than saturated soils; this Δu disparity diminishes progressively with increasing overconsolidation ratio (OCR). This behavior stems from gas bubbles inducing localized pore development and expansion within the soil matrix, generating microcracks and voids. Under elevated pore pressure, intensified stress concentration at bubble–soil interfaces amplifies during shear, causing collapse of bubble-adjacent voids and subsequent gas/void compression. These mechanisms enhance the shear contraction of gassy soil, thereby elevating $\Delta u/p'$.

For overconsolidated gassy clay specimens with an initial consolidation pore pressure u_0 = 200 kPa, scanning electron microscopy (SEM) imaging of shear failure planes revealed representative microstructural features, as shown in Figure 10. At elevated initial pore pressures, shear-induced collapse of cracks and voids adjacent to gas bubbles (the dashed line boxs in white) occurred, accompanied by significant bubble compression (mechanism illustrated in Figure 11a). Conversely, under lower initial pore pressures (u_0 = 0 kPa), higher gas content and larger bubble dimensions allowed pore water ingress into bubbles during shear, a phenomenon termed "bubble flooding" (Figure 11b), which reduces measured excess pore pressure. The trigger condition of bubble flooding can be calculated by the formula presented by Wheeler [24]:

$$u_w - u_g = \frac{2T}{R} \tag{3}$$

where u_w is the pore pressure at the bubble interface, u_g is the ambient pore water pressure, T is the temperature-dependent water surface tension, and R is the curvature radius of the water meniscus (equivalent to bubble radius).

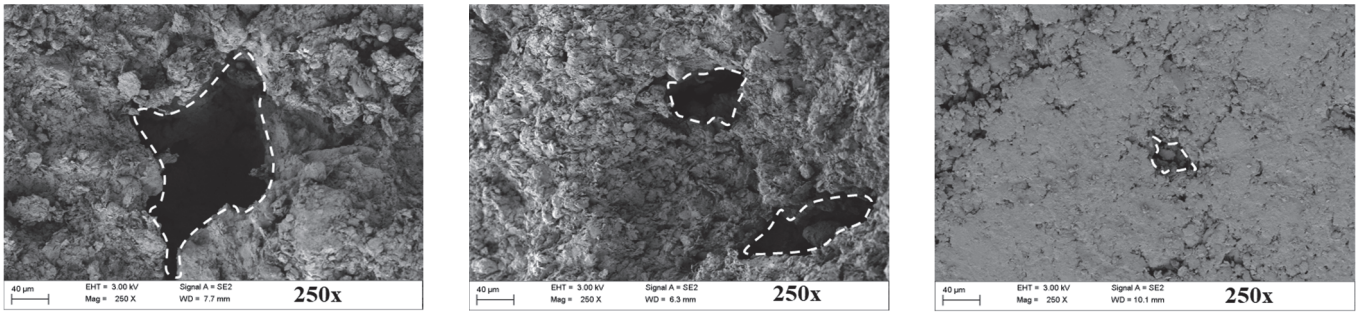

(**a**) (**b**) (**c**)

Figure 10. Microstructure of gassy soil after undrained shear failure: (**a**) OCR = 1; (**b**) OCR = 2; (**c**) OCR = 4.

Due to shear dilatancy, soil volume expansion facilitates water reentry from bubbles into the saturated matrix, mitigating excess pore pressure decline. In low initial pore pressure conditions, the excess pore pressure reduction trend at higher OCR is attenuated.

This is attributed to the lower initial gas content and smaller bubble volume in highly overconsolidated specimens, which limit shear dilatancy.

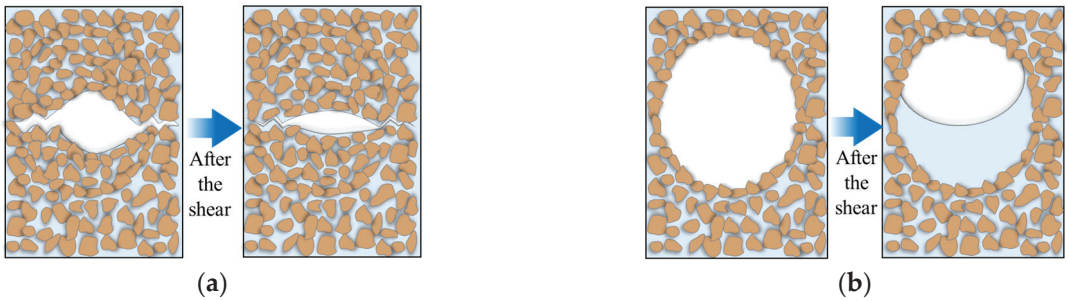

Figure 11. Schematic diagram of undrained shear process in gassy soil: (**a**) pore collapse at high initial pore pressure; (**b**) bubble flooding at low initial pore pressure.

3.2.2. Stress–Strain Relationship

The stress–strain relationship of soils reflects the undrained shear strength during shear. The stress–strain curves of overconsolidated gassy clay and saturated soils, as shown in Figure 12, exhibit similar patterns: during axial strains (ε) below 3%, the deviatoric stress (q) increases rapidly, with gassy clay under lower initial pore pressure (u_0 = 0 kPa) showing smaller q, likely attributed to larger bubble size and higher compressibility in low-pore-pressure conditions. As ε increases to 3–8%, the q growth rate slows, but gassy clay at u_0 = 0 kPa accelerates and surpasses other specimens. When ε exceeds 10%, all specimens reach peak q and stabilize.

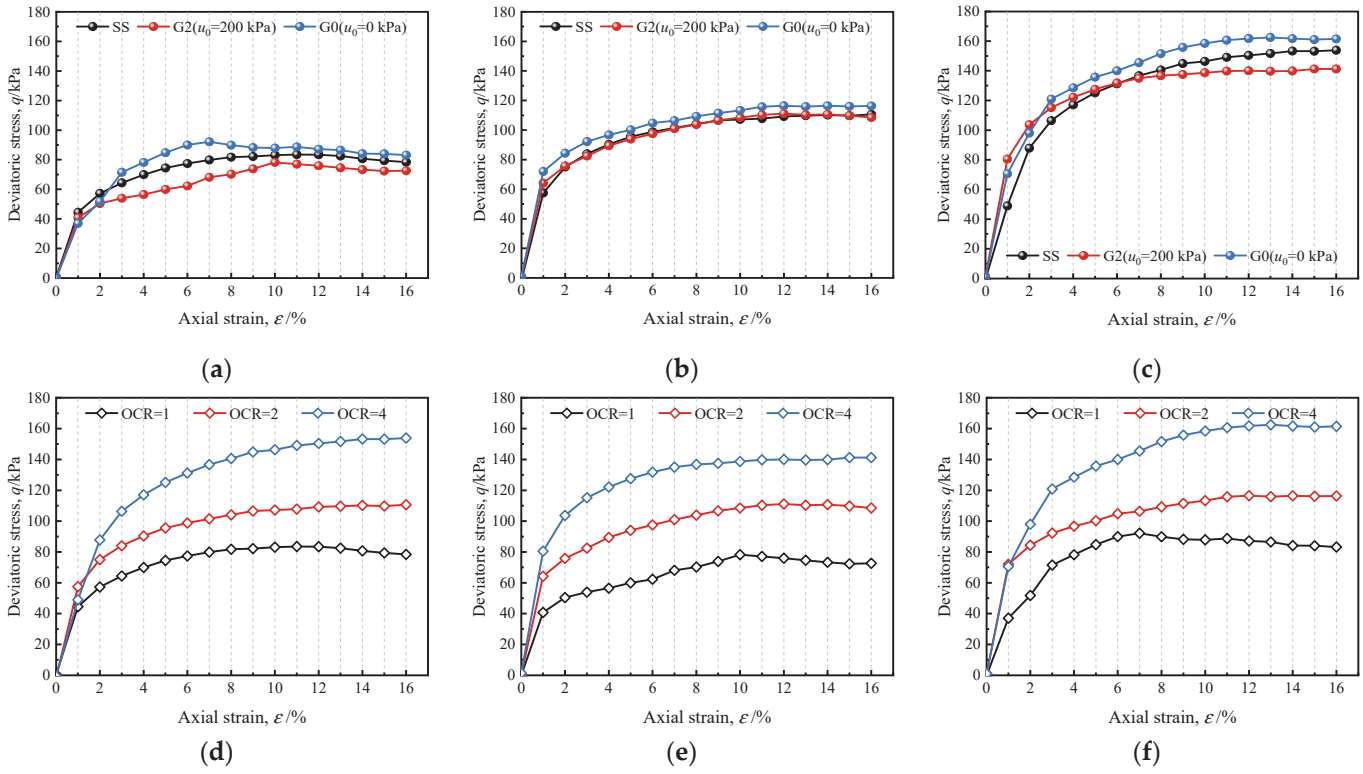

Figure 12. Stress–strain relationship of gassy soil with different overconsolidation ratios and initial pore pressure: (**a**) OCR = 1; (**b**) OCR = 2; (**c**) OCR = 4; (**d**) SS; (**e**) G2; (**f**) G0.

The undrained shear strength (s_u) in triaxial testing is calculated using the radius of Mohr's circle, which is taken as half of the failure strength(q_f). q_f can be determined as either the peak deviatoric stress or the deviatoric stress corresponding to an axial strain of 15% (ε = 15%). Figure 13 demonstrates the undrained shear strength (s_u) of gassy soil and saturated soils under different overconsolidation ratios (OCRs).

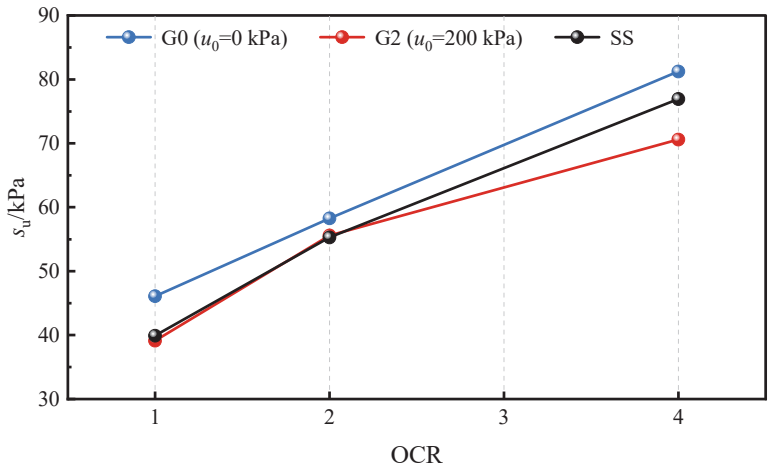

Figure 13. Variation curve of undrained shear strength with overconsolidation ratio OCR.

For OCR = 1, gassy soils exhibit higher s_u than saturated soils at low initial pore pressure (u_0 = 0 kPa) but lower s_u at u_0 = 200 kPa, with a 22% reduction in s_u observed as u_0 increases from 0 to 200 kPa. This reduction is attributed to larger bubble volume in gassy soil at low initial pore pressure, where bubble flooding enhances shear strength. For OCR = 2, s_u increases for both soil types: G2 specimens (u_0 = 200 kPa) show a 42% increase, while G0 specimens (u_0 = 0 kPa) improve by 26%, likely due to compressed bubbles reducing void collapse and weakening shear contraction. For OCR = 4, compared to OCR = 2, G2 and G0 specimens exhibit further s_u increases of 27% and 39%, respectively, with gassy soil at low initial pore pressure showing greater enhancement, consistent with Section 3.2.1 analyses on bubble-mediated mitigation of shear contraction attenuation and shear dilatancy intensification

3.2.3. Stress Path

Figure 14 illustrates the stress path curves of gassy soils and saturated soils, showing similar trends for specimens with identical overconsolidation ratios (OCRs) but significant divergence across different OCR values. With a rising OCR and decreasing initial pore pressure, the stress path slope progressively increases, which is consistent with previous research results [32,33]. For OCR = 1, the soil initially exhibits elastoplastic behavior during shear, characterized by rapid accumulation of excess pore pressure (excess pore pressure) and gradual reduction in mean effective stress (p'); gassy soils with lower initial pore pressure (u_0 = 0 kPa) demonstrate smaller excess pore pressure, resulting in less pronounced p' reduction. At later shear stages, dilative behavior emerges, slowing the growth of deviatoric stress (q) and excess pore pressure, with p' reaching its minimum value. For OCR = 2, stress paths adopt an S-shaped trajectory. At the initial stage of shear, the soil is in an elastic state, and the mean effective stress p' gradually increases. As the pores of the overconsolidated soil are compressed, the soil is in a state of dilatancy during the shear process, resulting in a small increase in the excess pore pressure and a decrease in the late shear period, and the mean effective stress p' decreases somewhat, but the decrease is lower than that of the soil with OCR = 1. Under OCR = 4, p' displays a sustained ascending

trend prior to critical state attainment, driven by lower void ratio and enhanced dilatancy in highly overconsolidated soils, which suppresses excess pore pressure generation and gradually decreases after the strain reaches its peak, thereby sustaining p' increase.

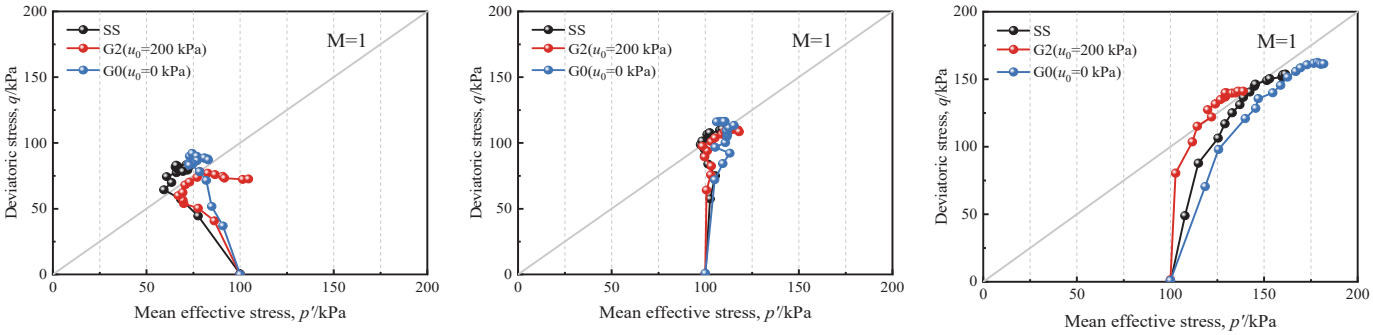

Figure 14. Stress paths of overconsolidated gassy soil: (**a**) OCR = 1; (**b**) OCR = 2; (**c**) OCR = 4.

The stress path slope of gassy clay with high initial pore pressure is smaller than that of saturated soils under a high overconsolidation ratio (OCR = 4), while closely resembling saturated soils at lower OCR values (OCR = 1, 2). This behavior likely arises from the smaller reduction in excess pore pressure observed in high-OCR gassy clay with high initial pore pressure compared to saturated soils, resulting in a less pronounced increase in mean effective stress (p'). For gassy clay with low initial pore pressure, the excess pore pressure generated under high OCR conditions is significantly lower than in both saturated soils and high-pore-pressure gassy clay, leading to the fastest growth of mean effective stress (p') during shear.

3.3. Cyclic Shear Characteristic

A total of nine cyclic simple shear tests were conducted according to the program outlined in Table 3. Among these, the gassy clay specimen G025 subjected to cyclic shear at $0.25\tau_{max}$ did not fail even after 10,000 cycles, prompting analysis of its first 1000 cycles to characterize pre-failure behavior [41].

3.3.1. Dynamic Strain

Figure 15 defines the parameters for mean shear strain (γ_a) and cyclic shear strain (γ_{cy}) in cyclic simple shear testing, expressed as follows:

$$\gamma_a = (\gamma_{max} + \gamma_{min})/2 \tag{4}$$

$$\gamma_{cy} = (\gamma_{max} - \gamma_{min})/2 \tag{5}$$

where γ_{max} and γ_{min} denote the maximum and minimum shear strains within a single cycle.

This study excludes mean shear stress and mean shear strain. Cyclic shear stress (τ_{cy}) is set to $0.5\tau_{max}$ and $0.25\tau_{max}$. The cyclic shear strain for each cycle is calculated via stress-strain hysteresis loops, with its evolution against cycle count plotted in Figure 16. Under a cyclic shear stress of $0.5\tau_{max}$, gassy clay exhibits greater cyclic failure resistance (higher cycle counts to failure) than saturated soils across all overconsolidation ratios (OCRs). This enhanced performance likely stems from bubble flooding during shear, which mitigates cyclic pore pressure accumulation and delays failure initiation. At a lower cyclic

shear stress of $0.25\tau_{max}$, gassy clay remains unfailed regardless of OCR, with cyclic shear strain accumulating gradually (maximum < 1%) throughout testing. This demonstrates that increasing the cyclic shear stress ratio (τ_{cy}/τ_{max}) under constant OCR conditions accelerates failure susceptibility in gassy clay during cyclic loading.

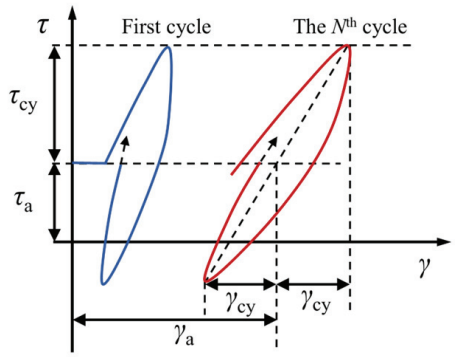

Figure 15. Schematic diagram of shear strain parameters in cyclic simple shear test [42].

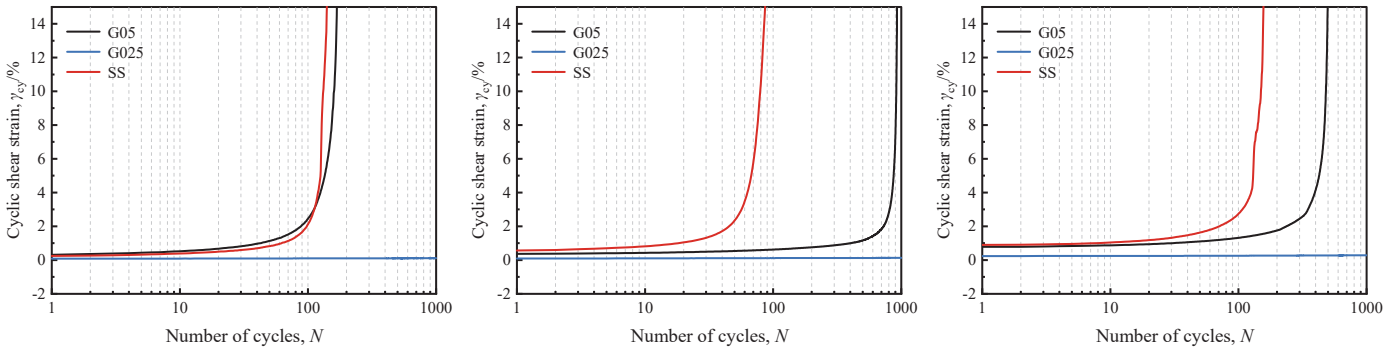

Figure 16. Cyclic shear strain curves of overconsolidated gassy soil under different dynamic shear stresses: (**a**) OCR = 1; (**b**) OCR = 2; (**c**) OCR = 4.

Under cyclic shear stress of $0.5\tau_{max}$, the cyclic failure cycles of gassy clay and saturated soils exhibit distinct trends across overconsolidation ratios (OCRs): at OCR = 1, gassy clay (N_{G05} = 169) surpasses saturated soil (N_{SS} = 141); at OCR = 2, gassy clay (N_{G05} = 928) significantly exceeds saturated soil (N_{SS} = 87); at OCR = 4, gassy clay (N_{G05} = 497) remains higher than saturated soil (N_{SS} = 157). The failure cycles of gassy clay first increase then decrease with rising OCR (peaking at OCR = 2), while saturated soils show the opposite trend (lowest at OCR = 2, highest at OCR = 4). This divergence is attributed to OCR-dependent shear strength variations and bubble compression in overconsolidated gassy clay, which modify its dilative/contractive behavior under cyclic loading.

3.3.2. Dynamic Pore Pressure

In cyclic simple shear testing, where the specimen height is maintained constant, the cyclic pore pressure is calculated from the variation in axial stress. Figure 17 illustrates the cyclic pore pressure evolution curves for gassy clay and saturated soils under different over-consolidation ratios (OCRs). The cyclic pore pressure evolution during shear exhibits three distinct phases: initially, at low cycle counts, pore pressure increases sharply; subsequently, it enters a prolonged phase of gradual growth with increasing amplitude; approaching the maximum cycle count, pore pressure surges rapidly again until failure occurs.

In cyclic simple shear testing, normally consolidated soils exhibit a gradual increase in cyclic pore pressure from zero at low cycle counts, whereas overconsolidated soils (OCR = 1, 2, 4) initially develop negative pore pressure before transitioning to positive values. For OCR = 4, the pore pressure reduction is most pronounced ($u_w < -20$ kPa), attributable to the denser structure and amplified dilative tendencies of overconsolidated soils, which suppress pore pressure generation or even induce negative pore pressure during the initial shear phase. As shear progresses, soil deformation and particle rearrangement drive cumulative pore pressure growth until failure.

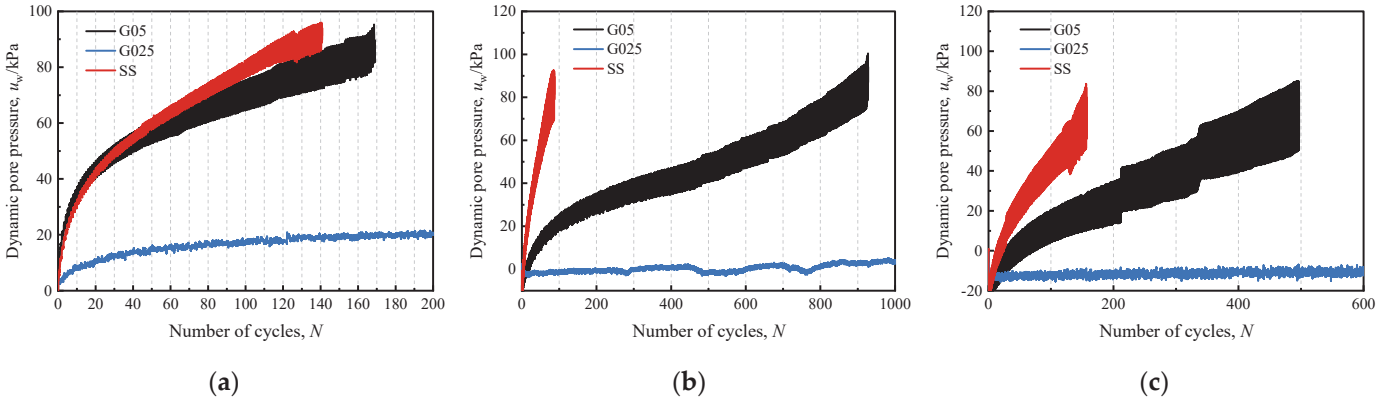

Figure 17. Dynamic pore pressure curves of overconsolidated gassy soil under different dynamic shear stresses: (**a**) OCR = 1; (**b**) OCR = 2; (**c**) OCR = 4.

A comparative analysis of cyclic pore pressure evolution between gassy clay and saturated soils under identical overconsolidation ratios (OCRs) and cyclic shear stress ratios (τ_{cy}/τ_{max}) reveals that gassy clay consistently exhibits slower pore pressure accumulation, with saturated soils demonstrating higher pore pressure values at equivalent cycle counts. This behavior arises from bubble flooding in gassy clay during shear, where partial pore water ingress into bubbles suppresses cyclic pore pressure increases. Furthermore, gassy clay's pore pressure response diverges across varying τ_{cy}/τ_{max} conditions: under lower cyclic shear stress ratios, pore pressure accumulates gradually, yielding significantly lower values at identical cycle counts compared to higher τ_{cy}/τ_{max} conditions.

Under identical cycle counts, the cyclic pore pressure amplitude increases with rising overconsolidation ratio (OCR), reaching a maximum of 18 kPa for OCR = 4 gassy clay, with gassy soils consistently exhibiting higher amplitudes than saturated soils. This behavior may stem from the enhanced dilative behavior of highly overconsolidated soils under cyclic loading, where greater particle rearrangement amplifies pore pressure generation. Simultaneously, the presence of gas bubbles in gassy clay further modifies dilative tendencies, though the precise mechanistic interplay between bubble dynamics and dilatancy remains unresolved and warrants further investigation.

3.3.3. Stiffness Softening Coefficient

The dynamic shear modulus (G), reflecting soil stiffness, is calculated from stress–strain hysteresis loops, as shown in Figure 18a, defined by the slope of the line connecting the coordinate origin to the stress peak of the hysteresis loop. Figure 18b demonstrates that increasing cycle counts lead to greater soil deformation, characterized by expanding hysteresis loop areas, progressive loop dispersion, and inclination toward the X-axis, indicating continuous stiffness softening. The stiffness softening coefficient, expressed

as G_N/G_1 (ratio of dynamic shear modulus at the Nth cycle to the 1st cycle), quantifies stiffness degradation under cyclic loading.

Experimental results for the stiffness softening coefficient (G_N/G_1) of overconsolidated gassy clay and saturated soils under varying cyclic shear stresses are shown in Figure 19. At a constant overconsolidation ratio (OCR), the stiffness softening coefficient of gassy clay decreases more gradually with increasing cycle counts than that of saturated soils under identical cyclic shear stress ratios (τ_{cy}/τ_{max}), indicating superior resistance to deformation and softening in gassy clay. This behavior likely stems from bubble flooding during shear, where partial pore water migration into gas bubbles reduces plastic strain accumulation. Furthermore, gassy clay subjected to lower cyclic shear stress ($0.25\tau_{max}$) exhibits significantly smaller reductions in G_N/G_1 compared to higher stress ($0.5\tau_{max}$), demonstrating that stiffness softening intensifies with larger τ_{cy}/τ_{max} values.

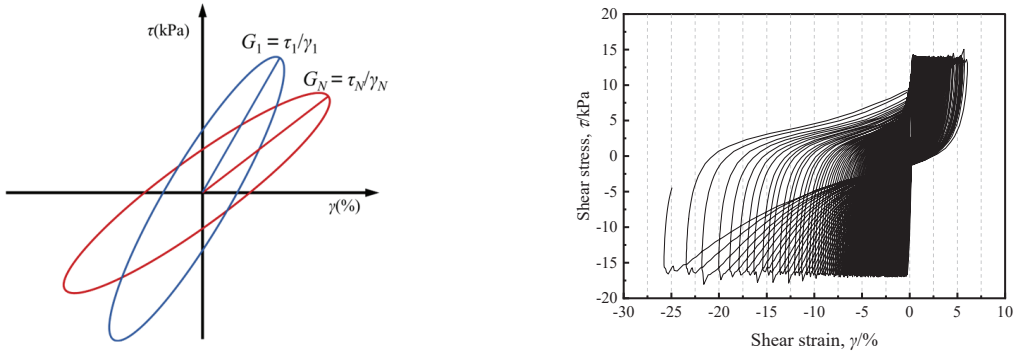

Figure 18. Stress–strain hysteresis curve and shear modulus diagram: (**a**) Shear modulus calculation diagram; (**b**) stress–strain hysteresis curve.

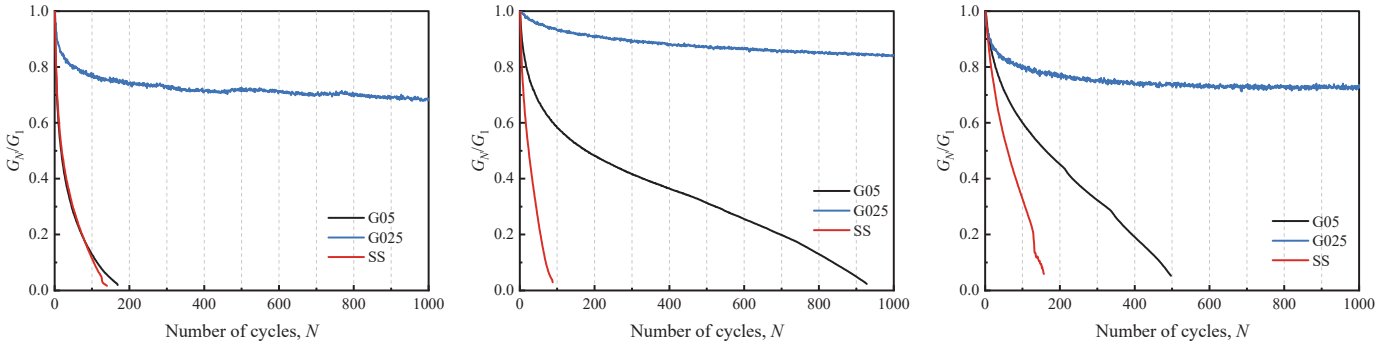

Figure 19. Stiffness softening coefficient curves of overconsolidated gassy soil under different dynamic shear stresses: (**a**) OCR = 1; (**b**) OCR = 2; (**c**) OCR = 4.

Under cyclic shear stress of $0.25\tau_{max}$, the stiffness softening magnitude of gassy clay within the first 1000 cycles initially increases then decreases with rising overconsolidation ratio (OCR): at OCR = 1, stiffness decreases by 32%; at OCR = 2, by 16%; and at OCR = 4, by 28%. A similar pattern emerges under $0.5\tau_{max}$, where the stiffness softening rate first decreases, then increases with higher OCR values, indicating that OCR = 2 gassy clay exhibits the strongest resistance to deformation and minimal softening under constant τ_{cy}/τ_{max} conditions. This trend directly explains why the cyclic failure cycles of gassy clay first rise and then decline with increasing OCR.

4. Conclusions

This study systematically investigates the microstructural and strength characteristics of overconsolidated gassy clay, elucidating the influence of overconsolidation ratio (OCR) and initial pore water pressure on its mechanical behavior, thereby providing critical theoretical and empirical foundations for constitutive modeling and engineering applications:

(1) Gassy clay was prepared via a porous medium infiltration method, with SEM imaging revealing that, under normal consolidation, soil particles primarily exist in granular or fragmentary forms, with gas distributed in discrete macro-bubbles. Increasing OCR induces irrecoverable plastic deformation, tighter particle packing, reduced porosity, and bubble compression, transitioning from spherical to collapsed morphologies.

(2) Triaxial tests demonstrate that the stress path and the response of excess pore pressure in the undrained shear process are closely related to the change of shear contraction and dilatancy of soil under an overconsolidation state. With rising OCR and decreasing initial pore pressure, the stress path slope progressively increases, mean effective stress (p') rises with deviatoric stress (q), and undrained shear strength (s_u) significantly improves, which is basically consistent with the experimental results of Gao, Cai et al. [32,33]. From OCR = 1 to 4, the shear strength of G0 increased by 76% and that of G2 increased by 80%, but the variation amplitudes were both lower than that of SS (93%). Excess pore pressure diminishes at higher OCR, even yielding negative pore pressure, attributable to suppressed bubble flooding and enhanced dilatancy under low initial pore pressure and overconsolidation.

(3) Cyclic simple shear tests reveal that, under $0.5\tau_{max}$ cyclic shear stress, gassy clay exhibits markedly higher cyclic failure resistance than saturated soil. At OCR = 2, the number of cycles to failure for gassy clay (NG05) peaked at 928, which is significantly higher than that of saturated clay (NSS = 87). Gassy clay remaining unfailed at $0.25\tau_{max}$ with minimal cumulative shear strain. Cyclic pore pressure evolution follows three phases: rapid initial increase, stabilized mid-term growth, and pre-failure surge. Overconsolidated soils generate negative pore pressure early due to dilatancy, which is less than -20 kPa at OCR = 4. Gassy clay's bubble-mediated suppression of pore pressure accumulation results in slower growth but higher amplitudes (increasing with OCR). Hysteretic stress–strain curves confirm gassy clay's lower stiffness softening rate, superior deformation resistance, and optimal anti-softening capacity at OCR = 2; higher τ_{cy}/τ_{max} exacerbates softening.

Author Contributions: Conceptualization, T.L., L.Z. and Y.Z. (Yan Zhang); methodology T.L. and C.Q. software, Y.Z. (Yan Zhang); validation, L.Z. and Y.Z. (Yuanzhe Zhan); formal analysis, T.L. and C.Q.; investigation L.Z., Y.Z. (Yan Zhang), C.Z. and J.J.; resources, T.L., L.Z. and Y.Z. (Yuanzhe Zhan); data curation, L.Z., C.Z. and J.J.; writing—original draft preparation, L.Z.; writing—review and editing, T.L., L.Z. and Y.Z. (Yan Zhang); visualization, L.Z.; supervision, T.L. and C.Q.; project administration T.L.; funding acquisition, T.L. All authors have read and agreed to the published version of the manuscript.

Funding: This research was funded by the National Natural Science Foundation of China (NO. 42207172, NO. 42277139) and the University Natural Science Research Project of Anhui Province (2023AH030037).

Data Availability Statement: The original contributions presented in this study are included in the article; further inquiries can be directed to the corresponding author.

Acknowledgments: The authors would like to thank Yi Jiang and Yue Zhao for their help during the experiment. Thanks to the Shandong Engineering Research Center of Marine Exploration and Conservation for providing the test equipment.

Conflicts of Interest: The authors declare no conflicts of interest.

References

1. Guo, Z.; Liu, L.; Liu, Z.; Pan, Y.; Shen, X.; Lei, L. Experimental and numerical challenges in multiscale study on geomechanical and hydrological systems. *Adv. Geo-Energy Res.* **2025**, *15*, 95–98. [CrossRef]
2. Guo, Z.; Gao, X.; Wu, H.; Liu, L.; Lei, L. Failure patterns in layered gas-storage systems. *Adv. Geo-Energy Res.* **2024**, *12*, 183–193. [CrossRef]
3. Liu, T.; Yang, X.; Zhang, Y. A Review of Gassy Sediments: Mechanical Property, Disaster Simulation and In-Situ Test. *Front. Earth Sci.* **2022**, *10*, 15–35. [CrossRef]
4. Kortekaas, S.; Sens, E.; Sarata, B. Shallow gas hazard linked to worldwide delta environments. In *Frontiers in Offshore Geotechnics II*; CRC Press: Boca Raton, FL, USA, 2010; pp. 221–225.
5. Anderson, A.L.; Hampton, L.D. Acoustics of gas-bearing sediments I. Background. *J. Acoust. Soc. Am.* **1980**, *67*, 1865–1889. [CrossRef]
6. Whelan, T.; Coleman, J.M.; Suhayda, J.N.; Roberts, H.H. Acoustical penetration and shear strength in gas-charged sediment. *Mar. Geotechnol.* **1977**, *2*, 147–159. [CrossRef]
7. Puzrin, A.; Tront, J.; Schmid, A.; Hughes, J. Engineered use of microbial gas production to decrease primary consolidation settlement in clayey soils. *Geotechnique* **2011**, *61*, 785–794. [CrossRef]
8. Chen, Z.; Lai, X.; Liao, L.; Huang, P. Submarine shallow gas detection method based on MIP-CPT technology: A case study in the Zhoushan sea area of the East China Sea. *Acta Pet. Sin.* **2016**, *37*, 8–16.
9. Xie, C.Y. Shallow natural gas in riverside soft soils along the Yangtze River in Anhui Province and its impact on hydraulic structures. *Water Resour. Hydropower Express* **2000**, *21*, 6–12.
10. Liu, L.; De Kock, T.; Wilkinson, J.; Cnudde, V.; Xiao, S.; Buchmann, C.; Uteau, D.; Peth, S.; Lorke, A. Methane bubble growth and migration in aquatic sediments observed by X-ray μCT. *Environ. Sci. Technol.* **2018**, *52*, 2007–2015. [CrossRef]
11. Abegg, F.; Anderson, A.L. The acoustic turbid layer in muddy sediments of Eckernfoerde Bay, Western Baltic: Methane concentration, saturation and bubble characteristics. *Mar. Geol.* **1997**, *137*, 137–147. [CrossRef]
12. Best, A.I.; Tuffin, M.D.J.; Dix, J.K.; Bull, J.M. Tidal height and frequency dependence of acoustic velocity and attenuation in shallow gassy marine sediments. *J. Geophys. Res. Solid Earth* **2004**, *109*, B08101. [CrossRef]
13. Kim, G.Y.; Narantsetseg, B.; Kim, J.W.; Chun, J.H. Physical properties and micro-and macro-structures of gassy sediments in the inner shelf of SE Korea. *Quat. Int.* **2014**, *344*, 170–180. [CrossRef]
14. Hong, Y.; Wang, L.; Yang, B.; Zhang, J. Stress-dilatancy behaviour of bubbled fine-grained sediments. *Eng. Geol.* **2019**, *260*, 105196. [CrossRef]
15. Sobkowikz, J.C. The Mechanics of Gassy Sediments. Ph.D. Thesis, University of Alberta, Edmonton, AB, Canada, 1982.
16. Grozic, J.; Nadim, F.; Kvalstad, T. On the undrained shear strength of gassy clays. *Comput. Geotech.* **2005**, *32*, 483–490. [CrossRef]
17. Hong, Y.; Wang, X.; Wang, L.; Gao, Z. A state-dependent constitutive model for coarse-grained gassy soil and its application in slope instability modelling. *Comput. Geotech.* **2021**, *129*, 103847. [CrossRef]
18. Sultan, N.; Garziglia, S. Mechanical behaviour of gas-charged fine sediments: Model formulation and calibration. *Geotechnique* **2014**, *64*, 851–864. [CrossRef]
19. Hong, Y.; Wang, L.; Ng, C.W.; Yang, B. Effect of initial pore pressure on undrained shear behaviour of fine-grained gassy soil. *Can. Geotech. J.* **2017**, *54*, 1592–1600. [CrossRef]
20. Wheeler, S.J. A conceptual model for soils containing large gas bubbles. *Geotechnique* **1988**, *38*, 389–397. [CrossRef]
21. Thomas, S.D. The Consolidation Behaviour of Gassy Soil. Ph.D. Thesis, Oxford University, Oxford, UK, 1987.
22. Ye, Z.B.; Li, J.R.; Ye, Q.Y.; Chen, X.X.; Zhou, W.T. Experimental study on consolidation settlement characteristics of fine-grained gassy soil. *Found. Treat.* **2022**, *4*, 472–478.
23. Sills, G.C.; Wheeler, S.J.; Thomas, S.D.; Gardner, T.N. Behaviour of offshore soils containing gas bubbles. *Geotechnique* **1991**, *41*, 227–241. [CrossRef]
24. Qin, A.; Sun, D.; Zhang, J. Semi-analytical solution to one-dimensional consolidation for viscoelastic unsaturated soils. *Comput. Geotech.* **2014**, *62*, 110–117. [CrossRef]
25. Wang, L. On the consolidation and creep behaviour of layered viscoelastic gassy sediments. *Eng. Geol.* **2021**, *293*, 296–298. [CrossRef]
26. Wheeler, S.J. The undrained shear strength of soils containing large gas bubbles. *Geotechnique* **1988**, *38*, 399–413. [CrossRef]
27. Wheeler, S.J.; Sham, W.K.; Thomas, S.D. Gas pressure in unsaturated offshore soils. *Can. Geotech. J.* **1990**, *27*, 79–89. [CrossRef]
28. Wheeler, S.J.; Gardner, T.N. Elastic moduli of soils containing large gas bubbles. *Geotechnique* **1989**, *39*, 333–342. [CrossRef]

29. Liu, T.; Qing, C.; Zheng, J.; Ma, X.; Chen, J.; Liu, X. Study on the Mechanical Behavior of Fine-Grained Gassy Soil Under Different Stress Conditions. *J. Mar. Sci. Eng.* **2025**, *13*, 373. [CrossRef]
30. Wang, H.; Zhang, Y.; Cai, G.; Liang, Y.; Liu, T.; Chen, J. Study on the CPTu inversion methods for strength and consolidation parameters of gassy soil with different gas contents. *Appl. Ocean. Res.* **2024**, *146*, 146103960. [CrossRef]
31. Hong, Y.; Chen, X.Y.; Wang, L.Z.; Yang, B.; Sanchez, M. Distinct Undrained Cyclic Behavior of Fine-Grained Gassy Soil at Various Initial Pore Water Pressures. *J. Geotech. Geoenviron. Eng.* **2021**, *147*, 06020027. [CrossRef]
32. Gao, Z.; Cai, H.; Hong, Y.; Lu, D. A critical state constitutive model for gassy clay. *Can. Geotech. J.* **2022**, *59*, 1033–1045. [CrossRef]
33. Cai, H.; Gao, Z.; Hong, Y.; Zhang, J. A bounding surface model for gassy clay. *Comput. Geotech.* **2023**, *161*, 105565. [CrossRef]
34. Nie, Y.; Luan, M.T.; Tang, X.W.; Guo, Y.; Zhang, Z.D.; Song, Y.X. Study on shear characteristics of overconsolidated clay under monotonic and coupled cyclic loading. *Rock Soil Mech.* **2009**, *30*, 2616–2622.
35. Bouriak, S.; Vanneste, M.; Saoutkine, A. Inferred gas hydrates and clay diapirs near the Storegga Slide on the southern edge of the Vøring Plateau, offshore Norway. *Mar. Geol.* **2000**, *163*, 125–148. [CrossRef]
36. Maslin, M.; Mikkelsen, N.; Vilela, C.; Haq, B. Sea-level-and gas-hydrate-controlled catastrophic sediment failures of the Amazon Fan. *Geology* **1998**, *12*, 26–52. [CrossRef]
37. Sultan, N.; De Gennaro, V.; Puech, A. Mechanical behaviour of gas-charged marine plastic sediments. *Géotechnique* **2012**, *62*, 751–766. [CrossRef]
38. Zhang, R.; Lunne, T. Deepwater sample disturbance due to stress relief. *Chin. J. Geotech. Eng.* **2003**, *25*, 356–360.
39. Hong, Y.; Zhang, J.F.; Wang, L.Z.; Liu, T. On evolving size and shape of gas bubble in marine clay under multi-stage loadings: Microcomputed tomography (μCT) characterization and cavity contraction analysis. *Can. Geotech. J.* **2020**, *57*, 1072–1091. [CrossRef]
40. Lehane, B.M.; O'Loughlin, C.D.; Gaudin, C. Rate effects on penetrometer resistance in kaolin. *Géotechnique* **2009**, *59*, 41–52. [CrossRef]
41. Tan, J. Research on Shear Characteristics of Soft Clay with Different Consolidation Degrees Under Static and Dynamic Loads. Master's Thesis, Wenzhou University, Wenzhou, China, 2021. [CrossRef]
42. Li, P.F.; Bi, Q.; Zhang, Y.H.; Yan, H.G.; Ren, B.; Tong, M. Research on the Cyclic Loading Characteristics of Silty Soil in the Sea Area of Eastern Guangdong. *Mar. Sci. Bull.* **2024**, *43*, 497–509.

Journal of
Marine Science and Engineering

MDPI

Article

Analysis of Offshore Pile–Soil Interaction Using Artificial Neural Network

Peiyuan Lin [1,2,3,*], Kun Li [1], Xiangwei Yu [1], Tong Liu [1], Xun Yuan [1] and Haoyi Li [1]

[1] School of Civil Engineering, Sun Yat-Sen University, Zhuhai 519082, China; likun57@mail2.sysu.edu.cn (K.L.); yuxw8@mail2.sysu.edu.cn (X.Y.); liut339@mail2.sysu.edu.cn (T.L.); yuanx35@mail2.sysu.edu.cn (X.Y.); lihy395@mail2.sysu.edu.cn (H.L.)
[2] State Key Laboratory for Tunnel Engineering, Guangzhou 510275, China
[3] Southern Marine Science and Engineering Guangdong Laboratory (Zhuhai), Zhuhai 519082, China
* Correspondence: linpy23@mail.sysu.edu.cn; Tel.: +86-0756-3668053

Abstract: Offshore wind power is one of the primary forms of utilizing marine green energy in China. Currently, near-shore wind power predominantly employs monopile foundations, with designs typically being overly conservative, resulting in high construction costs. Precise characterization of the interaction mechanisms between marine piles and surrounding soils is crucial for foundation design optimization. Traditional p-y curve methods, with simplified fitting functions, inadequately capture the complex pile–soil behaviors, limiting predictive accuracy and model uncertainty quantification. To address these challenges, this research collected 1852 empirical datasets of offshore wind monopile foundation pile–soil interactions, developing p-y curve and horizontal displacement prediction models using artificial neural network (ANN) expressions and comprehensive uncertainty statistical analysis. The constructed ANN model demonstrates a simple structure with satisfactory predictive performance, achieving average error margins below 6% and low to moderate prediction accuracy dispersion (26%~45%). In contrast, traditional p-y curve models show 30%~50% average biases with substantial accuracy dispersion near 80%, while conventional finite element methods exhibit approximately 40% error and dispersion. By strictly characterizing the probability cumulative function of the neural network model factors, a foundation is provided for reliability-based design. Through comprehensive case verification, it is demonstrated that the ANN-based model has significant advantages in terms of computational accuracy and efficiency in the design of offshore wind power foundations.

Keywords: offshore pile foundation; p-y curve; pile–soil interaction; uncertainty analysis; artificial neural network

1. Introduction

Although fossil fuels such as coal and oil remain the backbone of the global energy mix, offshore wind power—a renewable and low-carbon energy source—has emerged as a critical component of international efforts to achieve carbon neutrality and energy transition [1]. Rapid advancements in technology, coupled with cross-border policy coordination and collaboration (e.g., in the North Sea [2,3], Baltic Sea [4], and the Guangdong-Hong Kong-Macao Greater Bay Area [5] as a regional exemplar), have propelled offshore wind into a vital supplement to the world energy supply. In near-shore shallow water areas, offshore wind turbine foundations primarily utilize large-diameter steel pipe piles. Statis-

tics indicate that approximately 75% of marine engineering structures currently employ large-diameter monopile foundations [6,7].

The ideal objective in pile foundation design is to balance safety with economic efficiency. However, due to the potential catastrophic risks associated with complex wind, wave, and current loads in marine environments [8], coupled with nonlinear pile–soil interactions and the significant uncertainty in existing pile design methodologies [9,10], designers are compelled to adopt conservative approaches to ensure the stability and service life of offshore platform structures while hedging against the exorbitant repair costs of pile failure [11]. The direct consequence of overly conservative design is elevated construction costs. Accurately quantifying pile–soil interaction is the key to designing marine pile foundations that balance safety with economic considerations.

Currently, common methods for analyzing pile–soil interaction primarily include theoretical approaches [12,13], empirical methods [14,15], and numerical techniques [16–18]. Theoretical methods typically simplify piles as idealized models such as cantilever beams [19–21]; however, due to excessive simplification, these approaches fail to adequately account for complex factors in pile–soil interaction, including soil nonlinear mechanical properties and variations in pile–soil interface friction [22]. Empirical methods are analytical approaches developed from extensive engineering practice or experimental data, with the p-y curve method being a typical representative model. Due to its simple expression and convenient application, this method has been widely adopted in various international specifications [23–25]. The method constructs empirical expressions between pile displacement and soil reaction force by fitting experimental data [26,27].

The accuracy of the p-y curve method depends on the quantity of fitted data and the functional expressions employed. Additionally, the p-y curve method exhibits significant regional characteristics and typically cannot be directly applied to different regions [28,29]. Given the extreme complexity of marine environments, pile–soil interactions exhibit significant variability and uncertainty [30,31], imposing substantial limitations on applying the p-y curve method. Empirical investigations have demonstrated that the p-y curve method exhibits significantly compromised predictive accuracy when applied to large-diameter pile foundations and under specialized geotechnical conditions [32–35].

The finite element method (FEM) is a widely utilized numerical technique capable of accurately characterizing the boundary and initial conditions of pile–soil interaction systems [36]. However, the highly nonlinear mechanical properties inherent in marine soils present significant challenges to predictive modeling. Although FEM simulations are generally unbiased on average, they exhibit moderate variability in predictive accuracy due to these nonlinearities [37,38]. When confronted with complex environmental loads and unique geological formations, the FEM not only struggles to maintain precision but also encounters substantial hurdles, including significantly increased computational costs and prolonged processing times [39,40]. These limitations pose serious obstacles in practical engineering applications that demand high computational efficiency and rapid iterative analyses.

In recent years, machine learning methods have been widely applied to complex geotechnical engineering problem analysis due to their powerful nonlinear representation capabilities [41–44]. For example, support vector machines (SVMs) demonstrate high accuracy in landslide susceptibility analysis and rock deformation prediction [45,46], while artificial neural networks (ANNs) excel in soil classification [47] and in predicting earth dam settlement and foundation settlement [48]. Machine learning methods effectively compensate for the deficiencies of traditional techniques in handling highly nonlinear problems, overcoming the oversimplification of theoretical approaches, the applicability limitations of empirical

methods, and the accuracy and computational cost issues of numerical methods, making them highly suitable for analyzing pile–soil interactions in specialized marine geotechnical environments.

This study compiles a comprehensive dataset encompassing multi-dimensional parameters of marine large-diameter monopile foundations, including marine geological conditions, pile design specifications, horizontal displacement profiles, and soil pressure distribution characteristics. Leveraging this dataset, we develop a neural network model specifically tailored for analyzing pile–soil interactions in marine environments. The proposed framework achieves enhanced predictive accuracy for pile–soil interaction behaviors through systematic model training and rigorous application while significantly improving computational efficiency. This methodology substantially mitigates design risks associated with marine large-diameter pile foundations and provides a robust technical framework for cost-effective engineering solutions in offshore pile construction.

The subsequent section describes the database development process and its contents, while Section 3 details the construction of the neural network model, including fundamental concepts, development procedures, and the selection of key parameters. Sections 4 and 5 analyze the prediction results of the neural network model, discuss its performance and influencing factors, and validate the model's reliability using a real-world case study. Finally, the paper concludes with a summary of the research content and findings.

2. Database

This study collected 1852 datasets comprising field measurements and model test data from 29 monopile foundations across 24 offshore wind projects worldwide. Leveraging the compiled datasets, we established a marine geotechnical database to systematically investigate and predict pile–soil interactions of monopile foundations under complex loading and geological environments.

The database systematically documents three critical components for each monopile (Table 1): (i) soil parameters encompassing stratigraphic classification and strength characteristics (φ: internal friction angle; c: cohesion; E: elastic modulus; γ: soil's unit weight, et al.); (ii) geometric design specifications of steel tubular piles (L: pile length; D: outer diameter; t: wall thickness, et al.); and (iii) operational loading regimes with horizontal force (F) applied at the pile head. Depth-dependent soil–structure interaction data are parametrized by l (depth from pile head), with pile geometric configuration schematically detailed in Figure 1.

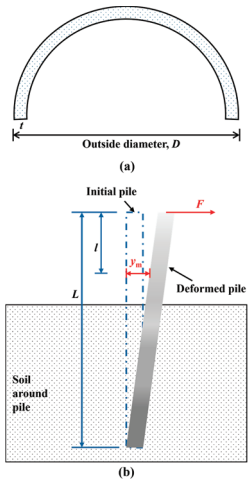

Figure 1. Pile foundation design parameters. (**a**) Cross-section view, (**b**) side-elevation view.

Table 1. Soil information and pile design parameters of the pile foundation in the database.

Pipe Number	Soil Type	Load	Soil Parameter				Pile Parameter			Reference
		F (kN)	*φ* (°)	*c* (kPa)	*E* (MPa)	*γ* (kN/m^3)	*L* (m)	*D* (m)	*t* (mm)	
P1	Clay, fine sand	200–650	18–42	0–15	10–180	18.5–20.5	78.5	2	30	[49]
P2	Clay, fine sand	200–650	18–42	0–15	10–180	18.5–20.5	78.5	2	30	[49]
P3	Medium-coarse sand, residual cohesive soil	148–1480	14–35	23–24	15–30	23.5–27.5	55	1.8	30	[50]
P4	Medium-coarse sand, residual cohesive soil	148–1480	14–35	23–24	15–30	23.5–27.5	53	1.9	30	[50]
P5	Silt	140–840	3.2–34.0	2–37	69–157	18.0–19.5	51	1.8	25	[51]
P6	Silty clay	400–800	8.1–33.6	7–37	8.0–33.6	17.8–20.0	72.7	2	-	[52]
P7	Marine clay, silty clay, residual soil	200–900	24–33	-	-	17.5–20.5	26.6	1.016	16	[53]
P8	Silt, fine sand, silty clay	150–900	31–35	-	-	6.5–9.5	89	2	26–30	[54]
P9	Silt, fine sand, silty clay	40–480	11–34.5	0.1–16.6	5.9–36.7	17.4–19.5	85.2	1.7	25–30	[55]
P10	Silt, silty clay, clay	40–480	11–34.5	0.1–16.6	5.9–36.7	17.4–19.5	85.2	1.7	25–30	[55]
P11	Silt, silty clay, medium sand, silty sand	100–700	30–37	-	2–50	5.8–10.9	105.4	2.4	40	[56]
P12	Clay	300–1300	-	-	16.02	17.9	83	2	26	[57]
P13	Soft clay, sandy	200–2000	35	-	12–17	6.7	66	2.2	30	[58]
P14	Silt, sandy silt, silty clay, fine sand	22–220	15–34	11–54.7	-	17.3–19.8	60	1.2	16	[59]
P15	Silty clay, clay, silt	20–300	8–34	7–18	8–36	17.4–20.5	82.1	30	1.7	[60]
P16	Silty clay, fine sand	50–425	8–35	2–17	20–60	18.3–20.0	93.7	35	2.8	[61]
P17	Silty clay, fine sand	100–500	8–35	2–17	20–60	18.3–20.0	93.7	35	2.8	[61]
P18	Silt, silty, sand	300–2000	8–18	15–16	8–30	17.7–20.2	70.0	30	2.2	[62]
P19	Silt, argillaceous sand	50–250	8–45	1–20	8–180	23.4–27.5	30.7	16	1.4	[63]
P20	Silt, argillaceous sand	50–250	8–45	1–20	8–180	23.4–27.5	32.2	16	1.4	[63]
P21	Sand	250–1500	38–43	-	-	8.1–19.5	0.41	0.079	1.2	[64]
P22	Silty soil	0–10	25	12	-	-	2.3·	0.089	4.0	[65]
P23	Silty soil	8.1–55.1	27	5	-	-	1.1	0.032	7.0	[66]
P24	Sand	0–3.8	38	-	8.23	15.1–16.5	1.4	0.102	6.4	[67]
P25	Sand	0.28–2.6	28.5	-	-	17.5	7.0	0.114	2.5	[68]
P26	Silt	0.26–1.5	35.5	0.1	-	15.7	2.0	0.165	3.0	[69]
P27	Silt, sand	0.72–6.1	30	-	-	19.3	4.5	0.159	4.5	[70]
P28	Sand	400–800	37	30	2.0	-	3.0	0.34	-	[71]
P29	Sand	148–1480	-	30	1.8	-	12	2.0	-	[72]

Field-monitored monopiles were predominantly embedded in clay and sand strata, with three cases (P3, P4, and P19) terminating in weathered rock formations. Laboratory tests employed reconstituted sand-silt mixtures. The soil unit weight (γ) exhibited limited variation, predominantly between 18.8 and 19.5 kN/m^3. While strength parameters demonstrated significant heterogeneity across the dataset. As illustrated in Figure 2, internal friction angle (φ) varied considerably from 5° to 42°; cohesion (c) predominantly clustered within 11–22 kPa, with only approximately 5% of specimens exceeding 50 kPa; the distribution of shear strength (c_u) exhibited considerable variability, ranging from 10 kPa to 80 kPa, with values predominantly concentrated within the 35–42 kPa interval; and soil elastic modulus (E) exhibited a wide distribution from 6 to 180 MPa, with half below 30 MPa and 80% below 69 MPa.

Figure 3 delineates the nonlinear correlation between lateral soil displacement (y) and mobilized soil resistance (p). Soil pressure on piles in clay typically ranged from 55 to 120 kN/m, whereas sand deposits demonstrated enhanced lateral resistance (215–412 kN/m) attributable to particulate interlocking and dilatant behavior.

Field tests revealed significant discrepancies in horizontal displacement magnitudes between clay- and sand-embedded piles. The clay-pile systems exhibited maximum displacements up to 255 mm, contrasting sharply with the sand systems' 122 mm maximum. The model test exhibited considerable scatter, with maximum displacements reaching 500 mm; however, 80% of the values were below 35 mm. This divergence underscores limitations in model testing: while capturing general load-displacement trends, scaled tests inadequately replicate in situ stress redistribution processes and strain localization patterns, particularly under large deformation regimes.

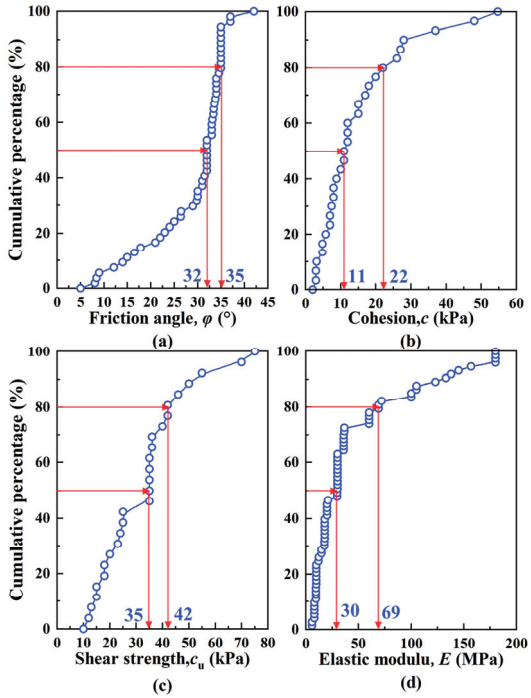

Figure 2. Cumulative percentage of soil strength parameters from field tests in the database (**a**). Friction angle, φ (°), (**b**) cohesion, c (kPa), (**c**) shear strength, c_u (kPa), (**d**) elastic modulus, E (MPa).

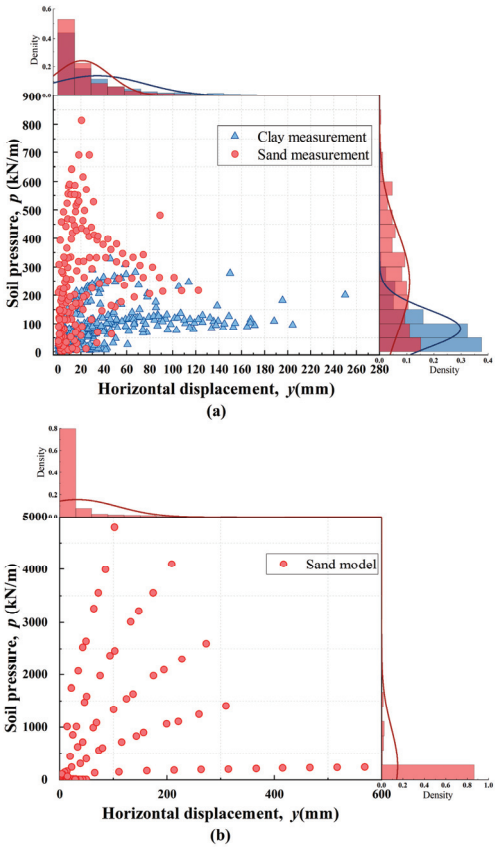

Figure 3. Nonlinear correlation between horizontal displacement and soil pressure. (**a**) Field measurement results for clay and sand, (**b**) model test results for sand.

The database reveals geometric scaling characteristics between prototype and model piles. Prototype monopile lengths (L) generally exceeded 50 m, with maximum values

reaching 105.4 m, whereas model piles exhibited significantly shorter dimensions ranging from 0.41 to 12.0 m. Diameter (D) distributions show marked divergence: prototype piles cluster in the 1.0–2.4 m range (80% within 1.8–2 m), while model diameters span three orders of magnitude (D: 0.032–2 m). Slenderness ratios (L/D) predominantly occupy 20–50 across both groups, satisfying prototype and model piles geometric proportional control criteria [73].

As illustrated in Figure 4a, normalized horizontal displacement (y/L) exhibits inverse proportionality to relative depth (l/L) in both clay and sand. Thickness (t) of field-measured piles ranged from 16 to 30 mm, with a predominance of 30 mm, while model piles featured substantially thinner walls of only 1.2–7 mm. Notably, geometric parameter covariation emerges: increasing L correlates with proportional D and t enhancements, reflecting design optimization for structural stability and bearing capacity across varying embedment depths.

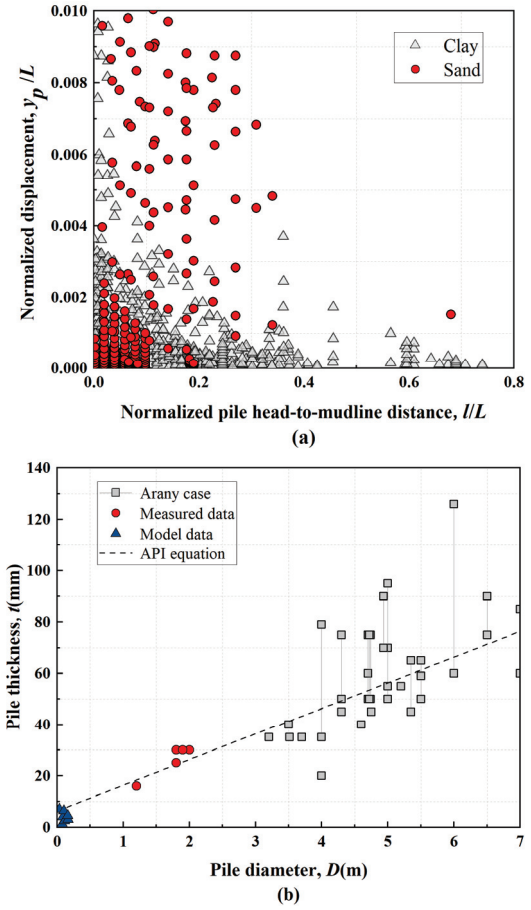

Figure 4. The design parameters of the piles in the database. (**a**) Normalized displacement versus normalized pile head-to-mudline distance for clay and sand, (**b**) pile thickness versus pile diameter.

To satisfy the installation requirements of steel pipe piles and prevent local buckling when the pile reaches its yield strength, the thickness needs to comply with the following criterion [23]:

$$t \geq 6.35 + \frac{D}{100} \tag{1}$$

Figure 4b illustrates the relationship between thickness and diameter for piles in the database, compared with data from other case studies [74]. The straight line in the figure represents the minimum thickness value recommended by the API specification. A

comparative analysis reveals that most field-tested piles in the database adhered to this standard, whereas the model test piles exhibited only basic compliance.

3. Neural Network Modeling of Pile–Soil Interaction

3.1. Artificial Neural Networks

Artificial neural networks (ANNs) are biologically inspired computational frameworks designed to emulate the information processing mechanisms of biological neural systems. As depicted in Figure 5, a standard ANN architecture consists of three hierarchical layers:

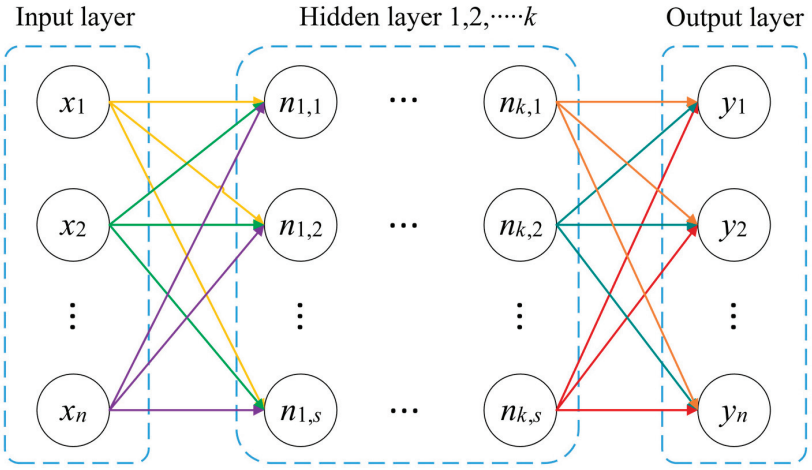

Figure 5. Neural network architecture.

(i). Input Layer: Receives normalized geotechnical parameters (e.g., pile diameter D, soil elastic modulus E).

(ii). Hidden Layer: Extracts nonlinear relationships through weighted transformations and activation functions.

(iii). Predicts target variables (e.g., pile head displacement, soil reaction forces).

The performance of the ANN depends on the number of layers and neurons. Increasing neurons or adjusting weights reduces the mean squared error (MSE).

3.2. Architecture Design & Workflow

3.2.1. Data Preprocessing

Input–output parameters are normalized to the interval [0, 1] to mitigate numerical instability caused by disparate units (e.g., MPa vs. mm):

$$x_{norm} = \frac{x - x_{min}}{x_{max} - x_{min}} \tag{2}$$

where x_{norm} is the normalized value; x is the raw data, and x_{max} or x_{min} denote the maximum or minimum values in the dataset.

3.2.2. Topology Structure

The hidden layer dimensionality is determined via Kolmogorov's superposition theorem [75], which prescribes a theoretical upper bound for the number of hidden nodes (m) as:

$$m = 2n + 1 \tag{3}$$

where n corresponds to the input dimension. This configuration balances model complexity and generalization capacity.

Equation (3) establishes the theoretical upper bound for nodes in the hidden layer. To systematically evaluate optimal network architecture, we conducted a parametric study by training networks with incrementally increasing hidden layer complexity (3, 5, 7, 9, 11, and 13 nodes) and assessed their performance against established metrics. Figure 6 plots the coefficient of determination (R^2) across training, validation, and test datasets. Increasing node count initially enhances model performance, as evidenced by rising R^2 values. However, beyond 5 nodes, R^2 exhibits pronounced fluctuations across all datasets. Networks with more than 9 nodes show a declining R^2 trend in training and test datasets, indicative of overfitting. This suggests that in geotechnical modeling, a moderate number of nodes (5–7 nodes) optimizes generalization capability, while excessive complexity degrades validation/test accuracy.

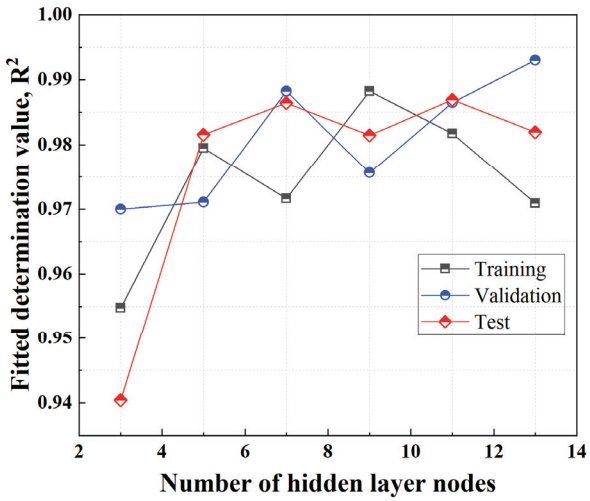

Figure 6. Effect of hidden layer node number on model performance (R^2) for training, validation and test datasets.

3.2.3. Propagation Mechanism & Training Algorithm

For an input vector $x = [x_1, x_2, \ldots, x_n]^T$, the pre-activation ($z_k$) and activation ($a_k$) of the k-th hidden neuron are computed as:

$$z_k = \sum_{p=1}^{s} n_{k,p} w_{k,p,t} + b_{k,t} \tag{4}$$

$$a_k = f(z_k) \tag{5}$$

where $w_{k,p,t}$ and $b_{k,t}$ denote the weight matrix and bias vector of the layer, respectively. f(x) represents activation functions (logistic) used to convey interlayer information.

The Levenberg–Marquardt (LM) optimization algorithm is employed for network training due to its hybrid mechanism that synergistically integrates the robustness of gradient descent in shallow regions of the error surface with the quadratic convergence properties of the Gauss–Newton method near minima. The weight update rule is formulated as:

$$\Delta W = -\left(J^T J + \mu I\right)^{-1} J^T e \tag{6}$$

where J is the Jacobian matrix of partial derivatives, μ is a damping factor, and e is the residual vector.

3.2.4. Learning Rate & Iterations

The learning rate (η) regulates the step magnitude in gradient-based optimization, critically balancing convergence stability and rate. Elevated η values (e.g., $\eta > 0.1$) accelerate convergence yet risk overshooting minima or inducing oscillatory behavior, whereas diminished values ($\eta < 0.001$) prioritize stability at the cost of computational inefficiency. This study adopts $\eta = 0.01$, a heuristically calibrated value within the empirically effective range $\eta \in [0.001, 0.1]$ for geotechnical systems [76–78].

Concurrently, the maximum iteration threshold ($N_{max} = 1000$) safeguards against overfitting by constraining parametric updates, with training termination triggered upon either reaching N_{max} or validation loss plateau ($\Delta\mathcal{L} < 10^{-5}$ sustained over 50 epochs).

3.2.5. Validation and Regularization

To prevent overfitting, a 70-15-15 data partitioning (training-validation-testing) is implemented, coupled with Bayesian regularization to penalize excessive weight magnitudes:

$$L_{reg} = \beta L + \alpha \sum_i \omega_i^2 \quad (7)$$

where α and β are hyperparameters optimized via cross-validation.

4. Results

4.1. Predictions of p-y Curves

A critical consideration lies in the selection of input parameters for the neural network model. While using all parameters from the database as inputs may theoretically maximize data utilization, it introduces computational complexity and risks overfitting due to redundant or low-sensitivity variables. Thus, the selection of which influencing factors to incorporate as input parameters is a task that requires careful engineering judgment. Fortunately, based on the physico-mechanical properties of clay and sand foundations and in conjunction with prior research [79–81], the primary influencing factors to be used as input parameters can be identified.

For the clay model, the selected inputs were pile diameter (D), length (L), depth (d), ultimate resistance (p_u), undrained shear strength (c_u), and lateral displacement (y). Similarly, the sand model incorporates D, L, d, internal friction angle (φ), soil unit weight (γ), and y as inputs, with soil pressure (p) as the output. The architecture of the clay p-y curve neural network is illustrated in Figure 7, while detailed structural hyperparameters for both models are tabulated in Table 2.

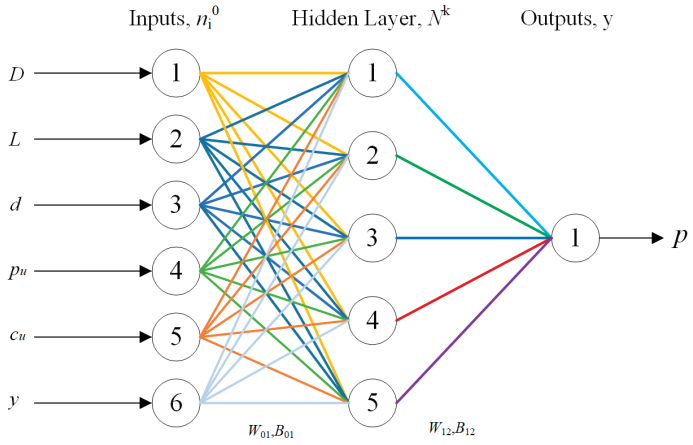

Figure 7. The ANN model for the p-y curve of clay.

Table 2. Neural network model structure parameters and predictive regression values.

Prediction	Input Nodes	Output Node	Hidden Nodes Number	Learning Rate	Maximum Iteration	R^2		
						Train	Validation	Test
Clay p-y curve	D, L, d, p_u, c_u, y (6)	p	5	0.01	1000	0.95	0.96	0.97
Sand p-y curve	D, L, d, φ, γ, y (6)	p	4			0.93	0.96	0.96
Pile horizontal displacement	F, L, D, d, l, E, φ, c (8)	y	5			0.97	0.96	0.98

It is also crucial to highlight another issue: the potential existence of size effects means that the results of model tests cannot fully replace those of field tests. Therefore, the data from model tests and field tests need to be separately employed to establish predictive models (primarily focused on sand). For ease of description in subsequent discussions, the predictive results from model tests and field tests are combined, and the use of ratios can effectively characterize these predictive outcomes. This will be elaborated in later sections.

The hidden layer neuron outputs are computed via the activation function as:

$$N^1 = 1 - \frac{2}{e^{[2(W_{01}N^0 + B_{01})]} + 1} \tag{8}$$

where W_{01} (5×6 weight matrix) and B_{01} (5×1 bias vector) govern the input-to-hidden layer transformations.

The output layer is expressed as:

$$\hat{Y}_{p,k} = Y_{(m,min)} + \left\{1 - \frac{2}{exp[2(W_{12}N^1 + B_{12})] + 1}\right\}\left(Y_{(m,max)} - Y_{(m,min)}\right) \tag{9}$$

where $Y_{m,min}$ and $Y_{m,max}$ denote the normalized bounds of measured input parameters (e.g., D, L, d, p_u, c_u, φ, γ, y) with subscript m indicating experimental measurements. W_{12} and B_{12} represent the hidden-to-output layer weight matrix and bias vector, respectively.

The squared error (ε_k^2) is calculated by comparing the observed values with their corresponding predicted values generated by the model.

$$\varepsilon_k^2 = \left(\hat{Y}_{p,k} - Y_{m,k}\right)^2 \tag{10}$$

By iterating over all samples in the dataset and aggregating these squared differences, the mean squared error (MSE) is obtained as a quantitative measure of the model's performance.

$$\varepsilon^2 = \sum_{k=1}^{i} \varepsilon_k^2 / i \tag{11}$$

The MSE serves as the objective function in the training of the artificial neural network. Minimizing the MSE through appropriate optimization algorithms allows for the determination of the optimal weights and biases (W_{01}, W_{12}, B_{01}, B_{12}).

The optimized parameters of the neural network for clay p-y curves are mathematically expressed as follows:

$$w_{01} = \begin{bmatrix} -9.45 & -6.45 & -1.90 & -4.33 & -4.38 & -0.09 \\ -0.79 & 0.49 & -0.41 & 1.87 & -1.76 & 5.65 \\ -6.83 & 7.93 & -12.76 & 7.72 & -13.25 & 3.78 \\ -2.92 & 3.42 & -3.98 & 1.39 & -9.06 & 0.89 \\ 2.22 & 0.08 & 2.29 & -3.61 & 0.54 & 0.24 \end{bmatrix}$$
$$w_{12} = \begin{bmatrix} 1.54 & 2.18 & 1.01 & -3.05 & 2.73 \end{bmatrix} \tag{12}$$

$$B_{01} = \begin{bmatrix} 4.0207 \\ 5.8339 \\ 0.1103 \\ -2.735 \\ -3.251 \end{bmatrix}, B_{12} = [-0.027] \tag{13}$$

Taking this model as an example, the simplified expression is as follows:

$$N^1 = \begin{bmatrix} n_1^1 \\ n_2^1 \\ n_3^1 \\ n_4^1 \\ n_5^1 \end{bmatrix} = \begin{bmatrix} f(-6.828D - 0.082L - 0.142d - 0.008p_u - 0.137c_u - 0.0004y + 14.972) \\ f(-0.573D + 0.006L - 0.031d + 0.003p_u - 0.055c_u + 0.023y + 6.59) \\ f(-4.935D + 0.101L - 0.954d + 0.014p_u - 0.414c_u + 0.015y + 5.754) \\ f(-2.109D + 0.043L - 0.298d + 0.002p_u - 0.283c_u + 0.004y + 0.933) \\ f(1.603D + 0.001L + 0.172d - 0.006p_u + 0.017c_u + 0.001y - 4.687) \end{bmatrix} \tag{14}$$

$$\begin{aligned} \hat{Y}_{p.k} &= [p_p] \\ &= \left[1.186 + \left(1 - \frac{2}{e^{2(1.5442n_1^1 + 2.175n_2^1 + 1.0083n_3^1 - 3.0477n_4^1 + 2.7265n_5^1 - 0.027)} + 1}\right) \times 577.443\right] \end{aligned} \tag{15}$$

where subscript p denotes predicted values from the neural network, contrasting with subscript m for measured data. f(x) represents the activation function.

For sand soils, the optimal weights and biases are derived as:

$$w_{01} = \begin{bmatrix} -0.736 & 0.744 & -1.277 & -0.114 & 0.543 & -1.756 \\ -0.469 & -1.337 & 1.254 & 0.092 & 0.574 & 1.524 \\ -2.774 & 1.539 & -2.097 & -0.011 & 1.499 & -2.119 \\ 0.777 & -1.179 & -1.835 & 0.729 & 0.485 & -0.239 \end{bmatrix}$$
$$w_{12} = \begin{bmatrix} 2.6457 & 3.3194 & -2.3985 & -2.2238 \end{bmatrix} \tag{16}$$

$$B_{01} = \begin{bmatrix} -0.296 \\ 1.4104 \\ -0.098 \\ 1.6015 \end{bmatrix}, B_{12} = [-1.1929] \tag{17}$$

As illustrated in Figure 8, the neural network demonstrates outstanding predictive performance. For the clay p-y curve model, both the training and testing phases exhibited strong convergence ($R^2 \geq 0.95$). The neural network model for sand p-y curves demonstrated robust correlation with experimental data, achieving a test set R^2 = 0.96. This statistical validated confirms the model's high predictive accuracy and reliability for both sandy soils and clayey soils.

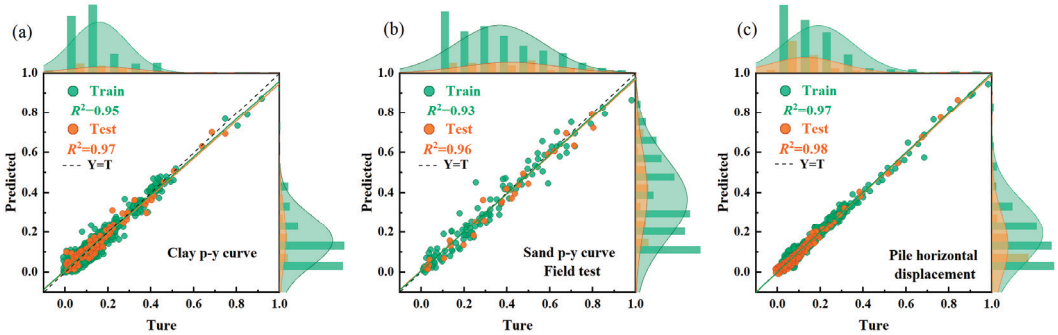

Figure 8. (**a**) Regression performance for Clay p-y curve prediction, (**b**) Regression performance for Sand p-y curve prediction, (**c**) Regression performance for Pile horizontal displacement prediction.

4.2. Pile Horizontal Displacement Prediction

The data were randomly extracted from the pile horizontal displacement database to construct an ANN-based model for predicting pile horizontal displacement. The structural parameters of the model are presented in Table 2. The input parameters include pile horizontal load (F), pile length (L), pile diameter (D), penetration depth (d), distance from the test point to the pile top (l), soil elastic modulus (E), internal friction angle (φ), and cohesion (c), with the pile horizontal displacement serving as the output parameter. Given the strong correlation between t and D as well as L, and considering that the research focus lies on the global horizontal displacement of the pile rather than its internal deformation characteristics, the input parameters of the model excluded the pile t.

For the constructed ANN model of pile horizontal displacement, the optimal values of parameters W_{01}, W_{12}, and B_{01}, B_{12} are determined.

$$w_{01} = \begin{bmatrix} -1.518 & 2.242 & 0.759 & -3.152 & 1.626 & 0.665 & -1.335 & -1.246 \\ 2.355 & -2.595 & -1.125 & 2.166 & 0.388 & -0.646 & -0.078 & 0.094 \\ 0.398 & 0.951 & -0.331 & -0.796 & -0.493 & 1.546 & 0.562 & -0.0402 \\ 0.299 & 1.628 & 3.163 & 0.779 & 0.238 & 2.878 & -4.888 & -1.2601 \\ 3.443 & 1.513 & 1.561 & -0.172 & -0.627 & 3.138 & 2.378 & -0.342 \end{bmatrix}$$
$$w_{12} = \begin{bmatrix} -1.9394 & 1.6094 & 2.5132 & 1.3983 & 3.1218 \end{bmatrix} \quad (18)$$

$$B_{01} = \begin{bmatrix} -1.2761 \\ 1.8069 \\ 1.1858 \\ 3.4579 \\ -3.103 \end{bmatrix}, B_{12} = [-0.91565] \quad (19)$$

The training and testing performance metrics of the model are systematically presented in Table 2 and Figure 8. The ANN framework demonstrated robust convergence characteristics, achieving exceptional agreement between predicted and observed displacements in the training dataset (R^2 =0.97). During validation and testing phases, the model maintained superior predictive capability with $R^2 > 0.96$ for both phases, confirming its reliability in horizontal displacement prediction across diverse geotechnical scenarios.

5. Discussion

5.1. Model Performance

To rigorously evaluate the performance of the neural network model, the model factor (λ) is used to evaluate the accuracy of the model:

$$\lambda_p = \frac{p_m}{p_p} \quad (20)$$

$$\lambda_y = \frac{y_m}{y_p} \quad (21)$$

where P_{m} and y_{m} denote measured soil resistance and displacement, respectively, while P_{p} and y_{p} represent predicted soil resistance and displacement, respectively.

Figure 9 presents the predicted p-y curves obtained from the neural network model and the API specification. It can be observed that the predictions from the neural network model closely align with the measured values along the 1:1 diagonal line, demonstrating a high degree of consistency. Only when the soil resistance is relatively low (less than 50 kN/m) do the data points exhibit some dispersion. In contrast, the values calculated

using the API specification show significant deviations from the actual measurements, underestimating clay resistance by approximately 50% and overestimating sand resistance by about 30%, with a greater degree of data scatter.

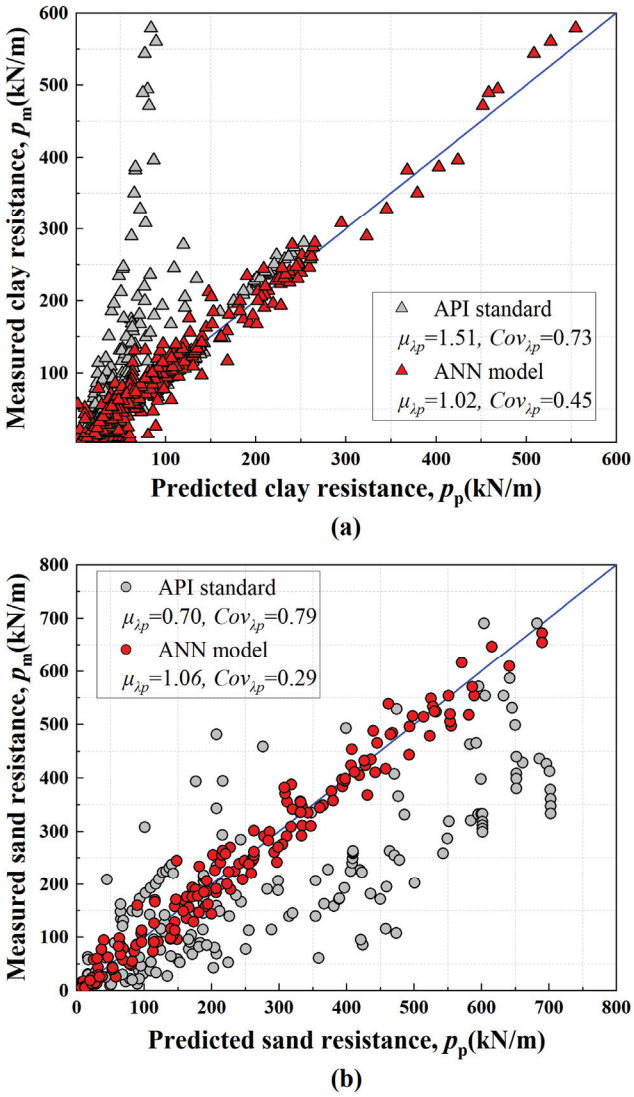

Figure 9. Comparison of predicted and measured soil resistance for clay and sand using the ANN model and API standard. (**a**) Clay resistance, (**b**) sand resistance.

For the clay p-y curves, the model factor λ of the neural network model has a mean value $\mu_{\lambda p}$ = 1.02 and a coefficient of variation COV_λ = 0.45. Compared to the clay p-y curves predicted by the API specification (μ_λ = 1.51, COV_λ = 0.73), the mean model factor of the neural network model is closer to 1. Similarly, for the sand p-y curves, the neural network model yields a mean model factor μ_λ = 1.06 with a coefficient of variation COV_λ = 0.29. In comparison, the API specification predicts a mean model factor of μ_λ =0.70 and COV_λ =0.79 for sand p-y curves.

These results demonstrate that the neural network model provides more accurate predictions, with average errors ranging from only 2% to 6%. According to the model accuracy classification [82], the variability in the prediction accuracy of the neural network model is classified as moderate to low. Overall, the soil resistance values computed by the neural network model, utilizing the selected input parameters and hidden nodes, effectively reflect the actual soil resistance behavior.

The measured data from field tests on the horizontal bearing capacity of offshore wind turbine pile foundations were input into the trained neural network model to obtain predicted values of horizontal displacement. These predicted values were then compared with the actual measured horizontal displacements, as illustrated in Figure 10. Observing the distribution of the data points, it is evident that the predictions from the neural network model are predominantly concentrated near the line along the 1:1 reference line, indicating low data dispersion. Specifically, the mean value of the model factor is $\mu_\lambda = 0.9$, with a coefficient of variation $COV_\lambda = 0.26$.

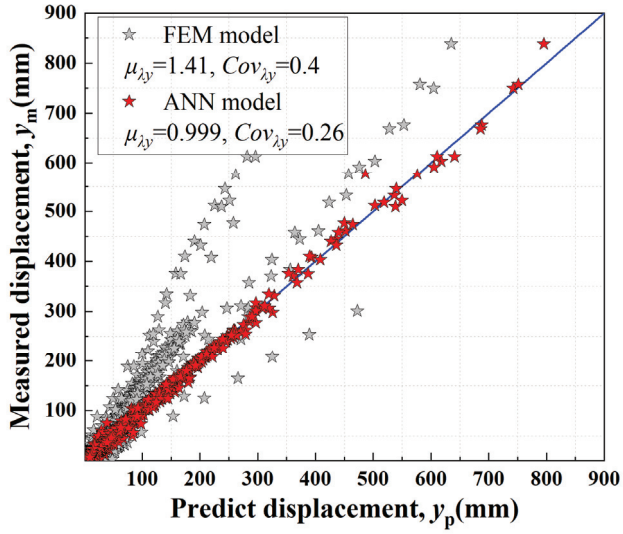

Figure 10. Comparison of horizontal displacement predictions from ANN model and FEM model with measured data.

To achieve a more rigorous comparative analysis, a finite element model (FEM) was utilized to predict the horizontal displacement of offshore wind turbine monopile foundations. For conciseness, the detailed description of the FEM is omitted here; the specific methodologies and parameters can be found in the work of [38]. The FEM results exhibited considerable dispersion and lower predictive accuracy, significantly underestimating the horizontal displacement around the pile. Specifically, the average value of the μ_λ was 1.41 with $COV_\lambda = 0.4$. The deviation of this result is closely related to the establishment of the model and the selection of data, and it may be attributed to issues such as the mixed use of model data and on-site measured data. This clearly demonstrates that the neural network model offers significant advantages and higher accuracy in predicting the horizontal displacement of offshore monopile foundations.

5.2. Parameter Sensitivity

Table 3 presents the Spearman rank correlation coefficients between the model factor λ and each input parameter at a significance level of 0.05. For the clay p-y curve model, λ exhibited positive correlations with P_u, d/L, y/D, and D/L; however, these correlations were relatively modest, with coefficients (ρ) not exceeding 0.20. Conversely, λ demonstrated slight negative correlations with D and L.

For the sand p-y curve model, λ displayed more pronounced positive correlations with y/D and D/L, with ρ values of 0.191 and 0.201, respectively. Negative correlations were observed with φ, d/L, y/L, D, and L. Notably, the correlation coefficients for D and L fell below -0.2, indicating that pile diameter and pile length significantly influence the sand p-y curve behavior. From an engineering standpoint, the strong negative correlation

with pile diameter (D) implies that the accuracy of the sand p-y curve model is particularly sensitive to this parameter. This underscores the importance of precise pile diameter specification and manufacturing control in design and construction, as variations can lead to considerable deviations in the predicted soil–pile interaction. Similarly, the significant influence of pile length (L) highlights its critical role in the overall response, demanding careful optimization during the design process.

Table 3. Spearman's rank correlation test results.

Model	Parameters	Spearman's Rank	
		p	ρ
Clay p-y curve	(λ, P_u)	0.039	0.142
	(λ, d/L)	0.023	0.183
	(λ, y/D)	0.028	0.153
	(λ, y/L)	0.150	0.072
	(λ, D/L)	0.048	0.109
	(λ, D)	0.046	−0.106
	(λ, L)	0.037	−0.125
Sand p-y curve	(λ, φ)	0.031	−0.163
	(λ, d/L)	0.046	−0.147
	(λ, y/D)	0.029	0.191
	(λ, y/L)	0.023	−0.178
	(λ, t/D)	0.068	−0.032
	(λ, D/L)	0.010	0.201
	(λ, D)	0.000	−0.401
	(λ, L)	0.000	−0.272
Pile horizontal displacement	(λ, φ)	0.000	−0.191
	(λ, F)	0.000	0.219
	(λ, E)	0.000	−0.241
	(λ, l/L)	0.001	0.106
	(λ, t/D)	0.001	−0.111
	(λ, D/L)	0.003	−0.093
	(λ, D)	0.000	0.158
	(λ, L)	0.000	−0.338

In the pile horizontal displacement model, F, l/L, and D exhibited positive correlations with λ. Negative correlations were identified with φ, E, t/D, D/L, and L. Particularly, parameters E and L had ρ values less than -0.2, suggesting that both the design parameters of the pile and the stiffness of the soil are significant factors affecting its horizontal displacement. The engineering significance of the strong negative correlation with soil modulus (E) is substantial; it emphasizes that accurate determination of soil stiffness through thorough geotechnical investigation is paramount for reliable predictions of horizontal pile displacement. Even minor uncertainties or variations in E can disproportionately affect the model's output, potentially impacting the safety and serviceability of the pile foundation. Likewise, the pile length (L), a fundamental design choice, also demonstrates a strong influence, reinforcing the need for its careful selection based on site conditions and load demands.

5.3. Probability Distribution

In reliability-based geotechnical design, the probability distribution of the λ, in addition to its μ_λ and COV_λ, constitutes a critical consideration. Kolmogorov–Smirnov (K–S) normality tests were performed on both the λ and its natural logarithm $\ln(\lambda)$, revealing that the model factors generated by the neural network deviated significantly from normal or

log-normal distributions. Further goodness-of-fit tests, including the corrected K-S test and Anderson–Darling (A-D) test, demonstrated that the model factor also failed to conform to Weibull, exponential, or gamma distributions.

To characterize the distribution pattern of the λ, a second-order Gaussian function was employed; this approach proves particularly effective in capturing the highly nonlinear distribution characteristics of model factors [83]. Figure 11 illustrates the fitting results, while Table 4 details the mathematical expression of the second-order Gaussian function and its optimized parameters. The coefficient of determination values approaching unity across all three investigated scenarios confirm the rationality and efficacy of utilizing Gaussian functions to model the distribution trends of the model factor λ.

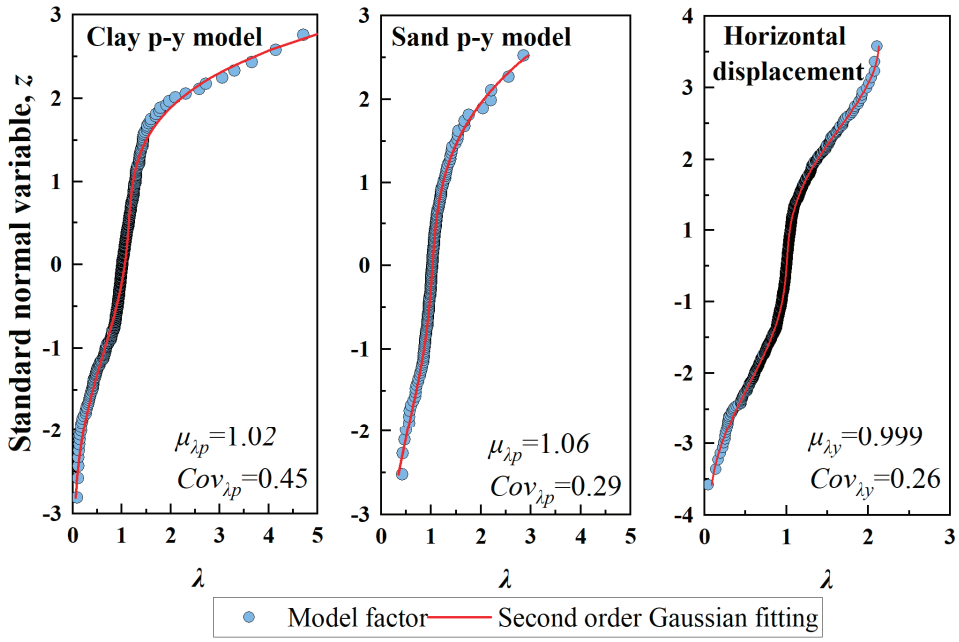

Figure 11. Probability distribution of ANN model factors.

Table 4. Gaussian fitting expression and parameters.

Model	Equation	Parameter	Value	R^2
Clay p-y curve	$\sum_{k=1}^{k=2} a_k \exp\left[-\left(\frac{z-b_k}{c_k}\right)^2\right]$	a_1	790.2102	0.97
		b_1	11.5655	
		c_1	3.90184	
		a_2	0.94124	
		b_2	0.08995	
		c_2	1.71666	
Sand p-y curve		a_1	0.75607	0.99
		b_1	−0.617	
		c_1	2.0571	
		a_2	169.8418	
		b_2	13.26167	
		c_2	5.31597	
Pile horizontal displacement		a_1	2.12399	0.99
		b_1	3.15144	
		c_1	2.16728	
		a_2	0.82494	
		b_2	−0.5293	
		c_2	1.68297	

To provide a more intuitive comparison of the accuracy among different predictive models, the μ_λ and the COV_λ for each model are summarized in Table 5. A comparative analysis reveals that the artificial neural network (ANN) model exhibits significant advantages in predictive accuracy over the API specification and the finite element model. Specifically, the average model factor of the ANN model is significantly closer to 1, and the relatively low coefficient of variation further validates the remarkable stability and reliability of the ANN model during the prediction process. In stark contrast, the FEM and the API approach, in practical applications, highly rely on precise parameter settings and simplified assumptions. When faced with complex and variable actual working conditions, it is difficult to comprehensively capture the subtle differences in the real environment, resulting in a significant reduction in the stability and reliability of their prediction results.

Table 5. The degree of dispersion and accuracy of the prediction methods of API, ANN, and FEM.

Model	μ_λ	COV_λ
API standard clay p-y curve	1.51	0.73
API standard sand p-y curve	0.70	0.79
ANN clay p-y curve	1.02	0.45
ANN sand p-y curve	1.06	0.29
FEM horizontal displacement	1.41	0.40
ANN horizontal displacement	0.99	0.26

5.4. Case Application

To further investigate the neural network model's performance, a case study was conducted using a monopile foundation from [84] work. It is critical to emphasize that the monopile analyzed here was excluded from the dataset used for prior model development and validation. The steel pipe pile has a length of 71.5 m, diameter of 2.0 m, and wall thickness of 30 mm. The surrounding soil strata consist of fine sand, silty sand, and clayey silt, with geotechnical properties detailed in Table 6.

Table 6. Design parameters for the example monopile.

Soil	Soil Thickness (m)	Elasticity Modulus (MPa)	Poisson Ratio	Cohesion (kPa)	Friction Angle (°)	Unit Weight (kN/m^3)
Sedimentary	11.1	18.0	0.3	15.5	16.5	18.4
Alluvial	25.7	20.1	0.3	15.0	17.0	18.8
Fine sand	13.9	36.0	0.2	8.0	33.4	19.5
Silt	20.7	30.3	0.2	24.6	30.5	19.0
Clay	14.5	18.5	0.3	26.2	18.3	20.0

Lateral displacement predictions along the pile depth were generated using both FEM and ANN models. As demonstrated in Figure 12, under five distinct loading scenarios, the FEM model consistently underestimated displacements, particularly in the supralittoral zone (above the mudline). This systematic bias correlates with the model accuracy evaluation outcomes, where the $\mu_\lambda > 1$ (refer to Figure 10). Such underestimation could lead to non-conservative design outcomes in engineering practice, potentially increasing operational risks for monopile foundations. Conversely, the ANN model predictions exhibit significantly better alignment with field monitoring data.

Progressive refinement of the ANN model is achievable through continuous accumulation of field measurements, involving both architectural optimization (e.g., hidden layer configuration) and parameter calibration (e.g., activation function tuning). This iterative process enhances predictive capability while reducing output variance, thereby enabling

more robust soil–pile interaction analysis for offshore foundation design. The ANN's superior predictive accuracy compared to conventional FEM methodologies underscores this study's contribution to advancing precision in geotechnical predictive modeling.

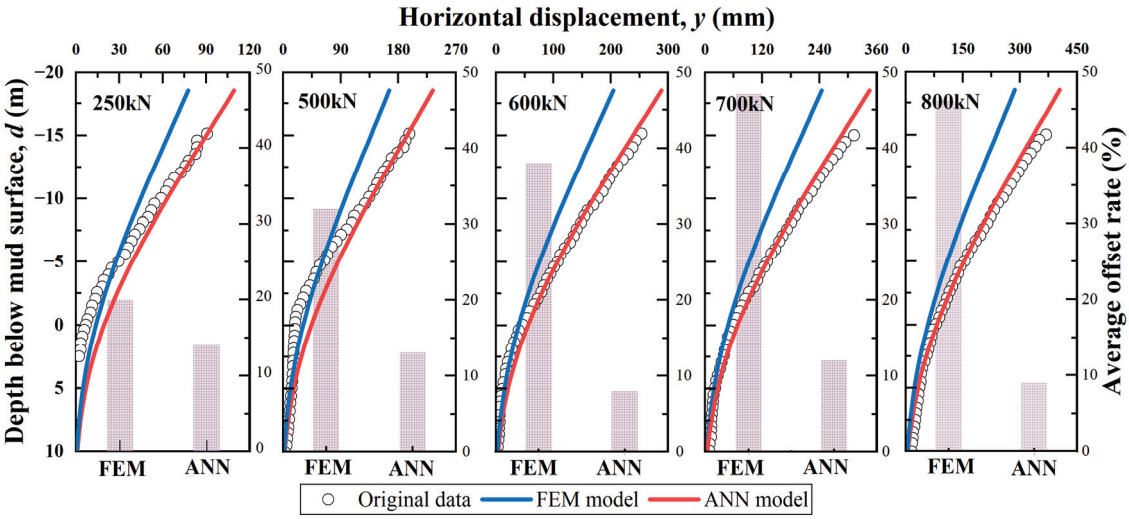

Figure 12. Predicted vs. measured horizontal displacement (ANN and FEM).

6. Conclusions

This study focuses on offshore wind turbine monopile foundations. By collecting data from literature sources, we established a marine pile–soil interaction database comprising 1852 datasets. Based on this database, predictive neural network models were developed for pile displacement and soil resistance around the pile, using pile design parameters, displacements, and soil strength parameters as input variables. The accuracy of these models was quantitatively evaluated, and their validity was verified. The main conclusions of this study are as follows:

(i) Artificial neural networks are established as p-y curve models for marine pile foundations in both clay and sand, as well as a predictive model for pile horizontal displacement. The developed pile–soil interaction ANN models exhibit nearly unbiased average accuracy, with an average error of less than 6%.

(ii) The cumulative distribution function of the model factor in the established neural network models can be approximated using a second-order Gaussian function. This simple expression can be directly applied to the reliability-based design of marine pile foundations.

(iii) Through analysis of practical cases and by comparing the finite element method with the neural network models developed in this study for predicting pile horizontal displacement, the superiority of the proposed ANN models in terms of computational accuracy and efficiency is highlighted.

Building upon the established model, subsequent research should prioritize the development of real-time data assimilation mechanisms for digital twin systems to achieve synchronized integration of monitoring data and numerical simulations, coupled with systematic expansion of engineering databases encompassing diverse marine geological conditions. The implementation of hybrid modeling frameworks that synergize 3D convolutional neural networks with physical principles is expected to significantly enhance predictive capabilities in pile–soil interaction analysis.

Author Contributions: Conceptualization, P.L.; methodology, P.L.; validation, K.L., X.Y. (Xiangwei Yu), T.L. and X.Y. (Xun Yuan); formal analysis, K.L. and X.Y. (Xiangwei Yu); data curation, H.L.;

writing—original draft preparation, P.L. and K.L.; writing—review and editing, P.L.; supervision, P.L.; funding acquisition, P.L. All authors have read and agreed to the published version of the manuscript.

Funding: This research was funded by the National Natural Science Foundation of China (Grant Nos. 52008408) and Natural Science Foundation of Guangdong Province (Grant Nos. 2021A1515012088). This financial support is gratefully acknowledged.

Data Availability Statement: Data are contained within the article.

Conflicts of Interest: The original contributions presented in this study are included in the article. Further inquiries can be directed to the corresponding author.

Abbreviations

The following abbreviations are used in this manuscript:

a_{k}	Activation of the k-th hidden neuron
A-D	Anderson–Darling
ANN	Artificial neural network
API	American Petroleum Institute
B_{01}	5×1 bias vector
B_{12}	Hidden-to-output layer bias vector
$\mathrm{b}_{\mathrm{k,t}}$	Bias vector of the layer
c	Cohesion
c_u	Shear strength
COV_λ	Coefficient of variation
d	Depth
D	Outer diameter
e	Residual vector
E	Elastic modulus
$f(x)$	Activation functions (logistic)
FEM	Finite element method
F	Horizontal force applied at the pile head
i	Total number of samples
I	Identity matrix
J	Jacobian matrix of partial derivatives
J^T	The transpose of the Jacobian matrix
K-S	Kolmogorov–Smirnov
l	Distance from the test point to the pile top
L	Pile length
L_{reg}	Regularized loss function
LM	Levenberg–Marquardt
m	Number of hidden nodes
MSE	Mean squared error
n	Input dimension
$n_{k,p}$	The p-th input to the k-th neuron
p_{u}	Ultimate resistance
P_{m}	Measured soil resistance
P_{p}	Predicted soil resistance
$\mathrm{N}_{\mathrm{max}}$	Maximum iteration threshold
N^0	Input vector
N^1	Output vector of the first hidden layer
p	Mobilized soil resistance
R^2	Coefficient of determination
SVM	Support vector machines

t	Wall thickness
$w_{k,p,t}$	Weight matrix of the layer
W_{01}	5×6 weight matrix
W_{12}	Hidden-to-output layer weight matrix
x	Raw data
x_{norm}	Normalized value
x_{max}	Maximum value
x_{min}	Minimum value
y	Lateral soil displacement
y_m	Measured displacement
y_p	Predicted displacement
$Y_{m,min}$	Normalized bound of measured input parameters
$Y_{m,max}$	Normalized bound of measured input parameters
$\hat{Y}_{p,k}$	Predicted value
$Y_{m,k}$	Actual value
z_k	Pre-activation of the k-th hidden neuron
$\Delta\mathcal{L}$	Change in validation loss
ΔW	Weight update vector
α	Hyperparameter optimized via cross-validation.
β	Hyperparameter optimized via cross-validation
φ	Internal friction angle
μ	Damping factor
η	Learning rate
γ	Soil's unit weight
λ	Model factor
μ_λ	Mean value
ε_k^2	Squared error
ε^2	Mean squared error
$\sum_i \omega_i^2$	Regularization penalty term

References

1. IEA. *Offshore Wind Outlook 2019*; IEA: Paris, France, 2019.
2. Hjelmeland, M.; Nøland, J.K. Correlation Challenges for North Sea Offshore Wind Power: A Norwegian Case Study. *Sci. Rep.* **2023**, *13*, 18670. [CrossRef] [PubMed]
3. Santhakumar, S.; Meerman, H.; Faaij, A.; Martinez Gordon, R.; Florentina Gusatu, L. The Future Role of Offshore Renewable Energy Technologies in the North Sea Energy System. *Energy Convers. Manag.* **2024**, *315*, 118775. [CrossRef]
4. Ponder, A.N.; Avdic, D.B. *Offshore Wind and Power-to-Hydrogen in the Baltic Sea Region*; BOWE2H Strategic Roadmap; IKEM: Berlin, Germany, 2024.
5. Ren, L.; Wang, Y.; Zhang, W.; Yang, H.; Wang, H.; Wei, J.; Mateos, L.M.F. Characterizing Wind Fields at Multiple Temporal Scales: A Case Study of the Adjacent Sea Area of Guangdong–Hong Kong–Macao Greater Bay Area. *Energy Rep.* **2022**, *8*, 212–223. [CrossRef]
6. Sun, Y. Experimental and Numerical Studies on a Laterally Loaded Monopile Foundation of Offshore Wind Turbine. Ph.D. Thesis, Zhejiang University, Hangzhou, China, 2016.
7. Zhang, J.; Wang, H. Development of Offshore Wind Power and Foundation Technology for Offshore Wind Turbines in China. *Ocean Eng.* **2022**, *266*, 113256. [CrossRef]
8. Buljac, A.; Kozmar, H.; Yang, W.; Kareem, A. Concurrent Wind, Wave and Current Loads on a Monopile-Supported Offshore Wind Turbine. *Eng. Struct.* **2022**, *255*, 113950. [CrossRef]
9. Yang, Y.F.; Zheng, Y.Q.; Ge, H.; Wang, C.Z. Nonlinear Interactions between Solitary Waves and Structures in a Steady Current. *Ocean Eng.* **2023**, *274*, 113920. [CrossRef]
10. Yu, Y.; Chen, X.; Guo, Z.; Zhang, J.; Lü, Q. Robust Design of Monopiles for Offshore Wind Turbines Considering Uncertainties in Dynamic Loads and Soil Parameters. *Ocean Eng.* **2022**, *266*, 112822. [CrossRef]
11. Qi, W.; Gao, F. Equilibrium Scour Depth at Offshore Monopile Foundation in Combined Waves and Current. *Sci. China Technol. Sci.* **2014**, *57*, 1030–1039. [CrossRef]

12. Gupta, B.K. Soil-Structure Interaction Analysis of Monopile Foundations Supporting Offshore Wind Turbines. Ph.D. Thesis, University of Waterloo, Waterloo, ON, Canada, 2018.
13. Poulos, H.G. Pile Behaviour—Theory and Application. *Géotechnique* **1989**, *39*, 365–415. [CrossRef]
14. Hansen, N.M. *Interaction Between Seabed Soil and Offshore Wind Turbine Foundations*; DCAMM Special Report; DTU Mechanical Engineering: Lyngby, Denmark, 2012; ISBN 9788790416805.
15. Zhu, B.; Wen, K.; Li, T.; Wang, L.; Kong, D. Experimental Study on Lateral Pile–Soil Interaction of Offshore Tetrapod Piled Jacket Foundations in Sand. *Can. Geotech. J.* **2019**, *56*, 1680–1689. [CrossRef]
16. Sheil, B.B.; McCabe, B.A. An Analytical Approach for the Prediction of Single Pile and Pile Group Behaviour in Clay. *Comput. Geotech.* **2016**, *75*, 145–158. [CrossRef]
17. Shi, S.; Zhai, E.; Xu, C.; Iqbal, K.; Sun, Y.; Wang, S. Influence of Pile-Soil Interaction on Dynamic Properties and Response of Offshore Wind Turbine with Monopile Foundation in Sand Site. *Appl. Ocean Res.* **2022**, *126*, 103279. [CrossRef]
18. Tang, H.; Yue, M.; Yan, Y.; Li, Z.; Li, C.; Niu, K. Influence of Soil–Structure Interaction Models on the Dynamic Responses of An Offshore Wind Turbine Under Environmental Loads. *China Ocean Eng.* **2023**, *37*, 218–231. [CrossRef]
19. Chow, Y.K.; Kencana, E.Y.; Leung, C.F.; Purwana, O.A. Spudcan-Pile Interaction in Thick Soft Clay and Soft Clay Overlying Sand: A Simplified Numerical Solution. *Appl. Ocean Res.* **2021**, *112*, 102684. [CrossRef]
20. Lin, Z.; Jiang, Y.; Xiong, Y.; Xu, C.; Guo, Y.; Wang, C.; Fang, T. Analytical Solution for Displacement-Dependent Active Earth Pressure Considering the Stiffness of Cantilever Retaining Structure in Cohesionless Soil. *Comput. Geotech.* **2024**, *170*, 106258. [CrossRef]
21. Randolph, M.F. The Response of Flexible Piles to Lateral Loading. *Géotechnique* **1981**, *31*, 247–259. [CrossRef]
22. Heidari, M.; Hesham El Naggar, M. Analytical Approach for Seismic Performance of Extended Pile-Shafts. *J. Bridge Eng.* **2018**, *23*, 04018069. [CrossRef]
23. American Petroleum Institute. *Planning, Designing, and Constructing Fixed Offshore Platforms: Working Stress Design*; API: Washington, DC, USA, 2020.
24. *DET NORSKE VERITAS DNVGL-ST-N001*; Marine Operations and Marine Warranty; DNV GL: Oslo, Norway, 2016.
25. MOT China Communications Press. *JTS 167-2018: Code for Design of Pile Foundations in Port and Waterway Engineering*; China Communications Press: Beijing, China, 2022.
26. Liu, P.; Jiang, C. A Modified P-y Curve Model for Offshore Piles near Sandy Slopes Considering the Soil-Pile-Slope Deformation Mechanism. *Mar. Struct.* **2024**, *98*, 103675. [CrossRef]
27. Stevens, J.B.; Audibert, J.M.E. Re-Examination Of P-Y Curve Formulations. In Proceedings of the Offshore Technology Conference, Houston, TX, USA, 30 April–3 May 1979.
28. Wang, H.; Wang, L.Z.; Hong, Y.; He, B.; Zhu, R.H. Quantifying the Influence of Pile Diameter on the Load Transfer Curves of Laterally Loaded Monopile in Sand. *Appl. Ocean Res.* **2020**, *101*, 102196. [CrossRef]
29. White, D.J.; Doherty, J.P.; Guevara, M.; Watson, P.G. A Cyclic P-y Model for the Whole-Life Response of Piles in Soft Clay. *Comput. Geotech.* **2022**, *141*, 104519. [CrossRef]
30. Lin, P.; Zhong, X.; Guo, C.; Yang, F.; Wang, F. Statistical Evaluation of Jacking-Installation Resistance Models for Suction Foundation of Offshore Wind Turbines in Sands. *Ocean Eng.* **2023**, *279*, 114605. [CrossRef]
31. Yeter, B.; Garbatov, Y.; Guedes Soares, C. Uncertainty Analysis of Soil-Pile Interactions of Monopile Offshore Wind Turbine Support Structures. *Appl. Ocean Res.* **2019**, *82*, 74–88. [CrossRef]
32. Byrne, B.W.; Houlsby, G.T.; Burd, H.J.; Gavin, K.G.; Igoe, D.J.P.; Jardine, R.J.; Martin, C.M.; McAdam, R.A.; Potts, D.M.; Taborda, D.M.G.; et al. PISA Design Model for Monopiles for Offshore Wind Turbines: Application to a Stiff Glacial Clay Till. *Géotechnique* **2020**, *70*, 1030–1047. [CrossRef]
33. Haiderali, A.; Madabhushi, G. Three-Dimensional Finite Element Modelling of Monopiles for Offshore Wind Turbines. In Proceedings of the Advances in Civil, Environmental, and Materials Research, Seoul, Republic of Korea, 26–29 August 2012.
34. McAdam, R.A.; Byrne, B.W.; Houlsby, G.T.; Beuckelaers, W.J.A.P.; Burd, H.J.; Gavin, K.G.; Igoe, D.J.P.; Jardine, R.J.; Martin, C.M.; Muir Wood, A.; et al. Monotonic Laterally Loaded Pile Testing in a Dense Marine Sand at Dunkirk. *Géotechnique* **2020**, *70*, 986–998. [CrossRef]
35. Xiao-ling, Z.; Rui, Z.; Yan, H. Study on P-y Curve of Large Diameter Pile under Long-Term Cyclic Loading. *Appl. Ocean Res.* **2023**, *140*, 103736. [CrossRef]
36. Sheil, B.; Finnegan, W. Numerical Simulations of Wave–Structure–Soil Interaction of Offshore Monopiles. *Int. J. Geomech.* **2017**, *17*, 04016024. [CrossRef]
37. Brinkgreve, R.B.; Bürg, M.; Andreykiv, A.; Lim, L. *Beyond the Finite Element Method in Geotechnical Analysis*; Bundesanstalt für Wasserbau: Karlsruhe, Germany, 2015; Volume 98, pp. 91–102.

38. Lin, P.; Ding, M.; Liu, H.; Liu, Y.; Wang, K. Statistical Accuracy of Finite Element Method in Predicting Horizontal Displacement of Monopiles for Offshore Wind Turbines. *Mar. Struct.* **2024**, *97*, 103641. [CrossRef]
39. Murphy, G.; Igoe, D.; Doherty, P.; Gavin, K. 3D FEM Approach for Laterally Loaded Monopile Design. *Comput. Geotech.* **2018**, *100*, 76–83. [CrossRef]
40. Wang, S.; Han, B.; Jiang, J.; Telyatnikova, N. Machine Learning and FEM-Driven Analysis and Optimization of Deep Foundation Pits in Coastal Area: A Case Study in Fuzhou Soft Ground. *Undergr. Space* **2025**, *22*, 55–76. [CrossRef]
41. Baghbani, A.; Choudhury, T.; Costa, S.; Reiner, J. Application of Artificial Intelligence in Geotechnical Engineering: A State-of-the-Art Review. *Earth-Sci. Rev.* **2022**, *228*, 103991. [CrossRef]
42. Lin, P.; Zhao, C.; Zhang, W.; Xue, Y. *Machine Learning Methods and Applications in Geotechnical Engineering*; China Architecture & Building Press: Beijing, China, 2023.
43. Vahab, M.; Shahbodagh, B.; Haghighat, E.; Khalili, N. Application of Physics-Informed Neural Networks for Forward and Inverse Analysis of Pile–Soil Interaction. *Int. J. Solids Struct.* **2023**, *277–278*, 112319. [CrossRef]
44. Zhang, W.; Li, H.; Li, Y.; Liu, H.; Chen, Y.; Ding, X. Application of Deep Learning Algorithms in Geotechnical Engineering: A Short Critical Review. *Artif. Intell. Rev.* **2021**, *54*, 5633–5673. [CrossRef]
45. Cui, C.; Zhang, S.; Chapman, D.; Meng, K. Dynamic Impedance of a Floating Pile Embedded in Poro-Visco-Elastic Soils Subjected to Vertical Harmonic Loads. *Geomech. Eng.* **2018**, *15*, 793–803. [CrossRef]
46. Dong, Y.; Cui, L.; Zhang, X. Multiple-GPU Parallelization of Three-dimensional Material Point Method Based on Single-root Complex. *Int. J. Numer. Methods Eng.* **2022**, *123*, 1481–1504. [CrossRef]
47. Cui, C.; Zhang, S.; Yang, G.; Li, X. Vertical Vibration of a Floating Pile in a Saturated Viscoelastic Soil Layer Overlaying Bedrock. *J. Cent. South Univ.* **2016**, *23*, 220–232. [CrossRef]
48. Zhang, Y.; Zhong, W.; Li, Y.; Wen, L.; Sun, X. ResGRU: A Deep Learning Approach for Settlement Prediction in CFRD Based on the Spatiotemporal Feature Fusion Method. *Comput. Geotech.* **2024**, *173*, 106518. [CrossRef]
49. Wang, W.; Yan, J.; Liu, J.P. Study on p-y Models for Large-Diameter Pile Foundation Based on In-Situ Tests of Offshore Wind Power. *Chin. J. Geotech. Eng.* **2021**, *43*, 1131–1138. [CrossRef]
50. Hu, Z.; Zhai, E.; Luo, L.; Yang, X. Study of P-y Curves of Large-Monopiles for Offshore Wind Power in Sand. *Acta Energiae Solaris Sin.* **2019**, *40*, 3571–3577.
51. Wu, R.; Ye, J.; Luo, G.; Shen, X.; Zhang, Q. Experimental Study on the Bearing Characteristics of Steel Pipe Pile in Radial Sandbar of Jiangsu Province. *Ocean Eng.* **2021**, *39*, 121–132. [CrossRef]
52. Luo, L.; Wang, Y.; Zhai, E.; Hu, Z.; Yang, X.; Li, Q. Study on P-y Curves of Monopile in Layered Soil Based on Field Test. *Acta Energiae Solaris Sin.* **2019**, *40*, 3258–3264.
53. Kim, Y.; Jeong, S.; Won, J. Effect of Lateral Rigidity of Offshore Piles Using Proposed P-y Curves in Marine Clay. *Mar. Georesources Geotechnol.* **2009**, *27*, 53–77. [CrossRef]
54. Zhang, Y. Study on Horizontal Load Test of Large-Diameter Steel Pipe Piles for Offshore Wind Power. *Energy Environ.* **2022**, *175*, 18–20. [CrossRef]
55. Gong, W.; Huo, S.; Yang, C.; Huang, X.; Guo, C. Experimental Study on Horizontal Bearing Capacity of Large Diameter Steel Pipe Pile for Offshore Wind Farm. *J. Hydraul. Eng.* **2015**, *46*, 34–39. [CrossRef]
56. Bao, J.; Su, J.; Wu, F. Field Horizontal Loading Test and P-y Curve Applicability of Large-Diameter Single Pile Foundation in Deep Soft Clay Groundsill. *J. Hohai Univ. (Nat. Sci.)* **2023**, *51*, 127–134. [CrossRef]
57. Liu, J.; Zhang, F.; Dai, G. Research on P-y Curve of Pile Foundation in Clay Based on Cpt Data. *Acta Energiae Solaris Sin.* **2023**, *44*, 172–180. [CrossRef]
58. Zhu, B.; Zhu, Z.; Li, T.; Liu, J.; Liu, Y. Field Tests of Offshore Driven Piles Subjected to Lateral Monotonic and Cyclic Loads in Soft Clay. *J. Waterw. Port. Coast. Ocean Eng.* **2017**, *143*, 05017003. [CrossRef]
59. Cai, W.; Ye, J. Experimental Investigation of Large Diameter Pipe Piles Under Vertical and Lateral Load in Ocean Engineering. *Shanghai Land Resour.* **2011**, *32*, 81–86. [CrossRef]
60. Zhu, Z.; Gong, W.; DAI, G. Field Test Research of Horizontal Bearing Capacity of Large Diameter Steel Pipe Pile. *Build. Sci.* **2010**, *26*, 32–36. [CrossRef]
61. Wang, Q.; Wang, S.; Wu, F. Research on Horizontal Load Testing of Large-Diameter Steel Pipe Piles. *Ocean Dev. Manag.* **2018**, *35*, 9–13. [CrossRef]
62. Bi, M.; Liu, D.; Wang, H. Calculation Method Study for the Horizontal Bearing Capacity of Offshore Wind Turbine Steel-Pile. *South. Energy Constr.* **2018**, *5*, 77–82. [CrossRef]
63. Lao, W.; Zhou, L.; Wang, Z. Field Test and Theoretical Analysis on Flexible Large-Diameter Rock-Socketed Steel Pipe Piles Under Lateral Load. *Chin. J. Rock. Mech. Eng.* **2004**, *23*, 1770–1777. [CrossRef]

64. Choo, Y.W.; Kim, D. Experimental Development of the P-y Relationship for Large-Diameter Offshore Monopiles in Sands: Centrifuge Tests. *J. Geotech. Geoenviron. Eng.* **2016**, *142*, 04015058. [CrossRef]
65. Wang, T.; Wang, T. Experimental Research on Silt P-Y Curves. *Rock. Soil. Mech.* **2009**, *30*, 1343–1346. [CrossRef]
66. Liu, H.; Zhang, D.; Lv, X. Model Tests on Lateral Bearing Capacity of Single Piles Under Cyclic Load Saturated Silt. *Period. Ocean Univ. China* **2015**, *45*, 76–82. [CrossRef]
67. Lin, H.; Ni, L.; Suleiman, M.T.; Raich, A. Interaction between Laterally Loaded Pile and Surrounding Soil. *J. Geotech. Geoenviron. Eng.* **2015**, *141*, 04014119. [CrossRef]
68. Zhu, B.; Zhu, R.; Chen, R.; Kong, L.; Luo, J. Model Tests on Characteristics of Ocean and Offshore Elevated Piles with Large Lateral Deflection. *Chin. J. Geotech. Eng.* **2010**, *32*, 521–530.
69. Wu, T.; Lu, Z.; Dou, D.; Wu, Q. Model Tests and Finite Element Analysis of Behaviors of Ocean and Offshore Elevated Piles under Lateral Load. *Sci. Technol. Eng.* **2013**, *13*, 7697–7702.
70. Zhu, B.; Chen, R.-P.; Guo, J.; Kong, L.; Chen, Y. Large-Scale Modeling and Theoretical Investigation of Lateral Collisions on Elevated Piles. *J. Geotech. Geoenviron. Eng.* **2012**, *138*, 461–471. [CrossRef]
71. Li, W.; Zhu, B.; Yang, M. Static Response of Monopile to Lateral Load in Overconsolidated Dense Sand. *J. Geotech. Geoenviron. Eng.* **2017**, *143*, 04017026. [CrossRef]
72. Yu, J.; Zhu, J.; Kanmin, S.; Huang, M.; Leung, C.; Tan, Q. Bounding-Surface-Based p-y Model for Laterally Loaded Piles in Undrained Clay. *Ocean Eng.* **2020**, *216*, 107997. [CrossRef]
73. Wood, D.M. *Geotechnical Modelling*; CRC Press: London, UK, 2017; ISBN 9781315273556.
74. Arany, L.; Bhattacharya, S.; Macdonald, J.; Hogan, S.J. Design of Monopiles for Offshore Wind Turbines in 10 Steps. *Soil Dyn. Earthq. Eng.* **2017**, *92*, 126–152. [CrossRef]
75. Kolmogorov, A.N. On the Representation of Continuous Functions of Many Variables by Superposition of Continuous Functions of One Variable and Addition. *Russ. Acad. Sci.* **1957**, *114*, 953–956.
76. Hsein Juang, C.; Lu, P.C.; Chen, C.J. Predicting Geotechnical Parameters of Sands from CPT Measurements Using Neural Networks. *Comput.-Aided Civ. Infrastruct. Eng.* **2002**, *17*, 31–42. [CrossRef]
77. Liu, C.; Macedo, J.; Rodríguez, A. Leveraging Physics-Informed Neural Networks in Geotechnical Earthquake Engineering: An Assessment on Seismic Site Response Analyses. *Comput. Geotech.* **2025**, *182*, 107137. [CrossRef]
78. Zhang, W.; Gu, X.; Hong, L.; Han, L.; Wang, L. Comprehensive Review of Machine Learning in Geotechnical Reliability Analysis: Algorithms, Applications and Further Challenges. *Appl. Soft Comput.* **2023**, *136*, 110066. [CrossRef]
79. Anglade, E.; Aubert, J.-E.; Sellier, A.; Papon, A. Physical and Mechanical Properties of Clay–Sand Mixes to Assess the Performance of Earth Construction Materials. *J. Build. Eng.* **2022**, *51*, 104229. [CrossRef]
80. Ouendi, F.; Zentar, R. Investigating the Influence of Particle Size Ranges on the Physical, Mineralogical, and Environmental Properties of Raw Marine Sediment. *Constr. Build. Mater.* **2023**, *409*, 133987. [CrossRef]
81. Wan, J.-H.; Zaoui, A. Mechanical Resistance behind Fiber-Reinforced Polymer Pile: Role of Clay Minerals. *Comput. Geotech.* **2024**, *168*, 106158. [CrossRef]
82. Phoon, K.-K.; Tang, C. Characterisation of Geotechnical Model Uncertainty. *Georisk Assess. Manag. Risk Eng. Syst. Geohazards* **2019**, *13*, 101–130. [CrossRef]
83. Yuan, J.; Lin, P. Reliability Analysis of Soil Nail Internal Limit States Using Default FHWA Load and Resistance Models. *Mar. Georesour. Geotechnol.* **2019**, *37*, 783–800. [CrossRef]
84. Xu, D.; Xu, X.; Li, W.; Fatahi, B. Field Experiments on Laterally Loaded Piles for an Offshore Wind Farm. *Mar. Struct.* **2020**, *69*, 102684. [CrossRef]

MDPI AG
Grosspeteranlage 5
4052 Basel
Switzerland
Tel.: +41 61 683 77 34

Journal of Marine Science and Engineering Editorial Office
E-mail: jmse@mdpi.com
www.mdpi.com/journal/jmse

Academic Open
Access Publishing

mdpi.com

ISBN 978-3-7258-5642-8